2020

Novel Insights Into The Genetic And Environmental Determinants Of Enteric Nervous System Biology

Sabine Schneider
University of Pennsylvania

Novel Insights Into The Genetic And Environmental Determinants Of Enteric Nervous System Biology

Abstract

The enteric nervous system (ENS) is a complex network of neurons and glia that resides within the bowel wall. It rivals the spinal cord in complexity and regulates crucial bowel functions like gastrointestinal motility. Dysfunction of the ENS, also called enteric neuropathy, can cause growth failure, abdominal distention, and, in some individuals, sepsis and early death. Hirschsprung disease, a developmental enteric neuropathy where the ENS is missing from the distal bowel, can be treated with surgical removal of the affected bowel segment. However, debilitating bowel problems including dysmotility persist in a subset of patients. Treatment options of chronic intestinal pseudo-obstruction (CIPO) are even more limited and mostly symptomatic. In CIPO, the ENS develops along the length of the bowel, but bowel motility is compromised. Due to the dearth of options, the scientific community is actively trying to develop effective therapeutic options to improve enteric neuropathy-related symptoms. Bowel problems in CIPO and Hirschsprung disease post-surgery have been attributed to loss or dysfunction of subtypes of enteric neurons. Ideally, curative treatment would involve postnatal replacement of the defective ENS or supplementation of these missing ENS cell types. Recently developed in vitro differentiation protocols that convert human pluripotent stem cells into enteric neurons and glia have made stem cell therapy an enticing avenue to pursue. However, we still do not sufficiently understand the nuances of enteric neuron subtype fate decisions to direct differentiation of enteric neuron precursors into specific neuron subtypes. In chapter 2, I describe our work characterizing the differential expression of transcriptional regulators in enteric neuron subtypes during embryonic development and in the adult colonic ENS. We show that the transcription factor Tbx3 is required for the development of a normal complement of nitrergic neurons in the neonatal ENS. In chapter 3, I describe our work towards designing a high throughput screen that will allow us to determine whether transcriptional regulators affect differentiation into cholinergic versus nitrergic enteric neuron subtypes. In chapter 4, I describe exciting new work that indicates that postnatal treatment of distal colon lacking an enteric nervous system with the neurotrophic factor GDNF can re-grow a normal, functional ENS in mice. This discovery may lay the foundation for the development of adjunct, non-invasive therapeutic options for the treatment of Hirschsprung disease. Lastly, in chapter 5, I introduce work towards understanding the function of the epigenetic regulator Bap1 in enteric nervous system development and postnatal maintenance.

Degree Type

Dissertation

Degree Name

Doctor of Philosophy (PhD)

Graduate Group

Cell & Molecular Biology

First Advisor

Robert O. Heuckeroth

Keywords

Chronic Intestinal Pseudo-Obstruction, differentiation, enteric nervous system, enteric neuropathy, Hirschsprung Disease

NOVEL INSIGHTS INTO THE GENETIC AND ENVIRONMENTAL DETERMINANTS OF ENTERIC NERVOUS SYSTEM BIOLOGY

Sabine Schneider

A DISSERTATION

in

Cell and Molecular Biology

Presented to the Faculties of the University of Pennsylvania

in

Partial Fulfillment of the Requirements for the

Degree of Doctor of Philosophy

2020

Supervisor of Dissertation

_____

Dr. Robert O. Heuckeroth, M.D. Ph.D.

Professor of Pediatrics and Professor of Cell and Developmental Biology

Graduate Group Chairperson

_____

Dr. Thomas A. Jongens, PhD.

Program Chair of Genetics and Epigenetics, Associate Professor of Genetics

Dissertation Committee

Dr. Paul Gadue, PhD. Associate Professor of Pathology and Laboratory Medicine

Dr. Stewart A. Anderson, MD. Professor of Psychiatry

Dr. Christopher J. Lengner, PhD. Associate Professor of Biomedical Sciences

Dr. Gregory J. Bashaw, PhD. Professor of Neuroscience

NOVEL INSIGHTS INTO THE GENETIC AND ENVIRONMENTAL DETERMINANTS OF ENTERIC NERVOUS SYSTEM BIOLOGY

This thesis is dedicated to Rebecca and Elijah, the reason why this work matters.

ACKNOWLEDGEMENT

To start out, I would like to thank my thesis mentor Dr. Robert Heuckeroth. I am immensely grateful that I was able to work with you for the past 5 years. You have supported my varied research pursuits with enthusiasm and taught me how to be a scientist, but I am most grateful to have found a mentor that so genuinely cares about my well-being. Thank you for always looking out for my best interests throughout the craziness that is a PhD.

To my current and former Heuckeroth lab colleagues: Thank you for teaching me, collaborating with me, for listening to and improving my ideas, for helping me out when I once again planned and started too many experiments at once, and most of all, thank you for becoming my friends: Christina Wright, Jessica Anderson, Rebecca Bradley, Briana Christophers, Marina Avetisyan, Chris Pai, Rebecca Bradley, Rajarshi Sengupta, Silvia Huerta-López, Josh Eisenberg, Rachel Cerón, Tao Gao, Beth Maguire, Jenny Yan, Kahleb Graham, Deepika Kothakapa and lastly Amanda Lemke without whom the Heuckeroth lab would not be able to function.

I would also like to thank my thesis committee chair Dr Paul Gadue and my thesis committee members Dr. Stewart Anderson, Dr. Gregory Bashaw, and Dr. Christopher Lengner for their support at various points during the past 5 years and the many helpful suggestions and valuable critical input into my projects.

Maggie, Maureen, David, and Maura, you are incredible. Thank you for making a complicated educational path a surprisingly smooth experience and thank you for recognizing when I am was not doing well, even when I was not ready to admit it to myself.

I am grateful to the many core facilities at CHOP that have supported my work throughout my PhD – without your expertise and this work would not have been possible. I want to mention in particular the CHOP flow cytometry core (Florin Tuluc, Lily Wu, John Lora, and Jennifer Murray), the CHOP Stem cell core (from, Dr. Deborah French, Chintan Jobaliya, Alyssa Gagne, and Jean-Ann Maguire), and the CHOP DVR staff including the animal care technicians (Amanda, Angie, and

Jules) and veterinary technicians (Kay, Melanie, Samyra, Stephanie, Samantha, Maria, and Amber).

Dr. Carter, I will be forever thankful that you took me under your wing as a freshman at St. John's University and selflessly and whole-heartedly supported my transfer to MIT. Without your help, I may not have made it to where I am today.

Rolf, you laid the foundation upon which all my academic achievements have been built throughout the years. Thank you for teaching me about discipline and hard work and that there can be joy in working with focus towards a distant goal.

Rocky and Sanja, I will be forever grateful for your support and the joy you brought to my life.

Sara, thank you for being the best roommate I have ever had, for being my family in Philadelphia when I was all alone and my support network during the first 3 years of the MD-PhD program. I still cannot believe a friend like you actually exists in real life!

I also want to thank Yuliya, one of the most brilliant, caring, and loyal people I have ever met. I am so grateful that 2020 brought us closer together again.

Mama und Papa, thank you for always supporting me and setting me up for academic success by expecting me to excel even when the easiest path would have been to blend in. Thank you for allowing me to go to the US for my undergraduate studies and supporting me throughout my higher education even though the educational system and my choice of degree programs continues to be unfamiliar and confusing. Oma, thank you for loving and supporting me and teaching me how to be an independent, confident, strong woman. I miss you very much. Johannes, thank you for being my biggest fan and always cheering me on. Thank you for believing in me when I could not and for pushing me even when I was kicking and screaming. Barbara, thank you for always being there for me, reaching out and making sure I am ok, and amazing me every time we talk with the many extracurricular pursuits a single person can be passionate about while also being enrolled in a demanding PhD program.

Lastly, and most importantly, thank you from the bottom of my heart, Sohaib! I cannot imagine what this PhD would have looked like without you. You were by my side during the difficult and heart-wrenching parts of the PhD and you shared my joy when I could finally make out a dim light at the end of the dark tunnel that was the third year of the PhD. Thank you for being my friend and partner and for patiently listening to me, challenging me, supporting me, pushing me, and making my life more wonderful than I could have ever imagined.

ABSTRACT

NOVEL INSIGHTS INTO THE GENETIC AND ENVIRONMENTAL DETERMINANTS OF ENTERIC NERVOUS SYSTEM BIOLOGY

Sabine Schneider

Robert O. Heuckeroth

The enteric nervous system (ENS) is a complex network of neurons and glia that resides within the bowel wall. It rivals the spinal cord in complexity and regulates crucial bowel functions like gastrointestinal motility. Dysfunction of the ENS, also called enteric neuropathy, can cause growth failure, abdominal distention, and, in some individuals, sepsis and early death. Hirschsprung disease, a developmental enteric neuropathy where the ENS is missing from the distal bowel, can be treated with surgical removal of the affected bowel segment. However, debilitating bowel problems including dysmotility persist in a subset of patients. Treatment options of chronic intestinal pseudo-obstruction (CIPO) are even more limited and mostly symptomatic. In CIPO, the ENS develops along the length of the bowel, but bowel motility is compromised. Due to the dearth of options, the scientific community is actively trying to develop effective therapeutic options to improve enteric neuropathy-related symptoms. Bowel problems in CIPO and Hirschsprung disease post-surgery have been attributed to loss or dysfunction of subtypes of enteric neurons. Ideally, curative treatment would involve postnatal replacement of the defective ENS or supplementation of these missing ENS cell types. Recently developed *in vitro* differentiation protocols that convert human pluripotent stem cells into enteric neurons and glia have made stem cell therapy an enticing avenue to pursue. However, we still do not sufficiently understand the nuances of enteric neuron subtype fate decisions to direct differentiation of enteric neuron precursors into specific neuron subtypes. In chapter 2, I describe our work characterizing the differential expression of transcriptional regulators in enteric neuron subtypes during embryonic development and in the adult colonic ENS. We show that the transcription factor *Tbx3* is required for the development of a normal

complement of nitrergic neurons in the neonatal ENS. In chapter 3, I describe our work towards designing a high throughput screen that will allow us to determine whether transcriptional regulators affect differentiation into cholinergic versus nitrergic enteric neuron subtypes. In chapter 4, I describe exciting new work that indicates that postnatal treatment of distal colon lacking an enteric nervous system with the neurotrophic factor GDNF can re-grow a normal, functional ENS in mice. This discovery may lay the foundation for the development of adjunct, non-invasive therapeutic options for the treatment of Hirschsprung disease. Lastly, in chapter 5, I introduce work towards understanding the function of the epigenetic regulator Bap1 in enteric nervous system development and postnatal maintenance.

TABLE OF CONTENTS

LIST OF TABLES

LIST OF ILLUSTRATIONS

CHAPTER 1: INTRODUCTION - UNEXPECTED ROLES FOR THE SECOND BRAIN: ENTERIC NERVOUS SYSTEM AS A MASTER REGULATOR OF BOWEL FUNCTION.

This chapter has been published in Annual Review of Physiology and reprinted here with permission. Authors: Sabine Schneider,* Christina M. Wright,* and Robert O. Heuckeroth. Unexpected roles for the second brain: enteric nervous system as a master regulator of bowel function. Annu Rev Physiol. 2019 Feb 10;81:235-259. doi: 10.1146/annurev-physiol-021317-121515.

*Co-first authors; contributed equally

1.1 Abstract

At the most fundamental level, the bowel facilitates absorption of small molecules, regulates fluid and electrolyte flux, and eliminates waste. To successfully coordinate this complex array of functions, the bowel relies on the enteric nervous system (ENS), an intricate network of more than 500 million neurons and supporting glia that are organized into distinct layers or plexi within the bowel wall. Neuron and glial diversity, as well as neurotransmitter and receptor expression in the ENS, resembles that of the central nervous system. The most carefully studied ENS functions include control of bowel motility, epithelial secretion, and blood flow, but the ENS also interacts with enteroendocrine cells, influences epithelial proliferation and repair, modulates the intestinal immune system, and mediates extrinsic nerve input. Here, we review the many different cell types that communicate with the ENS, integrating data about ENS function into a broader view of human health and disease. In particular, we focus on exciting new literature highlighting relationships between the ENS and its lesser-known interacting partners.

1.2 Introduction

Digesting nutrients that fuel our survival requires complex integration of many bowel functions and all must run smoothly to maintain a normal quality of life. Food must be broken into small particles and chemically digested for nutrient absorption. Indigestible components must efficiently pass through the gastrointestinal tract for elimination, while fluid and electrolyte balance is maintained. All of these processes occur in the setting of a complex microbiome that aids nutrient absorption, but can trigger inflammation and even infection should the system go awry. The intestine could not coordinate these functions without the enteric nervous system (ENS), a complex network of neurons and glia that reside in the bowel wall and send nerve fibers throughout the bowel. Like an orchestra conductor, the ENS is a critical regulator of many processes described above and interacts with an astounding array of cell types to facilitate bowel function.

The ENS is distributed all the way along the bowel in two layers called the myenteric and submucosal plexus (1). Each plexus is comprised of diverse enteric neuron and glial cell types that interact closely with each other and with other intestinal cells. Myenteric plexus cells cluster into ganglia between the outer longitudinal and inner circular smooth muscle of the bowel. Myenteric neurons provide the majority of direct innervation to the bowel's motor apparatus and the final output controlling bowel relaxation and contraction. Myenteric neurons interact closely with the tissue-resident macrophages (muscularis macrophages) that influence motility. Submucosal plexus ganglia reside between muscle and epithelium, where they regulate epithelial secretion and local blood flow. Neurons in both plexi respond to input from mucosal enteroendocrine cells and the autonomic nervous system. The ENS also interacts with immune and epithelial cells to promote barrier function that protects the bowel from pathogens in the gut lumen. Enteric neurons are currently classified by function, axon number, direction of axonal projections, synaptic connectivity, neurotransmitters, receptors, and electrophysiologic signatures. Approximately 20 enteric neuron subtypes and four glial subtypes have been characterized thus far, but a wealth of single cell sequencing data is expected to redefine enteric neuron and glial subtypes in the next few years.

Many excellent recent reviews detail known ENS circuitry, cell types, transmitters and functions (2-5) Instead of duplicating those efforts, our goal is to show how the ENS interacts with non-ENS cell types and the implications of these interactions for human disease.

To facilitate communication, enteric neurons extend an elaborate network of neurites with associated glia. These ENS components contact almost all bowel cells including muscle, epithelial cells, pacemaker cells (called the interstitial cells of Cajal, (ICC)), blood vessels and immune cells. Enteric neurons synapse on each other, but also release neurotransmitters from varicosities along neurites to regulate smooth muscle cell (SMC) and ICC activity. The ICC act as pacemakers since they have intrinsic slow waves of depolarization and hyperpolarization (6).

The contractile force for bowel motility is provided by SMC, which must coordinate activity to mix luminal contents or move undigested food toward the distal bowel for eventual elimination (7). To contract smooth muscle, myenteric plexus excitatory motor neurons project their axons predominantly orally. In contrast, inhibitory motor neurons project axons distally and cause smooth muscle relaxation. Simultaneous activation of excitatory and inhibitory motor neurons in a bowel region causes proximal bowel contraction and distal relaxation, a pattern called peristalsis that is frequently observed in the small intestine.

Additional enteric neuron types control epithelial secretion (secretomotor neurons), epithelial secretion and blood vessel dilation (secretomotor/vasodilator neurons), epithelial proliferation, or innervate enteroendocrine cells and lymphoid follicles. Enteric neurons also send intestinofugal fibers to pancreas, gallbladder, prevertebral sympathetic ganglia, and the central nervous system (CNS) (4). Finally, although the ENS can control many aspects of bowel function autonomously, *in vivo* ENS activity is modulated by luminal contents (nutrients and microbes), muscularis macrophages, parasympathetic neurons, sympathetic innervation from the celiac, superior and inferior mesenteric ganglia, and hormonal signals (e.g., adrenaline, thyroid hormone, corticotrophin releasing hormone, oxytocin). Many of these extrinsic signals are influenced by CNS activity, explaining how emotional responses like anxiety and fear can alter bowel function. The

remainder of this article will explore cell types that interact with the ENS, integrating basic science with human disease to explore how ENS function and dysfunction impact human health.

1.3 The ENS interfaces with the SIP syncytium to regulate motility

ENS interactions with SMC, ICC, and PDGFRα+ cells are critical for bowel motility. Many excellent manuscripts describe these interactions in detail (6-8), so here we highlight a few important interactions and recent developments.

Gap junctions connect **S**MC, **I**CC, and fibroblast-like **P**DGFRα+ cells into a multicellular syncytium commonly called the "SIP syncytium", whose name derives from the first letter of each cell type (**Figure 1.1A**) (6). The SIP syncytium receives input from excitatory and inhibitory motor neurons whose cell bodies reside within the myenteric plexus. Although SMC were once considered the main targets of excitatory and inhibitory ENS motor neurons, neural input onto ICC and PDGFRα+ cells is likely also critical for mediating smooth muscle contractility and for generating complex motility patterns necessary for life.

There are at least five types of ICC in the bowel: ICC-MY, located between the circular and longitudinal muscle layers, ICC-IM, located within the circular muscle layer in colon and stomach, ICC-DMP, between the inner and outer parts of the circular muscle layer of the small intestine, ICC-SM, on the submucosal surface of the circular muscle layer of colon, and ICC-SS, in the subserosal layer (**Figure 1.1B**). ICC-MY and ICC-SM, the "pacemaker" cells of the bowel, generate rhythmic electrical slow waves of depolarization and hyperpolarization that propagate passively to SMC via gap junctions and synchronize SMC contraction. This baseline electrical rhythm is present even when the ENS is absent. ICC-IM and ICC-DMP are closely associated with nerve varicosities (8) and electron microscopy suggests more nerve-ICC-IM contacts than nerve-SMC contacts (9). ICC-IM and ICC-DMP are believed to be the primary ICC that receive input from the ENS (8).

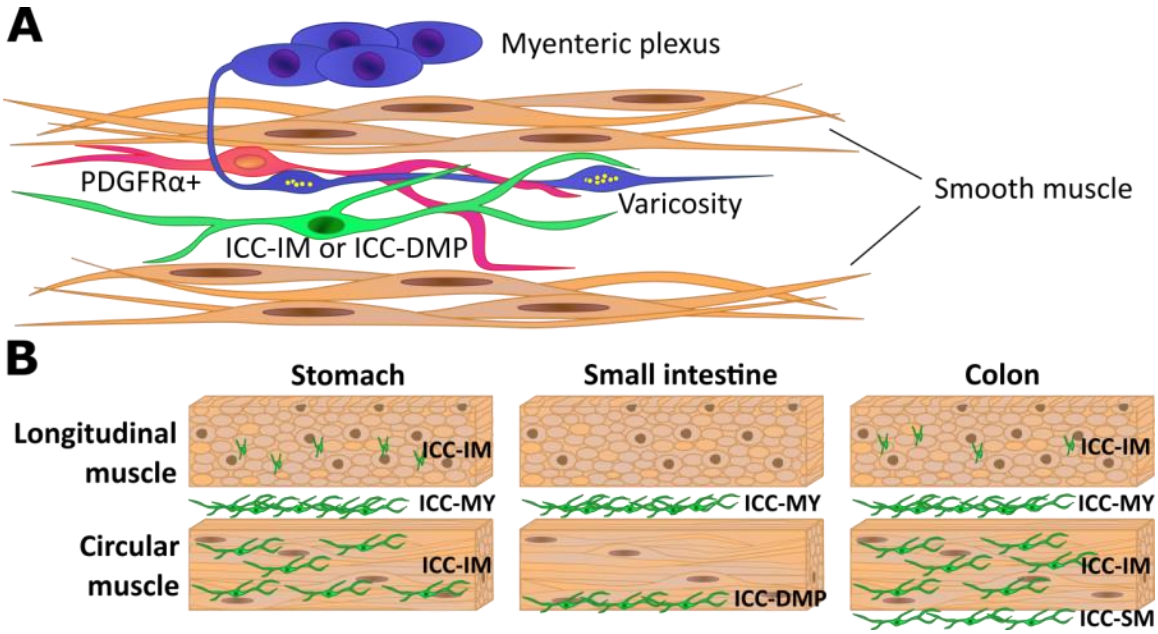

Figure 1.1: The SIP syncytium
(A) The SIP syncytium is composed of SMCs, ICCs, and PDGFR□+ cells which receive input from ENS varicosities. (B) ICC localization and composition varies with bowel region . Abbreviations: ICC-DMP, deep muscular plexus ICC; ICC-IM, intramuscular ICC; ICC-MY, myenteric ICC; ICC-SM, submucosal ICC.

To determine how ICC contribute to neuromuscular transmission, many early studies compared SMC recordings in wild type and ICC-IM-deficient animals during electric field stimulation (EFS). Although some investigators observed attenuated excitatory and/or inhibitory junction potentials in ICC-depleted smooth muscle, results were inconsistent (9-11). Possible explanations for the disparate findings include incomplete absence of ICC in certain model organisms (e.g., commonly used W/WV mouse has inconsistent and incomplete ICC loss (6)), strain and species differences, differences in level of tissue pre-contraction or pre-relaxation (12), use of nifedipine (422), differences between bowel regions, and developmental changes in innervation or smooth muscle reactivity in the absence of ICC. More recent studies test contributions of transduction pathways for specific neurotransmitters, often in genetically modified conditional knockout mice (10, 12, 13). These studies support the presence of parallel complementary pathways for signal transduction involving smooth muscle cells, ICC, and PDGFRα+ cells (**Figure 1.2A-B**).

Inhibitory signaling

Inhibitory junctional potentials (IJPs) recorded from colon smooth muscle are composed of a fast purinergic phase that is followed by a slower nitrergic phase (13). The purinergic contribution to the IJP is probably mediated by PDGFRα+ cells, which express high levels of the purine receptor P2Y1. The ligand for P2Y1 receptors in the bowel was once thought to be adenosine triphosphate (ATP), but in recent years β-nicotinamide adenine dinucleotide (β-NAD) and adenosine 5-diphosphate-ribose (ADPR) have emerged as more likely candidates (14). Applying β-NAD and ADPR to PDGFRα+ cells activates apamin-sensitive small-conductance Ca2+-activated K+ (SK) channels, leading to potassium efflux and membrane hyperpolarization (15). The change in membrane potential spreads via gap junctions to nearby SMC. Purinergic receptors are also expressed on SMC and ICC, but they are unlikely to mediate the strong fast hyperpolarization associated with the IJP (14, 16).

Nitric oxide (NO) is a major signaling molecule in inhibitory motor neurons that acts on both ICC and SMC. NO binds and activates nitric oxide-sensitive guanylyl cyclase (NO-GC). Guanylate cyclase converts GTP to cGMP, which activates GMP-dependent protein kinase I (PRKG1). PRKG1 in turn phosphorylates serines and threonines on many intracellular proteins, causing hyperpolarizing via mechanisms that remain incompletely understood. Molecules downstream of NO (e.g. NO-GC, Prkg1) have been deleted from subsets of ICC and SMC using conditional knockout mice. Although inconsistent findings have been reported, the results suggest that both ICC and SMC likely mediate NO signaling (10, 13). Interestingly, one study found that conditionally deleting NO-GC from ICC in mouse colon reduced IJP amplitude in response to EFS, but conditionally deleting NO-GC from ICC in mouse fundus completely abolished IJPs (13). This underscores an important and underemphasized issue in the literature: regulation of ICC, SMC, and PDGFRα+ cells by neural signaling may vary considerably depending on bowel region. Consistent with this observation, ICC localization and receptor expression differ in various bowel

regions (**Figure 1.1B**). For instance, ICC-MY in stomach do not express the NO-GC subunit sGCβ1, whereas most ICC-MY in colon express sGCβ1, and some ICC-MY in colon express sGCβ1 at high levels (17).

A few recent papers suggest that PRKG1-independent (but NO-GC and cGMP dependent) NO signal transduction may occur in ICC (18, 19). Pacemaker rhythms in cultured colon ICC were slowed by NO donors and cGMP, but not by a PRKG1 inhibitor (18). Small-molecule activation of NO-GC decreased spontaneous calcium transients in ICC-DMP in mouse small intestine, but PRKG1 inhibition had no effect (19). These findings are difficult to reconcile with data showing absent NO-mediated IJPs in Prkg1 conditional knockout mice (10). Possible explanations for the discrepancy include failure of the PRKG1 inhibitors to penetrate tissue, or differences between ICC subtypes studied.

Although the literature on how NO affects smooth muscle and ICC are sometimes contradictory, NO clearly has strong effects on both ICC and SMC in a guanylate cyclase-dependent manner. Further research is needed to determine (a) how members of the SIP syncytium in various bowel regions differ in receptor expression and response to signaling, (b) how innervation of the SIP syncytium differs in each bowel region, and (c) the significance of PRKG1-independent pathways in NO-mediated responses. Defining these characteristics may elucidate molecular mechanisms that generate diverse motility in each bowel region.

In addition to NO, inhibitory enteric neurons release vasoactive intestinal peptide (VIP) and pituitary adenylate cyclase activating peptide (PACAP). These neuropeptides likely signal through VIP receptors VIPR1 and VIPR2 and the PACAP receptor ADCYAP1R1, which are expressed on ICC and SMC (7). Typically, neuropeptides are released at high stimulus frequencies, so VIP and PACAP may play less prominent roles in direct motor neurotransmission than NO (7). In SMC, VIP/PACAP signaling is mediated via Gs which activates adenylyl cyclase, cyclic AMP (cAMP), and protein kinase A (PKA) (20). This increases Ca2+ transients that should increase the opening probability of Ca2+-activated K+ channels, causing membrane hyperpolarization (20). In ICC, VIP

may act via a different pathway. VIP decreases calcium transients dramatically in some ICC, and calcium transients increase when a VIP inhibitor is added. These calcium transients likely control the activity of calcium-dependent chloride channels (CaCC) which regulate slow waves (19). The mechanism behind this response is currently unknown.

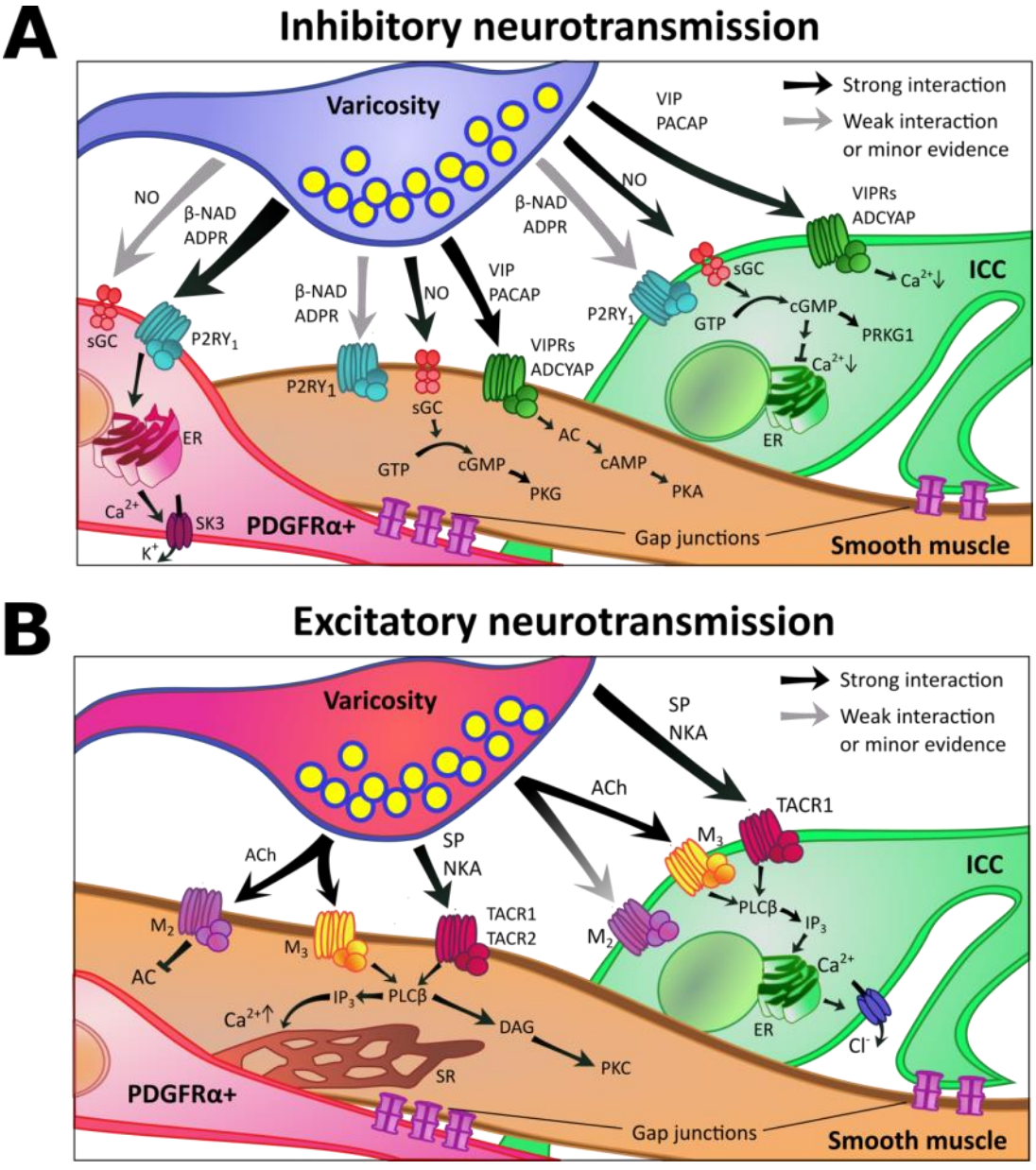

Figure 1.2: Inhibitory and excitatory motor neurotransmission.

(A) Inhibitory neurotransmission involves a combination of purine, NO, and VIP/PACAP signaling. (B) The primary neurotransmitters involved in excitatory neuromuscular transmission are acetylcholine and tachykinins. Abbreviations: AC, adenylate cyclase; ACh, acetylcholine; ADCYAP1R1, pituitary adenylate cyclase-activating polypeptide type 1 receptor; ADPR, ADP-Ribose; β-NAD, β-Nicotinamide adenine dinucleotide; cAMP, cyclic AMP; cGMP, cyclic GMP; DAG, diacylglycerol; GTP, guanosine triphosphate; ER, endoplasmic reticulum; ICC, interstitial cells of Cajal; IP3, inositol triphosphate; M2, muscarinic receptor 2; M3, muscarinic receptor 3; NKA, neurokinin A; NO, nitric oxide; PACAP, pituitary adenylate cyclase-activating peptide; PKA, protein kinase A; PKC, protein kinase C; PRKG1, protein kinase G; PLCβ, phospholipase C beta; sGC, soluble guanylate cyclase; SK3, small conductance calcium-activated potassium channel 3; SP, substance P; SR, sarcoplasmic reticulum; TACR1, tachykinin receptor 1; TACR2, tachykinin receptor 2; VIP, vasoactive intestinal peptide; VIPR, VIP receptors.

Excitatory signaling

The major excitatory neurotransmitters involved in direct motor neurotransmission are acetylcholine (ACh) and tachykinins (neurokinin A (NKA), and substance P (SP)). ACh binds muscarinic M_2 and M_3 receptors on SMC and ICC, while tachykinins bind tachykinin receptor 1 (TACR1) and tachykinin receptor 2 (TACR2) receptors on SMC and TACR1 on ICC (**Figure 1.2B**). In ICC-DMP, signal transduction via M_3 receptors likely occurs through G_q leading to Ca^{2+} release from the endoplasmic reticulum and activation of CaCC such as anoctamin 1 (Ano1). Opening of CaCC causes a depolarizing current predicted to enhance the likelihood of action potential generation and increase contraction amplitude (21, 22). M_2 receptors are also expressed on ICC but may play a less important role than M_3 receptors (21, 23). In contrast, evidence from knockout mice suggests that both M_3 and M_2 receptors influence SMC contractility (24).

Like muscarinic signaling in ICC, tachykinin signaling via TACR1 is hypothesized to act via G_q signaling coupled to Ca^{2+} release and CaCC opening. Tachykinin signaling may be more important than muscarinic signaling in ICC-DMP. Applying TACR1 receptor antagonists attenuated basal Ca^{2+} transients in small intestine ICC-DMP, suggesting that ICC-DMP are tonically excited by tachykinins (21). The same may not be true in colonic ICC, which do not express TACR1 receptor as highly (21). In SMC, tachykinin signaling is transduced by both TACR2 and TACR1 receptors (25). Second messenger signaling likely occurs through protein kinase C (PKC) and IP_3 (7), although other pathways may be involved (25).

ENS, the SIP syncytium, and bowel motility: putting it all together

When considering direct neural input to the SIP syncytium, it is important to remember that diverse motor patterns are needed for food to be digested and absorbed, and for waste to be eliminated. These motility patterns in human small intestine include peristalsis (waves of contraction and relaxation that propagate down the bowel), segmentation (alternating contraction and relaxation to mix food with digestive enzymes and bile), and the migrating motor complex (MMC) (where strong waves of contraction and relaxation propagate down the bowel during phase III to moves luminal contents toward distal bowel for elimination). In the colon there are high amplitude propagating contractions (HAPC) that move stool over long distances toward the rectum and occur only occasionally. Generation and maintenance of these motor patterns requires a complex interplay between neural signaling, ICC, PDGFRα+ cells, and SMC. In broad strokes, ICC continually produce oscillating electrical slow waves in the bowel that set the rhythm for many motor patterns. Slow wave electrical activity propagates from ICC to SMC, generating rhythmic SMC depolarization and contraction. Neural signaling onto the SIP syncytium generates and modulates ICC and SMC activity to produce the motor patterns described above. Stimuli from the environment alter ENS activity to determine which motor patterns should occur at specific times (7). For example, segmentation in the small bowel occurs after meals, but phase III MMC predominates once most nutrients are absorbed. Although the ENS is not essential for generating some motor patterns, the ENS is probably the primary inducer of complex motility patterns needed for survival (26).

To “decide” what to do, sensory neurons of the ENS (called intrinsic primary afferent neurons, IPANs) respond to diverse stimuli including stretch and mucosal distortion (1, 2). Stretch sensing is mediated by mechanoreceptors located within the myenteric plexus, which fire in response to distention (27). Historically, it has been assumed that stimulation of enterochromaffin (EC) cells in the bowel mucosa and the resulting serotonin (5-HT) release onto IPANs play a major role in evoking enteric neural reflexes such as the peristaltic reflex. However, recent papers question the

importance of serotonin release from EC cells for initiation of motility since mice lacking a critical enzyme involved in 5-HT biosynthesis in EC cells (tryptophan hydroxylase 1, or TPH1) survive to adulthood and have a normal gastrointestinal transit time (28). Further research has shown these mice have larger fecal pellets and aberrant colonic migrating motor complexes (29) suggesting that in the absence of 5-HT from EC cells, a higher degree of stretch is required to trigger contractions (30).

We have focused thus far on neurotransmission to the SIP syncytium, but enteric glia also influence bowel motility. Female mice lacking enteric glia have reduced gastrointestinal transit time and increased CMMC frequency compared to controls. Intriguingly, the same effect was not seen in males, suggesting potential glia-intrinsic sex-dependent differences, or sexual dimorphism in glial interacting partners (31). Other studies also suggest enteric glia influence bowel motility; for instance, mice lacking the glial-specific hemichannel connexin-43 had prolonged colonic transit, increased stool water content, and diminished contraction and relaxation amplitude (32). Mechanisms behind glial control of motility are not well understood. One hypothesis is that trophic factors produced by glia may prevent ENS dysfunction. Another possibility is that enteric glia directly modulate ICC slow wave activity (33).

Clinical relevance

Human bowel motility disorders include life threatening problems like Hirschsprung and chronic intestinal pseudo-obstruction (CIPO) syndrome. In these disorders, ENS or SIP syncytium function is so disrupted that surgical intervention or intravenous nutrition is often needed for survival

Hirschsprung disease. The ENS forms from neural crest-derived precursor cells (ENCDC) that colonize the bowel during first trimester fetal development. In about 1:5000 children, ENCDC never reach the distal bowel resulting in a region where the ENS is completely absent. This problem is called Hirschsprung disease. In children with Hirschsprung disease, the region of bowel that lacks

enteric ganglia (i.e. aganglionic bowel) is tonically contracted and does not have propagated motility, leading to functional obstruction. Because aganglionic bowel does not efficiently pass stool or air, Hirschsprung disease symptoms include distension, constipation, vomiting, abdominal pain, growth failure, and a predisposition to bowel inflammation (called enterocolitis) that may lead to death from sepsis. Hirschsprung disease provides absolute proof that the ENS is essential for life, since even a small region of aganglionosis can cause serious illness and premature death. Our recent review provides more detailed information about Hirschsprung disease symptoms and molecular mechanisms (34).

Chronic intestinal pseudo-obstruction syndrome (CIPO). When the ENS is present throughout the bowel, but bowel motility does not consistently support survival or growth without at least intermittent intravenous nutrition, CIPO is the likely diagnosis. Symptoms of CIPO include repetitive episodes of abdominal distension and pain, vomiting, growth failure, and weight loss (89). CIPO may occur as a primary disorder, or it may be secondary to complications of another disease. CIPO should not be confused with transient bowel motility defects such as ileus (the absence of bowel contractions) that commonly accompanies abdominal surgery, pancreatitis, appendicitis or sepsis.

The etiology of CIPO remains poorly understood, although clues are emerging from human and mouse genetics. Because so many cell types, transmitters, and signaling molecules impact ENS development and intestinal function, there are likely many underlying causes of CIPO, potentially including dysfunction of ENS, SMC, ICC, and/or PDGFRα+ cells. Unfortunately, even with advanced genetic tools like whole exome sequencing, causative genetic variants remain poorly defined. Only a few genetic causes of CIPO have been identified. These include mutations in the genes encoding filamin A (*FLNA*), DNA polymerase gamma (*POLG*), and gamma smooth muscle actin (*ACTG2*), leiomodin 1 (*LMOD*1), myosin heavy chain 11 (*MYH11*) and myosin light chain kinase (*MYLK*) (35, 36). Identifying more genetic causes of CIPO is critical as it will undoubtedly aid diagnosis. New medicines to treat CIPO are also desperately needed. Available prokinetic

medications prevent ACh degradation (e.g. Pyridostigmine), activate 5-HT4 receptors (enhancing ACh release from excitatory motor neurons and increasing bowel motility; e.g. Cisapride, Tegeserod, Prucalopride), inhibit dopamine receptors (Metoclopramide, Domperidone), activate somatostatin receptors (Octreotide) or activate receptors for motilin, a peptide that increases GI motility (e.g. Erythromycin). Unfortunately, many of these medicines have serious side effects or are only minimally effective at enhancing small bowel motility and resolving symptoms for people with serious motility disorders like CIPO (35, 37).

1.4 The ENS and vascular endothelium

During digestion, blood flow to intestinal mucosa increases as much as 2-fold owing in part to dilation of submucosal arterioles. Vasodilation and resulting hyperemia are needed to meet the high metabolic demands of the mucosa and to exchange nutrients, water, and solutes across bowel epithelium. Neurogenic vasodilation of submucosal arterioles is mediated by extrinsic and intrinsic (ENS) innervation. In contrast, vasoconstriction of bowel arterioles is wholly under control of extrinsic sympathetic innervation. Here we briefly review ENS control of vasodilation, which has been extensively characterized.

Most studies of submucosal arteriole vasodilation evaluated guinea pig small intestine, using varied preparations including isolated submucosa and full thickness intact bowel. These studies suggest many triggers for ENS-mediated vasodilation, including gently stroking bowel mucosa, distorting the mucosa with puffs of gas, and distending smooth muscle with a balloon. Small distortions of the mucosa (stroking, puffing gas) cause EC cells to release 5-HT onto enteric nerve terminals expressing 5-HT3 [myenteric IPANS (38)] and 5-HT4, and/or 5-HT1P [submucosal IPANs (39)]. Stimulation of these IPANs by 5-HT activates short (1–2 mm) reflex pathways within the submucosa, as well as longer reflex pathways that span submucosal and myenteric plexus (39). Stretching the bowel activates 5-HT_3 and 5-HT_4-insensitive mechanotransducers in the myenteric plexus (40) and possibly submucosal plexus (41) leading to vasodilation. Mechanical

deformation of the gut activates neurites and soma of a large number of mechanosensitive enteric neurons within the myenteric plexus (27). These mechanosensitive neurons are multifunctional (i.e. they may be afferents, interneurons, or efferents) and their responses to mechanical stimulation may be rapid-adapting, slow-adapting, or ultra-slow-adapting (42).

A final common pathway for ENS-mediated vasodilation in guinea pig small intestine is release of ACh onto endothelial cells which activates muscarinic M_3 receptors, leading to NO release and vasodilation (43). In guinea pig distal colon, substance P and/or VIP release from submucosal plexus neurons may contribute to vasodilation (44). The ENS may also stimulate mast cells to release the vasodilator histamine directly onto submucosal blood vessels (45) via SP and/or calcitonin gene-related peptide (CGRP) (45).

Clinical relevance

Impaired vascular control has been implicated in a number of inflammatory conditions, including necrotizing enterocolitis (NEC) and inflammatory bowel disease (IBD). NEC is a dangerous bowel disease in premature neonates, characterized by severe inflammation, ischemic necrosis, and sometimes bowel perforation. It is tempting to hypothesize that neuron dysfunction may contribute to development of necrotizing enterocolitis, for instance through dysregulation of vasodilation that occurs in response to feeding. Indeed, altered microcirculation involving constricted arterioles has been demonstrated in NEC (47) and damage to the ENS also occurs with NEC (47). However, there is not yet convincing evidence that ENS dysfunction is the primary cause of altered blood circulation in babies with NEC. Arguing against this hypothesis, vessel endothelial cells from bowel with NEC failed to generate NO in response to ACh, but vessels dilated in response to exogenous NO administration, suggesting dysfunction of endothelial cells may be paramount (48). This is similar to IBD, where vessel endothelium does not appropriately produce NO even when stimulated by ACh (49). Unfortunately, because defects seem intrinsic to endothelial cells, neuromodulators (e.g. AChE inhibitors) are unlikely to have therapeutic value in these

disorders, although gut derived neural stem cells do appear to prevent NEC-like injury in a rodent model (47).

1.5 Epithelial secretion and the ENS

5-HT released from enteroendocrine cells in response to mucosal stroking not only elicits peristalsis and supports vasodilation, but also activates fluid and electrolyte secretion into the gut lumen to facilitate digestion. 5-HT activates IPANS that in turn synapse on secretomotor neurons that release ACh or VIP. ACh acts via muscarinic receptors and VIP via VIPR1 receptors on crypt epithelial cells to increase intracellular Ca^{2+} (via phospholipase C and IP_3) and cAMP (via G_s) respectively. Cyclic AMP activates the cystic fibrosis transmembrane regulator (CFTR) chloride channel. Calcium activates the HCLCA1 chloride channel inducing more transient chloride flux. Movement of chloride into the gut lumen is accompanied by sodium and water. The details of these circuits are much better understood than this brief description suggests, and they are beautifully described in reviews (50, 51).

Interestingly, a recent publication has also defined a role for enteric glia in the regulation of epithelial ion transport. When glial cells lack the glial-specific hemichannel connexin-43 neuron-regulated electrogenic ion transport was reduced while transmural conductance and epithelial permeability were not significantly changed. Activation of GFAP-expressing glial cells stimulated electrogenic ion transport similar to that observed with direct neuronal stimulation. Inhibiting neuronal activation with tetrodotoxin only partially reduced glial-induced electrogenic ion transport, indicating that the enteric glia interactions with the epithelium do not require neuronal activity (52).

Clinical relevance

Dysfunctional regulation of epithelial secretion may lead to increased stool water content. VIP-producing tumors and SSRI-induced serotonin syndrome cause diarrhea by directly increasing neurotransmitters in the ENS circuit that controls epithelial secretion (53). Cholera, Rotavirus,

Clostridium difficile, Cryptosporidium, and enterotoxin producing Escherichia coli all cause profuse watery diarrhea at least in part by activating ENS circuits (54, 55).

1.6 The ENS, epithelial proliferation and repair

Bowel epithelium is replaced every few days via proliferation of stem cells and transit-amplifying cells in the crypt. Newly-generated cells differentiate into absorptive epithelial cells, goblet cells, and EC (among other cells types) before being lost via apoptosis. Regulation of epithelial proliferation and differentiation is carefully controlled since too little epithelial replacement reduces absorptive capacity and too much epithelial proliferation causes cancer. Among other regulatory mechanisms, accumulating data suggest the ENS influences epithelial proliferation and repair, as well as epithelial barrier function, but that effects of the ENS on bowel epithelium are complex.

For example, chemical ablation of the myenteric plexus with benzalkonium chloride increases epithelial proliferation, crypt depth and villus height (56) suggesting inhibitory effects of the ENS on epithelial renewal. Consistent with the hypothesis that ENS components reduce epithelial proliferation, mice with a hypomorphic ENS because of mutations in the tyrosine kinase receptor *Ret* have enhanced small bowel epithelial proliferation after small bowel resection during the adaptive response (57). In contrast, loss of the hepatocyte growth factor receptor *Met* within the ENS leads to reduced epithelial proliferation after dextran sodium sulfate (DSS)-induced bowel injury (58). Because *Met* and *Ret* are expressed in different subsets of myenteric neurons, these observations suggest some enteric neurons enhance and others suppress bowel epithelial proliferation depending on context.

Consistent with this hypothesis, ACh activates muscarinic receptors on intestinal stem or progenitor cells to enhance epithelial proliferation (59-62). Neuron-derived serotonin activates 5-HT(2A) receptors on cholinergic neurons, enhancing ACh release (63) and also enhancing epithelial proliferation. Interestingly, glucagon-like peptide 2 (GLP-2), a potent stimulant for epithelial

proliferation, might also work via the ENS since GLP-2 receptors are expressed by enteric neurons, but not intestinal epithelium (64). Alternatively, GLP-2 might support epithelial proliferation via subepithelial myofibroblasts that express GLP-2 receptor and release IGF-1 in response to GLP-2. In support of this hypothesis, IGF-1 is required for GLP-2 intestinotrophic effects and this mechanism could bypass the ENS (65).

In addition to regulating epithelial cell proliferation, enteric neurons appear to enhance epithelial barrier function. Co-culture of primary enteric neurons with primary intestinal epithelial stem cells, increases expression of tight junction associated protein zona occludens 1 (ZO-1), increases transepithelial resistance across the monolayer, and reduces apical to basolateral dextran permeability (66). Parallel studies suggest enteric glia may also influence intestinal epithelial barrier function (67-70). For these studies, enteric glia were eliminated using a transgenic GFAP-Cre driver to induce expression of HSV-TK or using the GFAP promoter to drive expression of the neoantigen haemagglutinin. In the former case, treatment with gancyclovir induced cell death in any cell that expressed the transgene by conversion of the antiviral agent to a toxic nucleotide analog. In the latter case, neoantigen expression led to CD8+-mediated cell death of any neoantigen-expressing cell. Eliminating glia in these ways led to massive bowel inflammation. Co-culture of epithelial cells and glia also changed gene expression (71) in epithelial cells, increasing tight junction proteins (like ZO1 and occludin) and decreasing transepithelial permeability in cultured epithelial monolayers (69-71). S-nitrosoglutathione was identified as a soluble glial-derived factor that increased epithelial barrier function *in vitro*. This compound drastically reduced the development of enterocolitis *in vivo* after HSV-TK-mediated damage to ENS and epithelium (69). Another study found that mucosal glia strongly upregulate their expression of GDNF in states of inflammation (72, 73). GDNF reduced epithelial apoptosis *in vitro* (74, 75) and in a mouse model of DSS-colitis, GDNF overexpression increased tight junction protein expression and decreased epithelial permeability (76). Collectively these studies provided substantial support for the hypothesis that enteric glia enhance epithelial barrier function. Interestingly, enteric glial cell-

derived GDNF also activates RET on type 3 innate lymphoid cells (ILC3) to induce release of IL-22, which enhances epithelial expression of genes that reduce bacterial translocation (77). Collectively these studies provided substantial support for the hypothesis that enteric glia enhance epithelial barrier function.

Surprisingly, an elegant set of experiments showed that enteric glial cells are not required for maintenance of epithelial integrity in mice. The authors eliminated all enteric glia by inducing cholera toxin subunit A expression under the control of the PLP1 promoter. In this system, no enterocolitis developed, and epithelial cell ultrastructure, proliferation and permeability were unaffected despite a dramatic loss of enteric glia. The absence of glia in the setting of DSS-induced colitis did not worsen symptom severity or specifically affect transepithelial permeability. Lastly, the authors showed that the discrepancy between their study and the previous *in vivo* studies could be explained by the aberrant GFAP-Cre transgene expression in a small number of epithelial cells which caused direct injury to the epithelial cell layer after ganciclovir treatment or induction of neoantigen expression (31).

Overall, it is clear the ENS influences intestinal barrier function in a normal physiologic state and during inflammation. The exact contributions of the different enteric neuron subtypes and of enteric glia have not yet been conclusively elucidated.

1.7 The ENS and macrophages

Two broad classes of tissue-resident macrophages contribute to intestinal immune function. The most abundant macrophage (Mφ) class resides in the lamina propria (LpMφ) directly beneath bowel epithelium (78) and are surrounded by dense submucosal neuron projections that innervate the epithelial layer. Direct functional interactions between ENS and LpMφ have not yet been document, but seem plausible. The second, relatively understudied group called muscularis macrophages (MMφ) are very closely associated with the myenteric plexus and emerging literature

suggests significant cross-talk and even developmental interdependence between these cell types (**Figure 1.3**).

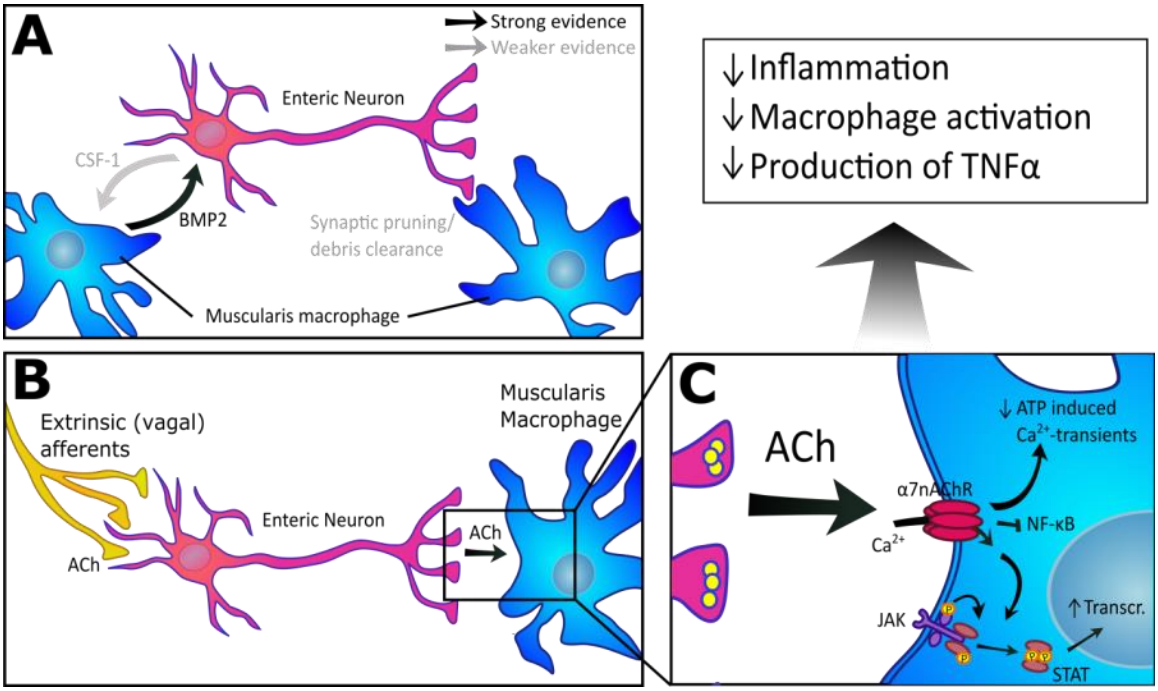

Figure 1.3: Interaction between muscularis macrophages and enteric neurons.
(A) Muscularis macrophages support enteric neurons through BMP2 signaling and possibly synaptic pruning and clearing of debris. (B) Enteric neurons are a key part of the cholinergic anti-inflammatory pathway (CAIP) reducing the activation of macrophages through vagal stimulation. (C) Activation of muscularis macrophages by ACh decreases macrophage activation and decreases production of TNFα. Abbreviations: α7nAChR, α7 nicotinic acetylcholine receptor; ACh, acetylcholine; ATP, adenosine triphosphate; BMP2, bone morphogenetic protein 2; CSF-1, colony stimulating factor 1; JAK, Janus kinase; NF-κB, nuclear factor kappa-light-chain-enhancer of activated B cells; STAT, signal transducer and activation of stimulation; TNFα, tumor necrosis factor alpha; Transcr., transcription.

1.8 The ENS depends on MMφ for normal structure and function

MMφ produce bone morphogenetic protein 2 (BMP2), a morphogen that binds its receptor BMPRII on neurons and influences ENS precursor differentiation, neurite fasciculation, and ganglion formation (79, 80). Mice lacking MMφ during development have increased numbers of enteric neurons and a disorganized ENS. Interestingly, this phenotype is similar what occurs when the BMP antagonist noggin is over-expressed *in vivo* (79, 81). Acute depletion of MMφ from the

bowel in adulthood enhanced colon contractility in response to stretch *ex vivo*, but delayed expulsion of a bead by the colon *in vivo*, suggesting problems with coordinating muscle activity. The motility changes were not limited to the colon since gastric emptying was also accelerated two days after acute MMφ depletion. The effects of MMφ depletion on *ex vivo* colon contractility could be mimicked by dorsomorphin (a BMP signaling inhibitor) or rescued by adding BMP2. Consistent with these observations, nuclear localization of pSMAD1/5/8 (a downstream effector complex for BMP signaling) was reduced in enteric neurons from MMφ-depleted bowel. Interestingly, antibiotic treatment to reduce luminal microbes reduced bowel MMφ, BMP2 levels, and nuclear pSMAD1/5/8 in enteric neurons. Antibiotics increased whole-bowel transit time and enhanced colon contractility *ex vivo*, suggesting dysfunctional bowel motility (81).

Taken together, these results offer strong evidence that enteric neurons rely on BMP2 produced by MMφ for normal morphology and function. These observations also suggest that postnatal acquisition of intestinal microbes critically shapes neuroimmune interactions in the bowel. Some authors have suggested that MMφ also contribute to normal ENS morphology by phagocytosing neuronal debris (82). This function of MMφ would be similar to that of microglia, the tissue-resident macrophages of the brain, which clear apoptotic neurons and eliminate unnecessary axons and synaptic connections (i.e. synaptic pruning). Further research is needed to determine the extent to which phagocytosis by MMφ shapes the ENS.

1.9 Activated MMφ regulate enteric neuron excitability during inflammation

Activated murine MMφ release chemokines, cytokines (interleukin 1, monocyte chemoattractant protein 1, interleukin 6, tumor necrosis factor alpha (TNFα)) and other bioactive compounds (NO, prostaglandins) (83, 84). NO regulates neuron excitability and directly relaxes SMC, so it is not surprising that increased NO reduces bowel contractility. Some enteric neurons also produce TNFα receptors, and TNFα activates neuropeptide Y (NPY) expression. NPY

increases bowel epithelial permeability during inflammation (85), suggesting a neuro-immune interaction that might be modulated to reduce intestinal inflammation.

1.10 The ENS modulates MMφ activation, and may affect MMφ survival

Macrophages express many neurotransmitter receptors, including α7 nicotinic acetylcholine (α7nAChR), tachykinin, glycine, and P2 purine receptors, all of which may alter MMφ function (84). The most well-characterized example of ENS modulation of MMφ is the cholinergic anti-inflammatory pathway (CAIP), a circuit involving the vagus, ENS, and MMφ. Stimulating the vagus nerve activates cholinergic enteric neurons near MMφ, leading to release of ACh and stimulation of α7nAChR on MMφ. This reduces inflammation by decreasing the ATP-induced calcium transients in MMφ, decreasing macrophage activation (86) and reducing TNFα production by macrophages (87). α7nAChR also activates the Jak2-STAT3 signaling pathway, which likely plays a role in attenuating macrophage activation (88). ENS-MMφ signaling is likely not limited to ACh-α7nAChR interactions given the large number of neurotransmitter receptors expressed by macrophages. Extrinsic nerves also modulate MMφ activation directly through norepinephrine signaling onto adrenoreceptor β2, but this pathway is probably independent of the ENS (78).

Intriguingly, adult enteric neurons express colony stimulating factor 1 (CSF-1), the primary survival factor for MMφ (450). Since other CSF-1 expressing cell types had not been identified in the bowel, we hypothesized that MMφ rely on CSF-1 produced by enteric neurons for normal development. Surprisingly, MMφ appear normal in neonatal bowel even in the absence of an ENS. Other intestinal cell types (endothelial cells, ICC) produce CSF-1 perinatally and may be the main cells supplying MMφ with CSF-1 in early life (89). Since a considerable ENS development occurs after birth, ENS-MMφ interactions likely mature postnatally, and it remains possible that CSF-1 expressed by neurons is critical for MMφ survival in adulthood. Global knockout models of CSF-1 (i.e. *Csf1*$^{op/op}$ mice) lack all MMφ, but thus far conditional depletion of CSF-1 from enteric neurons

has not been reported. This experiment would be needed to confirm that ENS-derived CSF-1 influences adult MMφ number or function.

Clinical relevance

Post-operative paralytic ileus is a common condition characterized by transiently impaired bowel motility after abdominal surgery. Post-operative ileus may be partially mediated by low-grade inflammation leading to impairment of muscle contractility. Supporting a role for MMφ in post-operative ileus, depletion of MMφ by clodronate or genetic MMφ loss in *Csf1*$^{op/op}$ mice protects against post-operative ileus (90). Intriguingly, vagal nerve stimulation reduced inflammation and improved post-operative ileus (91). This is likely mediated by the vagal-ENS-MMφ anti-inflammatory pathway described previously (86). MMφ activation has also been implicated in other gastrointestinal motility disorders such as gastroparesis, which also may be helped by vagal stimulation. This topic is summarized in a number of excellent recent reviews (83, 84).

1.11 ENS interactions with the microbiome

After birth, the bowel must grapple with drastic changes as it is exposed to a diverse array of microbes seeking to establish themselves within the gut lumen. Microbial colonization occurs while the ENS is still maturing, and we now believe these microbes substantially affect ENS development. At least two studies have shown reductions in neuron density in the small intestine and/or colon of young germ-free (GF) mice compared to age-matched gnotobiotic controls (92, 93). Oddly, one study reported an increased proportion of nitrergic myenteric neurons in their 3-day-old GF mice (93), while the other study, which used 4-week old GF mice, reported *decreased* nitrergic neuron numbers (92). The cause of this difference is unclear.

A few mechanisms for microbial effects on ENS development have been proposed. Interestingly, enteric neurons and glia express toll-like receptors (TLR), pattern recognition receptors that are activated by pathogen associated molecular patterns (PAMPs) as part of the

innate immune system. TLRs 3, 4, and 7 are expressed in enteric neurons and glia (94). Additionally, TLR2 may be expressed in ENS and in surrounding cells including SMC (95). Global deletion of TLR2 reduced the number of nitrergic neurons in colon, and accelerated gastrointestinal transit (95). Mice with a global deletion of TLR4, which detects lipopolysaccharide (LPS; a major component of gram-negative bacteria) had reduced numbers of nitrergic neurons, slow bowel motility, and reduced bowel relaxation in response to EFS. Conditional knockout mice missing *Myd88* selectively in neurons and glia also had delayed colon transit and reduced nitrergic neurons (92) MYD88 is a mediator of TLR4 activity. Finally, a high fat diet, which causes dysbiosis, also reduced NO-producing myenteric neuron number and slowed bowel motility in a TLR4-dependent fashion (96).

One possible explanation for these findings is that microbes could activate TLRs on enteric glia or mesenchymal cells, leading to release of the RET ligand glial cell line-derived neurotrophic factor (GDNF). GDNF provides trophic support for enteric neurons expressing RET and its co-receptor GDNF Family Receptor alpha 1 (GFRα1) during ENS development (97). In addition, GDNF contributes to motility by stimulating the ascending limb of the peristaltic response (98). In support of this theory, mice lacking TLR2 had significantly reduced GDNF in muscle. Administering recombinant GDNF to these mice subcutaneously for seven days restored neuron numbers and reversed dysmotility (95). Some evidence suggests enteric glia produce GDNF in response to inflammation (72), making them a plausible intermediary in this pathway, although SMCs or other mesenchymal cells could also be involved.

In addition to developmental effects, the microbiome can affect the ENS in adult life. Microbiome composition directly affects mature ENS function by altering electrophysiologic properties of neuron subtypes (99) and leading to changes in intestinal motility and neurally-mediated secretion (100, 101). Furthermore, giving mice antibiotics reduces neuron numbers and slows gastrointestinal transit (92). The ENS can also influence the composition of the microbiome. In a zebrafish model of HSCR, the pathogenic over-abundance of pro-inflammatory bacterial strains

could be corrected simply by restoring ENS function (102). These observations highlight just a few of the complex interactions between gut microbes and the ENS; a more detailed description of ENS-microbiome interactions can be found in recent reviews (103, 104).

1.12 ENS interactions with the adaptive immune system

Enteric neuron projections can be found within mucosal lymphoid follicles (Peyer's patches) (105, 106). When lymphocytes from Peyer's patches were exposed to neuropeptides, they significantly increased their proliferation rate and immunoglobulin synthesis (107). This suggests the exciting possibility that enteric neurons can directly influence the adaptive immune system. For example, the Y1 receptor that binds neuropeptide Y is expressed on monocytes, macrophages, lymphocytes, and granulocytes (108). Y1-deficient mice have reduced antigen presenting cell function, reduced effector T cells, and reduced production of TNFα and IL-12 by macrophages. Similarly, *Npy-/-* mice have lower TNFα levels and *Y1-/-* mice resist colitis that occurs after epithelial injury with dextran sodium sulfate (DSS) (109). VIP is produced by inhibitory motor neurons, descending interneurons and secretomotor neurons of the ENS to control motility and epithelial function. The VIP receptor is also expressed by T-cells, where VIP promotes a T-reg phenotype (110), by dendritic cells where VIP induces a tolerogenic phenotype (111, 112), and by macrophages where VIP inhibits production of TNFα, IL-6 and IL-12p40 (110). These anti-inflammatory effects of VIP *in vitro* contrast with the observation that *VIP-/-* mice are resistant to TNBS-induced colitis (113) and LPS-induced endotoxemia (114). The reason for this discrepancy is not known.

1.13 ENS interaction with enteroendocrine cells

Enteroendocrine cells (EEC) are a diverse group of neuroendocrine cells in the bowel epithelium that produce hormones and neuropeptides in response to stimulation from the gut lumen. The molecules produced by EEC act locally on cells within the mucosa, as well as

systemically via the bloodstream (115). Significant cross-talk occurs between EEC and the ENS to modulate vasodilation, motility and epithelial secretion. We already alluded to one mechanism by which enterochromaffin cells (EC), a subtype of EEC, signal enteric neurons through release of 5-HT onto nerve terminals. The triggers for 5-HT release are incredibly diverse and include mechanical deformation of the mucosa, macromolecules (e.g. glucose, fatty acids, amino acids), chemical irritants (e.g. allyl isothiocyanate), injury or stress (e.g. norepinephrine), and changes in the bacterial milieu (e.g. butyrate and other short chain fatty acids) (115, 116). In response to stimulation, EC activate neurons through the release of 5-HT onto nerve terminals. In addition to 5-HT, EEC produce neuropeptides such as somatostatin, motilin, VIP, glucagon-like peptide-1 (GLP-1) and cholecystokinin (CCK), which modulate ENS activity (117-119). It has traditionally been assumed that these neuroactive peptides signal in a paracrine manner. However, presynaptic and postsynaptic markers have been identified on EC, suggesting that EC communicate with nerves via synapse-like structures (116, 120). Even more compelling, monosynaptic transmission of modified rabies virus confirms the presence of functional efferent synapses (120). Unfortunately, the *in vivo* data does not address the question of whether the EC form synapses with enteric or extrinsic neurons (120). There is a paucity of research regarding EEC-ENS connections and particularly efferent ENS signaling onto hormone-producing EEC. Given the similarity in signaling molecules and receptors between EECs and the ENS, it seems highly likely that these cells communicate through additional pathways that remain to be discovered.

1.14 The ENS, CNS and the autonomic nervous system

A variety of extrinsic nerves innervate the bowel, including sympathetic nerves, the parasympathetic vagus and sacral plexus nerves, and the dorsal root ganglia. Some of these nerves interact directly with their targets in the bowel, but they may also mediate their effects indirectly by synapsing on enteric neurons. We already mentioned the cholinergic anti-inflammatory (CAIP) pathway, where vagal nerve fibers signal ENS intermediaries that then signal macrophages

to reduce inflammation. Here we provide a brief overview of other important ENS interactions with the autonomic nervous system. Please see the following reviews for a more in-depth discussion of this topic (4, 121),

1.15 Sympathetic neuron-ENS interactions

Sympathetic nerve endings contact the vast majority of enteric neurons (122), and may also activate enteric glia via ATP release (123). Sympathetic nerves indirectly regulate epithelial secretion by inhibiting secretomotor neurons in the submucosal plexus. This inhibition is likely tonic since transepithelial secretion is greatly enhanced after sympathectomy (122), and acute sympathetic inhibition effects on secretion are most apparent when the secretomotor reflex has been activated (124, 125).

The sympathetic nervous system coordinates motility across large segments of bowel. The changes in motility are mediated by reflex arcs that involve afferent sensory neurons of the ENS and efferent inhibition of enteric neurotransmission by the sympathetic nervous system. These reflex arcs may include or bypass the CNS, depending on context. Sympathetic reflexes have been worked out in detail and are well described elsewhere (122).

1.16 Parasympathetic-ENS interactions

Parasympathetic innervation of the upper gastrointestinal tract is exclusively provided by the vagus nerve and vagal projections are known to reach as far as the colon. Whether the entire bowel is innervated by the vagus nerve is still contested. Evidence suggests that the innervation includes the distal colon at least in some animal models (126). The pelvic nerves may provide additional parasympathetic innervation to the lower gastrointestinal tract. However, a recent study argues that these nerves are actually part of the sympathetic nervous system (127).

Most enteric ganglia in the small intestine and stomach are innervated by vagal nerve fibers (128). The vast majority of vagal nerve fibers are sensory and transmit afferent input to the CNS. It

is unclear if afferent vagal signaling to the CNS is directly influenced by the ENS. Vagal-enteric (efferent) neurotransmission is predominantly cholinergic, although additional neurotransmitters have been identified in preganglionic vagal neurons (catecholamines and NO) and could have an auxiliary role (129, 130). Efferent vagal input affects all functions of the ENS, including the regulation of bowel motility, epithelial secretion, and vasoconstriction (4). Additionally, the vagus nerve mediates anti-inflammatory effects on the bowel through enteric neurons as part of the CAIP as described earlier (86).

1.16 Clinical relevance

The pathways described above confirm bidirectional communication between the ENS and CNS that has important effects on bowel function, but the gut also influence the brain, an interaction referred to as the “Gut-Brain Axis” (131). An additional intriguing hypothesis is that these pathways may lead to CNS disease since protein misfolding events that occur in the ENS could be initiators for certain CNS diseases such as Parkinson’s disease (PD). PD involves the prion-like misfolding of α-synuclein which aggregates into deposits called Lewy bodies, leading to neurodegeneration and dementia. Genetic changes or ingested toxins like the pesticide rotenone could first cause α-synuclein aggregation in the ENS (132), which then travels to the CNS via the vagus, where they induce misfolding of additional α-synuclein to cause the characteristic Lewy body pathology. Support for this hypothesis includes the observation that Lewy body-type pathology is found within enteric neurons of people with PD (133), bowel symptoms often precede CNS symptoms and correlate with disease severity (134), and that α-synuclein aggregates can travel from the bowel to the brain via the vagus nerve (135, 136). In humans, truncal vagotomy may reduce PD risk (137, 138). Similar transit of misfolded protein from the bowel to the brain could also explain the spread of prion diseases like kuru, variant Creutzfeldt-Jakob, scrapie, chronic wasting disease and spongiform encephalopathy where ingestion of misfolded prion proteins initiates disease pathogenesis (139). More details are provided in excellent reviews (140-142).

1.17 ENS and the CNS

Since the ENS shares many neurotransmitters, receptors, and transcription factors with the CNS, it is not surprising that many people with CNS disease also have problems with bowel function. People with autism spectrum disorder (ASD) are 3-4 times more likely to have gastrointestinal symptoms than unaffected individuals; intriguingly, mutations in chromodomain-helicase-DNA binding protein 8 (CDH8), haploinsufficiency for the transcription factor TCF4, an activating mutation in the sodium-dependent 5-HT transporter (SERT/SLC6A4), and MET mutations are all directly linked to ASD and GI motility disorders (58,143-146). Mice expressing mutant forms of amyloid precursor protein associated with familial Alzheimer disease accumulate amyloid beta in enteric neurons, have a reduced enteric neuron number, dysmotility and increased vulnerability to bowel inflammation (147, 148). Mutations in TAR DNA-binding protein 43 (TDP-43) that cause familial amyotrophic lateral sclerosis (ALS), may also cause ENS defects, including intestinal obstruction in the Prp-TDP43^{Ala315Thr} mouse model (149, 150). There is much more to learn about links between ENS and CNS disease.

1.18 Summary

The enteric neurons and glia richly integrate sensory stimuli to control bowel motility, epithelial function, blood flow, and immune system activity. To do this, almost every cell of the bowel wall closely interacts with the ENS including smooth muscle, ICC, PDGFRα+ cells, EEC, epithelial cells, blood vessels, and many hematopoietic lineages. The ENS also interacts with extrinsic sympathetic, parasympathetic and sensory nerves, and is influenced by hormonal signals to modulate bowel function to meet systemic needs. Mechanisms and cell types that impact ENS activity remain under-investigated. Defining molecular and cellular mechanisms of ENS activity promises new approaches to dangerous bowel motility disorders (Hirschsprung disease, CIPO, gastroparesis), common and less dangerous motility problems (irritable bowel syndrome, chronic

constipation, functional dyspepsia), inflammatory bowel disease, necrotizing enterocolitis, and ischemic bowel disease. Given links between gut microbes, bowel motility, epithelial function and CNS activity, ENS biology may also provide new approaches to addressing complex problems like anxiety, depression, autism, Parkinson's and ALS, and Alzheimer's disease as we begin to define the interplay along the gut brain axis.

1.19 Acknowledgements

ROH is supported by the Irma and Norman Braman Endowment, the Suzi and Scott Lustgarten Center Endowment, The Children's Hospital of Philadelphia Research Institute, March of Dimes 6-FY15-235, FDA (1R01FD005312-01), Canadian Institute of Health Research (377028) and the NIH SPARC Program OT2OD023859. CMW is supported by NIH NIDDK (1F30 DK117546-01). CMW and SS would like to thank Sanja Popovic, Tiancheng Wang, Sohaib Hashmi, and Natania Field for their unwavering support and insightful feedback.

1.20 References

1. Furness JB. 2006. The Enteric Nervous System. Malden, MA: Blackwell
2. Vanner S, Greenwood-Van Meerveld B, Mawe G, Shea-Donohue T, Verdu EF, et al. 2016. Fundamentals of neurogastroenterology: basic science. Gastroenterology 150:1280–91
3. Furness JB. 2016. Integrated neural and endocrine control of gastrointestinal function. Adv. Exp. Med. Biol. 891:159–73
4. Furness JB, Callaghan BP, Rivera LR, Cho HJ. 2014. The enteric nervous system and gastrointestinal innervation: integrated local and central control. Adv. Exp. Med. Biol. 817:39–71
5. Furness JB. 2012. The enteric nervous system and neurogastroenterology. Nat. Rev. Gastroenterol. Hepatol. 9:286–94

6. Sanders KM, Kito Y, Hwang SJ, Ward SM. 2016. Regulation of gastrointestinal smooth muscle function by interstitial cells. Physiology 31:316–26
7. Sanders KM, Koh SD, Ro S, Ward SM. 2012. Regulation of gastrointestinal motility—insights from smooth muscle biology. Nat. Rev. Gastroenterol. Hepatol. 9:633–45
8. Sanders KM, Hwang SJ, Ward SM. 2010. Neuroeffector apparatus in gastrointestinal smooth muscle organs. J. Physiol. 588:4621–39
9. Beckett EA, Horiguchi K, Khoyi M, Sanders KM, Ward SM. 2002. Loss of enteric motor neurotransmission in the gastric fundus of Sl/Sld mice. J. Physiol. 543:871–87
10. Klein S, Seidler B, Kettenberger A, Sibaev A, Rohn M, et al. 2013. Interstitial cells of Cajal integrate excitatory and inhibitory neurotransmission with intestinal slow-wave activity. Nat. Commun. 4:1630
11. Huizinga JD, Liu LW, Fitzpatrick A, White E, Gill S, et al. 2008. Deficiency of intramuscular ICC increases fundic muscle excitability but does not impede nitrergic innervation. Am. J. Physiol. Gastrointest. Liver Physiol. 294:G589–94
12. Groneberg D, Lies B, Konig P, J ¨ ager R, Seidler B, et al. 2013. Cell-specific deletion of nitric oxide- sensitive guanylyl cyclase reveals a dual pathway for nitrergic neuromuscular transmission in the murine fundus. Gastroenterology 145:188–96
13. Lies B, Gil V, Groneberg D, Seidler B, Saur D, et al. 2014. Interstitial cells of Cajal mediate nitrergic inhibitory neurotransmission in the murine gastrointestinal tract.Am. J. Physiol. Gastrointest. Liver Physiol. 307:G98–106
14. Kurahashi M, Mutafova-Yambolieva V, Koh SD, Sanders KM. 2014. Platelet-derived growth factor receptor-α-positive cells and not smooth muscle cells mediate purinergic hyperpolarization in murine colonic muscles. Am. J. Physiol. Cell Physiol. 307:C561–70
15. Kurahashi M, Zheng H, Dwyer L, Ward SM, Koh SD, Sanders KM. 2011. A functional role for the ‘fibroblast-like cells’ in gastrointestinal smooth muscles. J. Physiol. 589:697–710

16. Peri LE, Sanders KM, Mutafova-Yambolieva VN. 2013. Differential expression of genes related to purinergic signaling in smooth muscle cells, PDGFRα-positive cells, and interstitial cells of Cajal in the murine colon. Neurogastroenterol. Motil. 25:e609–20
17. Iino S, Horiguchi K, Nojyo Y. 2008. Interstitial cells of Cajal are innervated by nitrergic nerves and express nitric oxide-sensitive guanylate cyclase in the guinea-pig gastrointestinal tract.Neuroscience 152:437–48
18. Shahi PK, Choi S, Jeong YJ, Park CG, So I, Jun JY. 2014. Basal cGMP regulates the resting pacemaker potential frequency of cultured mouse colonic interstitial cells of Cajal. Naunyn Schmiedebergs Arch. Pharmacol. 387:641–48
19. Baker SA, Drumm BT, Cobine CA, Keef KD, Sanders KM. 2018. Inhibitory neural regulation of the Ca2+ transients in intramuscular interstitial cells of Cajal in the small intestine. Front. Physiol. 9:328
20. Hagen BM, Bayguinov O, Sanders KM. 2006. VIP and PACAP regulate localized Ca2+ transients via cAMP-dependent mechanism. Am. J. Physiol. Cell Physiol. 291:C375–85
21. Baker SA, Drumm BT, Skowronek KE, Rembetski BE, Peri LE, et al. 2018. Excitatory neuronal responses of Ca2+ transients in interstitial cells of Cajal in the small intestine. eNeuro 5. https://doi.org/10.1523/ENEURO.0080-18.2018
22. Zhu MH, Sung IK, Zheng H, Sung TS, Britton FC, et al. 2011. Muscarinic activation of Ca2+-activated Cl− current in interstitial cells of Cajal. J. Physiol. 589:4565–82
23. So KY, Kim SH, Sohn HM, Choi SJ, Parajuli SP, et al. 2009. Carbachol regulates pacemaker activities in cultured interstitial cells of Cajal from the mouse small intestine. Mol. Cells 27:525–31
24. Unno T, Matsuyama H, Izumi Y, Yamada M, Wess J, Komori S. 2006. Roles of M2 and M3 muscarinic receptors in cholinergic nerve-induced contractions in mouse ileum studied with receptor knockout mice. Br. J. Pharmacol. 149:1022–30

25. Lecci A, Capriati A, Altamura M, Maggi CA. 2006. Tachykinins and tachykinin receptors in the gut, with special reference to NK2 receptors in human. Auton. Neurosci. 126–127:232–49
26. Huizinga JD, Martz S, Gil V, Wang XY, Jimenez M, Parsons S. 2011. Two independent networks of interstitial cells of Cajal work cooperatively with the enteric nervous system to create colonic motor patterns. Front. Neurosci. 5:93
27. Kugler EM, Michel K, Zeller F, Demir IE, Ceyhan GO, et al. 2015. Mechanical stress activates neurites and somata of myenteric neurons. Front. Cell Neurosci. 9:342
28. Li Z, Chalazonitis A, Huang YY, Mann JJ, Margolis KG, et al. 2011. Essential roles of enteric neuronal serotonin in gastrointestinal motility and the development/survival of enteric dopaminergic neurons. J. Neurosci. 31:8998–9009
29. Heredia DJ, Gershon MD, Koh SD, Corrigan RD, Okamoto T, Smith TK. 2013. Important role of mucosal serotonin in colonic propulsion and peristaltic reflexes: in vitro analyses in mice lacking tryptophan hydroxylase 1. J. Physiol. 591:5939–57
30. Kendig DM, Grider JR. 2015. Serotonin and colonic motility. Neurogastroenterol. Motil. 27:899–905
31. Rao M, Rastelli D, Dong L, Chiu S, Setlik W, et al. 2017. Enteric glia regulate gastrointestinal motility but are not required for maintenance of the epithelium in mice. Gastroenterology 153:1068–81.e7
32. McClain J, Grubišić V, Fried D, Gomez-Suarez RA, Leinninger GM, et al. 2014. Ca ´ 2+ responses in enteric glia are mediated by connexin-43 hemichannels and modulate colonic transit in mice. Gastroenterology 146:497–507.e1
33. Bassotti G, Villanacci V, Antonelli E, Morelli A, Salerni B. 2007. Enteric glial cells: New players in gastrointestinal motility? Lab. Investig. 87:628–32
34. Heuckeroth RO. 2018. Hirschsprung disease—integrating basic science and clinical medicine to improve outcomes. Nat. Rev. Gastroenterol. Hepatol. 15:152–67

35. Antonucci A, Fronzoni L, Cogliandro L, Cogliandro RF, Caputo C, et al. 2008. Chronic intestinal pseudo-obstruction. World J. Gastroenterol. 14:2953–61
36. Ravenscroft G, Pannell S, O'Grady G, Ong R, Ee HC, et al. 2018. Variants in ACTG2 underlie a substantial number of Australasian patients with primary chronic intestinal pseudo-obstruction. Neurogastroenterol. Motil. 2018:e13371
37. Di Nardo G, Di Lorenzo C, Lauro A, Stanghellini V, Thapar N, et al. 2017. Chronic intestinal pseudoobstruction in children and adults: diagnosis and therapeutic options. Neurogastroenterol. Motil. 29:e12945
38. Bertrand PP, Kunze WA, Furness JB, Bornstein JC. 2000. The terminals of myenteric intrinsic primary afferent neurons of the guinea-pig ileum are excited by 5-hydroxytryptamine acting at 5-hydroxytryptamine-3 receptors. Neuroscience 101:459–69
39. Vanner S, Macnaughton WK. 2004. Submucosal secretomotor and vasodilator reflexes. Neurogastroenterol. Motil. 16(Suppl. 1):39–43
40. Reed DE, Vanner SJ. 2003. Long vasodilator reflexes projecting through the myenteric plexus in guineapig ileum. J. Physiol. 553:911–24
41. Weber E, Neunlist M, Schemann M, Frieling T. 2001. Neural components of distension-evoked secretory responses in the guinea-pig distal colon. J. Physiol. 536:741–51
42. Mazzuoli-Weber G, Schemann M. 2015. Mechanosensitivity in the enteric nervous system. Front. Cell Neurosci. 9:408
43. Vanner S, Surprenant A. 1996. Neural reflexes controlling intestinal microcirculation. Am. J. Physiol. 271:G223–30
44. Vanner S, Surprenant A. 1991. Cholinergic and noncholinergic submucosal neurons dilate arterioles in guinea pig colon. Am. J. Physiol. 261:G136–44
45. Stead RH, Tomioka M, Quinonez G, Simon GT, Felten SY, Bienenstock J. 1987. Intestinal mucosal mast cells in normal and nematode-infected rat intestines are in intimate contact with peptidergic nerves. PNAS 84:2975–79

46. Downard CD, Grant SN, Matheson PJ, Guillaume AW, Debski R, et al. 2011. Altered intestinal microcirculation is the critical event in the development of necrotizing enterocolitis. J. Pediatr. Surg. 46:1023–28
47. Zhou Y, Yang J, Watkins DJ, Boomer LA, Matthews MA, et al. 2013. Enteric nervous system abnormalities are present in human necrotizing enterocolitis: potential neurotransplantation therapy. Stem Cell Res. Ther. 4:157
48. Nowicki PT, Caniano DA, Hammond S, Giannone PJ, Besner GE, et al. 2007. Endothelial nitric oxide synthase in human intestine resected for necrotizing enterocolitis. J. Pediatr. 150:40–45
49. Hatoum OA, Binion DG, Otterson MF, Gutterman DD. 2003. Acquired microvascular dysfunction in inflammatory bowel disease: loss of nitric oxide-mediated vasodilation. Gastroenterology 125:58–69
50. Xue J, Askwith C, Javed NH, Cooke HJ. 2007. Autonomic nervous system and secretion across the intestinal mucosal surface. Auton. Neurosci. 133:55–63
51. Banks MR, Farthing MJ. 2002. Fluid and electrolyte transport in the small intestine. Curr. Opin. Gastroenterol. 18:176–81
52. Grubišić V, Gulbransen BD. 2017. Enteric glial activity regulates secretomotor function in the mouse colon but does not acutely affect gut permeability. J. Physiol. 595:3409–24
53. Lane R, Baldwin D. 1997. Selective serotonin reuptake inhibitor-induced serotonin syndrome: review. J. Clin. Psychopharmacol. 17:208–21
54. Jones SL, Blikslager AT. 2002. Role of the enteric nervous system in the pathophysiology of secretory diarrhea. J. Vet. Intern. Med. 16:222–28
55. Eklund S, Jodal M, Lundgren O. 1985. The enteric nervous system participates in the secretory response to the heat stable enterotoxins of Escherichia coli in rats and cats. Neuroscience 14:673–81
56. Hernandes L, Zucoloto S, Alvares EP. 2000. Effect of myenteric denervation on intestinal epithelium proliferation and migration of suckling and weanling rats. Cell Prolif. 33:127–38

57. Hitch MC, Leinicke JA, Wakeman D, Guo J, Erwin CR, et al. 2012. Ret heterozygous mice have enhanced intestinal adaptation after massive small bowel resection. Am. J. Physiol. Gastrointest. Liver Physiol. 302:G1143–50
58. Avetisyan M, Wang H, Schill EM, Bery S, Grider JR, et al. 2015. Hepatocyte growth factor and MET support mouse enteric nervous system development, the peristaltic response, and intestinal epithelial proliferation in response to injury. J. Neurosci. 35:11543–58
59. Takahashi T, Shiraishi A, Murata J. 2018. The coordinated activities of nAChR and Wnt signaling regulate intestinal stem cell function in mice. Int. J. Mol. Sci. 19:738
60. Greig CJ, Cowles RA. 2017. Muscarinic acetylcholine receptors participate in small intestinal mucosal homeostasis. J. Pediatr. Surg. 52:1031–34
61. Lundgren O, Jodal M, Jansson M, Ryberg AT, Svensson L. 2011. Intestinal epithelial stem/progenitor cells are controlled by mucosal afferent nerves. PLOS ONE 6:e16295
62. Muise ED, Gandotra N, Tackett JJ, Bamdad MC, Cowles RA. 2017. Distribution of muscarinic acetylcholine receptor subtypes in the murine small intestine. Life Sci. 169:6–10
63. Gross ER, Gershon MD, Margolis KG, Gertsberg ZV, Li Z, Cowles RA. 2012. Neuronal serotonin regulates growth of the intestinal mucosa in mice. Gastroenterology 143:408–17.e2
64. Bjerknes M, Cheng H. 2001. Modulation of specific intestinal epithelial progenitors by enteric neurons. PNAS 98:12497–502
65. Leen JL, Izzo A, Upadhyay C, Rowland KJ, Dube PE, et al. 2011. Mechanism of action of glucagon-like peptide-2 to increase IGF-I mRNA in intestinal subepithelial fibroblasts. Endocrinology 152:436–46
66. Puzan M, Hosic S, Ghio C, Koppes A. 2018. Enteric nervous system regulation of intestinal stem cell differentiation and epithelial monolayer function. Sci. Rep. 8:6313
67. Cornet A, Savidge TC, Cabarrocas J, Deng WL, Colombel JF, et al. 2001. Enterocolitis induced by autoimmune targeting of enteric glial cells: a possible mechanism in Crohn's disease? PNAS 98:13306–11

68. Aube AC, Cabarrocas J, Bauer J, Philippe D, Aubert P, et al. 2006. Changes in enteric neurone phenotype and intestinal functions in a transgenic mouse model of enteric glia disruption. Gut 55:630–37
69. Savidge TC, Newman P, Pothoulakis C, Ruhl A, Neunlist M, et al. 2007. Enteric glia regulate intestinal barrier function and inflammation via release of S-nitrosoglutathione. Gastroenterology 132:1344–58
70. Bush TG, Savidge TC, Freeman TC, Cox HJ, Campbell EA, et al. 1998. Fulminant jejuno-ileitis following ablation of enteric glia in adult transgenic mice. Cell 93:189–201
71. Van Landeghem L, Mahe MM, Teusan R, Leger J, Guisle I, et al. 2009. Regulation of intestinal epithelial cell's transcriptome by enteric glial cells: impact on intestinal epithelial barrier functions. BMC Genom. 10:507
72. von Boyen GB, Schulte N, Pfluger C, Spaniol U, Hartmann C, Steinkamp M. 2011. Distribution of enteric glia and GDNF during gut inflammation. BMC Gastroenterol. 11:3
73. Xiao WD, Chen W, Sun LH, Wang WS, Zhou SW, Yang H. 2011. The protective effect of enteric glial cells on intestinal epithelial barrier function is enhanced by inhibiting inducible nitric oxide synthase activity under lipopolysaccharide stimulation. Mol. Cell Neurosci. 46:527–34
74. Xiao W, Wang W, Chen W, Sun L, Li X, et al. 2014. GDNF is involved in the barrier-inducing effect of enteric glial cells on intestinal epithelial cells under acute ischemia reperfusion stimulation. Mol. Neurobiol. 50:274–89
75. Steinkamp M, Geerling I, Seufferlein T, von Boyen G, Egger B, et al. 2003. Glial-derived neurotrophic factor regulates apoptosis in colonic epithelial cells. Gastroenterology 124:1748–57
76. Zhang DK, He FQ, Li TK, Pang XH, Cui DJ, et al. 2010. Glial-derived neurotrophic factor regulates intestinal epithelial barrier function and inflammation and is therapeutic for murine colitis. J. Pathol. 222:213–22

77. Ibiza S, Garc´ıa-Cassani B, Ribeiro H, Carvalho T, Almeida L, et al. 2016. Glial-cell-derived neuroregulators control type 3 innate lymphoid cells and gut defence. Nature 535:440–43
78. Gabanyi I, Muller PA, Feighery L, Oliveira TY, Costa-Pinto FA, Mucida D. 2016. Neuro-immune interactions drive tissue programming in intestinal macrophages. Cell 164:378–91
79. Chalazonitis A, Pham TD, Li Z, Roman D, Guha U, et al. 2008. Bone morphogenetic protein regulation of enteric neuronal phenotypic diversity: relationship to timing of cell cycle exit. J. Comp. Neurol. 509:474–92
80. Fu M, Vohra BPS, Wind D, Heuckeroth RO. 2006. BMP signaling regulates murine enteric nervous system precursor migration, neurite fasciculation, and patterning via altered Ncam1 polysialic acid addition. Dev. Biol. 299:137–50
81. Muller PA, Koscso B, Rajani GM, Stevanovic K, Berres ML, et al. 2014. Crosstalk between muscularis macrophages and enteric neurons regulates gastrointestinal motility. Cell 158:300–13
82. Kulkarni S, Micci MA, Leser J, Shin C, Tang SC, et al. 2017. Adult enteric nervous system in health is maintained by a dynamic balance between neuronal apoptosis and neurogenesis. PNAS 114:E3709–18
83. De Schepper S, Stakenborg N, Matteoli G, Verheijden S, Boeckxstaens GE. 2017. Muscularis macrophages: key players in intestinal homeostasis and disease. Cell Immunol. 330:142–50
84. Cipriani G, Gibbons SJ, Kashyap PC, Farrugia G. 2016. Intrinsic gastrointestinal macrophages: their phenotype and role in gastrointestinal motility. Cell Mol. Gastroenterol. Hepatol. 2:120–30.e1
85. Chandrasekharan B, Jeppsson S, Pienkowski S, Belsham DD, Sitaraman SV, et al. 2013. Tumor necrosis factor-neuropeptide Y cross talk regulates inflammation, epithelial barrier functions, and colonic motility. Inflamm. Bowel Dis. 19:2535–46

86. Matteoli G, Gomez-Pinilla PJ, Nemethova A, Di Giovangiulio M, Cailotto C, et al. 2014. A distinct vagal anti-inflammatory pathway modulates intestinal muscularis resident macrophages independent of the spleen. Gut 63:938–48
87. Wang H, Yu M, Ochani M, Amella CA, Tanovic M, et al. 2003. Nicotinic acetylcholine receptor α7 subunit is an essential regulator of inflammation. Nature 421:384–88
88. de Jonge WJ, van der Zanden EP, The FO, Bijlsma MF, van Westerloo DJ, et al. 2005. Stimulation of the vagus nerve attenuates macrophage activation by activating the Jak2-STAT3 signaling pathway. Nat. Immunol. 6:844–51
89. Avetisyan M, Rood JE, Huerta Lopez S, Sengupta R, Wright-Jin E, et al. 2018. Muscularis macrophage development in the absence of an enteric nervous system. PNAS 115:4696–701
90. Wehner S, Behrendt FF, Lyutenski BN, Lysson M, Bauer AJ, et al. 2007. Inhibition of macrophage function prevents intestinal inflammation and postoperative ileus in rodents. Gut 56:176–85
91. The FO, Cailotto C, van der Vliet J, de Jonge WJ, Bennink RJ, et al. 2011. Central activation of the cholinergic anti-inflammatory pathway reduces surgical inflammation in experimental post-operative ileus. Br. J. Pharmacol. 163:1007–16
92. Anitha M, Vijay-Kumar M, Sitaraman SV, Gewirtz AT, Srinivasan S. 2012. Gut microbial products regulate murine gastrointestinal motility via Toll-like receptor 4 signaling. Gastroenterology 143:1006–16.e4
93. Collins J, Borojevic R, Verdu EF, Huizinga JD, Ratcliffe EM. 2014. Intestinal microbiota influence the early postnatal development of the enteric nervous system. Neurogastroenterol. Motil. 26:98–107
94. Barajon I, Serrao G, Arnaboldi F, Opizzi E, Ripamonti G, et al. 2009. Toll-like receptors 3, 4, and 7 are expressed in the enteric nervous system and dorsal root ganglia. J. Histochem. Cytochem. 57:1013–23

95. Brun P, GironMC, QesariM, Porzionato A, Caputi V, et al. 2013. Toll-like receptor 2 regulates intestinal inflammation by controlling integrity of the enteric nervous system. Gastroenterology 145:1323–33

96. Reichardt F, Chassaing B, Nezami BG, Li G, Tabatabavakili S, et al. 2017. Western diet induces colonic nitrergic myenteric neuropathy and dysmotility in mice via saturated fatty acid- and lipopolysaccharideinduced TLR4 signalling. J. Physiol. 595:1831–46

97. Uesaka T, Nagashimada M, Enomoto H. 2013. GDNF signaling levels control migration and neuronal differentiation of enteric ganglion precursors. J. Neurosci. 33:16372–82

98. Grider JR, Heuckeroth RO, Kuemmerle JF, Murthy KS. 2010. Augmentation of the ascending component of the peristaltic reflex and substance P release by glial cell line-derived neurotrophic factor. Neurogastroenterol. Motil. 22:779–86

99. McVey Neufeld KA, Mao YK, Bienenstock J, Foster JA, Kunze WA. 2013. The microbiome is essential for normal gut intrinsic primary afferent neuron excitability in the mouse. Neurogastroenterol. Motil. 25:183-e88

100. Lomasney KW, Cryan JF, Hyland NP. 2014. Converging effects of a Bifidobacterium and Lactobacillus probiotic strain on mouse intestinal physiology. Am. J. Physiol. Gastrointest. Liver Physiol. 307:G241–47

101. Wang B, Mao YK, Diorio C, Wang L, Huizinga JD, et al. 2010. Lactobacillus reuteri ingestion and IKCa channel blockade have similar effects on rat colon motility and myenteric neurones. Neurogastroenterol. Motil. 22:98–107.e33

102. Rolig AS, Mittge EK, Ganz J, Troll JV, Melancon E, et al. 2017. The enteric nervous system promotes intestinal health by constraining microbiota composition. PLOS Biol. 15:e2000689

103. Hyland NP, Cryan JF. 2016. Microbe-host interactions: Influence of the gut microbiota on the enteric nervous system. Dev. Biol. 417:182–87

104. Kabouridis PS, Pachnis V. 2015. Emerging roles of gut microbiota and the immune system in the development of the enteric nervous system. J. Clin. Investig. 125:956–64

105. Chiocchetti R, Mazzuoli G, Albanese V, Mazzoni M, Clavenzani P, et al. 2008. Anatomical evidence for ileal Peyer's patches innervation by enteric nervous system: a potential route for prion neuroinvasion? Cell Tissue Res. 332:185–94

106. Vulchanova L, Casey MA, Crabb GW, Kennedy WR, Brown DR. 2007. Anatomical evidence for enteric neuroimmune interactions in Peyer's patches. J. Neuroimmunol. 185:64–74

107. Stanisz AM, Befus D, Bienenstock J. 1986. Differential effects of vasoactive intestinal peptide, substance P, and somatostatin on immunoglobulin synthesis and proliferations by lymphocytes from Peyer's patches, mesenteric lymph nodes, and spleen. J. Immunol. 136:152–56

108. Farzi A, Reichmann F, Holzer P. 2015. The homeostatic role of neuropeptide Y in immune function and its impact on mood and behaviour. Acta Physiol. 213:603–27

109. Wheway J, Mackay CR, Newton RA, Sainsbury A, Boey D, et al. 2005. A fundamental bimodal role for neuropeptide Y1 receptor in the immune system. J. Exp. Med. 202:1527–38

110. Gonzalez-Rey E, Fernandez-Martin A, Chorny A, Delgado M. 2006. Vasoactive intestinal peptide induces CD4+, CD25+ T regulatory cells with therapeutic effect in collagen-induced arthritis. Arthritis Rheum. 54:864–76

111. Gonzalez-Rey E, Chorny A, Fernandez-Martin A, Ganea D, Delgado M. 2006. Vasoactive intestinal peptide generates human tolerogenic dendritic cells that induce CD4 and CD8 regulatory T cells. Blood 107:3632–38

112. Delgado M, Gonzalez-Rey E, Ganea D. 2005. The neuropeptide vasoactive intestinal peptide generates tolerogenic dendritic cells. J. Immunol. 175:7311–24

113. Abad C, Cheung-Lau G, Coute-Monvoisin AC, Waschek JA. 2015. Vasoactive intestinal peptide-deficient mice exhibit reduced pathology in trinitrobenzene sulfonic acid-induced colitis. Neuroimmunomodulation 22:203–12

114. Abad C, Tan YV, Cheung-Lau G, Nobuta H, Waschek JA. 2012. VIP deficient mice exhibit resistance to lipopolysaccharide induced endotoxemia with an intrinsic defect in proinflammatory cellular responses. PLOS ONE 7:e36922

115. Latorre R, Sternini C, De Giorgio R, Greenwood-Van Meerveld B. 2016. Enteroendocrine cells: a review of their role in brain-gut communication. Neurogastroenterol. Motil. 28:620–30

116. Bellono NW, Bayrer JR, Leitch DB, Castro J, Zhang C, et al. 2017. Enterochromaffin cells are gut chemosensors that couple to sensory neural pathways. Cell 170:185–98.e16

117. He Y, Wang H, Yang D, Wang C, Yang L, Jin C. 2015. Differential expression of motilin receptor in various parts of gastrointestinal tract in dogs. Gastroenterol. Res. Pract. 2015:970940

118. Amato A, Cinci L, Rotondo A, Serio R, Faussone-Pellegrini MS, et al. 2010. Peripheral motor action of glucagon-like peptide-1 through enteric neuronal receptors. Neurogastroenterol. Motil. 22:664-e203

119. Sayegh AI, Ritter RC. 2003. Cholecystokinin activates specific enteric neurons in the rat small intestine. Peptides 24:237–44

120. Bohorquez DV, Shahid RA, Erdmann A, Kreger AM, Wang Y, et al. 2015. Neuroepithelial circuit formed by innervation of sensory enteroendocrine cells. J. Clin. Investig. 125:782–86

121. Berthoud HR, Jedrzejewska A, Powley TL. 1990. Simultaneous labeling of vagal innervation of the gut and afferent projections from the visceral forebrain with Dil injected into the dorsal vagal complex in the rat. J. Comp. Neurol. 301:65–79

122. Lomax AE, Sharkey KA, Furness JB. 2010. The participation of the sympathetic innervation of the gastrointestinal tract in disease states. Neurogastroenterol. Motil. 22:7–18

123. Gulbransen BD, Bains JS, Sharkey KA. 2010. Enteric glia are targets of the sympathetic innervation of the myenteric plexus in the guinea pig distal colon. J. Neurosci. 30:6801–9

124. Sjövall H, Redfors S, Hallbäck DA, Eklund S, Jodal M, Lundgren O. 1983. The effect of splanchnic nerve stimulation on blood flow distribution, villous tissue osmolality and fluid and electrolyte transport in the small intestine of the cat. Acta Physiol. Scand. 117:359–65

125. Sjövall H, Redfors S, Jodal M, Lundgren O. 1983. On the mode of action of the sympathetic fibres on intestinal fluid transport: evidence for the existence of a glucose-stimulated secretory nervous pathway in the intestinal wall. Acta Physiol. Scand. 119:39–48

126. Altschuler SM, Escardo J, Lynn RB, Miselis RR. 1993. The central organization of the vagus nerve innervating the colon of the rat. Gastroenterology 104:502–9

127. Espinosa-Medina I, Saha O, Boismoreau F, Chettouh Z, Rossi F, et al. 2016. The sacral autonomic outflow is sympathetic. Science 354:893–97

128. Walter GC, Phillips RJ, Baronowsky EA, Powley TL. 2009. Versatile, high-resolution anterograde labeling of vagal efferent projections with dextran amines. J. Neurosci. Methods 178:1–9

129. Kalia M, Fuxe K, Goldstein M, Harfstrand A, Agnati LF, Coyle JT. 1984. Evidence for the existence of putative dopamine-, adrenaline- and noradrenaline-containing vagal motor neurons in the brainstem of the rat. Neurosci. Lett. 50:57–62

130. Hyland NP, Abrahams TP, Fuchs K, Burmeister MA, Hornby PJ. 2001. Organization and neurochemistry of vagal preganglionic neurons innervating the lower esophageal sphincter in ferrets. J. Comp. Neurol. 430:222–34

131. Powell N, Walker MM, Talley NJ. 2017. The mucosal immune system: master regulator of bidirectional gut-brain communications. Nat. Rev. Gastroenterol. Hepatol. 14:143–59

132. Pan-Montojo F, Anichtchik O, Dening Y, Knels L, Pursche S, et al. 2010. Progression of Parkinson’s disease pathology is reproduced by intragastric administration of rotenone in mice. PLOS ONE 5:e8762

133. Braak H, de Vos RA, Bohl J, Del Tredici K. 2006. Gastric α-synuclein immunoreactive inclusions in Meissner's and Auerbach's plexuses in cases staged for Parkinson's disease-related brain pathology. Neurosci. Lett. 396:67–72

134. Edwards LL, Pfeiffer RF, Quigley EM, Hofman R, Balluff M. 1991. Gastrointestinal symptoms in Parkinson's disease. Mov. Disord. 6:151–56

135. Holmqvist S, Chutna O, Bousset L, Aldrin-Kirk P, Li W, et al. 2014. Direct evidence of Parkinson pathology spread from the gastrointestinal tract to the brain in rats. Acta Neuropathol. 128:805–20

136. Ulusoy A, Rusconi R, Perez-Revuelta BI, Musgrove RE, Helwig M, et al. 2013. Caudo-rostral brain spreading of α-synuclein through vagal connections. EMBO Mol. Med. 5:1119–27

137. Liu B, Fang F, Pedersen NL, Tillander A, Ludvigsson JF, et al. 2017. Vagotomy and Parkinson disease: a Swedish register-based matched-cohort study. Neurology 88:1996–2002

138. Svensson E, Horvath-Puh ´ o E, Thomsen RW, Djurhuus JC, Pedersen L, et al. 2015. Vagotomy and subsequent risk of Parkinson's disease. Ann. Neurol. 78:522–29

139. Kaatz M, Fast C, Ziegler U, Balkema-Buschmann A, Hammerschmidt B, et al. 2012. Spread of classic BSE prions from the gut via the peripheral nervous system to the brain. Am. J. Pathol. 181:515–24

140. Rao M, Gershon MD. 2016. The bowel and beyond: the enteric nervous system in neurological disorders. Nat. Rev. Gastroenterol. Hepatol. 13:517–28

141. Del Tredici K, Braak H. 2016. Sporadic Parkinson's disease: development and distribution of α-synuclein pathology. Neuropathol. Appl. Neurobiol. 42:33–50

142. Natale G, Ferrucci M, Lazzeri G, Paparelli A, Fornai F. 2011. Transmission of prions within the gut and towards the central nervous system. Prion 5:142–49

143. Bernier R, Golzio C, Xiong B, Stessman HA, Coe BP, et al. 2014. Disruptive CHD8 mutations define a subtype of autism early in development. Cell 158:263–76114.

144. Grubišić V, Kennedy AJ, Sweatt JD, Parpura V. 2015. Pitt-Hopkins mouse model has altered particular gastrointestinal transits in vivo. Autism Res. 8:629–33

145. Margolis KG, Li Z, Stevanovic K, Saurman V, Israelyan N, et al. 2016. Serotonin transporter variant drives preventable gastrointestinal abnormalities in development and function. J. Clin. Investig. 126:2221–35

146. Peng Y, Huentelman M, Smith C, Qiu S. 2013. MET receptor tyrosine kinase as an autism genetic risk factor. Int. Rev. Neurobiol. 113:135–65

147. Puig KL, Lutz BM, Urquhart SA, Rebel AA, Zhou X, et al. 2015. Overexpression of mutant amyloid-β protein precursor and presenilin 1 modulates enteric nervous system. J. Alzheimers Dis. 44:1263–78

148. Semar S, Klotz M, Letiembre M, Van Ginneken C, Braun A, et al. 2013. Changes of the enteric nervous system in amyloid-β protein precursor transgenic mice correlate with disease progression. J. Alzheimers Dis. 36:7–20

149. Guo Y, Wang Q, Zhang K, An T, Shi P, et al. 2012. HO-1 induction in motor cortex and intestinal dysfunction in TDP-43 A315T transgenic mice. Brain Res. 1460:88–95

150. Esmaeili MA, Panahi M, Yadav S, Hennings L, Kiaei M. 2013. Premature death of TDP-43 (A315T) transgenic mice due to gastrointestinal complications prior to development of full neurological symptoms of amyotrophic lateral sclerosis. Int. J. Exp. Pathol. 94:56–64

CHAPTER 2: scRNA-SEQUENCING REVEALS NEW ENTERIC NERVOUS SYSTEM ROLES FOR GDNF, NRTN, AND TBX3

This manuscript is under review. Authors: Christina M. Wright*, Sabine Schneider*, Kristen M. Smith-Edwards, Fernanda Mafra, Anita J.L. Leembruggen, Michael V. Gonzalez, Deepika R. Kothakapa, Jessica B. Anderson, Beth A. Maguire, Tao Gao, Tricia A. Missall, Marthe J. Howard, Joel C. Bornstein, Brian M. Davis, and Robert O. Heuckeroth.

*Co-first authors; contributed equally

2.1 Abstract

Bowel function requires coordinated activity of many enteric neuron subtypes. Clear definition of subtype-specific gene expression may facilitate molecular diagnoses for bowel motility disorders. Using adult mouse colon RNAseq data from 635 myenteric neurons and 707 E17.5 neurons, we defined seven adult myenteric neuron subtypes, eight E17.5 neuron subtypes and hundreds of differentially- expressed genes. Manually dissected human colon myenteric plexus yielded data from 48 neurons, 3798 glia, 5568 smooth muscle, 377 interstitial cells, and 2153 macrophages. Immunohistochemistry demonstrated differential protein abundance for BNC2, PBX3, RBFOX1, TBX2, and TBX3 in enteric neuron subtypes. Conditional *Tbx3* loss reduced NOS1-expressing myenteric neurons. Differential *Gfra1* and *Gfra2* expression coupled with calcium imaging revealed that GDNF and neurturin acutely and differentially regulate activity of ~50% of myenteric neurons with distinct effects on smooth muscle contractions. This insight into enteric nervous system biology provides a foundation for future studies of bowel motility disorders.

2.2 Introduction

The enteric nervous system (ENS) is a network of neurons and glia within the bowel wall that controls gut motility, mucosal immunity, epithelial function and proliferation, along with vasodilation in response to local and extrinsic stimuli (1–3). Thus, ENS defects can cause debilitating bowel dysfunction. Defects include developmental anomalies like Hirschsprung disease (HSCR) and primary chronic intestinal pseudo-obstruction. Acquired ENS defects occur in achalasia, Parkinson's disease, Chagas, and probably gastroparesis and irritable bowel syndrome. Unfortunately, we currently have limited ability to identify missing or defective ENS cell populations in people with bowel dysmotility and available therapies are often ineffective. Even if missing cells were identified, neurotransmitters, receptors, and signaling pathways that may be therapeutic targets in the ENS are poorly defined. Potential new therapies include stem cell replacement (4), trophic factor-induced regeneration (5) and repurposing medicines based on genetic polymorphisms that underlie symptoms. Each strategy would benefit from detailed data about ENS gene expression.

Our goal was to use single cell RNAseq in mouse and human enteric neurons to gain new insight into enteric neuron subtype identity, regional neuron identity, and to learn more about how RET ligands impact neural activity and motility in adult mice. As our studies proceeded, other groups described single cell ENS RNAseq data from P21 mouse small bowel (6) and adult mouse bowel with or without gut microbes (7). New bioRxiv papers also provide single cell RNAseq data from adult mouse and human colon (8), and from E15.5, E18.5, and P21 mouse small bowel (9). Each manuscript has a unique focus. These data, along with our analyses, provide the rich tapestry of ENS gene expression information needed for progress in diagnosing and treating bowel motility disorders.

The RNA-seq data collectively define 8-12 myenteric neuron types and >20 total enteric neuron types, plus 4-7 types of enteric glia, consistent with anatomic and functional analyses over decades (2,10–13). Here we focus on distinctions between myenteric nitrergic (nitric oxide

producing) and cholinergic (acetylcholine producing) neurons, which comprise >89% of human and >95% of mouse myenteric neurons (14,15). We found many cell type-specific ion channels, neurotransmitters, adhesion proteins, and signaling pathways supporting functional connectivity, and identified >40 differentially expressed transcriptional regulators, including *Tbx3*, which is preferentially expressed in neuronal nitric oxide synthase (NOS1)-producing myenteric neurons. *Tbx3*-/- mice had a 30% reduction in NOS1 neurons. We also found that *Pbx3* is preferentially expressed in cholinergic neurons, consistent with a report that *Pbx3*-/- mice have fewer CALB1+ cholinergic neurons (9). Further, *Pou3f3* marks colon, but not small bowel, neurons from early development to adulthood, consistent with distinct ENS organization and function in colon versus small bowel.

An additional major distinction is that nitrergic neurons predominantly express Gfra1, but cholinergic neurons express *Gfra2* in adult and E17.5 mouse myenteric plexus. GFRA1 and GFRA2 are cell surface receptors that bind preferentially to glial cell line-derived neurotrophic factor (GDNF) and neurturin (NRTN), respectively, and this binding activates RET kinase. RET impacts many signaling pathways and has clear trophic effects (16), but if the only purpose of GDNF/GFRA1 and of NRTN/GFRA2 signaling was to activate RET, it is unclear why distinct trophic factors and co-receptors would be advantageous once development is complete. We thus used calcium imaging to test the hypothesis that GDNF and NRTN acutely affect ENS function and bowel motility. We discovered strikingly different effects of these trophic factors on GCaMP6s activity in enteric neurons. Collectively, our single cell RNAseq data provide highly validated information about gene expression in mouse and human ENS and a new foundation for ENS cell classification. Our novel observations about TBX3, GDNF/GFRA1, NRTN/GFRA2, POU3F3, and many other genes also offer distinct new insights that could facilitate stem cell or trophic factor based therapies for human bowel motility disorders.

2.3 Results

Single nucleus RNA-sequencing defines mouse distal colon enteric neuron subpopulations

Isolating ENS cells from adult mouse distal colon was challenging. Many approaches did not work well (**Supplementary Table 2.1**). Ultimately, myenteric plexus nuclei were isolated from 47-52 day old *Wnt1-Cre*$^{Cre/wt}$*; R26R-LSL-H2B-mCherry* mice that express the fluorescent nuclear protein Histone 2B-mCherry (**Supplementary Figure 2.1A-D**). Cryosectioning disrupted muscle, improving yield. Dounce homogenization released nuclei (**Figure 2.1A**). 10x Genomics platform generated data from 1,520 mCherry+ neuronal (**Figure 2.1B**) and glial nuclei. Because of low read depth we included intronic reads, yielding a mean of 2,970 unique molecular identifiers (UMI, number of unique RNA molecules sequenced) and 1,549 genes per cell.

Using CellRanger and Seurat (17,18), we identified 12 clusters: 4 glial (*Plp1*+ and *Sox10*+), 4 neuronal (*Elavl4*+), and several non-ENS (6.5% of total), including *Pdgfra*+ (PDGFRα+ cells), *Kit*+ (interstitial cells of Cajal, ICC), and *Actg2*+ (smooth muscle cells (SMC); **Supplementary Figure 2.1E-J**). Mean UMI and gene counts were higher for neurons than glia (Neurons: 4,629 UMI and 2,217 genes; Glia: 1,780 UMI, 1,069 genes; **Figure 2.1C**). To refine analyses, we re-clustered neuronal groups (**Figure 2.1B**) and identified 7 clusters (635 neurons total).

Two neuron groups (Nos1 and Nos2) express *Nos1*, *Vip*, and *Gal*, consistent with known co-expression in inhibitory motor neurons and interneurons that have NOS1+/VIP+ nerve terminals within circular smooth muscle and myenteric ganglia respectively (13,19). Chat1 cells express choline acetyl-transferase (*Chat*) and preprotachykinin (substance P precursor, Tac1), but not proenkephalin (*Penk*), consistent with excitatory motor neurons or intrinsic sensory neurons (20,21). Chat2 cells express *Chat*, *Tac1* and *Penk*, a combination marking guinea pig ileum excitatory motor neurons and ascending interneurons. Chat3 cells express *Chat*, *Tac1, Penk,* and hepatocyte growth factor receptor *Met* (**Figure 2.1D, E, Supplementary Figure 2.2E**). We tested if *Tac1* and *Penk* expression could differentiate between motor- and interneurons. Immunohistochemistry showed that in circular smooth muscle, 55.3± 8.4% of varicosities

containing substance P (SP) do not contain enkephalin (ENK; **Supplementary Figure 2.1K-M, S**), but in myenteric ganglia, ~25% of SP terminals lack ENK and vice versa (**Supplementary Figure 2.1N-P, S**). An additional clustered neuron group appeared heterogeneous. We manually divided these neurons into Chat4 that express *Chat, Penk*, and *Slc17a6* (encodingVGLUT2) and Calcb that express *Calcb* (Calcitonin Related Polypeptide Beta)*, Grp* (Gastrin releasing peptide) and *Nmu* (Neuromedin U)). We hypothesize that Chat4 are interneurons since VAChT+/VGLUT2+ terminals were reported in mouse distal colon myenteric ganglia, but not muscle (22) *Chat/Penk/Vglut2* neurons also express *Calb1*, a calcium-binding protein in mouse interneurons (13,23,24). To further validate *Vglut2*/*Chat* co-expression, we bred *Vglut2-IRES-Cre;TdTomato* x *ChAT-L10A-EGFP* and found 95.9 ± 0.9% of TDTOMATO+ neurons in myenteric plexus co-expressed EGFP (**Supplementary Figure 2.1T-V**).

Many neurotransmitters (**Figure 2.1E; Supplementary Figure 2.2A**) and neurotransmitter receptors (**Figure 2.1F; Supplementary Figure 2.2B**) were differentially expressed between neuron subgroups, including receptors for acetylcholine, glutamate, serotonin, opioids, and purines. Neuron groups also differentially expressed ion channels (**Supplementary Figure 2.2C,D**), signaling molecules (**Supplementary Figure 2.2E,F**), axon guidance molecules, adhesion proteins, and survival factors and receptors.

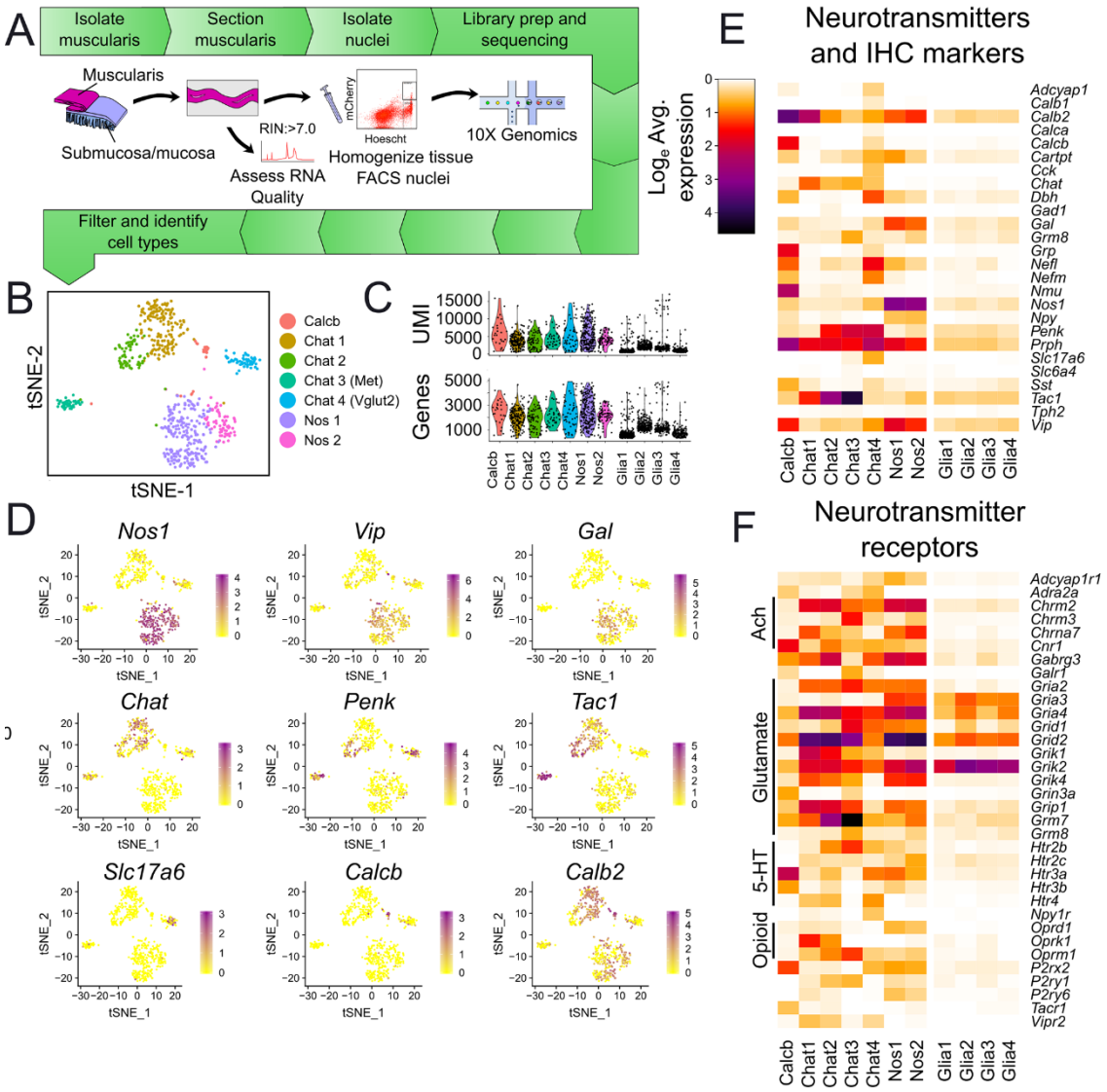

Figure 2.1: Adult mouse distal colon myenteric plexus RNAseq defines neuron and glia subtypes.

(A) Single nucleus RNAseq workflow. (B) T-SNE plot of enteric neuron and glial clusters. (C) Violin plots for neuron and glia clusters. (D) Feature plots for selected markers highlight neuron subtypes. Color shows $\log_e$(normalized gene expression). (E, F) Heatmaps show expression of commonly used enteric neuron markers with >0 detected reads (E) and neurotransmitter receptors (F). (E-F) Colors show $\log_e$(normalized mean gene expression).

Single-nucleus sequencing reveals distinct roles for GDNF and NRTN in mouse distal colon.

We were particularly intrigued that *Gfra1* and *Gfra2*, preferred receptors for GDNF and NRTN respectively, were abundant in glia but differentially expressed in neuron subsets. *Gfra2* was primarily in *Chat*+ neurons (**Figure 2. 2A-B**), consistent with prior studies (25,26). *Gfra1* was primarily in *Nos/Vip/Gal*+ neurons. We could not find prior reports of *Gfra1*-restricted expression in adult mouse ENS, so we tested if NOS1 colocalized with GFP in distal colon of *Gfrα1*$^{Gfp/wt}$ mice that express GFP from a *Gfra1* locus (27). GFP was in 88.9±1.8% of NOS1+ neurons, 8.8±5.7% of NOS1-negative neurons (**Figure 2.2D-E**), and in S100β+ glia (**Supplementary Figure 2.3A**) consistent with RNAseq. Coupled with the observation that GDNF acts acutely in the ascending peristaltic response (28), our data suggest GDNF and NRTN have opposing acute effects on bowel contractility, although both activate RET.

To test this, we recorded myenteric neuron calcium transients in GDNF or NRTN-treated full-thickness colon of *E2a-Cre;R26R-GCaMP6s* mice that express the calcium indicator GCaMP6s in all cells (**Figure 2.2F-G**). We also simultaneously monitored colon movement, an indirect measure of muscle tension (29). GDNF and NRTN increased or decreased spontaneous GCaMP6s activity in 50% (260/523) of all myenteric neurons (**Figure 2.2H-J**). Only 8.3% responded to both GDNF and NRTN (**Figure 2.2I**) suggesting most effects are via their preferred receptors, GFRA1 and GFRA2 respectively. To test this, we identified nitrergic neurons *post-hoc* in 3 fields. 63% (29/48) of neurons responding only to GDNF were nitrergic, while 25% (17/68) NRTN-only responders were nitrergic (**Supplementary Figure 2.3B-G**). The high percentage of non-nitrergic neurons responding to GDNF suggested some changes in GCaMP6s activity were due to synaptic connectivity. Remarkably, when we added the voltage-gated sodium channel blocker, tetrodotoxin (TTX), only 3-4% of myenteric neurons were GDNF- or NRTN-responsive, and only 7-8% responded in the presence of the nicotinic acetylcholine receptor antagonist, hexamethonium, with almost no overlap between GDNF- and NRTN-influenced cells (**Figure 2.2K-L and Supplementary Figure 2.3H-I**). This suggests that GDNF and NRTN have direct and indirect effects on GCaMP6s activity in distinct myenteric neurons.

GDNF also increased myenteric neurons responding to oral electrical field stimulation (EFS) by 71.3 ± 17.5% (p=0.0068), but did not affect responses to EFS applied aboral to recorded ganglia (p=0.49; **Suppl. Fig. 3J-K**). In contrast, NRTN did not affect the percentage of EFS-responsive myenteric neurons, regardless of stimulus location (p=0.116 aboral, p=0.188 oral; **Supplementary Figure 2.3L-M**). GDNF and NRTN both altered which neurons responded to oral and/or aboral EFS (data not shown). Further, GDNF robustly increased spontaneous and oral EFS-induced movement in the imaging field (p=0.0230, **Supplementary Figure 2.3J,N**). NRTN decreased movement in 3 of 5 preparations, but this was not statistically significant (**Figure 2.2M-O**). These observations suggest that GDNF and NRTN influence distinct myenteric neurons and that GDNF acutely enhances colon contractility.

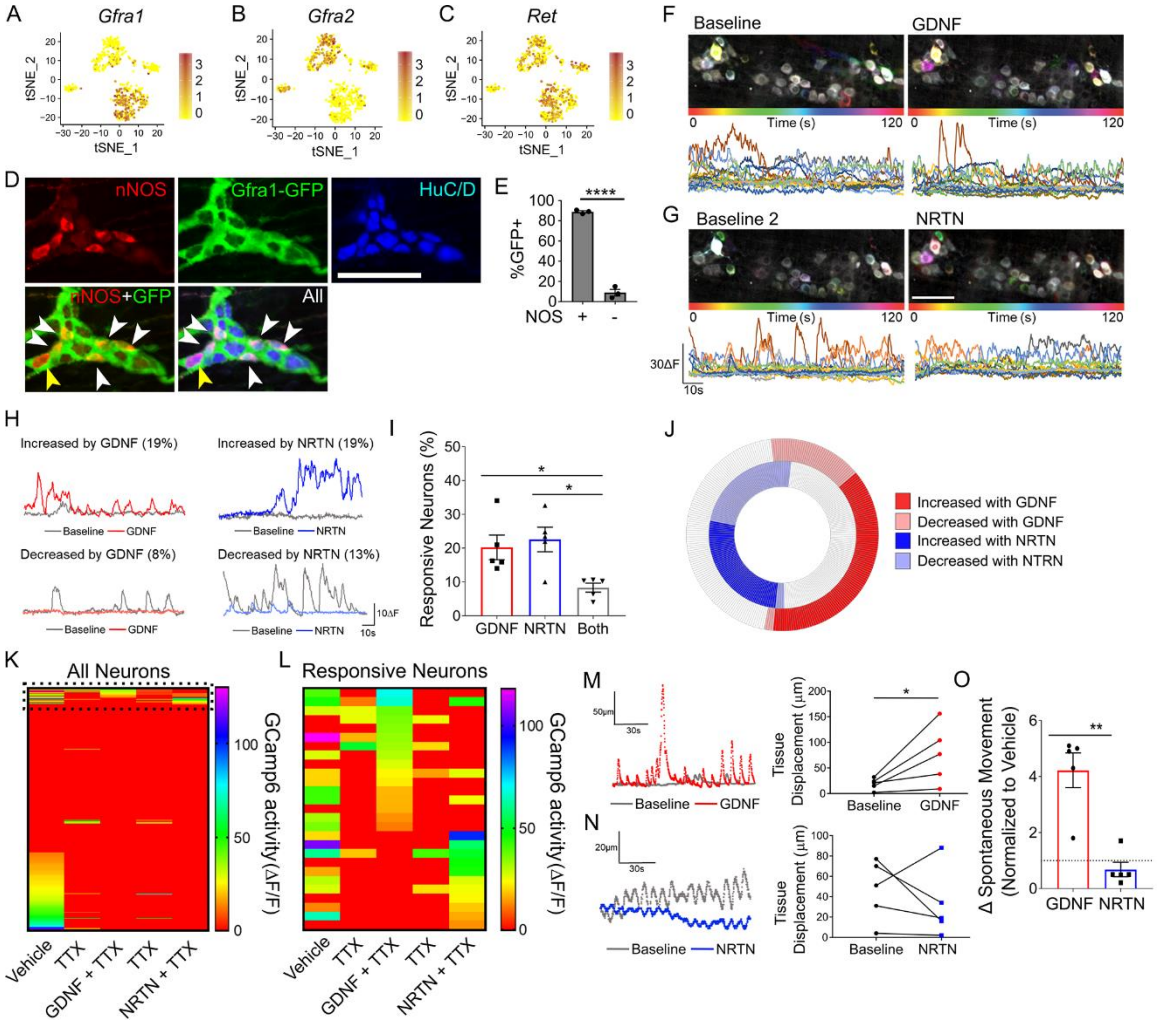

Figure 2.2: GDNF and NRTN acutely influence GCaMP activity of largely non-overlapping adult distal colon myenteric neuron populations.

(A-C) Feature plots show *Gfra1* is primarily in *Nos1/Vip/Gal* neurons (A), *Gfra2* is in *Chat* neurons (B), and *Ret* is in almost all neurons except *Chat 3 (*C). (D) Whole mount immunohistochemistry shows GFP (green) in most NOS1+ (red) neurons of *Gfra1*$^{Gfp/wt}$ distal colon. White arrowheads, GFP+, NOS1+ neurons. Yellow arrowhead, GFP-, NOS1+ neuron. (E) Most NOS1+ neurons are GFP+. Most NOS1- neurons are GFP-, consistent with RNAseq ($p<0.0001$, Student's t-test, n=3 mice (*Gfra1*$^{Gfp/wt}$)). (F-G) Time-lapse images (top; pixels assigned color based on timing of transients; i.e., color=activity) and traces (bottom) of GCaMP6s activity from ROIs on myenteric neurons during baseline (left) and after addition of 10 nM GDNF (F) or NRTN (G) (right). (H) Sample traces from neurons with activity increased (top) or decreased (bottom) by GDNF (red) or NRTN (blue). Baseline (gray) and percent neurons (in parentheses) with increased or decreased activity (>2 standard deviation change). (I) Percent neurons responding only to GDNF (red), only to NRTN (blue), or both (gray) ($P<0.05$, one-way ANOVA with Tukey's multiple comparisons test). (J) Iris plot of GDNF and NRTN responsive myenteric neurons (49.7% of total neurons, 260 of 523 total

neurons). GDNF (outer circle, red). NRTN (inner circle, blue) (n=5 mice). White, no ligand-induced activity change. Light shades indicate decreased activity after ligand addition. Most responsive neurons are affected by either GDNF or NRTN, but not both. (K-L) Heatmaps of GCaMP6s activity before and after adding the voltage-gated sodium channel blocker tetrodotoxin (TTX) and during sequential addition of GDNF and NRTN. Colors indicate GCaMP signal amplitude (red, no activity). (K) Heatmap of all neurons (n=301 neurons, 4 independent colon sections, 1 mouse). Dotted box shows GDNF- and NRTN-responsive neurons. (L) Expanded heatmap of 13 neurons that were only GDNF-responsive, 11 neurons only NRTN-responsive, and 3 neurons that responded to both. (M, N) Sample traces (left) and graph (right) of tissue displacement at baseline and after GDNF (M) (P=0.022, ratio paired t-test) or NRTN (N) (P=0.1583, ratio paired t-test). (O) GDNF, but not NRTN, enhanced tissue movement (P<0.01, unpaired t-test). (E,I,O) Mean +/- SEM. (D,F,G) Scale bar=100 microns. *p<0.05, **<0.01, ****p<0.0001.

Sequencing suggests combinatorial transcription factor codes define neuron subtypes.

To gain insight into neuronal subtype identity, we examined transcription and splicing factors ('regulatory genes') in adult colon myenteric neurons. Some genes that affect ENS subtype ratios (e.g. *Ascl1, Hand2,* and *Sox6*) were not differentially expressed in adults, but others not yet known to affect subtype specification were differentially expressed (e.g. *Tbx3*, *Tlx2,* and *Zeb2*; (30–32); **Figure 2.3A; Supplementary Figure 2.2G**). Many other transcription factors had distinct expression patterns in neuron subgroups including *Pbx3*, *Etv1*, *Casz1*, *Bnc2*, and *Zfhx3.* Consistent with data from other nervous system regions (33), few transcription factors were expressed in only one neuron subpopulation, suggesting combinatorial codes regulate enteric neuron phenotype (**Figure 2.3A; Supplementary Figure 2.2G**).

We focused on regulatory genes differentially expressed in cholinergic or nitrergic neurons, as most myenteric neurons express *Chat* or *Nos1*, but not both. We used *ChAT-EGFP-L10A* mice that reliably express EGFP at high levels in CHAT+ cells, since antibody staining is often weak (34). Consistent with RNAseq, SATB1, RBFOX1, and PBX3 immunoreactivity was preferentially in *Chat*-EGFP+ neurons, and TBX3 was primarily in NOS1+ neurons (**Figure 2.3B-F; I-L**). RNAseq also suggested *Etv1* enrichment in NOS1+ neurons. To validate this, we treated *Etv1-CreERT2$^{Cre/wt}$;R26R-TdTomato* mice with high-dose tamoxifen to induce TDTOMATO from *Etv1*+ regulatory elements. TDTOMATO was in 56.4±3.6% of NOS1+ and 5.6±0.9% of NOS1- myenteric

neurons (**Figure 2.3B,H, N**). Also consistent with RNAseq, PHOX2B protein had similar abundance in *Chat*-EGFP+ and *Chat*-EGFP- myenteric neurons (**Figure 2.3B,G, M**). Distribution of these transcription factors between *Chat-EGFP*+ and NOS1+ neurons is summarized in **Figure 2.3O-P**. These quantitative analyses show substantial correlation between protein and single-nucleus RNAseq data (**Figure 2.3A**).

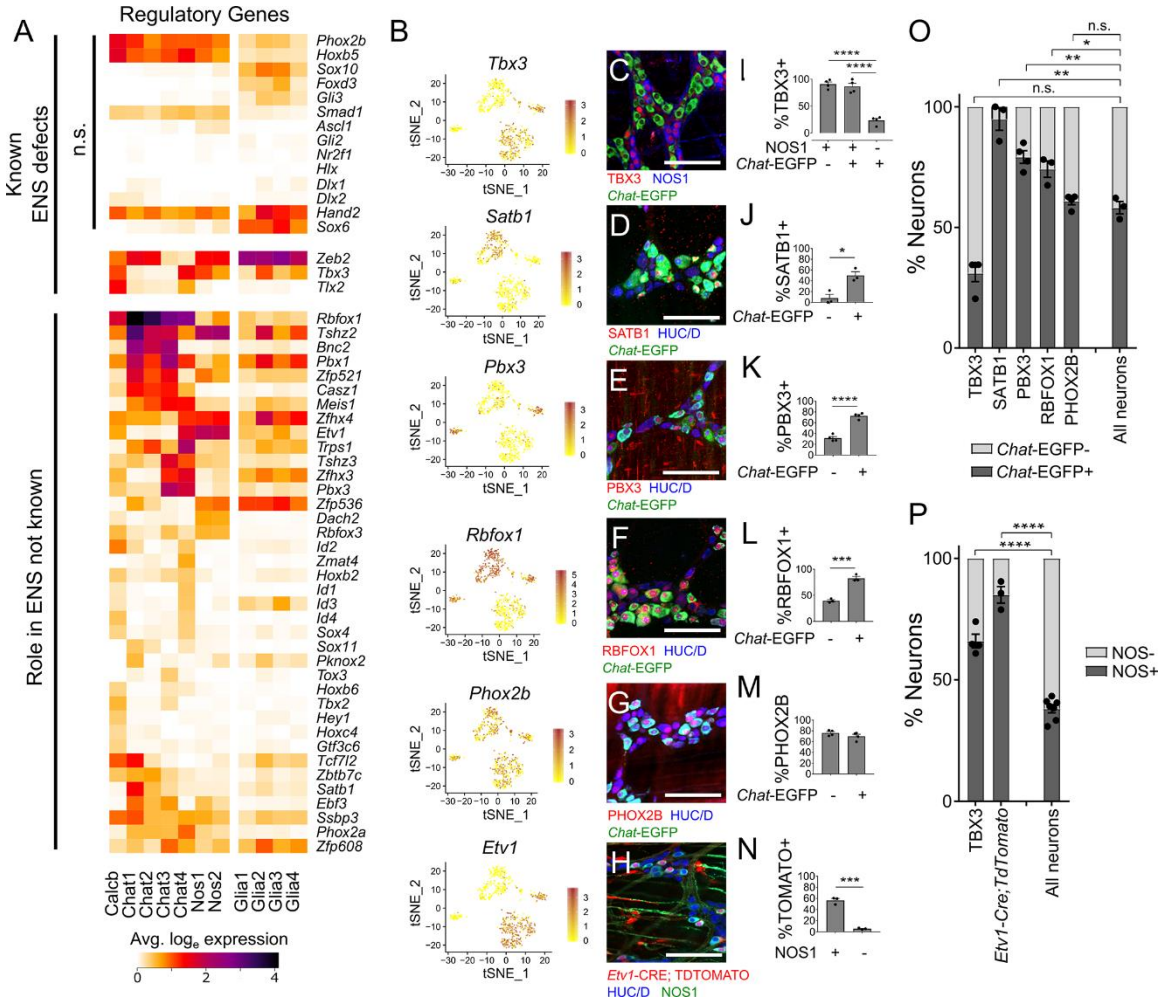

Figure 2.3: Regulatory genes in distinct adult ENS subsets.
(A) Transcription and splicing factors with known roles in ENS development (top). Differentially expressed factors newly identified in this study (bottom). n.s. = not significantly differentially expressed between neuron clusters. Color key shows $\log_e$(normalized mean gene expression within each cluster). (B) Feature plots of select regulatory genes. Color key shows $\log_e$(normalized gene expression). (C-G) Myenteric plexus wholemount immunohistochemistry in young adult *ChAT-EGFP-L10A* distal colon shows expression in neuron subsets. (H) Wholemount myenteric

plexus immunohistochemistry in distal colon from tamoxifen-treated *Etv1-Cre^{Ert2};R26R-TdTomato* mice. TDTOMATO is in many NOS1+ neurons and some non-neuronal cells with ICC morphology. (I-M) Quantification of immunohistochemistry. TBX3 is mostly in nitrergic (NOS1+) neurons (I, p<0.0001, n=3). SATB1 (J, p=0.013, n=3), PBX3 (K, p<0.0001, n=3), and RBFOX1 (L, p=0.0006, n=3) are mostly in cholinergic (EGFP+) neurons, consistent with single-cell data. PHOX2B is equally abundant in *Chat*-EGFP+ and *Chat*-EGFP- cells (M, p=0.2193, n=4). (N) Quantification of (H) shows 56.4±3.6% of NOS1+ neurons are TDTOMATO+. Only 5.6±0.9% of NOS1- neurons are TDTOMATO+ (p=0.0002, n=3). (O-P) Cholinergic (*Chat*-EGFP+, O) and nitrergic (NOS1+, P) identity for cells expressing select factors. SATB1 (p=0.0022), PBX3 (p=0.0026), and RBFOX1 (p=0.019) are largely restricted to cholinergic (*Chat*-GFP+) neurons. PHOX2B is in both cholinergic and non-cholinergic neurons (p=0.370) (P values compare Transcription factor+EGFP+/Transcription factor+ versus EGFP+/Total neuron ratios). TBX3 (p<0.0001) and ETV1 (p<0.0001) are primarily in nitrergic (NOS1+) neurons (P values compare Transcription factor+NOS1+/Transcription factor+ versus NOS1+/Total neuron ratios). (J-P) Student's t-test. (I) ANOVA with Tukey's post-hoc test. Scale bar = 100 microns. *ChAT-EGFP-L10A* = *Chat*-EGFP. *p<0.05, **p<0.01, ***p<0.001, ****p<0.0001.

Adult neuron subtype transcription factor patterns are largely established by E17.5

In mice, CHAT+ and NOS1+ enteric neurons are identifiable by late gestation and appear lineage committed (35,36). To identify lineage specific transcription factors at E17.5, we performed RNAseq using whole bowel from *ChAT-L10a-EGFP $^{wt/wt}$; Nos1-CreERT2$^{Cre/wt}$;TdTomato*+ and *ChAT-L10a-EGFP+; Nos1-CreERT2$^{wt/wt}$;TdTomato*+ littermates after E15.5 tamoxifen treatment. In these mice, EGFP marks CHAT-lineage and TDTOMATO identifies *NOS1*-lineage neurons (**Figure 2.4A**). 1005 cells were sequenced at 83% saturation. We normalized after removing outliers, leaving 707 neurons (*Elavl4*+), 179 epithelial (*Epcam*+), and 67 smooth muscle cells (*Actg2*+) (**Supplementary Figure 2.4A-B**). Reclustering without epithelia and muscle yielded 8 neuron clusters (**Figure 2.4B**), which all had high *Ret* expression, but were still *Dcx*+, a marker of immature neurons (37). Enteric glia were rare based on *Plp1* and *Sox10* (**Supplementary Figure 2.4E**).

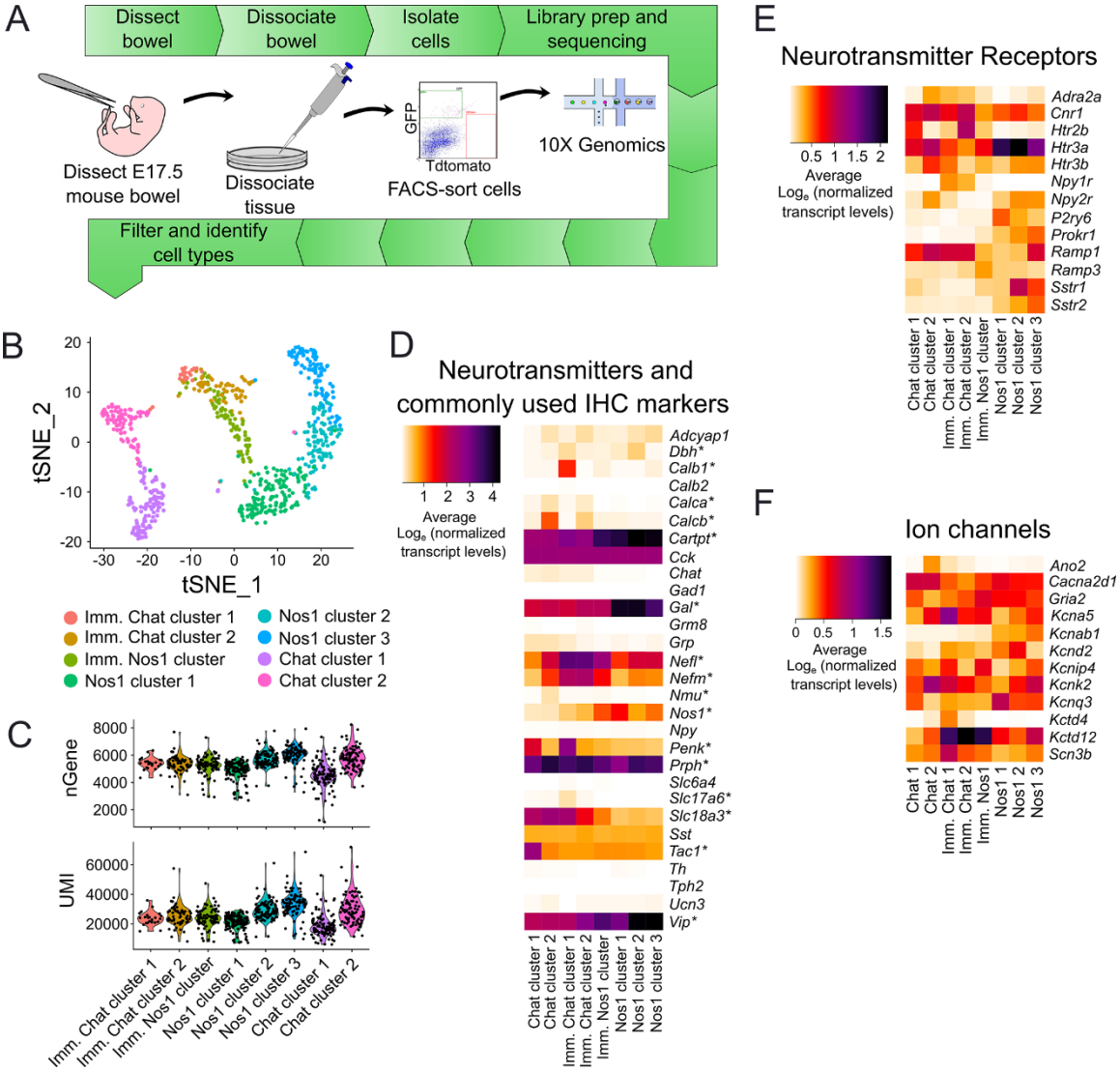

Figure 2.4: Single-cell RNAseq of E17.5 *ChAT-EGFP-L10A+* and *Nos1-CreERT2$^{Cre/wt}$;R26R-TdTomato+* neurons show distinct nitrergic and cholinergic clusters.

(A) Workflow for RNAseq. (B) T-SNE plot shows neuron subpopulations. (C) Violin plots show subgroups had 25,319.7±5562.2 unique RNA transcripts (UMI) and 5291.6±558.8 detected genes (nGene) per cell. (D-F) Heatmaps show commonly used enteric neuron markers with > 0 detected reads (E), neurotransmitter receptors (F), and ion channels. Color shows $\log_e$(normalized mean gene expression). (D) *Indicates differential expression across neuron subtypes. (E-F) Genes listed are differentially expressed across subtypes.

Chat transcripts were rare as others reported (8,9), but vesicular acetylcholine transporter *Slc18a3* was highly expressed in neuron clusters with low *Nos1* (**Supplementary Figure 2.4C-D**). Three clusters appeared less mature, prominently expressing neurite projection and cytoskeleton reorganization genes, based on Gene Ontology (GO) term analysis. Other clusters expressed synaptogenesis and maintenance genes suggesting more mature neurons (**Supplementary Figure 2.4F-G**). As in adults, many neurotransmitters, receptors, ion channel subunits, and signaling molecules were differentially expressed between subgroups (**Figure 2.4D-F and Supplementary Figure 2.5A-E**), including *Gfra1* and *Gfra2* (**Supplementary Figure 2.5D-E**). Many differentially expressed regulatory genes identified in adult mouse ENS were also differentially expressed in neuron subsets at E17.5, including *Casz1, Bnc2, Etv1, Pbx3, Tbx2, Tbx3, and Rbfox1* (**Figure 2.5 and Supplementary Figure 2.5F-G**), suggesting they could influence subtype identity.

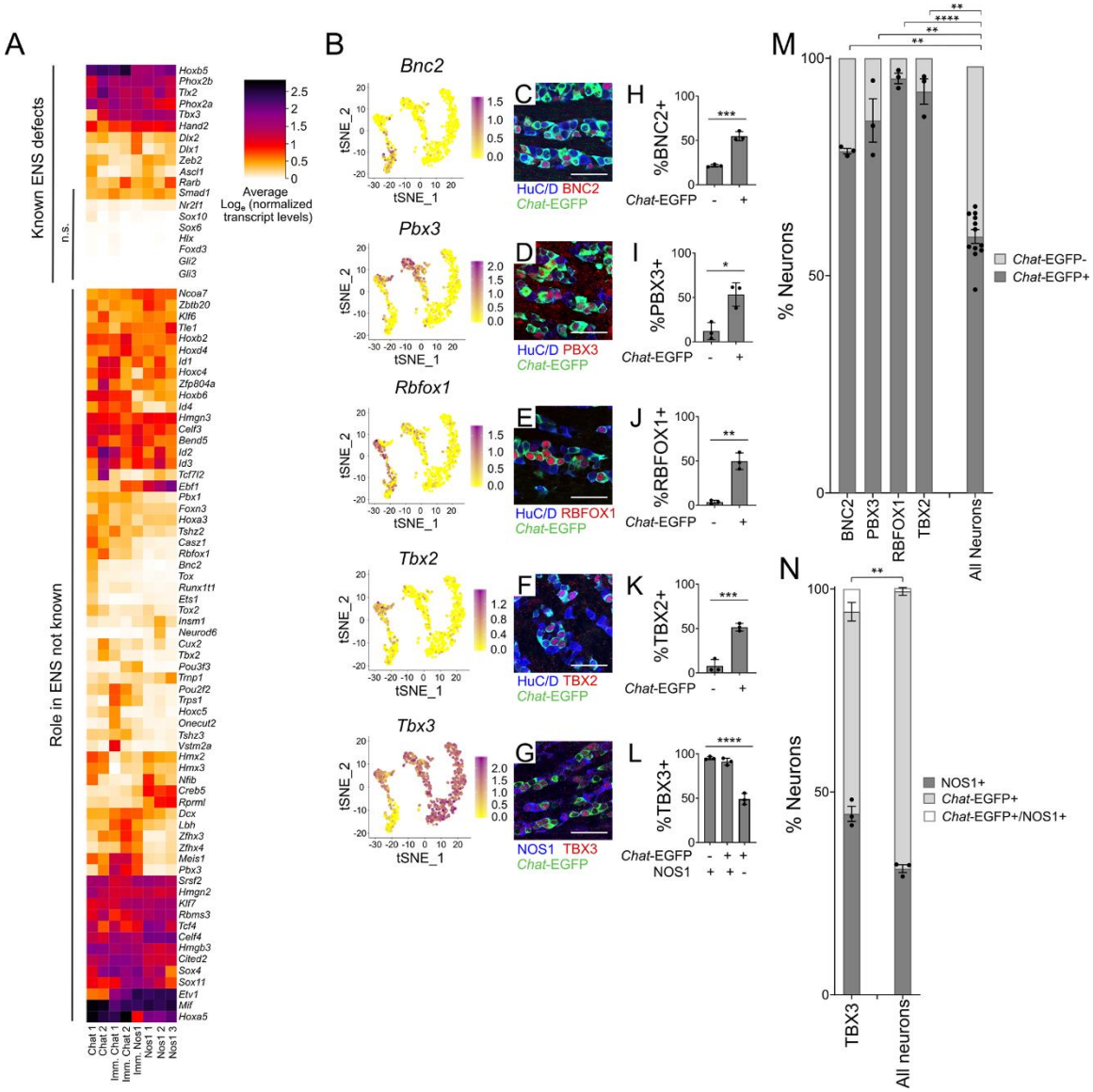

Figure 2.5: Many differentially expressed regulatory genes at E17.5 are also differentially expressed in adult distal colon.

(A) Transcription and splicing factors with known roles in ENS development (top), and newly-identified in this study (bottom). n.s. = not significantly differentially expressed between clusters. (B) Feature plots. (A,B) Colors show $\log_e$ (normalized mean gene expression). (C-G) Whole-mount immunohistochemistry of E17.5 *ChAT-EGFP-L10A* mid-small intestine. (H-L) Quantification of immunohistochemistry. BNC2 (H, p=0.0005, n=3), PBX3 (I, p=0.0119, n=3), RBFOX1 (J, p=0.0012, n=3), and TBX2 (K, p<0.001, n=3) are primarily in cholinergic (*Chat*-GFP+) neurons. TBX3 (L, p<0.0001, n=3, ANOVA with Tukey's post-hoc test) is primarily in NOS1+ neurons. (M-N) Quantification of cholinergic (*Chat*-EGFP+, M) and nitrergic (NOS1+, N) identity. Neurons expressing BNC2 (p=0.0018), PBX3 (p=0.0165), RBFOX1 (p<0.0001), and TBX2 (p=0.0016) are

primarily cholinergic (*Chat*-GFP+) neurons (P values compare Transcription factor+EGFP+/Transcription factor+ versus EGFP+/Total neuron ratios). TBX3+ neurons (p=0.003) are primarily nitrergic neurons (P values compare Transcription factor+NOS1+/Transcription factor+ versus NOS1+/Total neuron ratios). (H-L) Mean +/- SEM. (C-P) *ChAT-EGFP-L10A* reporter = *Chat*-EGFP. (H-K,M-N) Student's t-test. (L) ANOVA with Tukey's post-hoc test. Scale bar = 50 µm. *p<0.05, **p<0.01, ***p<0.001, ****p<0.0001.

Conditional Tbx3 loss reduced NOS1+ myenteric neuron density, but Etv1 and Rbfox1 loss did not alter CHAT/NOS1 subtype ratios

For several differentially expressed regulatory genes we determined if mutations altered nitrergic or cholinergic enteric neuron abundance. We found that P0 *Wnt1-Cre;Tbx3$^{fl/fl}$;R26R-Tdtomato* mice lacking TBX3 in ENS had a ~30% lower NOS1+ neuron density in small bowel, despite normal total neuron density (**Figure 2.6A-D**). In contrast, P0 mice lacking *Etv1* (*Etv1-Cre-ERT2$^{cre/cre}$;ChAT-L10A-EGFP*), which is enriched in nitrergic neurons, had normal NOS1+ to *Chat*-EGFP+ enteric neuron ratios (**Figure 2.6E-H**). *Chat*-EGFP+ neuron density was also normal in *Rbfox1* mutants (*Wnt1-Cre;Rbfox1$^{fl/fl}$;Chat-EGFP-L10A*) despite *Rbfox1* enrichment in cholinergic neurons (**Figure 2.6J-M**). Colonic bead expulsion latency tests were also normal in adult *Etv1* (**Figure 2.6I**) and *Rbfox1* (**Figure 2.6N**) mutant mice, suggesting intact ENS-mediated distal colon motility. Collectively, these findings suggest TBX3 impacts NOS1+ neurons, but ETV1 and RBFOX1 mutations do not alter CHAT/NOS1 neuron numbers.

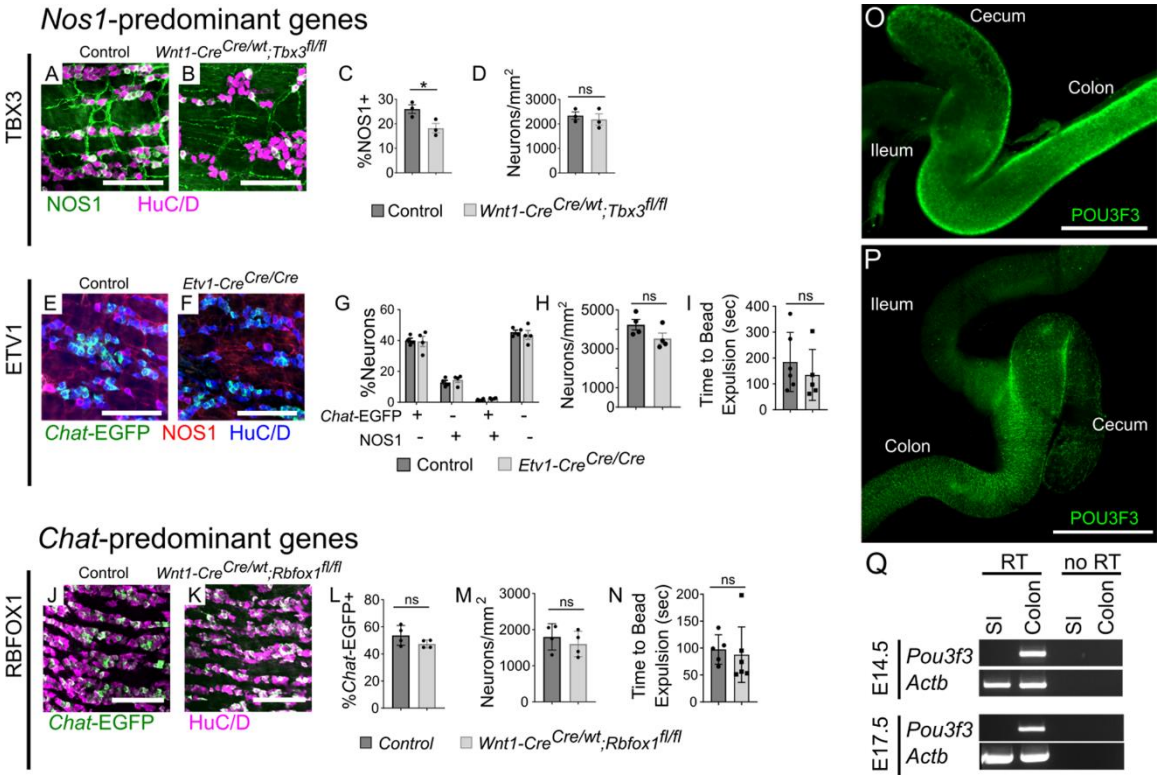

Figure 2.6: *Tbx3* loss in ENS reduces NOS1+ myenteric neurons, but NOS1+ or *Chat*-EGFP+ neuron abundance and colon bead expulsion was normal in *Etv1* and *Rbfox1* mutants. POU3F3 is restricted to colon ENS.

(A-B) Confocal maximum-intensity projections of NOS1+ (green) and total HuC/D (magenta) neurons in *Tbx3* mutant and control P0 small bowel. (C-D) Quantification shows 30% reduction in NOS1+/Total neuron ratio in *Wnt1-Cre*$^{Cre/wt}$*;Tbx3*$^{fl/fl}$ P0 small bowel (C; p=0.041, n=3 per group) despite normal total neuron density (D; p=0.601, n=3 per group). (E-F) Confocal maximum-intensity projections of P0 small bowel. (E) Control and (F) *Etv1-CreERT2*$^{Cre/Cre}$ bred to *Chat-EGFP-L10A* and stained for EGFP (green), NOS1 (red), and HuC/D (blue). (G) Quantification shows normal NOS1+ and Chat-EGFP+ neuron ratios (p=0.797, two-way ANOVA, n=4 in each group) and normal neuron density (H; p=0.117, n=4 in each group) in *Etv1* mutant P0 small bowel. (I) Colonic bead expulsion latency is normal in *Etv1-CreERT2*$^{Cre/Cre}$ mice (p=0.429, n=6 control, M=3/F=3, P45-50 at start of assay), n=5(*Etv1-CreERT2*$^{Cre/Cre}$, M=3/F=2, P49-58 at start of assay)). (J-K) Single confocal planes in P0 small bowel of control (J) and *Wnt1-Cre*$^{Cre/wt}$*;Rbfox1*$^{fl/fl}$ (K) bred to *Chat-EGFP-L10A* and stained for EGFP (green) and HuC/D (magenta). (L,M) Quantification shows that proportion of EGFP+ neurons (p=0.162, n=4 per group) and total neuron density (p=0.470, n=4 per group) are normal in *Rbfox1* mutants. (N) Colon bead expulsion latency is normal in *Wnt1-Cre*$^{Cre/wt}$*;Rbfox1*$^{fl/fl}$ mice (N; p=0.2677, n=5(control, M=2/F=3, P44-46 at start of assay), n=6(*Wnt1-Cre*$^{Cre/wt}$*;Rbfox1*$^{fl/fl}$, M=2/F=4, P46-58 at start of assay)). (O-P) Whole mount shows POU3F3 in colon and cecum but not ileum at E14.5 (O) and E17.5 (P). (O) Epifluorescence, unstitched. (P) Flattened, stitched confocal Z-stack. (Q) Representative RT-PCR for flow sorted TDTOMATO+ ENS cells from *Wnt1-Cre;R26R-TdTomato* mice confirms *Pou3f3* in fetal colon but not small

intestine (SI). (C-D, G-I, L-N) Mean +/- SEM. (C-D,H,K-L) Student's t-test. (I,N) Mann-Whitney. (A-B,E-F,J-K) Scale bar=100 µm. (O) Scale bar = 500 µm. (P) Scale bar = 1 mm. *ChAT-EGFP-L10A* = *Chat*-EGFP. *p<0.05.

Pou3f3 is expressed in colon, but not small intestine ENS

In addition to subtype identity, regional differences in neurons could promote different motility patterns. We were intrigued by the observation that *Pou3f3* (a.k.a. *Brn1*), a transcription factor important for CNS development (38), was mostly restricted to E17.5 immature Chat2 and immature Nos1 clusters (**Supplementary Figure 2.6A-B**). Since colon ENS matures after small bowel, this could be explained by *Pou3f3* enrichment in colon ENS, a hypothesis confirmed by RT-PCR (**Figure 2.6Q**). Immunohistochemistry using two antibodies showed POU3F3 marks all immature and mature colon neurons, but no small bowel neurons (**Figure 2.6O-P**, **Supplementary Figure 2.6C-X**), as recently reported by others (7). Human colon also showed POU3F3 in the nucleus of all submucosal and myenteric neurons. Human small bowel submucosal neurons lacked POU3F3, but some small bowel myenteric neurons had cytoplasmic POU3F3 immunoreactivity of uncertain significance (**Supplementary Figure 2.6Y-V'**). These data significantly extend recent reports that colon, but not small bowel, enteric neurons express POU3F3.

Using *Pou3f3* to mark E17.5 colon neurons (**Supplementary Figure 2.6W'**) and restricting comparisons to only mature or immature clusters based on GO terms, we identified 5 genes differentially expressed in *Pou3f3*+ versus *Pou3f3*- enteric neurons of immature clusters (*Slc18a3, Klhl1, Dpysl3, Gna14,* and *Itm2a*, **Supplementary Figure 2.6X'**) and 3 genes differentially expressed in *Pou3f3*+ versus *Pou3f3*- enteric neurons of mature clusters (*Ahr, Pantr1, Zfhx3*, **Supplementary Figure 2.66Y'**). *Ahr, Pantr1,* and *Zfhx3* patterns resemble *Pou3f3* (Pearson Correlation, compare **Supplementary Figure 2.6B** to **Supplementary Figure 2.6A''**) and others recently reported *Ahr* enrichment in colon ENS (7). Differentially expressed genes in immature clusters seem less likely to be colon restricted since patterns (**Supplementary Figure 2.6Z'**) are distinct from *Pou3f3* (**Supplementary Figure 2.6B**). Instead, differential expression of *Slc18a3*

(vesicular acetylcholine transporter) and *Klhl1* (P/Q-type calcium current density modulator) may reflect neuron maturation (39). *Dpysl3*, a cytoskeletal regulator, was in all groups, but 32% more abundant in *Pou3f3*+ cells (**Supplementary Figure 2.6Z'**). *Gna14,* and *Itm2a* are under-investigated, but at the highest levels in immature Chat clusters.

Adult human myenteric plexus

From human colon we sequenced single nuclei of the myenteric plexus region. Human enteric neurons comprise <1/10,000 cells and separating ENS from surrounding muscle was difficult. To identify ENS and aid microdissection of the myenteric plexus layer, we stained live colon with 4-Di-2-Asp (**Supplementary Figure 2.7A**), a dye taken up by mitochondria in presynaptic nerve terminals. We unsuccessfully attempted single cell RNAseq after ENS microdissection. Isolating neuronal nuclei using NeuN (40) or PHOX2B antibody staining was likewise unsuccessful. Ultimately, we obtained data from a limited number of human colon myenteric neuron nuclei by microdissecting using 4-Di-2-Asp, freezing in O.C.T., sectioning, Dounce homogenizing, and flow sorting Hoechst+ single nuclei from cell debris. 10x Genomics (**Figure 2.7A**) yielded RNAseq data from 20,167 nuclei of 16 adult colons (**Supplementary Table 2.4**) with a mean of 1,455 UMI and 894 genes per nucleus (**Supplementary Table 2.5**). Our data included many smooth muscle, ICC, PDGFRα+ cells, enteric glia, muscularis macrophage, vascular endothelial and hematopoietic cells (**Figure 2.7B; Supplementary Figure 2.7B-J**; i.e., most cells that impact bowel motility). One cluster of 48 cells was strongly positive for neuronal genes like *ELAVL4*, *SNAP25*, and *UCHL1* (**Supplementary Figure 2.7N-R**). Because of small cell numbers, we used hierarchical Euclidean clustering based on the top 50 markers distinguishing neurons from other cells. This gave two distinct clusters (**Figure 2.7C**) that differ in *NOS1*/*VIP/GAL*+ expression. *CHAT* and *SLC18A3* (*VAChT*) transcripts were not detected in either neuron subgroup, probably due to low read depth, as low *CHAT* was also noted by other groups (8,9). We next asked if any of the 41 transcription or splicing factors differentially expressed in

mouse *Nos1+* versus *Chat+* myenteric neurons were also differentially expressed in human enteric neuron subtypes. Consistent with mouse data, *ETV1* was most abundant in *NOS1+* neurons, while *RBFOX1* and *BNC2* were enriched in *NOS1-* neurons (**Figure 2.7D**) after multiple comparison testing. Immunohistochemistry confirmed BNC2 (**Figure 2.7E-H,Y**), PBX3 (**Figure 2.7I-L,Z**), RBFOX1 (**Figure 2.7M-P,A'**), TBX2 (**Figure 2.7Q-T,B'**), and TBX3 (**Figure 2.7U-X,C'**) were differentially expressed in human enteric neuron subtypes, with patterns similar to mouse (i.e. most RBFOX1+, PBX3+, BNC2+, and TBX2+ cells are CHAT+; most TBX3+ cells are NOS+; **Figure 2.7D'-E'**).

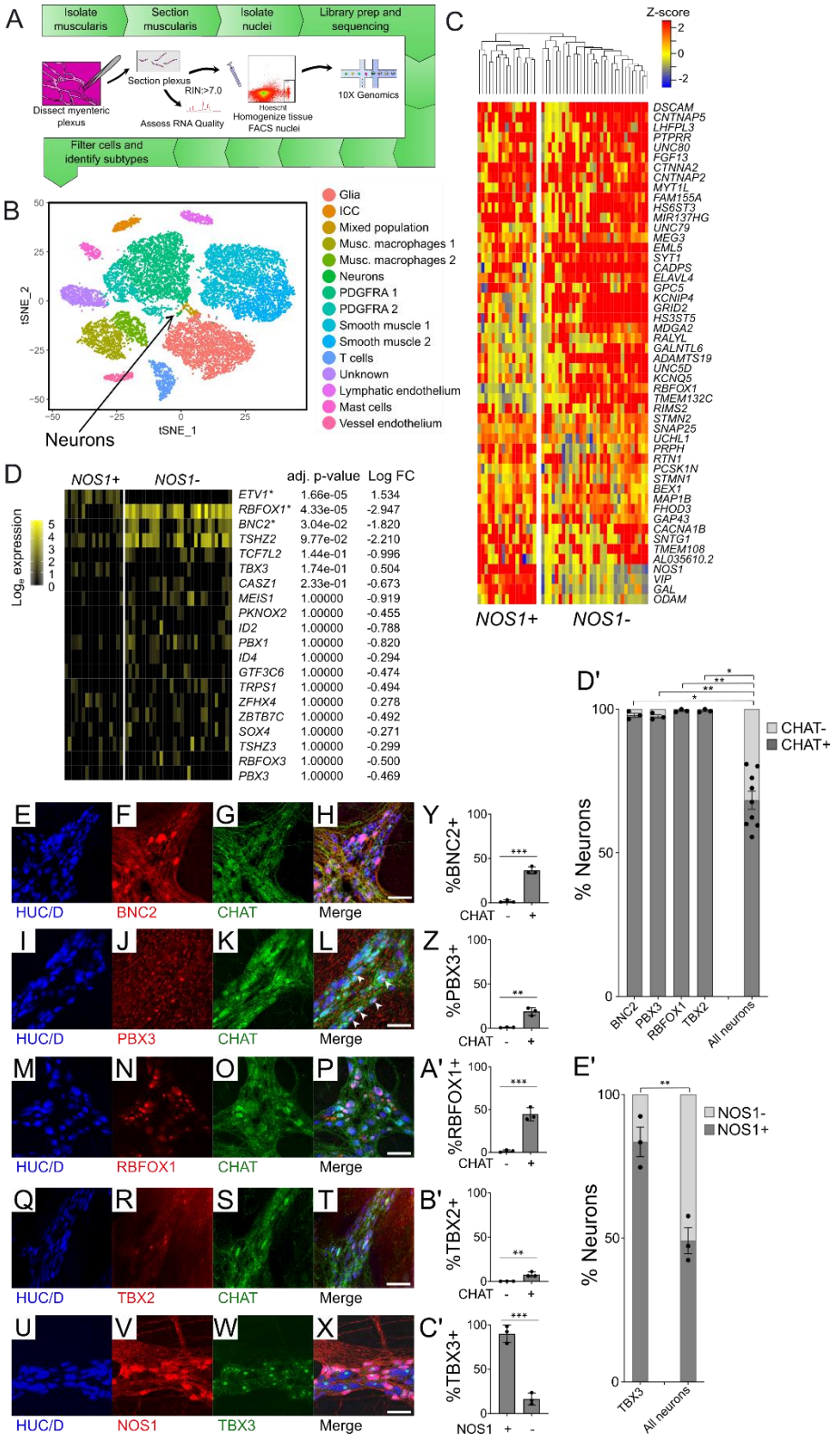
A
Isolate muscularis
Section muscularis
Isolate nuclei
Library prep and sequencing
Dissect myenteric plexus
Section plexus
RIN:>7.0
Assess RNA Quality
Hoescht
Homogenize tissue
FACS nuclei
10X Genomics
Filter cells and identify subtypes
B
tSNE_2
tSNE_1
Neurons
Glia
ICC
Mixed population
Musc. macrophages 1
Musc. macrophages 2
Neurons
PDGFRA 1
PDGFRA 2
Smooth muscle 1
Smooth muscle 2
T cells
Unknown
Lymphatic endothelium
Mast cells
Vessel endothelium
C
Z-score
DSCAM
CNTNAP5
LHFPL3
PTPRR
UNC80
FGF13
CTNNA2
CNTNAP2
MYT1L
FAM155A
HS6ST3
MIR137HG
UNC79
MEG3
EML5
SYT1
CADPS
ELAVL4
GPC5
KCNIP4
GRID2
HS3ST5
MDGA2
RALYL
GALNTL6
ADAMTS19
UNC5D
KCNQ5
RBFOX1
TMEM132C
RIMS2
STMN2
SNAP25
UCHL1
PRPH
RTN1
PCSK1N
STMN1
BEX1
MAP1B
FHOD3
GAP43
CACNA1B
SNTG1
TMEM108
AL035610.2
NOS1
VIP
GAL
ODAM
NOS1+
NOS1-
D
NOS1+
NOS1-
Log2 expression
adj. p-value
Log FC
ETV1* 1.66e-05 1.534
RBFOX1* 4.33e-05 -2.947
BNC2* 3.04e-02 -1.820
TSHZ2 9.77e-02 -2.210
TCF7L2 1.44e-01 -0.996
TBX3 1.74e-01 0.504
CASZ1 2.33e-01 -0.673
MEIS1 1.00000 -0.919
PKNOX2 1.00000 -0.455
ID2 1.00000 -0.788
PBX1 1.00000 -0.820
ID4 1.00000 -0.294
GTF3C6 1.00000 -0.474
TRPS1 1.00000 -0.494
ZFHX4 1.00000 0.278
ZBTB7C 1.00000 -0.492
SOX4 1.00000 -0.271
TSHZ3 1.00000 -0.299
RBFOX3 1.00000 -0.500
PBX3 1.00000 -0.469
D'
% Neurons
CHAT-
CHAT+
BNC2
PBX3
RBFOX1
TBX2
All neurons
E
F
G
H
HUC/D
BNC2
CHAT
Merge
Y
%BNC2+
CHAT
I
J
K
L
HUC/D
PBX3
CHAT
Merge
Z
%PBX3+
CHAT
M
N
O
P
HUC/D
RBFOX1
CHAT
Merge
A'
%RBFOX1+
CHAT
Q
R
S
T
HUC/D
TBX2
CHAT
Merge
B'
%TBX2+
CHAT
U
V
W
X
HUC/D
NOS1
TBX3
Merge
C'
%TBX3+
NOS1
E'
% Neurons
NOS1-
NOS1+
TBX3
All neurons

Figure 2.7: Human myenteric plexus *NOS1/VIP/GAL+* and *NOS1/VIP/GAL-* neurons differentially express many regulatory genes also differentially expressed in mouse ENS. (A) Workflow for single-nucleus RNAseq of adult human colon myenteric plexus. (B) T-SNE plot of 20,167 nuclei shows glia, ICC, muscularis macrophages, *Pdgfrα*+ cells, smooth muscle, T cells, endothelium, and unknown groups. Neurons comprise one small cluster (~48 cells). (C) Heatmap shows 50 genes with the highest fold difference between neurons and other cells. Hierarchical clustering suggests 2 subgroups: *NOS1+/VIP+/GAL+* (17 neurons) and *NOS1-/VIP-/GAL-* (31 neurons). (D) Heatmap shows transcription and splicing factors differentially expressed in mouse colon that were in >10% of human myenteric neurons. *RBFOX1, ETV1,* and *BNC2* were differentially expressed between *NOS1/VIP/GAL+* and *NOS1/VIP/GAL-* human neurons (Wilcoxon rank-sum test with Bonferroni correction). (E-X) Maximum intensity projections of confocal Z-stacks show adult human colonic ENS. BNC2 (E-H). PBX3 (I-L, white arrowheads indicate nuclear PBX3 in neurons.), RBFOX1 (M-P), TBX2 (Q-T) and TBX3 (U-X) are present in subsets of human myenteric neurons. (Y-C') Quantification of immunohistochemistry shows BNC2 (Y, p=0.0001, n=3), PBX3 (Z, p=0.0021, n=3), RBFOX1 (A', p=0.0007, n=3), and TBX2 (B', p=0.0089, n=3) are primarily in CHAT+ neurons. TBX3 (C', p=0.0004, n=3) is primarily expressed in NOS1+ neurons. (Z-A') Quantification of CHAT+ (D') and NOS1+ (E' cells reveals BNC2 (p=0.0102), PBX3 (p=0.0021), RBFOX1 (p=0.0016), and TBX2 (p=0.0162) are largely restricted to CHAT+ neurons in adult human ENS (P values compare Transcription factor+EGFP+/Transcription factor+ versus EGFP+/Total neuron ratios). TBX3 (p=0.0073) is primarily in NOS1+ neurons (P values compare Transcription factor+NOS1+/Transcription factor+ versus NOS1+/Total neuron ratios). (Y-E') Mean +/- SEM and Student's t-test. *p<0.05, **p<0.01, ***p<0.001.

2.4 Discussion

Life-threatening bowel motility disorders like HSCR and chronic intestinal pseudo-obstruction (41) are challenging to treat and difficult to diagnose. To facilitate molecular diagnostics, enhance understanding of ENS function, and advance new strategies like stem cell therapy (42,43), we used single-cell transcriptomics to identify a vast array of neurotransmitters, receptors, ion channels, signaling molecules, and mRNA regulatory genes. These data identified 7 mouse myenteric neuron subclasses in adult distal colon and 8 neuron groups at E17.5. Immunohistochemistry in mouse and human validated RNAseq, and functional studies identified new ENS roles for TBX3, GDNF and NRTN. Our analyses complement recent data from others examining different ages and bowel regions (6–9), providing a foundation for novel diagnostics and disease management.

Several transcription factors were differentially expressed in nitrergic versus cholinergic neurons. We therefore tested if gene loss altered *Chat* or *Nos1* subtype abundance. We found that *Tbx3* loss in *Wnt1*-lineage cells reduced NOS1+ myenteric neuron density, but not total neuron density. Interestingly, *Tbx3* expression in limb bud is induced by the transcription factor HAND2 (44), and *Hand2* mutations cause complete loss of NOS1+/VIP+ enteric neurons (45), suggesting TBX3 also acts downstream of HAND2 in the ENS. In contrast, NOS1+ and *Chat*-EGFP+ neuron density was normal in *Etv1* mutant mice although most adult NOS1+ myenteric neurons express *Etv1* and ETV1 regulates CNS neuron subtype differentiation (46). Similarly, while the splicing and mRNA binding protein RBFOX1 (47,48) is present in most ENS cholinergic neurons and RBFOX1 regulates CNS neuron subtype differentiation (49), the percentage of *Chat*-EGFP+ myenteric neurons was normal in *Wnt1-Cre*$^{Cre/wt}$*; Rbfox1*$^{fl/fl}$ mice. Normal colonic bead expulsion latency in *Etv1* and *Rbfox1* mutant mice suggests redundant mechanisms in the ENS prevent obvious anatomic or functional defects.

Another striking observation is that the transcription factor POU3F3 is found in the nucleus of all mouse and human colon enteric neurons, but not in small bowel neurons as another group recently confirmed (7). POU3F3 function in colon ENS is not known, but POU3F3 regulates cortical neuron migration and neurogenesis (50,51). Human mutations cause intellectual disability, speech delay, autism, epilepsy, craniofacial anomalies and cryptorchidism (52), but effects of POU3F3 mutation on bowel function were not reported. Restricted colon expression is interesting because colon motility and ENS structure differ between colon and small bowel (13,19,23,24,53), but we know little about underlying developmental mechanisms. The observation that there are colon-restricted ENS transcription factors suggests more intense investigation of regional gene expression in the ENS may be valuable.

Human RNAseq yielded data from 17 *NOS1*+ and 31 *NOS1*- myenteric neurons as well as from many other cells that impact bowel motility. Guided by RNAseq, we found *ETV1* was more abundant in human nitrergic neurons, while *RBFOX1* and *BNC2* were enriched in non-nitrergic

neurons, suggesting subtype-specific genes may be conserved between humans and mice. Immunohistochemistry confirmed TBX3, PBX3, and TBX2 are also present in subsets of human enteric neurons as predicted by mouse data.

Many other genes differentially expressed in enteric neuron subclasses may merit investigation. For example, *ZEB2* mutations cause Mowat-Wilson syndrome, characterized by Hirschsprung disease (HSCR), intellectual disability and distinctive facial features. Post-surgical outcomes in Mowat-Wilson syndrome are worse than for isolated HSCR and *ZEB2* mutations cause chronic constipation without HSCR (54,55) suggesting *Zeb2* might have roles beyond bowel colonization by ENS precursors. *Zfhx3*, another HSCR-associated gene (56) drives neuronal differentiation in other regions, but roles in ENS subtype specification are unexplored.

Integrating new and old data about ENS subtypes

Using neurotransmitter-associated markers in adults (**Supplementary Table 2.2**) and at E17.5 (**Supplementary Table 2.3**), we correlated our RNAseq data with known ENS subtype markers. Subtype designations at E17.5 include small bowel and colon neurons (distinguished by *Pou3f3*) and immature clusters defined by Gene Ontology (GO) Term modules (**Supplementary Figure 2.4F, G**). The similarities between E17.5 small bowel and adult colon suggest that some aspects of neuron differentiation are similar across bowel regions and completed by E17.5. Many newly identified differentially expressed genes are highlighted in **Supplementary Tables 2.2** and **2.3**. Some genes known to be expressed in enteric neuron subtypes were not detected (see **Supplementary Table 2.2**), but lack of expression is uninterpretable, because of limited read depth in adult colon nuclei. In adults, Calcb neurons appear to be AH/Dogiel type II intrinsic sensory neurons that express neurofilament M (*Nefm*), Nav1.9 (*Scn11.1a*), calretinin (*Calb2*), NK1 tachykinin receptor (*Tacr1*), serotonin receptors *Htr3A* and *Htr3b*, and purine receptor *P2rx2* (19,57,58). Chat1 neurons express the mechanosensitive channel *Piezo1* suggesting these cells are stretch sensitive intrinsic sensory neurons, but other sensory neuron markers are absent. There

are reports of mechanosensitive interneurons and motor neurons (59), so Chat1 neurons may correspond to these. *Tac1* and *Penk* co-expression make Chat2 and Chat3 clusters excitatory motor neurons or interneurons (19), **Supplementary Figure 2.1K-S**). Unexpectedly, however, Chat3 neurons also express hepatocyte growth factor receptor *Met* and do not express CGRP (*Calcb*), suggesting Met+ colonic neurons may differ from small bowel where MET and CGRP were found in the same neurons by immunohistochemistry (60). Finally, Chat4 cells appear to be interneurons based on co-expression of *Slc18a3*, *Chat*, *Nos1*, *Vip*, and *Calb1*. Thus, many findings fit well with known neuron subtypes, and immunohistochemistry correlates well with RNAseq, providing high confidence in our results. We point out unexpected findings to suggest there is more to learn and that future studies based on our RNAseq are needed to fully define adult enteric neuron subtypes.

Defining neuron subtypes at E17.5 presents an added challenge because differentiation is incomplete. **Supplementary Table 2.3** highlights some markers differentially expressed in neuron subtypes. Since almost all cholinergic and nitrergic neurons at E17.5 remain cholinergic or nitrergic respectively in adults (35,36), we extrapolate from adult data. Assessment of maturity is based on GO Term analysis. Colon neurons were identified by *Pou3f3* expression. Chat cluster 1 and Chat cluster 2 markers suggest small bowel excitatory motor neurons and intrinsic sensory neurons, respectively. Chat cluster 2 also expresses BMP and TGFβ signaling antagonists (*Nog*, *Bambi*, *Smad7*), which may provide new insights into ENS development. Immature Chat cluster 1 appears to be developing myenteric interneurons that express *Slc17a6*, similar to the adult Chat4 cluster. Nos1 clusters 1 and 3 are most likely inhibitory motor neurons, but could also be interneurons. Nos1 cluster 2 represents possible inhibitory interneurons based on the expression of the transcription factor Neurod6 (9). Interestingly, Nos1 cluster 1 differentially expresses *Ednrb*, but the role of Ednrb/EDN3 signaling at this time is not known. We highlight these observations to emphasize how mining our data might provide new insight into development.

GDNF and NRTN acutely affect calcium signaling in distinct adult enteric neuron populations

Our data also provide new insight into adult gene function. We knew already that GDNF/GFRA1/RET signaling is essential during gestation for ENS precursor survival, proliferation, and bowel colonization (61). As the ENS matures, GDNF/GFRA1/RET signaling enhances neuronal differentiation, increases neurite growth, and alters axon trajectories for NOS1+ enteric neurons (62). Then, in adults, GDNF increases the strength of bowel contraction in the ascending limb of the peristaltic response (28). We were therefore unsurprised that GDNF altered calcium signaling in some enteric neurons and that GDNF acutely enhanced basal and EFS-evoked motor patterns. In contrast, although NRTN/GFRA2/RET are known to influence bowel motility and support acetylcholinesterase+ and substance P+ neurites (25,26), acute effects of NRTN on the ENS or bowel motility had not been demonstrated. Our data confirm and extend prior observations. *Gfra1* and *Gfra2*, preferred co-receptors for GDNF and NRTN respectively, are expressed in largely non-overlapping populations of *Ret*+ E17.5 and adult myenteric neurons. GFRA1 is in ~90% of NOS1+ myenteric neurons, but in very few NOS1- neurons, so we anticipated GDNF effects primarily in NOS1+ neurons. However, 44% (33/75) of GDNF influenced neurons were non-nitrergic. This might occur because GDNF activates RET via GFRA2 (NRTN's preferred co-receptor) at high (pharmacologic) concentrations (63–65), but this seems unlikely since GCaMP6s signaling was altered by both GDNF and NRTN in only 8% of myenteric neurons. Instead, the observation that some neurons had increased and others decreased GCaMP activity in response to each trophic factor suggests both direct and indirect effects were measured and that responses may depend on synaptic inputs, as confirmed by TTX/hexamethonium data. The hypothesis that GDNF and NRTN sensitize responsive neurons to incoming stimuli is also supported by our prior studies of dorsal root ganglion neurons where these factors acutely potentiate TRPV1-induced calcium signals and induce hyperalgesia when injected into hindpaw (66). Although we do not know the source of calcium (e.g., intra- or extracellular) or whether evoked GCaMP signals were activity-

dependent, our data collectively show that NRTN and GDNF acutely influence non-overlapping sets of myenteric neurons and differentially regulate bowel motility.

Summary

Bowel motility disorders remain poorly defined in part because the ENS is complicated and under-investigated. As we move into an era of advanced genetic testing for people with life-threatening medical problems like chronic intestinal pseudo-obstruction, we remain hampered by inadequate data about enteric neuron subtypes that support normal bowel function. In addition to defining many subtype specific molecules, we demonstrated new roles for *Tbx3,* GDNF and NRTN, and showed colon- specific POU3F3 expression in enteric neurons at many ages, combining data from mouse and human myenteric plexus. Many additional studies will build on this work.

2.5 Methods

Study approval

Studies adhere to ARRIVE (Animals in Research: Reporting In Vivo Experiments) guidelines (69). Mouse experiments were performed in accordance with Institutional Animal Care and Use Committee (IACUC) approval from Children's Hospital of Philadelphia (IACUC#19-001041) and University of Pittsburgh (IACUC#IS00013297) or University of Melbourne Animal Experimentation Ethics Committee (project number 1714308.2). Human colon was acquired with Institutional Review Board approval from Perelman School of Medicine at University of Pennsylvania (IRB#804376) and from Children's Hospital of Philadelphia (IRB#13-010357).

Animals

B6.FVB(Cg)-Tg(Chat-EGFP/Rpl10a,Slc18a3)DW167Htz/J mice (referred to as *ChAT-EGFP-L10a* (RRID:IMSR_JAX:030250; C57BL/6J) were a kind gift from Dr. Joseph Dougherty at Washington University School of Medicine in St. Louis. *Tbx3tm3.1Moon* mice (referred to as *Tbx3*;

RRID:MGI:5538564; described previously (22); mixed background) were a kind gift from Dr. Anne Moon at Geisinger Commonwealth School of Medicine. *B6.129S2-Rbfox1tm1.1Dblk/J* mice (referred to as *Rbfox1*; RRID:IMSR_JAX:014089; C57BL6/J) were a kind gift from Dr. Douglas Black at the University of California Los Angeles. *Gfra1tm2.1Jmi* mice (referred to as *Gfra1-Gfp*; RRID:MGI:3715157, C57BL/6) were a kind gift of Dr. Sanjay Jain at Washington University School of Medicine in St. Louis. *C57BL/6J* mice (RRID:IMSR_JAX:000664), *H2az2*(*Tg(Wnt1cre)11Rth* mice (referred to as *Wnt1-Cre*; RRID:IMSR_JAX:003829), *B6;129S6-Gt(ROSA)26Sortm1(CAG-tdTomato*,-EGFP*)Ees/J* mice (referred to as *ROSA$^{nT\text{-}nG}$*; RRID:IMSR_JAX:023035), *B6;129S-Gt(ROSA)26Sortm1.1Ksvo/J* mice (referred to as *R26R-H2b-mCherry*; RRID:IMSR_JAX:023139), *B6(Cg)-Etv1tm1.1(cre/ERT2)Zjh/J* mice (referred to as *Etv1-CreERT2* mice; RRID:IMSR_JAX:013048), *Slc17a6tm2(cre)Lowl/J* mice (referred to as *Vglut2-IRES-Cre* mice; RRID:IMSR_JAX:016963), *B6;129S-Nos1tm1.1(cre/ERT2)Zjh/J* mice (referred to as *Nos1-CreERT2*; RRID:IMSR_JAX:014541), *Gt(ROSA)26Sortm9(CAGtdTomato)Hze* mice (referred to as *R26R-TdTomato*; RRID:IMSR_JAX:007909), *B6.FVB-Tg(EIIa-cre)C5379Lmgd/J* (referred to as *E2a-Cre* RRID:IMSR_JAX:003724; C57BL/6), and *B6J.Cg-Gt(ROSA)26Sortm96(CAG-GCaMP6s)Hze/MwarJ* (referred to *R26R-Gcamp6s*; RRID:IMSR_JAX:028866; C57BL/6) were obtained from The Jackson Laboratory (Bar Harbor, ME). *Wnt1-Cre* mice on a mixed C57BL/6J x CBA/J)F1 background were bred into *R26R-H2b-mCherry* mice on a mixed 129S4/SvJaeSor x C57BL/6J background and maintained on a mixed C57BL/6J x 129S4/SvJaeSor x CBA/J)F1 background. *Etv1-CreERT2* mice were bred to *R26R-TdTomato* mice and *ChAT-EGFP-L10a* mice to generate *Etv1-CreERT2;R26R-TdTomato;ChAT-EGFP-L10a* mice on a C57BL/6J background. *Vglut2-IRES-Cre* mice on a C57BL/6;FVB;129S6 background were bred to *R26R-TdTomato* on a C57BL/6J background and maintained on a mixed C57BL/6;FVB;129S6 background. *Nos1-CreERT2* mice were crossed with *R26R-TdTomato* mice and *ChAT-EGFP-L10a* mice to generate *ChAT-EGFP-L10a; Nos1-CreERT2; R26R-TdTomato* mice and maintained on a C57BL/6 background. *Rbfox1;Wnt1-Cre;R26R-TdTomato;ChAT-EGFP-L10a* mice were generated by

crossing *Rbfox1* mice to *Wnt1-Cre* mice, *ChAT-EGFP-L10a* mice, and *R26R-TdTomato* mice and were maintained on a mixed background. *Wnt1-Cre;Tbx3* mice were generated by crossing *Wnt1-Cre* mice to *Tbx3* mice and were maintained on a mixed background. *E2a-Cre* mice were crossed with *R26R-Gcamp6s* mice to generate mice that express GCaMP6s (a genetically encoded calcium indicator) in all cells. *E2a-Cre;R26R-GCaMP6s* mice were maintained on a pure C57BL/6 background. Genotyping was performed using previously published and novel primers (**Supplementary Table 2.9**) and by Transnetyx (Cordova, TN). Vaginal plug day was considered day E0.5. Experimental animals of the correct strain, genotype, and age were randomly selected from the total pool of mice available. General animal husbandry information for the mice used in this study is provided in **Supplementary Table 2.10**.

Human colon

Colon tissue was acquired with Institutional Review Board approval from Perelman School of Medicine at University of Pennsylvania (IRB #804376) and the Children's Hospital of Philadelphia Institutional Review Board (IRB#13-010357) using the Abramson Cancer Center Tumor Bank. Colon was de-identified, providing limited clinical data. Resected colons were maintained at ambient temperature until arrival in pathology, where they were transferred to ice-cold Dulbecco-modified PBS (DPBS) 1-4 hours after resection. Pathologists selected regions of colon without gross abnormalities, and colon specimens were transferred to the laboratory in DPBS on ice.

Tamoxifen treatment

Tamoxifen (10mg/mL or 20mg/mL; Sigma, Cat#T5648) was prepared by first adding 200 uL ethanol and then 1800 uL sunflower oil (Sigma, Cat#S5007). Tamoxifen was dissolved by alternately vortexing and incubating in a 37ºC water bath. *Nos1-creERT2;Chat-EGFP-L10A;R26-TdTomato* E15.5 dams were injected once with 200mg/kg tamoxifen at 10mg/mL concentration. *Etv1-CreERT2;Chat-EGFP-L10A;R26-TdTomato* E15.5 dams were gavaged once with tamoxifen

at 200mg/kg concentration at 20mg/mL concentration and pups were dissected at E17.5. Adult *Etv1-CreERT2;R26-TdTomato* adult mice were gavaged twice (two days apart) with 233mg/kg tamoxifen at 20mg/mL concentration three weeks prior to dissection.

Preparing young adult mouse colon for nuclei isolation

Wnt1-Cre$^{Cre/wt}$*;R26R-H2b-mCherry+* 47-52-day-old mice (8 females, 1 male) were euthanized with CO_2. Colon was removed, flushed with cold, sterile Dulbecco's phosphate buffered saline (DPBS) using a 20 mL syringe to remove luminal contents, and placed in fresh cold, sterile DPBS. Colon was carefully cut along the mesentery, pinned mucosal side down on dishes treated with Sylgard Elastomer 184 (Sylgard Elastomer 184 Silicone Encapsulant Clear, Dow Corning, Midland, MI). Muscularis was carefully peeled from the mucosa and placed in cold O.C.T. compound (Fisher Healthcare Tissue-Plus O.C.T. Compound; Thermo Fisher Scientific, Hampton, NH; Cat#23-730-571) in a biopsy specimen cryomold (VWR, Radnor, PA; Cat#4565), frozen in methylbutane on dry ice, and stored at -80°C.

Preparing adult human colon for nuclei isolation

Using insect pins (Fine Science Tools, Cat# 26002-20), colons were maximally stretched and pinned serosa side up on 30 mm dishes treated with Sylgard Elastomer 184 (Sylgard Elastomer 184 Silicone Encapsulant Clear, Dow Corning, Midland, MI). Tissue was incubated in 9 parts carboxygenated (95% oxygen, 5% CO_2) Krebs-Ringer solution (118 mM NaCl (Sigma, Cat#S6191), 4.6 mM KCl (Thermo Fisher Scientific, Cat#BP366-500), 2.5 mM $CaCl_2$ (Cat# C7902), 1.2 mM $MgSO_4$ (Sigma, Cat#M-7506), 1 mM NaH_2PO_4 (Sigma, Cat#S0751), 11 mM D-(+)-Glucose (Sigma, Cat#G-7021), 25 mM $NaHCO_3$ (Thermo Fisher Scientific, Cat#BP328-500), pH 7.4) and 1 part 4-(4-(Dimethylamino)styryl) -N-Methylpyridinium Iodide (4-Di-2-Asp; Abcam, Cambridge, U.K, Cat# ab145266) at room temperature in sterile DPBS. After 10 minutes, the tissue was transferred to ice-cold carboxygenated Krebs-Ringers solution under a SteREO Discovery.V20 fluorescence

dissecting scope (ZEISS, Oberkochen, Germany, 488 nm filter). Fluorescent ENS was carefully dissected from muscularis by peeling away longitudinal muscle strips with Dumont #5 forceps (Fine Science Tools, Cat#11251-30), placed in cold O.C.T. compound (Fisher Healthcare Tissue-Plus O.C.T. Compound; Thermo Fisher Scientific, Hampton, NH; Cat#23-730-571) in a biopsy specimen cryomold (VWR, Radnor, PA; Cat#4565), frozen in methylbutane (Thermo Fisher Scientific Cat#O3551-4) on dry ice, and stored at -80°C.

RNA extraction for RIN assessment prior to sequencing

One to three days before sequencing, frozen mouse or human tissues were sectioned on a Microm HM 505 E Cryostat (GMI, Ramsey, MN; 100 µM sections, -20°C). RNA was extracted from several (1-5) 100 µM sections using the Qiagen RNeasy Plus Micro kit (Qiagen, Hilden, Germany; Cat# 74034) and using Qiagen's RNase Free DNase Set (Qiagen, Cat# 79254). Samples were run on an 2100 Agilent Bioanalyzer using an RNA 6000 Pico Kit (Agilent, Santa Clara, CA, Cat#5067-1513), and tissue was used if RNA Integrity Number (RIN) was > 7.0.

Nuclei isolation and sorting

To isolate nuclei, frozen colon sections (100 µm) in ice-cold lysis buffer (10mM Tris HCl pH 7.5 (Cat# 15567-027), 10 mM NaCl (Sigma, Cat#S6191), 3 mM $MgCl_2$ (Cat# BP214-500), 0.005% Nonidet P40 Substitute (Thermo Fisher Scientific, Cat#AM9010; Sigma, Cat#74385) were chopped rapidly with iridectomy scissors (1 minute), transferred to a pre-cooled Dounce homogenizer (VWR, Cat#357538) on ice, homogenized 15 strokes with the loose pestle and 40 strokes with the tight pestle, filtered through MACS SmartStrainer (Miltenyi Biotec, Cat#130-098-458), centrifuged (590xg, 8 minutes, 4°C), and resuspended in staining buffer (1x phosphate-buffered saline (PBS), 1% w/v Ultrapure BSA (Life Technologies, Cat#AM2618), 0.2U/mL Protector RNase inhibitor, (Sigma, Cat#3335399001)), 2.5µg/mL Hoechst 33342 Trihydrochloride Trihydrate (Thermo Fisher Scientific, Cat# H3570) was added to a final concentration of 2.5 µg/mL before

filtering (FlowMi strainer, VWR, Cat#H13680-0040) and flow sorting (MoFlo Astrios) into 5µL staining buffer using a 70µm nozzle to isolate Hoechst+/mCherry+ nuclei (mouse) or Hoechst+ nuclei (human).

Whole cell isolation from E17.5 mice

An E17.5 *Nos1-CreERT2;ChAT-L10A-EGFP;R26R-TdTomato* dams, tamoxifen treated (200 mg/kg) at E15.5 was euthanized, and pups were rapidly dissected on ice (2 TdTomato+, 3 GFP+). For RNA-seq, full-length small intestines and colon dissociated together were used for RNA-seq. For RT-PCR, TdTomato+ E14.5 and E17.5 small intestine and colon from *Wnt1-Cre+;R26-TdTomato+* mice were analyzed separately. Tissue in carboxygenated 1x Hanks' Balanced Salt Solution (HBSS, Thermo Fisher Scientific, Cat#14025092) was cut into small pieces with insulin needles, and dissociated with Liberase (Sigma, Cat#5401135001) plus DNase I (0.02U/µL, Roche, Basel, Switzerland; Cat#04716728001), $MgCl_2$ (6mM, Cat# BP214-500) and $CaCl_2$ (1mM, Cat# C7902) in HBSS (37^{o}C, 40 minutes) with repeated trituration (P1000). Dissociated cells were, passed 2-3x through 35 µm filters (Falcon, Cat#352235), pelleted (170xg, 3 minutes, 4°C) in 10% fetal bovine serum (FBS)/Iscove's DMEM (Corning, Cat#10-016-CM), resuspended in FACS buffer (0.04% w/v BSA (Thermo Fisher Scientifics, Cat#AM2618) in HBSS (Thermo Fisher Scientific, Cat#14025092)), filtered again, and sorted (BD FACSJazz, 100µm nozzle) into 300µL FACS buffer for sequencing. For RT-PCR, tdTomato+ cells were collected in 1mL Iscove's DMEM/10% FBS, centrifuged (600xg, 5 minutes, 4°C) and resuspended in Buffer RLT plus (Qiagen, Cat#74034).

Library generation, sequencing, and data processing

Libraries prepared with Chromium Single Cell 3' Reagent Kits v2, (Cat#120237, 10X Genomics, Pleasanton, CA) were sequenced on an Illumina HiSeq 2500. Cell Ranger pipeline (10x Genomics) was used to convert BCL files into FASTQ files, perform STAR alignment (70), filter,

count UMI, and generate gene-barcode matrices. Cell Ranger Aggr pipeline (10x genomics, v. 3.0.0) was used to aggregate multiple samples, normalize outputs, and re-compute gene-barcode matrices on combined data.

Analysis of murine single-nucleus and single cell sequencing data

Using Seurat (17,18), gene-barcode matrices were imported into R, filtered to remove low-expressors or doublets (nGene=200-5000 for adult distal colon, nGene = 1000-9000 for E17.5 whole bowel) and mitochondrial contaminants (percent mitochondria <10% for adult distal colon, percent mitochondria <5% for E17.5 whole bowel), normalized, scaled to regress out UMI and percent mitochondria. Cells were clustered using the most statistically significant principal components. To cluster the E17.5 mouse data, we excluded genes located on the X- and Y-Chromosomes from the principal components and included principal components up to the point where either any additional principal component contributed less than 5% of standard deviation and the principal components cumulatively contributed to 90% of the standard deviation or when the variation changes by less than 0.1% between consecutive principal components (71). This turned out to be 15 principal components. For adult mouse distal colon data, we found that taking all of the recommended statistically significant principal components resulted in difficult-to-interpret clustering, possibly due to batch effects in our dataset, and that the first ~11 components were sufficient to cluster our data in a biologically meaningful way. When reclustering was performed on subsets of data (i.e., to filter out contaminants), subsetted data was rescaled and reclustered using the same method described above, minus the normalization step. To identify genes that were differentially- expressed between clusters, clusters were compared one at a time to all other cells in the dataset using a Wilcoxon Rank Sum test with Bonferroni multiple testing correction (Seurat's FindAllMarkers command). A cutoff of at least 10% of cells in a group expressing a gene of interest was required for genes to be tested, and only genes with $\log_e$(fold change) > 0.25 were included in the analysis. Heatmaps (**Figures 2.1, 2.3-2.5, Suppl. Figures 2.2, 2.5**) were generated by taking

the mean of the log-normalized data scaled by Seurat for cells within each cluster. Except where indicated, only genes that were differentially expressed between neuronal clusters are shown. Hierarchical clustering (**Figure 2.7C**) was performed using the complete linkage method. For the GO Term analysis, we combined the three putative immature clusters into one and compared gene expression for these three clusters with the gene expression of all other clusters using a Wilcoxon Rank Sum test with Bonferroni multiple testing correction (Seurat's FindMarkers command). We performed GO Enrichment Analysis for GO biological processes (PANTHER Overrepresentation Test, GO Ontology database released 2020-02-21) using Fisher's exact test with FDR correction. We submitted differentially expressed genes for the immature clusters (immature Chat cluster1, immature Chat cluster 2, immature Nos1 cluster) and compared these to the reference gene list for *mus musculus* (22265 genes). We also submitted differentially expressed genes for the more mature cluster (Chat cluster 1, Chat cluster 2, Nos1 cluster 1, Nos1 cluster 2, Nos1 cluster 3) and compared these to the reference gene list for mus musculus (22265 genes). We reported the 20 most enriched GO Terms. To identify genes differentially expressed between colon and small intestine, we defined colonic neurons as all cells with detectable *Pou3f3* expression. We compared gene expression using a Wilcoxon Rank Sum test with Bonferroni multiple testing correction (Seurat's FindMarkers command) for neurons within the immature clusters (Immature Chat cluster 1, Immature Chat cluster 2, Immature Nos1 cluster) or within the mature clusters (Chat cluster 1, Chat cluster 2, Nos1 cluster 1, Nos1 cluster 2, and Nos1 cluster 3) to normalize for the relatively more immature state of development of the majority of *Pou3f3*-expressing cells (40 mature *Pou3f3*-expressing neurons versus 503 other mature neurons and 94 immature *Pou3f3*-expressing neurons versus 62 other immature neurons). We followed up the identification of potentially colon-specific genes by correlating the gene expression of the gene in question with *Pou3f3* expression in all neurons (pairwise Pearson Correlation).

Analysis of human single-nucleus sequencing data

Using Seurat (17,18), gene-barcode matrices were imported into R, filtered to remove low-expressors or doublets (nGene=200-5000) and mitochondrial contaminants (percent mitochondria <10%), normalized, and scaled to regress out UMI and percent mitochondria. Nuclei were clustered using the most statistically significant principal components identified by elbow plot (11 principle components). Since unbiased clustering initially did not detect the small group of neurons as a distinct group, we identified 48 neurons by isolating all nuclei expressing any copies of *ELAVL4, UCHL1*, or *SNAP25* (**Supplementary Figure 2.7N-P**). These nuclei were reclustered. We saw 7 subgroups that we believe are doublets containing neuronal and non-neuronal nuclei based on co-expression of genes like *ACTG2, PLP1, KIT* 9 (**Supplementary Figure 2.7Q-R**). One subgroup appeared to be pure single neuron data based on high expression of other neuronal markers like *SYT1* and *DSCAM* and the absence of markers for other well-defined cell populations (**Supplementary Figure 2.7Q-R**). The strongly-positive cluster (48 neurons) was mapped back onto the t-SNE plot. To identify neuron-specific genes, we compared this cluster of neurons against all other cell populations using a Wilcoxon Rank Sum test with Bonferroni multiple testing correction (Seurat's FindMarkers command). A cutoff of at least 25% of cells in a group with expression > 0 was required for genes to be tested. Neuron gene expression for the top 50 neuron-specific genes was graphed and neurons were clustered using the Euclidean distance method (**Figure 2.7C**). This revealed two groups of neurons, one which was NOS1+, and another that was NOS1-. We imported a list of 36 transcription and splice factors identified as significantly different in mouse adult colon *Nos1* and *Chat* expressing neurons. Using this list and Seurat's FindMarkers command, we compared expression for these genes between NOS1+ and NOS1- neurons and found differential expression for a subset of transcription factors (**Figure 2.7D**).

Preparing bowel for whole mount immunochemistry

E17.5 bowel was washed in PBS, straightened with stainless steel insect pins (Fine Science Tools, 26002-20) on Sylgard® Elastomer 184 (Silicone Encapsulant Clear, Dow Corning, Midland, MI), and fixed (4% paraformaldehyde (PFA), 20 min, room temperature (RT)). P0 small intestine in ice-cold PBS was opened along mesenteric border, pinned with insect pins serosal side up without stretching onto Sylgard® Elastomer 184 (Sylgard Elastomer 184 Silicone Encapsulant Clear, Dow Corning, Midland, MI), before fixing (4% PFA, 20-30 minutes, RT) and peeling muscularis from mucosa/submucosa. Adult distal colon flushed with ice-cold PBS, was opened along the mesenteric border. Muscle layers were peeled from mucosa/submucosa using Dumont #5 forceps (Fine Science Tools, Cat# 11251-30), maximally stretched, pinned (insect pins) to Sylgard® Elastomer 184, fixed (4% PFA, 20-30 minutes, RT), briefly washed (1x PBS), equilibrated in 50% glycerol/50% PBS (30 minutes, RT or overnight, 4ºC) before storage (-20°C). For high magnification anti-enkephalin and anti-substance P staining, colon opened along mesenteric border was stretched, pinned, and fixed (4% PFA, overnight, 4°C), rinsed in 1x PBS (3 x 10min), and the dissected with fine forceps to remove mucosa, submucosa, and circular muscle from myenteric plexus attached to longitudinal muscle.

Anti-enkephalin and anti-substance P antibodies studies used C57BL6 wild-type mice. Proximal, mid and distal-colon tissue was removed, opened along the mesenteric border, cleaned of fecal matter, stretched and pinned to Sylgard Elastomer 184 and post-fixed (4% PFA, overnight, 4°C). After rinsing 3 times (10-minute/rinse) in 1x phosphate-buffered saline, mucosa, submucous plexus and circular muscle were removed with fine forceps, leaving preparations of myenteric plexus attached to longitudinal muscle.

Whole mount immunohistochemistry

Bowel stored at -20ºC in 50% glycerol/50% PBS was rinsed in PBS, blocked (2 hours, PBS + 0.5% Triton X-100 (Sigma, Cat# T8787) (PBST) with 5% Normal Donkey Serum (NDS; Jackson

ImmunoResearch Laboratory, West Grove, PA, RRID: AB_2337258), incubated in primary antibody (**Supplementary Table 2.7**) with gentle rocking (4°C, 2 days) except for ANNA-1 which was incubated overnight (4°C). After washing (3 x 5 minutes, 0.5% PBST) and secondary antibody (**Supplementary Table 2.7**) incubation in blocking solution with gentle rocking (1 hour, RT), tissue was washed (3 x 5 minutes, PBS), and mounted in 50% glycerol/50% PBS.

For high magnification imaging, longitudinal muscle with exposed myenteric plexus was placed in 10% Casblock (Thermo Fisher Scientific, Cat# 008120) with 0.1% Triton X-100 (ProSciTech, Thuringowa, QLD) in PBS (30 minutes, RT), then in primary antisera (**Supplementary Table 2.7**) (24-48 hours, 4°C) before rinsing (PBS, 3x 10min), and secondary antisera staining (**Supplementary Table 2.7**) (2 hours, RT). After rinsing (PBS, 3x 10min), preparations were mounted using fluorescence mounting medium (DAKO, Carpenteria, CA).

NADPH diaphorase staining

Bowel was pinned flat and fixed (4% PFA, 20min, RT), briefly washed (1xPBS), incubated in 0.1M phosphate buffer, pH7.4 with 1mg/mL beta-nicotinamide adenine dinucleotide phosphate (beta-NADPH, Sigma, Cat# N750), 0.1mg/mL nitroblue tetrazolium (Sigma, Cat#11383213001), 0.3% Triton-X 100 (1 hour, 37ºC), washed in PBS, and imaged immediately in a custom-made holding chamber.

Preparing human colon for whole mount immunochemistry

Human colon with fat trimmed was pinned serosa side up on Sylgard® Elastomer 184 plates in ice-cold PBS using stainless steel insect pins. Tissue was maximally stretched during pinning to make the colon as thin as possible. Pinned tissue was fixed overnight (4ºC, 4% PFA), washed in DPBS, and stored at 4ºC in 50% PBS/50% glycerol/0.05% sodium azide until staining.

Immunofluorescence staining of human colon whole mount

Following our new protocol (14), 0.7-1cm x 0.7-1cm colon pieces were washed (1x PBS, RT), incubated in 100% methanol on ice (1 hour), treated with Dent's bleach (1 mL 30% hydrogen peroxide (Thermo Fisher Scientific, Cat #H1009), 1 mL dimethyl sulfoxide (Sigma, Cat#D2650), 4 mL 100% methanol (72)) at room temperature (2 hours), washed again (1x PBS, 3x5 minutes, room temperature), blocked (0.5% Triton X-100, 5% NDS in PBS, 3 days) and then incubated 14 days in blocking solution with primary antibodies (**Supplementary Table 2.7**, 37ºC, 40-100 rpm). Following PBS washing (1 day, 3 washes, gentle rocker, RT), colon was incubated in secondary antibodies 3 days, 37ºC, 40-100 rpm), washed in PBS over 1 day, dehydrated in a methanol series, placed in Murray's clear (2:1 benzyl benzoate:benzyl alcohol, gentle rocking, RT) until translucent (30-60 min). Transparent colon mounted on glass slides in Murray's clear was imaged within 1 day. For details see (dx.doi.org/10.17504/protocols.io.wyeffte).

Microscopy

Images were acquired with a Zeiss LSM 710 confocal microscope with 20x/0.8 air or 63x/1.4 oil DIC M27 Plan-Apochromat objectives and Zeiss Zen software version 2.3 14.0.14.201 (Zeiss, Oberkochen, Germany) or upright fluorescent Olympus BX60 microscope with Axiocam CCD camera and Axiovision software. ImageJ (NIH) and Photoshop CS6 (Adobe, San Jose, CA) were used to crop and uniformly adjust color. High magnification myenteric plexus images were acquired with a Zeiss LSM 880 Airyscan microscope with a Plan-Apochromat 63x1.40 Oil DIC M27 objective (Carl Zeiss Microscopy, North Ryde, NSW, Cat#420782-990-799) at the Biological Optical Microscopy Platform (BOMP), University of Melbourne.

Image analysis

Counting for adult mouse distal colon and human colon was performed on >5 randomly-selected x20 fields per animal in each region using ImageJ's CellCounter module (NIH). Because

of high cell density at E17.5, only half of each 20X field was counted. Investigators were blinded to genotype when comparing knockout to control mice. High magnification myenteric plexus images were processed to quantify substance P and enkephalin colocalization using Imaris 9.0.0 (Bitplane) (22).

RNA extraction and RT-PCR for *Pou3f3* expression analysis

Wnt1-Cre;R26-TdTomato E14.5 and E17.5 dams were euthanized with 5% CO_2, and pups were removed from the mother. For each litter, all TdTomato+ small intestines and colons were combined to increase cell count. Small intestines and colons were dissected in ice-cold Dulbecco-modified PBS, transferred to HBSS (Thermo Fisher Scientific, Cat No: 14025092), separated, divided into small pieces using insulin needles (Beckton Dickerson, Cat#08290-3284-18), and dissociated for 30 minutes at 37°C in Liberase (Sigma, Cat#5401135001) supplemented with DNase I (Roche, Basel, Switzerland; Cat#04716728001), $MgCl_2$ (6 mM) and $CaCl_2$ (1 mM) in HBSS with P1000 trituration. Cells were filtered, washed with Iscove's DMEM (Corning, Cat#10-016-CM), and resuspended in FACS buffer (10mM HEPES, 1mg/mL BSA, 1% penicillin and streptomycin (Thermo Fisher Scientific, Cat#15140122) in HBSS). Fluorescent TdTomato+ cells were sorted on a BD FACSJazz and collected in Iscove's DMEM with 10% FBS. Cells were spun down at 600xg, resuspended in Buffer RLT plus, and RNA was isolated using the Qiagen RNeasy Plus Micro Kit (Qiagen, Hilden, Germany; Cat# 74034) with DNase treatment (Qiagen, Cat#79254).

RNA integrity and concentrations were measured on a 2100 Agilent Bioanalyzer using an RNA 6000 Pico Kit (Agilent, Santa Clara, CA, Cat#5067-1513). All samples used had RIN ≥ 7. cDNA was generated using Superscript II RNase H (Thermo Fisher Scientific, Cat#18064022). RT-PCR was performed using KAPA mixture (KAPA biosystems, Cat#KK7352) and previously-described primers (**Supplementary Table 2.8**). Three replicates were run for all experiments.

Colon Bead Expulsion studies

Young adult mice (P44-58 at begin of assay, P49-64 at end of assay) were anesthetized with 2L/min carbogen with 2.5% (v/v) isoflurane (Piramal, Cat#NDC 66794-017-10) for 1.5 minutes before the start of the experiment, anesthesia was continued until completed bead insertion. A glass bead (3 mm, Sigma, Cat#Z143928) lubricated with sunflower seed oil (Sigma, Cat#S5007) was inserted 2 cm into the colon using a custom-made 3-mm rounded glass rod. Glass rod was removed, isoflurane stopped, mice were placed in empty cages, and time to bead expulsion was recorded. If a mouse regained consciousness before bead insertion, mice were anesthetized for an additional 2-4min. Assay was repeated 3 times per mouse (48-96 hours between procedures). Mice had free access to food and water prior to the experiment.

Calcium imaging full thickness colon

Colons from *E2a-Cre;R26R-Gcamp6s* mice aged 12-16 weeks were cut longitudinally and pinned (mucosa facing down) in a Sylgard-lined dish superfused with carbogenated (95% O2, 5% CO2) artificial cerebrospinal fluid (ACSF) (29), freshly prepared, maintained at 35ºC. Nifedipine (1µM, Sigma, Cat# N7634) in ACSF improved stability for calcium imaging analyses. GCaMP6s in myenteric neurons was imaged with an upright DM6000FS Leica fluorescence microscope (Leica, Buffalo Grove, IL) and EMCCD camera (Photometrics; Roper Scientific, Tucson, AZ) using a x20 objective. Images were collected with Metamorph software (Molecular Devices, San Jose, CA) at 10 Hz sampling rate. For each field, spontaneous activity was imaged 2 min, before two 30s movies were collected in response to electrical field stimulation (EFS; 100 µs pulse, 20 Hz, 1 s) using concentric electrodes 5 mm oral or aboral to imaging fields (order randomized). Recombinant rat GDNF (Cat. #512-GF, R&D Systems) or NRTN (Cat. #450-11, PeproTech) were added at 10nM final concentration (order of presentation randomized). We recorded spontaneous activity in 2-min movies collected intermittently while ligands continuously superfused circulating ACSF for 10 min. Responses to oral and aboral stimulation were then re-imaged. Colon was washed for 30 min and

baseline activity and responses were re-imaged before the next receptor ligand was applied. In a subset of experiments, the addition of tetrodotoxin (TTX, 0.5μM, Cat. #T8024, Sigma) or hexamethonium (HEX, 300μM, Cat. #H0879, Sigma) blocked all neural transmission or excitatory synaptic transmission, respectively, allowing for identification of myenteric neurons directly activated by GDNF or NRTN. Spontaneous activity was recorded (three 2-min movies) at baseline, 10 min following TTX or HEX, and during application of GDNF or NRTN (in the presence of either TTX or HEX; order of presentation of GDNF/NRTN was randomized). Colon tissue was then "washed" with the particular blocker, activity was re-imaged, and the next receptor ligand was applied while imaging responses.

Analysis of live GCaMP6s imaging

Metamorph (Molecular Devices, Downington, PA) image files exported to ImageJ (NIH) were coded for blind analysis. Circular ROIs were drawn on all myenteric neurons in each field. Amplitude of GCaMP6s signals were analyzed and quantified as described (Smith-Edwards et al. 2016). We calculated ΔF/F0 [% = ((F − F0)/F0) x 100], where F is peak fluorescence and F0 is baseline mean fluorescence; ΔF/F0 of 4SD > baseline was considered a response. Time control studies, in which GCaMP6s activity from individual neurons was measured over time, were used to determine whether changes in activity were significantly altered due to GDNF or NRTN application. Tissue movement along x- and y-axes was measured using ImageJ Template-Matching plugin. Time-lapse color-coded images created in ImageJ use pixel color to indicate when pixels reached maximum F, providing spatial and temporal information about activity.

Statistics

We used Prism 7.03 (GraphPad Software, San Diego, CA) software. A cutoff of $p < 0.05$ was considered significant. Data represent mean ± standard error of the mean (SEM).

2.6 Author Contributions

Conceptualization: CMW, SS, ROH; Methodology: CMW, SS, KMSE, AJLL, ROH, MJH, BMD, JCB; Formal Analysis: SS, CMW, MVG, KMSE, Investigation: CMW, SS, FM, KMSE, AJLL, DRK, MVG, TAM, JBA, BM, TG; Writing - original draft: CMW, SS, ROH, KMSE; Writing - Review and Editing: CMW, SS, ROH, KMSE, BMD, AJLL, JCB, MJH; Funding Acquisition: ROH, MJH, JCB, BMD; Supervision: ROH, BMD, JCB.

2.7 Acknowledgements and Funding

We thank Dr. Emma Furth, Dr. Federico Valdivieso, Dr. Michael Feldman, Dr. Ali Naji, Rachel H. Céron, Silvia Huerta López, Caitlin Feltcher, Andrew Kromer, Lauren Schmucker, and Jennifer Finan for help with human tissue acquisition. We are grateful to Scott Gianino for initial studies of POU3F3. This work was supported by the Irma and Norman Braman Endowment, The Children's Hospital of Philadelphia Research Institute, the Suzi and Scott Lustgarten Center Endowment, NIH grants 5 F30 DK117546-02 (CMW), F32 DK120115 (KMSE), R01DK122798 (Brian Davis PI, Robert Heuckeroth and Marthe Howard co-PIs) and from NIH SPARC Program OT2OD023859 (Marthe Howard PI, Robert Heuckeroth, Brian Davis and Joel Bornstein co-PIs).

2.8 Supplementary Materials

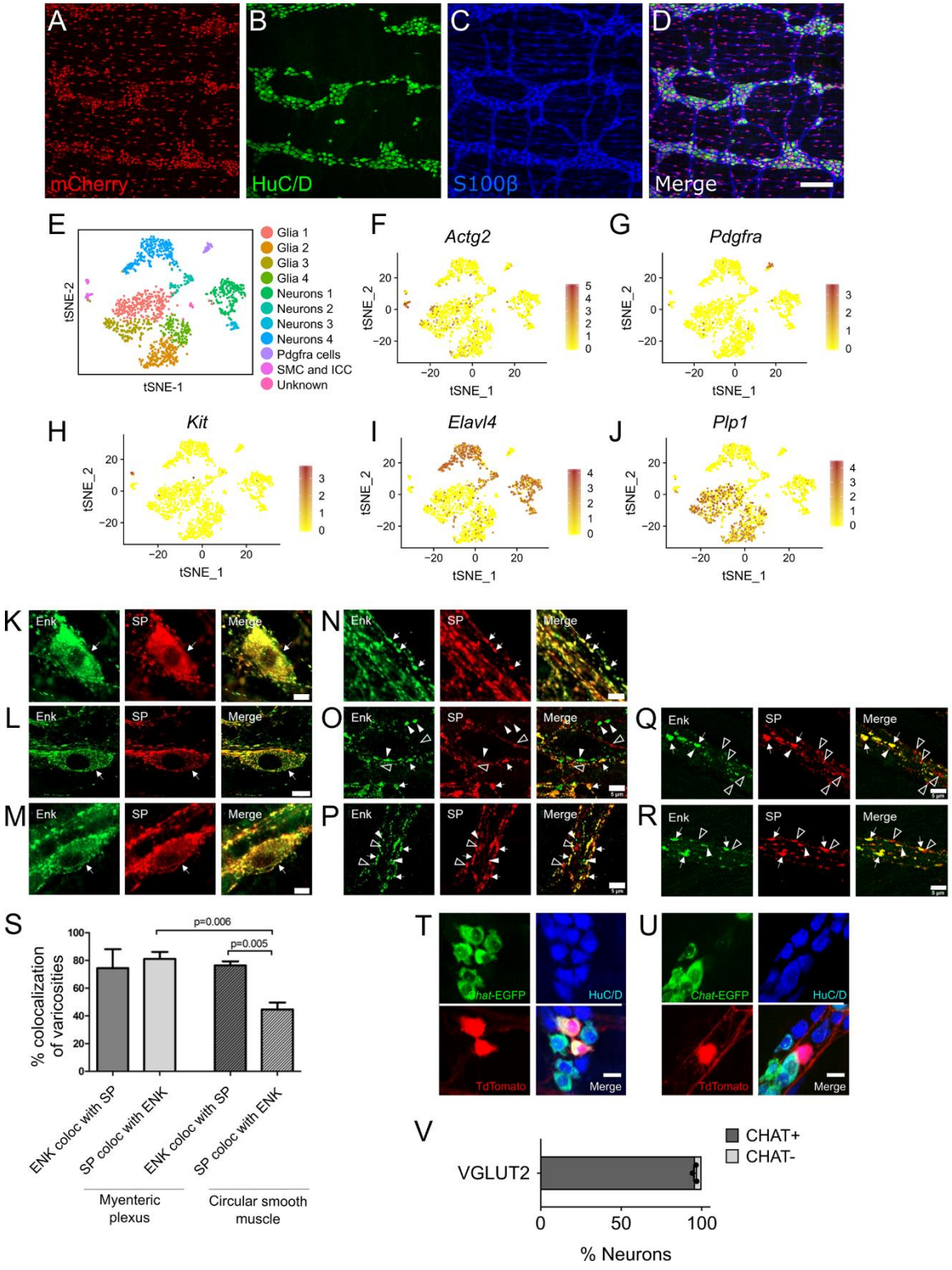

Supplementary Figure 2.1: Initial processing of single nucleus RNA-seq data from young adult *Wnt1-cre$^{cre/wt}$; R26R-H2B-mCherry$^{ch/wt}$* mouse colon with validation of enkephalin and substance P co-expression.

(A-D) H2B-mCherry fluorescence (red) in 50 day old *Wnt1-cre$^{cre/wt}$; R26R-H2B-mCherry$^{ch/wt}$* mice colocalizes with HuC/D+ neurons (green) and S100β+ glia (blue) in the ENS. ~73% of HuC/D+ neurons were H2B-mCherry+. (E) T-SNE plot of all cell groups from distal colon of *Wnt1-cre$^{cre/wt}$; R26R-H2B-mCherry$^{ch/wt}$* mice. (F-J) Feature plots for *Actg2* (F), *Pdgfrα* (G), *Kit* (H), *Elavl4* (I), and *Plp1* (J) indicate the locations of SMC, Pdgfrα+ cells, ICC, neurons, and glia respectively. Color key represents $\log_e$(normalized gene expression). Scale bar 100μm. (K-M) Enkephalin (green) colocalizes with substance P (red) in myenteric neuron cell bodies in proximal (K), mid (L), and distal colon (M). (N-P) Most myenteric intraganglionic neuron varicosities in proximal (N), mid (O), and distal colon (P) express both enkephalin (green) and substance P (red). (Q-R) Most enkephalin+ (green) neuron varicosities in circular smooth muscle in mid-colon (Q) and distal colon (R) also express substance P (red), but only a subset of substance P-expressing neuron varicosities in circular smooth muscle express enkephalin. (K-R) Images representative of n=3 preparations per colon region and n=3 images per preparation. (S) Quantification of colocalization of enkephalin and substance P in varicosities within mid-colon myenteric ganglia and within circular smooth muscle. (T) EGFP (green) fluorescence signal colocalizes with TDTOMATO+ (red) neurons (blue) in *Vglut2-IRES-Cre; R26R-TdTomato; ChAT-EGFP-L10A* mice. (U) In a small subset of HuC/D+ neurons (blue), TDTOMATO+ (red) does not colocalize with EGFP fluorescence signal in *Vglut2-IRES-Cre; R26R-TdTomato; ChAT-EGFP-L10A* mice. (V) Quantification of the colocalization of EGFP fluorescence with TDTOMATO fluorescence in *Vglut2-IRES-Cre; R26R-TdTomato* mice. (K-M) Scale bar = 10μm. (N-R) Scale bar 5μm. (K-R) White arrows point towards cells and varicosities that express both enkephalin and substance P. (N-R) White arrowheads point towards varicosities that express enkephalin only. Empty arrowheads point towards varicosities that express substance P only. (S, V) Mean +/- SEM.

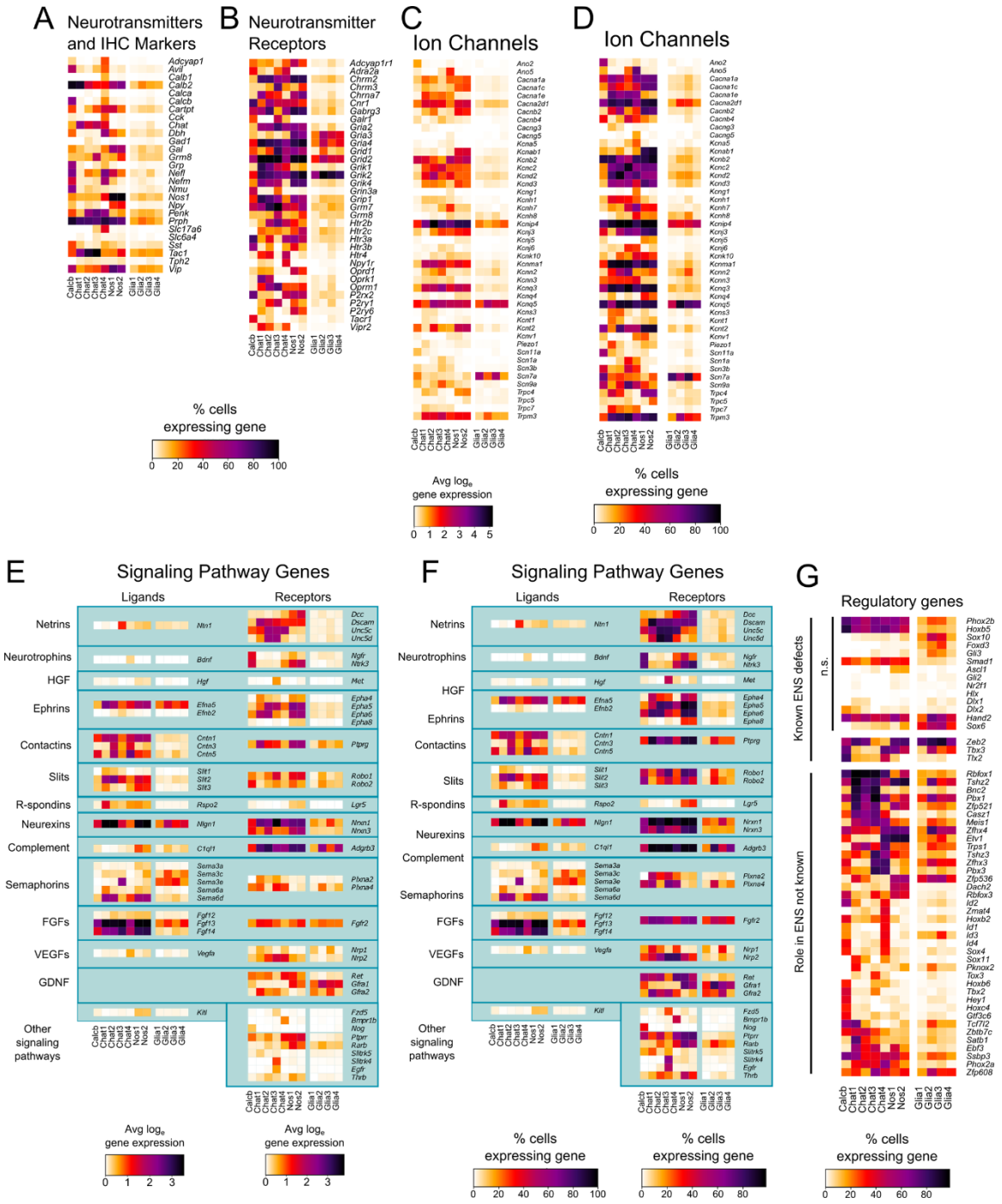

Supplementary Figure 2.2: Percent of cells per cluster with detectable levels of differentially expressed neurotransmitters, commonly used enteric neuron immunohistochemical markers, neurotransmitter receptors, and regulatory factors in adult distal mouse colon. Average expression per cluster and percent of cells per cluster with detectable levels of

differentially expressed ion channels and signaling pathway molecules in adult distal mouse colon.

(A-B) Proportion of cells per cluster with expression values >0 for differentially expressed neurotransmitters, immunohistochemical markers (A) and neurotransmitter receptors (B). Color bar applies to both panels. (C) Average expression of differentially expressed ion channel (subunit) genes for different neuron and glial groups. (D) Proportion of cells per cluster with expression values >0 for differentially expressed ion channels. (E) Average expression for selected ligands (left) and receptors (right) that were differentially expressed between different neuron and glial subclasses. (F) Proportion of cells per cluster with expression values >0 for differential expressed ligands (left) and receptors (right). (G) Proportion of cells per cluster with expression values >0 for transcription and splicing factors with known roles in ENS development(top), and regulatory genes (transcription factors and splicing factors) newly-identified in the ENS in this study (bottom). n.s. = not significantly differentially expressed between neuron clusters. (C-E) Color key represents $\log_e$(normalized average gene expression within each cluster).

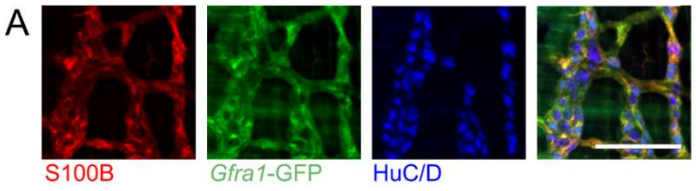

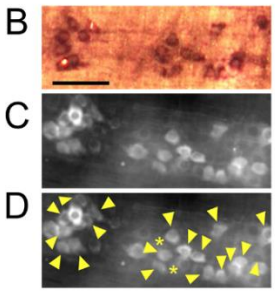

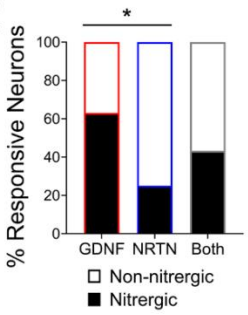

F

Nitrergic neurons	GDNF/ No change	GDNF/ increased response	GDNF/ decreased response	SUM
NRTN/No change	65	13	16	94
NRTN/increased response	9	5	3	17
NRTN/decreased response	8	3	2	13
	82	21	21	124

G

Non-nitrergic neurons	GDNF/ No change	GDNF/ increased response	GDNF/ decreased response	SUM
NRTN/No change	131	12	5	148
NRTN/increased response	28	10	1	39
NRTN/decreased response	23	0	6	29
SUM	182	22	12	216

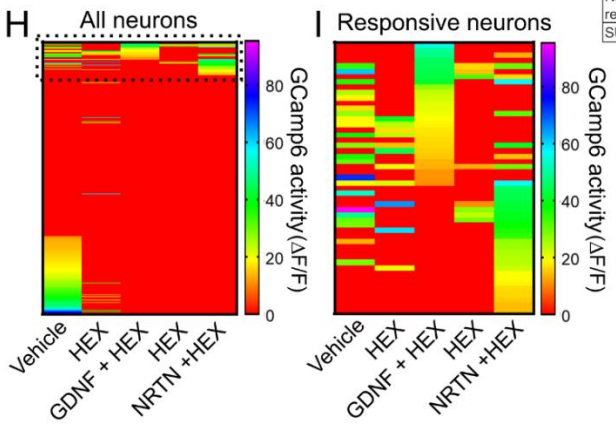

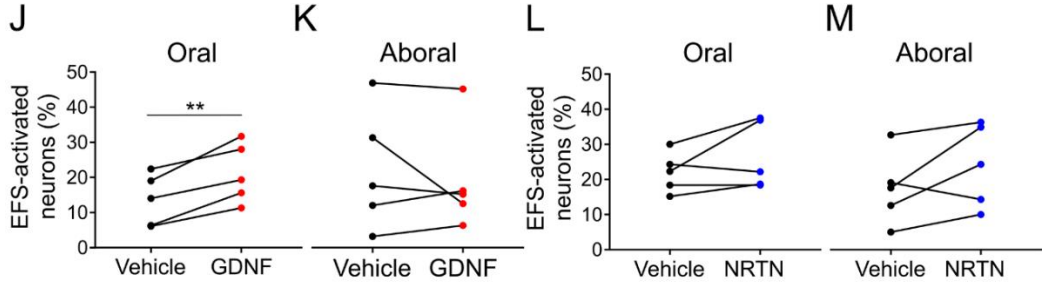

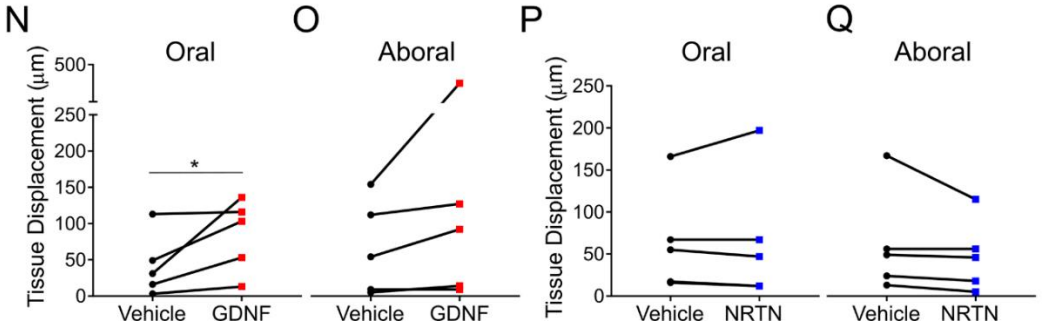

Supplementary Figure 2.3: *Gfra1* is expressed in adult enteric neurons and glia. GDNF modulates activity in some myenteric neurons and enhances colon muscularis movement. (A) Whole mount immunohistochemistry using *Gfra1*$^{Gfp/wt}$ distal colon shows colocalization of GFP (green) with S100B+ (red) glia and HuC/C (blue) neurons. Scale bar = 100 microns. (B) NADPH diaphorase stained colon identifies nitric oxide producing neurons. (C) Corresponding GCaMP6s imaging field. (D) GCaMP6s imaging field in (C) where yellow arrowheads identify putative nitrergic myenteric neurons and asterisks indicate putative NADPH diaphorase positive neurons with low GCaMP6s signal. (E) Quantification of GDNF- and NRTN-responsive nitrergic neurons (n=3 fields from separate experiments, p=0.0298, Fisher Exact test, 2x2 contingency table (NOS+/NOS- and GDNF response/NRTN response)). (F, G) Quantitative data for GCaMP6s imaging fields stained *post-hoc* for NADPH diaphorase, indicating response to GDNF and NRTN. (F) Responsive nitrergic neurons. (G) Responsive non-nitrergic neurons. (H) Heatmap illustrating GCaMP6s activity before and after addition of the nicotinic acetylcholine receptor antagonist hexamethonium (HEX) and during the sequential application of GDNF and NRTN. Each row represents a single neuron and colors represent the magnitude of the change in GCaMP6s activity (red = no activity change). Dotted line shows GDNF and NRTN responsive neurons. Activity was assessed for 352 total neurons in 4 independent colon sections from 1 mouse. (I) Heatmap focusing only on GDNF- and NRTN-responsive neurons illustrating GCaMP6s activity before and after hexamethonium (HEX) addition and during the sequential application of GDNF and NRTN. 28 neurons were only GDNF-responsive, 24 neurons only NRTN-responsive, and 9 neurons responded to both GDNF and NRTN. Each row represents a single neuron and colors represent the magnitude of the change in GCaMP6s activity (red = no activity change). (J-M) Percent of total observed neurons per GCaMP6s imaging field with increased activity after electrical field stimulation (EFS) applied 5 mm oral (J, L) or aboral (K,M) relative to the imaging field at baseline (vehicle) and in the presence of GDNF (J, K) and NRTN (L, M). GDNF increases the percent of activated neurons after orally applied EFS (J, p=0.0068, ratio paired t-test). (N-Q) Tissue displacement (micrometers) after EFS applied 5 mm oral (N, P) or aboral (O,Q) relative to the imaging field at baseline (vehicle) and in the presence of GDNF (N, O) and NRTN (P-Q). Tissue displacement is increased in the presence of GDNF after orally applied EFS (N, p=0.0230, ratio paired t-test). (B-G) n=3 fields of view from separate mice. *p<0.05 **p<0.01

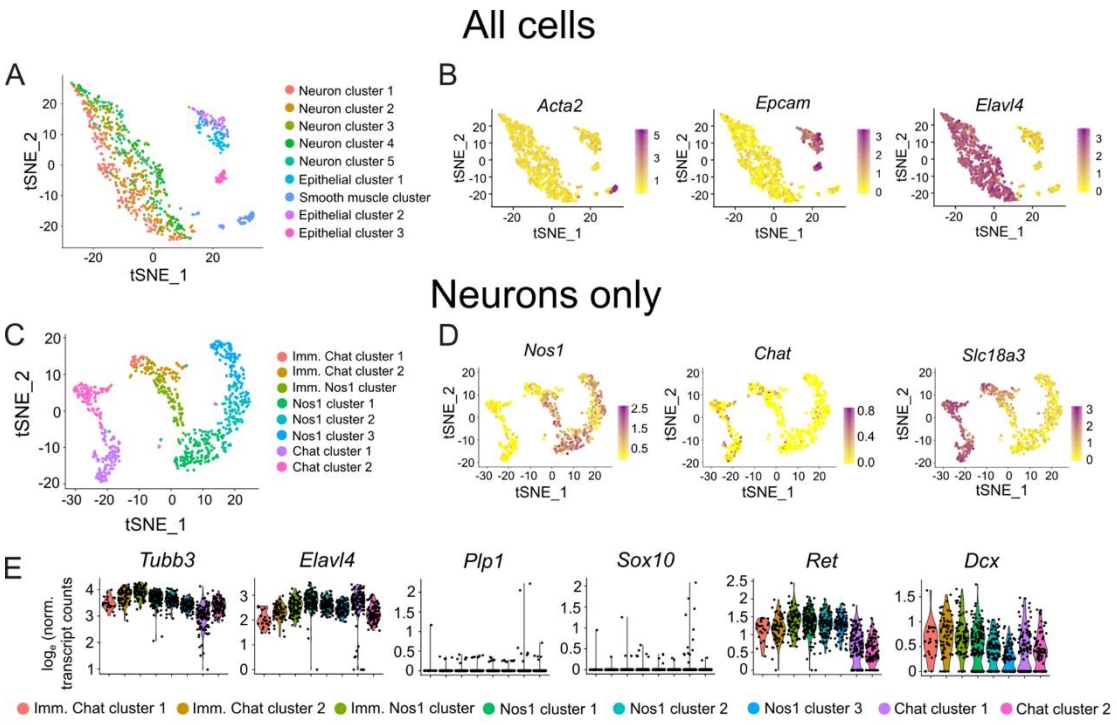

F

GO Terms (biological process) enriched in immature neuron clusters

GO biological process	GO Term	Fold enrichm.	raw p-value	FDR
intermediate filament polymerization or depolymerization	GO:0045105	> 100	9.78E-05	1.32E-02
neurofilament bundle assembly	GO:0033693	> 100	1.63E-04	1.93E-02
regulation of axon diameter	GO:0031133	81.56	4.52E-04	4.41E-02
noradrenergic neuron differentiation	GO:0003357	81.56	4.52E-04	4.38E-02
neurofilament cytoskeleton organization	GO:0060052	73.4	1.81E-05	3.25E-03
limb bud formation	GO:0060174	66.73	2.30E-05	4.04E-03
axon regeneration	GO:0031103	43.18	7.07E-05	9.89E-03
synaptic membrane adhesion	GO:0099560	27.19	2.45E-04	2.74E-02
lens morphogenesis in camera-type eye	GO:0002089	26.21	2.70E-04	2.98E-02
negative regulation of cardiac muscle tissue growth	GO:0055022	25.31	2.97E-04	3.26E-02
negative regulation of stress fiber assembly	GO:0051497	24.47	3.26E-04	3.43E-02
cardiac septum morphogenesis	GO:0060411	15.49	2.40E-05	4.12E-03
neural crest cell development	GO:0014032	15.29	2.54E-05	4.31E-03
outflow tract morphogenesis	GO:0003151	12.55	3.53E-04	3.62E-02
regulation of extent of cell growth	GO:0061387	9.56	2.13E-04	2.43E-02
dendrite development	GO:0016358	8.8	3.08E-04	3.31E-02
neuron migration	GO:0001764	8.55	3.50E-04	3.61E-02
negative regulation of ion transport	GO:0043271	8.11	1.17E-04	1.51E-02
negative regulation of neuron differentiation	GO:0045665	7.65	1.24E-05	2.39E-03
axon guidance	GO:0007411	6.7	3.18E-04	3.39E-02

G

GO Terms (biological process) enriched in mature neuron clusters

GO biological process	GO Term	Fold enrichm.	raw p-value	FDR
positive regulation of timing of catagen	GO:0051795	> 100	1.16E-04	3.12E-02
modulation of excitatory postsynaptic potential	GO:0098815	20.65	5.49E-05	1.97E-02
positive regulation of cation channel activity	GO:2001259	14.64	1.95E-04	4.34E-02
regulation of release of sequestered calcium ion into cytosol	GO:0051279	14.64	1.95E-04	4.28E-02
negative regulation of transmembrane transport	GO:0034763	10.33	1.46E-04	3.78E-02
axonogenesis	GO:0007409	5.92	2.01E-04	4.30E-02
positive regulation of neuron differentiation	GO:0045666	4.93	2.36E-04	4.78E-02
positive regulation of cell population proliferation	GO:0008284	3.89	2.78E-05	1.42E-02
regulation of anatomical structure morphogenesis	GO:0022603	3.71	2.17E-05	1.18E-02
positive regulation of phosphate metabolic process	GO:0045937	3.28	1.53E-04	3.66E-02
negative regulation of signal transduction	GO:0009968	3.18	2.05E-04	4.32E-02
negative regulation of multicellular organismal process	GO:0051241	3.1	1.50E-04	3.71E-02
positive regulation of cell communication	GO:0010647	2.87	3.89E-05	1.66E-02
positive regulation of signaling	GO:0023056	2.86	4.09E-05	1.66E-02
positive regulation of RNA metabolic process	GO:0051254	2.81	1.48E-04	3.77E-02
positive regulation of cellular biosynthetic process	GO:0031328	2.72	7.69E-05	2.38E-02

Supplementary Figure 2.4: Single-cell sequencing of E17.5 *ChAT-EGFP-L10A*+ and *Nos1-CreERT2*$^{Cre/wt}$*;R26R*-TdTomato+ cells reveals several neuron clusters at different stages of maturity.

(A) T-SNE plot of all cell groups isolated from E17.5 bowel. (B) Feature plots of *Acta2* as smooth muscle marker, *Epcam* as an intestinal epithelial marker, and *Elavl4* as a pan-neuronal marker.

Color key represents $\log_e$(normalized gene expression). (C) After removing the epithelial and smooth muscle cells from the dataset and reclustering, T-SNE plot reveals multiple neuron subpopulations. (D) Expression of *Nos1* and the cholinergic marker *Slc18a3/VachT* verifies the presence of the expected cholinergic and nitergic neuronal subpopulations. *Chat* expression was low throughout, but overlapped with *Slc18a3* expression. Color key represents $\log_e$(normalized gene expression). (E) All neurons have high expression of pan-neuronal markers *Tubb3* and *Elavl4*. There is minimal contamination with glial cells based on the expression of enteric glial marker *Plp1*. *Sox10*, which marks enteric glia and enteric neural crest precursors was also low, but *Ret*, which is expressed in ENS precursors and many neurons, was present in all clusters. This suggests that these cells are lineage-restricted neurons, however, all neurons still express the immature pan-neuronal marker *Dcx*. (F) GO Term analysis of differentially expressed genes in the three more immature neuron clusters (immature chat cluster 1, immature chat cluster 2, immature Nos1 cluster) compared to all other clusters indicates that these neurons are actively involved in cytoskeletal reorganization and neurite extension. (G) GO Term analysis of differentially expressed genes in the five more mature neuron clusters (Chat cluster 1, Chat cluster 2, Nos1 cluster 1, Nos1 cluster 2, and Nos1 cluster 3) compared to the immature clusters (Immature Chat cluster 1, Immature Chat cluster 2, and Immature Nos1 cluster) indicates that these neurons are actively involved in synapse formation.

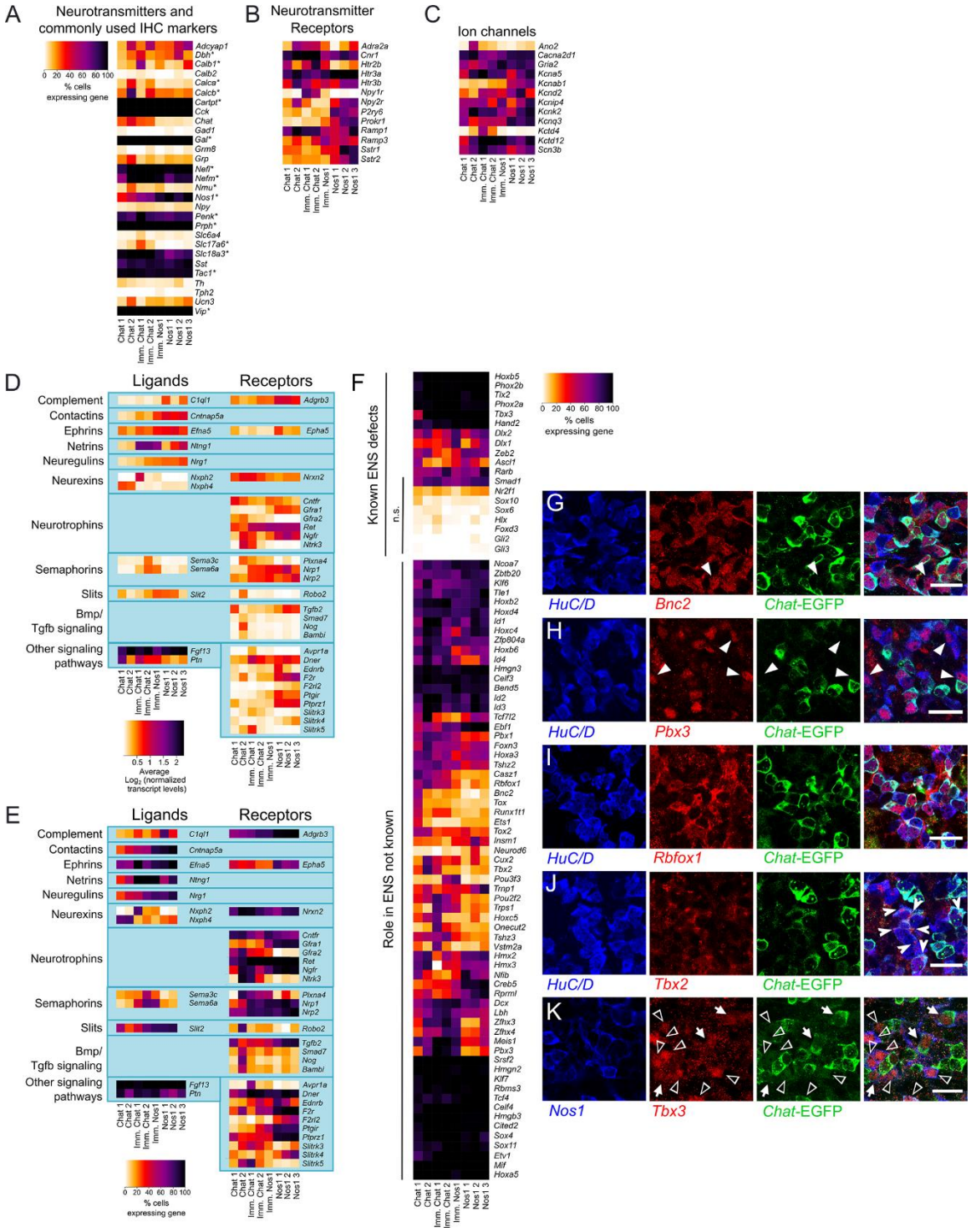

Supplementary Figure 2.5: Cholinergic and nitrergic neuron subsets at E17.5 differentially express ion channels and signaling pathway molecules as well as many regulatory genes found in adult distal colon ENS.

(A) Neurotransmitter and commonly used enteric neuron immunohistochemical markers with > 0 detected reads. Asterisks mark genes differentially expressed across the distinct neuron subclasses. Color key represents proportion of cells per cluster with expression values >0. (B-C) Neurotransmitter receptor (B) and ion channel (C) genes differentially expressed across distinct neuron subclasses. Color key represents proportion of cells per cluster with expression values >0. (D-E) Genes involved in extracellular signaling pathways differentially expressed across neuron subclasses. (D) Color key represents $\log_e$(normalized average gene expression within each cluster). (E) Color key represents proportion of cells per cluster with expression values >0. (F) Transcription and splicing factors with known roles in ENS development (top), and newly-identified in the ENS in this study (bottom). n.s. = not significantly differentially expressed between neuron clusters. Color key represents proportion of cells per cluster with expression values >0. (G-K) Whole-mount immunohistochemistry of select regulatory genes in E17.5 *ChAT-EGFP-L10A* reporter mouse mid-colon shows gene localization in neuron subsets. BNC2 (G), PBX3 (H), and RBFOX1 (I) are predominantly expressed in cholinergic (EGFP+) neurons. (B-D) White arrowheads indicate neurons that express the regulatory gene in question, but are not cholinergic. (J) TBX2 does not have nuclear or diffuse cytoplasmic staining in the E17.5 colon. Instead, TBX2 immunoreactive cytoplasmic aggregates were detected in a subset of cholinergic (EGFP+) neurons (notched white arrowheads). (K) TBX3 is expressed in some cholinergic (EGFP+, white arrows) and most nitrergic (NOS1+, empty arrowheads) neurons. (G-K) *ChAT-EGFP-L10A* reporter = *Chat*-EGFP. Scale bar = 20µm (B-G).

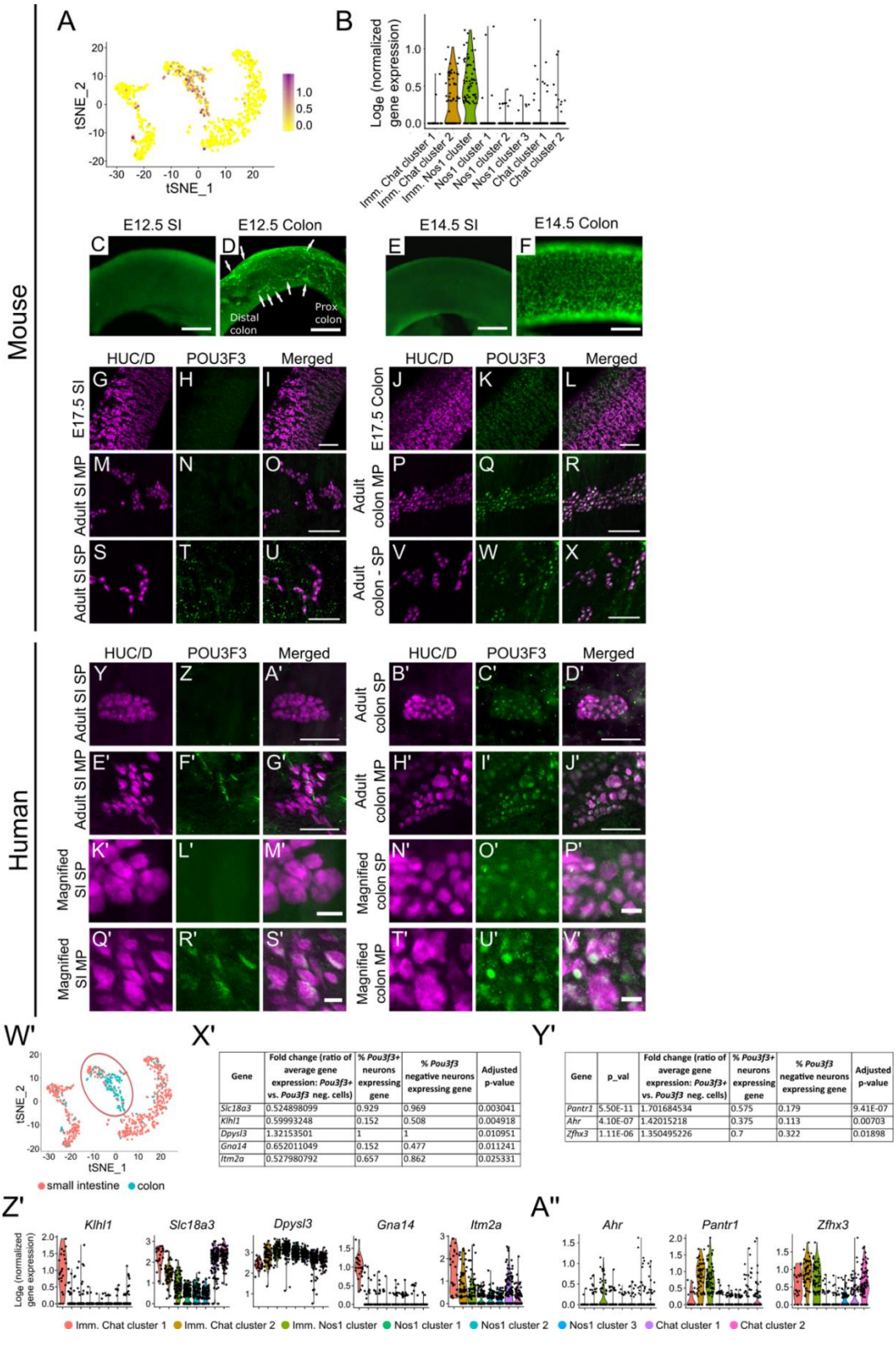

Gene	Fold change (ratio of average gene expression: *Pou3f3+* vs. *Pou3f3* neg. cells)	% *Pou3f3+* neurons expressing gene	% *Pou3f3* negative neurons expressing gene	Adjusted p-value
Slc18a3	0.524898099	0.929	0.969	0.003041
Klhl1	0.59993248	0.152	0.508	0.004918
Dpysl3	1.32153501	1	1	0.010951
Gna14	0.652011049	0.152	0.477	0.011241
Itm2a	0.527980792	0.657	0.862	0.025331

Gene	p_val	Fold change (ratio of average gene expression: *Pou3f3+* vs. *Pou3f3* neg. cells)	% *Pou3f3+* neurons expressing gene	% *Pou3f3* negative neurons expressing gene	Adjusted p-value
Pantr1	5.50E-11	1.701684534	0.575	0.179	9.41E-07
Ahr	4.10E-07	1.42015218	0.375	0.113	0.00703
Zfhx3	1.11E-06	1.350495226	0.7	0.322	0.01898

Supplemental Figure 2.6: *Pou3f3* is expressed in mouse colon but not small intestine ENS. (A) Feature plot shows scattered E17.5 enteric neurons expressing *Pou3f3* throughout the neuron clusters. Color key represents $\log_e$(normalized gene expression). (B) Violin plot of *Pou3f3* expression in E17.5 enteric neurons indicates that *Pou3f3* is predominantly expressed in Immature Chat cluster 2 and Immature Nos1 cluster. (C-X) Whole mount immunohistochemistry confirms that POU3F3 immunoreactivity (green) is not detected in most of the small bowel at E12.5 (C), E14.5 (E), E17.5 (H), or in adulthood (N,T). POU3F3 immunoreactivity is easily detected in proximal colon (D) at E12.5 (arrows) and throughout the colon at E14.5 (F), E17.5 (K), and in adulthood (Q,W). (L,R,X) At E17.5 and in adulthood, colonic POU3F3 co-localizes with the enteric neuron marker HuC/D. (Y-V') Confocal z-stack maximum intensity projections at lower magnification (Y-J') and high magnification (K'-V') of whole mount immunohistochemistry for POU3F3 in adult human small intestine (Y-A', E'-G', K'-M', Q'-S') and adult human colon (B'-D', H'-J', N'-P', T'-V') shows nuclear POU3F3 localization only in colonic neurons. No POU3F3 staining was detectable in human small intestine submucosal plexus (Y-A', K'-M'), whereas clear nuclear POU3F3 staining could be seen in human colon submucosal neurons (B'-D', N'-P'). Cytoplasmic POU3F3 antibody staining was present in a subpopulation of human small intestine myenteric neurons (E'-G', Q'-S'). In the human colon myenteric plexus all neurons showed clear nuclear POU3F3 localization (H'-J', T'-V'). (W') Feature plot showing scattered E17.5 enteric colonic neurons. Cells expressing *Pou3f3* were assigned colonic identity. Red circle marks immature clusters: immature Chat cluster 1, immature Chat cluster 2, and immature Nos1 cluster. (X') Genes differentially expressed by cells assigned colon identity compared to cells assigned small intestine identity within the three immature clusters (immature Chat cluster 1, immature Chat cluster 2, immature Nos1 cluster). (Y') Genes differentially expressed by cells assigned colon identity compared to cells assigned small intestine identity within the three mature clusters (Chat cluster 1 and 2 and Nos1 cluster 1, 2, and 3). (Z') Violin plots showing expression of the differentially expressed genes across all E17.5 neuron clusters indicate that the genes identified in (X') are specific to immature Chat cluster 1 and not colon or small intestine (Pearson Correlation between the expression of the identified gene and *Pou3f3* supports this conclusion: p>0.1 for all, except *Dpysl3*, corr. coeff.=0.0819, p=0.0294) (A'') Violin plots showing expression of the differentially expressed genes across all E17.5 neuron clusters suggest that the expression of genes *Ahr* and *Pantr1* and possibly *Zfhx3* are specific to colon myenteric neurons (Pearson Correlation between the expression of the identified gene and *Pou3f3* supports this conclusion: *Ahr*, corr. coeff.= 0.3581, $p<2.2x10^{-6}$; *Pantr1*, corr.coeff.=0.5640, $p<2.2x10^{-6}$; *Zfhx3*, 0.4034, $p<2.2x10^{-6}$). SP = submucosal plexus, MP = myenteric plexus. Images are representative of 3 independent biological replicates. Scale bar = 100 µM (C, E-J'), 200 µM (D), 20 µM (K'-V').

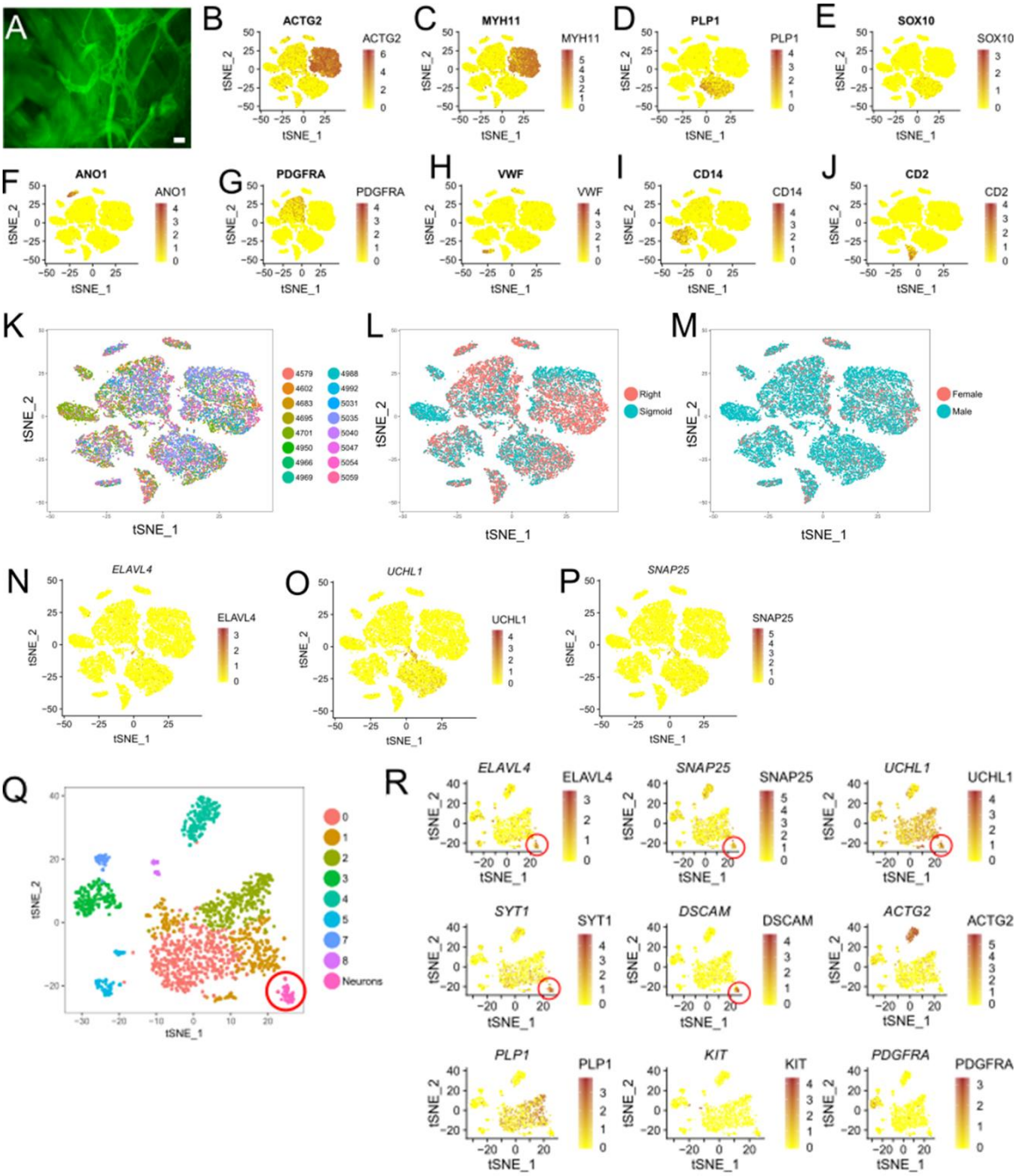

Supplementary Figure 2.7: Human single nucleus RNA-seq analysis from 20,167 cells yielded data from 48 definitive neurons and many other cells that impact bowel motility including SMC, ICC, PDGFRA+ cells, muscularis macrophage, and glia.

(A) Human myenteric plexus after incubation with 4-Di-2-Asp, with muscle layers partially peeled away. **(**B-J) Feature plots showing genes expressed highly in adult human smooth muscle (B, C; *ACTG2, MYH11*), glial cells (D, E; *PLP1, SOX10*), ICC (F; *ANO1*), PDGFRA+ cells (G; *PDGFRA*),

vessel endothelial cells (H; *VWF*), muscularis macrophages (I; *CD14*), and T cells (J; *CD2*). Color key represents $\log_e$(normalized gene expression). Scale bar = 50µm. (K-M) T-SNE plots of human nuclei colored by sample number (K), colon location (right versus sigmoid; L), and sex (M). Cells from different colon regions and different sexes largely form the same t-SNE clusters. (N-P) Feature plots show location of *ELAVL4* (N)*, UCHL1* (O), and *SNAP25* (P) expression suggest that a small population of neurons expressing all three is present in this dataset, but most of the 20,000 nuclei are not *ELAVL4, SNAP25,* or *UCHL1*-positive. Color key represents $\log_e$(normalized gene expression). (Q) T-SNE plot of all human nuclei expressing *ELAVL4*, *UCHL1*, or *SNAP25* (inclusive or) reveals many populations that may be doublets because they cluster with nuclei expressing non-neuronal cell markers. For this manuscript, we only describe in detail expression data for the tight cluster of cells we believe are single neurons based on high expression of *ELAVL4*, *SNAP25*, *UCHL1*, *SYT1*, and *DSCAM* (highlighted with red circle) (R) Feature plots of neuronal markers (*ELAVL4*, *SNAP25*, *UCHL1*, *SYT1*, and *DSCAM*), SMC markers (*ACTG2*), glial cell markers (*PLP1*), ICC markers (*KIT*), and PDGFRA+ cell markers (*PDGFRA*) suggest that other populations are not neurons. Color key represents $\log_e$(normalized gene expression).

Supplementary Table 2.1: Methods used to isolate cells or nuclei for RNA-seq.

Genotype	Whole cells, or nuclei?	Description
Wnt1-Cre;R26R-EGFP	Cells	The EGFP signal in *Wnt1-Cre;R26R-EGFP* animals was too weak to flow sort effectively given the high degree of background in the 488 channel.
Wnt1-Cre;R26R-tdTomato	Cells	The localization of tdTomato to neurites in our *Wnt1-Cre;R26R-Tdtomato* line was problematic, since we desired clean separation of single cells. Sorting myenteric plexus from this mouse line often resulted in preps with neurites attached to tdTomato- cells. We tried dissociating with different proteases (cold active protease, dispase and collagenase), different incubation times (15 minutes, 30 minutes), multiple methods of trituration (pipette-based, needle-based), and different bowel layers, with little improvement in outcome
Wnt1-Cre;ROSA^{NT-NG}	Nuclei	*Wnt1-Cre;Rosa^{NT-NG}* mice had tdTomato in their nuclei at baseline; with CRE-induced recombination, they accumulated EGFP in their nuclei instead of tdTomato. Unfortunately, these mice lost fluorescent signal during the Dounce homogenization procedure. We hypothesize that membrane damage associated with homogenization led to diffusion of GFP and loss of signal.
Wnt1-Cre;Rosa26 LSL H2B mCherry	Nuclei	Successful and used to generate data in **Figures 1** through **4.**
Wild type	Nuclei	We attempted to use directly-conjugated NeuN and PHOX2B antibodies to isolate mouse ENS nuclei with flow sorting, since some neuronal nuclei in mouse stain with this NeuN antibody by immunohistochemistry. We were unsuccessful.

Supplementary Table 2.2: Predicted adult enteric neuron subtype classification based on RNA-seq

Cluster name (Adult Colon)	**Chat 1**	**Chat 2**	**Chat 3 (Met)**	**Chat 4 (Vglut2)**	**Calcb**	**Nos 1**	**Nos 2**
Suggested neuron type	Intrinsic sensory neurons, interneurons (with mechanosensitive properties)	Interneurons or excitatory motor neurons	Interneurons or excitatory motor neurons	Interneuron	Intrinsic Sensory Neuron	Inhibitory motor neurons +/- interneurons?	Inhibitory motor neurons +/- interneurons?
Expressed markers supporting conclusion (differential expression marked by *)	*Chat*, Slc18a3, Tac1, (Piezo1*)*	*Chat, Tac1*, Penk**	*Chat, Met*, Penk*, Tac1**	*Slc18a3*, Chat, Nos1, Vip, Calb1*, Penk*, Nefm**	*Calcb*, Nefm, Scn11a*, Calb2*, Tacr1*, Htr3a*, Htr3b*, P2rx2**	*Nos1*, Vip*, Gal*, Npy**	*Nos1*, Vip, Gal, Npy*
Other genes of note differentially expressed	*Calb2**			*Slc17a6**	*Nmu*, Grp*, Avil**	*Htr3a*, P2rx2**	
Corresponding neuron subtype designations from Drokhlyansky et al., 2019, BioXRIV (Adult Mouse Colon)	PEMN 1, 3, 4, 6 (based on *Chat, Tac1, Piezo1*)	PEMN 2, or PIN1, PIN2 (based on *Chat, Penk, Tac1*, and absent *Piezo1*)	PIN1, PIN2 or PEMN 2 (based on *Chat, Penk, Tac1, Calcrl, Ramp1*)	PIN3 or PSN3 (based on *Chat, Slc17a6, Nxph2*)	PSN_1 (based on *Nmu, Grp, Calcb*)	PIMN_1-7 (based on *Nos1, Vip, Gal*)	PIMN_1-7 (based on *Nos1, Vip, Gal*)
Corresponding neuron subtype designations in Morarach et al, 2020 (P21 mouse Small Intestine)- very limited data available	ENC1,7 (*Chat, Tac1,* absent *Penk*)	ENC2-4 (*Chat, Tac1, Penk*)	ENC4 (*Chat, Tac1, Penk, Fut9, Nfatc1*),	ENC12 > ENC7 (*Slc17a6*, *Penk, Nxph2, Nefm*)	ENC6 > ENC5 (*Calcb, Nmu, Nog, Sst*)	ENC8-10 (*Nos, Vip, Gal*)	ENC8-10 (*Nos, Vip, Gal*)

Cluster name (Adult Colon)	**Chat 1**	**Chat 2**	**Chat 3 (Met)**	**Chat 4 (Vglut2)**	**Calcb**	**Nos 1**	**Nos 2**
Corresponding neuron subtype designations from Zeisel et al 2018 (P21 mouse Small Intestine) - http://mousebrain.org/genesearch.html?	ENT5 (*Chat, Tac1, Dmkn, Hoxb5,* absent *Penk*)	No equivalent cluster in this small intestine dataset. *Penk* is only expressed in ENT6 and ENT7, but neither of these clusters are a good match due to *Slc17a6* expression and lack of *Fut9* and *Nfatc1* expression in this cluster.	No equivalent cluster in this small intestine dataset. ENT6 is closest (*Chat, Tac1, Penk, Fut9, Nfatc1*, but ENT6 is missing *Met* expression)	ENT7 (based on *Chat, Penk, Slc17a6, Calb1, Nxph2, Phox2a*)	ENT9 (*Nmu, Myl1, P2rx2*)	ENT2 > ENT1, EN3 (*Cartpt, Nos1, Ass1, Bglap*)	ENT1,3 > ENT2 (*Nos1, Ass1, Cox8b, Gal, Moxd1)*
Markers missing					*Kcnn4, Piezo1*		
Citations	20,21,59,67	20,21	60	9,23,58	58	10,19	10,19

Supplementary Table 2.3: Predicted E17.5 enteric neuron subtype classification based on RNA-seq

Cluster Name (E17.5 whole bowel)	**Immature Chat cluster 1**	**Chat cluster 1**	**Chat cluster 2**	**Nos1 cluster 1**	**Nos1 cluster 2**	**Nos1 cluster 3**	**Immature Chat cluster 2**	**Immature Nos1 cluster**
Suggested neuron type	Small intestine inter-neurons	Small intestine excitatory motor neurons	Small intestine intrinsic sensory neurons	Small intestine inhibitory motor neurons or inter-neurons	Small intestine inter-neurons	Small intestine inhibitory motor neurons or inter-neurons	Colon (+/- some small intestine) cholinergic neurons	Colon (+/- some small intestine) nitrergic neurons
Differentially Expressed markers supporting conclusion	*Slc18a3, Chat, Penk, Calb1*	Slc18a3, Chat, Penk, Tac1	*Calca, Calcb, Htr3b, Nmu*	*Nos1, Vip, Gal*	*Nos1, Vip, Gal, Neurod6*	*Nos1, Vip, Gal*	*Slc18a3*	*Nos1, Pou3f3*
Other genes of note differentially expressed	*Slc17a6, Npy1r, Avpr1a*	*Tgfb2, Htr2b*	*Nmu, Nog, Bambi, Smad7, Adra2a, Ntrk3, Npy2r*	*Ednrb, C1ql1, P2ry6, Htr3a, Cartpt, Npy2r*	*Dbh, Sstr1, Sstr2, Cartpt, Htr3a, Npy2r*	*Sstr1, Sstr2, Cartpt, Prokr1, Npy2r*	*Htr2b, Npy1r, Ramp1*	*Npy1r, Ramp3*
Markers missing				*+/- Npy*	*+/- Npy*	*+/- Npy*		
Corresponding P21 small intestine neuron subtype designations from Morarach *et al*., 2020, BioXRIV	ENC12 (based on *Chat, Slc18a3, Slc17a6, Calb1, Penk*)	ENC2 > ENC3 (based on *Chat, Slc18a3, Penk, Tac1, Gda, Ndufa4l2*)	ENC6 (based on *Calcb, Nmu*)	ENC8 or ENC9 (based on *Nos1, Vip, Gal, C1ql1*)	ENC10 (based on *Nos1, Vip, Gal, Neurod6*)	ENC8 or ENC9 (based on *Nos1, Vip, Gal*)	N/A	N/A
Corresponding P21 small intestine neuron subtype designations from	ENT7 (based on *Chat, Slc18a3, Slc17a6, Calb1, Penk*)	ENT6 > ENT6 and ENT4 (based on *Chat, Slc18a3, Penk,*	ENT9 (based on *Calcb, Nmu, Nog*)	ENT3 > ENT2 (based on *Nos1, Vip, Gal, Cartpt*)	ENT1 (based on *Nos1, Vip, Gal, Cartpt, Neurod6*)	ENT2 > ENT3 (based on *Nos1, Vip, Gal, Cartpt, Ltk*)	N/A	N/A

Cluster Name (E17.5 whole bowel)	**Immature Chat cluster 1**	**Chat cluster 1**	**Chat cluster 2**	**Nos1 cluster 1**	**Nos1 cluster 2**	**Nos1 cluster 3**	**Immature Chat cluster 2**	**Immature Nos1 cluster**
Zeisel *et al*., 2018, Cell		*Tac1, Gda, Ndufa4l2*)						
Citations	9,13,23,24 ,58)	13,19,24 Our own data	9,19,58	13,23,68	9,68	13,23,68	Our own data	Our own data

Supplementary Table 2.4: Characteristics of colon resection samples

Sample ID	Age	Sex	History	Colon region	RNA Integrity #: Plexus	RNA Integrity #: Surrounding muscle
4579	54	M	Cecal polyp	Right colon	7.6	7.9
4602	75	M	Hx of cecal lesion	Right colon	7.5	6.9
4683	38	M	Goblet cell carcinoma	Right colon	7.9	8
4695	77	F	Colonic mass	Right colon	7.4	7.4
4701	78	M	Rectal cancer	Sigmoid colon	8.2	6.3
4950	78	M	Bowel obstruction	Sigmoid colon	6.50, 6.90, and 7.10 (3 pieces)	7.6
4969	83	M	Adenocarcinoma	Right colon	6.5	7.90, 5.80 (2 pieces)
4966	71	F	Bowel obstruction	Right colon	7.2	8.1, 7.9 (2 pieces)
4988	65	F	Colon polyp	Right colon	5.20 and 2.90 (RNA conc. v low)*	7.5 and 7.4 (2 pieces)
4992	47	M	Rectal carcinoma	Sigmoid colon	4.4 (RNA conc v. low)*	7.1
5031	70	M	Colon polyp	Right colon	7.8	7.4 and 7.2
5035	24	M	Volvulus	Sigmoid colon	8	6.6 and 7.2
5040	44	M	Colonic mass	Right colon	7.7	7.5 and 7.8
5047	65	M	Rectal adenocarcinoma	Sigmoid colon	6.6	7.4
5054	36	F	Bowel adhesions	Right colon	7.6	7.20 and 7.70
5059	59	F	Adenocarcinoma	Right colon	7.2	7.50 and 6.40

Supplementary Table 2.5: UMI and gene counts from colon resection samples

Sample ID	Cells or nuclei loaded (predicted from FACS)	# of Cells with RNA-seq data	Ratio of sequenced cells to loaded cells	Avg UMI count with intronic reads mapped	Avg gene count with intronic reads mapped
4579	4000	680	0.17	2,474	1,559
4602	6900	2,316	0.3356522	2,004	1,268
4683	6300	2,081	0.3303175	1,397	876
4695	4000	833	0.20825	1,487	974
4701	12300	4,414	0.3588618	1,296	780
4950	5200	1,237	0.2378846	1,415	910
4969	5300	653	0.1232075	1,262	1,262
4966	2100	432	0.2057143	1,856	1,193
4988	1200	237	0.1975	2,354	1554
4992	673	60	0.089153	3,939	2336
5031	5200	1728	0.3323077	1,538	967
5035	7100	2524	0.355493	1,886	1119
5040	2300	755	0.3282609	1,941	1212
5047	5000	957	0.1914	1,701	1013
5054	3100	1219	0.3932258	2,071	1216
5059	1200	338	0.2816667	2470	1474

Supplementary Table 2.6: Numbers of Biological Replicates and Numbers of Cells/Terminals Counted

Experiment	**Biological replicate number**	**Total neurons or nerve terminals counted**	**Statistical tests used**	**Descriptive Statistics: Mean ± standard deviation // Median (range if n=3, interquartile range if n>3)**
Figure 1 - Enkephalin and substance P staining quantification	3	11628 (myenteric ganglia) 2918(circular muscle)	Unpaired t-test	Varicosities within myenteric ganglia: % of Enk+ varicosities that were SP+: 74.5 ± 23.6 // 86.9 (41.9) % of SP+ varicosities that were Enk+: 81.2 ± 8.7 // 78.0 (16.5) Varicosities in circular muscle: % of Enk+ varicosities that were SP+: 76.5 ± 5.0 // 78.7 (9.3) % of SP+ varicosities that were Enk+: 44.7 ± 8.4 // 41.9 (16.0)
Figure 2 - *Gfra1*-GFP quantification (mouse adult distal colon)	3	614	Student's t-test	% of NOS1+ that were GFP+: 88.9 ± 1.8 //89.1 (3.7) % of NOS- neurons that were GFP+: 8.8 ± 5.7 //7.7 (11.2)
Figure 2 - NADPH diaphorase staining	5	340	Fisher Exact Test (2x2 contingency table)	N/A
Figure 3 - *Etv1-CreERT2;TdTomato* x NOS1 quantification (mouse adult distal colon)	3	1101	Student's t-test	% of NOS+ neurons that were TDT+: 56.4 ± 6.3 // 59.7 (11.3) % of NOS- neurons that were TDT+: 5.6 ± 1.5 // 5.6 (3.0) % of TDTOMATO+ neurons that were NOS+: 85.0 ± 5.8 // 85.7 (11.6) % of TDTOMATO neurons that were NOS-: 15.0 ± 5.8 // 14.3 (11.6)
Figure 3 - PBX3 x *Chat*-EGFP quantification (mouse adult distal colon)	4	2684	Student's t-test	% of EGFP- neurons that were RBFOX1+: 31.4 ± 6.0 // 29.5 (10.9) % of EGFP+ neurons that were RBFOX1+: 72.7 ± 5.4 // 74.2 (9.8)

Experiment	Biological replicate number	Total neurons or nerve terminals counted	Statistical tests used	Descriptive Statistics: Mean ± standard deviation // Median (range if n=3, interquartile range if n>3)
				% of PBX3+ neurons that were EGFP+: 79.2 ± 5.3 // 79.4 (12.3) % of PBX3+ neurons that were EGFP-: 20.8 ± 5.3 // 20.6 (10.2)
Figure 3 - PHOX2B x *Chat*-EGFP quantification (mouse adult distal colon)	4	2136	Student's t-test	% of EGFP- neurons that were PHOX2B+: 69.9 ± 7.3 // 72.0 (13.5) % of EGFP+ neurons that were PHOX2B+: 76.1 ± 5.1 // 76.3 (9.5) % of PHOX2B+ neurons that were EGFP+: 60.8 ± 2.9 // 62.1 (4.9) % of PHOX2B+ neurons that were EGFP-: 39.2 ± 2.9 // 37.9 (4.9)
Figure 3 - RBFOX1 x *Chat*-EGFP quantification (mouse adult distal colon)	3	993	Student's t-test	% of EGFP- neurons that were RBFOX1+: 39.4 ± 3.8 // 38.7 (7.6) % of EGFP+ neurons that were RBFOX1+: 82.5 ± 6.7 // 78.8 (11.8) % of RBFOX1+ neurons that were EGFP+: 74.2 ± 5.8 // 76.9 (10.7) % of RBFOX1+ neurons that were EGFP-: 25.8 ± 5.8 // 23.1 (10.7)
Figure 3 - SATB1 x *Chat*-EGFP quantification (mouse adult distal colon)	3	1028	Student's t-test	% of EGFP- neurons that were SATB1+: 7.9 ± 12.3 // 1.6 (22.1) % of EGFP+ neurons that were SATB1+: 50.0 ± 12.0 // 45.3 (22.5) % of SATB1+ neurons that were EGFP+: 94.8 ± 7.9 // 98.8 (14.3) % of SATB1+ neurons that were EGFP-: 5.2 ± 7.9 // 1.2 (14.3)
Figure 3 - TBX3 x NOS1 quantification (mouse adult distal	4	1033	Student's t-test	% of NOS+/EGFP- neurons that were TBX3+: 90.9 ± 8.2 // 92.0 (15.7) % of NOS+/EGFP+ neurons that were TBX3+: 86.5 ± 12.1 // 85.6 (22.6)

Experiment	Biological replicate number	Total neurons or nerve terminals counted	Statistical tests used	Descriptive Statistics: Mean ± standard deviation // Median (range if n=3, interquartile range if n>3)
colon)				% of NOS-/EGFP+ neurons that were TBX3+: 23.4 ± 7.7 // 26.3 (13.1) % of TBX3+ neurons that were EGFP+: 31.0 ± 7.0 // 34.5 (10.6) % of TBX3+ neurons that were EGFP-: 69.0 ± 7.0 // 65.5 (10.6) % of TBX3+ neurons that were NOS+: 66.0 ± 5.6 // 64.5 (10.0) % of TBX3+ neurons that were NOS-: 34.0 ± 5.6 // 35.5 (10.0)
Figure 3 - All neurons (mouse adult distal colon)	3 (EGFP) 7 (NOS)		N/A	% of total neurons that were EGFP+:58.1 ± 4.4 // 58.8 (8.8) % of total neurons that were EGFP-: 41.9 ± 4.4 // 41.2 (8.8) % of total neurons that were NOS+: 38.1 ± 4.5 // 39.2 (7.9) % of total neurons that were NOS-: 61.9 ± 4.5 // 60.8 (7.9)
Supplementary Figure 1 - *Vglut-Ires-Cre;TdTomato* x *Chat*-EGFP quantification (mouse adult distal colon)	3	114	N/A	% TDTOMATO+/EGFP+/HUC+: 4.1 ± 1.5 // 3.5 (2.7) % TDTOMATO+/EGFP-/HUC+: 95.9 ± 1.5 // 96.5 (2.7)
Figure 5 - BNC2 x *Chat*-EGFP quantification (mouse E17.5 mid-small intestine)	3	6186	Student's t-test	BNC2+EGFP+/EGFP+: 54.8 ± 5.2 // 52.3 (9.5) BNC2+EGFP-/EGFP-: 21.6 ± 1.5 // 21.3 (2.94) BNC2+EGFP+/BNC2+: 78.7 ± 1.1 // 78.7 (2.1) EGFP+HUC+/HUC+: 59.2 ± 4.4 // 57.0 (8.0)

Experiment	**Biological replicate number**	**Total neurons or nerve terminals counted**	**Statistical tests used**	**Descriptive Statistics: Mean ± standard deviation // Median (range if n=3, interquartile range if n>3)**
Figure 5 - PBX3 x *Chat*-EGFP quantification (mouse E17.5 mid-small intestine)	3	10259	Student's t-test	PBX3+EGFP+/EGFP+: 53.4 ± 13.3 // 60.6 (23.4) PBX3+EGFP-/EGFP-: 12.1 ± 9.5 // 9.7 (18.6) PBX3+EGFP+/PBX3+: 85.7 ± 8.6 // 84.5 (17.1) EGFP+HUC+/HUC+: 56.2 ± 9.6 // 55.8 (19.1)
Figure 5 - RBFOX1 x *Chat*-EGFP quantification (mouse E17.5 mid-small intestine)	3	11522	Student's t-test	RBFOX1+EGFP+/EGFP+: 49.7 ± 9.4 // 48.3 (18.7) RBFOX1+EGFP-/EGFP-: 3.7 ± 2.1 // 4.0 (4.2) RBFOX1+EGFP+/RBFOX1+: 95.3 ± 2.1 // 95.7 (4.1) EGFP+HUC+/HUC+: 59.7 ± 2.8 // 60.6 (5.3)
Figure 5 - TBX2 x *Chat*-EGFP quantification (mouse E17.5 mid-small intestine)	3	8369	Student's t-test	TBX2+EGFP+/EGFP+: 51.5 ± 4.3 // 51.4 (8.5) TBX2+EGFP-/EGFP-: 7.8 ± 7.3 // 3.7 (12.7) TBX2+EGFP+/TBX2+: 92.3 ± 5.1 // 94.7 (9.3) EGFP+HUC+/HUC+: 60.9 ± 5.1 // 63.3 (9.4)
Figure 5 - TBX3 x *Chat*-EGFP x NOS1 quantification (mouse E17.5 mid-small intestine)	3	4235	ANOVA with Tukey's post-hoc test	TBX3+EGFP+/EGFP+: 49.1 ± 6.3 // 48.1 (12.5) TBX3+NOS1+/NOS1+: 95.2 ± 1.7 // 94.6 (3.4) TBX3+NOS1+EGFP+/NOS1+EGFP+: 91.2 ± 3.9 // 91.4 (7.8) TBX3+EGFP+/TBX3+: 60.9 ± 5.1 // 0.5 (0.1) TBX3+NOS1+/TBX3+: 44.6 ± 3.2 // 43.9 (6.3) TBX3+EGFP+NOS1+/TBX3+: 5.6 ± 0.9 // 5.4 (1.7)

Experiment	Biological replicate number	Total neurons or nerve terminals counted	Statistical tests used	Descriptive Statistics: Mean ± standard deviation // Median (range if n=3, interquartile range if n>3)
				EGFP+/(sum of EGFP+,NOS1+,NOS1+EGFP+): 68.3 ± 1.6 // 67.5 (3.0) NOS1+/(sum of EGFP+,NOS1+,NOS1+EGFP+): 31.1 ± 1.7 // 32.0 (3.0) EGFP+NOS1+/(sum of EGFP+,NOS1+,NOS1+EGFP+): 0.8 ± 0.0 // 0.8 (0.1)
Figure 6 - *Etv1-CreERT2; TdTomato* neuron numbers (mouse P0 mid-small intestine)	4 (control), 4 (KO)	5620 (control), 5157 (KO)	ANOVA with Tukey's post-hoc test	% *Chat*-EGFP+ neurons: KO: 39.5 ± 6.6 // 41.03 (12.4) Control: 40.0 ± 2.9 // 39.6 (5.5) % NOS1+ neurons: KO: 14.5 ± 3.2 // 15.8 (5.4) Control: 12.9 ± 2.7 // 12.6 (5.2) % *Chat*-EGFP+/NOS1+ neurons: KO: 2.4 ± 0.5 // 2.5 (0.9) Control: 1.6 ± 0.6 // 1.5 (1.1) % *Chat*-EGFP-/NOS1- neurons: KO: 43.6 ± 5.7 // 43.1 (10.5) Control: 45.5 ± 2.6 // 45.4 (4.9) Total Neuron Density: KO: 3530 ± 563.3 // 3334 (980) Control: 4241 ± 535.6 // 4144 (1009)
Figure 6 - *Wnt1-Cre;Tbx3 flox* neuron numbers (mouse P0 mid-small intestine)	3 (control), 3 (KO)	8618 (control), 3983 (KO)	Student's t-test	% NOS1+ neurons: KO: 18.2 ± 3.3 // 17.4 (6.6) Control: 26.0 ± 3.0 // 26.4 (6.0) Total Neuron Density: KO: 2180 ± 403.2 // 2075 (786) Control: 2337 ± 260.6 // 2302 (517)
Figure 6 - *Wnt1-*	4 (control),	6871	Student's t-	% *Chat*-EGFP+ neurons:

Experiment	**Biological replicate number**	**Total neurons or nerve terminals counted**	**Statistical tests used**	**Descriptive Statistics: Mean ± standard deviation // Median (range if n=3, interquartile range if n>3)**
Cre;Rbfox1 flox neuron numbers (mouse P0 mid-small intestine)	4 (KO)	(control), 5348 (KO)	test	KO: 47.4 ± 2.9 // 47.3 (5.1) Control: 53.6 ± 7.3 // 53.6 (14.1) Total Neuron Density: KO: 1603 ± 352.2 //1589 (674) Control: 1789 ± 364.6 // 1903 (665)
Figure 7 - BNC2 x CHAT quantification (human colon)	3	2675	Student's t-test	BNC2+CHAT+/CHAT+: 36.6 ± 4.1 // 34.3 (7.1) BNC2+CHAT-/CHAT-: 1.6 ± 1.3 // 0.8 (2.3) BNC2+CHAT+/BNC2+: 97.9 ± 1.3 // 97.9 (2.7) CHAT+HUC+/HUC+: 66.6 ± 11.8 // 60.0 (20.6)
Figure 7 - PBX3 x CHAT quantification (human colon)	3	2439	Student's t-test	PBX3+CHAT+/CHAT+: 19.0 ± 4.3 // 19.9 (8.6) PBX3+CHAT-/CHAT-: 1.1 ± 0.3 // 1.1 (0.6) PBX3+CHAT+/PBX3+: 97.5 ± 1.1 // 97.2 (2.2) CHAT+HUC+/HUC+: 68.7 ± 6.9 // 67.7 (13.8)
Figure 7 - RBFOX1 x CHAT quantification (human colon)	3	2825	Student's t-test	RBFOX1+CHAT+/CHAT+: 44.4 ± 7.7 // 41.4 (14.4) RBFOX1+CHAT-/CHAT-: 1.5 ± 1.4 // 1.6 (2.8) RBFOX1+CHAT+/RBFOX+: 99.4 ± 0.5 // 99.3 (1.0) CHAT+HUC+/HUC+: 87.4 ± 2.7 // 86.9 (5.3)
Figure 7 - TBX2 x CHAT quantification (human colon)	3	3427	Student's t-test	TBX2+CHAT+/CHAT+: 7.8 ± 2.8 // 6.2 (4.8) TBX2+CHAT-/CHAT-: 0.1 ± 0.1 // 0.1 (0.2) TBX2+CHAT+/TBX2+: 99.4 ± 0.5 // 99.3 (1.0)

Experiment	Biological replicate number	Total neurons or nerve terminals counted	Statistical tests used	Descriptive Statistics: Mean ± standard deviation // Median (range if n=3, interquartile range if n>3)
				CHAT+HUC+/HUC+: 69.6 ± 12.9 // 72.5 (25.3)
Figure 7 - TBX3 x NOS1 quantification (human colon)	3	972	Student's t-test	TBX2+NOS1+/NOS1+: 90.0 ± 9.7 // 92.4 (19.0) TBX2+NOS1-/NOS1-: 16.4 ± 6.5 // 14.9 (12.8) TBX3+NOS1+/TBX3+: 83.5 ± 8.9 // 83.3 (17.7) NOS1+HUC+/HUC+: 49.1 ± 7.8 // 47.3 (15.3)

Supplementary Table 2.7: List of Antibodies

Antibody	Concentration	Catalog number	Source
Rabbit anti-NOS1	1:200 (mouse), 1:100 (human)	AB5380	Sigma, RRID:AB_91824
Goat anti-CHAT	1:100 (human)	AB144P	Sigma, RRID:AB_2079751
ANNA-1 (HuC/D)	N/A (mouse)	N/A	Kind gift from Dr. V. Lennon, Mayo Clinic
Mouse anti-HuC/D	1:200 (human)	A21271	Thermo Fisher Scientific, RRID:AB_221448
Goat anti-TBX3	1:100 (human and mouse)	AF4509-SP	R&D Systems, RRID:AB_2240328
Goat anti-PHOX2B	1:100 (mouse)	AF4940-SP	R&D Systems, RRID:AB_10889846
Rabbit anti-SATB1	1:100 (mouse)	ab109122	Abcam, RRID:AB_10862207
Chicken anti-GFP	1:500 (mouse)	#GFP-1020	Aves Labs, RRID:AB_10000240
Rabbit anti-S100B	1:200 (mouse)	Ab52642	Abcam; RRID:AB_882426
Rabbit anti-PBX3	1:100 (human and mouse)	12571-1-AP	Proteintech Group; RRID:AB_2160469
Rabbit anti-TBX2	1:100 (human and mouse)	22346-1-AP	Proteintech Group
Rabbit anti-POU3F3	1:100 (human and mouse)	HPA067151	Sigma; RRID:AB_2685790
Rabbit anti-RBFOX1	1:100 (human and mouse)	HPA040809	Sigma; RRID:AB_10796228
Goat anti-BRN1 (also called POU3F3 protein)	1:100 (mouse)		Santa Cruz; no longer sold
Rabbit anti-BNC2	1:100 (human and mouse)	HPA018525	Sigma; RRID:AB_1845402
Rabbit anti-Met Enkephalin	1:500 (mouse)	AB5026	Sigma; RRID:AB_91644
Rat anti-Substance P (NC1/34)	1:800 (mouse)	AB150349	Abcam
Alexa Fluor goat anti-human 647	1:400 (mouse and human)	A21445	Thermo Fisher Scientific; RRID:AB_2535862
AlexaFluor donkey anti-rabbit 488	1:400 (mouse and human)	A21206	Thermo Fisher Scientific; RRID:AB_2535792
AlexaFluor donkey anti-rabbit 594	1:400 (mouse and human)	A21207	Thermo Fisher Scientific; RRID:AB_141637

Antibody	Concentration	Catalog number	Source
AlexaFluor donkey anti-rabbit 647	1:400 (mouse and human)	A31573	Thermo Fisher Scientific; RRID:AB_2536183
AlexaFluor goat anti-rat 594	1:500 (mouse)	A11007	Thermo Fisher Scientific; RRID:AB_10561522
AlexaFluor donkey anti-goat 594	1:400 (mouse and human)	A11058	Thermo Fisher Scientific; RRID:AB_2534105
AlexaFluor goat anti-chicken 488	1:400 (mouse and human)	A11039	Thermo Fisher Scientific; RRID:AB_142924
AlexaFluor donkey anti-goat 647	1:400 (mouse and human)	A21447	Thermo Fisher Scientific; RRID:AB_141844
AlexaFluor donkey anti-goat 488	1:400 (mouse and human)	A11055	Thermo Fisher Scientific; RRID:AB_2534102
AlexaFluor goat anti-rabbit 488	1:400 (mouse and human)	A31556	Thermo Fisher Scientific; RRID:AB_221605

Supplementary Table 2.8: List of RT-PCR primers

Gene	Primer Sequence	Band size	Genotyping solution	Reference
Pou3f3 (mouse)	5'-CAACAGCCACGACCCTCACT-3' 5'-CAGAACCAGACCCGCACGAC-3'	450 bp	KAPA (KAPA Biosystems, Cat #KK7352)	(74)
Actb (mouse)	5'-GAGAGGGAAATCGTGCGTGAC-3' 5'-AGCTCAGTAACAGTCCGCCTA-3'	534 bp	KAPA ((KAPA Biosystems, Cat #KK7352)	(75)

Supplementary Table 2.9: List of PCR primers for mouse genotyping

Gene (Strain)	Primer Sequence	Band size	Genotyping solution	Reference
Tbx3	F: 5'-GTG TGA GAC AGA GAA ATC AGT GG-'3 R: 5'-5' CCA ACT GGT ATC TTG ATA AAC CTC-'3	Mut: 480bp WT: 320bp	KAPA (KAPA Biosystems, Cat #KK7352), Taq (NEB, Cat #M0271L)	(30)
Gfp (ChAT-EGFP-L10a)	F: 5'-TCA TAG AGG CGC AGA GTT CC-3' R: 5'-CTG AAC TTG TGG CCG TTT AC-3'	Mut: 250bp	KAPA (KAPA Biosystems, Cat #KK7352)	JAX genotyping protocol (Stock No: 030250)
Rbfox1	F: 5-ATGCCCATGCAGTGAAA AAT-3' R: 5'-TGCAGCACATTGAAACCT TC-3'	Mut: 397bp WT: 294bp	KAPA (KAPA Biosystems, Cat #KK7352)	(76)
Gfra1-Gfp	Common F: 5'-CTTCCAGGTTGGGTCGG AACTGAACCC-3' Mut R: 5'-GCCGTTTACGTCGCCGT CCAGCTCGACCAG-3' WT R: 5'-AGAGAGCTCAGCGTGCA GAGATC-3'	WT: ~200bp Mut: ~300bp	KAPA (KAPA Biosystems, Cat #KK7352)	(27) and personal correspondence with Dr. Sanjay Jain's laboratory
Cre (Wnt1-Cre)	F: 5'- GCA TTA CCG GTC GAT GCA ACG AGT GAT GAG-3' R: 5'-GAG TGA ACG AAC CTG GTC GAA ATC AGT GCG-3'	408bp	KAPA (KAPA Biosystems, Cat #KK7352), Taq (NEB)	https://mgc.wustl.edu/protocols/pcr_genotyping_primer_pairs
R26R-mCherry (R26R-H2b-mCherry)	Common F: 5'-AAA GTC GCT CTG AGT TGT TAT-3' Mutant R: 5'-TTA TGT AAC GCG GAA CTC CA-3' WT R: 5'GGA GCG GGA GAA ATG GAT ATG-3'	Mut: 309bp WT: 603bp	KAPA (KAPA Biosystems, Cat #KK7352)	JAX genotyping protocol (Stock No: 023139)

Gene (Strain)	Primer Sequence	Band size	Genotyping solution	Reference
Cre (Vglut2-IRES-Cre)	F: 5’-GCA TTA CCG GTC GAT GCA ACG AGT GAT GAG-3’ R: 5’-GAG TGA ACG AAC CTG GTC GAA ATC AGT GCG-3’	408bp	KAPA (KAPA Biosystems, Cat #KK7352), Taq (NEB, Cat #M0271L)	https://mgc.wustl.edu/protocols/pcr_genotyping_primer_pairs
Cre (Nos1-CreERT2)	F: 5’-GCA TTA CCG GTC GAT GCA ACG AGT GAT GAG-3’ R: 5’-GAG TGA ACG AAC CTG GTC GAA ATC AGT GCG-3’	408bp	KAPA (KAPA Biosystems, Cat #KK7352), Taq (NEB, Cat #M0271L)	https://mgc.wustl.edu/protocols/pcr_genotyping_primer_pairs
R26R-TdTomato	Common F: 5'-AAAGTCGCTCTGAGTTGTTAT-3'Mut R: 5’-GCGAAGAGTTTGTCCTCAACC-3’ WT R: 5'-GGAGCGGGAGAAATGGATATG-3'	Mut: ~350bp WT: ~600bp	KAPA (KAPA Biosystems, Cat #KK7352), Taq (NEB, Cat #M0271L)	JAX genotyping protocol (Stock No: 007900)
Etv1-CreERT2	WT F: 5’-CCC TCC CCT CTC ATT TTC TC-3’ Mut F: 5’-TGG TTT GTC CAA ACT CAT CAA-3’ Common R: 5’-ACA GTT TCT CCC ACG CTG AC-3’	Mut: 170bp WT: 459bp	KAPA ((KAPA Biosystems, Cat #KK7352)	JAX genotyping protocol (Stock No: 013048)
Cre (E2a-Cre)	F: 5’-GCG GTC TGG CAG TAA AAA CTA TC-3’ R: 5’-GTG AAA CAG CAT TGC TGT CAC TT-3’	100bp	HotStar Taq Kit (Qiagen, Cat# 203443)	JAX genotyping protocol (Stock No: 003724)
R26R-GCaMP6s	Mut F: 5’-ACG AGT CGG ATC TCC CTT TG-3’ Mut R: 5’-AGA CTG CCT TGG GAA AAG CG-3’ WT F: 5’-AAG GGA GCT GCA GTG GAG TA-3’	Mut: 356bp WT: 297bp	KAPA (KAPA Biosystems, Cat #KK7352)	JAX genotyping protocol (Stock No: 028866)

Gene (Strain)	Primer Sequence	Band size	Genotyping solution	Reference
	WT R: 5’-CCG AAA ATC TGT GGG AAG TC-3’			

Supplementary Table 2.10: ARRIVE Guidelines - General animal husbandry information

Location of Animal facility (types of experiments)	**CHOP (all experiments, except listed elsewhere)**	**University of Pittsburgh (Live calcium imaging experiments)**	**University of Melbourne (High magnification images of myenteric plexus stained with substance P and enkephalin)**
Facility Type	Conventional: cages are opened at room air, face masks are not required when handling mice	Barrier housing and maintained with caging opened under Animal Transfer Station/Biosafety Cabinets	Individually Ventilated Cages (IVC, Tecniplast): cages opened under Animal Transfer Station
Facility Type	Specific pathogen free, Pathogens detected in room within the past 2 years: MNV (mouse norovirus), Helicobacter not tested but likely present	Specific pathogen free; sentinel testing for excluded pathogens and MNV	Specific pathogen free; sentinel testing for excluded pathogens and MNV
Animal welfare assessment	Daily	Daily	Daily (food and water) Weekly (health check)
Bedding	¼ inch corn cob (The Andersons, Product 4B)	P.J Murphy Coarse Certified Aspen Sani-chip	Compressed paper-based bedding
Cage type	Lab Products (Seaford, DE) 75 sq. in. Ventilated.	Allentown mouse IVC caging	Tecniplast IVC caging (Green line)

Location of Animal facility (types of experiments)	**CHOP (all experiments, except listed elsewhere)**	**University of Pittsburgh (Live calcium imaging experiments)**	**University of Melbourne (High magnification images of myenteric plexus stained with substance P and enkephalin)**
Cage cleaning/sterilization	Standard tunnel washer	Standard tunnel washer, boxes autoclaved before use	Rack washer (Tecniplast), steam sterilisation
Mouse diet	Mouse Diet 5015 (Lab Diet), direct from manufacturer: not autoclaved, not irradiated	Prolab Isopro RMH 3000 (5P75) irradiated	Jackson labs: LabDiet® 5K52 formulation (6% fat). Animal Facility: Barastoc WEHI Mice Cubes, irradiated
Light-dark cycle	12/12	12/12	12/12
Temperature	72°F +/- 2°F	72°F +/- 4°F	18-24°C +/- 1°C
Humidity	30-70% depending on the day/season	30-70% depending on the day/season	30-70% depending on the day/season
Water pH and quality	Reverse Osmosis, pH~7, Edstrom automatic watering system	Reverse Osmosis, pH~7, Edstrom automatic watering system	Filtered water bottles (down to 0.2 microns), pH~7

Location of Animal facility (types of experiments)	**CHOP (all experiments, except listed elsewhere)**	**University of Pittsburgh (Live calcium imaging experiments)**	**University of Melbourne (High magnification images of myenteric plexus stained with substance P and enkephalin)**
Access to food and water	Continuous	Continuous	Continuous
Number of mice per cage	1-5 (20-30g)	1- 4 males, 1-5 females	1-5
Cage Enrichment	house/dome (Bioserve, S3174) and nestlet (Ancare)	house/dome (Bioserve, S3174) and nestlet (Ancare)	house/dome, tissues, chewing wooden block for single-housed mice
Mating strategy	Continuous	Continuous	not applicable in this study
Age at weaning	19-20 days	19-28 days	19-21 days (not applicable for this study)

2.9 References

1. Furness JB. The Enteric Nervous System. Malden, Mass: Wiley; 2006. 288 p.

2. Schneider S, Wright CM, Heuckeroth RO. Unexpected Roles for the Second Brain: Enteric Nervous System as Master Regulator of Bowel Function. Annu Rev Physiol. 2019 Feb 10;81:235–59.

3. Fung C, Vanden Berghe P. Functional circuits and signal processing in the enteric nervous system. Cell Mol Life Sci [Internet]. 2020 May 18; Available from: http://dx.doi.org/10.1007/s00018-020-03543-6

4. Burns AJ, Goldstein AM, Newgreen DF, Stamp L, Schäfer K-H, Metzger M, et al. White paper on guidelines concerning enteric nervous system stem cell therapy for enteric neuropathies. Dev Biol. 2016 Sep 15;417(2):229–51.

5. Soret R, Schneider S, Bernas G, Christophers B, Souchkova O, Charrier B, et al. Glial Cell Derived Neurotrophic Factor Induces Enteric Neurogenesis and Improves Colon Structure and Function in Mouse Models of Hirschsprung Disease. Gastroenterology [Internet]. 2020 Jul 17; Available from: http://dx.doi.org/10.1053/j.gastro.2020.07.018

6. Zeisel A, Hochgerner H, Lönnerberg P, Johnsson A, Memic F, van der Zwan J, et al. Molecular Architecture of the Mouse Nervous System. Cell. 2018 Aug 9;174(4):999–1014.e22.

7. Obata Y, Castaño Á, Boeing S, Bon-Frauches AC, Fung C, Fallesen T, et al. Neuronal programming by microbiota regulates intestinal physiology. Nature. 2020 Feb;578(7794):284–9.

8. Drokhlyansky E, Smillie CS, Van Wittenberghe N, Ericsson M, Griffin GK, Dionne D, et al. The enteric nervous system of the human and mouse colon at a single-cell resolution [Internet].

bioRxiv. 2019 [cited 2020 Jun 24]. p. 746743. Available from: https://www.biorxiv.org/content/10.1101/746743v4

9. Morarach K, Mikhailova A, Knoflach V, Memic F. Diversification of molecularly defined myenteric neuron classes revealed by single cell RNA-sequencing. bioRxiv [Internet]. 2020; Available from: https://www.biorxiv.org/content/10.1101/2020.03.02.955757v1.abstract

10. Lomax AE, Furness JB. Neurochemical classification of enteric neurons in the guinea-pig distal colon. Cell Tissue Res. 2000 Oct;302(1):59–72.

11. Furness JB, Callaghan BP, Rivera LR, Cho H-J. The enteric nervous system and gastrointestinal innervation: integrated local and central control. Adv Exp Med Biol. 2014;817:39–71.

12. Knowles CH, Veress B, Kapur RP, Wedel T, Farrugia G, Vanderwinden J-M, et al. Quantitation of cellular components of the enteric nervous system in the normal human gastrointestinal tract--report on behalf of the Gastro 2009 International Working Group. Neurogastroenterol Motil. 2011 Feb;23(2):115–24.

13. Sang Q, Young HM. Chemical coding of neurons in the myenteric plexus and external muscle of the small and large intestine of the mouse. Cell Tissue Res. 1996 Apr;284(1):39–53.

14. Graham KD, López SH, Sengupta R, Shenoy A, Schneider S, Wright CM, et al. Robust, 3-Dimensional Visualization of Human Colon Enteric Nervous System Without Tissue Sectioning. Gastroenterology [Internet]. 2020 Feb 27; Available from: http://dx.doi.org/10.1053/j.gastro.2020.02.035

15. Jiang Y, Dong H, Eckmann L, Hanson EM, Ihn KC, Mittal RK. Visualizing the enteric nervous system using genetically engineered double reporter mice: Comparison with immunofluorescence. PLoS One. 2017 Feb 3;12(2):e0171239.

16. Arighi E, Borrello MG, Sariola H. RET tyrosine kinase signaling in development and cancer. Cytokine Growth Factor Rev. 2005 Aug;16(4-5):441–67.

17. Stuart T, Butler A, Hoffman P, Hafemeister C, Papalexi E, Mauck WM 3rd, et al. Comprehensive Integration of Single-Cell Data. Cell. 2019 Jun 13;177(7):1888–902.e21.

18. Butler A, Hoffman P, Smibert P, Papalexi E, Satija R. Integrating single-cell transcriptomic data across different conditions, technologies, and species. Nat Biotechnol. 2018 Jun;36(5):411–20.

19. Qu Z-D, Thacker M, Castelucci P, Bagyánszki M, Epstein ML, Furness JB. Immunohistochemical analysis of neuron types in the mouse small intestine. Cell Tissue Res. 2008 Nov;334(2):147–61.

20. Furness JB, Costa M, Miller RJ. Distribution and projections of nerves with enkephalin-like immunoreactivity in the guinea-pig small intestine. Neuroscience. 1983 Apr;8(4):653–64.

21. Bornstein JC, Costa M, Furness JB, Lees GM. Electrophysiology and enkephalin immunoreactivity of identified myenteric plexus neurones of guinea-pig small intestine. J Physiol. 1984 Jun;351:313–25.

22. Swaminathan M, Hill-Yardin EL, Bornstein JC, Foong JPP. Endogenous Glutamate Excites Myenteric Calbindin Neurons by Activating Group I Metabotropic Glutamate Receptors in the Mouse Colon. Front Neurosci. 2019 May 1;13:426.

23. Sang Q, Williamson S, Young HM. Projections of chemically identified myenteric neurons of the small and large intestine of the mouse. J Anat. 1997 Feb;190 (Pt 2):209–22.

24. Sang Q, Young HM. The identification and chemical coding of cholinergic neurons in the small and large intestine of the mouse. Anat Rec. 1998 Jun;251(2):185–99.

25. Rossi J, Herzig K-H, Võikar V, Hiltunen PH, Segerstråle M, Airaksinen MS. Alimentary tract innervation deficits and dysfunction in mice lacking GDNF family receptor alpha2. J Clin Invest. 2003 Sep;112(5):707–16.

26. Heuckeroth RO, Enomoto H, Grider JR, Golden JP, Hanke JA, Jackman A, et al. Gene targeting reveals a critical role for neurturin in the development and maintenance of enteric, sensory, and parasympathetic neurons. Neuron. 1999 Feb;22(2):253–63.

27. Uesaka T, Jain S, Yonemura S, Uchiyama Y, Milbrandt J, Enomoto H. Conditional ablation of GFRα1 in postmigratory enteric neurons triggers unconventional neuronal death in the colon and causes a Hirschsprung's disease phenotype. Development. 2007 Jun 1;134(11):2171–81.

28. Grider JR, Heuckeroth RO, Kuemmerle JF, Murthy KS. Augmentation of the ascending component of the peristaltic reflex and substance P release by glial cell line-derived neurotrophic factor. Neurogastroenterol Motil. 2010 Jul;22(7):779–86.

29. Smith-Edwards KM, Najjar SA, Edwards BS, Howard MJ, Albers KM, Davis BM. Extrinsic Primary Afferent Neurons Link Visceral Pain to Colon Motility Through a Spinal Reflex in Mice. Gastroenterology. 2019 Aug;157(2):522–36.e2.

30. López SH, Avetisyan M, Wright CM, Mesbah K, Kelly RG, Moon AM, et al. Loss of Tbx3 in murine neural crest reduces enteric glia and causes cleft palate, but does not influence heart development or bowel transit. Dev Biol [Internet]. 2018 Oct 5; Available from: http://dx.doi.org/10.1016/j.ydbio.2018.09.017

31. Shirasawa S, Yunker AM, Roth KA, Brown GA, Horning S, Korsmeyer SJ. Enx (Hox11L1)-deficient mice develop myenteric neuronal hyperplasia and megacolon. Nat Med. 1997 Jun;3(6):646–50.

32. Van de Putte T, Francis A, Nelles L, van Grunsven LA, Huylebroeck D. Neural crest-specific removal of Zfhx1b in mouse leads to a wide range of neurocristopathies reminiscent of Mowat-Wilson syndrome. Hum Mol Genet. 2007 Jun 15;16(12):1423–36.

33. Thompson CL, Ng L, Menon V, Martinez S, Lee C-K, Glattfelder K, et al. A high-resolution spatiotemporal atlas of gene expression of the developing mouse brain. Neuron. 2014 Jul 16;83(2):309–23.

34. Wright CM, Garifallou JP, Schneider S, Mentch HL, Kothakapa DR, Maguire BA, et al. Dlx1/2 mice have abnormal enteric nervous system function. JCI Insight [Internet]. 2020 Feb 27;5(4). Available from: http://dx.doi.org/10.1172/jci.insight.131494

35. Hao MM, Bornstein JC, Young HM. Development of myenteric cholinergic neurons in ChAT-Cre;R26R-YFP mice. J Comp Neurol. 2013 Oct 1;521(14):3358–70.

36. Bergner AJ, Stamp LA, Gonsalvez DG, Allison MB, Olson DP, Myers MG Jr, et al. Birthdating of myenteric neuron subtypes in the small intestine of the mouse. J Comp Neurol. 2014 Feb 15;522(3):514–27.

37. Liu M-T, Kuan Y-H, Wang J, Hen R, Gershon MD. 5-HT4 receptor-mediated neuroprotection and neurogenesis in the enteric nervous system of adult mice. J Neurosci. 2009 Aug 5;29(31):9683–99.

38. Dominguez MH, Ayoub AE, Rakic P. POU-III transcription factors (Brn1, Brn2, and Oct6) influence neurogenesis, molecular identity, and migratory destination of upper-layer cells of the cerebral cortex. Cereb Cortex. 2013 Nov;23(11):2632–43.

39. Aromolaran KA, Benzow KA, Koob MD, Piedras-Rentería ES. The Kelch-like protein 1 modulates P/Q-type calcium current density. Neuroscience. 2007 Mar 30;145(3):841–50.

40. Lake BB, Ai R, Kaeser GE, Salathia NS, Yung YC, Liu R, et al. Neuronal subtypes and diversity revealed by single-nucleus RNA sequencing of the human brain. Science. 2016 Jun 24;352(6293):1586–90.

41. Heuckeroth RO. Hirschsprung disease - integrating basic science and clinical medicine to improve outcomes. Nat Rev Gastroenterol Hepatol. 2018 Mar;15(3):152–67.

42. Barber K, Studer L, Fattahi F. Derivation of enteric neuron lineages from human pluripotent stem cells. Nat Protoc. 2019 Apr;14(4):1261–79.

43. McCann CJ, Thapar N. Enteric neural stem cell therapies for enteric neuropathies. Neurogastroenterol Motil. 2018 Oct;30(10):e13369.

44. Osterwalder M, Speziale D, Shoukry M, Mohan R, Ivanek R, Kohler M, et al. HAND2 targets define a network of transcriptional regulators that compartmentalize the early limb bud mesenchyme. Dev Cell. 2014 Nov 10;31(3):345–57.

45. Lei J, Howard MJ. Targeted deletion of Hand2 in enteric neural precursor cells affects its functions in neurogenesis, neurotransmitter specification and gangliogenesis, causing functional aganglionosis. Development. 2011 Nov;138(21):4789–800.

46. Abe H, Okazawa M, Nakanishi S. The Etv1/Er81 transcription factor orchestrates activity-dependent gene regulation in the terminal maturation program of cerebellar granule cells. Proc Natl Acad Sci U S A. 2011 Jul 26;108(30):12497–502.

47. Lee J-A, Damianov A, Lin C-H, Fontes M, Parikshak NN, Anderson ES, et al. Cytoplasmic Rbfox1 Regulates the Expression of Synaptic and Autism-Related Genes. Neuron. 2016 Jan 6;89(1):113–28.

48. Weyn-Vanhentenryck SM, Mele A, Yan Q, Sun S, Farny N, Zhang Z, et al. HITS-CLIP and integrative modeling define the Rbfox splicing-regulatory network linked to brain development and autism. Cell Rep. 2014 Mar 27;6(6):1139–52.

49. Zhang X, Chen MH, Wu X, Kodani A, Fan J, Doan R, et al. Cell-Type-Specific Alternative Splicing Governs Cell Fate in the Developing Cerebral Cortex. Cell. 2016 Aug 25;166(5):1147–62.e15.

50. McEvilly RJ, de Diaz MO, Schonemann MD, Hooshmand F, Rosenfeld MG. Transcriptional regulation of cortical neuron migration by POU domain factors. Science. 2002 Feb 22;295(5559):1528–32.

51. Sugitani Y, Nakai S, Minowa O, Nishi M, Jishage K-I, Kawano H, et al. Brn-1 and Brn-2 share crucial roles in the production and positioning of mouse neocortical neurons. Genes Dev. 2002 Jul 15;16(14):1760–5.

52. Snijders Blok L, Kleefstra T, Venselaar H, Maas S, Kroes HY, Lachmeijer AMA, et al. De Novo Variants Disturbing the Transactivation Capacity of POU3F3 Cause a Characteristic Neurodevelopmental Disorder. Am J Hum Genet. 2019 Aug 1;105(2):403–12.

53. Li Z, Hao MM, Van den Haute C, Baekelandt V, Boesmans W, Vanden Berghe P. Regional complexity in enteric neuron wiring reflects diversity of motility patterns in the mouse large intestine. Elife [Internet]. 2019 Feb 12;8. Available from: http://dx.doi.org/10.7554/eLife.42914

54. Dastot-Le Moal F, Wilson M, Mowat D, Collot N, Niel F, Goossens M. ZFHX1B mutations in patients with Mowat-Wilson syndrome. Hum Mutat. 2007;28(4):313–21.

55. Coyle D, Puri P. Hirschsprung's disease in children with Mowat-Wilson syndrome. Pediatr Surg Int. 2015 Aug;31(8):711–7.

56. Zhang Z, Li Q, Diao M, Liu N, Cheng W, Xiao P, et al. Sporadic Hirschsprung Disease: Mutational Spectrum and Novel Candidate Genes Revealed by Next-generation Sequencing. Sci Rep. 2017 Nov 1;7(1):14796.

57. Nurgali K, Stebbing MJ, Furness JB. Correlation of electrophysiological and morphological characteristics of enteric neurons in the mouse colon. J Comp Neurol. 2004 Jan 1;468(1):112–24.

58. Furness JB, Robbins HL, Xiao J, Stebbing MJ, Nurgali K. Projections and chemistry of Dogiel type II neurons in the mouse colon. Cell Tissue Res. 2004 Jul;317(1):1–12.

59. Mazzuoli G, Schemann M. Multifunctional rapidly adapting mechanosensitive enteric neurons (RAMEN) in the myenteric plexus of the guinea pig ileum. J Physiol. 2009 Oct 1;587(Pt 19):4681–94.

60. Avetisyan M, Wang H, Schill EM, Bery S, Grider JR, Hassell JA, et al. Hepatocyte growth factor and MET support mouse enteric nervous system development, the peristaltic response, and intestinal epithelial proliferation in response to injury. Journal of Neuroscience. 2015;35(33):11543–58.

61. Lake JI, Heuckeroth RO. Enteric nervous system development: migration, differentiation, and disease. Am J Physiol Gastrointest Liver Physiol. 2013 Jul 1;305(1):G1–24.

62. Wang H, Hughes I, Planer W, Parsadanian A, Grider JR, Vohra BPS, et al. The timing and location of glial cell line-derived neurotrophic factor expression determine enteric nervous system structure and function. J Neurosci. 2010 Jan 27;30(4):1523–38.

63. Creedon DJ, Tansey MG, Baloh RH, Osborne PA, Lampe PA, Fahrner TJ, et al. Neurturin shares receptors and signal transduction pathways with glial cell line-derived neurotrophic factor in sympathetic neurons. Proc Natl Acad Sci U S A. 1997 Jun 24;94(13):7018–23.

64. Baloh RH, Tansey MG, Golden JP, Creedon DJ, Heuckeroth RO, Keck CL, et al. TrnR2, a novel receptor that mediates neurturin and GDNF signaling through Ret. Neuron. 1997 May;18(5):793–802.

65. Klein RD, Sherman D, Ho WH, Stone D, Bennett GL, Moffat B, et al. A GPI-linked protein that interacts with Ret to form a candidate neurturin receptor. Nature. 1997 Jun 12;387(6634):717–21.

66. Malin SA, Molliver DC, Koerber HR, Cornuet P, Frye R, Albers KM, et al. Glial cell line-derived neurotrophic factor family members sensitize nociceptors in vitro and produce thermal hyperalgesia in vivo. J Neurosci. 2006 Aug 16;26(33):8588–99.

67. Spencer NJ, Smith TK. Mechanosensory S-neurons rather than AH-neurons appear to generate a rhythmic motor pattern in guinea-pig distal colon. J Physiol. 2004 Jul 15;558(Pt 2):577–96.

68. Branchek TA, Gershon MD. Time course of expression of neuropeptide Y, calcitonin gene-related peptide, and NADPH diaphorase activity in neurons of the developing murine bowel and the appearance of 5-hydroxytryptamine in mucosal enterochromaffin cells. J Comp Neurol. 1989 Jul 8;285(2):262–73.

69. Kilkenny C, Browne WJ, Cuthill IC, Emerson M, Altman DG. Improving bioscience research reporting: the ARRIVE guidelines for reporting animal research. Osteoarthritis Cartilage. 2012 Apr;20(4):256–60.

70. Dobin A, Davis CA, Schlesinger F, Drenkow J, Zaleski C, Jha S, et al. STAR: ultrafast universal RNA-seq aligner. Bioinformatics. 2013 Jan 1;29(1):15–21.

71. Piper M, Pantano L, Mistry M, Khetani R. Single-cell RNA-seq: Clustering Analysis [Internet]. In-depth-NGS-Data-Analysis-Course. 2018 [cited 2020 Jul 3]. Available from: https://hbctraining.github.io/In-depth-NGS-Data-Analysis-Course/sessionIV/lessons/SC_clustering_analysis.html

72. Dent JA, Polson AG, Klymkowsky MW. A whole-mount immunocytochemical analysis of the expression of the intermediate filament protein vimentin in Xenopus. Development. 1989 Jan;105(1):61–74.

73. Smith-Edwards KM, DeBerry JJ, Saloman JL, Davis BM, Woodbury CJ. Profound alteration in cutaneous primary afferent activity produced by inflammatory mediators. Elife [Internet]. 2016 Nov 2;5. Available from: http://dx.doi.org/10.7554/eLife.20527

74. Jin Z, Liu L, Bian W, Chen Y, Xu G, Cheng L, et al. Different transcription factors regulate nestin gene expression during P19 cell neural differentiation and central nervous system development. J Biol Chem. 2009 Mar 20;284(12):8160–73.

75. Ngan ES-W, Garcia-Barceló M-M, Yip BH-K, Poon H-C, Lau S-T, Kwok CK-M, et al. Hedgehog/Notch-induced premature gliogenesis represents a new disease mechanism for Hirschsprung disease in mice and humans. J Clin Invest. 2011 Sep;121(9):3467–78.

76. Gehman LT, Stoilov P, Maguire J, Damianov A, Lin C-H, Shiue L, et al. The splicing regulator Rbfox1 (A2BP1) controls neuronal excitation in the mammalian brain. Nat Genet. 2011 May 29;43(7):706–11.

CHAPTER 3: Development of a screening platform to identify transcription factors directing enteric neuron subtype specification and differentiation

This manuscript is being prepared for publication. This chapter details progress towards establishing a high-throughput screening system to test the effect of transcription factor overexpression on enteric neuron subtype differentiation. Authors: Sabine Schneider, Sohaib K Hashmi, Chinmay Kalluraya, Paul Gadue, Deborah L. French, Robert O. Heuckeroth. (2020)

3.1 Abstract

Enteric neuropathies, dysfunction of the enteric nervous system (ENS), can cause devastating disease in affected individuals. The symptoms include abdominal pain, diarrhea, vomiting, distention and in severe cases sepsis and death. Our current treatment options remain limited to supportive treatment and surgical resection of the most severely affected bowel regions. The underlying cause of enteric neuropathy is loss or dysfunction of one or more enteric neuron subtypes. One enticing way to study these disorders and develop new therapy takes advantage of recently developed *in vitro* differentiation protocols for human pluripotent stem cells (hPSCs). Stem cell therapies aim to replace or supplement missing or defective ENS cell types to re-establish functioning neural circuits. However, *in vitro* differentiation protocols are not yet sophisticated enough to direct differentiation into specific neuronal subtype fates. My hypothesis was that a better understanding of the extracellular signals and transcriptional regulation that controls subtype specification and differentiation would facilitate protocol development for directed differentiation of stem cells to specific ENS subtype fates. Here, we present progress towards the goal of testing the effects of select transcriptional regulators on stem cell differentiation into cholinergic versus nitrergic enteric neuron fates. To pursue this work we established an *in vitro* ENS differentiation protocol in our lab and created a small library of doxycycline-inducible lentiviral vectors that express transcriptional regulators differentially expressed in developing enteric neuron subtypes. We are

currently validating *CHAT* and *NOS1* fluorescent reporter hPSC lines to facilitate future screening of the transcriptional regulator library.

3.2 Introduction

The enteric nervous system (ENS) is a complex network of 500 million neurons and glia that spans the entire length of the bowel. More than 20 specialized enteric neuron subtypes form repeating neural circuits that coordinate vital functions like muscle contraction and epithelial ion transport (1–4). For this reason, congenital and acquired imbalances in enteric neuron subtypes may cause debilitating and potentially life-threatening gastrointestinal motility disorders (5–7). Symptoms include constipation, nausea, vomiting, abdominal pain and distention, and in some cases sepsis and early death (5, 7). For all of these ENS disorders, quality of life can be poor and few effective treatments exist (7–9). If an obvious ENS abnormality is regionally restricted, surgical removal of the affected bowel region is routine. An example is Hirschsprung disease where the ENS is completely missing in the distal bowel and surgical resection of the abnormal region can be curative. However, in many children, debilitating symptoms persist after Hirschsprung disease surgery (10–12). One explanation for post-surgical problems appears to be dysfunctional ENS circuitry in areas of the bowel where the ENS looks grossly normal (13–17). When bowel motility is abnormal in many regions, the problem is called chronic intestinal pseudo-obstruction (CIPO). For CIPO, treatment options are particularly limited (8, 9). Neuropathic CIPO is presumed to be caused by altered enteric neuron subtype ratios and neuron subtype dysfunction, but exact genetic mutations and the mechanisms of disease are still only rarely identified (see our work in **chapter 2** to address this problem).

For both Hirschsprung disease and CIPO, an ideal therapy would replace the missing or defective ENS cell types (18). Recent advances in stem cell biology have made stem cell therapy an enticing possibility. Patient-derived human pluripotent stem cells (hPSCs) can now be robustly generated. hPSCs can be cultured long-term in serum-free, chemically-defined, and xeno-free

culture media without loss of pluripotency (19) and innovations in genome-editing technology (20) have dramatically simplified the process of correcting gene defects. Even more excitingly, several differentiation protocols have been developed to convert human pluripotent stem cells into enteric nervous system cells (21–26). However, no differentiation protocol is optimized to generate specific ENS subtypes. This is not surprising since only limited mouse (27, 28) and human (28) gene expression data sets were available to guide hypothesis-driven protocol development. Most importantly, only a few extracellular signaling molecules (BMP2/4 and Noggin (29–31), NRTN (32, 33), 5-HT (34), and GDNF (35)), extracellular matrix components (laminin-I, heparan sulfate, collagen-I, and collagen-IV (36)), and transcription factors (*Ascl1/Mash1* (37), *Sox6* (28), *Hand2* (38, 39), *Dlx1/Dlx2* (40), and *Smad1* (31)) have been shown to affect specification or differentiation of enteric neuron subtypes in experimental models. Our work (**Chapter 2**) and that of others (41–44) now provide exciting new gene expression data defining extracellular factors and transcriptional regulatory networks that could facilitate directed enteric neuron subtype differentiation. Using our own data, I decided to explore a fundamental question of enteric nervous system development: Is the expression of a defined number of transcription factors sufficient to direct differentiation of a multipotent enteric neural precursor into a cholinergic versus a nitrergic enteric neuron fate?

Cholinergic and nitrergic cell types make up the vast majority of enteric myenteric neurons and include excitatory and inhibitory motor neurons respectively. In mouse small intestine myenteric plexus, ~30% of all neurons are nitrergic, ~60% cholinergic, and ~3% both cholinergic and nitrergic (45, 46). In human colon myenteric plexus, 43-51% of all neurons are nitrergic only, 28-52% cholinergic only, and 4-10% both nitrergic and cholinergic (see **Chapter 6 Supplemental Table 6.4 and 6.5** for a more in depth discussion of human myenteric plexus staining). These cholinergic and nitrergic neurons are derived from a common enteric neuron precursor and the subtype fate decision is made at or after the penultimate cell division (27). The observation that enteric neuron subtypes diverge from a common precursor late in differentiation supports the hypothesis that a few transcriptional regulators could control enteric neuron subtype differentiation.

Even more compellingly, one myenteric interneuron subtype appears to differentiate post-mitotically from a common precursor that also produces inhibitory motor neurons in a *Pbx3*-dependent manner (42). To more broadly investigate the transcriptional regulation of cholinergic versus nitrergic enteric neuron subtype fate, we established an hPSC differentiation protocol that generates enteric neuron and glial subtypes. We are currently developing fluorescent reporter hPSC lines to facilitate identification of nitrergic and cholinergic enteric neurons and we have generated doxycycline-inducible lentiviruses that express selected transcriptional regulators. We are now poised to use this system to test the hypothesis that specific transcription factors can direct enteric neuron subtype differentiation into either cholinergic or nitrergic fate. This system can also be easily adapted to systematically study extracellular signaling pathways regulating cholinergic and nitrergic neuron subtype differentiation.

3.3 Results

Reproducible differentiation of human pluripotent stem cell-derived into enteric neuron and glial subtypes

We used the differentiation protocol developed by Fattahi *et al*. (22), as well as the feeder-free version of the protocol by Barber *et al*. (25) to reproducibly differentiate human pluripotent stem cells (hPSCs) into enteric neurons and glia (called **E**nteric **N**eural Crest-derived **C**ells or ENC). On day 11/12 of ENC differentiation, we were able to verify the presence of CD49D+/p75+ enteric neuron precursors (**Figure 3.1A-B**) (22, 47). Cells expressing high levels of CD49D were isolated via FACS and ENC differentiation was continued with purified enteric neuron precursors. By day 17 of differentiation, enteric neuron precursors had a mesenchymal appearance (flat, low nucleus:cytoplasm ratio), were highly migratory (data not shown) and individual cells were often connected to neighboring cells by thin neurites (**Figure 3.1C**), similar to migrating enteric neuron precursors in mouse (48, 49). Around day 25 of differentiation, cells adopted a more rounded appearance with longer, more robust neurites (**Figure 3.1D**). Immature enteric neurons and glia

then started aggregating after day 30 (**Figure 3.1E**). These cell body aggregates connected by fasciculated neurites closely resemble enteric ganglia, the clusters of neurons and glia that are characteristic of a normal mature ENS (50). By day 36, tubulin 3 beta (TuJ1+)- expressing neuron cell bodies and a dense network of long TuJ1+ axons were interspersed with S100B+ glial cells (**Figure 3.1F**). After day 60 of differentiation, the cultures were dominated by small, tight "ganglion"-like cell aggregates (**Figure 3.1G**) and larger, dense cell accumulations (**Figure 3.1H**) connected to each other by thick strands of fasciculated neurites (**Figure 3.1G-H**).

The "mature" ENC differentiation cultures after day 60 contained enteric neurons that expressed a wide variety of important enteric neuron subtype markers: CALB2 (calretinin), GABA (gamma butyric acid), NPY (neuropeptide Y), NOS1 (nitric oxide synthase I), RET(REarranged during Transformation proto-oncogene), SST (somatostatin), TAC1 (substance P), TH (tyrosine hydroxylase), TPH2 (tryptophan hydroxylase 2), and VIP (vasoactive intestinal peptide) (Figure 3.1I). "Mature" ENC cultures included large numbers of p75+ enteric glia (**Figure 3.1I**) co-expressing combinations of the glial markers S100B, GFAP, and SOX10 (**Figure 3.1J-K**) (51). We detected the pan-enteric neuron marker PHOX2B (52) in most of the enteric neurons within our culture, including TH+ neurons (**Figure 3.1L**). We also assessed co-expression of some neuron subtype marker combinations in our cultures. As expected based on immunohistochemical characterization of mouse enteric neuron subtypes (45, 53), NOS1 and CALB2 were generally not expressed by the same neurons (**Figure 3.1M**) while many neurons co-expressed calretinin (CALB2) and vesicular acetylcholine transporter (SLC18A3), a combination present in most cholinergic neurons (**Figure 3.1N**) (46, 53). A small subset of neurons co-expressed vasoactive intestinal peptide (VIP) and somatostatin (SST, **Figure 3.1O**), a neuropeptide combination that marks interneurons and submucosal secretomotor neurons in guinea pig (54). These observations extend previous immunohistochemical characterizations of the enteric neuron and glial subtypes found in "mature" ENC cultures (22, 24–26). The presence of all expected enteric neuron subtype

markers indicates that these two ENC differentiation protocols allow for the differentiation of many important categories of enteric neuron subtypes.

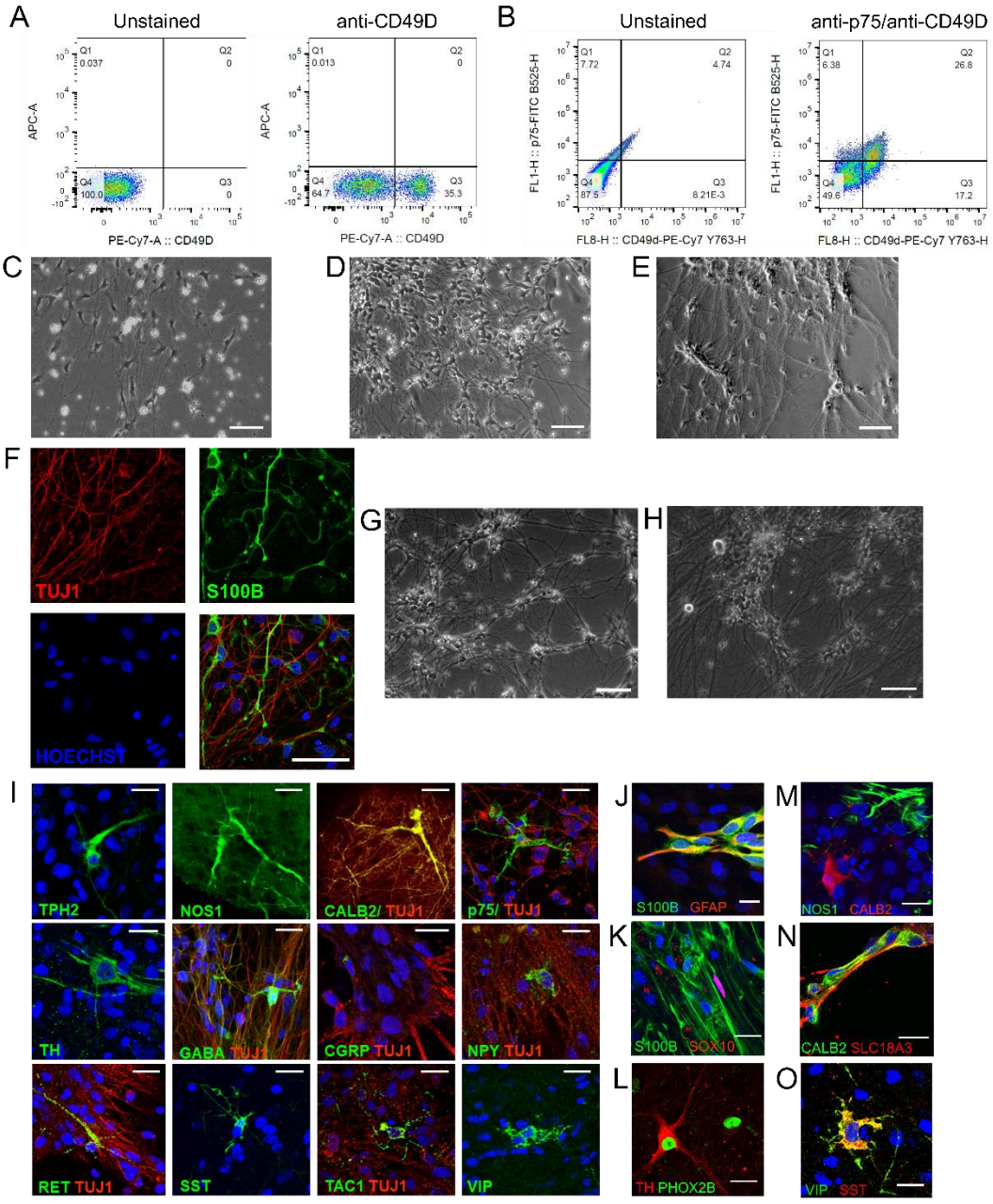

Figure 3.1: Reproducible differentiation of hPSC-derived enteric neuron and glia
A) Fluorescence activated cell sorting at day 11 of differentiation shows robust generation of CD49D (α4 integrin)-expressing enteric nervous system precursor cells. Compare unstained cells (left) to CD49D-stained cells (right). (B) CD49D-expressing cells also express the enteric nervous system precursor marker p75 (LNFR, low-affinity nerve growth factor receptor) by fluorescence

activated cell sorting at day 11 of differentiation. Compare unstained cells (left) with p75/CD49D-stained cells (right). (C) At day 17 of differentiation, the enteric neural precursor cells have a mesenchymal appearance and extend thin neurites. (D-E) The cells gain a more rounded appearance up by day 28 of differentiation (D) and start aggregating into “ganglia”-like structures by day 33 (E). (F) By day 36 of differentiation, expression of the pan-neuronal marker TuJ1 (tubulin 3 beta) and the glial marker S100B can be appreciated in distinct cell populations. (G-H) Extensive networks of fasciculated neurites connect tight “ganglia”-like cell clusters and looser cell aggregates after day 60 of differentiation. (I) The expected wide variety of enteric glial markers and enteric neuron subtype markers can be detected in mature cultures after day 60 of differentiation. TPH2 (tryptophan hydroxylase 2), NOS1 (nitric oxide synthase 1), CALB2 (calretinin), p75 (LNFR, low-affinity nerve growth factor receptor), TH (tyrosine hydroxylase), GABA (gamma aminobutyric acid), CGRP (calcitonin gene-related peptide), NPY (neuropeptide Y), RET (**re**arranged during **t**ransfection proto-oncogene), SST (somatostatin), TAC1 (substance P), and VIP (vasoactive intestinal peptide). Pan-neuronal marker TUJ1 (tubulin 3 beta) is shown for context in a subset of panels. (J-O) Coexpression was assessed from a limited number of glial and neuron subtype markers: (J) S100B and GFAP as well as (K) S100B and SOX10 are coexpressed by subsets of enteric glia. (L) Pan-enteric neuron marker PHOX2B is expressed in differentiated neurons (including TH-expressing neurons). (M) NOS1 and CALB2 are *not* expressed in the same neurons. (N) CALB2+ neurons co-express the pan-cholinergic neuron marker SLC18A3 (vesicular acetylcholine transporter and lastly, (O) VIP and SST are coexpressed in a subset of neurons. (F,I,J) Blue pan-nuclear marker is Hoechst. (C-E, G-H) Scale bar = 100 μm. (F) Scale bar = 50 μm. (I-O) Scale bar = 20 μm.

Generating a *NOS1* and *CHAT* fluorescent reporter H9-hESC cell line to facilitate identification of nitrergic and cholinergic enteric neurons

Quantification of cholinergic and nitrergic neurons in mature ENC cultures is necessary to determine if transcription factor overexpression enhances enteric neuron differentiation into cholinergic or nitrergic neurons. However, commonly used immunohistochemical markers choline acetyltransferase (CHAT), vesicular acteylchine transporter (SLC18A3), and neuronal nitric oxide synthase (NOS1) are in neuron cell bodies and their extensive neurites (45) making it difficult to count individual cell bodies in dense neuron aggregates. To address this problem, I decided to generate fluorescent reporter H9-hESC lines that label cholinergic and nitrergic neurons. Using CRISPR/CAS9, we generated two independent reporter lines with a nuclear localized tandem dimer red fluorescent protein (tdRFP) knocked into the 3’ untranslated region (3’ UTR) of either the endogenous *NOS1* locus or the endogenous *CHAT* locus. An internal ribosome entry site (IRES) sequence after the *NOS1* and *CHAT* stop codons permits expression of nuclear tdRFP from the

same mRNA as the endogenous *NOS1* and *CHAT* transcripts, respectively. Thus, tdRFP expression can serve as a proxy for NOS1 or CHAT expression. We included a floxed puromycin selection cassette at the 3' end of the CRISPR insertion template (**Figure 3.2A**) and screened ~300 clones by PCR for correct genomic insertion of the IRES-NLS-tdRFP-puromycin selection cassette (**Figure 3.2B-E**). We expanded one morphologically healthy hPSC clone for each of *NOS1* or *CHAT* fluorescent reporter genomic insertion. Chromosomal G band analysis for the *CHAT* reporter line confirmed the absence of chromosomal aberrations (**Supplementary Figure 3.1**). The *NOS1* reporter line has not yet been karyotyped.

Both reporter clones were subsequently transfected with pCAG-Cre-GFP to excise the floxed puromycin selection cassette, which was verified by PCR (**Figure 3.2G-J**). We attempted differentiations with *NOS1* and *CHAT* fluorescent reporter lines, but unfortunately saw only faint cytoplasmic tdRFP with no nuclear-localized tdRFP (data not shown). Upon re-examination of the repair template, we found a 10 bp spacer between the NLS and tdRFP sequences that introduced a frameshift preventing production of normal protein. However, the tdRFP sequence itself has an ATG start codon that could explain the faint cytoplasmic tdRFP signal.

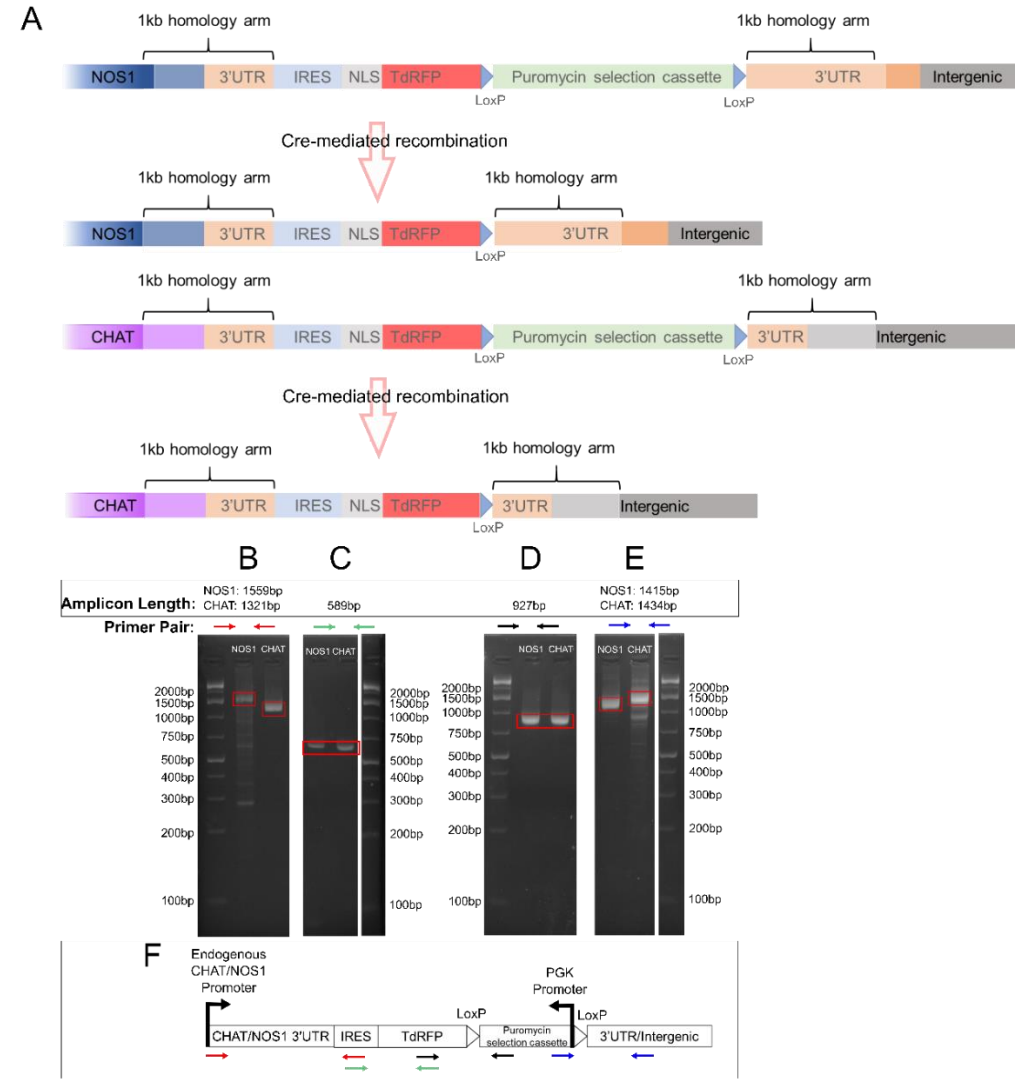
A
1kb homology arm
1kb homology arm
NOS1
3'UTR
IRES
NLS
TdRFP
Puromycin selection cassette
3'UTR
Intergenic
LoxP
LoxP
Cre-mediated recombination
1kb homology arm
1kb homology arm
NOS1
3'UTR
IRES
NLS
TdRFP
3'UTR
Intergenic
LoxP
1kb homology arm
1kb homology arm
CHAT
3'UTR
IRES
NLS
TdRFP
Puromycin selection cassette
3'UTR
Intergenic
LoxP
LoxP
Cre-mediated recombination
1kb homology arm
1kb homology arm
CHAT
3'UTR
IRES
NLS
TdRFP
3'UTR
Intergenic
LoxP
B
C
D
E
Amplicon Length:
NOS1: 1559bp
CHAT: 1321bp
589bp
927bp
NOS1: 1415bp
CHAT: 1434bp
Primer Pair:
NOS1 CHAT
2000bp
1500bp
1000bp
750bp
500bp
400bp
300bp
200bp
100bp
F
Endogenous
CHAT/NOS1
Promoter
PGK
Promoter
LoxP
LoxP
CHAT/NOS1 3'UTR
IRES
TdRFP
Puromycin
selection cassette
3'UTR/Intergenic

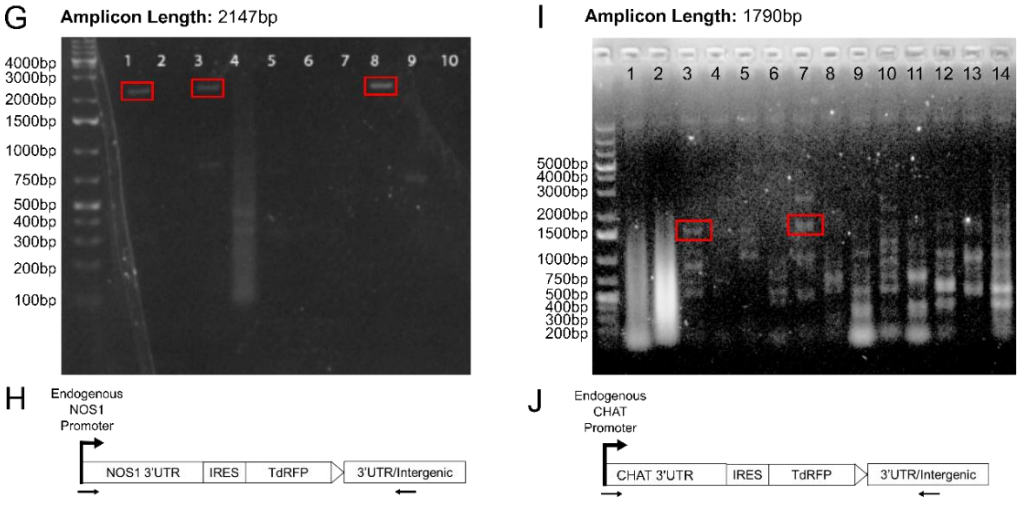
G
Amplicon Length: 2147bp
4000bp
3000bp
2000bp
1500bp
1000bp
750bp
500bp
400bp
300bp
200bp
100bp
1 2 3 4 5 6 7 8 9 10
I
Amplicon Length: 1790bp
5000bp
4000bp
3000bp
2000bp
1500bp
1000bp
750bp
500bp
400bp
300bp
200bp
1 2 3 4 5 6 7 8 9 10 11 12 13 14
H
Endogenous
NOS1
Promoter
NOS1 3'UTR
IRES
TdRFP
3'UTR/Intergenic
J
Endogenous
CHAT
Promoter
CHAT 3'UTR
IRES
TdRFP
3'UTR/Intergenic

Figure 3.2: Development of CHAT and NOS1 3'UTR fluorescent reporter knock-in h9-hESC cell lines

A) Schematic of the CRISPR repair template integrated into the genomic CHAT and NOS1 loci. An internal ribosomal entry site (IRES), the coding sequence for tandem-dimer RFP (TdRFP) with a nuclear localization sequence (NLS), and a purmycin selection cassette were introduced into the 3'UTR of the CHAT and NOS1 loci. The dsDNA repair template homology arms extend 1kb both upstream (5') and downstream (3') from the Cas9 cut site within the CHAT and NOS1 3'UTRs. (B-E) Four sets of primers were used to verify a complete insertion of the repair template into the correct genomic location (see **Supplementary Table 3.3**). (F) Schematic of the genomic locus with inserted repair template. The approximate location of the primer pairs (B-D) are marked by colored arrows. (G) Transient expression of CRE removed the puromycin selection cassette from the NOS1 clone with correct insertion of the repair template (see B-D) and allowed us to select 3 clones (1,3 and 8) with retained correct genomic insertion (see **Supplementary Table 3.3**). (H) Schematic of the NOS1 genomic locus with inserted repair template. The approximate location of the primer pair (G) is marked by arrows. (I) Transient expression of CRE removed the puromycin selection cassette from the CHAT clone with correct insertion of the repair template (see B-D) and allowed us to select 2 clones (3 and 7) with retained correct genomic insertion (see **Supplementary Table 3.3**). (J) Schematic of the CHAT genomic locus with inserted repair template. The approximate location of the primer pair (G) is marked by arrows.

Lentiviral overexpression of transcription factors specific to enteric neuron subtypes

I chose nine transcription factors to overexpress in differentiating ENC cultures. These transcription factors were selected based on differential expression in myenteric cholinergic or nitrergic enteric neuron subtypes as defined by single cell RNA-sequencing data at embryonic day 17.5 (E17.5) and single nucleus sequencing in adult mouse colon (see **Chapter 2** and **Figure 3.3A-B**). Some selected transcription factors are expressed in all cholinergic neuron clusters, but few nitrergic neuron clusters in E17.5 mouse ENS (*Casz1* and *Meis1*), some are only detected in specific cholinergic clusters (*Bnc2*, *Tbx2*, and *Pbx3*), and some are primarily restricted to nitrergic neuron clusters (*Creb5*, *Etv1*, *Ebf1*) (**Figure 3.3B** and **Chapter 2**).

I decided to introduce the transcription factors into enteric neural precursors via lentiviral infection. Transcription factor expression was controlled by a doxycycline-inducible *cis* regulatory element for tight temporal control (**see Supplementary Figure 3.2A**). As proof-of-principle, I infected enteric neural precursors at day 22 of differentiation with high titer lentiviral particles carrying the cDNA sequence for doxycycline-responsive transcriptional activator, reverse

tetracycline-controlled transactivator (rtTA), and *EBF1* cDNA with added V5 and His tag sequences. Differentiating ENC cultures were treated with doxycycline from day 24 to day 27 and analyzed for EBF1 expression at day 27 of differentiation. Enteric neuron precursors were identified by SOX10 expression and nuclear expression of both V5 and His protein tags verified efficient EBF1 expression in the vast majority of cells (**Figure 3.3C**).

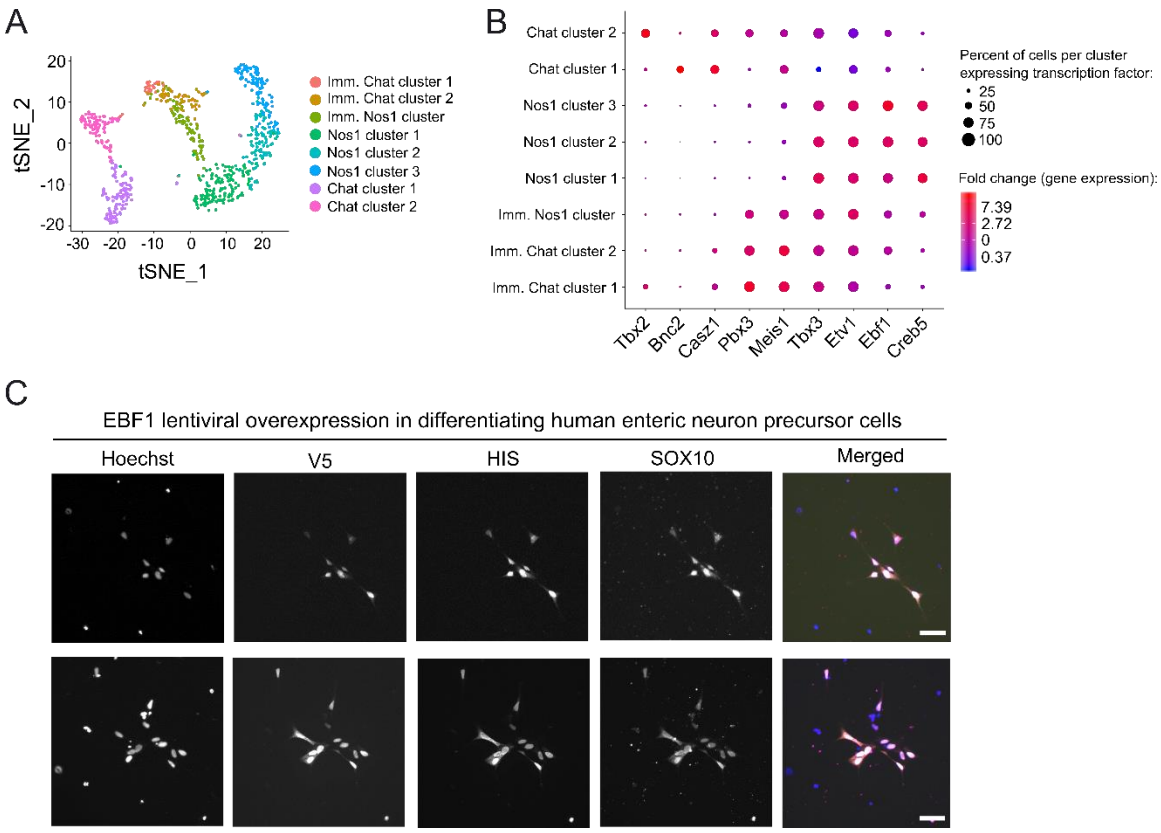

Figure 3.3: Successful generation of lentiviral overexpression vectors for select transcription factors to be used in overexpression screen

(A) TSNE plot of embryonic day 17.5 (E17.5) mouse enteric neuron single cell sequencing data shows 4 clusters of nitrergic neurons (1 immature and 3 mature clusters) and 4 clusters of cholinergic neurons (2 immature and 2 mature clusters) (see **chapter 2**). (B) Dot plot with nine transcription factors differentially expressed in cholinergic or nitrergic E17.5 enteric neuron cluster(s). The transcription factors were selected for the overexpression screen and cloned into the FU-tetO-Gateway lentiviral expression vector under control of a tetracycline response element (see **Supplementary Table 3.4** and **Supplementary Figure 3.2**). Dot plot illustrates both the fold change in transcription factor differential expression per cluster (denoted by color shades ranging from blue to red) and percent of cells per cluster expressing the transcription factor (denoted by circle diameter). (C) Transcription factor EBF1 is successfully expressed in enteric neuron

precursors (SOX10+) at day 27 of differentiation. Enteric neuron precursors at day 22 of differentiation were infected with lentiviral expression vector carrying the EBF1 coding sequence and expression of the HIS and V5 tag can be verified. Hoechst is used to mark all nuclei in the field of view. (A-B) Imm.= immature. (B) Color legend denotes fold change (average normalized gene expression level in cluster of interest/ average normalized gene expression level in all other clusters). (C) Scale bar = 50 μm.

3.4 Discussion and Future Directions

The future of targeted stem cell therapies for enteric neuropathies like CIPO depends on understanding the transcriptional regulation of enteric neuron subtype specification and differentiation. Some studies using conditional knockout mouse models studies have already implicated transcription factors in enteric neuron subtype differentiation (28, 31, 37–40, 42, 55). However, conditional knockout mouse models are a low-throughput tool to identify transcription factors that critically influence differentiation. In contrast, high-throughput screening in pluripotent cells could rapidly identify transcriptional regulators that alter enteric neuron subtype differentiation.

An important consideration is that redundancy in transcription factor regulatory networks frequently obscures regulatory functions of single transcription factors in loss-of-function studies (56, 57). Gain-of-function studies thus may have a higher chance of revealing a regulatory role for a given transcription factor. However, only rare transcription factors can induce the expression of genes in transcriptionally silent chromatin regions (58, 59) which may encompass gene loci with cell type or cell subtype-specific expression. Limited combinations of pioneer factors are able to initiate gene regulatory networks that can convert one distantly related mature cell type to another (60–62) or, rarely, single-handedly establish a specific cell fate (63). Therefore, the overexpression system I established may increase the likelihood of elucidating regulatory functions of specific transcription factors in differentiating enteric neurons. Candidate transcription factors can be expressed in immature enteric neurons. These cells have already established enteric neuron-specific transcriptional regulatory networks, and may express required transcriptional coregulators

for subtype specific gene modules. Most importantly, subtype-specific gene loci may already be accessible to transcription factor binding due to permissive chromatin modifications (64).

My selection of transcription factors was based on my newly generated mouse single cell and single nucleus data. Mouse models well-recapitulate a number of human enteric neuropathies (65–67) and regulatory relationships between specific genes and transcription factors appear to be largely conserved between mammals (68). However, there are interspecies differences in enteric neuron subtype neurotransmitter expression (45) and enteric neuron subtype ratios (52). It is possible that transcriptional regulation of enteric neuron subtype differentiation is altered in subtle but important ways when comparing mouse and human. This makes it even more important that the role of candidate transcriptional regulators is assessed in human cells.

We chose transcription factors based on their differential expression in fetal and adult cholinergic versus nitrergic myenteric neuron subsets. Most selected transcription factors also have roles in CNS neuron subtype differentiation (**Supplementary Table 3.4**). Our novel data shows that *Tbx3* is required for normal perinatal numbers of myenteric nitrergic neurons (**Chapter 2**) and others reported *Pbx3* is required for differentiation of a subset of myenteric interneurons (*Pbx3*, (42)). This makes these transcription factors perfect candidates to test and validate the transcription factor overexpression screen as we differentiate hESC into enteric neurons.

To facilitate the identification of cholinergic and nitrergic neurons in dense enteric nervous system cultures (after day 60 of ENC differentiation), I decided to generate fluorescent reporter lines that will label any nitrergic (NOS1-expressing) or cholinergic (CHAT-expressing) cells. Addition of a nuclear localization sequence to the tdRFP protein should further simplify quantification of these neurons since dense networks of neurites will not contain tdRFP. I decided to introduce the tdRFP sequence into the 3'UTR to avoid having to select for heterozygous insertion of the construct into hPSC. Homozygous loss of *Chat* (69) and *Nos1* leads to structural ENS defects (70) and beyond that, we wanted to minimize changes in endogenous gene expression as much as possible. One drawback of this design decision is the dependence of *tdRFP* translation efficiency

on the transcription rate of the endogenous *CHAT* and *NOS1* transcripts. Recent data we and others generated shows that in both mouse and human, *NOS1* transcripts are abundant in nitrergic neurons, however, *CHAT* transcripts are rare (**Chapter 2** and (42, 43)). This may reflect low *CHAT* RNA transcript stability or possibly predominantly local *CHAT* protein translation at pre-synaptic terminals (71, 72). Since the tdRFP has been introduced into the 3'UTR after an IRES sequence, translation of *tdRFP* will likely be less efficient than that of the endogenous *CHAT* and *NOS1* transcripts (73) and thus tdRFP signal could be very low even in unambiguously cholinergic neurons. However, the half-life of RFP proteins is around 20-26 hours (74–76), so even a low translation rate may be sufficient to detect tdRFP fluorescence.

Unfortunately, we detected a frameshift in both the CHAT and NOS1 fluorescent lines, which likely explains the lack of nuclear tdRFP signal and low tdRFP signal overall. We will continue the characterization of the lines we generated to see if the reporters can be used despite the design error. However, it is likely that we will have to repeat the reporter line CRISPR screen with a correct CRISPR repair template without the frame-shift. At this point, we do not predict this to take very long since all tools have already been generated and validated in our hands.

Our screen currently only focuses on cholinergic versus nitrergic fate decisions, but could be extended to look at other functionally relevant neuron subtypes like intrinsic sensory neurons or motor neurons (1). We have already extended the previously published characterization of enteric neuron subtypes that spontaneously arise in ENC differentiation cultures (22, 25) by staining for known mouse and human enteric neuron subtype markers. We were able to verify the presence of many important markers and the expected co-expression patterns for a much smaller subset. To better understand the possibilities and limitations of the current ENC differentiation protocols, we plan on quantifying the proportions of total neurons co-expressing unique combinations subtype markers using single cell/nucleus RNA sequencing data that has only recently been generated (**Chapter 2** and (42–44)).

Since at least some subtype fate decisions are made late in the enteric neuron differentiation timeline (27, 42) and may require tight temporal control of transcriptional regulator expression, we chose a lentiviral vector with a doxycycline-responsive *cis* regulatory element (TRE) 5' to the transcription factor sequences (**Supplementary Figure 3.2A**) (77, 78). Introduction of doxycycline in the cell culture medium for differentiating enteric neuron precursors would then permit us to control the timing of transcription factor gene expression. Stable genomic insertion of the construct allows us to infect differentiating enteric neural precursors before they form tight aggregates (compare **Figure 3.1C** to **Figure 3.1F**), thereby maximizing infection efficiency. Differentiating cells are thus infected days to weeks before "mature" enteric neuron subtypes are observed in culture. We currently plan to infect enteric neural precursors at day 20-22 of differentiation and to start transcription factor overexpression by day 25 (concurrent with the change in enteric neural precursor morphology to a rounded cell shape and shortly before first detection of pan-neuronal marker tubulin III beta (**Figure 3.1D-F**). Cultures will be monitored closely for the appearance of cholinergic/nitrergic neurons (nuclear RFP+ neurons) and mature ENC cultures will be quantified for the absolute numbers and cholinergic/nitrergic to total neuron ratio (**Supplementary Figure 3.2B**).

We are now poised to use this system to study the effects of select transcription factors on enteric neuron subtype differentiation into either cholinergic or nitrergic fate. Furthermore, this system can easily be expanded to study fate decisions for functionally important sub-categories of cholinergic and nitrergic neurons (e.g. intrinsic sensory neurons or inhibitory motor neurons) as well as the effects of extracellular signaling pathway modulation (e.g. addition of trophic factors and small molecule inhibitors) on neuron subtype differentiation.

3.5 Methods

Cell Culture

Maintenance of pluripotent stem cells on a feeder layer

Human pluripotent stem cells (hPSCs, H9-hESCs; WA09, WiCell, Madison, WI; NIH Registration Number 0062) were maintained in HES medium (see Reagents and Solutions in Supplementary Data) on a layer of irradiated mouse embryonic fibroblasts (MEFs) plated on gelatin-coated tissue culture dishes. HPSCs were examined daily by brightfield microscopy to verify normal morphology and passaged once colonies were compact, rounded, and almost touching (every 3-4 days) without being raised. 1-4 days before passaging hPSCs, irradiated MEFs were plated on 6-well plates coated with 0.1% gelatin (Sigma-Aldrich; Cat# G1890) in MEF medium (see Reagents and Solutions in Supplementary Data). Before plating PSCs on the MEF feeder-layer, the wells were washed 1x with Iscove's Modified Dulbecco's Eagle Medium (IMDM, ThermoFisher, Cat#12440053). To passage one well of a 6-well plate of hPSCs, 1 mL of TrypLE Express (Invitrogen, Cat#12605010) was added to the hPSC plate and incubated at room temperature (RT) for 3 minutes. The well was then gently agitated and inspected by brightfield microscopy. Once most of the MEFs had detached and the edges of the hPSC colonies had lifted off while the center remained firmly attached, TrypLE was aspirated and the well was washed once with IMDM. IMDM was then aspirated and 1 mL of HES medium was added to the well. The hPSC colonies were gently removed from the bottom of the well using a rubber cell scraper (Fisher Scientific, Cat#50-809-208). Cells were triturated three times with a P1000 pipet tip and a subset of cells (1:10 passaging ratio for maintenance culture) was transferred to a 14 mL Falcon tube (Corning, Cat#352059) containing HES medium supplemented with 10 μM Rho-associated kinase inhibitor (ROCKi) (Y-27632 dihydrochloride, R&D Systems, Cat#1254/1). 2 mL of cell suspension was plated per well and cultured at 37°C in 5% carbon dioxide, 5% oxygen, and 90% nitrogen. HES medium with ROCKi was replaced with normal HES medium after allowing cells to attach overnight and replaced daily until cells were ready for their next passage. To freeze cells, the normal

passaging protocol was followed (as above), but cells were scraped into IMDM after dissociation with TrypLE. PSCs were triturated, and the cell suspension was transferred to a 15 mL Falcon tube, and centrifuged at 270 x*g* for 3 minutes. The media was aspirated and the cell pellet was resuspended in 50% FBS, 40% HES media, and 10% dimethyl sulfoxide (DMSO) (Sigma, Cat#2650-100ml). Resuspended cells were transferred into labeled cryovials and placed into freezing containers containing isopropanol at -80°C for 24 hours before being transferred to liquid nitrogen for long-term storage.

Maintenance of pluripotent stem cells in feeder-free conditions

To transition hPSCs from MEF feeders to feeder-free conditions, tissue culture plates were coated with Corning® Matrigel® hESC-Qualified Matrix, LDEV-free (Corning, Cat#354277). The Matrigel was diluted 1:100 in DMEM/F12 (Dulbecco's Modified Eagle Medium: Nutrient Mixture F-12, ThermoFisher, Cat#11320033) and incubated at room temperature for 45 min to 1 hour. Matrigel was then aspirated and replaced with IMDM and used right away or stored at 37°C in 5% carbon dioxide for up to 1 week. HPSCs on a MEF feeder layer were dissociated with TrypLE as previously described and plated on the Matrigel-coated plates at a ratio of 1:6 in Essential 8 (E8) Flex medium (Gibco, Cat#A2858501). Cells were cultured at 37°C in 5% carbon dioxide. Cells were fed every day with 2 mL/well (6-well plate) of fresh E8 medium. HPSCs were adapted to feeder-free conditions after 2-3 passages. To passage feeder-free hPSCs, colonies were observed by brightfield microscopy daily. Once colonies were large but still tightly formed and covered close to 75% of the well, the well was washed once with 1x Dulbecco's Phosphate Buffered Saline (DPBS) without calcium and magnesium (Cat#21-031-CV), and 0.5 mM EDTA (EDTA Buffer, pH 8, 0.5 M, Invitrogen, Cat#15575020) diluted in 1x DPBS (EDTA-PBS) (pre-warmed to 37°C) was added. Cells were incubated with EDTA-PBS for 4 minutes while closely observing the well under a brightfield microscope. When the cells in the colonies appeared rounded and cells at the center began to separate from each other, EDTA-PBS was gently removed and 1 mL E8 Flex medium

was added to the well followed by gentle agitation to lift off cell aggregates. A P10 pipet tip was used to gently draw up the cell aggregates into a 14 mL Falcon tube with E8 media and cells were plated at a passaging ratio of 1:3-1:5 on a new plate coated with 1:100 Matrigel. For cryopreserving feeder-free PSCs, cells were passaged with 0.5 mM EDTA-PBS as previously described. After removing EDTA-PBS, 1 mL/well of STEM-CellBanker-GMP Grade (Amsbio LLC, Cat#NC0400932) was added and cell aggregates were lifted off by gentle agitation. After triturating once, resuspended cells were transferred into labeled cryovials and placed into freezing containers with isopropanol at -80°C for 24 hours before being transferred to liquid nitrogen for long-term storage.

Differentiation of pluripotent stem cells into enteric neural crest precursor cells

Differentiation of hPSCs into enteric neurons and glia starting from hPSCs maintained on a MEF feeder-cell layer *(22)*

Up to a week before starting a differentiation, 6-well plates were prepared for differentiation by coating with Matrigel (Corning Matrigel Basement Membrane Matrix, Corning, Cat#354234). The Matrigel was thawed on ice and diluted 1:20 with DMEM/F12 medium (Dulbecco's Modified Eagle Medium: Nutrient Mixture F-12, ThermoFisher, Cat#11320033). The diluted Matrigel was added to the wells and allowed to incubate at 37°C for 1-2 hours. The plates were monitored carefully under a brightfield microscope to identify the ideal Matrigel layer thickness at which regular, elongated, feathery aggregates were visible on the well bottom (79).

One to three days before the start of differentiation, hPSCs were passaged onto 1:20 Matrigel. Differentiations were carried out in tissue culture-treated 6-well plates. For passaging, the wells were washed briefly with Iscove's Modified DMEM (IMDM). 0.05% Trypsin-EDTA (Mediatech, Cat#MT25-052-CI) was added to each well (1 mL/well). During the incubation with Trypsin at room temperature for 1-2 minutes, the plate was continuously agitated with vigorous side-to-side motions across the cell culture hood surface. This allowed the MEF feeder layer cells to detach very quickly while the hPSC stayed firmly attached to the bottom of the well. Once most of the MEF had

detached, the trypsin was carefully aspirated from the side of the well and the dish was left without any medium for another 1-2 minutes at room temperature. At this point, HES medium was added to the wells (1mL/well) and the cells were triturated 2-3 times with a P100 pipet before they were counted and replated on 1:20 Matrigel at a cell density of 100,000 cells/cm^2. Differentiation was started 1 to 3 days after plating on 1:20 Matrigel once hPSCs reached a 70-80% confluent monolayer (see Fattahi et al. 2015 for images denoting the optimal cell density at the start of differentiation (79)).

On day 0 of differentiation, HES medium was replaced with 2 mL/well KSR medium for differentiation day 0-1 (see Supplementary Materials - Reagents and Solutions). Differentiating cultures were maintained in 37°C in 5% carbon dioxide. On day 2 of differentiation, KSR medium for differentiation day 0-1 was replaced with 2 mL/well KSR medium for differentiation day 2-11 (see Reagents and Solutions in Supplementary Data). On day 4 of differentiation, the medium was replaced with 2 mL/well 75% (v/v) KSR medium for differentiation day 2-11 and 25% (v/v) N2 medium (see Reagents and Solutions in Supplementary Data). On day 6 of differentiation, the medium was replaced with 4 mL/well 50% (v/v) KSR medium for differentiation day 2-11 and 50% (v/v) N2 medium plus the addition of 1 µM retinoic acid (100mM, Sigma, Cat#R2625). On day 8 of differentiation, the medium was replaced with 4 mL/well 25% (v/v) KSR medium for differentiation day 2-11, 75% (v/v) N2 medium, and 1 µM retinoic acid (100mM, Sigma, Cat#R2625). On day 10 of differentiation, the medium was replaced with 4 mL/well N2 medium with 1 µM retinoic acid. CD49D-expressing enteric neural precursors were purified via fluorescence activated cell sorting on day 11 of differentiation.

Differentiation of hPSCs into enteric neurons and glia starting from hPSCs maintained in feeder-free conditions *(25)*

Two days before start of differentiation, hPSCs in feeder-free conditions were passaged according to the methods specified above, but with a passaging ratio of 5:6 (cell aggregates from 5x wells of a 6-well plate are seeded in 6x wells of a 6-well plate) on a plate coated with 1:100

Matrigel (Corning, Cat#354234). Culture medium is replaced with fresh Essential 8 Flex medium (Gibco, Cat#A2858501) the next day. Two days after plating, differentiation was started if the hPSC cultures had proliferated to a confluent monolayer. This was considered day 0 of differentiation and the maintenance medium (Essential 8 Flex medium) was switched to 2mL/well differentiation medium A (see Reagents and Solutions in Supplementary Data). Whenever medium was aspirated, care was taken to slowly aspirate from the edge of the wells in order to not disrupt the cell layer in the wells. On day 4 of differentiation, differentiation medium A was replaced with differentiation medium B (see Reagents and Solutions in Supplementary Data) at 2mL/well. On day 6, the medium in the wells was replaced with fresh differentiation medium B at 4mL/well. On day 8, differentiation medium B was replaced with differentiation medium C (see Reagents and Solutions in Supplementary Data) at 4mL/well. On day 10 of differentiation, the medium in the wells was replaced with 6mL/well fresh differentiation medium C. CD49D-expressing enteric neural precursors were purified via fluorescence activated cell sorting on day 12 of differentiation.

Differentiation of enteric neural crest precursor cells into enteric neurons and glia

ENC spheroid phase (differentiation days 11/ 12 to 15)

After FACS-mediated purification of CD49D+ enteric neural crest precursor cells on day 11/12 of differentiation, the sorted cells were resuspended in NC medium (see Reagents and Solutions in Supplementary Data) at a concentration of 2.5 million cells/mL NC medium and plated at 2mL/well in a 6-well plate (Costar® 6-well Clear Flat Bottom Ultra-Low Attachment 6-Well Plate; Corning, Cat#3471). During these 3-4 days, the cells aggregated into and proliferated as floating spheroids. Two days after plating (differentiation day 13/14), the old NC medium was removed by gently swirling the plate with the ENC spheroids so that they group at the center of the well. This allowed careful aspiration of the old NC medium with a P1000 pipet from the edge of the well while actively avoiding the removal of any ENC spheroids. 2 mL/well fresh NC medium was added.

Enteric Neuron Induction (differentiation days 15 to >60)

On day 15 of differentiation, the ENC spheroids are grouped at the center of their wells by gently swirling the plate and the NC medium was carefully aspirated from the edge of the well with a P1000 pipet. 1 mL/well accutase was added to the wells and the plate was incubated at 37°C for 30 minutes to dissociate the ENC spheroids. The spheroids were then mechanically dissociated with a P1000 pipet and cells were pelleted (270*xg*, 3 min). The cells were resuspended in EN medium (see Reagents and Solutions in Supplementary Data) and plated on poly-L-ornithine/laminin/fibronectin-coated glass coverslips in 12-well plates at a cell density of 100,000 cells/cm^2. EN medium was replaced every 2 days until day 50 of differentiation. After that EN medium was supplemented with 2 µg/mL laminin-I (L, R&D Systems, Cat#3400-010-01) and 2 µg/mL fibronectin (FN, BD Biosciences, Cat#356008) and replaced weekly.

Preparation of poly-L-ornithine/laminin/fibronectin-treated long-term ENC culture plates

Two to seven days before ENC spheroids were plated for enteric neuron induction (between day 6 and 13 of differentiation), the plates used for long-term ENC culture were prepared for seeding. Glass coverslips were placed into each well (18mm glass coverslips (Fisherbrand, Cat#12-546) were used for 12-well plates) and 15 µg/mL poly-L-ornithine hydrobromide (Sigma, Cat#P3655) in 1xPBS was added. The plate was then incubated overnight at 37°C. The next day, the poly-L-ornithine hydrobromide solution was replaced with 2 µg/mL laminin-I (R&D Systems, Cat#3400-010-01) and 2 µg/mL fibronectin (BD Biosciences, Cat#356008) in 1x PBS and the plate was incubated overnight at 37°C and used the next day or left at 37°C until needed (up to 6 days). Before cell seeding, the laminin/fibronectin solution was aspirated and replaced with EN medium.

Flow cytometry to confirm maintenance of pluripotency

To confirm pluripotency, hPSCs were assessed by flow cytometry for expression of cell surface markers associated with the pluripotent state. One well of PSCs was washed once with 1x Dulbecco's Phosphate Buffered Saline (DPPBS) (Invitrogen, Cat#14190136), treated with 1 mL

0.25% Trypsin-EDTA (Invitrogen, Cat#25200056) for 5 minutes at 37°C to dissociate colonies into single cells, neutralized with 0.5 mL Fetal Bovine Serum (FBS) (Tissue Culture Biologicals, Cat#101), and centrifuged at 270 x*g* for three minutes. The pellet was resuspended in 500 µL FACS Buffer (see Reagents and Solutions in Supplementary Data) and 100 µl each was pipetted into 4x wells of a 96-well plate. The plate was spun down for two minutes at 750x*g.* The pellets were resuspended once more in 100 µL of FACS buffer and spun down for two minutes at 750 x*g*. Each well was resuspended in fluorophore-conjugated antibody mixtures as follows: 1 - Unstained control (100 µl FACS buffer), 2 - SSEA3 (1:50)/SSEA4 (1:400) in 100 µl FACS buffer, 3 - Tra 1-60 (1:50)/Tra 1-81 (1:50) in 100 µL FACS buffer, and 4 - SSEA1 (1:50)/SSEA5 (1:200) in 100 µL FACS buffer. Antibody catalog numbers are in **Supplementary Table 3.1**. Cells were incubated with the antibodies for 15 minutes in the dark at room temperature. 80 µL of FACS buffer was added to each well and the plate is spun down at 750 x*g* for 2 minutes. The pellet was resuspended in 200 µL FACS buffer and spun down once more at 750 x*g* for 2 minutes. Finally, the cells were resuspended in 100 µL of FACS buffer and analyzed for cell surface marker expression using the Cytoflex LX (Beckman Coulter).

Purification of enteric neural precursors via FACS at day 11/ 12 of differentiation

On day 11 of differentiation (if hPSCs were maintained on a feeder layer) or day 12 of differentiation (if PSC were maintained in feeder-free conditions), all wells were washed once with 2 mL/well sterile 1x DPBS before dissociation with 1mL/well Accutase (Innovative Cell Technologies, Cat#AT104) at 37°C for 20-30 min. After gentle agitation of the plate, all cells were collected with a P1000 pipet, titrated 2-3 times, and transferred into one 14 mL Falcon tube per 6-well plate. The cells were pelleted (270 *xg*, 3 min) after addition of 4 mL 10% FBS in IMDM. The cell pellet was then resuspended in 600µL IMDM supplemented with 10% FBS, 10 uL/mL DNaseI (EMD Millipore; Cat#260913), and 3 µL/mL monothioglycerol (MTG, Sigma Aldrich; Cat#M6145) plus anti-CD49D antibody (see **Supplementary Table 3.1**). The cells were incubated on ice for 15

min protected from light exposure with periodic agitation. The cells were subsequently washed twice by the addition of 5 mL IMDM supplemented with 10% FBS and subsequent pelleting (270 *xg*, 3 min). After the second wash, the cells were resuspended in IMDM supplemented with 10% FBS, 10 uL/mL DNaseI (EMD Millipore; Cat#260913), and 3 µL/mL monothioglycerol (MTG, Sigma Aldrich; Cat#M6145), passed through a mesh strainer (Falcon, Cat#352235), and sorted on a BD FACSJazz (BD Biosciences), MoFlo Astrios (Beckman-Coulter), or BD FACSAria Fusion (BD Biosciences) to isolate CD49D-expressing cells. Cells were sorted into IMDM supplemented with 10% FBS, 10 µL/mL DNaseI, and 3 µL/mL MTG (Sigma Aldrich; Cat#M6145), centrifuged (270 *xg*, 3 min), and resuspended in NC medium (see Reagents and Solutions in Supplementary Data) for plating.

Immunofluorescence staining

Cells on glass coverslips were washed with phosphate-buffered saline (PBS), fixed (4% paraformaldehyde, 20 minutes, RT), washed twice with PBS, blocked (5% normal donkey serum (NDS), 0.5% Triton X-100 in PBS (0.5% PBST)) (1 hour, RT), incubated in primary antibodies (5% NDS, 0.5% PBST 1 hour, RT) (see **Supplementary Table 3.1**, washed 3 x 5 minutes (0.5% PBST), and then incubated in secondary antibodies (see **Supplementary Table 3.1**) (0.5% PBST, 30 minutes, dark, RT). Cells washed three times in PBS, incubated in Hoechst 3342 nuclear dye (1:1000, Invitrogen, Cat#H3570) (30 minutes, RT) were washed two times in PBS, mounted in Prolong Gold AntiFade Mountant (Life Technologies; Cat#P36934) and allowed to set (overnight, dark, RT) before long-term storage at 4°C.

Microscopy

Immunofluorescence images were acquired on a Zeiss LSM 710 laser scanning confocal microscope and Zeiss ZEN 2.3 SP1 FP3 (black) (Version 14.0.18.201; Zeiss, Oberkochen, Germany) software with a 20x/0.8 air or 63x/1.4 oil DIC M27 Plan-Apochromat objective. The Zeiss

LSM 710 condenser numerical aperture is 0.55. Confocal images were processed in ImageJ to crop, scale, and uniformly color adjust. Brightfield images were acquired on a Leica DFC340 FX camera attached to a Leica DMI4000B microscope with Leica Application Suite X version 1.5.1.13187 (Leica Microsystems, Wetzlar, Germany).

Generating NOS1 3'UTR and CHAT 3'UTR fluorescent reporter human embryonic stem cells (hESCs)

Guide RNA design

The genomic sequence for human *NOS1* (Transcript ID ENST00000618760.4, NOS1-202, Location Chromosome 12: 117,208,142-117,452,170) and *CHAT* ITranscript ID ENST00000395562.2, CHAT-205, Chromosome 10:49,609,095-49,665,104) were obtained from the Ensembl Genome Browser (*NOS1*: Ensembl 87 December 2016 release, *CHAT*: Ensembl 89 May 2017) (80). A region of 150 bp within the 3'UTR of *NOS1* starting from 30bp 3' of the STOP codon was analyzed for suitable CRISPR/Cas9 guide RNAs (gRNAs) using the Broad Institute software crispr.mit.edu (Feb. 2017) (81). A 150bp region encompassing the entire CHAT 3'UTR and a short region upstream from the STOP codon was analyzed for suitable gRNAs using the software http://crispor.tefor.net/ (July 2017) (82) and genome version "UCSC Feb. 2009 (GRCh37/hg19) + SNPs: 1000 Genomes, ExaC". Four gRNAs were chosen for testing based on the best combinations of specificity/quality scores (see **Supplementary Table 3.2**). Each gRNA has a 20 bp sequence with a NGG protospacer adjacent motif (PAM) sequence at the 3' end. The sequences were edited in the following way for cloning into the empty gRNA cloning vector (Addgene Plasmid #41824; RRID:Addgene_41824; gRNA_Cloning Vector was a gift from George Church) (83): 1) The PAM sequence was removed. 2) The nucleotide at the 5' end was changed to a G if it was not already a G. 3) Homology arms were added as follows:

5'- *TTTCTTGGCTTTATATATCTTGTGGAAAGGACGAAACACC*- **add gRNA sequence here** -3'

5’- *GACTAGCCTTATTTTAACTTGCTATTTCTAGCTCTAAAAC*- **add reverse complement of gRNA sequence here** -3’

The 60 bp oligos (sequence and reverse complement of sequence) were ordered as 25 nmole oligos (Purification: Standard desalting) (Integrated DNA Technologies, IDT) and annealed in a 1:1 ratio (95°C for 5 minutes, cool at RT for 10 minutes). The annealed product was amplified using Phusion High-Fidelity DNA Polymerase (New England Biolabs Catalog#M0530S) (98°C for 30s, 30 cycles (98°C for 10s, 55°C for 20s, 72°C for 30s), 72°C for 5 min, 4°C hold). The PCR product was visualized by agarose gel electrophoresis using a 1.5% agarose gel. The product band was excised under ultraviolet light and purified using the NucleoSpin Gel and PCR Clean-Up kit (Machery-Nagel,PA, USA; Cat#740609).

The gRNA empty cloning vector was digested using the AflII restriction enzyme and Gibson Assembly (Gibson Assembly Master Mix; New England Biolabs, Catalog#E2611) was used to clone the PCR-amplified gRNA sequences into the vector. The assembled gRNA vectors were transformed into NEB 5-alpha Competent E. coli (High Efficiency) (New England Biolabs, Catalog#C2987H), colonies were picked and amplified by miniprep, and plasmids were purified using the QIAprep Spin Miniprep Kit (QIAGEN, Catalog#27106). Sequences were verified by Sanger sequencing.

Guide RNA testing

H9-hESCs (H9-hESCs; WA09, WiCell, Madison, WI; NIH Registration Number 0062) were plated in a 6-well dish on a feeder layer of irradiated MEFs to reach 30-60% confluency after 24 hours. Media was changed 4 hours before transfection. H9-hESCS were transfected with the identified gRNAs and pCas9_GFP (pCas9_GFP was a gift from Kiran Musunuru (Addgene plasmid#44719; http://n2t.net/addgene:44719; RRID:Addgene_44719)) (84) using 0.104 µg of plasmid/cm^2 of plate surface area and Lipofectamine Stem Transfection Reagent (ThermoFisher Scientific, Cat#STEM00003) following manufacturer instructions. Transfected cells were incubated for 48 hours in 5% oxygen, 5% carbon dioxide, and 90% nitrogen at 37°C and sorted for GFP

positive cells. Sorted hESCs were plated in conditioned HES medium (see Reagents and Solutions in Supplementary Data) at 5000 cells/plate on 100 mm dishes coated with Corning® Matrigel® hESC-Qualified Matrix, LDEV-free (Corning, Cat#354277) (diluted 1:3 in DMEM/F12). Up to 20 colonies were manually picked using a 200 µL pipet tip after 10-15 days when they reached ~1 mm in diameter and transferred into PCR strip tubes. After triturating 3-4 times, the colonies in PCR strip tubes were pelleted at 10,000 x *g* for 5 minutes and the supernatant was removed. 20 µL Proteinase K buffer (see Reagents and Solutions in Supplementary Data) was added to each tube followed by incubation at 55°C for 1 hour and inactivation at 94°C for 10 minutes. The digest was vortexed and centrifuged at 10,000 x *g* for 5 minutes and 5 µL of digest was used in a PCR reaction using primers specified in **Supplementary Table 3**. The PCR products were analyzed by agarose gel electrophoresis using a 2.5% agarose gel. Size changes and presence of doublets was used to determine cutting efficiency and gRNAs CHAT-1 and NOS1-2 were chosen.

NOS1 3'UTR and CHAT 3'UTR fluorescent reporter cell line creation

NOS1 3'UTR and *CHAT* 3'UTR fluorescent reporter cell lines were created using H9 human embryonic stem cells (H9-hESCs; WA09) (WiCell, Madison, WI; NIH Registration Number 0062). A tandem dimer red fluorescent protein (tdRFP) reporter was introduced in separate screens into the 3' untranslated regions (3'UTRs) of *NOS1* and *CHAT* in H9-hESCs. gRNA binding sequences in the *CHAT* and *NOS1* 3'UTR were identified. A gRNA screen was performed (see methods above and gRNA sequences in **Supplementary Table 3.2**) and gRNAs CHAT-1 and NOS1-2 were chosen for subsequent gene editing. A plasmid was created to serve as the homology-directed repair template after the Cas9-induced double-stranded DNA break. The repair template consisted of an internal ribosome entry site (IRES) followed by tdRFP with a 5' nuclear localization signal (NLS) (repair constructs are referred to as *NOS1* 3'UTR IRES-NLS-tdRFP and *CHAT* 3'UTR IRES-NLS-tdRFP). 1 kb homology arms were added at the 5' and 3' ends of the repair template. The repair template also included a *loxP*-flanked puromycin selection cassette.

However, this was not utilized due to the unavailability of puromycin-resistant MEFs at the time of the experiment.

H9-hESCS were transfected with the identified gRNAs and pCas9_GFP (pCas9_GFP was a gift from Kiran Musunuru (Addgene plasmid#44719; http://n2t.net/addgene:44719; RRID:Addgene_44719)) (84) using 0.104 µg of plasmid/cm^2 of plate surface area and Lipofectamine Stem Transfection Reagent (ThermoFisher Scientific, Cat#STEM00003) following manufacturer instructions. Transfected cells were incubated for 48 hours in 5% oxygen, 5% carbon dioxide, and 90% nitrogen at 37°C and sorted for GFP positive cells. Sorted hESCs were plated in conditioned HES medium (see Reagents and Solutions in Supplementary Data) at 5000 cells/plate on 100 mm dishes coated with Corning® Matrigel® hESC-Qualified Matrix, LDEV-free (Corning, Cat#354277) (diluted 1:3 in DMEM/F12). All healthy-looking colonies were manually picked using a 200 µL pipet tip after 10-15 days when they reached ~1 mm in diameter and transferred into PCR strip tubes. After triturating 3-4 times, half of the volume was plated in HES medium on 48-well plates coated with Corning® Matrigel® hESC-Qualified Matrix, LDEV-free (Corning, Cat#354277) (diluted 1:3 in DMEM/F12) and seeded with irradiated MEFs 24 hours prior to seeding of the picked colonies.The other half of the cell suspension was pelleted at 10,000 x *g* for 5 minutes and the supernatant was removed. 20 µL Proteinase K buffer (see Reagents and Solutions in Supplementary Data) was added to each tube followed by incubation at 55°C for 1 hour and inactivation at 94°C for 10 minutes. The digest was vortexed and centrifuged at 10,000 x *g* for 5 minutes and 5 µL of digest was used in a PCR reaction. Primers for PCR screening of CRISPR clones are listed in **Supplementary Table 3.3**. The PCR products were analyzed by agarose gel electrophoresis. Any colonies that showed a correct insertion of the repair template were expanded into progressively larger wells with MEF feeder cells plated on 0.1% gelatin (Sigma-Aldrich; Cat# G1890) until they could be maintained as normal (see above) and stocks of the cell line clone could be frozen for long-term storage.

To excise the puromycin selection cassette, clones with the correct insertion were expanded and transfected with pCAG-Cre-GFP (pCAG-Cre:GFP was a gift from Connie Cepko (Addgene plasmid # 13776; http://n2t.net/addgene:13776 ; RRID:Addgene_13776)) (85) using Lipofectamine Stem. GFP positive cells were FAC-sorted after 48 hours and plated at 5000 cells per 100 mm dish, and individual colonies were manually picked, as previously described. Colonies were screened for excision of the puromycin selection cassette using the primers outside of the inserted sequence including the 1kb homology arms (sequences in **Supplementary Table 3.3**).

Transcription factor cloning into lentiviral expression vector

Transcription factor cDNA sequences (see **Supplemental Table 3.4**) were amplified using primers that added the Gateway recombination sequence attB1 flanking the ORF: attB1 Fwd: 5'-GGGGACAAGTTTGTACAAAAAAGCAGGCT-3' and attB1 Rev: 5'-GGGGACCACTTTGTACAAGAAAGCTGGGTA-3'. The PCR reaction was run on a 0.7% agarose gel and the product band was excised under ultraviolet light and purified using the NucleoSpin Gel and PCR Clean-Up kit (Machery-Nagel,PA, USA; Cat#740609). The amplified transcription factor sequences were then inserted into the FU-tetO-Gateway lentiviral expression vector (kind gift from John Gearhart, Addgene plasmid # 43914 ; http://n2t.net/addgene:43914 ; RRID:Addgene_43914) (77) using a One Tube Gateway cloning reaction (86). 100 fM (315 ng) of Gateway pDONR221 Vector (ThermoFisher, Cat#12536017) and 300 fM of the amplified transcription factor sequences were combined with 3 µL BP Clonase II enzyme mix (ThermoFisher, Cat#11789100) and TE buffer pH 8.0 was added up to a final volume of 15 µL. The reaction mixture was incubated at room temperature overnight. To assess the efficiency of the first step of the reaction (BP reaction), 0.5 µl of proteinase K solution (ThermoFisher, Cat#11789100) was added to 5 µL of the BP reaction mixture and incubated at 37°C for 10min and then transformed into OneShot TOP10 Competent Cells (ThermoFisher, Cat#C404003). 100 fM (678 ng) of FU-tetO-Gateway lentiviral expression vector and 3 µL LR Clonase II enzyme mix (ThermoFisher, Cat#11791100) were added to the

remaining 10 µL of BP reaction and TE buffer pH 8.0 was added up to a final volume of 15 µL. The reaction mixture was incubated at room temperature overnight and to stop the reaction, the reaction was incubated at 37°C for 10 minutes in the presence of 2 µl of proteinase K solution (ThermoFisher, Cat#11791100). 2 µl of LR clonase reaction was subsequently transformed into OneShot TOP10 Competent Cells (ThermoFisher, Cat#C404003), colonies were picked, amplified by miniprep, and plasmids were purified using the QIAprep Spin Miniprep Kit (QIAGEN, Catalog#27106). Sequences were verified by Sanger sequencing.

Lentivirus production

This protocol closely follows the recommendations made by Wang *et al.* (87). HEK293T cells (ATCC, Cat#CRL-3216) were seeded at a cell density of $3.5x10^6$ cells/plate on 2x 10 cm plates per transcription factor lentiviral expression vector in HEK293T culture medium (see Reagents and Solutions in Supplementary Data). The next day, the culture medium was exchanged and the cells were transfected: Per 10 cm plate, 48 µL FuGENE transfection reagent (Promega, Cat#E2311) was added to 600 µL IMDM (ThermoFisher, Cat#12440053) without touching the side of the well or microcentrifuge tube. The FuGENE/IMDM mixture was left at room temperature for 5 minutes. 4 µg of each lentiviral packaging vector pVSV-G (88), pMDLg/pRRE (89), and pRSVREV (89) and 4 µg of the FU-tetO-Gateway lentiviral expression vector were combined separately before addition to the FuGENE/IMDM mixture. The FuGENE/IMDM/DNA mixture was gently mixed (several inversions of microcentrifuge tube) and left undisturbed at room temperature for 20 minutes. The transfection mix was then slowly added to the culture medium on the HEK293T culture plate and the plate was tilted several times to mix the contents. The plates were left undisturbed for 3 days at 37°C in 5% carbon dioxide before the media was collected and passed through a Millex-HV Syringe Filter Unit, 0.45 µm, PVDF, 33 mm (Sigma, Cat#SLHV033RS) using a 20mL syringe (Becton Dickinson, Cat#302830) into ultraclear centrifuge tubes (Beckman Coulter, Cat#344058) and the viral particles were pelleted at 24,000 rpm for 90 minutes (no breaking at the end of the

spin) in a SW-28 Ti rotor (Beckman Coulter, SW 28 Ti Swinging-Bucket Aluminum Rotor Package, Cat#342204). The ultracentrifuge tubes were then inverted to remove the supernatant and added 100uL of 1x Dulbecco's Phosphate Buffered Saline (DPBS, Cat#21-031-CV). After 1 hour at 4°C, the virus was aliquoted into 10 µL aliquots and frozen at -80°C for long-term storage.

To facilitate titering of the FU-tetO-Gateway lentiviral expression vector that only expresses the gene product of interest in the presence of doxycycline hyclate (doxycycline, Sigma, Cat#D9891-25G) and a reverse tetracycline-controlled transactivator (rtTA), a polyclonal HEK293T cell line stably expressing rtTA was created. Briefly, HEK293T cells were infected with FUdeltaGW-rtTA vector (kind gift from Konrad Hochedlinger, Addgene plasmid # 19780 ; http://n2t.net/addgene:19780 ; RRID:Addgene_19780) (90) and maintained in the presence of 0.5 µg/mL doxycycline for 14 days. 0.5 µg/mL doxycycline, which had been empirically determined to be the lowest concentration of doxycycline to kill 100% of HEK293T cells within 48 hours.

For titering, this polyclonal rtTA-expressing cell line was passaged into a 48-well plate at a cell density of 60,000 cells/well. The next day, a subset of the wells was infected with FUdeltaGW-rtTA-lentivirus. The virus was serially diluted (1:2 serial dilution from 1:250 to 1:16,000) in the presence of 1:2000 protamine sulfate (Fresenius Kai, Cat#C22905, NDC 63323-229-05) and 0.5 µg/mL doxycycline. The virus-containing culture medium was replaced 24 hours after infection with fresh HEK293T culture medium with 0.5 µg/mL doxycycline and the virus was titered 48 hours after infection using intracellular flow cytometry.

Intracellular Flow Cytometry for virus titering

The wells with infected HEK293T were washed once with 1x Dulbecco's Phosphate Buffered Saline (DPBS) (Invitrogen, Cat#14190136), treated with 1 mL 0.25% Trypsin-EDTA (Invitrogen, Cat#25200056) for 5 minutes at 37°C to dissociate colonies into single cells, neutralized with 0.5 mL Fetal Bovine Serum (FBS) (Tissue Culture Biologicals, Cat#101), and centrifuged at 270 x*g* for three minutes. The cells were resuspended in IMDM and centrifuged at

270 x*g* for three minutes. The cells were then fixed for 30 minutes at 37°C in 1.6% (v/v) PFA in Dulbecco's Phosphate Buffered Saline (DPBS, Cat#21-031-CV) and then centrifuged (700 *xg* two minutes). The cells were then resuspended in DPBS and centrifuged at 700 x*g* for two minutes. For permeabilization, the cells were washed twice in 1x Intracellular Staining Permeabilization Wash Buffer (10x stock, BioLegend, Cat#421002) in DPBS and centrifuged at 700 *xg* for two minutes. The cells were then resuspended in anti-His or anti-V5 primary antibody (details in **Supplementary Table 3.3**) in 1x Intracellular Staining Permeabilization Wash Buffer in DPBS with and incubated for 30 minutes at room temperature. The cells were washed twice with 1x Intracellular Staining Permeabilization Wash Buffer in DPBS, centrifuged (700 *xg*, 2 min), and supernatant was aspirated. The cells were then resuspended in Alexa Fluor 488-conjugated secondary antibody (details in Supplementary Table 3) in 1x Intracellular Staining Permeabilization Wash Buffer in DPBS with and incubated for 30 minutes at room temperature. The cells were subsequently washed twice with 1x Intracellular Staining Permeabilization Wash Buffer in DPBS, centrifuged (700 *xg*, 2 min), the supernatant was aspirated, and cells were resuspended in FACS Buffer (see Reagents and Solutions in Supplementary Data) for analysis on a Cytoflex LX (Beckman Coulter).

Lentiviral infection of ENC differentiations

Differentiating enteric neuron precursors were infected with EBF1-FU-tetO-Gateway-lentivirus and FUdeltaGW-rtTA-lentivirus on day 22 of differentiation: EN medium was aspirated from the wells and replaced with EN medium supplemented with EBF1-FU-tetO-Gateway-lentivirus (1:1000 dilution of concentrated virus stock, ~$2x10^8$ viral particles/mL), FUdeltaGW-rtTA-lentivirus (1:1000 dilution of concentrated virus stock, viral titer unknown), and 1:2000 protamine sulfate (Fresenius Kai, Cat#C22905, NDC 63323-229-05). The EN medium was replaced the next morning and on day 24 of differentiation, EN medium was supplemented with 0.5 µg/mL doxycycline hyclate (Sigma, Cat#D9891-25G) to start expression of the EBF1 coding sequence. On day 27 of

differentiation, the wells were briefly washed with phosphate-buffered saline (PBS), fixed with 4% paraformaldehyde, and then immunofluorescence stained for V5- and His-tag expression.

3.5 Acknowledgments

We wish to thank Chintan Jobaliya (logistical support) and Jean Ann Maguire (karyotype analysis of cell lines) from the CHOP Stem Cell Core for their technical expertise. We thank Jenny Yan for her invaluable assistance with lentiviral vector generation, Somdutta Mukherjee for technical expertise and encouragement, and Aileen Ren and Briana R. Christophers for their assistance in setting up our tissue cell culture room. We thank the staff of the Flow Cytometry Core Laboratory at the Children's Hospital of Philadelphia Research Institute for their invaluable assistance. Funding for the work comes from the Irma and Norman Braman Endowment, The Children's Hospital of Philadelphia Research Institute, and the Suzi and Scott Lustgarten Center Endowment.

3.6 Author Contributions

Conceptualization: SS; Methodology: SS, SKH, ROH; Formal Analysis: SS, SKH; Investigation: SS, SKH, CK; Resources: ROH, PG and DLF; Writing - original draft and editing: SS, SKH, ROH; Funding Acquisition: ROH; Supervision: DLF, PG and ROH.

3.7 Supplementary Data

Supplementary Figures and Tables

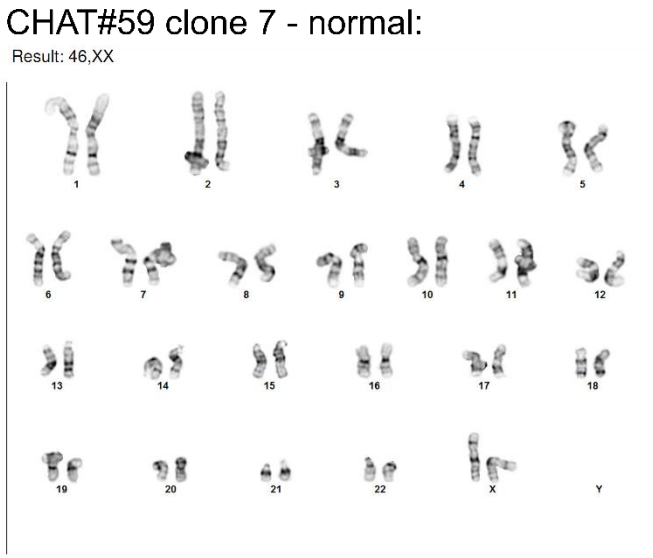

Supplementary Figure 3.1: Chromosomal G-band analysis (karyotyping) of CHAT 3' UTR IRES-NLS-tdRFP fluorescent reporter iPSC line
Cre recombinase overexpression was used to excise the puromycin selection cassette from one clone with the correctly inserted full-length CRISPR repair template, CHAT#59. Chromosomal G-Band analysis of one clone (#7) was normal.

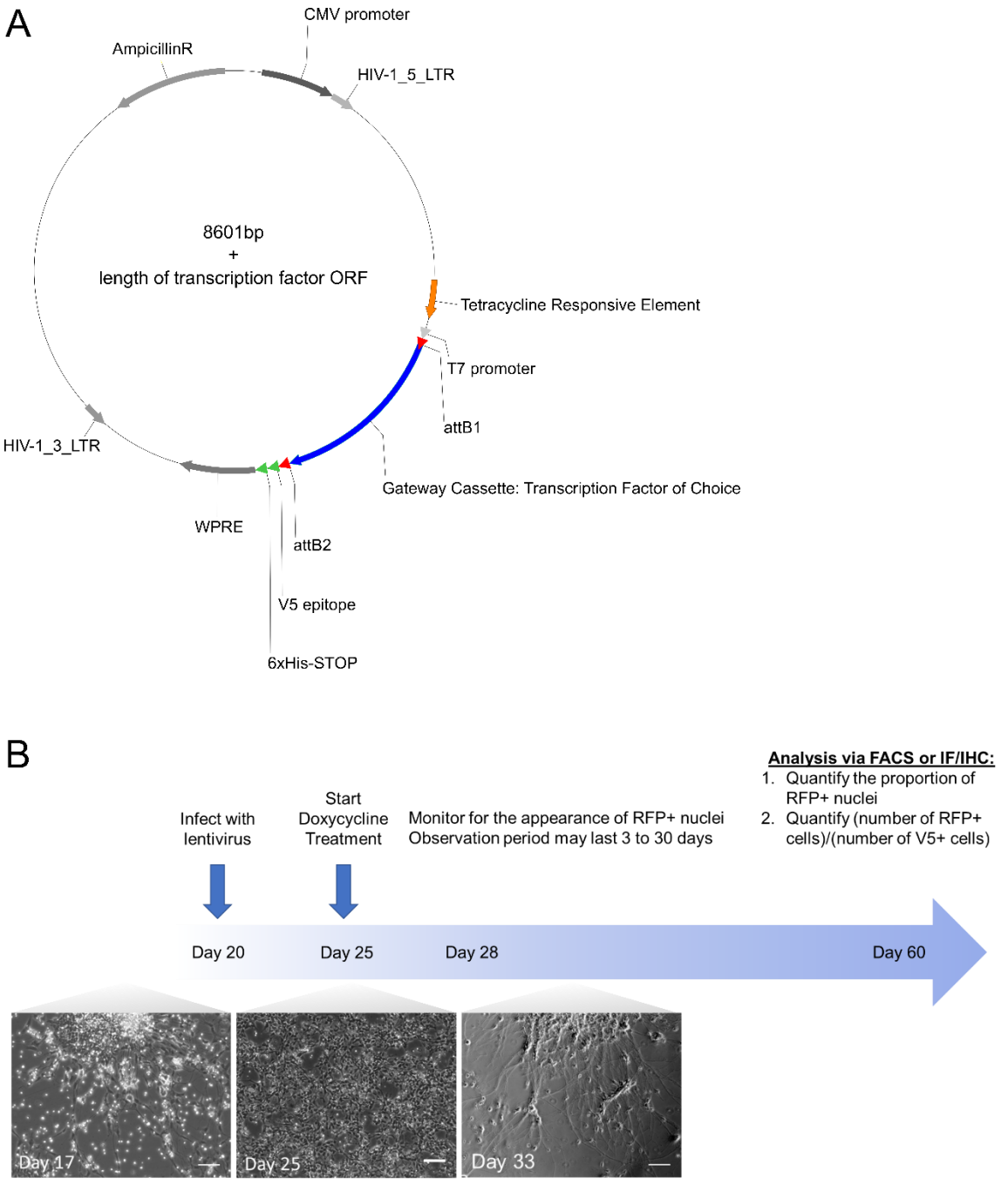

Supplementary Figure 3.2: Looking ahead - the candidate transcription factor overexpression screen

A) Plasmid map of the FU-tetO-Gateway lentiviral expression vector used for this screen (77). The Gateway recombination sites (attR1 and attR2) allow for efficient insertion of coding sequences into the expression vector "Gateway cassette" under control of a tetracycline response element and a T7 promoter. The coding sequence is tagged with a V5 and HIS tag, simplifying verification of

infection and expression. (B) Schematic of the planned transcription factor overexpression screen. Differentiating enteric neural precursors will be transfected at day 20-22 when the cells are transitioning from a mesenchymal phenotype (image on the bottom left, Day 17) to a more rounded cell type (image on the bottom middle, Day 25). Doxycycline treatment to turn on transcription factor expression is started on day 25, before the cells start aggregating into “ganglia”-like structures (image on the bottom right, Day 33). The cells will then be monitored for the appearance of RFP+ nuclei, indicating the emergence of NOS1+ or CHAT+ neurons, and the proportion of RFP+ neurons will be quantified in mature cultures at or beyond day 60.

Supplementary Table 3.1: Antibodies

Antibody Name (species)	Application (Concentration)	Manufacturer	Catalog
Hoechst 33342, Trihydrochloride, Trihydrate	Immunofluorescence (1:1000)	Invitrogen	Cat#:H3570
SOX10 (goat)	Immunofluorescence (1:200)	Santa Cruz	Cat#:sc-17342, RRID:AB_2195374
SOX10 (goat)	Immunofluorescence (1:200)	R&D Systems	Cat#:AF2864, RRID:AB_442208
TUJ1 (rabbit)	Immunofluorescence (1:5000)	Covance, BioLegend	Cat#:PRB-435P (Covance), Cat#:802001 (BioLegend), RRID:AB_2564645
TUJ1 (chicken)	Immunofluorescence (1:400)	Aves Labs	Cat#:TUJ, RRID:AB_2313564
HUC/D (clone 16A11, mouse)	Immunofluorescence (1:200)	Invitrogen	Cat#:A21271, RRID:AB_221448
NOS1 (rabbit)	Immunofluorescence (1:100)	Millipore	Cat#:AB5380, RRID:AB_91824
Tyrosine hydroxylase (TH, sheep)	Immunofluorescence (1:800)	Chemicon (Millipore)	Cat#:AB1542, RRID:AB_90755
CGRP (goat)	Immunofluorescence (1:500)	Abcam	Cat#:Ab36001, RRID:AB_725807

Antibody Name (species)	Application (Concentration)	Manufacturer	Catalog
TAC1 (N-18, goat)	Immunofluorescence (1:500)	Santa Cruz	Cat#:Sc-9758, RRID:AB_661439
CALB2 (rabbit)	Immunofluorescence (1:1000)	Chemicon (Millipore)	Cat#:AB5054, RRID:AB_2068506
TPH2 (sheep)	Immunofluorescence (1:400)	Chemicon (Millipore)	Cat#:AB1541, RRID:AB_90754
VACHT (rabbit)	Immunofluorescence (1:1000)	Synaptic Systems	Cat#:139103, RRID:AB_887864
GABA (rabbit)	Immunofluorescence (1:1000)	Sigma	Cat#:A2052, RRID:AB_477652
NPY	Immunofluorescence (1:500)	Peninsula Laboratories International	Unknown
SST (YC7, rat)	Immunofluorescence (1:500)	Millipore	Cat#:MAB354, RRID:AB_2255365
RET (rabbit)	Immunofluorescence (1:400)	Immuno-Biological Laboratories	Cat#:18121, RRID:AB_2301042
VIP (rabbit)	Immunofluorescence (1:250)	Abcam	Cat#:ab78536, RRID:AB_1604043

Antibody Name (species)	Application (Concentration)	Manufacturer	Catalog
GFAP (chicken)	Immunofluorescence (1:500)	BioLegend	Cat#:PCK-591P (Covance), Cat#:829401 (BioLegend), RRID:AB_2564929
P75 (rabbit)	Immunofluorescence (1:400)	Chemicon (Millipore)	Cat#:AB1554, RRID:AB_90760
S100B (rabbit)	Immunofluorescence (1:100)	abcam	Cat#:Ab52642, RRID:AB_882426
RFP (5F8, Rat)	Immunofluorescence (1:150)	Chromotek	Cat#:5F8-100, RRID:AB_2336064
V5 tag (rabbit)	Immunofluorescence (1:200) and Intracellular flow Cytometry (1:100)	Cell Signaling Technology	Cat#:D3H8Q, RRID:AB_2687461
HIS tag (ad1.1.10, mouse)	Immunofluorescence and Intracellular Flow cytometry (1:200)	R&D Systems	Cat#:MAB050, RRID:AB_357353
Goat anti-Chicken IgG (H+L) Highly Cross-Adsorbed Secondary Antibody, Alexa Fluor 488	Immunofluorescence (1:400)	Life Technologies	Cat#:A11039, RRID:AB_142924
Goat anti-Chicken IgG (H+L) Highly Cross-Adsorbed Secondary Antibody, Alexa Fluor 594	Immunofluorescence (1:400)	Life Technologies	Cat#:A11042, RRID:AB_2534099

Antibody Name (species)	Application (Concentration)	Manufacturer	Catalog
Goat anti-Chicken IgG (H+L) Highly Cross-Adsorbed Secondary Antibody, Alexa Fluor 647	Immunofluorescence (1:400)	Life Technologies	Cat#:A21449, RRID:AB_1500594
Donkey anti-Goat IgG (H+L) Highly Cross-Adsorbed Secondary Antibody, Alexa Fluor 488	Immunofluorescence (1:400)	Life Technologies	Cat#:A11055, RRID:AB_2534102
Donkey anti-Goat IgG (H+L) Highly Cross-Adsorbed Secondary Antibody, Alexa Fluor 647	Immunofluorescence (1:400)	Life Technologies	Cat#:A21447, RRID:AB_141844
Donkey anti-Mouse IgG (H+L) Highly Cross-Adsorbed Secondary Antibody, Alexa Fluor 488	Immunofluorescence and Intracellular Flow cytometry (1:400)	Life Technologies	Cat#:A21202, RRID:AB_141607
Donkey anti-Mouse IgG (H+L) Highly Cross-Adsorbed Secondary Antibody, Alexa Fluor 647	Immunofluorescence (1:400)	Life Technologies	Cat#:A31571, RRID:AB_162542
Donkey anti-Rabbit IgG (H+L) Highly Cross-Adsorbed Secondary Antibody, Alexa Fluor 488	Immunofluorescence and Intracellular Flow cytometry (1:400)	Life Technologies	Cat#:A21206, RRID:AB_2535792

Antibody Name (species)	Application (Concentration)	Manufacturer	Catalog
Donkey anti-Rabbit IgG (H+L) Highly Cross-Adsorbed Secondary Antibody, Alexa Fluor 594	Immunofluorescence (1:400)	Life Technologies	Cat#:A21207, RRID:AB_141637
Donkey anti-Rabbit IgG (H+L) Highly Cross-Adsorbed Secondary Antibody, Alexa Fluor 647	Immunofluorescence (1:400)	Life Technologies	Cat#:A31573, RRID:AB_2536183
Donkey anti-Rat IgG (H+L) Highly Cross-Adsorbed Secondary Antibody, Alexa Fluor 488	Immunofluorescence (1:400)	Life Technologies	Cat#:A21208, RRID:AB_141709
Donkey anti-Rat IgG (H+L) Highly Cross-Adsorbed Secondary Antibody, Alexa Fluor 594	Immunofluorescence (1:400)	Life Technologies	Cat#:A21209, RRID:AB_2535795
Donkey anti-Sheep IgG (H+L) Highly Cross-Adsorbed Secondary Antibody, Alexa Fluor 488	Immunofluorescence (1:400)	Life Technologies	Cat#:A11015, RRID:AB_141362
Donkey anti-Sheep IgG (H+L) Highly Cross-Adsorbed Secondary Antibody, Alexa Fluor 594	Immunofluorescence (1:400)	Life Technologies	Cat#:A11016, RRID:AB_10562537

Antibody Name (species)	Application (Concentration)	Manufacturer	Catalog
Alexa Fluor® 488 anti-human SSEA-3 Antibody	Flow cytometry (1:50)	BioLegend	Cat#:330305 RRID:AB_1279441
Alexa Fluor® 647 anti-human SSEA-4 Antibody	Flow cytometry (1:400)	BioLegend	Cat#:330407 RRID:AB_1089201
Alexa Fluor® 488 anti-human TRA-1-60-R Antibody	Flow cytometry (1:50)	BioLegend	Cat#:330613 RRID:AB_2295395
Alexa Fluor® 647 anti-human TRA-1-81 Antibody	Flow cytometry (1:50)	BioLegend	Cat#:330705 RRID:AB_1089245
Alexa Fluor® 488 anti-mouse/human CD15 (SSEA-1) Antibody	Flow cytometry (1:50)	BioLegend	Cat#:125609, RRID:AB_1089191
APC anti-human SSEA-5 Antibody	Flow Cytometry (1:200)	BioLegend	Cat#:355209, RRID:AB_2562012
FITC anti-human CD271 (LNGFR/p75) Antibody	Flow Cytometry (1:200)	Miltenyi Biotec	Cat#:130-098-103, RRID:AB_2661083
PE/Cy7 anti-human CD49D Antibody	Flow Cytometry (1:200)	BioLegend	Cat#:304313, RRID:AB_10642817

Supplementary Table 3.2: Candidate gRNAs identified using CRISPR Guide RNA Design tools for *NOS1 3'UTR IRES-NLS-tdRFP* (http://crispr.mit.edu) and *CHAT 3'UTR IRES-NLS-tdRFP* (http://crispor.tefor.net/). Selected gRNAs are highlighted in grey.

gRNA	Cut in Sense or Antisense Strand	Sequence (5' → 3')	Sequence with homology arms	Software annotation of gRNA sequence
NOS1-1	antisense	**A**CTGAGGG GCGAGAAG CCCG**AGG**	*TTTCTTGGCTTTATATA TCTTGTGGAAAGGACG AAACACC**G**CTGAGGG GCGAGAAGCCCG*	Quality Score: 77, Predicted off-target sites: 129 (31 in genes)
	sense	**CCT**CGGGC TTCTCGCC CCTCAG**T**	*GACTAGCCTTATTTTAA CTTGCTATTTCTAGCT CTAAAACCGGGCTTCT CGCCCCTCAG**C***	
NOS1-2	sense	**T**CGGGCTT CTCGCCCC TCAG**TGG**	*TTTCTTGGCTTTATATA TCTTGTGGAAAGGACG AAACACC**G**CGGGCTTC TCGCCCCTCAG*	Quality Score: 76, Predicted off-target sites: 96 (21 in genes)
	antisense	**CCA**CTGAG GGGCGAGA AGCCCG**A**	*GACTAGCCTTATTTTAA CTTGCTATTTCTAGCT CTAAAACCTGAGGGGC GAGAAGCCCG**C***	
NOS1-3	sense	**A**GTGGTTT CCTCGGCC CTCC**TGG**	*TTTCTTGGCTTTATATA TCTTGTGGAAAGGACG AAACACC**G**GTGGTTTC CTCGGCCCTCC*	Quality Score: 71, Predicted off-target sites: 183 (29 in genes)
	antisense	**CCA**GGAGG GCCGAGGA AACCAC**T**	*GACTAGCCTTATTTTAA CTTGCTATTTCTAGCT CTAAAACGGAGGGCC GAGGAAACCAC**C***	
NOS1-4	antisense	**G**AAACCAG GGCACAGC GACA**AGG**	*TTTCTTGGCTTTATATA TCTTGTGGAAAGGACG AAACACC**G**AAACCAGG GCACAGCGACA*	Quality Score: 70, Predicted off-target sites: 265 (37 in genes)
	sense	**CCT**TGTCG CTGTGCCC TGGTTT**C**	*GACTAGCCTTATTTTAA CTTGCTATTTCTAGCT CTAAAACTGTCGCTGT GCCCTGGTTT**C***	

gRNA	Cut in Sense or Antisense Strand	Sequence (5' → 3')	Sequence with homology arms	Software annotation of gRNA sequence
CHAT-1	antisense	**G**CAGGGTC TGGCTGTT CTAG **AGG**	*TTTCTTGGCTTTATATA TCTTGTGGAAAGGACG AAACACC**G**CAGGGTCT GGCTGTTCTAG*	Specificity score: 82, Predicted efficiency: 53 (Doench '16)/ 52 (Mor.-Mateos)
		CCTCTAGA ACAGCCAG ACCCTG**C**	*GACTAGCCTTATTTTAA CTTGCTATTTCTAGCT CTAAAACAGTGGCAGG AGTCAAGGTT**C***	
CHAT-2	sense	**C**AACCTTG ACTCCTGC CACT **AGG**	*TTTCTTGGCTTTATATA TCTTGTGGAAAGGACG AAACACC**G**AACCTTGA CTCCTGCCACT*	Specificity score: 71, Predicted efficiency: 54 (Doench '16)/ 26 (Mor.-Mateos)
		CCTAGTGG CAGGAGTC AAGGTT**G**	*GACTAGCCTTATTTTAA CTTGCTATTTCTAGCT CTAAAACAGTGGCAGG AGTCAAGGTT**C***	
CHAT-3	antisense	**G**TTTGGGA GGTGAAAC CTAG **TGG**	*TTTCTTGGCTTTATATA TCTTGTGGAAAGGACG AAACACC**G**TTTGGGAG GTGAAACCTAG*	Specificity score: 69, Predicted efficiency: 56 (Doench '16)/ 50 (Mor.-Mateos)
		CCACTAGG TTTCACCT CCCAAA**C**	*GACTAGCCTTATTTTAA CTTGCTATTTCTAGCT CTAAAACCTAGGTTTC ACCTCCCAAA**C***	
CHAT-4	antisense	**C**TGTTCTA GAGGCTGG GTTT **GGG**	*TTTCTTGGCTTTATATA TCTTGTGGAAAGGACG AAACACC**G**TGTTCTAG AGGCTGGGTTT*	Specificity score: 60, Predicted efficiency: 67 (Doench '16)/ 48 (Mor.-Mateos)
		CCCAAACC CAGCCTCT AGAACA**G**	*GACTAGCCTTATTTTAA CTTGCTATTTCTAGCT CTAAAACAAACCCAGC CTCTAGAACA**C***	

Supplementary Table 3.3: PCR primers for screening *CHAT* and *NOS1* 3'UTR NLS-tdRFP reporter CRISPR clones

Forward Primer	Sequence (5' → 3')	Tm (°C)	Reverse Primer	Sequence (5' → 3')	Tm (°C)	PCR Product Size (kb)
CHAT Fwd	AGTCTGCTGCCGCCTACTGAGA	64	CHAT Rev	GCTGTGGAAAGCTGGGGTAAGG	61	176 - gRNA screen
NOS1 Fwd	CTGAGCCCAGAGCATGGGTGATTT	63	NOS1 Rev	GGAGTGGGAACAGAGTTTTGTAAGAGCC	63	364 - gRNA screen
tdRFP unique internal Fwd	GCATGGCACCGGCAGCACCG	68	CHAT 3'UTR genomic Rev	ACATCTCAACTCTGCCTCTGCTG	60	1790 - after puromycin selection cassette removal
tdRFP unique internal Fwd	GCATGGCACCGGCAGCACCG	68	NOS1 3'UTR genomic Rev	GCAACTCTTTCCAACCTCATCCAC	60	2147 - after puromycin selection cassette removal
PGK Prom Fwd	CTGTCCATCTGCACGAGACTAGTG	61	CHAT 3'UTR genomic Rev	CTGCCTCATAGGGTTGTGGTGAG	61	1434
PGK Prom Fwd	CTGTCCATCTGCACGAGACTAGTG	61	NOS1 3'UTR genomic Rev	GCAACTCTTTCCAACCTCATCCAC	60	1415
CHAT 3'UTR Fwd	CTCAGCACACAGCACCAGAAAC	60	IRES_R	CAGTTCCTCTGGAAGCTTCTTGA	58	1.321
NOS1 3'UTR Fwd	GAAGCAAGAGGATGGCCTGATC	59	IRES_R	CAGTTCCTCTGGAAGCTTCTTGA	58	1.559

Forward Primer	Sequence (5’ → 3’)	Tm (°C)	Reverse Primer	Sequence (5’ → 3’)	Tm (°C)	PCR Product Size (kb)
IRES Fwd	TGGCTCT CCTCAAG CGTATTC AACAAGG GG	67	tdRFP unique internal rev	CGGTGCT GCCGGTG CCATGC	68	0.927
PGK Fwd	TGGCAAA ACAATAC TGAGAAT GAAGTG	58	Puro Rev	AACCTCC CCTTCTA CGAGCG	60	0.589

Supplementary Table 3.4: Transcription factor coding sequences cloned into FUdeltaGW-rtTA lentiviral expression vector

Transcription Factor	RefSeq Accession Number	Source, Catalog Number	Literature supporting a possible role in neuronal subtype differentiation	Citations
Homo sapiens basonuclin 2 (BNC2), transcript variant 1, mRNA	NM_017637	Genscript, Cat#: OHu25354	Expressed in subset of dorsal horn neurons in mouse, Loss causes neural crest- derived craniofacial abnormalities	(91–93)
Homo sapiens castor zinc finger 1 (CASZ1), transcript variant 2, mRNA	NM_017766	Genscript, Cat#: OHu12480	Loss causes reduced CNS axonal network and aberrant gene expression in D. melanogaster CNS, Expression restricted to a subset of CNS neurons, Possibly regulates differentiation of dorsal horn neurons	(94, 95)
Homo sapiens cAMP responsive element binding	NM_182898.3	Genscript, Cat#: OHu31208D	Differentially expressed in spinal motor neurons	(96)

Transcription Factor	RefSeq Accession Number	Source, Catalog Number	Literature supporting a possible role in neuronal subtype differentiation	Citations
protein 5 (CREB5), transcript variant 1, mRNA				
Homo sapiens early B cell factor 1 (EBF1), transcript variant 1, mRNA	NM_001290360	Genscript, Cat#: OHu23556	Required for coupling to cell cycle exit to neuronal differentiation during mouse hindbrain development	(97)
Homo sapiens ETS variant 1 (ETV1), transcript variant 1, mRNA	NM_004956	Genscript, Cat#: OHu14889	Required for cerebellar granule cell differentiation in mouse	(98)
Homo sapiens Meis homeobox 1 (MEIS1), mRNA	NM_002398	Genscript, Cat#: OHu19435	Expressed in specific murine CNS neuron subtypes, Regulates mouse cerebellar granule development, Required for murine sympathetic neuron survival	(99–101)
Homo sapiens PBX homeobox 3 (PBX3), transcript variant 1, mRNA	NM_006195	Genscript, Cat#: OHu10595	Regulates post-mitotic differentiation of putative enteric interneurons in mouse, Regulates segment-specific neuron subtype specification in D. melanogaster, Required for medullary respiratory control center development and dorsal horn interneuron differentiation in mouse	(42, 102, 103)

Transcription Factor	RefSeq Accession Number	Source, Catalog Number	Literature supporting a possible role in neuronal subtype differentiation	Citations
Homo sapiens T-box 2 (TBX2), mRNA	NM_005994	Genscript, Cat#: OHu11986	Required for UV photoreceptor specification in zebrafish retina, regulates anterior neural specification in xenopus	(104, 105)
Homo sapiens T-box transcription factor 3 (TBX3), transcript variant 1, mRNA	NM_005996.3	Genscript, Cat#: OHu17127	Reduced numbers of nitrergic enteric neurons in ENS conditional knockout in mouse	Chapter 2

Reagents and Solutions

Proteinase K Buffer

10x buffer stock of 50 mM Tris·HCl (pH 7.4), 15 mM ammonium sulfate (pH 9.3), 2.5 mM $MgCl_2$, 0.1% (v/v) Tween 20, 100 µg/ml Proteinase K (QIAGEN, Catalog#19133).

HES Medium

Combine DMEM/F12 medium (Dulbecco's Modified Eagle Medium: Nutrient Mixture F-12, ThermoFisher, Cat#11320033), 15% (v/v) knockout serum replacement (ThermoFisher, Cat#A3181502), 100 µM nonessential amino acids (NEAA, 100x stock, Thermofisher, Cat#11140-050), 2 mM GlutaMAX (100x stock, ThermoFisher, Cat#35050061), 1x Penicillin-Streptomycin (100x stock, ThermoFisher, Cat#15140122), 0.1 mM β-mercaptoethanol (ThermoFisher, Cat#21985-023), and 10 ng/ml human bFGF (can vary from 5-10 ng/µL depending on the cell line, R&D Systems, Cat# 233-FB). Store at 4°C for no longer than 1 month.

Conditioned HES medium

Wash 0.1% gelatin-coated wells with MEF at least 24 hours after plating (see methods above) with IMDM to remove traces of FBS. Add HES medium with 15 ng/mL bFGF (R&D Systems, Cat# 233-FB)) at 200 µL/cm^2 to the wells and incubate the medium with the MEF feeder layer at 37°C in 5% carbon dioxide. Collect the medium after 48 hours and remove any cellular debris by passing the medium through a vacuum filter.

MEF medium

Iscove's Modified Dulbecco's Medium (IMDM, ThermoFisher, Cat#12440053), 15% Fetal bovine serum (Tissue Culture Biologicals, Cat#101), 100 µL monothioglycerol (MTG, Sigma Aldrich; Cat#M6145) per 100 mL total media volume (from stock diluted 13 µL/mL in IMDM; make fresh

daily), 1x Penicillin-Streptomycin (100x stock, ThermoFisher, Cat#15140122). Store at 4°C for no longer than 1 month.

KSR medium for differentiation day 0-1

Add 10 µM SB431542 (10 mM stock; R&D Systems, Cat#1614), 100nM LDN1931189 (500 µM stock, Stemgent, Cat#04-0074-02), 15% (v/v) knockout serum replacement (ThermoFisher, Cat#A3181502), 2 mM L-Glutamine (100x stock, ThermoFisher, Cat#25030081), 100 µM nonessential amino acids (NEAA, 100x stock, Thermofisher, Cat#11140-050), 1x Penicillin-Streptomycin (100x stock, ThermoFisher, Cat#15140122), 0.1 mM β-mercaptoethanol (ThermoFisher, Cat#21985-023) to KnockOut DMEM (ThermoFisher, Cat#10829018). Store at 4°C for no longer than 2 weeks.

KSR medium for differentiation day 2-11

Add 10 µM SB431542 (10 mM stock; R&D Systems, Cat#1614), 100nM LDN1931189 (500 µM stock, Stemgent, Cat#04-0074-02), 3 µM CHIR99021 (6 mM stock; R&D Systems, Cat#4423), 15% (v/v) knockout serum replacement (ThermoFisher, Cat#A3181502), 2 mM L-Glutamine (100x stock, ThermoFisher, Cat#25030081), 100 µM nonessential amino acids (NEAA, 100x stock, Thermofisher, Cat#11140-050), 1x Penicillin-Streptomycin (100x stock, ThermoFisher, Cat#15140122), 0.1 mM β-mercaptoethanol (ThermoFisher, Cat#21985-023) to KnockOut DMEM (ThermoFisher, Cat#10829018). Store at 4°C for no longer than 2 weeks. Starting with day 6 of differentiation, add 1 µM retinoic acid (100mM, Sigma, Cat#R2625) to the culture medium the day of use.

N2 medium

Add 3 µM CHIR99021 (6 mM stock; R&D Systems, Cat#4423), 10 µM SB431542 (10 mM stock; R&D Systems, Cat#1614), 100nM LDN1931189 (500 µM stock, Stemgent, Cat#04-0074-02), 1%

(v/v) N2 supplement (Stemcell Technologies, Cat#07156), 2 mM L-Glutamine (100x stock, ThermoFisher, Cat#25030081), 1x Penicillin-Streptomycin (100x stock, ThermoFisher, Cat#15140122), to Neurobasal medium (ThermoFisher, Cat#21103049). Store at 4°C for no longer than 2 weeks. Starting with day 6 of differentiation, add 1 µM retinoic acid (100mM, Sigma, Cat#R2625) to the culture medium the day of use.

Differentiation medium A

Add 1 ng/mL BMP4 (100 µg/mL stock; R&D Systems, Cat#314-BP), 600 nM CHIR99021 (6 mM stock; R&D Systems, Cat#4423), and 10 µM SB431542 (10 mM stock; R&D Systems, Cat#1614) to Essential 6 medium (ThermoFisher, Cat#A1516401). Store at 4°C for no longer than 2 weeks.

Differentiation medium B

Add 1.5 µM CHIR99021 (6 mM stock; R&D Systems, Cat#4423) and 10 µM SB431542 (10 mM stock; R&D Systems, Cat#1614) to Essential 6 medium (ThermoFisher, Cat#A1516401). Store at 4°C for no longer than 2 weeks.

Differentiation medium C

Add 1.5 µM CHIR99021 (6 mM stock; R&D Systems, Cat#4423), 10 µM SB431542 (10 mM stock; R&D Systems, Cat#1614), and 1 µM retinoic acid (100mM, Sigma, Cat#R2625) to Essential 6 medium (ThermoFisher, Cat#A1516401). Store at 4°C for no longer than 2 weeks.

NC medium

Combine Neurobasal medium (ThermoFisher, Cat#21103049) with 2% (v/v) B27 supplement (ThermoFisher, Cat#17504044), 1% (v/v) N2 supplement (Stemcell Technologies, Cat#07156), 2 mM GlutaMAX (100x stock, ThermoFisher, Cat#35050061), 1x Penicillin-Streptomycin (100x stock,

ThermoFisher, Cat#15140122), 10 ng/mL FGF2 (R&D Systems, Cat# 233-FB), and 3 µM CHIR99021 (6 mM stock; R&D Systems, Cat#4423). Store at 4°C for no longer than 2 weeks.

EN medium

Combine Neurobasal medium (ThermoFisher, Cat#21103049) with 2% (v/v) B27 supplement (ThermoFisher, Cat#17504044), 1% (v/v) N2 supplement (Stemcell Technologies, Cat#07156), 2 mM GlutaMAX (100x stock, ThermoFisher, Cat#35050061), 1x Penicillin-Streptomycin (100x stock, ThermoFisher, Cat#15140122), and 10 ng/mL GDNF (Peprotech, Cat#450-10). Store at 4°C for no longer than 2 weeks. The day of use, add 100 µM ascorbic acid (Sigma, Cat#A8960).

HEK293T culture medium

Add 10% FBS (Tissue Culture Biologicals, Cat#101) and 1x Penicillin-Streptomycin (100x stock, ThermoFisher, Cat#15140122) to Dulbecco's Modified Eagle Medium (DMEM, Corning, Cat#10-013-CV).

FACS Buffer

Combine phosphate-buffered saline (PBS), 2% fetal bovine serum, 1 mM EDTA, and 0.1% sodium azide.

3.8 References

1. Fung C, Vanden Berghe P. Functional circuits and signal processing in the enteric nervous system [Internet]. *Cell. Mol. Life Sci.* [published online ahead of print: May 18, 2020]; doi:10.1007/s00018-020-03543-6

2. Schneider S, Wright CM, Heuckeroth RO. Unexpected Roles for the Second Brain: Enteric Nervous System as Master Regulator of Bowel Function [Internet]. *Annu. Rev. Physiol.* [published online ahead of print: October 31, 2018]; doi:10.1146/annurev-physiol-021317-121515

3. Furness JB, Callaghan BP, Rivera LR, Cho H-J. The enteric nervous system and gastrointestinal innervation: integrated local and central control. *Adv. Exp. Med. Biol.* 2014;817:39–71.

4. Furness JB. *The Enteric Nervous System*. Malden, Mass: Wiley; 2006:

5. Knowles CH, Lindberg G, Panza E, De Giorgio R. New perspectives in the diagnosis and management of enteric neuropathies. *Nat. Rev. Gastroenterol. Hepatol.* 2013;10(4):206–218.

6. Rivera LR, Poole DP, Thacker M, Furness JB. The involvement of nitric oxide synthase neurons in enteric neuropathies. *Neurogastroenterol. Motil.* 2011;23(11):980–988.

7. Heuckeroth RO. Hirschsprung disease - integrating basic science and clinical medicine to improve outcomes. *Nat. Rev. Gastroenterol. Hepatol.* 2018;15(3):152–167.

8. Antonucci A et al. Chronic intestinal pseudo-obstruction. *World J. Gastroenterol.* 2008;14(19):2953–2961.

9. Nardo GD et al. Chronic intestinal pseudo-obstruction in children and adults: diagnosis and therapeutic options [Internet]. *Neurogastroenterology & Motility* 2017;29(1):e12945.

10. Yanchar NL, Soucy P. Long-term outcome after Hirschsprung's disease: patients' perspectives. *J. Pediatr. Surg.* 1999;34(7):1152–1160.

11. Jarvi K, Laitakari EM, Koivusalo A, Rintala RJ, Pakarinen MP. Bowel function and gastrointestinal quality of life among adults operated for Hirschsprung disease during childhood: a population-based study. *Ann. Surg.* 2010;252(6):977–981.

12. Neuvonen MI, Kyrklund K, Rintala RJ, Pakarinen MP. Bowel Function and Quality of Life After Transanal Endorectal Pull-through for Hirschsprung Disease: Controlled Outcomes up to Adulthood. *Ann. Surg.* 2017;265(3):622–629.

13. Musser MA, Correa H, Southard-Smith EM. Enteric neuron imbalance and proximal dysmotility in ganglionated intestine of the Sox10(Dom/+) Hirschsprung mouse model. *Cell Mol Gastroenterol Hepatol* 2015;1(1):87–101.

14. Roberts RR, Bornstein JC, Bergner AJ, Young HM. Disturbances of colonic motility in mouse models of Hirschsprung's disease. *Am. J. Physiol. Gastrointest. Liver Physiol.* 2008;294(4):G996–G1008.

15. Zaitoun I et al. Altered neuronal density and neurotransmitter expression in the ganglionated region of Ednrb null mice: implications for Hirschsprung's disease. *Neurogastroenterol. Motil.* 2013;25(3):e233–44.

16. Coyle D, O'Donnell AM, Gillick J, Puri P. Altered neurotransmitter expression profile in the ganglionic bowel in Hirschsprung's disease. *J. Pediatr. Surg.* 2016;51(5):762–769.

17. Cheng LS, Schwartz DM, Hotta R, Graham HK, Goldstein AM. Bowel dysfunction following pullthrough surgery is associated with an overabundance of nitrergic neurons in Hirschsprung disease. *J. Pediatr. Surg.* 2016;51(11):1834–1838.

18. Burns AJ et al. White paper on guidelines concerning enteric nervous system stem cell therapy for enteric neuropathies. *Dev. Biol.* 2016;417(2):229–251.

19. Fan Y, Wu J, Ashok P, Hsiung M, Tzanakakis ES. Production of human pluripotent stem cell therapeutics under defined xeno-free conditions: progress and challenges. *Stem Cell Rev Rep* 2015;11(1):96–109.

20. Hockemeyer D, Jaenisch R. Induced Pluripotent Stem Cells Meet Genome Editing. *Cell Stem Cell* 2016;18(5):573–586.

21. Li W et al. Characterization and transplantation of enteric neural crest cells from human induced pluripotent stem cells [Internet]. *Mol. Psychiatry* [published online ahead of print: October 25, 2016]; doi:10.1038/mp.2016.191

22. Fattahi F et al. Deriving human ENS lineages for cell therapy and drug discovery in Hirschsprung disease [Internet]. *Nature* [published online ahead of print: February 10, 2016]; doi:10.1038/nature16951

23. Workman MJ et al. Engineered human pluripotent-stem-cell-derived intestinal tissues with a functional enteric nervous system [Internet]. *Nat. Med.* [published online ahead of print: November 21, 2016]; doi:10.1038/nm.4233

24. Lai FP-L et al. Correction of Hirschsprung-Associated Mutations in Human Induced Pluripotent Stem Cells Via Clustered Regularly Interspaced Short Palindromic Repeats/Cas9, Restores Neural Crest Cell Function [Internet]. *Gastroenterology* [published online ahead of print: March 23, 2017]; doi:10.1053/j.gastro.2017.03.014

25. Barber K, Studer L, Fattahi F. Derivation of enteric neuron lineages from human pluripotent stem cells [Internet]. *Nat. Protoc.* [published online ahead of print: March 25, 2019]; doi:10.1038/s41596-019-0141-y

26. Lau S-T et al. Activation of Hedgehog Signaling Promotes Development of Mouse and Human Enteric Neural Crest Cells, Based on Single-Cell Transcriptome Analyses. *Gastroenterology* 2019;157(6):1556–1571.e5.

27. Lasrado R et al. Lineage-dependent spatial and functional organization of the mammalian enteric nervous system. *Science* 2017;356(6339):722–726.

28. Memic F et al. Transcription and Signaling Regulators in Developing Neuronal Subtypes of Mouse and Human Enteric Nervous System. *Gastroenterology* 2018;154(3):624–636.

29. Chalazonitis A et al. Bone morphogenetic protein regulation of enteric neuronal phenotypic diversity: relationship to timing of cell cycle exit. *J. Comp. Neurol.* 2008;509(5):474–492.

30. Chalazonitis A et al. Bone morphogenetic protein-2 and -4 limit the number of enteric neurons but promote development of a TrkC-expressing neurotrophin-3-dependent subset. *J. Neurosci.* 2004;24(17):4266–4282.

31. Liu X, Liu S, Xu Y, Liu X, Sun D. Bone morphogenetic protein 2 regulates the differentiation of nitrergic enteric neurons by modulating Smad1 signaling in slow transit constipation. *Mol. Med. Rep.* 2015;12(5):6547–6554.

32. Chalazonitis A et al. Neurotrophin-3 Is Required for the Survival–Differentiation of Subsets of Developing Enteric Neurons. *J. Neurosci.* 2001;21(15):5620–5636.

33. Rossi J et al. Retarded Growth and Deficits in the Enteric and Parasympathetic Nervous System in Mice Lacking GFRa2, a Functional Neurturin Receptor. *Neuron* 1999;22:243–252.

34. Li Z et al. Essential roles of enteric neuronal serotonin in gastrointestinal motility and the development/survival of enteric dopaminergic neurons. *J. Neurosci.* 2011;31(24):8998–9009.

35. Wang H et al. The timing and location of glial cell line-derived neurotrophic factor expression determine enteric nervous system structure and function. *J. Neurosci.* 2010;30(4):1523–1538.

36. Raghavan S, Bitar KN. The influence of extracellular matrix composition on the differentiation of neuronal subtypes in tissue engineered innervated intestinal smooth muscle sheets. *Biomaterials* 2014;35(26):7429–7440.

37. Memic F et al. Ascl1 Is Required for the Development of Specific Neuronal Subtypes in the Enteric Nervous System. *J. Neurosci.* 2016;36(15):4339–4350.

38. Blaugrund E et al. Distinct subpopulations of enteric neuronal progenitors defined by time of development, sympathoadrenal lineage markers and Mash-1-dependence. *Development* 1996;122(1):309–320.

39. Hendershot TJ et al. Expression of Hand2 is sufficient for neurogenesis and cell type-specific gene expression in the enteric nervous system. *Dev. Dyn.* 2007;236(1):93–105.

40. Wright CM et al. Dlx1/2 mice have abnormal enteric nervous system function [Internet]. *JCI Insight* 2020;5(4). doi:10.1172/jci.insight.131494

41. Zeisel A et al. Molecular Architecture of the Mouse Nervous System. *Cell* 2018;174(4):999–1014.e22.

42. Morarach K, Mikhailova A, Knoflach V, Memic F. Diversification of molecularly defined myenteric neuron classes revealed by single cell RNA-sequencing [Internet]. *bioRxiv* [published online ahead of print: 2020];https://www.biorxiv.org/content/10.1101/2020.03.02.955757v1.abstract. cited

43. Drokhlyansky E et al. The enteric nervous system of the human and mouse colon at a single-cell resolution [Internet]. *bioRxiv* 2019;746743.

44. May-Zhang AA et al. Combinatorial transcriptional profiling of mouse and human enteric neurons identifies shared and disparate subtypes in situ [Internet]2020;2020.07.03.187211.

45. Qu Z-D et al. Immunohistochemical analysis of neuron types in the mouse small intestine. *Cell Tissue Res.* 2008;334(2):147–161.

46. Sang Q, Young HM. The identification and chemical coding of cholinergic neurons in the small and large intestine of the mouse. *Anat. Rec.* 1998;251(2):185–199.

47. Hao MM, Young HM. Development of enteric neuron diversity. *J. Cell. Mol. Med.* 2009;13(7):1193–1210.

48. Young HM et al. Dynamics of neural crest-derived cell migration in the embryonic mouse gut. *Dev. Biol.* 2004;270(2):455–473.

49. Druckenbrod NR, Epstein ML. The pattern of neural crest advance in the cecum and colon. *Dev. Biol.* 2005;287(1):125–133.

50. Fu M, Vohra BPS, Wind D, Heuckeroth RO. BMP signaling regulates murine enteric nervous system precursor migration, neurite fasciculation, and patterning via altered Ncam1 polysialic acid addition. *Dev. Biol.* 2006;299(1):137–150.

51. Boesmans W, Lasrado R, Vanden Berghe P, Pachnis V. Heterogeneity and phenotypic plasticity of glial cells in the mammalian enteric nervous system. *Glia* 2015;63(2):229–241.

52. Graham KD et al. Robust, 3-Dimensional Visualization of Human Colon Enteric Nervous System Without Tissue Sectioning [Internet]. *Gastroenterology* [published online ahead of print: February 26, 2020]; doi:10.1053/j.gastro.2020.02.035

53. Sang Q, Young HM. Chemical coding of neurons in the myenteric plexus and external muscle of the small and large intestine of the mouse. *Cell Tissue Res.* 1996;284(1):39–53.

54. Hansen MB. The enteric nervous system I: organisation and classification. *Pharmacol. Toxicol.* 2003;92(3):105–113.

55. Lei J, Howard MJ. Targeted deletion of Hand2 in enteric neural precursor cells affects its functions in neurogenesis, neurotransmitter specification and gangliogenesis, causing functional aganglionosis. *Development* 2011;138(21):4789–4800.

56. Niwa H. The principles that govern transcription factor network functions in stem cells [Internet]. *Development* 2018;145(6). doi:10.1242/dev.157420

57. Jiang J et al. A core Klf circuitry regulates self-renewal of embryonic stem cells. *Nat. Cell Biol.* 2008;10(3):353–360.

58. Zaret KS, Carroll JS. Pioneer transcription factors: establishing competence for gene expression. *Genes Dev.* 2011;25(21):2227–2241.

59. Iwafuchi-Doi M, Zaret KS. Cell fate control by pioneer transcription factors. *Development* 2016;143(11):1833–1837.

60. Ieda M et al. Direct reprogramming of fibroblasts into functional cardiomyocytes by defined factors. *Cell* 2010;142(3):375–386.

61. Son EY et al. Conversion of mouse and human fibroblasts into functional spinal motor neurons. *Cell Stem Cell* 2011;9(3):205–218.

62. Morris SA. Direct lineage reprogramming via pioneer factors; a detour through developmental gene regulatory networks. *Development* 2016;143(15):2696–2705.

63. Davis RL, Weintraub H, Lassar AB. Expression of a single transfected cDNA converts fibroblasts to myoblasts. *Cell* 1987;51(6):987–1000.

64. Minoux M et al. Gene bivalency at Polycomb domains regulates cranial neural crest positional identity [Internet]. *Science* 2017;355(6332). doi:10.1126/science.aal2913

65. Hosoda K et al. Targeted and Natural (Piebald-Lethal) Mutations f Endothelin-B Receptor Gene Produce Megacolon Associated with Spotted Coat Color in Mice. *Ceil, Voi.* 1994;79:1267–1276.

66. Fujimoto T. Natural history and pathophysiology of enterocolitis in the piebald lethal mouse model of Hirschsprung's disease. *J. Pediatr. Surg.* 1988;23(3):237–242.

67. Cantrell VA et al. Interactions between Sox10 and EdnrB modulate penetrance and severity of aganglionosis in the Sox10Dom mouse model of Hirschsprung disease. *Hum. Mol. Genet.* 2004;13(19):2289–2301.

68. Stergachis AB et al. Conservation of trans-acting circuitry during mammalian regulatory evolution. *Nature* 2014;515(7527):365–370.

69. Johnson CD et al. Deletion of choline acetyltransferase in enteric neurons results in postnatal intestinal dysmotility and dysbiosis. *FASEB J.* 2018;32(9):4744–4752.

70. McCann CJ et al. Transplantation of enteric nervous system stem cells rescues nitric oxide synthase deficient mouse colon. *Nat. Commun.* 2017;8:15937.

71. Holt CE, Martin KC, Schuman EM. Local translation in neurons: visualization and function. *Nat. Struct. Mol. Biol.* 2019;26(7):557–566.

72. Koenig E. Synthetic mechanisms in the axon—I. Local axonal synthesis of acetylcholinesterase. *J. Neurochem.* 1965;12(5):343–355.

73. Mizuguchi H, Xu Z, Ishii-Watabe A, Uchida E, Hayakawa T. IRES-dependent second gene expression is significantly lower than cap-dependent first gene expression in a bicistronic vector. *Mol. Ther.* 2000;1(4):376–382.

74. Corish P, Tyler-Smith C. Attenuation of green fluorescent protein half-life in mammalian cells. *Protein Eng.* 1999;12(12):1035–1040.

75. Khmelinskii A et al. Tandem fluorescent protein timers for in vivo analysis of protein dynamics. *Nat. Biotechnol.* 2012;30(7):708–714.

76. Lo C-A et al. Quantification of Protein Levels in Single Living Cells. *Cell Rep.* 2019;26(11):3172.

77. Addis RC et al. Efficient conversion of astrocytes to functional midbrain dopaminergic neurons using a single polycistronic vector. *PLoS One* 2011;6(12):e28719.

78. Das AT, Tenenbaum L, Berkhout B. Tet-On Systems For Doxycycline-inducible Gene Expression. *Curr. Gene Ther.* 2016;16(3):156–167.

79. Fattahi F, Studer L, Tomishima MJ. Neural Crest Cells from Dual SMAD Inhibition. *Curr. Protoc. Stem Cell Biol.* 2015;33:1H.9.1–9.

80. Yates AD et al. Ensembl 2020. *Nucleic Acids Res.* 2020;48(D1):D682–D688.

81. Hsu PD et al. DNA targeting specificity of RNA-guided Cas9 nucleases. *Nat. Biotechnol.* 2013;31(9):827–832.

82. Concordet J-P, Haeussler M. CRISPOR: intuitive guide selection for CRISPR/Cas9 genome editing experiments and screens. *Nucleic Acids Res.* 2018;46(W1):W242–W245.

83. Mali P et al. RNA-guided human genome engineering via Cas9. *Science* 2013;339(6121):823–826.

84. Ding Q et al. Enhanced efficiency of human pluripotent stem cell genome editing through replacing TALENs with CRISPRs. *Cell Stem Cell* 2013;12(4):393–394.

85. Matsuda T, Cepko CL. Controlled expression of transgenes introduced by in vivo electroporation. *Proc. Natl. Acad. Sci. U. S. A.* 2007;104(3):1027–1032.

86. Gateway Cloning Protocols - US [Internet]https://www.thermofisher.com/us/en/home/life-science/cloning/gateway-cloning/protocols.html. cited August 19, 2020

87. Wang X, McManus M. Lentivirus production [Internet]. *J. Vis. Exp.* [published online ahead of print: October 2, 2009];(32). doi:10.3791/1499

88. Qin X-F, An DS, Chen ISY, Baltimore D. Inhibiting HIV-1 infection in human T cells by lentiviral-mediated delivery of small interfering RNA against CCR5. *Proc. Natl. Acad. Sci. U. S. A.* 2003;100(1):183–188.

89. Dull T et al. A third-generation lentivirus vector with a conditional packaging system. *J. Virol.* 1998;72(11):8463–8471.

90. Maherali N et al. A high-efficiency system for the generation and study of human induced pluripotent stem cells. *Cell Stem Cell* 2008;3(3):340–345.

91. Bhoj EJ et al. Human balanced translocation and mouse gene inactivation implicate Basonuclin 2 in distal urethral development. *Eur. J. Hum. Genet.* 2011;19(5):540–546.

92. Chamessian A et al. Transcriptional Profiling of Somatostatin Interneurons in the Spinal Dorsal Horn. *Sci. Rep.* 2018;8(1):6809.

93. Vanhoutteghem A et al. The importance of basonuclin 2 in adult mice and its relation to basonuclin 1. *Mech. Dev.* 2016;140:53–73.

94. Mellerick DM, Kassis JA, Zhang SD, Odenwald WF. castor encodes a novel zinc finger protein required for the development of a subset of CNS neurons in Drosophila. *Neuron* 1992;9(5):789–803.

95. Monteiro CB et al. Zinc finger transcription factor Casz1 expression is regulated by homeodomain transcription factor Prrxl1 in embryonic spinal dorsal horn late-born excitatory interneurons [Internet]. *European Journal of Neuroscience* 2016;43(11):1449–1459.

96. Delile J et al. Single cell transcriptomics reveals spatial and temporal dynamics of gene expression in the developing mouse spinal cord [Internet]. *Development* 2019;146(12):dev173807.

97. Garcia-Dominguez M, Poquet C, Garel S, Charnay P. Ebf gene function is required for coupling neuronal differentiation and cell cycle exit. *Development* 2003;130(24):6013–6025.

98. Abe H, Okazawa M, Nakanishi S. The Etv1/Er81 transcription factor orchestrates activity-dependent gene regulation in the terminal maturation program of cerebellar granule cells. *Proc. Natl. Acad. Sci. U. S. A.* 2011;108(30):12497–12502.

99. Barber BA et al. Dynamic expression of MEIS1 homeoprotein in E14.5 forebrain and differentiated forebrain-derived neural stem cells. *Ann. Anat.* 2013;195(5):431–440.

100. Bouilloux F et al. Loss of the transcription factor Meis1 prevents sympathetic neurons target-field innervation and increases susceptibility to sudden cardiac death [Internet]. *Elife* 2016;5. doi:10.7554/eLife.11627

101. Owa T et al. Meis1 Coordinates Cerebellar Granule Cell Development by Regulating Pax6 Transcription, BMP Signaling and Atoh1 Degradation. *J. Neurosci.* 2018;38(5):1277–1294.

102. Rhee JW et al. Pbx3 deficiency results in central hypoventilation. *Am. J. Pathol.* 2004;165(4):1343–1350.

103. Rottkamp CA, Lobur KJ, Wladyka CL, Lucky AK, O'Gorman S. Pbx3 is required for normal locomotion and dorsal horn development. *Dev. Biol.* 2008;314(1):23–39.

104. Alvarez-Delfin K et al. Tbx2b is required for ultraviolet photoreceptor cell specification during zebrafish retinal development. *Proc. Natl. Acad. Sci. U. S. A.* 2009;106(6):2023–2028.

105. Cho G-S, Park D-S, Choi S-C, Han J-K. Tbx2 regulates anterior neural specification by repressing FGF signaling pathway. *Dev. Biol.* 2017;421(2):183–193.

CHAPTER 4: A MOLECULAR-BASED REGENERATIVE MEDICINE APPROACH FOR THE TREATMENT OF HIRSCHSPRUNG DISEAS

This manuscript is in press at Gastroenterology (September 2020) and reprinted here with permission. Authors: Rodolphe Soret, Sabine Schneider, Guillaume Bernas, Briana Christophers, Ouliana Souchkova, Baptiste Charrier, Franziska Righini-Grunder, Ann Aspirot, Mathieu Landry, Steven W. Kembel, Christophe Faure, Robert O. Heuckeroth, Nicolas Pilon.

4.1 Abstract

BACKGROUND & AIMS: Hirschsprung disease (HSCR) is a life-threatening birth defect where distal colon is devoid of enteric neural ganglia. Current HSCR treatment is surgical removal of aganglionic bowel, but many children continue to have severe problems after surgery. Here, we tested a non-surgical therapy based on the hypothesis that post-natal administration of Glial cell line-Derived Neurotrophic Factor (GDNF) might induce enteric nervous system regeneration.

METHODS: GDNF was administered via rectal enema to several HSCR mouse models from postnatal day (P) 4 to P8. We assessed survival, ENS structure and regeneration, colon bead expulsion, colon epithelial permeability, muscle thickness, neutrophil infiltration, and stool microbiome in GDNF-treated and untreated mice. Time-lapse imaging and genetic cell lineage tracing were used to identify a source of GDNF-targeted enteric neural progenitors. Human aganglionic colon explants from children with HSCR were also cultured with GDNF and evaluated for enteric neurogenesis.

RESULTS: Three different HSCR-model mice had prolonged survival after GDNF enema treatment. GDNF-treated mice developed enteric neurons and glia in distal bowel that should have been aganglionic, had enhanced colon motility, reduced distal colon epithelial permeability, reduced muscle thickness, reduced neutrophil infiltration and partial normalization of aganglionosis-induced dysbiosis.

Exogenous luminal GDNF penetrated aganglionic colon epithelium, triggering production of endogenous GDNF. Some new enteric neurons appear to arise from Dhh-Cre+ lineage Schwann cells within extrinsic nerves. Ex vivo cultured explants of human aganglionic bowel also respond to GDNF.

CONCLUSIONS: This study provides hope that GDNF-based regenerative therapy might supplement or replace current HSCR treatment.

4.2 Introduction

The enteric nervous system (ENS) extends along the entire gastrointestinal tract to control bowel motility and epithelial activity in response to sensory stimuli (1). Interconnected enteric ganglia containing neurons and glia develop from neural crest-derived progenitors before birth. Incomplete colonization of distal colon by these ENS progenitors causes Hirschsprung disease (HSCR), a condition affecting 1 in 5000 newborns (2). In HSCR, distal colon without ganglia (i.e., aganglionic colon) remains tonically contracted, causing functional intestinal obstruction. Symptoms also include bowel inflammation and a high risk of sepsis and premature death (2).

HSCR is subdivided into short-segment (S-HSCR) and long-segment forms (L-HSCR) (2). In S-HSCR (>80% of cases), the ENS is absent from rectum and sigmoid colon only. L-HSCR means longer regions of distal bowel are aganglionic. Many genes influence HSCR risk (2), and genetic risk variants may combine with non-genetic factors (3). The major HSCR-associated gene is *RET*, a transmembrane tyrosine kinase activated when GDNF binds the co-receptor GFRα1. GDNF-GFRα1-RET signaling is needed for survival, proliferation, and migration of ENS progenitors (4-6). Accordingly, >90% of children with S-HSCR bear non-coding variants that reduce *RET* expression (7). Protein altering *RET* variants are not common in S-HSCR, but occur in ~35% of people with L-HSCR (8, 9). Other genes influencing HSCR risk encode EDNRB signaling pathway molecules, transcription factors, guidance and extra-cellular matrix molecules, and diverse additional factors (7, 9-11). Male sex also increases HSCR risk ~4-fold, while Down syndrome

increases HSCR risk ~100-fold (2). Collectively, these observations mean that most children with HSCR have reduced, but not absent RET signaling, and that diverse additional factors impact HSCR occurrence.

Since 1948, surgical removal of aganglionic bowel has been life-saving for most children with HSCR (12). However, post-surgical complications are common and can be long-lasting, impacting survival and/or quality of life (2). One ideal alternative approach would be to rebuild the ENS and reduce the need for surgery. This idea prompted many groups to develop cell transplantation-based HSCR therapies (13). However, despite many encouraging results, some difficulties remain (14). The optimal source of stem cells, ideal amplification and/or differentiation strategies prior to transplantation, methods of cell delivery, and cell fate after transplantation are not yet well defined.

Here we tested the hypothesis that endogenous ENS progenitors could be activated after birth and generate enteric neurons *de novo*. Our cell-free strategy is based on the idea that HSCR is due to incomplete rostrocaudal colonization of distal bowel by the main subpopulation of ENS progenitors, namely neural crest cells of vagal origin (15). Since extracellular matrix in colon becomes refractory to migration after a certain developmental window (16), reactivating vagal-derived ENS progenitor migration seemed unlikely after birth. However, it seemed possible that ENS progenitors of sacral (17) or Schwann cell lineage (18) origin, which are already present in aganglionic colon, could be induced to proliferate and differentiate into functioning neurons. Schwann cells in particular are abundant in hypertrophic extrinsic nerve tracts that populate both muscular and submucosal layers of distal aganglionic bowel (19). GDNF appeared as a primary candidate for postnatal reactivation of ENS progenitors in the aganglionic zone notably because of its ability to stimulate migration and proliferation of Schwann cells in a RET-independent but GFRα1-dependent manner through its alternative receptor NCAM (20, 21).

4.3 Materials and Methods

Mice

Details about all mouse lines used are in Supp. Methods. Enema treatments of most mouse lines were performed at Université du Québec à Montréal, except for Ret9/- that were treated with mycophenolate (22) and GDNF at the Children's Hospital of Philadelphia Research Institute (as detailed in Supplementary Methods). Where indicated, some $Hol^{Tg/Tg}$ and $Ednrb^{s\text{-}l/s\text{-}l}$ were also GDNF-treated at the Children's Hospital of Philadelphia Research Institute after reciprocal exchange of mice between Philadelphia and Montreal. Unless specified otherwise (see Supplementary Figure 4.1), 10 µl enemas consisting of a 1 µg/µl solution of human recombinant GDNF (Peprotech, Cat# 450-10) diluted in PBS were administered daily between P4 to P8 (see Supp. Methods for more detail). Clinical grade GDNF (Medgenesis Therapeutix Inc., Canada) and a previously described 6XHis-tagged version (23) used for some experiments had similar efficiency (see Supp. Methods for other tested molecules). For EdU incorporation assays, mouse pups received 10 µl intraperitoneal injections of a 10 mM EdU solution (ThermoFisher Scientific, Cat# C10337) once a day during the 5-day (P4 to P8) GDNF enema treatment.

Tissue processing, immunohistochemistry, and imaging

Bowel was cut longitudinally along the mesentery, washed in PBS, pinned onto Sylgard-coated petri dishes, fixed with 4% PFA at 4°C overnight, and finally microdissected to separate longitudinal/circular muscles from the submucosa/mucosa layer. For *ex vivo* analyses of living tissues, unfixed tissues were microdissected in ice-cold oxygenated Krebs solution. For histological analyses, fixed full-thickness bowel segments were embedded in paraffin and transversally sectioned at 10 µm. For Western blotting, unfixed organs were weighed and dissolved in RIPA buffer, using 1 mL for every 100 mg of tissue (further details are provided in Supplementary Methods). Details about immunohistochemistry and imaging can be found in Supplementary Methods.

Analysis of colonic motility and permeability. In vivo analysis of distal colonic motility in P20 mice was performed using the bead latency test, as detailed in Supplementary Methods. For *ex vivo* analysis of colonic motility, strips of living muscles from most distal colon (1 cm from the anus) of P20 mice were prepared as described above, and attached in the longitudinal direction in a Schuler organ bath (Harvard apparatus) filled with oxygenated Krebs solution. Contraction/relaxation of longitudinal muscles was then recorded as detailed in Supplementary Methods. For *ex vivo* analysis of mucosal barrier function, segments of living mucosa from most distal colon of P20 mice were prepared as described above, mounted in Ussing chambers with 0.5 cm^2 exposed surface area (Warner Instruments, Model U-9926), and evaluated for paracellular permeability as described in Supplementary Methods.

Microbiome analysis

Stool isolation, microbiome sequencing and data analysis were performed as previously described (details are provided in Supplementary Methods) (24).

Ex vivo time-lapse imaging and culture of murine aganglionic colon

For time-lapse imaging, strips of living muscles from the last cm of distal colon from P4 *Hol*$^{Tg/Tg}$;*G4-RFP* double transgenic pups were prepared as described above, and pinned onto Sylgard-coated 35mm ibidi µ-dishes (ibidi, Cat# 81156). Muscle strips were then cultured in suspension as detailed in Supplementary Methods. For *ex vivo* induction of neurogenesis, strips of living muscles from the last cm of distal colon from P4 *Hol*$^{Tg/Tg}$ pups were cultured as for time-lapse imaging in presence of 0.5 µM EdU. After 96h of culture, tissues were fixed with PFA and processed for immunofluorescence and EdU labelling.

Culture of human aganglionic colon tissues

Human sigmoid colon tissue was obtained from 12 HSCR patients undergoing Swenson-type surgical resection of the aganglionic zone. Nine patients (7 boys and 2 girls; aged between 28 and 1638 days at the time of surgery) were recruited at the Centre hospitalier universitaire Sainte-Justine (Montreal, Canada) while 3 patients were recruited at the Children's Hospital of Philadelphia (2 boys and 1 girl; aged between 300 and 1177 days at the time of surgery). After the surgery, full-thickness colon tissues were placed in ice-cold Krebs solution or Belzer UW Cold Storage Solution (Bridge to Life Ltd.) and immediately brought to the relevant research laboratory. Muscle strips were then prepared as described above and cut in smaller pieces of 0.5 cm X 0.5 cm. One piece was kept aside for validation of aganglionosis via immunofluorescence, while the others were cultured for 96h as described above for inducing neurogenesis in mouse tissues. Samples from two patients (86 and 1638 days of age at surgery) were in addition cultured for 7 days, under the same conditions. At the end of culture period, all tissues were fixed with PFA and processed for immunofluorescence and EdU labelling.

Study approval

All experiments with mice were approved by animal research ethics committees of the Université du Québec à Montréal (CIPA reference # 878) and the Children's Hospital of Philadelphia Research Institute (IAC reference # 16-001041). Likewise, experiments with human samples were approved by human research ethics committees of the Université du Québec à Montréal (CIEREH protocol # 491), the Centre hospitalier universitaire Sainte-Justine (CER protocol # 4172) and the Children's Hospital of Philadelphia (IRB protocol # 13-010357). Informed consent for the collection and use of human tissues was obtained from all donors, and parents or legal guardian except for one piece of de-identified human colon.

Statistics

All experiments employed a minimum of three biological replicates. Where relevant, the exact number of independent replicates (n) and statistical tests used to calculate P values are included in figures and/or legends. P values were determined using GraphPad Prism 6, with the exception of microbiome data that were analyzed with R.

4.4 Results

GDNF enemas rescue aganglionosis in three mouse models of S-HSCR

Using rectal enemas, we tested if early postnatal administration of GDNF could enhance survival of four mouse models of S-HSCR: *Holstein* (*Hol*$^{Tg/Tg}$; a fully-penetrant model for trisomy 21 [Collagen VI over-expression]-associated HSCR) (25), *TashT* (*TashT*$^{Tg/Tg}$; a partially-penetrant model for male-biased HSCR) (26), *Piebald-lethal* (*Ednrb*$^{s\text{-}l//s\text{-}l}$; a fully-penetrant model for *EDNRB* mutation-associated HSCR) (27) and *Ret*$^{9/-}$ mutant mice (a hypomorphic model where aganglionosis is induced by mycophenolic acid) (22). The enema volume necessary to fill whole colon, GDNF concentration, treatment time window, as well as duration and frequency of therapy were first empirically determined with *Hol*$^{Tg/Tg}$ pups (**Supplementary Figure 4.1A-E**). Remarkably, our selected treatment (i.e., daily administration of 10 µg GDNF in PBS as 10 µl enemas for 5 consecutive days between postnatal day [P] 4 to P8) prevented death in about half of *Hol*$^{Tg/Tg}$ mice at P28, the maximum age of survival for control *Hol*$^{Tg/Tg}$ mice (**Figure 4.1A**). Most animals surviving to P28 reached adult age after GDNF treatment and mice evaluated could reproduce (two tested breeding pairs were fertile). The few animals that were allowed to survive beyond P56 (our adult reference age) eventually died from megacolon or dystocia between P68 and P250 (**Supplementary Figure 4.1C**). Importantly, the same GDNF enema treatment also prevented premature death for more than 60% of *Ednrb*$^{s\text{-}l//s\text{-}l}$ mice **(Figure 4.1B)** and for all male *TashT*$^{Tg/Tg}$ pups (**Figure 4.1C**). Nine GDNF-treated male *TashT*$^{Tg/Tg}$ mice kept for over a year looked healthy without any sign of adverse effects. Enema treatment of *Hol*$^{Tg/Tg}$ mice using Noggin, endothelin-3,

or the serotonin receptor (5-HT4R) agonist RS67506 (rationale provided in **Supplementary Table 4.1**) failed to increase life expectancy, suggesting specific benefit to GDNF (**Supplementary Figure 4.1F**). We also failed to further increase the overall survival rate of GDNF-treated *Hol*$^{Tg/Tg}$ animals either by replacing standard chow with a gel diet (**Figure 4.1G**) or by combining GDNF with vitamin C, serotonin or endothelin-3 (**Figure 4.1H**).

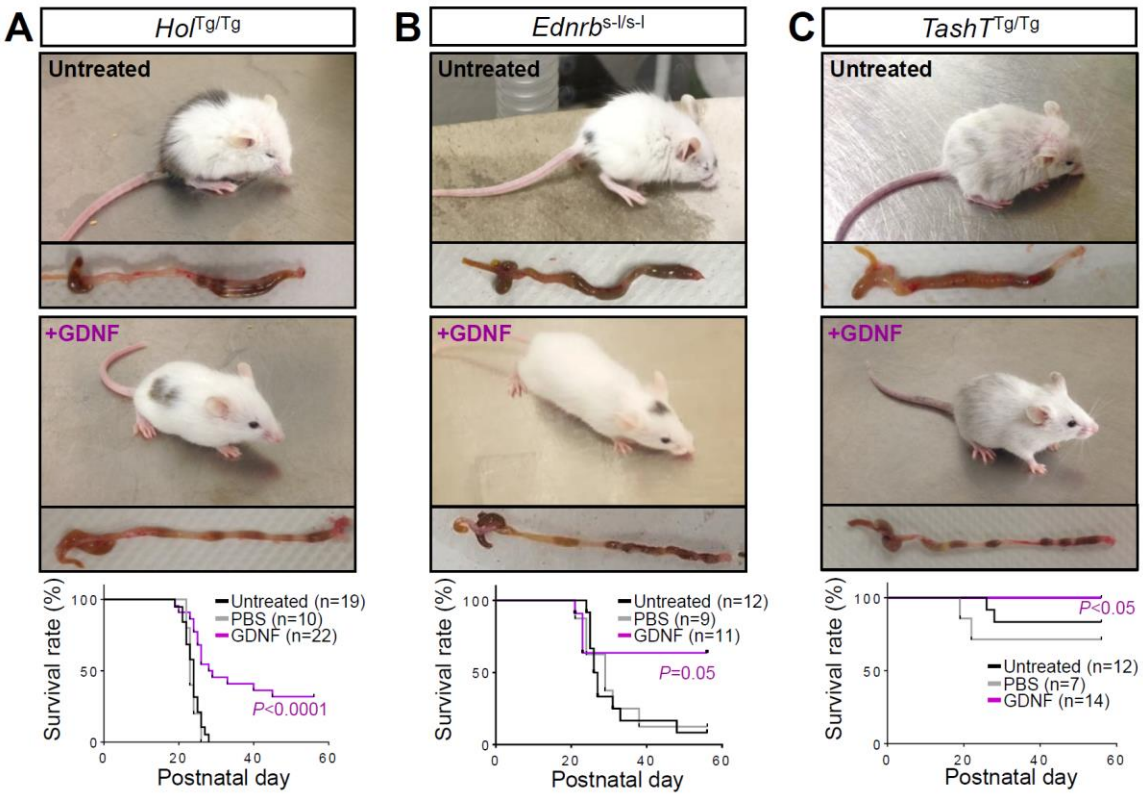

Figure 4.1: GDNF enemas rescue aganglionic megacolon in HSCR mouse models
(A-C) Daily administration of GDNF enemas to *Hol*$^{Tg/Tg}$ (**A**), *Ednrb*$^{S-l/s-l}$ (**B**) and *TashT*$^{Tg/Tg}$ (**C**) mice between P4-P8 positively impacts both megacolon symptoms and survival rates (Mantel-Cox statistical test, GDNF-treated *vs* PBS-treated groups).

Because modest reductions in RET function are common in people with HSCR, we wanted to determine if GDNF enemas could work in RET hypomorphic mice. Unfortunately, there are no good mouse models for *RET* mutation- associated HSCR. *Ret*-null mice have total intestinal aganglionosis (28) whereas *Ret* heterozygotes are overtly normal (4). We therefore decided to use

our established protocol to induce distal bowel aganglionosis in *Ret*$^{9/-}$ hypomorphic mice using mycophenolate mofetil (22). Surprisingly, far less prenatal mycophenolate was needed to cause dose-dependent aganglionosis in our novel experimental conditions (with *Ret* mutants rederived in a new animal facility) (**Supplementary Figure 4.2A**) compared to our prior studies (22), and postnatal GDNF enemas did not improve survival compared to PBS alone (**Supplementary Figure 4.2B**). Instead, many pups died with distended bowel before the end of GDNF treatment, even at the lowest mycophenolate concentration (**Supplementary Figure 4.2C**). Moreover, many ill pups had ganglia throughout the bowel (**Supplementary Figure 4.2D**), suggesting highly variable efficiency of mycophenolate treatment and additional toxicity that complicates data interpretation.

To determine how GDNF enemas enhanced survival in the other three HSCR mouse models, we tested the hypothesis that GDNF induced postnatal neurogenesis in aganglionic distal colon. We focused on the *Holstein* line for practical reasons (fertility is low in *Piebald-lethal* and megacolon incidence is lower in *TashT*), and analyzed P20 animals because *Hol*$^{Tg/Tg}$ mice generally reach this stage even without enema treatment (**Figure 4.1A**). As we reported (25), myenteric HuC/D^{+} neurons and SOX10^{+} glia were abundant in WT distal colon and absent from the last cm of *Hol*$^{Tg/Tg}$ colon (**Figure 4.2A**). In contrast, in *Hol*$^{Tg/Tg}$ distal colon, SOX10^{+} cells were mainly within thick extrinsic nerve fibers (**Figure 4.2A**) where Schwann cells reside (18). Remarkably, distal colon from GDNF-treated *Hol*$^{Tg/Tg}$ animals had numerous HuC/D^{+} neurons and SOX10^{+} glia organized into ganglia primarily adjacent to extrinsic nerves (**Figure 4.2A**). These GDNF-induced ganglia formed Tuj1^{+} interconnected networks in both myenteric and submucosal plexuses (**Figure 4.2B**). Quantification of myenteric neuron density in whole colon of *Hol*$^{Tg/Tg}$ and male *TashT*$^{Tg/Tg}$ mice showed GDNF effects are most prominent in distal colon (i.e., final 3 cm), with minor effects in proximal colon (**Figure 4.2A** and **Supplementary Figure 4.3).** In the mid-colon of GDNF-treated *Hol*$^{Tg/Tg}$ mice, the increased neuron density (**Figure 4.2A**) was mainly due to an enlargement of pre-existing myenteric ganglia (**Supplementary Figure 4.3A**). In the most distal colon, where untreated *Hol*$^{Tg/Tg}$ mice are normally devoid of enteric neurons, GDNF-treated *Hol*$^{Tg/Tg}$ mice had an

average neuron density that was about 40% that of WT mice (**Figure 4.2A**). When neuron density in the distal colon was too low, GDNF-treated *Hol*$^{Tg/Tg}$ mice developed megacolon (**Supplementary Figure 4.1I**). Remarkably, in GDNF-treated *TashT*$^{Tg/Tg}$ males, neuron density in the most distal colon was completely restored (**Supplementary Figure 4.3B-C**).

EdU incorporation assays confirmed that GDNF induced proliferation of neuron and glia progenitors during the 5-day treatment from P4 to P8. Staining of P20 *Hol*$^{Tg/Tg}$ colon from mice that received daily EdU injections during GDNF treatment revealed many EdU^{+} HuC/D^{+} (presumptive neurons) and EdU^{+} SOX10^{+} (presumptive glia or neuron/glia progenitors) in both myenteric and submucosal ganglia (**Figure 4.2C-D** and **Supplementary Figure 4.4**). Yet, only a few, very small ganglia (i.e., 3 neurons) were fully populated by EdU^{+} neurons (**Supplementary Figure 4.4C**). Collectively these data suggest that GDNF enemas induce proliferation and differentiation of ENS progenitors in distal colon and that some of induced neurons and glia cluster into new ganglia.

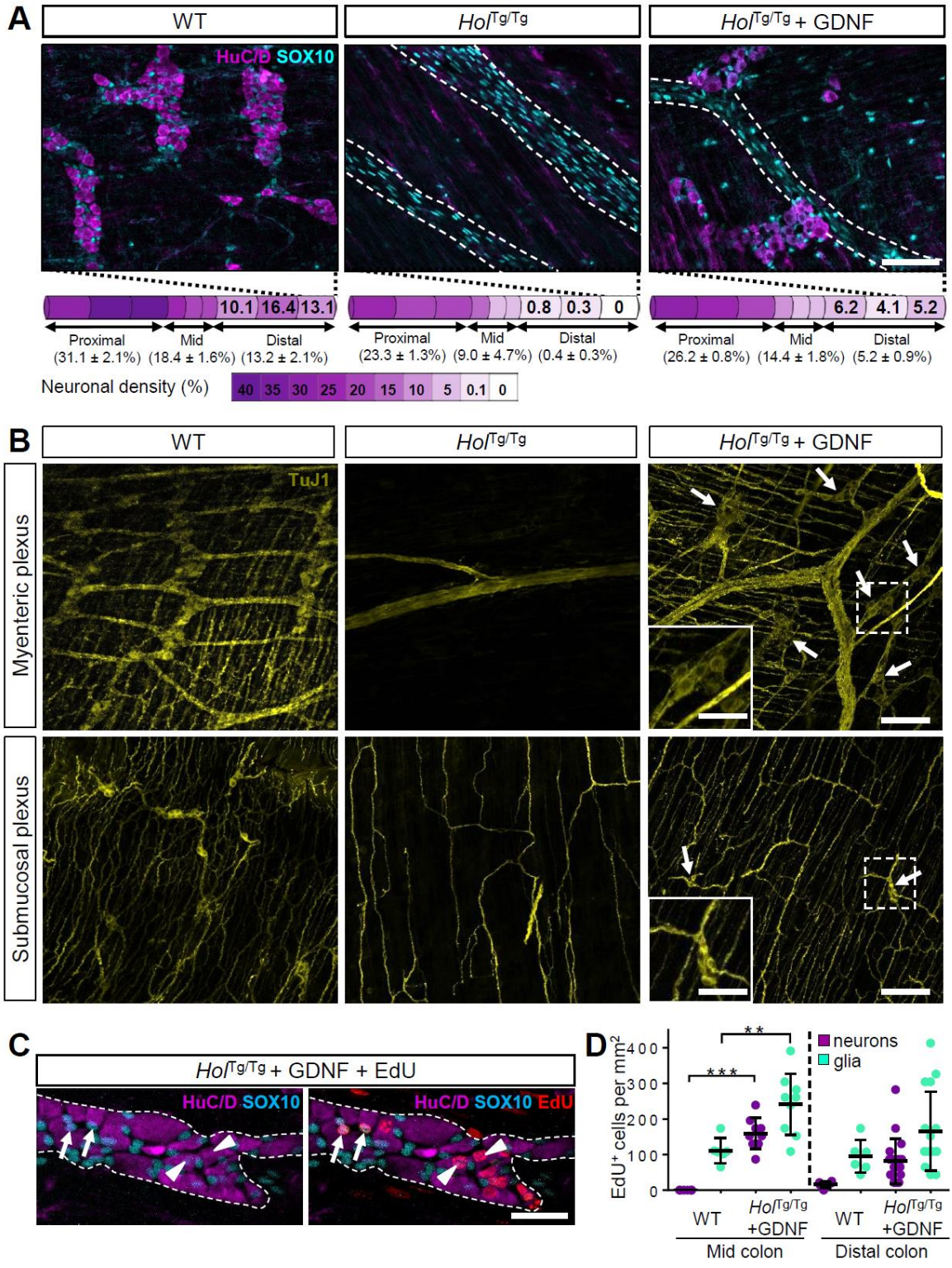
A
WT
Hol Tg/Tg
Hol Tg/Tg + GDNF
HuC/D SOX10
10.1 16.4 13.1
0.8 0.3 0
6.2 4.1 5.2
Proximal
Mid
Distal
(31.1 ± 2.1%) (18.4 ± 1.6%) (13.2 ± 2.1%)
(23.3 ± 1.3%) (9.0 ± 4.7%) (0.4 ± 0.3%)
(26.2 ± 0.8%) (14.4 ± 1.8%) (5.2 ± 0.9%)
Neuronal density (%)
40 35 30 25 20 15 10 5 0.1 0
B
WT
Hol Tg/Tg
Hol Tg/Tg + GDNF
TuJ1
Myenteric plexus
Submucosal plexus
C
Hol Tg/Tg + GDNF + EdU
HuC/D SOX10
HuC/D SOX10 EdU
D
EdU+ cells per mm2
neurons
glia
WT
Hol Tg/Tg +GDNF
Mid colon
Distal colon

Figure 4.2: GDNF enemas induce a new ENS in the otherwise aganglionic region of P20 *Hol*$^{Tg/Tg}$ mice

(A) GDNF treatment induces myenteric ganglia containing HuC/D$^+$ neurons and SOX10$^+$ glia. For each colon subregion (cylinders), average neuronal density (color-coded) is expressed as the percentage of area occupied by HuC/D$^+$ cells in the myenteric plexus (n=6 mice per group; 3 fields of view per subregion). **(B)** Immunofluorescence analysis of TuJ1$^+$ neuronal structures in myenteric and submucosal plexus, including GDNF-induced ganglia (arrows). Insets are zoomed-in views of dashed boxes. **(C-D)** EdU incorporated in GDNF-induced myenteric neurons (arrowheads) and glia (arrows) during the 5-day treatment. Quantitative results in **D** are expressed as the number of EdU$^+$ cells per mm^2 (n=3 WT and 3 GDNF-treated *Hol*$^{Tg/Tg}$ mice; 2-7 fields of view per animal; ***P<0.001; ****P<0.0001; one-way ANOVA with post-hoc Sidak's test). All images show a z-stack projection representative of observations made from 3 mice. Dashed outlines delineate extrinsic nerve fibers (**A**) or a single ganglion (**C**). Scale bars, 100 µm (**A, B**) and 50 µm (**B insets**, **C**).

GDNF-induced ENS is morphologically and functionally similar to WT

Again focusing on the *Hol*$^{Tg/Tg}$ model, we next asked to what extent GDNF-induced ENS in the distal colon resembles WT at P20. Average neuron-to-glia ratio within GDNF-induced myenteric ganglia was statistically similar to WT (P=0.16) **(Figure 4.3A**). Relative proportions of major myenteric neuron subtypes, including cholinergic (ChAT$^+$) and nitrergic (nNOS$^+$) neurons, were also very similar to WT **(Figure 4.3B-C)**. Moreover, many other neuronal subtypes were detected including TH$^+$ dopaminergic neurons, CalR$^+$ excitatory motor neurons, VIP$^+$ inhibitory motor neurons, and SubP$^+$ excitatory motor neurons (**Figure 4.3C**). Interestingly, in proximal and mid colon of *Hol*$^{Tg/Tg}$ mice (Fig.S5), GDNF treatment also corrected the imbalance of nitrergic (increased) and cholinergic (decreased) neuron subtypes that is observed proximal to the aganglionic segment in both HSCR mouse models and human patients (29-32).

To evaluate function of P20 GDNF-induced myenteric ganglia, we analyzed colonic motility *in vivo*, using the bead latency test. In contrast to untreated *Hol*$^{Tg/Tg}$ mice that never expelled a rectally-inserted glass bead during our 30 minute observation period, a subset of GDNF-treated *Hol*$^{Tg/Tg}$ expelled the bead in 10-21 min, a bit slower than WT mice (range of 2-8 min) (**Figure 4.3D**). Analysis of neuron density in these GDNF-treated *Hol*$^{Tg/Tg}$ mice revealed a robust inverse

correlation between time to expel the bead and neuron density in the distal colon (**Supplementary Figure 4.6A**). We also evaluated motility *ex vivo* using muscle strips from P20 distal colons attached to force transducers in organ baths. This system allows electric field stimulation-induced contractions of WT colon muscles to be slightly increased by inhibition of nitric oxide synthase with L-NAME, which can then be robustly counteracted by inhibition of cholinergic signaling with atropine. Reminiscent of *in vivo* data, colon muscle strips from GDNF-treated *Hol*$^{Tg/Tg}$ mice displayed one of two distinct response patterns (**Figure 4.3E** and **Supplementary Figure 4.6B**), either similar to WT or similar to untreated *Hol*$^{Tg/Tg}$. To indirectly test function of P20 GDNF-induced submucosal ganglia, we analyzed epithelial permeability to small fluorescently labeled dextran molecules (FD4) in Ussing chambers. Once more, distal colonic tissues from GDNF-treated *Hol*$^{Tg/Tg}$ mice displayed two distinct response types, with mucosa either impermeable to FD4 like WT tissues, or permeable to FD4 like control *Hol*$^{Tg/Tg}$ tissues from untreated mice (**Figure 4.3F**).

To complement ENS analyses, we evaluated other HSCR-associated bowel anomalies. *Hol*$^{Tg/Tg}$ mouse colon had thicker smooth muscles and more neutrophils than WT mice, but GDNF-treated *Hol*$^{Tg/Tg}$ mouse colon was similar to WT (**Figure 4.3G-I** and **Supplementary Figure 4.7**). Similarly, stool microbiome profiling demonstrated dysbiosis in P20 *Hol*$^{Tg/Tg}$ mouse colon, but average abundance of several bacterial genera in *Hol*$^{Tg/Tg}$ mouse colon were indistinguishable from WT after GDNF treatment (**Figure 4.3J**). A notable exception was *Bacteroides* abundance, which was low in *Hol*$^{Tg/Tg}$ mice and even lower after GDNF treatment. Accordingly, beta diversity analysis revealed distinct microbial communities among WT, *Hol*$^{Tg/Tg}$ and GDNF-treated *Hol*$^{Tg/Tg}$ mice (**Figure 4.3K**).

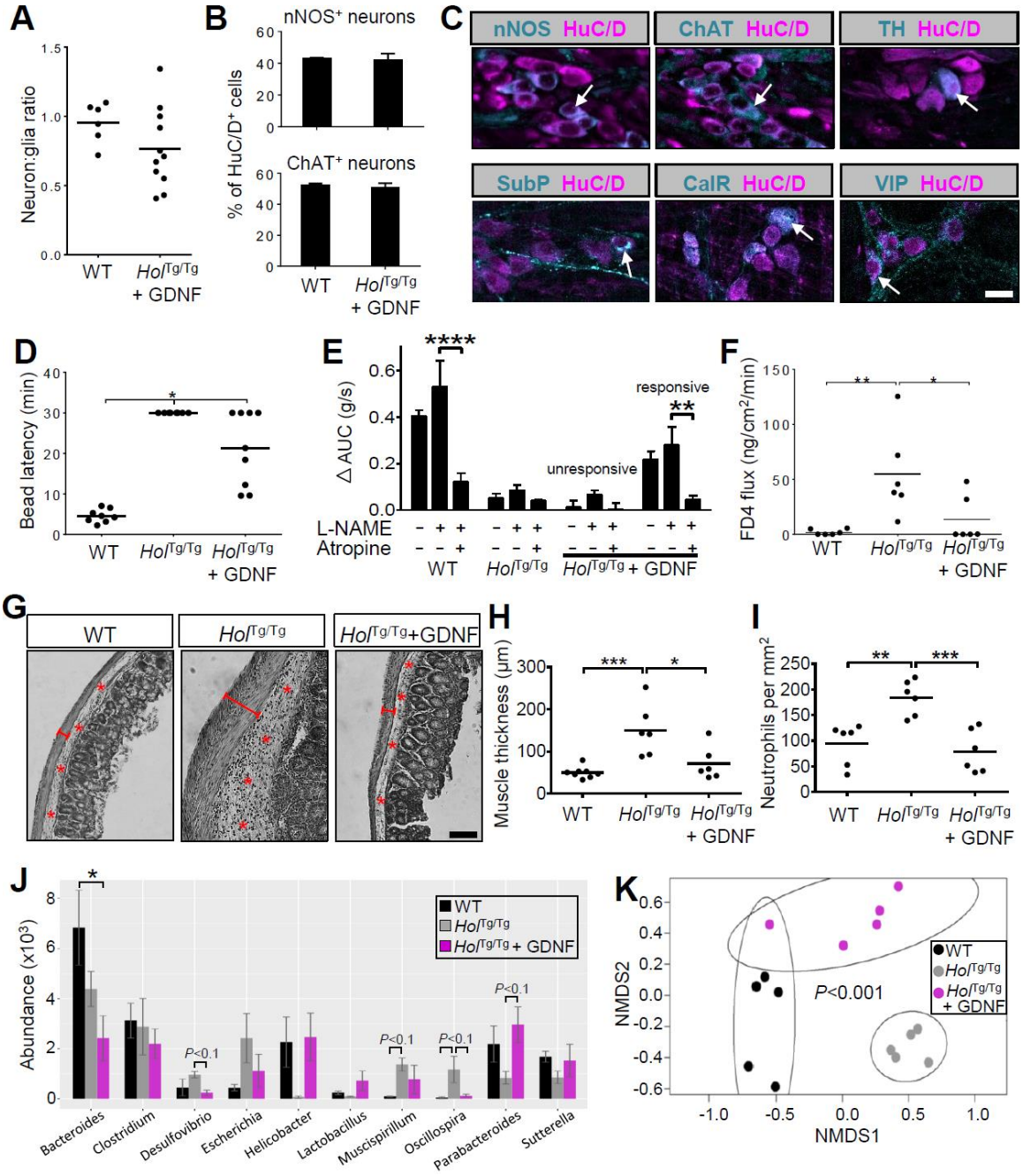

Figure 4.3: Phenotypic and functional characterization of the GDNF-induced ENS in P20 *Hol*$^{Tg/Tg}$ mice

(A-B) WT-like neuron (HuC/D$^+$) to glia (SOX10$^+$) ratio (**A**), and proportions of nitrergic and cholinergic neurons (**B**) in GDNF-induced myenteric ganglia from distal colon of *Hol*$^{Tg/Tg}$ mice (n=6 mice per group; 3 fields of view per animal). **(C)** GDNF-induced myenteric ganglia include many neuron subtypes (arrows; n=3 mice per marker). Scale bar, 20μm. **(D)** Bead latency test (n=8-9 mice per group, **P*<0.05; one-way ANOVA with post-hoc Sidak's test). **(E)** Electric field-stimulated

and drug-modulated patterns of longitudinal muscle contraction-relaxation (n=6 WT and *Hol*$^{Tg/Tg}$, n=7 *Hol*$^{Tg/Tg}$ + GDNF; ***P*<0.01; *****P*<0.0001; two-way ANOVA with post-hoc Tukey's test). Contractile strength is expressed as the difference from baseline of the area under the curve (AUC) values obtained after stimulation (see Fig.S6B). Muscle strips from GDNF-treated *Hol*$^{Tg/Tg}$ mice are either unresponsive (i.e., like untreated *Hol*$^{Tg/Tg}$ mice; 3/7) or responsive (i.e., similar to WT; 3/7). **(F)** Mucosal permeability to FD4 in Ussing chambers (n=6 mice per group; **P*<0.05; ***P*<0.01; one-way ANOVA with post-hoc Sidak's test). **(G-I)** H&E staining-based analysis of smooth muscle thickness (brackets in **G** and quantification in **H**) and neutrophil invasion (asterisks in **G** and quantification in **I**) in distal colon sections (n=6 mice per group; Scale bar, 150µm; **P*<0.05; ***P*<0.01; ****P*<0.001; one-way ANOVA with post-hoc Sidak's test). **(J-K)** 16S rRNA sequencing-based microbiome profiling (n=5 mice per group). Bar histograms (**J**) display the average relative abundance at the genera level (**P*<0.05; one-way ANOVA with post-hoc Tukey's test). Beta-diversity comparisons (**K**) with 95% confidence interval ellipses are based on non-metric multidimensional scaling (NMDS) of Bray-Curtis dissimilarity of the relative abundance of operational taxonomic units among samples (*P*<0.001; PERMANOVA).

Schwann cells within extrinsic nerves are a target of GDNF in aganglionic colon

To elucidate how GDNF induces enteric neurogenesis, we first evaluated GDNF distribution in P8 bowel via Western blot, taking advantage of size differences between recombinant (15 kDa) and endogenous (20 kDa, glycosylated) GDNF monomers. Recombinant GDNF was detected in GDNF-treated *Hol*$^{Tg/Tg}$ distal colon but not in proximal colon (**Figure 4.4A**). Surprisingly, while endogenous GDNF is normally only detected in ileum, recombinant GDNF enemas triggered robust increases in endogenous GDNF throughout the colon (**Figure 4.4A**). Recombinant GDNF was no longer detected in colon nor in any other tissue at P20, suggesting that administered GDNF primarily acts during the treatment period (**Supplementary Figure 4.8**). To assess precise locations of recombinant GDNF during treatment, we treated *Hol*$^{Tg/Tg}$ mice using a 6xHis-tagged version of GDNF ($_{His}$GDNF) (23). Time-course analysis of distal colon 2h after GDNF treatment on P4, P6 and P8 revealed $_{His}$GDNF accumulated over time in colon submucosa (**Figure 4.4B**), smooth muscles, and subsets of enteric neurons (**Figure 4.4C** and **Supplementary Figure 4.9**) of *Hol*$^{Tg/Tg}$ mice. Interestingly, RET levels also increased (**Figure 4.4B** and **Supplementary Figure 4.9**), supporting the hypothesis that GDNF-RET auto-regulatory loops are activated in GDNF-treated colon. Remarkably, both $_{His}$GDNF and RET were detected in induced neurons close to

extrinsic nerves of $_{His}$GDNF-treated animals, not only in *Hol*$^{Tg/Tg}$ mice (**Figure 4.4C**) but also in *Ednrb*$^{s\text{-}l/s\text{-}l}$ mice (**Supplementary Figure 4.10A**), and in both of our mouse facilities in Montreal and Philadelphia (**Supplementary Figure 4.10A-B**).

Given that induced neurons and glia were often closely associated with extrinsic nerves, we hypothesized that nerve-associated Schwann cells might be GDNF-targeted ENS progenitors. We first assessed response of Schwann cells to GDNF using live explants of distal colon *muscularis externa* from P4 *Hol*$^{Tg/Tg}$;*G4-RFP* double transgenic pups. In these mice, neural crest derivatives including Schwann cells are marked by RFP fluorescence (33). Time-lapse imaging of explants after 72h of culture suggested GDNF (5 µg/ml) stimulates both migration and proliferation of Schwann cells (**Figure 4.4D**). Impact of GDNF on proliferation of these Schwann cells was confirmed via immunofluorescence after 96h of culture, which revealed a 3-fold increase in Ki67^{+} SOX10^{+} double positive cells upon exposure to GDNF (**Figure 4.4E-F**).

To more definitely demonstrate Schwann cells are GDNF targets, we used *in vivo* genetic cell lineage tracing with the Schwann lineage-specific *Dhh-Cre* driver and the *R26*$^{[Floxed\ Stop]YFP}$ Cre reporter allele in the *Holstein* [FVB/N] mutant background. Analysis of proximal and mid colons from untreated *Dhh-Cre*$^{Tg/+}$;*R26*$^{YFP/+}$ and *Hol*$^{Tg/Tg}$;*Dhh-Cre*$^{Tg/+}$;*R26*$^{YFP/+}$ animals at P20 showed that the proportion of Schwann cell lineage-derived (YFP^{+}) myenteric neurons increased from 5-7% in a pure FVB/N genetic background to 10-11% in presence of homozygous *Holstein* mutation (**Supplementary Figure 4.11A-B**). Remarkably, the Schwann cell lineage contribution further increased to 34% of myenteric neurons in the distal colon of GDNF-treated *Hol*$^{Tg/Tg}$;*Dhh-Cre*$^{Tg/+}$;*R26*$^{YFP/+}$ animals (**Figure 4.4G-H**). By daily EdU administration during GDNF treatment, we identified four subgroups of induced myenteric neurons based on cellular origin (YFP fluorescence) and/or EdU incorporation (**Figure 4.4G-H** and **Supplementary Figure 4.11C**). While this work supports the hypothesis that Schwann cells are a source of GDNF-induced neurons and glia in both myenteric (**Figure 4.4G-H**) and submucosal (**Supplementary Figure 4.11C**) plexus, it also revealed that a majority of induced neurons (66%) were YFP-negative, suggesting a stronger

contribution by non-*Dhh*-expressing cell type(s). Regardless of cellular origin, a majority of induced neurons (62%) also did not incorporate EdU, raising the possibility that neurogenesis might result from transdifferentiation (i.e., direct differentiation of a post-mitotic cell into another type of specialized cell) instead of requiring proliferating precursor cells (**Figure 4.4G-H**).

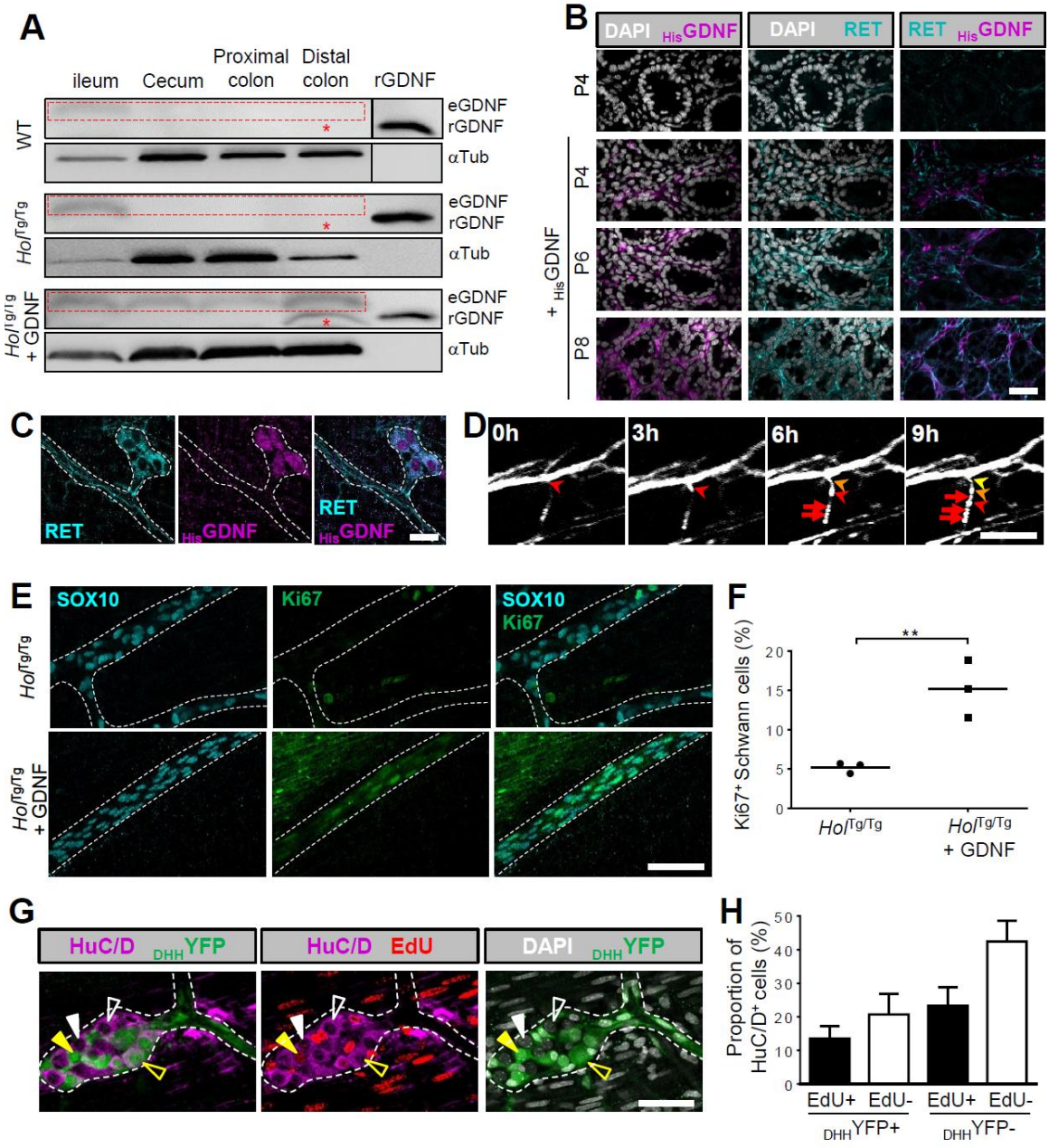

Figure 4.4: Extrinsic Schwann cells are a source of GDNF-induced neurons and glia in the otherwise aganglionic colon

(A) Distribution of recombinant (r)GDNF (asterisks) and endogenous (e)GDNF (dashed boxes) in different subregions of the GI tract from WT, *Hol*$^{Tg/Tg}$ and GDNF-treated *Hol*$^{Tg/Tg}$ mice at P8. **(B-C)** Accumulation of 6xHis-tagged GDNF ($_{His}$GDNF) and RET during enema treatments of *Hol*$^{Tg/Tg}$ mice, in the submucosa between P4-P8 (**B**) and in induced myenteric neurons at P8 (**C**). **(D)** 10-hour long time-lapse recordings of GDNF-cultured aganglionic colon tissues from P4 *Hol*$^{Tg/Tg}$;*G4-RFP* mice showing dividing (arrows) and migrating (arrowheads) Schwann cells on extrinsic nerves (50 µm-thick z-stacks). **(E-F)** GDNF exposure for 96h increases Schwann cell proliferation (SOX10^{+} Ki67^{+}) in distal colon explants from P4 *Hol*$^{Tg/Tg}$ mice (***P*<0.01; two-tailed Student's *t*-test). **(G-H)** Myenteric ganglia from the distal colon of P20 *Hol*$^{Tg/Tg}$;*Dhh- Cre*$^{Tg/+}$;*R26*$^{YFP/+}$ mice that were administered GDNF and EdU between P4-P8. Four categories of induced neuron are detected: 1) EdU-positive Schwann-derived (filled yellow arrowhead); 2) EdU-negative Schwann-derived (empty yellow arrowhead); 3) EdU-positive unknown origin (filled white arrowhead); 4) EdU-negative unknown origin (empty white arrowhead). All blots/images are representative of observations made from 3 mice. Quantifications were performed using 3 fields of view per mouse. Dashed outlines delineate either an extrinsic nerve fiber (**E**), or an extrinsic nerve fiber and an adjacent single ganglion (**C** and **G**). Scale bar, 20µm (**B-C**), 100µm (**D**), 50µm (**E-F**).

GDNF can induce new neurons in human aganglionic colon *ex vivo*

To test if GDNF could induce new enteric neurons in human tissue, we needed an *ex vivo* model. We discovered that 96h of *ex vivo* GDNF treatment induced neurons in all *Hol*$^{Tg/Tg}$ distal colon aganglionic tissues, but neurogenesis was much less efficient than *in vivo* (**Figure 4.5A** and **Supplementary Figure 4.12A**). Induced neurons rarely clustered into ganglia and such ganglia were always very small (**Figure 4.5B**). In marked contrast to widespread EdU incorporation into Schwann cells (**Figure 4.5C** and **Supplementary Figure 4.12B**), EdU incorporation in induced neurons was also minimal (**Figure 4.5B-C**). Although not perfect, we used this *ex vivo* system to test if GDNF could induce neurogenesis in aganglionic human colon muscle from children who had pull-through surgery to resect aganglionic distal bowel. Our cohort consisted of 12 children with epidemiologic characteristics typical of HSCR (i.e., mostly sporadic, male-biased, short-segment) (**Table 4.1**). Culturing small pieces of freshly- isolated *muscularis externa* with GDNF for 96h markedly increased the proportion of EdU^{+} Schwann cells in 9/9 human tissues where EdU was added to media (**Figure 4.5D-E**). Most importantly, we also detected new neurons expressing

HuC/D, βIII-Tubulin (Tuj1), RET, PGP9.5 and PHOX2B in three HSCR explants (**Figure 4.5F-G** and **Supplementary Figure 13**). These three explants were from the youngest children of our cohort (28 to 44 days old) (**Figure 4.5G** and **Table 4.1**). Two of these young children had sporadic HSCR with unknown genetic causes. The third child had a MEN2A syndrome- associated *RET* mutation (**Table 4.1**). For older children (n=2; 86 and 1638 days old), we found that extending GDNF treatment to 7 days could yield neurons that incorporated EdU (**Figure 4.5H**). Collectively these data suggest our observations in mice may be extended to humans.

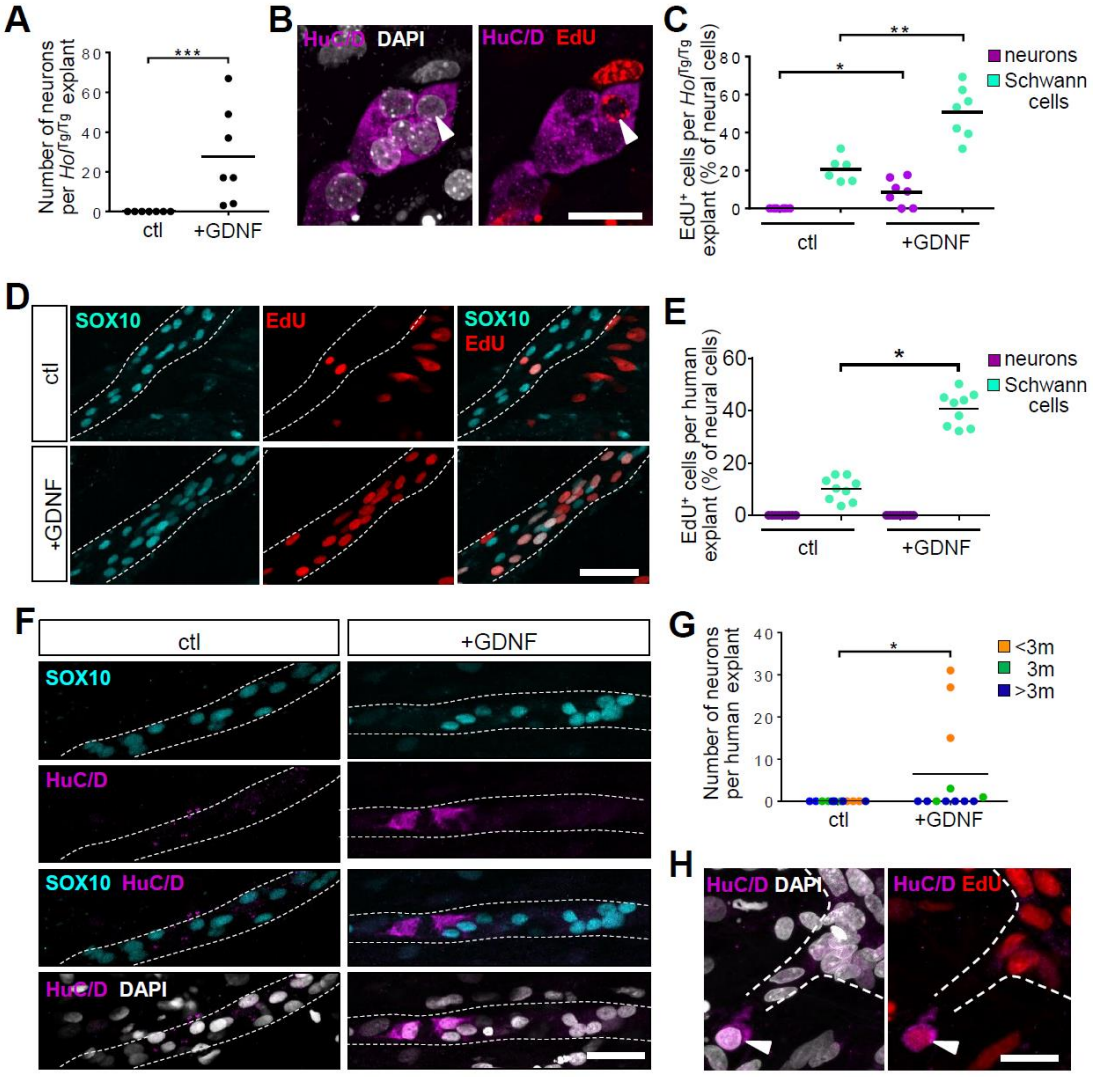

Figure 4.5: *Ex vivo* preclinical testing of GDNF therapy on explants of aganglionic colon from *Hol*$^{Tg/Tg}$ mice and human HSCR patients

(A-C) Distal colon explants from P4 *Hol*$^{Tg/Tg}$ mice cultured for 96h with GDNF and EdU (+GDNF) or EdU alone (ctl). GDNF-induced HuC/D^{+} neurons (**A**) rarely form ganglia (**B**) and are less likely to show EdU incorporation than SOX10^{+} Schwann cells (arrowhead in **B** and quantification in **C**) (n=7 explants per condition; **P*<0.05; ***P*<0.01; ****P*<0.001; two-tailed Mann-Whitney U test). **(D-G)** Aganglionic colon explants from human HSCR patients cultured for 96h with GDNF and EdU (+GDNF) or EdU alone (ctl). EdU incorporation was detected in SOX10^{+} Schwann cells but not in HuC/D^{+} neurons (**D-E**). GDNF-induced HuC/D^{+} neurons were detected in a subset of explants (**F**), all originating from patients less than 3 months of age at the time of surgery (**G**) (n=12 explants per condition; **P*<0.05; two-tailed Mann-Whitney U test). **(H)** Extended culture in presence of GDNF for 7 days yielded neurons in explants from older patients, including some that incorporated EdU (arrowhead). All displayed images were taken at myenteric plexus level. Dashed outlines delineate extrinsic nerve fibers. Scale bars, 50 µm (**B** and **H**) and 100 µm (**D** and **F**).

Table 4.1: Overview of HSCR colon samples used for *ex vivo* preclinical testing of GDNF therapy

Age at surgery (days)	Genetic status	Sex	Clinical Classifi-cation	Extent of aganglion-osis (cm)	Number of neurons	EdU^+ Schwann cells (%)
28	Sporadic, unknown mutation	M	Short segment disease	5	31	38
36	Sporadic, unknown mutation	M	Short segment disease	25	27	33
44	MEN2a syndrome, *RET* mutation	M	Short segment disease	6	15	44
80	Sporadic, unknown mutation	M	Short segment disease	7	3	34
85	Sporadic, unknown mutation	M	Short segment disease	6	1	32
86	Sporadic, unknown mutation	M	Short segment disease	7	0	46
249	Mowat-Wilson syndrome, *ZFHX1B* mutation	F	Short segment disease	30	0	32
300	Data not available	M	Data not available	Data not available	0	Not quantified
344	Sporadic, unknown mutation	M	Short segment disease	26	0	Not quantified
349	Sporadic, unknown mutation	M	Short segment disease	9	0	43
1177	Bardet-Biedl Syndrome, BBS1 mutation	F	Long segment disease	40	0	Not quantified
1638	Sporadic, unknown mutation	F	Short segment disease	8	0	50

4.5 Discussion

Here we report that GDNF enemas can regenerate a functional ENS *in situ* and prevent death in three genetically- distinct mouse models of S-HSCR. Detailed mechanistic studies in $Hol^{Tg/Tg}$ mice showed that exogenous GDNF can penetrate the permeable distal aganglionic colon,

leading to increased levels of endogenous GDNF and RET in the whole colon. At least some of the new neurons and glia appear to arise from extrinsic *Dhh-Cre*+ lineage Schwann cells, and newly organized enteric ganglia appear to be self-sustaining until at least P56 (**Supplementary Figure 4.14**).

One concern for GDNF-based therapy is that RET signaling is often reduced in children with HSCR, suggesting GDNF responsiveness would also be reduced. However, most children with S-HSCR must have substantial RET activity in ENS precursors because complete RET absence causes a much more severe phenotype (i.e., total intestinal aganglionosis) in mice and humans (28, 34). Supporting this idea, recent whole genome sequencing studies of people with S-HSCR found only 4.3% (out of 443 patients) (7) and 6.3% (out of 190 patients) (9) had *RET* rare coding variants predicted to be damaging. Furthermore, rectal GDNF therapy increased levels of RET and endogenous GDNF in mouse colon, suggesting positive feedback loops that could enhance RET signaling even if initial RET levels were low. This could be particularly valuable since RET provides trophic support to some enteric neurons in adults (4) and RET is expressed in a subset of GDNF-induced neurons after rectal therapy (**Figure 4.4C**, **Supplementary Figure 4.10A-B** and **Supplementary Figure 4.11D**). Finally, although some of the GDNF-induced neurons that express RET are derived from Schwann cells (**Supplementary Figure 4.11D),** RET is most likely not needed to activate these precursors in aganglionic bowel. GDNF signaling in Schwann cells is instead mediated by NCAM (20), and our data show NCAM but not RET expression in Schwann cells of extrinsic nerves in aganglionic mouse colon (**Supplementary Figure 4.15**). Nonetheless, we tried to directly determine if reduced RET levels affected GDNF therapy using our previously published model of *Ret* hypomorphic mice exposed to mycophenolate (22). However, several problems complicated interpretation in our new experimental conditions, including the occurrence of HSCR-like dilated bowel even in absence of aganglionosis (**Supplementary Figure 4.2C-D**). Future studies would need to test GDNF enema effects in other models where reduced RET activity is associated with short- segment aganglionosis, but the “ideal” model is not readily apparent.

In contrast to *Ret* mutants, *Hol*$^{Tg/Tg}$, *TashT*$^{Tg/Tg}$ and *Ednrb*$^{s\text{-}l/s\text{-}l}$ mice are all reliable models of S-HSCR (25-27), recapitulating key hallmarks of the human disease in both aganglionic segment and proximal ENS-containing colonic regions (29-32). Although not all GDNF-treated mutant mice have prolonged survival, the survival advantage after GDNF treatment in Montreal is dramatic and the *in situ* generation of new enteric neurons in previously aganglionic bowel, which was observed in both Montreal and Philadelphia (**Supplementary Figure 4.10A-B**), is unprecedented. The reason why some mice responded better to GDNF than others might be due to the degree of aganglionosis-associated inflammation (**Figure 4.3G-I**). Indeed, although GDNF is known to have anti-inflammatory properties (35), the inflammatory microenvironment present in aganglionic bowel before GDNF treatment might help trigger a neurogenic response as it does in the context of inflammatory bowel disease (36). Unfortunately, the exact inflammatory mediators that enhance enteric neurogenesis are not yet known, but once identified we could develop adjunct treatments that enhance the effect of GDNF therapy.

Adjunct treatments might also be developed based on a serendipitous finding we made when we tried to replicate our Montreal survival data (**Figure 4.1A-C**) using *Hol*$^{Tg/Tg}$ and *Ednrb*$^{sl/sl}$ mice in Philadelphia. We unexpectedly discovered that these mouse lines live much longer in Philadelphia than in Montreal without any specific treatment, even though all our mice originated from the same colonies (**Supplementary Figure 4.10C-D**). The prolonged survival in Philadelphia compared to Montreal was especially dramatic for untreated *Ednrb*$^{s\text{-}l/s\text{-}l}$ (**Supplementary Figure 4.10C**) that lived much longer than previously described in any other mouse facility (27, 30, 37). Intriguingly, the survival advantage for untreated HSCR models in Philadelphia occurred despite the confirmed presence of distal bowel aganglionosis and/or megacolon (**Supplementary Figure 4.10C-D**). In fact, Philadelphia-based untreated mice survived as long as GDNF-treated mice in Montreal (**Supplementary Figure 4.10E-F**) and survival could not be further enhanced in Philadelphia by GDNF treatment (**Supplementary Figure 4.10E-F**) even though GDNF-induced neurogenesis was similar in both Montreal and Philadelphia (**Supplementary Figure 4.10A-B**).

One especially attractive hypothesis for all these observations is that GDNF treatment in Montreal and non-genetic factors in Philadelphia might both improve a critical pro-survival bowel function (e.g., promoting enhanced epithelial barrier function or modulating mucosal immune responses), either indirectly (via induced ENS ganglia) in Montreal or directly (bypassing the need for induced ENS ganglia) in Philadelphia. Although we suspect that food- and/or microbiota-based mechanisms underlie the survival advantage in Philadelphia, there are many variables so defining mechanisms is complicated.

A potentially more straightforward approach to improve GDNF therapy would be to identify GDNF-targeted ENS progenitors other than *Dhh*-lineage Schwann cells that appear to contribute only about a third of GDNF-induced neurons. This could lead to an improved GDNF-based cocktail that includes additional trophic factor(s) that bind receptors on these other cells. In this regard, substantial literature suggests the existence of ENS "stem cells" in postnatal mouse and human bowel[38, 39], even in aganglionic regions (40, 41). Interestingly, extrinsic nerve fibers of aganglionic regions were previously identified as a niche for these ENS stem cells (41). Our data confirm this prior observation and further suggest that at least some of these stem cells are in fact *Dhh*-lineage Schwann cells. It is possible that the other ENS progenitors are also Schwann cells that do not express CRE in *Dhh-Cre* mice. In accordance with this possibility, we noted that some SOX10$^+$ Schwann cells are not YFP$^+$ in extrinsic nerves from the aganglionic colon of *Hol*$^{Tg/Tg}$;*Dhh-Cre*$^{Tg/+}$;*R26*$^{YFP/+}$ mice at P8 (**Supplementary Figure 4.16**). The strong contribution of non-*Dhh*-expressing cells combined with the location of some GDNF-induced ganglia away from extrinsic nerves, however, also suggests the involvement of additional cell type(s), which might include sacral neural crest-derived cells. Sacral-derived ENS progenitors can colonize the aganglionic colon during prenatal development (42), and our SOX10 immunofluorescence data suggest that some of these cells persist in postnatal aganglionic tissues as scattered progenitors and/or enteric glia, also expressing the alternative GDNF receptor NCAM (**Figure 4.2A** and **Supplementary Figure 4.15**). A contribution by differentiated enteric glia of sacral origin might also help explain the

observation that many GDNF-induced neurons had not incorporated EdU suggesting they were generated via transdifferentiation (**Figure 4.4G-H**).

In theory, GDNF-based rectal therapy would be easy to implement since normal saline enemas are already commonly used in children with HSCR both before and after pull-through surgery. If penetration of GDNF beyond the epithelium was limited, GDNF could be directly injected into the colon wall with currently available endoscopes or via a specially designed delivery tool. Ideally, GDNF-based rectal therapy would prevent the need for pull-through surgery. Even if GDNF enemas did not work as primary HSCR treatment, GDNF therapy might nevertheless improve post-surgical outcomes by normalizing ENS structure in the retained distal bowel of the "transition zone" (i.e., correcting hypoganglionosis and neuronal subtype imbalance). In addition, since ENS stem cell-based therapies are being considered for the treatment of HSCR, GDNF might be a useful adjunct to these therapies to promote engraftment. All these considerations make a human clinical trial of GDNF-based rectal therapy in children with HSCR appealing.

4.6 Acknowledgments

The authors thank Denis Flipo (UQAM) for assistance with confocal imaging, Dr. Natalie Patey (CHU Ste-Justine), Ben Wilkins and Archana Shenoy (CHOP) for help with collection of human samples, and MedGenesis Therapeutix Inc. for generously providing clinical grade human recombinant GDNF.

4.7 Author Contributions

RS and NP conceived the study; ROH and NP supervised the study; RS, SS, ROH and NP designed the experiments; RS, SS, GB, BC, OS, BC and ML performed the experiments and collected data; RS, SS, GB, BC, ML, SWK, ROH and NP analyzed and interpreted data; FRG, AA and CF provided samples; RS, SS, ROH and NP drafted and edited the manuscript; All authors revised the manuscript.

4.8 Funding

This work was supported by catalyst grants from the Fondation du grand défi Pierre Lavoie to NP and by an operating grant from the Canadian Institutes of Health Research (CIHR #377028) to NP and ROH. RS was supported by a postdoctoral fellowship from the Fonds de la recherche du Québec – Santé (FRQS). SWK holds the Canada Research Chair in Plant Microbiomes. NP is a FRQS Senior Research Scholar and the recipient of the UQAM Research Chair on Rare Genetic Diseases. ROH was also supported by the March of Dimes 6-FY15-235, the Irma and Norman Braman Endowment, the Suzi and Scott Lustgarten Center Endowment, and The Children's Hospital of Philadelphia Research Institute. The funders had no role in study design, data collection and analysis, decision to publish, or preparation of the manuscript.

4.9 Supplementary Materials

Supplementary Methods

Mice

Holstein (*Tg[Sox3-GFP,Tyr]HolNpln*), *TashT* (*Tg[SRY-YFP,Tyr]TashTNpln*), and *G4-RFP* (*Gata4p[5kb]-RFP*) lines were as previously described (all maintained on a FVB/N genetic background) (25, 26, 33), whereas *Piebald-lethal* (*Ednrb$^{s-l;}$* JAX stock # 000308; C3H/HeJ-C57BL/6 mixed background) and *Dhh-Cre* (*Tg[Dhh-cre]1Mejr*; JAX stock # 012929; FVB/N background) were obtained from The Jackson Laboratory. Other mouse lines used were *R26$^{[Floxed\ Stop]YFP}$* (*Gt[ROSA]26Sor$^{tm1(EYFP)Cos}$*; provided by F. Costantini (Columbia University, USA) and maintained on a FVB/N background) (43), *Ret^{TGM}* (here referred to as *Ret*-null; *Ret^{tm1Jmi}*; maintained on a C57BL/6 background) (44), and *Ret^{9}* (*Ret$^{tm2(RET)Jmi}$*; provided by S. Jain (Washington University School of Medicine, USA) and maintained on a 129X1/Sv1 background) (45).

For mycophenolate mofetil treatments (22), timed pregnancies were set up by mating *Ret$^{+/-}$* with *Ret$^{9/+}$* or *Ret$^{9/9}$* mice, considering noon of the day of plug detection as E0.5. At E7.5, the drinking water of pregnant dams was replaced with 0.25X PBS adjusted to pH3.6 with added prodrug mycophenolate mofetil (Accord Healthcare, NDC Cat# 16729-094) at varying concentrations (250 µg/mL, 187.5 µg/mL, and 125 µg/mL). Dams remained on mycophenolate mofetil-supplemented drinking water from E7.5 to E18.5.

Enemas were administered using a 24-gauge gavage needle (Fine Science Tools, Canada) attached to a micropipette. The head of the gavage needle was introduced in the rectum just beyond the anus, and enemas were injected over the course of a few seconds. Pups were then placed back with their mother, and either sacrificed for tissue analysis (at age indicated in relevant figure legends) or checked daily to track survival.

Tissue labelling and imaging

For immunofluorescence staining, whole microdissected tissues were permeabilized for 2 hours in blocking solution (10% FBS and 1% Triton X-100, in PBS) before being sequentially incubated with specific primary (at 4°C overnight) and relevant secondary (at room temperature for 2 hours) antibodies, both diluted in blocking solution that was also used to wash tissues between all steps. All antibodies and dilution factors, are listed in **Supplementary Table 4.2**. EdU was detected using the Invitrogen Click-iT EdU Imaging Kit (ThermoFisher Scientific, Cat# C10337) in accordance with the manufacturer's instructions. For histological analyses, cross-sections of full-thickness bowel tissues were stained with hematoxylin and eosin (H&E) as previously described (46).

All immunofluorescence images were acquired with either a 20X or a 60X objective on a confocal microscope (either Nikon A1R or Zeiss 710), with the exception of H&E-stained sections that were imaged with a 10X objective using an Infinity-2 camera (Lumenera Corporation) mounted on a Leica DM 2000 microscope (Leica Microsystems Canada). Image analysis was performed with ImageJ, using the "Subtract background" function to decrease non-specific background signal, the "Multi-point" function for cell counting, and the "Polygon selection" function for calculation of surface area.

Western blot analysis

Organs dissolved in RIPA buffer (containing 1X Roche Complete protease inhibitors) were sonicated on ice and centrifuged at 14,000 rpm for 15 minutes at 4°C, keeping the supernatants for western blot analysis. Equal volumes of samples were electrophoretically separated in an 18% sodium dodecyl sulfate-polyacrylamide gel (SDS-PAGE) and transferred to Immun-blot® PVDF membranes (Bio-Rad, Cat# 1620177). Membranes were subsequently incubated in blocking solution (5% skimmed milk and 0.1% Tween 20, in TBS), followed by incubation with either mouse anti-GDNF (Santa Cruz Biotechnology, Cat# sc-13147; 1:500 dilution factor) or rabbit anti-βTubulin

(Abcam, Cat# ab176560; 1:70 000 dilution factor) primary antibodies, and then relevant horseradish peroxydase-conjugated secondary antibodies, all diluted in blocking solution. Each incubation was for 60 min at room temperature, each time interspersed by 3 washes with blocking solution. Proteins were finally visualized using Immobilon western chemiluminescent HRP substrate (Millipore Sigma, Cat# WBKLS0050) and Fusion FX imaging system (Vilber).

Ex vivo culture for time-lapse imaging

Muscle strips were cultured in suspension as previously described for time-lapse imaging of embryonic guts (25), in DMEM/F12 medium (Wisent, Cat# 319-085-CL) supplemented with 10% FBS and 100IU/ml antibiotic-antimycotic with or without 5 µg/ml GDNF under standard culture conditions (37°C, 5% CO_2). After 72h of culture, each petri dish was placed in a microscope incubation chamber (Okolab) for 10 hours under the same culture conditions, and image stacks (250µm-thick) of RFP-labelled extrinsic nerves and Schwann cells were acquired every 10 min, using a 20X objective on a Nikon A1R confocal unit as previously described (25).

In vivo and ex vivo analysis of colonic motility

For bead latency test, mice were anesthetized with 2% isoflurane and a 2mm glass bead (Sigma, Cat# 1.04014) was inserted into the distal colon with a probe over a distance of 0.5 cm from the anus. Each mouse was then isolated in its cage without access to food and water and monitored for the time required to expel the glass bead. For *ex vivo* analysis of contractility, muscle strips were initially stretched with a preload of 2 g of tension for 60 min, and contraction/relaxation of longitudinal muscles was then continuously recorded with a myograph (Narco Biosystems Inc., Model F-60) coupled to a computer equipped with the BIOPAC student Lab 4.0.2 software (BIOPAC Systems Inc.). Electrical field stimulation (EFS) was applied with a voltage stimulator (BIOPAC Systems Inc., Model BSL MP36/35) connected to electrodes, using parameters that activate enteric neurons without directly activating muscles (12 V, 20 Hz, 10s train duration, and

300µs stimulus pulse duration). This procedure was repeated 3 times, with 10 min washout periods between stimulations. To characterize the nitrergic and cholinergic components of EFS-induced contractile responses, N-nitro-L-arginine methyl ester (L-NAME; Sigma, Cat# N5751) and atropine (Sigma, Cat# A01132) were added to Krebs solution at a final concentration of 0.5µM and 1µM, respectively. The area under the curve (AUC) was measured during each EFS-induced response, and data were expressed in ΔAUC (corresponding to the difference between the AUC measured 20s after stimulation minus the AUC measured 20s before stimulation).

Ex vivo analysis of paracellular permeability

Each Ussing chamber contained 5ml of DMEM/F12 medium (Wisent, Cat# 319-085-CL), which was maintained at 37ºC and continuously oxygenated (95% O_2 / 5% CO_2). After a 30 min equilibration period, 200µl of apical medium was replaced with 200µl of a 1mg/ml solution of FITC-conjugated dextran 4 kDa (FD4; Sigma, Cat# 60842-46-8). Fluorescence intensity of basolateral aliquots of 150ul, reflecting paracellular transit from the luminal surface, was then measured every 30 min over a period of 3 hours, using a fluorimeter (TECAN, Model Infinite M1000). Fluorescence intensity was finally converted in amount of FD4 by comparison to a standard curve, and the average value for the 3 hour period was used to calculate paracellular permeability, which was expressed in ng of FD4 per surface of mucosa area per min (ng/cm^2/min).

Microbiome analysis

Mice were sacrificed at P20 and their feces were directly collected from the colon (3 fecal pellets per mouse). Bacterial DNA was then extracted using the QIAamp® Fast DNA Stool Mini Kit (QIAGEN, Cat# 51604), and the V5-V6 region of the *16S* rRNA gene was PCR amplified with a collection of previously described barcoded primers (47). Raw sequences generated with an Illumina MiSeq sequencer were paired and processed using the MOTHUR pipeline (48), and the

BIOM package (49) was subsequently used to transfer biom files into R (50) for generating graphs of relative taxa abundance and beta diversity.

Supplementary Figures and Tables

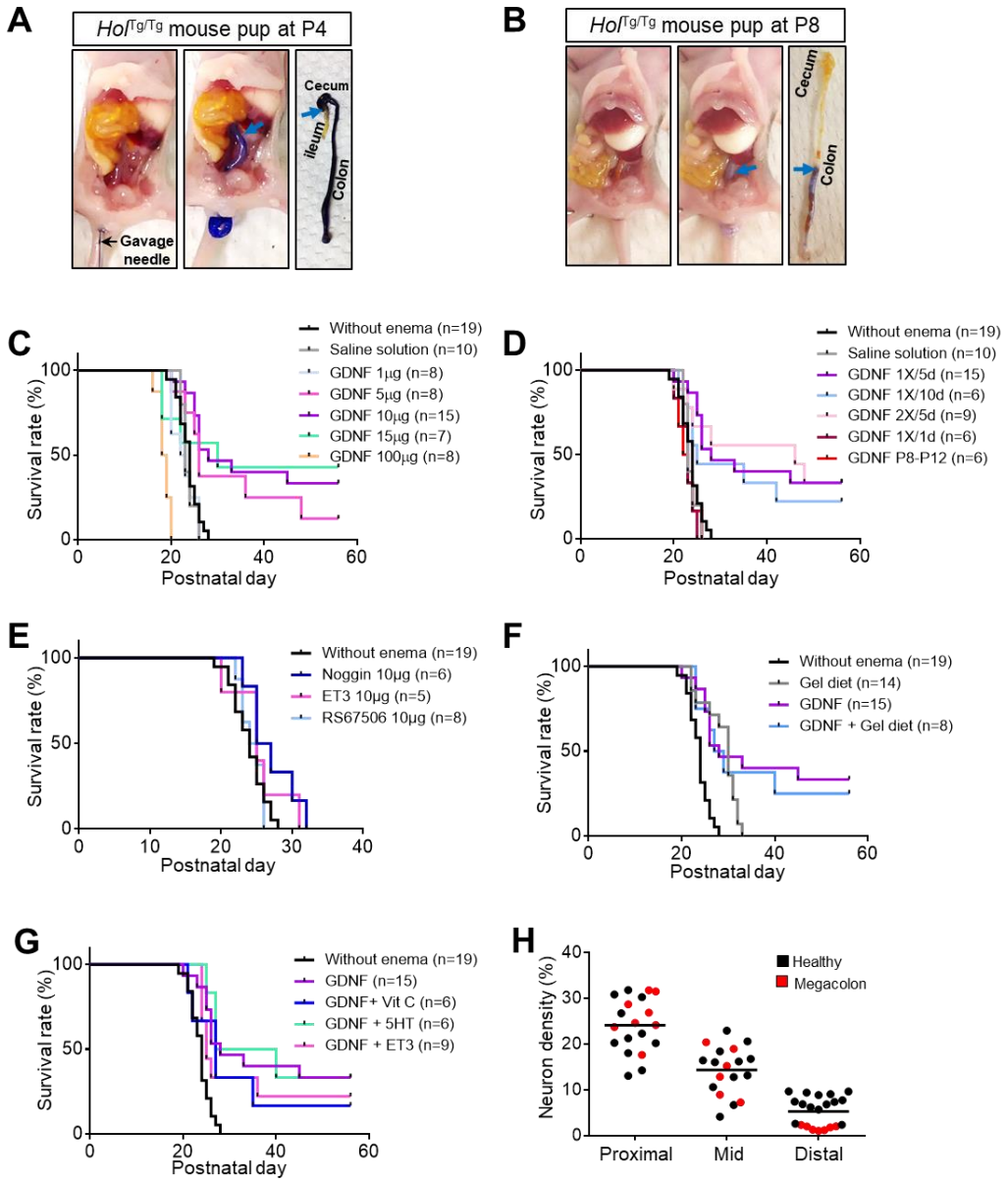

Supplementary Figure 4.1: Set-up of GDNF therapy parameters in Hol$^{Tg/Tg}$ mice
(A-B) Distribution of 10µl methylene blue enemas in the colon of P4 (**A**) and P8 (**B**) *Hol$^{Tg/Tg}$* pups. **(C)** Impact of GDNF concentration on survival of *Hol$^{Tg/Tg}$* pups that received 10µl enemas once

daily between P4-P8. Indicated amounts correspond to the total quantity of GDNF that was administered each day. **(D)** Impact of treatment time window (P4-P8 *vs* P8-P12), duration (1d, 5d or 10d; starting at P4) and frequency (once or twice a day, for 5 days) on the survival of *Hol*$^{Tg/Tg}$ pups treated with GDNF enemas (quantity of GDNF administered per single enema was kept constant at 10µg in 10µl). **(E)** Survival rate of *Hol*$^{Tg/Tg}$ pups that were administered 10µl enemas containing the indicated neurotrophic molecule (Noggin, Endothelin-3, or the serotonin receptor agonist RS67506; all at 1µg/µl final concentration) once daily between P4-P8. **(F)** Impact of food consistency (regular chow *vs* gel diet) on survival of *Hol*$^{Tg/Tg}$ pups that received GDNF enemas (10µg in 10µl) on a daily basis between P4-P8. **(G)** Impact of co-administration of ascorbic acid (Vit.C; 100µM final concentration), serotonin (5-HT; 1µg/µl final concentration) and Endothelin-3 (ET3; 1µg/µl final concentration) on survival of *Hol*$^{Tg/Tg}$ pups that received GDNF enemas (10µg in 10µl) once daily between P4-P8. **(H)** Neuron density in the colon (expressed in % of surface area) and associated health status of P20 *Hol*$^{Tg/Tg}$ mice that received GDNF enemas (10µg in 10µl) on a daily basis between P4-P8.

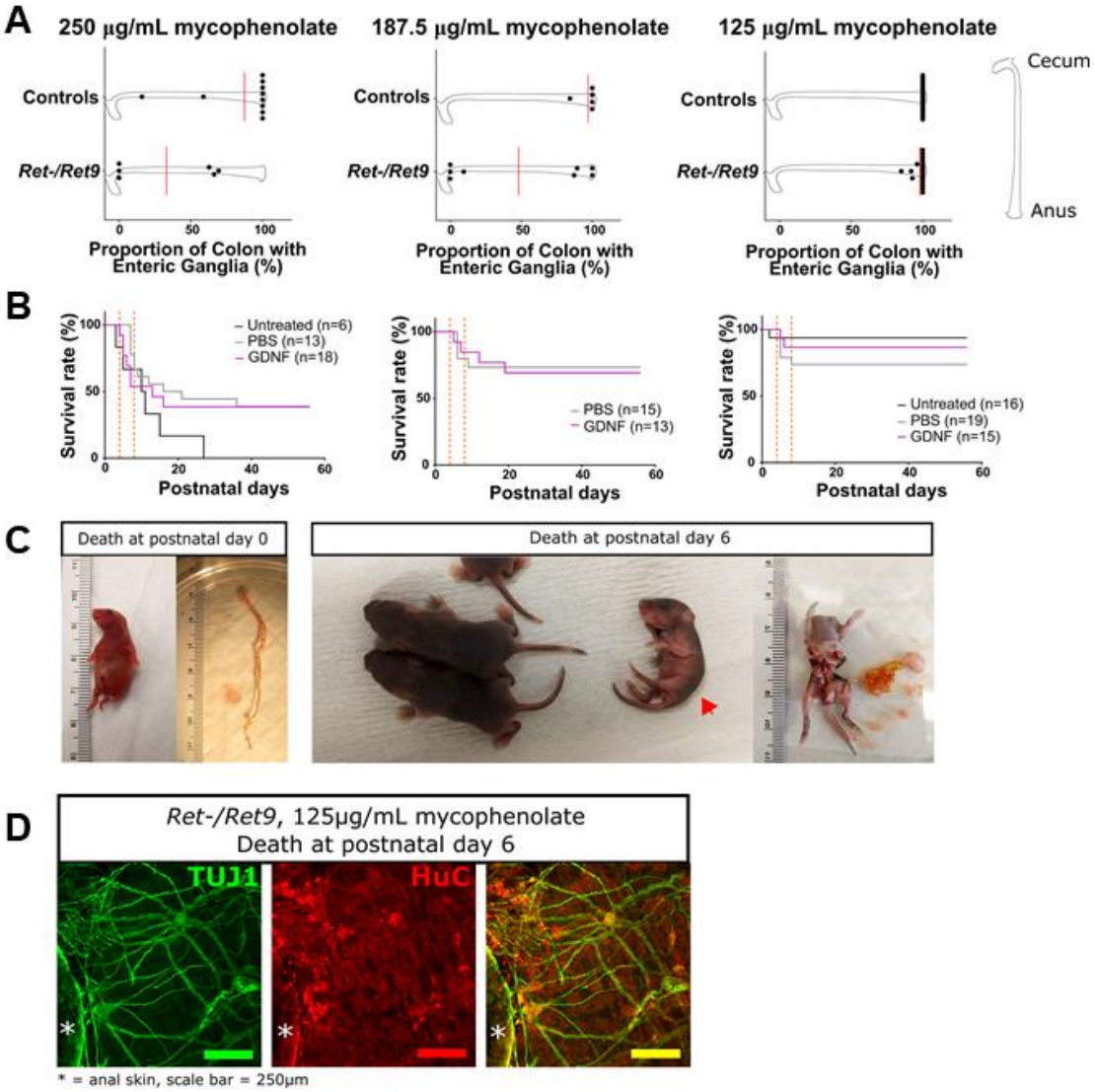

Supplementary Figure 4.2: GDNF enemas do not rescue survival in RET hypomorph mouse model of HSCR

(A) Treatment of pregnant dams with increasing doses of mycophenolate mofetil from E7.5 to E18.5 increases penetrance of HSCR-like aganglionosis and the length of aganglionic bowel in the newborn *Ret*$^{-/9}$ pups. A few *Ret*$^{wt/9}$ littermates (graphed as part of the control group) also exhibited aganglionosis. **(B)** There is no survival difference for mice treated from P4-P8 with GDNF versus PBS for all mycophenolate mofetil concentrations. (Log-rank test and Gehan-Breslow-Wilcoxon test for all data sets $P > 0.1$). **(C)** *Ret*$^{-/9}$ mice died during the P4-P8 treatment period with bowel distention. **(D)** Representative image of the distal colon of 125µg/mL mycophenolate-treated *Ret*$^{-/9}$ pups that died during the treatment period. This specific pup died at post-natal day 6 (as seen in **C**) even though myenteric neurons (HuC/D^{+}) completely colonized the bowel (anal skin marked with *). Extrinsic nerve fibers are also visualized (TuJ1^{+}). Scale bar, 250µm (**D**).

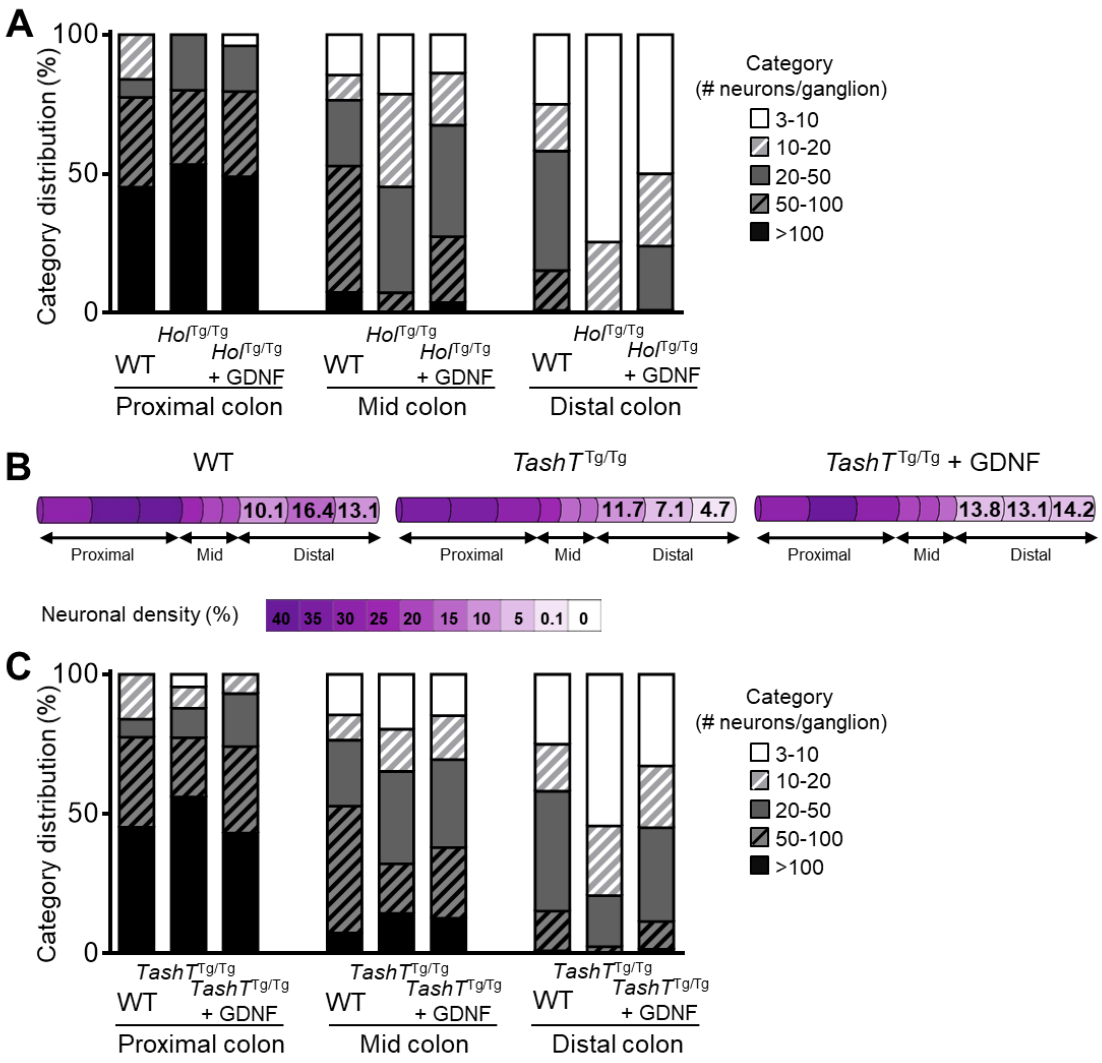

Supplementary Figure 4.3: Analysis of myenteric ganglion size and neuronal density in the colon of P20 *Hol*$^{Tg/Tg}$ and *TashT*$^{Tg/Tg}$ mice that were treated or not with GDNF between P4-P8
(A) Analysis of myenteric ganglion size *in Hol*$^{Tg/Tg}$ mice. **(B)** Analysis of neuronal density in *TashT*$^{Tg/Tg}$ mice. The average neuronal density (color-coded) is indicated for each colon sub-region (represented by cylinders) along the length of the colon. Neuronal density is expressed as the percentage of area occupied by HuC/D^{+} cells in a single focal plane at the level of the myenteric plexus within the bowel wall (n=6 mice per group; 3 fields of view per sub-region). For each distal colon subregion, the neuronal density is also given as a numerical value. **(C)** Analysis of myenteric ganglion size *in TashT*$^{Tg/Tg}$ mice.

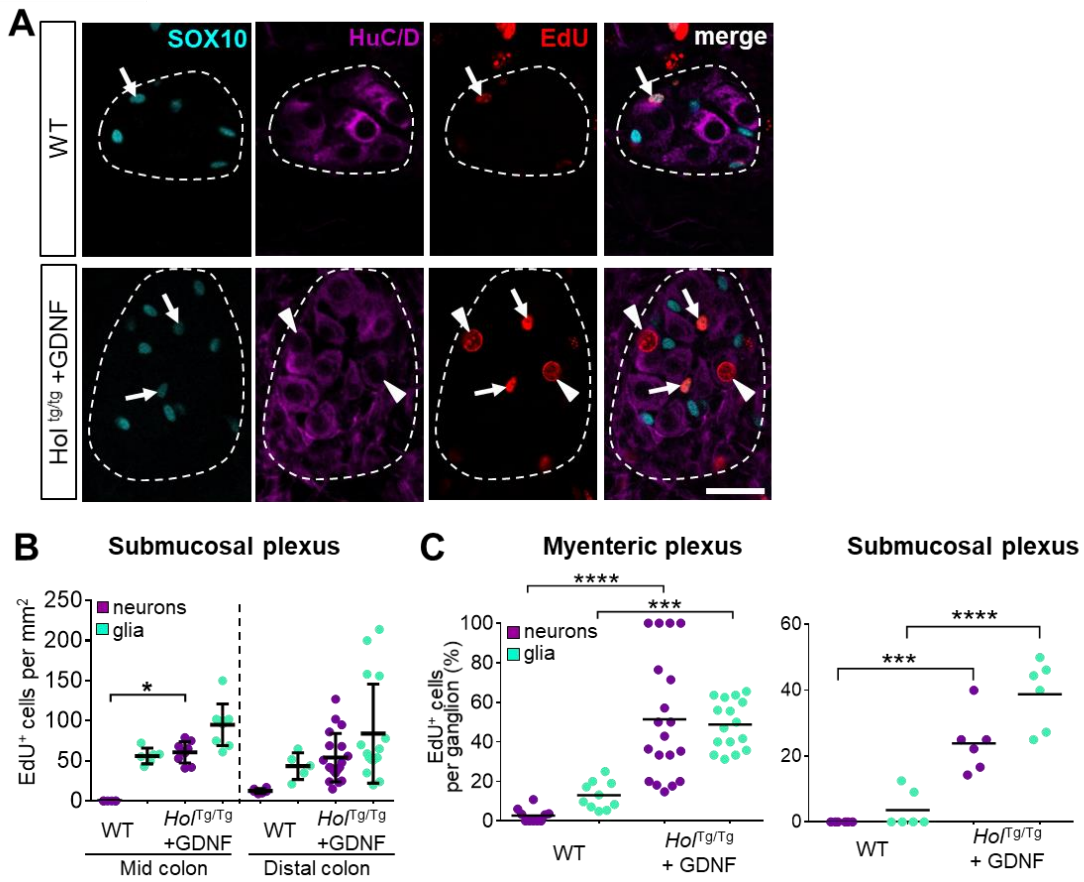

Supplementary Figure 4.4: Analysis of EdU incorporation in myenteric and submucosal ganglia of the colon from P20 WT and GDNF-treated *Hol$^{Tg/Tg}$* mice that were administered EdU between P4-P8

(A) *Example* of EdU incorporation in a z-stack projection of submucosal neurons (arrowheads) and glia (arrows) in the distal colon. Dashed outline marks area occupied by a single ganglion. Scale bar, 50 µm. **(B)** *Quantitative analysis of EdU incorporation* in submucosal neurons (HuC/D$^+$) and glia (SOX10$^+$) in mid and distal colon. Results are expressed as the number of EdU$^+$ cells per mm^2 (n=3 WT and 3 GDNF-treated *Hol$^{Tg/Tg}$* mice; 2-7 fields of view per animal; **P*<0.05; one-way ANOVA with post-hoc Sidak's test). **(C)** Quantitative analysis of EdU incorporation in myenteric (left panel) and submucosal (right panel) neurons (HuC/D$^+$) and glia (SOX10$^+$) in distal colon. Results are expressed in percentage of EdU$^+$ cells per ganglion (n=3 WT and 3 GDNF-treated *Hol$^{Tg/Tg}$* mice; 2-7 fields of view per animal; ****P*<0.001; *****P*<0.0001; one-way ANOVA with post-hoc Sidak's test). GDNF-treated mice received 10µg GDNF in 10µL enemas once daily between P4-P8.

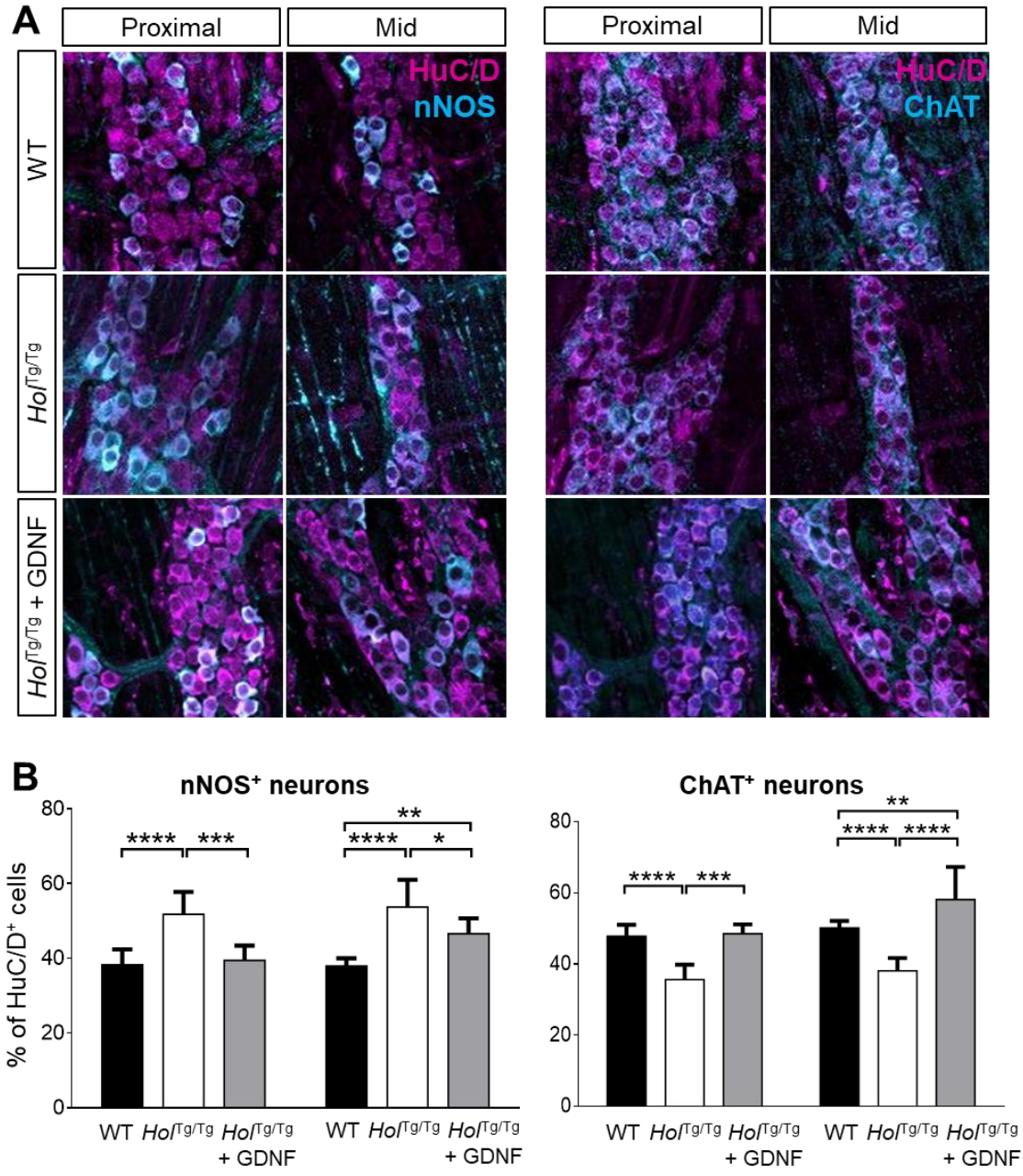

Supplementary Figure 4.5: Proportion of nitrergic and cholinergic myenteric neurons in the proximal and mid colon of WT, untreated *Hol*$^{Tg/Tg}$ or GDNF-treated *Hol*$^{Tg/Tg}$ mice at P20

(A) Qualitative analysis of the proportion of nitrergic (left panel) and cholinergic (right panel) neurons. Scale bar, 50 µm. **(B)** Quantitative analysis of the proportion of nitrergic (left panels) and cholinergic (right panels) neurons (n=3 WT and 3 GDNF-treated *Hol*$^{Tg/Tg}$ mice; 3 fields of view per animal; **P*<0.05; ***P*<0.01; ****P*<0.001; *****P*<0.0001; one-way ANOVA with post-hoc Sidak's test). GDNF-treated mice received 10µg GDNF in 10µL enemas once daily between P4-P8.

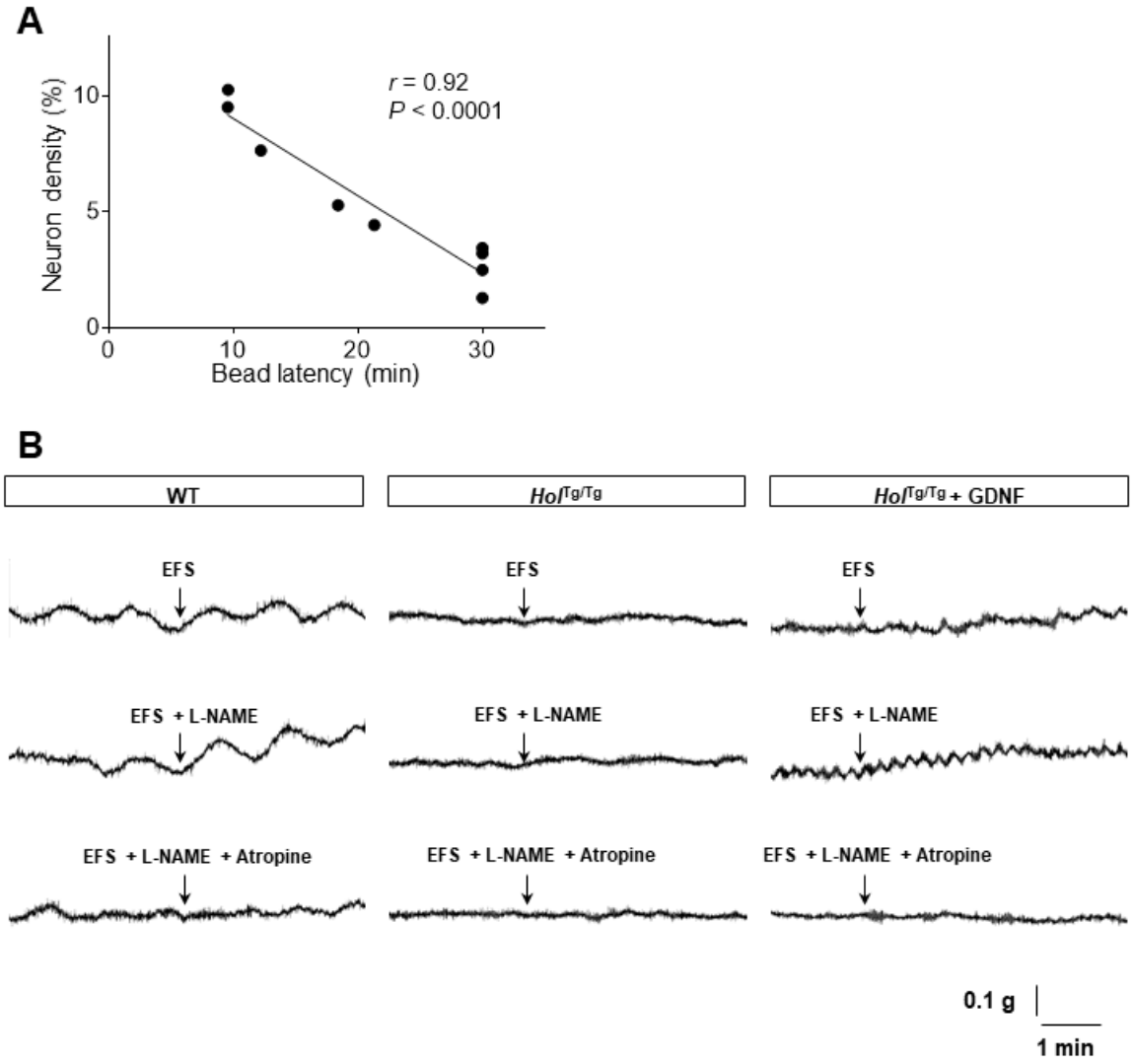

Supplementary Figure 4.6: Supporting information for in vivo and ex vivo analyses of motility in the distal colon of WT, untreated HolTg/Tg or GDNF-treated HolTg/Tg mice at P20 **(A)** Correlation between neuron density in distal colon and time for bead expulsion in GDNF-treated *Hol*$^{Tg/Tg}$ mice at P20 (in support of **Figure 4.3D**). **(B)** Examples of electric field-stimulated and drug-modulated patterns of longitudinal smooth muscle contraction-relaxation in an organ bath equipped with a force transducer (in support of **Figure 4.3E**). In responsive tissues, electric field stimulation (EFS) triggers contractions of colonic muscles that can be slightly increased by L-NAME-mediated inhibition of nitrergic signaling, and robustly counteracted by atropine-mediated inhibition of cholinergic signaling. GDNF-treated mice received 10µg GDNF in 10µL enemas once daily between P4-P8.

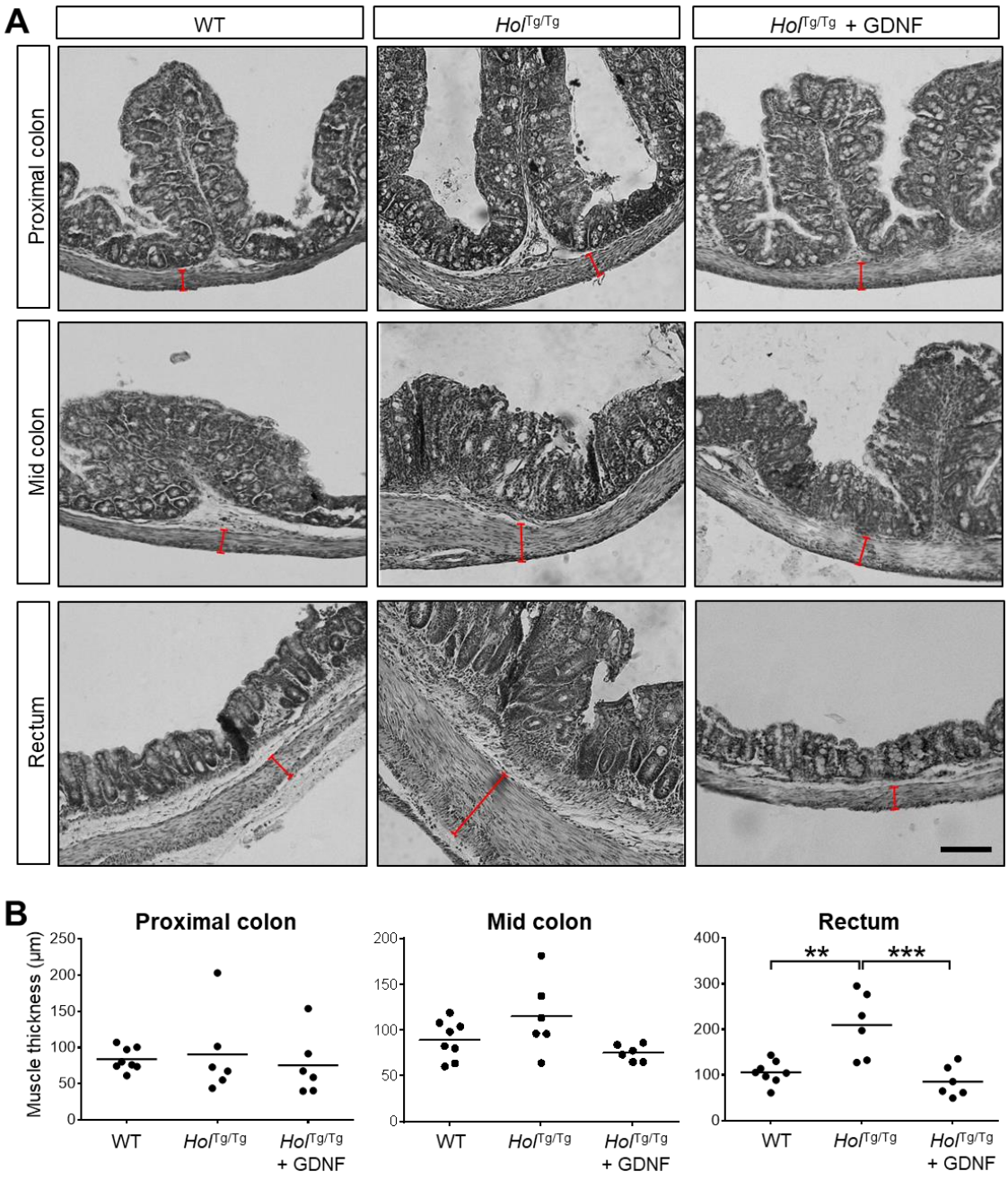

Supplementary Figure 4.7: Analysis of smooth muscle thickness in the distal colon of WT, untreated *Hol*$^{Tg/Tg}$ or GDNF-treated *Hol*$^{Tg/Tg}$ mice at P20

(A) *Representative* H&E-stained cross-sections of different colon segments, with smooth muscle thickness indicated by red brackets. Scale bar, 150 µm. **(B)** Average muscle thickness for each colon segment (n=6 mice per group; ***P*<0.01; ****P*<0.001; one-way ANOVA with post-hoc Tukey's test). GDNF-treated mice received 10µg GDNF in 10µL enemas once daily between P4-P8.

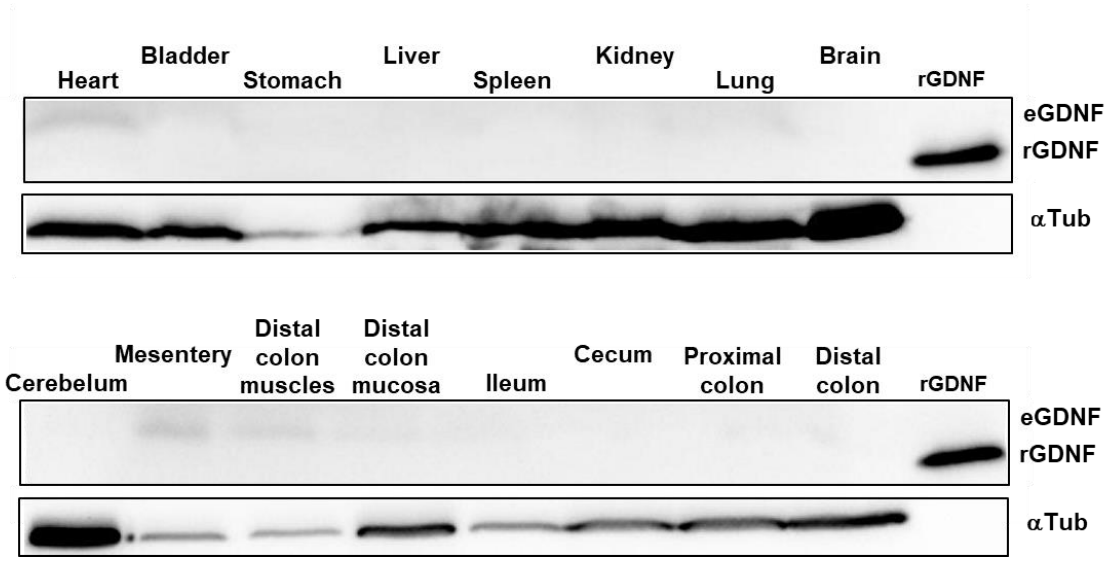

Supplementary Figure 4.8: Analysis of GDNF distribution in multiple tissues of GDNF-treated *Hol*$^{Tg/Tg}$ mice at P20

Western bolt analysis of □Tubulin-normalized levels of endogenous GDNF (eGDNF) and recombinant GDNF (rGDNF) in different tissues of P20 *Hol*$^{Tg/Tg}$ mice that received 10µg GDNF in 10µL enemas once daily between P4-P8. The displayed blots are representative of observations made from 3 mice.

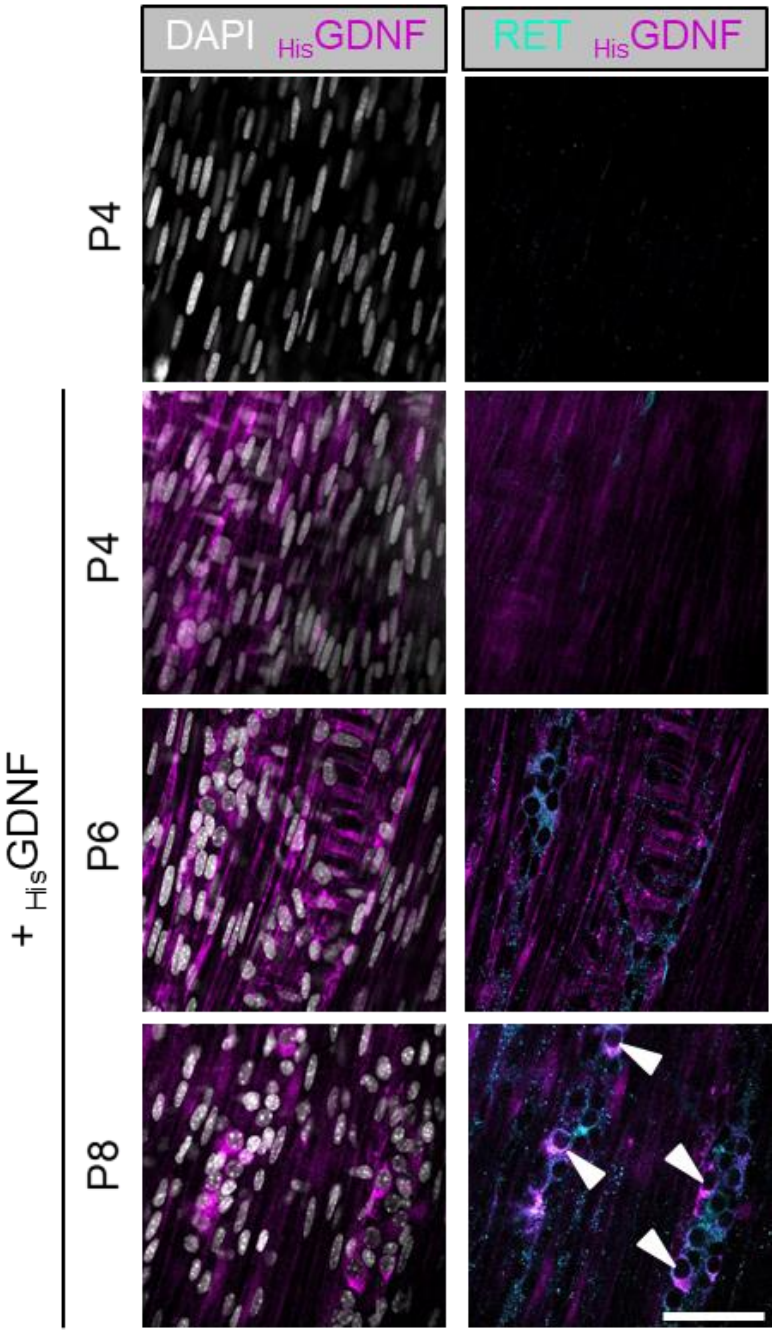

Supplementary Figure 4.9: Time-course analysis of $_{His}$GDNF distribution and RET expression in colonic smooth muscles of P4-P8 *Hol*$^{Tg/Tg}$ mice treated with $_{His}$GDNF

Immunofluorescence analysis of $_{His}$GDNF distribution and RET expression in distal colon muscularis of $_{His}$GDNF-treated *Hol*$^{Tg/Tg}$ mice. White arrowheads point to RET^{+} neurons that also stain positive for $_{His}$GDNF. All images show a single focal plane representative of observations made from 3 mice. Scale bar, 20µm.

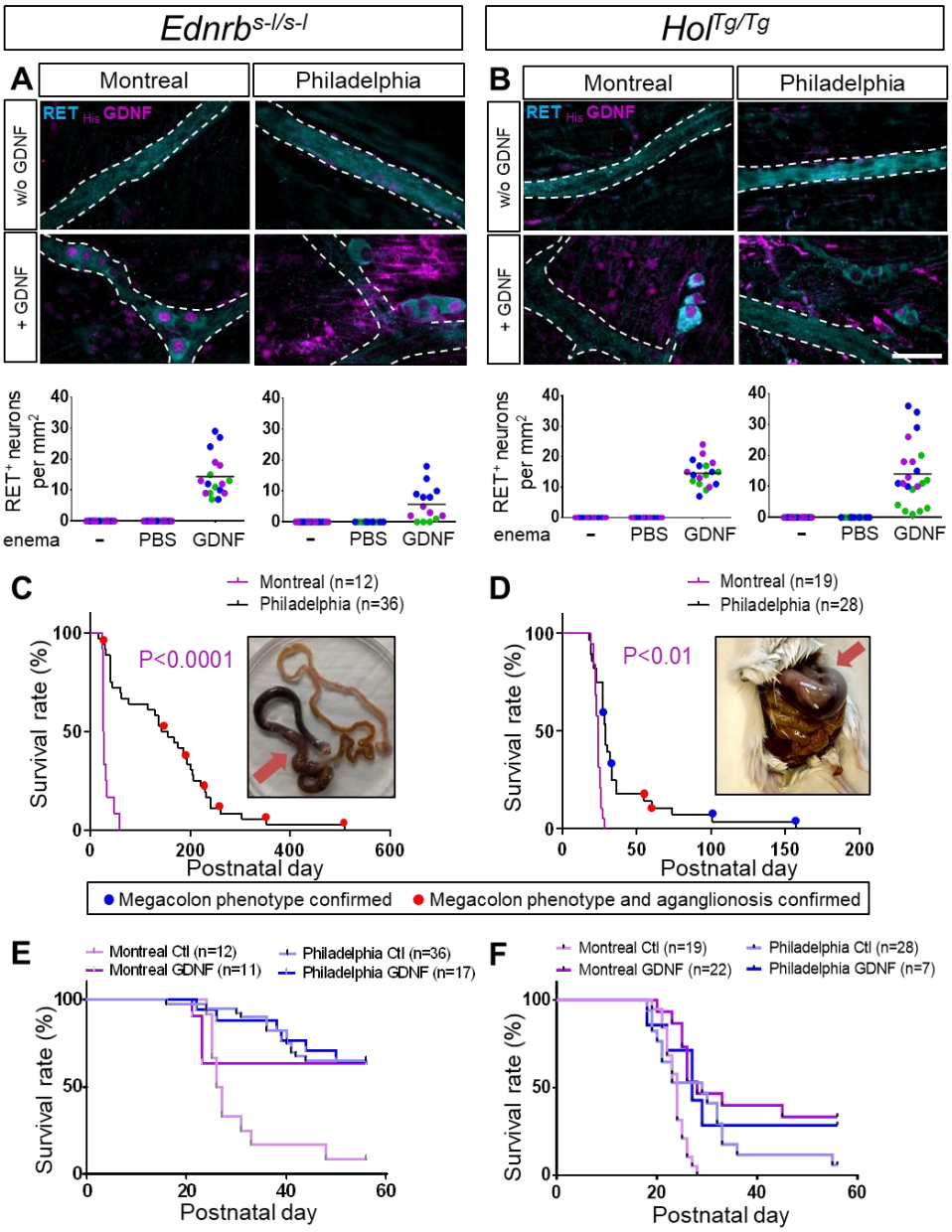

Supplementary Figure 4.10: GDNF enemas trigger enteric neurogenesis without prolonging already extended survival of HSCR mouse models in Philadelphia

(**A-B)** In both Montreal and Philadelphia, daily administration of $_{His}$GDNF enemas (10µg $_{His}$GDNF in 10µL of PBS) between P4-P8 trigger enteric neurogenesis in both *Ednrb*$^{s-l/s-l}$ (**A**) and *Hol*$^{Tg/Tg}$ (**B**) mice (in support of **Figure 4.4C**). Upper panels are representative images of immunolabeled distal colons (last cm) at P8 showing the presence of RET and $_{His}$GDNF double-positive myenteric neurons close to an extrinsic nerve fiber (dashed outlines; Scale bar, 50µm). Lower panels are quantitative analyses with results expressed in number of RET^{+} myenteric neurons per mm^2. Each dot corresponds to a field of view, with color code meaning that samples were from the same animal

(n=3 for GDNF enemas; n=2 for untreated and PBS enemas; 4-8 fields of view per animal). **(C-D)** Untreated *Ednrb*$^{s\text{-}l/s\text{-}l}$ (**C**) and *Hol*$^{Tg/Tg}$ (**D**) mice live longer in Philadelphia than in Montreal. For many mice that were found dead, megacolon phenotype (distended feces-filled colon, as shown in insets) was visually confirmed (marked by red dots). In addition, some moribund mice were euthanized in order to prevent colon tissue alteration, thereby allowing to confirm distal aganglionosis by HuC-TuJ1 double-immunofluorescence (marked by blue dots). (**E-F**) For both *Ednrb*$^{s\text{-}l/s\text{-}l}$ (**E**) and *Hol*$^{Tg/Tg}$ (**F**) mice, GDNF treatment in Montreal increases survival to rates seen in untreated mice in Philadelphia ($P > 0.5$ for GDNF-treated *Ednrb*$^{s\text{-}l/s\text{-}l}$ mice in Montreal versus untreated *Ednrb*$^{s\text{-}l/s\text{-}l}$ mice in Philadelphia; $P > 0.7$ for GDNF-treated *Hol*$^{Tg/Tg}$ mice in Montreal versus untreated *Hol*$^{Tg/Tg}$ mice in Philadelphia). GDNF treatment did not further enhance the survival advantage of *Ednrb*$^{s\text{-}l/s\text{-}l}$ and *Hol*$^{Tg/Tg}$ mice in Philadelphia ($P > 0.9$ for untreated *Ednrb*$^{s\text{-}l/s\text{-}l}$ mice in Philadelphia versus GDNF-treated *Ednrb*$^{s\text{-}l/s\text{-}l}$ mice in Philadelphia; $P > 0.5$ for untreated *Hol*$^{Tg/Tg}$ mice in Philadelphia versus GDNF-treated *Hol*$^{Tg/Tg}$ mice in Philadelphia). Log-rank (Mantel-Cox) and Gehan-Breslow-Wilcoxon tests.

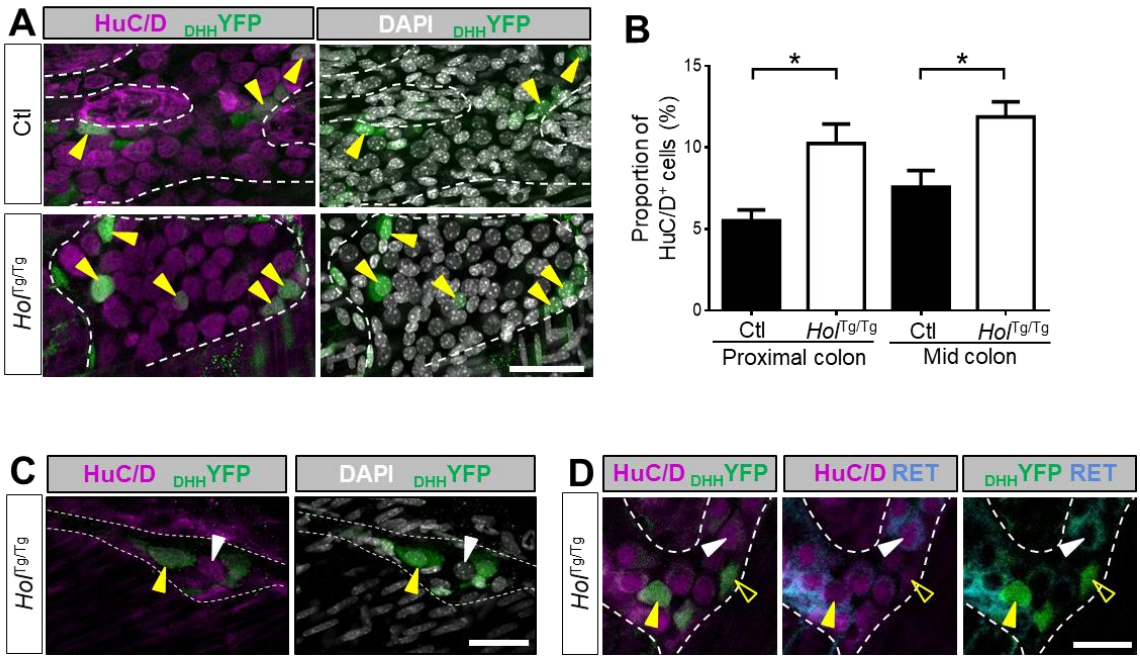

Supplementary Figure 4.11: Analysis of Schwann cell lineage-derived neurogenesis in myenteric and submucosal ganglia of *Dhh-Cre*$^{Tg/+}$;*R26*$^{YFP/+}$ and *Hol*$^{Tg/Tg}$;*Dhh-Cre*$^{Tg/+}$;*R26*$^{YFP/+}$ mice at P20

(A) Analysis of myenteric neurons (HuC/D$^+$) and YFP expression in the proximal colon of *Dhh-Cre*$^{Tg/+}$;*R26*$^{YFP/+}$ (Ctl) and *Hol*$^{Tg/Tg}$;*Dhh-Cre*$^{Tg/+}$;*R26*$^{YFP/+}$ (*Hol*$^{Tg/Tg}$) mice. Yellow arrowheads point to Schwann lineage-derived neurons. **(B)** Quantitative analyses of myenteric neurons (HuC/D$^+$) that are YFP+ in the proximal and mid-colon of *Dhh-Cre*$^{Tg/+}$;*R26*$^{YFP/+}$ (Ctl) and *Hol*$^{Tg/Tg}$;*Dhh-Cre*$^{Tg/+}$;*R26*$^{YFP/+}$ (*Hol*$^{Tg/Tg}$) mice (n=3 Ctl and 3 *Hol*$^{Tg/Tg}$ mice; 3 fields of view per animal; *P<0.05; one-way ANOVA with post-hoc Sidak's test). **(C)** Analysis of submucosal neurons (HuC/D$^+$) and YFP expression in the distal colon of *Hol*$^{Tg/Tg}$;*Dhh-Cre*$^{Tg/+}$;*R26*$^{YFP/+}$ (*Hol*$^{Tg/Tg}$) mice that were treated with GDNF between P4-P8. Neurons of either Schwann lineage (yellow arrowhead) or unknown (white arrowhead) origin are detected. **(D)** Analysis of RET-expressing myenteric neurons (HuC/D$^+$) and YFP expression in the distal colon of *Hol*$^{Tg/Tg}$;*Dhh-Cre*$^{Tg/+}$;*R26*$^{YFP/+}$ (*Hol*$^{Tg/Tg}$) mice that were treated with GDNF between P4-P8. RET is expressed in a subset of neurons, regardless of Schwann lineage (RET$^+$, filled yellow arrowhead; RET$^-$, empty yellow arrowhead) or non-Schwann lineage (white arrowhead) origin. All displayed images are z-stack projections representative of observations made from 3 mice. Scale bar, 50µm. Dashed outline marks area occupied by a single ganglion.

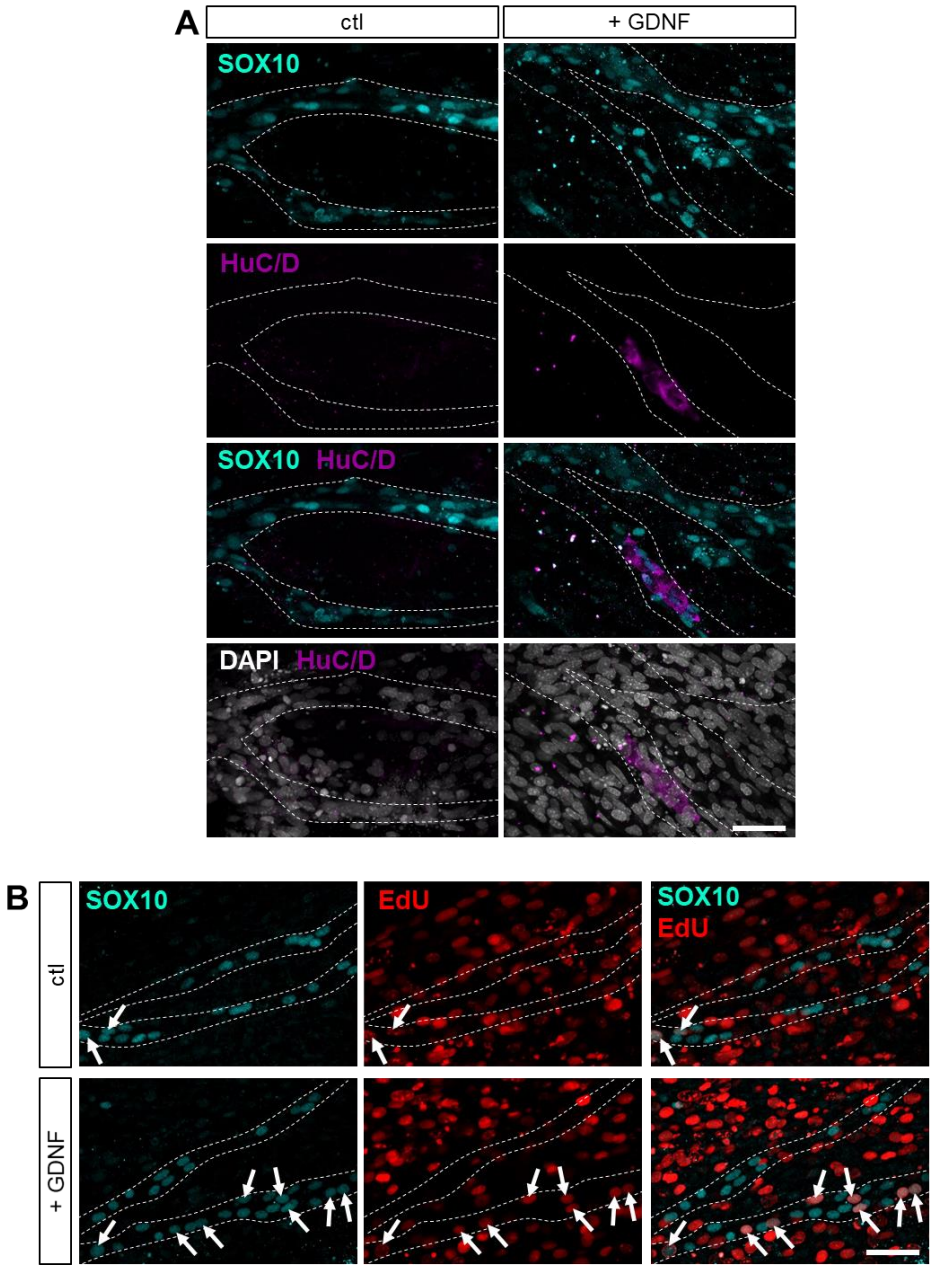

Supplementary Figure 4.12: Analysis of neurogenesis and Schwann cell proliferation in distal colon explants from P4 Hol$^{Tg/Tg}$ mice and cultured in the presence or absence of GDNF for 96h

(A-B) Representative images of HuC/D^{+} neurons (**A**), and EdU^{+} SOX10^{+} proliferating Schwann cells (arrows in **B**) in explants of distal colon from *Hol*$^{Tg/Tg}$ mice cultured in presence of GDNF and EdU (+GDNF) or EdU alone (ctl). The displayed images are single focal planes representative of observations made from 7 mice. Scale bar, 50µm. Dashed outline marks area occupied by extrinsic nerve fibers.

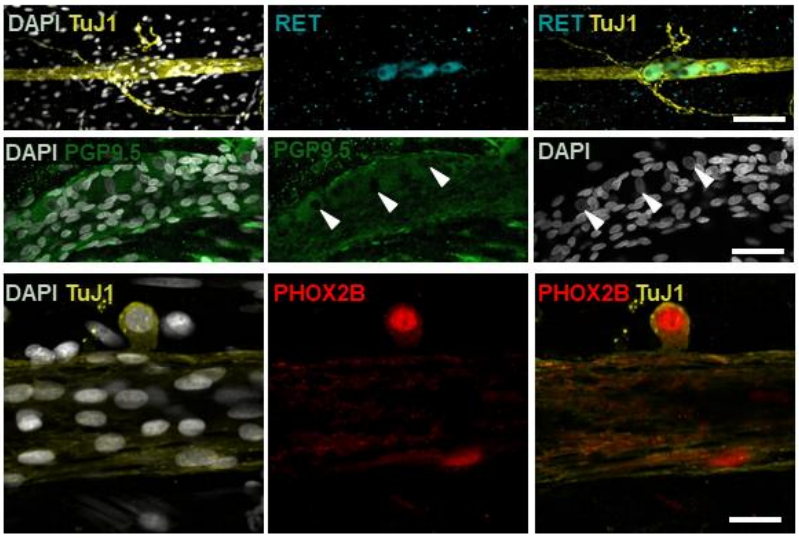

Supplementary Figure 4.13: Marker analysis of GDNF-induced neurons in sigmoid colon explants prepared from HSCR patients and cultured in presence of GDNF for 96h
Immunofluorescence analysis showing that human GDNF-induced neurons are closely associated with extrinsic nerves and express βIII-Tubulin (TuJ1), RET, PGP9.5 and PHOX2B (in support of Figure 4.5F). Arrowheads in middle panels point to round/ovoid nuclei of PGP9.5^{+} neurons. The displayed images are single focal planes representative of observations made from 3 human samples. Scale bar, 100µm (upper panels), 50µm (middle panels) and 25µm (lower panels).

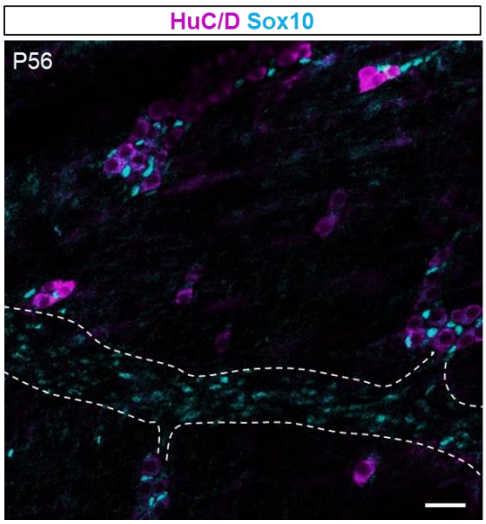

Supplementary Figure 4.14: GDNF-induced myenteric ganglia are self-sustaining until adulthood
Immunofluorescence analysis of HuC/D and SOX10 expression in myenteric ganglia from distal colon of GDNF-treated *Hol*$^{Tg/Tg}$ mice at P56. The displayed image is a single focal plane representative of observations made from 3 mice. Scale bar, 50µm.

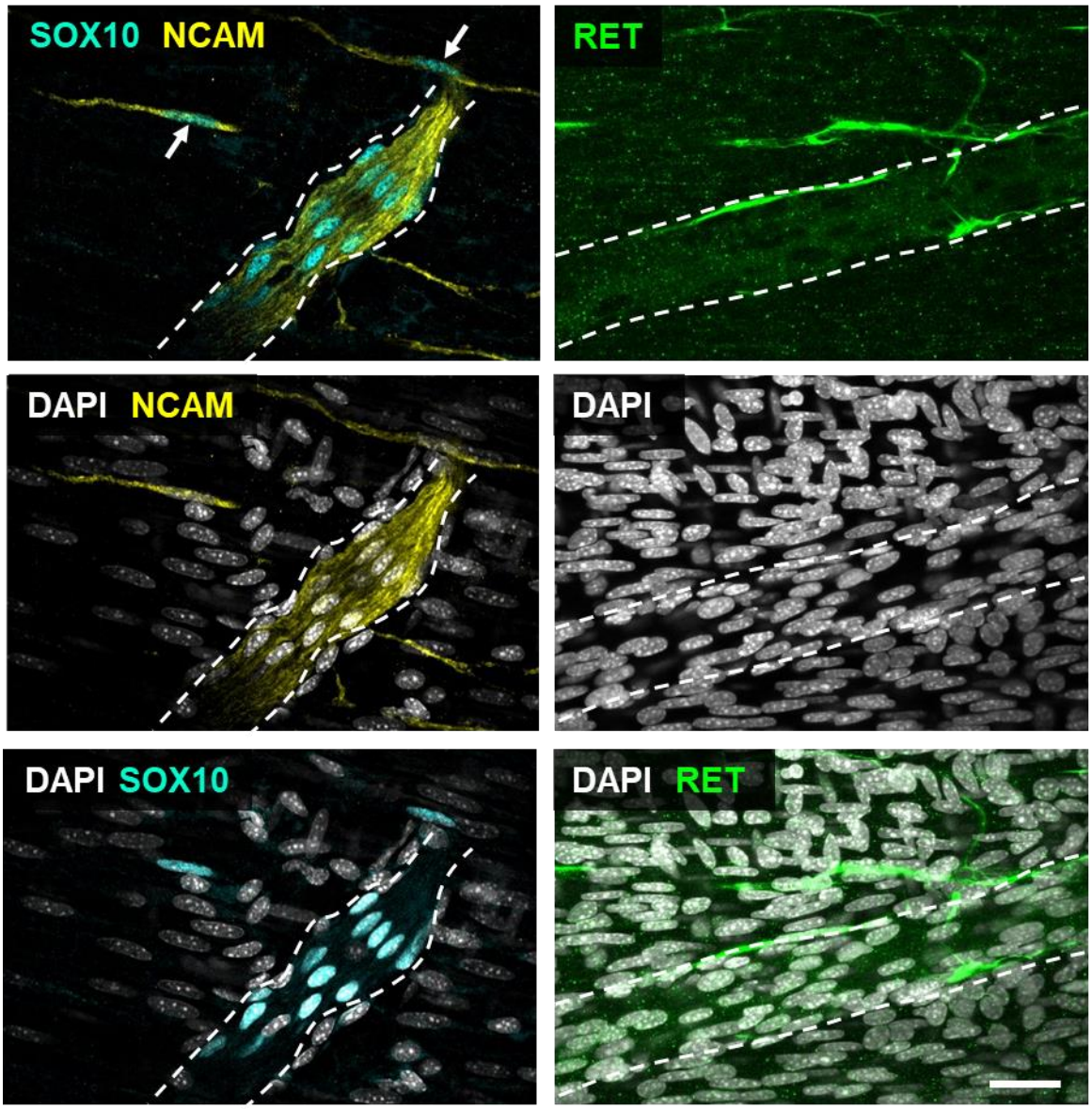

Supplementary Figure 4.15: Schwann cells in the aganglionic distal colon of *Hol*$^{Tg/Tg}$ mice express NCAM but not RET

Immunofluorescence analysis of NCAM and RET expression in extrinsic nerve fibers (delineated by dashed lines) from distal colon of untreated *Hol*$^{Tg/Tg}$ mice at P20. NCAM but not RET is expressed in SOX10^{+} Schwann cells and putative enteric glia/ENS progenitors (arrows). The displayed images are single focal planes representative of observations made from 3 mice. Scale bar, 50µm.

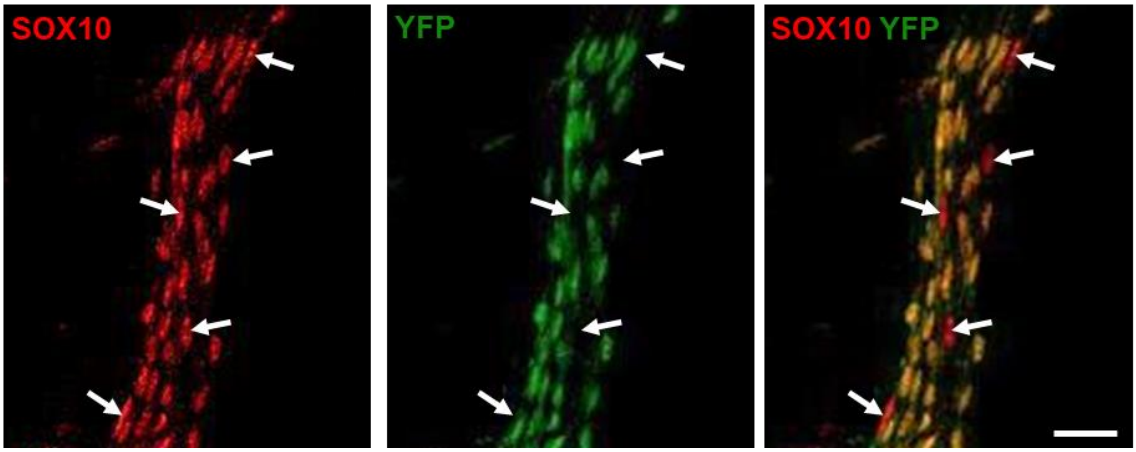

Supplementary Figure 4.16: Schwann cells in the aganglionic distal colon of *Hol*$^{Tg/Tg}$;*Dhh-Cre*$^{Tg/+}$;*R26*$^{YFP/+}$ mice are not all YFP-labeled

Immunofluorescence analysis of SOX10 and YFP expression in an extrinsic nerve fiber from distal colon of untreated *Hol*$^{Tg/Tg}$;*Dhh-Cre*$^{Tg/+}$;*R26*$^{YFP/+}$mice at P8. A subset of SOX10^{+} Schwann cells are negative for YFP (arrows). The displayed images are single focal planes representative of observations made from 3 mice. Scale bar, 50µm.

Supplementary Table 4.1. Rationale for selection of supplemental neurotrophic molecules

Molecule	Reason for selecting	Reference
Noggin	NSE promoter-driven Noggin overexpression increases enteric neuron numbers in transgenic mice	Chalazonitis et al., *J Neurosci* 2004 (51)
Endothelin-3	Ex vivo culture of avian hindgut in presence of endothelin-3 increases ENS density	Nagy and Goldstein, *Dev Biol* 2006 (52)
RS67506	Systemic administration of the serotonin receptor (5-HT4R) agonist RS67506 triggers enteric neurogenesis in adult mice	Liu et al., *J Neurosci* 2009 (53)
Serotonin	Serotonin (5-HT) enhances *in vitro* neuronal differentiation of murine enteric neural precursors	Fiorica-Howells et al., *J Neurosci* 2000 (54)
Vitamin C	Ascorbic acid is needed for *in vitro* differentiation and maturation of human enteric neural precursors	Fattahi et al., *Nature* 2016 (55)

Supplementary Table 4.2. List of primary antibodies and dilution factors used for immunofluorescence

Antibody	Source	Catalog number	RRID reference	Dilution
6X His	R&D systems	MAB050	AB_357353	1:500
CalR	Swant,	CG1	AB_10000342	1:500
ChAT	Millipore	AB144P	AB_2079751	1:100
GFP	Abcam	Ab290	AB_303395	1:500
HuC/D	Molecular Probes	A-21271	AB_221448	1:500
HuC/D (ANNA-1)	Gift from Vanda Lennon	---	AB_2313944	1:2000
Ki67	Abcam	ab15580	AB_443209	1:500
NCAM	Abcam	ab5032	AB_2291692	1:500
NOS1	Santa Cruz Biotechnology	sc-648	AB_630935	1:200
PHOX2B	R&D systems	AF4940	---	1:250
RET	R&D systems	MAB718	AB_2232594	1:500
SOX10	Santa Cruz Biotechnology	sc-17342	AB_2195374	1:200
SubP	Abcam	ab67006	AB_1143173	1:500
TH	Abcam	ab137869	---	1:500
TUJ1	Covance	MRB-435P	AB_663339	1:1000
VIP	Abcam	ab8556	AB_306628	1:500

4.10 References

1. Furness JB. The enteric nervous system and neurogastroenterology. Nat Rev Gastroenterol Hepatol 2012;9:286-94.
2. Heuckeroth RO. Hirschsprung disease - integrating basic science and clinical medicine to improve outcomes. Nat Rev Gastroenterol Hepatol 2018;15:152-167.
3. Heuckeroth RO, Schafer KH. Gene-environment interactions and the enteric nervous system: Neural plasticity and Hirschsprung disease prevention. Dev Biol 2016;417:188-97.
4. Gianino S, Grider JR, Cresswell J, et al. GDNF availability determines enteric neuron number by controlling precursor proliferation. Development 2003;130:2187-98.
5. Natarajan D, Marcos-Gutierrez C, Pachnis V, et al. Requirement of signalling by receptor tyrosine kinase RET for the directed migration of enteric nervous system progenitor cells during mammalian embryogenesis. Development 2002;129:5151-60.
6. Young HM, Hearn CJ, Farlie PG, et al. GDNF is a chemoattractant for enteric neural cells. Dev Biol 2001;229:503-16.
7. Tang CS, Li P, Lai FP, et al. Identification of Genes Associated With Hirschsprung Disease, Based on Whole-Genome Sequence Analysis, and Potential Effects on Enteric Nervous System Development. Gastroenterology 2018;155:1908-1922 e5.
8. Emison ES, Garcia-Barcelo M, Grice EA, et al. Differential contributions of rare and common, coding and noncoding Ret mutations to multifactorial Hirschsprung disease liability. Am J Hum Genet 2010;87:60-74.
9. Tilghman JM, Ling AY, Turner TN, et al. Molecular Genetic Anatomy and Risk Profile of Hirschsprung's Disease. N Engl J Med 2019;380:1421-1432.
10. Gui H, Schriemer D, Cheng WW, et al. Whole exome sequencing coupled with unbiased functional analysis reveals new Hirschsprung disease genes. Genome Biol 2017;18:48.

11. Tang CS, Zhuang X, Lam WY, et al. Uncovering the genetic lesions underlying the most severe form of Hirschsprung disease by whole-genome sequencing. Eur J Hum Genet 2018;26:818-826.
12. Swenson O, Bill AH, Jr. Resection of rectum and rectosigmoid with preservation of the sphincter for benign spastic lesions producing megacolon; an experimental study. Surgery 1948;24:212-20.
13. Burns AJ, Goldstein AM, Newgreen DF, et al. White paper on guidelines concerning enteric nervous system stem cell therapy for enteric neuropathies. Dev Biol 2016;417:229-51.
14. McCann CJ, Borrelli O, Thapar N. Stem cell therapy in severe pediatric motility disorders. Curr Opin Pharmacol 2018;43:145-149.
15. Yntema CL, Hammond WS. The origin of intrinsic ganglia of trunk viscera from vagal neural crest in the chick embryo. J Comp Neurol 1954;101:515-41.
16. Hotta R, Anderson RB, Kobayashi K, et al. Effects of tissue age, presence of neurones and endothelin-3 on the ability of enteric neurone precursors to colonize recipient gut: implications for cell-based therapies. Neurogastroenterol Motil 2010;22:331-e86.
17. Le Douarin NM, Teillet MA. The migration of neural crest cells to the wall of the digestive tract in avian embryo. J Embryol Exp Morphol 1973;30:31-48.
18. Uesaka T, Nagashimada M, Enomoto H. Neuronal Differentiation in Schwann Cell Lineage Underlies Postnatal Neurogenesis in the Enteric Nervous System. J Neurosci 2015;35:9879-88.
19. Watanabe Y, Ito F, Ando H, et al. Morphological investigation of the enteric nervous system in Hirschsprung's disease and hypoganglionosis using whole-mount colon preparation. J Pediatr Surg 1999;34:445-9.
20. Paratcha G, Ledda F, Ibanez CF. The neural cell adhesion molecule NCAM is an alternative signaling receptor for GDNF family ligands. Cell 2003;113:867-79.

21. Sjostrand D, Ibanez CF. Insights into GFRalpha1 regulation of neural cell adhesion molecule (NCAM) function from structure-function analysis of the NCAM/GFRalpha1 receptor complex. J Biol Chem 2008;283:13792-8.

22. Lake JI, Tusheva OA, Graham BL, et al. Hirschsprung-like disease is exacerbated by reduced de novo GMP synthesis. J Clin Invest 2013;123:4875-87.

23. Creedon DJ, Tansey MG, Baloh RH, et al. Neurturin shares receptors and signal transduction pathways with glial cell line-derived neurotrophic factor in sympathetic neurons. Proc Natl Acad Sci U S A 1997;94:7018-23.

24. Toure AM, Landry M, Souchkova O, et al. Gut microbiota-mediated Gene-Environment interaction in the TashT mouse model of Hirschsprung disease. Sci Rep 2019;9:492.

25. Soret R, Mennetrey M, Bergeron KF, et al. A collagen VI-dependent pathogenic mechanism for Hirschsprung's disease. J Clin Invest 2015;125:4483-96.

26. Bergeron KF, Cardinal T, Toure AM, et al. Male-Biased Aganglionic Megacolon in the TashT Mouse Line Due to Perturbation of Silencer Elements in a Large Gene Desert of Chromosome 10. PLoS Genet 2015;11:e1005093.

27. Hosoda K, Hammer RE, Richardson JA, et al. Targeted and natural (piebald-lethal) mutations of endothelin-B receptor gene produce megacolon associated with spotted coat color in mice. Cell 1994;79:1267-76.

28. Schuchardt A, D'Agati V, Larsson-Blomberg L, et al. Defects in the kidney and enteric nervous system of mice lacking the tyrosine kinase receptor Ret. Nature 1994;367:380-3.

29. Cheng LS, Schwartz DM, Hotta R, et al. Bowel dysfunction following pullthrough surgery is associated with an overabundance of nitrergic neurons in Hirschsprung disease. J Pediatr Surg 2016;51:1834-1838.

30. Ro S, Hwang SJ, Muto M, et al. Anatomic modifications in the enteric nervous system of piebald mice and physiological consequences to colonic motor activity. Am J Physiol Gastrointest Liver Physiol 2006;290:G710-8.

31. Toure AM, Charrier B, Pilon N. Male-specific colon motility dysfunction in the TashT mouse line. Neurogastroenterol Motil 2016;28:1494-507.

32. Zaitoun I, Erickson CS, Barlow AJ, et al. Altered neuronal density and neurotransmitter expression in the ganglionated region of Ednrb null mice: implications for Hirschsprung's disease. Neurogastroenterol Motil 2013;25:e233-44.

33. Pilon N, Raiwet D, Viger RS, et al. Novel pre- and post-gastrulation expression of Gata4 within cells of the inner cell mass and migratory neural crest cells. Dev Dyn 2008;237:1133-43.

34. Shimotake T, Go S, Inoue K, et al. A homozygous missense mutation in the tyrosine E kinase domain of the RET proto-oncogene in an infant with total intestinal aganglionosis. Am J Gastroenterol 2001;96:1286-91.

35. Zhang DK, He FQ, Li TK, et al. Glial-derived neurotrophic factor regulates intestinal epithelial barrier function and inflammation and is therapeutic for murine colitis. J Pathol 2010;222:213-22.

36. Belkind-Gerson J, Hotta R, Nagy N, et al. Colitis induces enteric neurogenesis through a 5-HT4-dependent mechanism. Inflamm Bowel Dis 2015;21:870-8.

37. Fujimoto T. Natural history and pathophysiology of enterocolitis in the piebald lethal mouse model of Hirschsprung's disease. J Pediatr Surg 1988;23:237-42.

38. Kruger GM, Mosher JT, Bixby S, et al. Neural crest stem cells persist in the adult gut but undergo changes in self-renewal, neuronal subtype potential, and factor responsiveness. Neuron 2002;35:657-69.

39. Laranjeira C, Sandgren K, Kessaris N, et al. Glial cells in the mouse enteric nervous system can undergo neurogenesis in response to injury. J Clin Invest 2011;121:3412-24.

40. Badizadegan K, Thomas AR, Nagy N, et al. Presence of intramucosal neuroglial cells in normal and aganglionic human colon. Am J Physiol Gastrointest Liver Physiol 2014;307:G1002-12.

41. Wilkinson DJ, Bethell GS, Shukla R, et al. Isolation of Enteric Nervous System Progenitor Cells from the Aganglionic Gut of Patients with Hirschsprung's Disease. PLoS One 2015;10:e0125724.

42. Burns AJ, Champeval D, Le Douarin NM. Sacral neural crest cells colonise aganglionic hindgut in vivo but fail to compensate for lack of enteric ganglia. Dev Biol 2000;219:30-43.

43. Srinivas S, Watanabe T, Lin CS, et al. Cre reporter strains produced by targeted insertion of EYFP and ECFP into the ROSA26 locus. BMC Dev Biol 2001;1:4.

44. Enomoto H, Crawford PA, Gorodinsky A, et al. RET signaling is essential for migration, axonal growth and axon guidance of developing sympathetic neurons. Development 2001;128:3963-74.

45. Jain S, Naughton CK, Yang M, et al. Mice expressing a dominant-negative Ret mutation phenocopy human Hirschsprung disease and delineate a direct role of Ret in spermatogenesis. Development 2004;131:5503-13.

46. Boulende Sab A, Bouchard MF, Beland M, et al. An Ebox element in the proximal Gata4 promoter is required for Gata4 expression in vivo. PLoS ONE 2011;6:e29038.

47. Laforest-Lapointe I, Paquette A, Messier C, et al. Leaf bacterial diversity mediates plant diversity and ecosystem function relationships. Nature 2017;546:145-147.

48. Schloss PD, Westcott SL, Ryabin T, et al. Introducing mothur: open-source, platform-independent, community-supported software for describing and comparing microbial communities. Appl Environ Microbiol 2009;75:7537-41.

49. McDonald D, Clemente JC, Kuczynski J, et al. The Biological Observation Matrix (BIOM) format or: how I learned to stop worrying and love the ome-ome. Gigascience 2012;1:7.

50. Team RC. R: A language and environment for statistical computing. R Foundation for Statistical Computing, Vienna, Austria. 2014.

51. Chalazonitis A, D'Autreaux F, Guha U, et al. Bone morphogenetic protein-2 and -4 limit the number of enteric neurons but promote development of a TrkC-expressing neurotrophin-3-dependent subset. J Neurosci 2004;24:4266-82.

52. Nagy N, Goldstein AM. Endothelin-3 regulates neural crest cell proliferation and differentiation in the hindgut enteric nervous system. Dev Biol 2006;293:203-17.

53. Liu MT, Kuan YH, Wang J, et al. 5-HT4 receptor-mediated neuroprotection and neurogenesis in the enteric nervous system of adult mice. J Neurosci 2009;29:9683-99.

54. Fiorica-Howells E, Maroteaux L, Gershon MD. Serotonin and the 5-HT(2B) receptor in the development of enteric neurons. J Neurosci 2000;20:294-305.

55. Fattahi F, Steinbeck JA, Kriks S, et al. Deriving human ENS lineages for cell therapy and drug discovery in Hirschsprung disease. Nature 2016.

CHAPTER 5: THE EPIGENETIC REGULATOR BAP1 IS REQUIRED FOR MAINTENANCE OF POSTNATAL ENTERIC NERVOUS SYSTEM ANATOMY AND FUNCTION BUT NOT EMBRYONIC ENTERIC NERVOUS SYSTEM FORMATION

This manuscript is being prepared for publication. In this chapter we present progress towards understanding the role of epigenetic regulator Bap1 in murine enteric nervous system development and postnatal function. Authors: Sabine Schneider, Jessica B. Anderson, Rebecca P. Bradley, Christina M. Wright, J. William Harbour, Robert O. Heuckeroth

5.1 Abstract

Epigenetic regulatory mechanisms are underappreciated but likely critical for the development of the enteric nervous system. We decided to explore the role of the epigenetic regulator *Bap1* in ENS development after a serendipitous discovery that embryonic *Bap1* loss causes drastic bowel dysfunction and early death. *Bap1* has well-defined roles in cancer genesis, however, its role in development is still barely understood. In this study, we report that deletion of *Bap1* in enteric neural precursors does not affect enteric neural precursor migration or neonatal proximal small intestine motility and enteric neuron density. However, by postnatal day 15, *in vitro* and *in vivo* bowel motility as well as myenteric and submucosal enteric neuron density is significantly reduced in both small and large intestines. This loss of enteric neuron density can be partially explained by loss of neurons derived from *Bap1-/-* enteric neuron precursors. However, tamoxifen-induced postnatal deletion of *Bap1* in most enteric neurons in either early life or adulthood does not cause obvious morbidity. We are now working on elucidating the mechanism through which embryonic *Bap1* loss causes postnatal ENS dysfunction.

5.2 Introduction

The enteric nervous system (ENS) is a complex network of neurons and glia that resides within the bowel wall. The ENS rivals the spinal cord in complexity, with more than 20 neuron subtypes and at least four glial subtypes forming the basis of repeating neural circuits along the length of the bowel (1–3). Enteric neural circuits regulate crucial bowel functions like fluid homeostasis across the epithelium, epithelial homeostasis, blood flow within the bowel wall, immune system activity, and coordinated smooth muscle contraction and relaxation (3–5). Due to its vital role in bowel health, dysfunction of the ENS has devastating consequences. Congenital or acquired defects in enteric nervous system function, also called enteric neuropathies, most notably disrupt the propulsive gut smooth muscle contractions. This causes abdominal distention, constipation, vomiting, pain, and in some cases sepsis and early death (6–8).

The most severe congenital ENS defect, Hirschsprung disease, is caused by incomplete migration of enteric neuron precursors from the proximal to the distal end of the developing embryonic bowel (6, 9). Hirschsprung disease is thus characterized by a complete lack of enteric neurons at the distal end of the bowel. If the ENS forms along the entire length of the bowel, but there are no or only subtle anatomic abnormalities, the enteric neuropathy is called chronic intestinal pseudo-obstruction (CIPO). A number of causative gene mutations and genomic risk loci for Hirschsprung disease have been identified over the past few decades (9–12). Two examples that have been studied extensively are loss of *EDNRB* (13–18) and *SOX10* (19–23), two monogenic causes of Hirschsprung disease. However, only a few genetic causes of neuropathic CIPO have been identified in humans (*SOX10* (24), *FLNA* (25), *SGOL1* (26), *RAD21* (27), and mitochondrial genes *POLG* and *TYMP* (28)). Cumulatively, these genes only explain a small proportion of the total number of CIPO cases (29). A number of recent studies have advanced our understanding of gene expression in enteric neuron subtypes at different stages of ENS development ((22, 30–32) and Chapter 2) and greatly increased the number of possible candidate

CIPO risk loci. A handful of genes are now also known to affect enteric neuron subtype differentiation and function in mice (30, 31, 33–37).

Neural crest precursors undergo drastic changes in cell identity during their migration and differentiation into the many cell types of the ENS. These changes include epithelial-to-mesenchymal transition to become multipotent migratory neural crest precursors (38, 39), a transition to migratory multipotent enteric neural crest precursors that gives rise to immature enteric neurons and glia (40), and ultimately neural precursors make fate decisions to become specialized enteric neuron subtypes (31, 40). All of these processes require epigenetic reorganization of the chromatin landscape and coordinated transcriptional regulation of cell type and developmental stage-specific gene sets (41, 42).

Epigenetic regulatory mechanisms are likely critical for the development of the ENS. For example, loss of *Aebp2* and *Ezh2*, subunits of the epigenetic regulator complex polycomb repressor complex 2 (PRC2) in mouse enteric neuron precursors cause Hirschsprung Disease (43, 44). DNA Methyltransferase 3b (*Dnmt3b*), an enzyme necessary for the generation of important epigenetic marks, has also been implicated in ENS development (45). However, given the obvious importance of epigenetic mechanisms in ENS development, the dearth of knowledge about specific epigenetic mechanisms involved in ENS formation is surprising. We were thus intrigued by the serendipitous discovery that deletion of the epigenetic regulator *Bap1* in the ENS leads to bowel dysfunction and early death in mice. Elucidating the role of *Bap1* in enteric nervous system development and function will add to the critical fund of ENS biology knowledge needed to ultimately develop curative therapies for ENS-related human diseases like Hirschsprung disease and CIPO.

BAP1 is a deubiquitinase and well-known tumor suppressor gene with diverse nuclear and cytoplasmic functions within the cell (46, 47). As a nuclear protein, BAP1 is involved in DNA replication fork elongation (48) and double-stranded DNA damage repair (49, 50). BAP1 also regulates gene expression. In association with other transcription factors, it can act as a transcriptional activator or repressor itself (51, 52), it can change the activity of other transcription

factors indirectly through its deubiquitinase activity (53, 54), and it can change gene expression patterns at a larger scale as an epigenetic regulator (55–57). In the cytoplasm, BAP1 regulates intrinsic apoptosis initiation through its deubiquitinase activity (46). However, BAP1's role in development is not well understood. Global knock-out of *Bap1* leads to early embryonic lethality in mice (52). In xenopus, Bap1 is required for lineage commitment of pluripotent cells to the germ layers and neural crest lineages (55). Intriguingly, loss of *Bap1* in uveal melanoma cells causes downregulation of HSCR-associated genes *Sox10* and *Ednrb* (58). *Bap1* also has a role in regulating retinoic acid-induced gene expression (57, 59). Reduced retinoic acid signaling is a known cause of Hirschsprung disease (60–62). Therefore, we hypothesized that *Bap1* knockout in the enteric nervous system would lead to disrupted migration of enteric neuron precursors resulting in Hirschsprung disease.

To investigate the role of *Bap1* in enteric nervous system development, we used two Cre recombinase driver mouse lines to conditionally delete *Bap1* in different subsets of neural crest derivatives. In *Bap1;Wnt1-Cre* mice, Cre expression is regulated by the *Wnt1* promoter and *Bap1* alleles are excised in all neural crest lineages early in neural crest development after embryonic day 8.5 (E8.5) (63). In *Bap1;Tyr-Cre* mice, Cre recombinase is expressed under the control of the tyrosinase promoter and *Bap1* alleles are excised in the majority of migrating neural crest cells by E 10.5. However, in the adult ENS, only a subset of enteric neurons are still derived from *Tyr-Cre* lineage precursors (64). In this chapter, we present work towards anatomically and functionally defining the ENS defect caused by *Bap1* loss as well as preliminary work towards understanding the underlying mechanisms.

5.3 Methods

Study approval

Studies adhere to ARRIVE (Animals in Research: Reporting In Vivo Experiments) guidelines (65). Mouse experiments were performed in accordance with Institutional Animal Care and Use Committee (IACUC) approval from Children's Hospital of Philadelphia (IACUC#19-001041).

Animals

Bap1tm1.1Geno mice (referred to as *Bap1*; RRID:MGI:5439652, C57BL/6) (66) bred into *Tg(Tyr-cre)1Gfk* mice (referred to as *Tyr-Cre*; RRID:MGI:3580524, C57BL/6) were a kind gift from Dr. J. William Harbour at the University of Miami Miller School of Medicine. *Hdac4tm2.1Eno* mice (referred to as *Hdac4*; RRID: MGI:4418117, C57BL/6) were a kind gift from Dr. Kelly A. Hyndman at the University of Alabama at Birmingham. *Rettm2(cre/ERT2)Ddg* mice (referred to as *Ret-CreERT2*; RRID:MGI:4437245, C57BL/6) were a kind gift from Dr. Jeffrey Milbrandt, Washington University. *H2az2*(*Tg(Wnt1cre)11Rth* mice (referred to as *Wnt1-Cre*; RRID:IMSR_JAX:003829, (C57BL/6J x CBA/J)F1) and *Gt(ROSA)26Sortm9(CAGtdTomato)Hze* mice (referred to as *R26R-TdTomato*; RRID:IMSR_JAX:007909, C57BL/6) were obtained from The Jackson Laboratory (Bar Harbor, ME). *Wnt1-Cre* mice on a mixed background were bred into *R26R-TdTomato* mice on a pure C57BL/6J background and maintained on a mixed (C57BL/6J x CBA/J)F1xC57BL/6 background. *Wnt1-Cre* mice were bred into *Bap1* mice and maintained on a mixed (C57BL/6J x CBA/J)F1xC57BL/6 background. *Bap1* mice were bred into *Tyr-Cre* and maintained on a pure C57BL/6 background. For specific experiments, *Bap1;Tyr-Cre* mice were bred into *R26-TdTomato* mice and maintained in a pure C57BL/6 background. Lastly, *Hdac4* mice were bred into *Bap1;Tyr-Cre;R26-TdTomato* mice and maintained on a pure C57BL/6 background. *Ret-CreERT2* mice were bred to *R26R-TdTomato* and *Bap1* mice and maintained on a pure C57BL/6 background. General animal husbandry information can be found in **Supplementary Table 1**. Genotyping was performed

with previously published and novel primers (**Supplementary Table 3**) and by Transnetyx (Cordova, TN) using tail or ear biopsies. Vaginal plug day was considered day E0.5.

Tamoxifen treatment of *Bap1;Ret-CreERT2;TdTomato* mice

Tamoxifen (20 mg/mL; Sigma, Cat#:T5648) was prepared by first dissolving tamoxifen in 200 µL ethanol at 37°C and then adding 1800 µL sunflower oil (Sigma, Cat#:S5007). Adult *Bap1;Ret-CreERT2;TdTomato* were gavaged with 200 mg/kg tamoxifen once daily on 4 days in a 5 day time window. Nursing dams (starting when litters are at postnatal day 1 to 3) were gavaged with 200 mg/kg tamoxifen once daily on 4 days in a 5 day time window.

Whole Mount Immunofluorescence staining

P0 mice were euthanized by decapitation. P15 mice were euthanized by cervical dislocation. Adult mice were euthanized with carbon dioxide (CO_2, 3 minutes) followed by cervical dislocation. Full-length bowel was removed from the abdominal cavity, placed in 1x PBS, and opened along the mesenteric border. Bowel borders were pinned out serosa-side up to a Sylgard 184 Elastomer (Ellsworth Adhesives, Cat#:184 SIL ELAST KIT 0.5KG) coated plate using insect pins (Fine Science Tools, Cat#:26002-20) and fixed for 20 minutes at RT in 4% paraformaldehyde (PFA; Thermo Fisher, Cat#:O4042-500). After fixation, the tissue was washed 3 times for 5 min each with 1x PBS and stored in 50% glycerol (Sigma, Cat#:G9012-2L)/50% 1x PBS (Quality Biological, Cat#:A611-E404-99) until use at 4°C (if up to a week) or -20°C (if stored longer than one week). When tissue samples were ready to be stained, they were rinsed 3 times for 5 min each in 1x PBS and blocked for 2 hours at RT in 5% normal donkey serum (Jackson ImmunoResearch Laboratories, Cat#:017-000-121) in 0.1-0.5% Triton X-100 (Sigma, Cat#:T8787) in PBS (0.1-0.5% PBST). HuC/D antibody (ANNA1) was incubated with tissue either for 3 hours at RT or overnight at 4°C. The tissue was then transferred into primary antibody after a single 5 min wash in 1x PBS at RT. Primary antibody (see **Supplementary Table 2**) in 5% normal donkey serum in 0.1-0.5%

PBST was incubated with tissue either for 3 hours at RT or overnight at 4°C. The tissue was then washed 3 times for 30min each in 1x PBS and transferred into secondary antibody (see **Supplementary Table 2**) in 5% normal donkey serum in 0.1-0.5% PBST for incubation at RT for 60-90 min. The tissue was then washed 3 times for 30min each in 1x PBS and mounted in 50% glycerol/ 50% 1x PBS on microscope slides (Fisherbrand, Cat#:1255015) using cover slips (ThermoFisher, Cat#:125485P). All incubation and wash steps were performed on a benchtop rocker (Speed 2-4, Cole-Parmer, Cat#:S2035-CP-A).

Immunohistochemistry for paraffin-embedded samples.

Bowel was removed from mice at postnatal day 15, opened at the mesenteric border, and proximal small intestine, distal small intestine, and colon were stretched maximally and pinned out with insect pins. The tissue was fixed in 4% PFA (20 min, RT). The tissue was prepared for paraffin-embedding by briefly washing the tissue in 1x DPBS and then leaving the tissue in 70% Ethanol for at least 3 hours at RT or overnight at 4°C. Pieces of 0.7 cm length were cut from the most proximal and most distal ends of both small intestine and colon.

The tissue was dehydrated and pre-processed for paraffin-embedding using a Thermo Scientific Excelsior Es Processor: 4 stages of graded ethanol 80%, 90%, 100%, 100% (30 min each), then 3 stages of Xylene (30 min, 30 min, 45 min, Sigma, Cat#:EM-XX0060-4), then 3 stages of paraffin (45 min, 30 min, 30 min). Care was taken to embed the tissue in paraffin with as little horizontal or vertical curvature as possible. Tissue sections of 5µm were cut on a HM 355s Microm microtome so that the full 0.7 cm proximo-distal length of the tissue piece is visible in a single section. The tissue sections were then rehydrated (xylene - 3x 5 min, 100% ethanol - 5min, 5 min, 95% ethanol - 5 min, 80% ethanol - 5 min, 70% ethanol - 5 min, dH_2O - 5min) in preparation for immunohistochemical staining.

For hematoxylin and eosin (H&E) staining, the tissue was first stained at hematoxylin (Harris Modified Method Hematoxylin Stains, Fisher, Cat#:SH30-500D - 7 min), then rinsed in tap

water for 5 min, differentiated in 1% acid alcohol (1% concentrated HCl (VWR, Cat# 470301-260) in 70% ethanol, 23 sec), and blued in Scott's tap water substitute concentrate (Scott's tap water; Sigma, Cat#:S5134) for 5 min. The slides were then washed with running tap water a couple of times, dipped in 80% ethanol and directly afterwards transferred into alcoholic Eosin Y Solution (Sigma, Cat#:HT110116) for 60-90s. To finish, the slides were rinsed in fresh dH_2O a couple of times, and then dehydrated (95% Ethanol > 1 min, 95% Ethanol - 2 min, 100% Ethanol - 2 min, Xylene - 2x 2 min) and mounted (Richard-Allan Scientific Cytoseal XYL, ThermoFisher, Cat#:8312-4).

For periodic acid-Schiff/Alcian blue (PAS/AB) staining, the sections were incubated with Alcian blue (pH2.5, RT, 6 min, Sigma, Cat#A5268), then washed in running tap water (2 min), rinsed in dH_2O, treated with 0.5% periodic acid solution (RT, 5 min, Fisher, Cat#:A223-25), and again washed with dH_2O. The slides were subsequently incubated with Schiff's reagent (RT, 15 min, Sigma, Cat#:3952016), washed with running tap water (5min), stained with hematoxylin (45 sec - 1 min), washed again in running tap water (2 min), differentiated with acid alcohol (1% concentrated HCl in 70% ethanol; 22sec), then blued in Scott's tap water (1min), and rinsed in running tap water a couple of times before dehydration (95% Ethanol - 2x 2 min, 100% Ethanol - 2 min, Xylene - 2x 2 min) and mounting (Richard-Allan Scientific Cytoseal XYL, ThermoFisher, Cat#:8312-4).

Colon Bead Expulsion

Adult mice (P95-P210) were anesthetized with 2 L/min carbogen with 2.5% (v/v) isoflurane for 1.5 minutes before start of the experiment, anesthesia was continued until completed bead insertion. A glass bead (3 mm, Sigma, Cat#:Z143928) lubricated with sunflower seed oil (Sigma, Cat#:S5007) was inserted 2 cm into the colon using a custom-made 3-mm rounded glass rod. Mice were placed in empty cages, and time to bead expulsion was recorded. Assay was repeated 3 times per mouse with at least 48 hours between procedures. If a mouse regained consciousness

before bead insertion, mice were anesthetized for an additional 2-4min. If the bead insertion was met with increased resistance due to the presence of feces in the colon, the experiment was halted to allow the mouse to regain consciousness. After 10 minutes the bead insertion was attempted a second time. If there was still resistance, the experiment was not continued on that day and a new attempt was made 48 hours later. Mice were allowed to eat ad libitum before testing.

FITC-Dextran small intestinal transit assay

P15 *Tyr-Cre;Bap1* mice were gavaged with 70-100 µL of 10 mg/mL FITC-Dextran, MW 70,000, (Sigma, Cat#:FD70S) dissolved in 2% methylcellulose (Sigma, Cat:#274429). Mice were kept in a normal cage environment for 90 min post gavage, but without access to their mother or food and water. The mice were then euthanized and the small intestine was cut into 12 segments of equal length. Colon was cut into 5 segments of equal length. The segments were each placed into individually labeled Eppendorf tubes containing 400 µL 1xPBS. Bowel segments in PBS were first minced with scissors and then vortexed for 40 sec until FITC was fully released from tissue. The samples were centrifuged (4000 *xg*, 10 min) and 100 µL of supernatant from each sample was transferred into a 96 well plate. Absolute fluorescence intensity in each well was measured with a Modulus II microplate Multimode Reader and a filter Cube with Excitation 490 nm and Emission 510-570 nm. Data is presented as percent fluorescence intensity ([fluorescence intensity measured in a specific bowel segment]/[sum of fluorescence intensities measured for all bowel segments] x100). Geometric mean is calculated as follows: $\boldsymbol{i=119ixi}$. Where “i” refers to each of the 19 bowel segments (ordered from most proximal (stomach; segment 1) to most distal segment (distal colon; segment 19) and “x” refers to the measured fluorescence intensity in the corresponding segment.

***In vivo* colon transit assay**

P15 *Tyr-Cre;Bap1* mice were separated into individual opaque holding containers and placed in a dark, undisturbed location. The welfare of the mice was confirmed every hour. The
260

number of stool pellets in the container at the end of an 8 hour time period was counted and the presence of liquid diarrhea or feces-matted perianal fur was noted.

In Vitro Organ Bath Experiments

For *Tyr-Cre;Bap1* mice at postnatal day 15 (P15), full-length colon was removed from the abdomen and immediately placed in a dish with warm (37°C), oxygenated (95% O_2 and 5% CO_2) Krebs-Ringers solution (118 mM NaCl (Sigma, Cat#:S6191), 4.6 mM KCl (Thermo Fisher Scientific, Cat#:BP366-500), 2.5 mM $CaCl_2$ (Sigma, Cat#:C-7902), 1.2 mM $MgSO_4$ (Sigma, Cat#:M-7506), 1 mM NaH_2PO_4 (Sigma, Cat#:S0751), 25 mM $NaHCO_3$ (Sigma, Cat#:BP328-500), 11 mM D-glucose (Sigma, Cat#:G7021, pH 7.4). To remove stool from the bowel lumen, Krebs-Ringers solution was pushed into the bowel lumen through a 21-gauge needle (BD Biosciences, Cat#:BD305167). Care was taken to touch the epithelium as little as possible. After flushing, the entire colon was transferred to the organ bath (Hugo Sachs Elektronik - Harvard Apparatus, Cat#:D-79232) which was pre-filled with warm, oxygenated Krebs-Ringers solution flowing through the chamber at a rate of 9.189 mL/min. The colon was cannulated on both ends (Hugo Sachs Elektronik - Harvard Apparatus, Cat#:S#16105) and the tissue was secured to the cannula with thread. Intraluminal pressure was created and maintained with a liquid reservoir suspended level to the water surface in the bath. The height of the water column in the reservoir was maintained at 2cm above the surface of the water bath. The fluid reservoir was connected to the proximal colon and the distal colon was connected to an outflow tube that opened 1 cm above the fluid level in the chamber to facilitate continuous flow of the oxygenated Krebs-Ringers solution through the colon.

For newborn (P0) *Wnt1-Cre;Bap1* mice, the most proximal 3 cm of small bowel from P0 *Wnt1-Cre;Bap1* mice was removed from the mice and immediately placed in warm Krebs-Ringers solution. The small bowel was then transferred to the organ bath (Hugo Sachs Elektronik Harvard Apparatus, Cat#:D-79232) which was pre-filled with warm, oxygenated Krebs-Ringers solution flowing through the chamber at a rate of 9.189 mL/min. P0 proximal small bowel was cannulated

on the proximal end using a 10 µL pipette tip as a cannula (Fisher Scientific, Cat#:21-277-2A) and secured to the cannula using string. The distal end of the small bowel segment was pinned to sylgard through the mesentery. The cannula was connected to a 3 mL syringe via a 2 mm diameter plastic, L-shaped tube. Intraluminal pressure was created and maintained with a liquid reservoir suspended level to the height of the water in the bath with fluid levels maintained 1 cm above the surface level of the water bath. The fluid reservoir was connected only to the proximal bowel and allowed to freely flow out of the distal bowel, facilitating continuous flow of the warm, oxygenated Krebs-Ringers solution through the bowel.

The bowel was equilibrated for 30 minutes. Video was recorded for 20 minutes. Tetrodotoxin (Abcam, Cat#:ab120054; 1mM stock in sodium citrate buffer [40mM citric acid monohydrate (EMD Millipore, Cat#:CX1725-1) and 60mM trisodium citrate dihydrate (Sigma, Cat#:C3434), pH 4.8]) was then added to the warm, oxygenated Krebs-Ringers solution at a final concentration of 1 µM. Video was recorded 20 minutes immediately following application.

Video Imaging and data processing

An E-PM1 Olympus digital camera was mounted on a dissecting microscope to video the bowel at 15 frames per second, 1,920 × 1,080 pixel resolution. The organ bath chamber was illuminated using the dissecting microscope's light source, and contrast was provided between the bath and the bottom of the chamber by securing a piece of black paper to the bottom of the chamber (in the case of the P0 small bowel organ baths, beneath the sylgard). The files were converted from .MTS to .mp4 using VLC Media Player and spatiotemporal information was converted to matrices using a MATLab script created by Dr. Christina M. Wright (https://github.com/christinawright100/BowelSegmentation/commit/095850905504f6ac29c7311f56fd9bf089ad4574, commit ID 958509). The script first thresholds the image, then separates and distinguishes the bowel from the background. The thresholded image was used to determine bowel width across the bowel for the duration of the video to create a graph depicting bowel width over

time for each location along the proximo-distal axis of the bowel segment in question. CMCs (defined as a neurogenic contraction characterized by being repetitive and containing a defined peak point of contraction) were quantified by blinded trained laboratory personnel.

Microscopy

Images of whole mount immunofluorescence staining were acquired with a Zeiss LSM 710 confocal microscope with a x20 (20x/0.8 air) Plan-Apochromat objective and Zeiss Zen software version 2.3 14.0.14.201 (Zeiss, Oberkochen, Germany). Images of Hematoxylin and Eosin as well as Periodic Acid-Schiff/Alcian Blue staining were acquired with a Leica DMC 2900 camera attached to a Leica DM 6000B epifluorescence microscope with an x20 (20x/0.7 air) HC Plan-Apochromat objective and Leica Application Suite X version 2.0.0.14332.2 (Leica Microsystems, Wetzlar, Germany). Confocal images show either single optical slices or maximum intensity z-projections as indicated in the figure legends. ImageJ (NIH) was used to color-adjust images. ImageJ or Inkscape (67); http://www.inkscape.org/) were used to crop images.

Biological sample size and technical replicates.

For H&E and PAS/AB immunohistochemistry, five slides per mouse for each bowel region were stained. Each slide held 3-5 consecutive sections separated by a minimum distance of 200 µm. Only one section was imaged per slide: the section with the highest number of “intact” villi or crypts (full-length epithelial crypts and/or villi with an uninterrupted epithelial monolayer). For proximal small intestine and distal colon, only fields of view containing at least one “intact” villus and/or crypt were imaged. For distal small intestine and proximal colon, the entire section was imaged and analyzed.

For whole mount immunofluorescence staining of P0 and P15 mouse bowel, at least 4x randomly chosen full-thickness confocal Z-stacks at 20x magnification were acquired and analyzed as technical replicates for each individual bowel region. For P15 ENS quantifications, cells in the entire field of view were counted. For P0 ENS quantifications, cells in two randomly

chosen quadrants of the imaged field of view were counted. Quadrant choice was adjusted if tissue damage was identified.

Statistics

We used Prism 7.03 - 8 (GraphPad Software, San Diego, CA) for statistical analysis. A cutoff of $p < 0.05$ was considered significant. All data was tested for normality and appropriate tests were chosen. Statistical analysis was only attempted if the sample number in all comparison groups exceeded n=3.

5.4 Results

Loss of *Bap1* in the enteric nervous system causes failure to thrive

Bap1 fl/fl;Tyr-Cre+ (*Tyr-Cre* cKO) mice failed to thrive and died prematurely with a median survival of only 18 days (**Figure 5.1A**). A few *Tyr-Cre* cKO pups were able to live beyond day 40, however, only when they were left with parents and in the presence of soft, moist food. At birth, *Tyr-Cre* cKO pups could not be differentiated from their littermates (data not shown). However, *Tyr-Cre* cKO pups gained weight more slowly (**Figure 5.1B**), stayed smaller than their littermates, and developed visibly distended abdomens towards the end of their lives (**Figure 5.1C**). At death, *Tyr-Cre* cKO colon and distal small intestine were distended with accumulated feces (**Figure 5.1D**). This distention and accumulated feces developed with increasing age. At postnatal day 15 (P15), rare *Tyr-Cre* cKO pups still had a normal-appearing bowel with well-formed fecal pellets in the distal colon, but for most pups the proximal colon was already distended by accumulated feces (**Figure 5.1E-E''**). The colon of some *Tyr-Cre* cKO mice even became deformed by the accumulated feces within (**Figure 5.1E-E'**). By P20 and beyond, the vast majority of *Tyr-Cre* cKO mice presented with a deformed colon and accumulated feces throughout the colon (**Figure 5.1E-E'**). Accumulation of feces in the distal small intestine also increased with age. At P15, we observed distal small intestine

fecal aggregation and distention for 30.4% of *Tyr-Cre* cKO mice, but that percentage increased to 89.9% beyond postnatal day 20 (**Figure 5.1F**). We also noticed white patches of abdominal fur for most *Tyr-Cre* cKO pups, indicating incomplete embryonic melanocyte migration (**Figure 5.1G-H**).

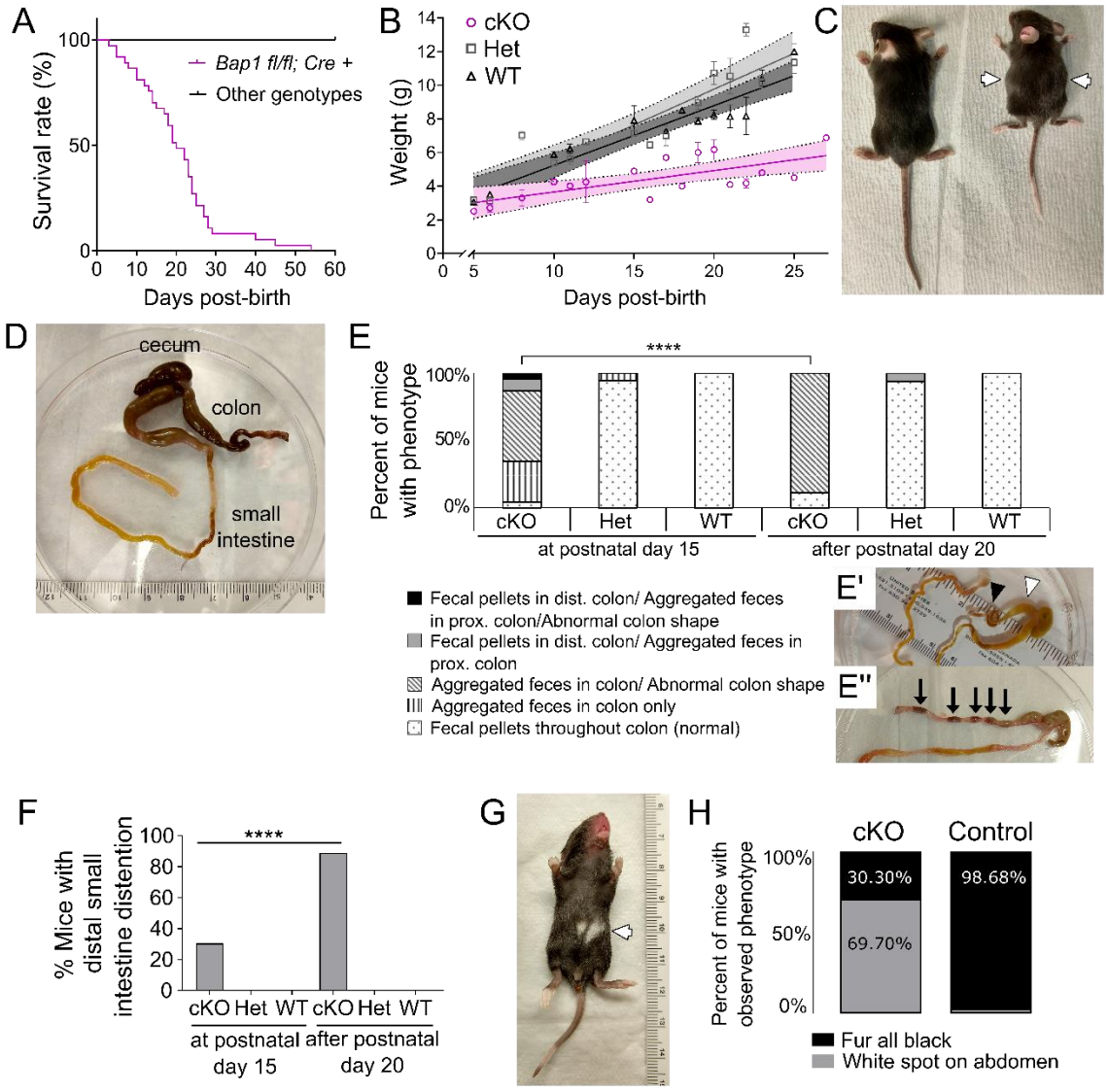

Figure 5.1: *Bap1 fl/fl; Tyr-Cre+* mice failed to thrive and died with massively dilated bowel. (A) *Bap1 fl/fl;Tyr-Cre* + (cKO) mice died early in life (median survival 20 days, n=30). Only mice left with parents and in the presence of softened, moist food lived beyond postnatal day 25 (P25). (B) cKO mice (n=111 measurements across all ages, 6.76 +/- 10.25 measurements per time point, R^2=0.4861) gained weight more slowly than their heterozygous (Het, n=177 measurements across all ages, 10.50 +/- 15.58 measurements per time point, R^2=0.8334) and wild-type (WT, n=168 measurements across all ages, 11.06 +/- 15.49 measurements per time point, R^2=0.8873) littermates. Graph shows simple regression with 95% confidence interval of mean weight per time

point with standard error of the mean (p = 0.001, Repeated Measures One-way ANOVA mixed effects model). (C) cKO mice (right) were smaller than their unaffected littermates (left). At P20, the representative cKO mouse also had a visibly distended abdomen (white arrows). (D) The colon and distal small intestine of cKO mice became severely distended due to aggregated feces later in life. The representative image of a cKO bowel was taken at P27. (E) cKO mice presented with abnormal colon phenotype beyond P15 (p<0.0001 comparing Het to cKO for both P15 and beyond P20, Binomial test). The severity of the observed bowel phenotype increased with age for cKO mice. At P15, the colons of the majority of cKO mice had a range of abnormal appearances (cKO: n=23, Het: n=19, WT: n=15), however, beyond P20 (>P20; cKO: n=9, Het: n=17, WT: n=20) most of the cKO mice presented with the most severe abnormal phenotype of aggregated feces with a deformed colon and a lack of formed fecal pellets (p=0.0142, Binomial test comparing P15 and >P20 cKO). (E') An example of an unusual deformation (black arrowhead) in the mid-colon and accumulated, unformed feces in the proximal colon (white arrowhead) as well as distal small intestine (no arrow) in a P15. (E'') A normal-appearing colon of a P15 WT pup shows well-formed stool pellets starting at the distal end of the proximal colon. (F) Feces also aggregated in the distal small intestine of cKO mice (P<0.0001 for both P15 and >P20, Binomial test) and distal small intestine involvement increased with age from 30.4% at P15 to 88.9% for cKO mice >P20. (P<0.0001, Binomial test). Sample size at P15: cKO: n=23, Het: n=19, WT: n=15. Sample size for ages >P20: cKO: n=9, Het: n=17, WT: n=20. (G) Example of a spot of white fur on the abdomen of a P10 cKO pup (white arrow). This indicates incomplete melanocyte migration. (H) Melanocyte migration was incomplete for the majority of cKO mice as compared to WT mice (cKO: n=33, WT: n=76, Binomial test, P<0.00001). (A-H) cKO refers to *Bap1 fl/fl;Tyr-Cre* + genotype. (B,E-F) Het refers to *Bap1 fl/wt; Tyr-Cre* + genotype. (E,H) WT refers to *Bap1 wt/wt;Tyr-Cre* + genotype. (B) WT includes the genotypes *Bap1 wt/wt; Tyr-Cre* + genotype plus any mice not carrying a *Cre* allele. Data not significant unless otherwise indicated. ****p<0.0001

Bowel motility is reduced in *Bap1* conditional knockout mice

To better understand the fecal stasis phenotype observed in the *Tyr-Cre* cKO mice, we decided to assess bowel motility *in vivo* and *in vitro*. We decided to focus our analysis on P15 mice. This is a time point where 83.3% of the *Tyr-Cre* cKO pups are still alive, but where a clearly abnormal bowel phenotype can already be observed in the vast majority of *Tyr-Cre* cKO pups (**Figure 5.1A** and **E-F**). We never observed gross abnormalities in the proximal small intestine like gas or fecal accumulation. However, *in vivo* bowel motility was significantly reduced in this part of the bowel based on slower transit of FITC Dextran dye along the proximal small intestine (**Figure 5.2A-B**). Since fecal accumulation was most severe in the colon and was also first observed there, we assessed *in vivo* colon motility. We quantified the number of fecal pellets expelled within an 8 hour time window by P15 *Tyr-Cre* cKO pups and control littermates. Unlike their littermates, all but

one *Tyr-Cre* cKO pup did not pass any fecal pellets in the 8 hour time window and if any feces were evident, it was watery diarrhea (**Fig. 5.2C-D**). The inability to pass stool could be explained by either a complete lack of colonic bowel motility or uncoordinated motility, where contractions can be observed but are unable to productively move stool pellets towards the anus. To differentiate between these possibilities, we took full-length colons from P15 mice, subjected them to constant intraluminal pressure in oxygenated Krebs-Ringers solution and recorded spontaneous contractility patterns. We observed repetitive contractions involving the whole colon with a defined peak point of contraction in all wild-type mice (**Figure 5.2E**). These contraction patterns matched the definition of "colonic motor complexes" (CMC) as proposed by Corsetti *et al*. (68). As expected for neurogenic contractions, these colonic motor complexes disappeared in the presence of the voltage-gated sodium channel inhibitor tetrodotoxin which blocks all neurotransmission (**Supplementary Figure 5.1A-B**). In contrast, the majority of *Tyr-Cre* cKO mice had no neurogenic contractions (5/10, **Figure 5.2F**, **Supplementary Figure 5.1C-D,F**). We observed abnormal neurogenic contractions in three *Tyr-Cre* cKO mice (e.g. only retrograde propulsive contractions or very slow contractions involving only part of the colon, **Supplementary Figure 5.1E-F**). A single *Tyr-Cre* cKO colon exhibited both abnormal contractions as well as a single CMC. However, we also noted exclusively normal neurogenic motility for two of the *Tyr-Cre* cKO mice (**Figure 5.2F**). This is consistent with the observation that the bowel of some P15 mice still looks grossly normal and that a small number of cKO mice can still pass stool pellets. Overall, significantly fewer neurogenic colonic motility patterns were observed for *Tyr-Cre* cKO mice *in vitro* (**Figure 5.2G**). Dysfunction or loss of specific neuron subtypes could cause bowel dysmotility by causing imbalances in inhibitory and excitatory neuroeffector signaling to gut smooth muscle. This would result in tonic contraction or relaxation and abnormal motility of the affected gut segment (34). To assess this possibility, we assessed colon diameter before and after the addition of tetrodotoxin but could not detect a difference in either absolute colon diameter or percent change in bowel diameter before and after tetrodotoxin between *Bap1* wild-type and cKO colons. (**Supplementary Figure 5.1G-H**).

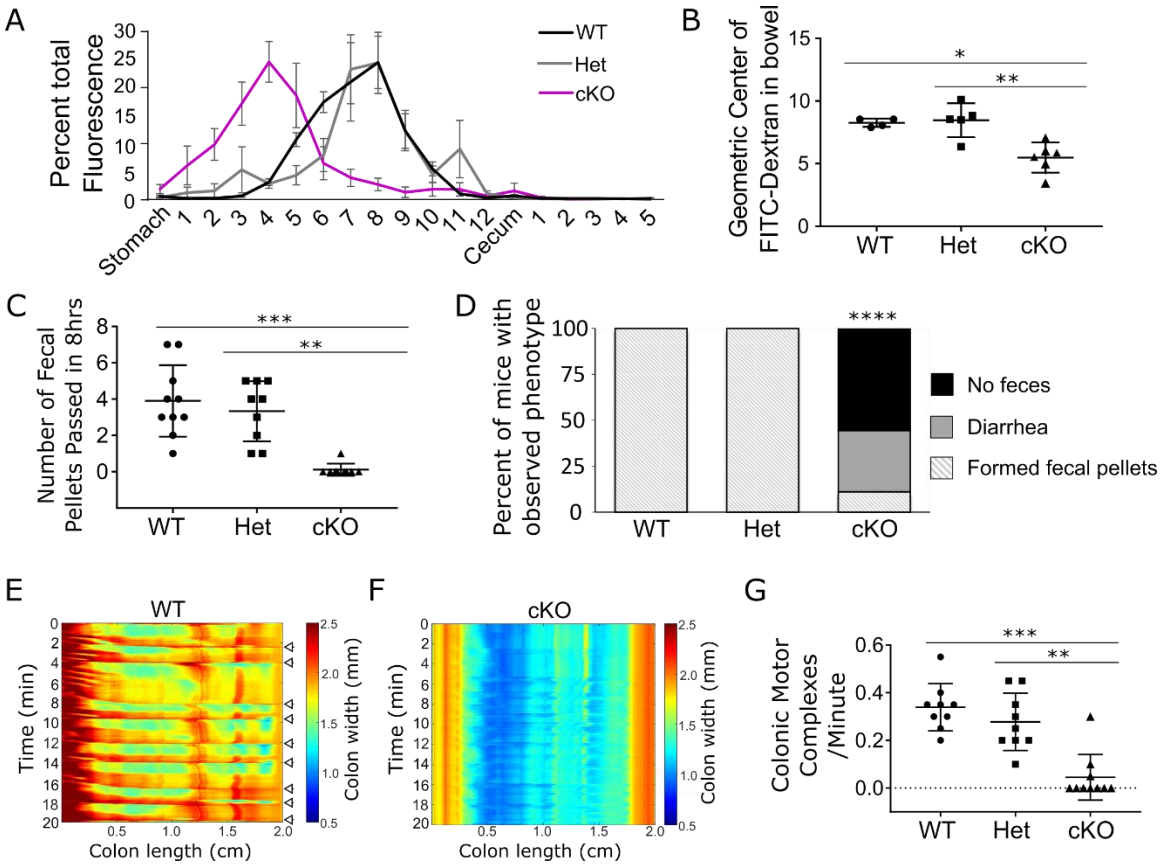

Figure 5.2: Proximal small intestine and colon motility were significantly reduced in *Bap1 fl/fl; Tyr-Cre+* mice at postnatal day 15.

(A) Mean FITC fluorescence intensity (+/- standard error of the mean) measured along the full length of the bowel indicates that FITC-conjugated Dextrans traveled more slowly through the cKO (n=6, sex unknown) proximal small intestine as compared to Het (n=5, sex unknown) and WT (n=4, sex unknown) bowels at postnatal day 15 (P15). (B) The geometric center of measured FITC fluorescence was more proximal for cKO mice than for Het and WT mice (P=0.0017, Kruskal-Wallis Test with Dunn's Multiple Comparisons Test, cKO vs Het: P=0.0086, cKO vs WT: P=0.0452, cKO: n=6, 5.48 ± 1.21; Het: n=5, 8.47 ± 1.35; WT: n=4, 8.26 ± 0.33 (mean ± stdev)). (C) P15 cKO mice passed fewer stool pellets in an 8 hour time window than Het and WT mice (P=0.0001, Kruskal-Wallis Test with Dunn's Multiple Comparisons Test, cKO vs Het: P=0.0016, cKO vs WT: P=0.0004, cKO: n=9 (4F/3M/2 unknown), 0.11 ± 0.33; Het: n=9 (4F/5M), 3.33 ± 1.66; WT: n=10 (6F/4M), 3.90 ± 1.97 (mean ± stdev)). (D) The majority of P15 cKO mice had abnormal stool (diarrhea or no feces at all, P<0.0001, Binomial test comparing cKO and WT). (E-F) Representative kymographs depicting bowel width as a function of time and distance along the proximo-distal axis of the cannulated colon for P15 WT (E) and cKO (F) mice. (G) Fewer colonic motor complexes (CMC) were recorded for cKO as compared to Het and WT colons (P=0.0003, Kruskal-Wallis Test with Dunn's Multiple Comparisons Test, Het vs cKO: P = 0.0065, WT vs. cKO: P=0.0003, cKO: n=10 (4 females/ 6 males), 0.05 ± 0.10 CMC/min; Het: n=9 (6 females/ 3 males), 0.28 ± 0.12 CMC/min;

WT: n=9 (6 females/ 3 males), 0.34 ± 0.10 CMC/min (mean ± stdev)). (A-G) cKO refers to *Bap1 fl/fl;Tyr-Cre*+ genotype and Het refers to *Bap1 fl/wt; Tyr-Cre*+ genotype. (A-B) WT includes *Bap1 wt/wt; Tyr-Cre* + genotype plus any mice not carrying a *Cre* allele. (C-G) WT refers to *Bap1 wt/wt;Tyr-Cre* + genotype. (B,C,G) Graphs show mean +/- standard deviation. Data not significant unless otherwise indicated. *P<0.05, **P<0.01, ***P<0.001, ****P<0.0001

Loss of *Bap1* in the enteric nervous system alters bowel epithelium

The deformed colon shape commonly observed in c*Tyr-Cre* cKO mice beyond P15 (**Figure 5.1E-E'**) led us to ask if the normally soft and flexible distal bowel wall had stiffened due to fibrosis and/or inflammatory infiltrates. Increased stiffness of the bowel wall also could directly affect bowel motility. To address this question, we first stained cross-sections of proximal and distal small intestine as well as proximal and distal colon with trichrome stain to visualize collagen-I deposition within the bowel wall. We did not observe any differences in *Tyr-Cre* cKO versus control bowels (**Supplementary Figure 5.2A-H**). We also did not see any inflammatory infiltrates within the bowel wall (**Supplementary Figure 5.2A-H, I-J, O-R, A'-D',** and **I'-J'**). However, we noticed a possible reduction in goblet cells in *Tyr-Cre* cKO distal small intestine and proximal colon epithelium as compared to control epithelium (**Supplementary Figure 5.2B-C** versus **F-G**). Goblet cells produce mucus which lubricates stool and facilitates movement of the stool along the bowel. Mucus also forms an important protective layer between luminal contents and the epithelial layer and prevents access of potentially pathogenic bacteria to the epithelium (69). Thus, loss of goblet cells could increase susceptibility to sepsis and death. However, these preliminary observations were not confirmed. Proximal small intestine epithelium appeared grossly normal (**Supplementary Figure 5.2I-N**), whereas distal small intestine epithelium was normal except for a significantly increased presence of relatively more immature goblet cells in *Tyr-Cre* cKO epithelial crypts that was no longer apparent in epithelial villi where mature epithelial cells are located (**Supplementary Figure 5.2O-Z**). *Tyr-Cre* cKO epithelial crypts in proximal colon were deeper than in control mice and contained proportionally more goblet cells (**Supplementary Figure 5.2A'-H'**). No obvious differences in *Tyr-Cre* cKO versus control distal colon epithelium could be detected

(**Supplementary Figure 5.2I'-L'**). Overall, we were able to detect small differences in *Tyr-Cre* cKO epithelium in the distal bowel, however, the significance of these changes is unclear.

Enteric neuron density along the length of the bowel is normal at birth but significantly reduced by postnatal day 15 in *Bap1* conditional knock-out mice

Bap1 is an epigenetic regulator with known roles in differentiation (55) and regulation of genes important for ENS precursor migration (58). Loss of *Bap1* also affects fetal migration of melanocytes, another neural crest derivative (**Figure 5.1G-H**). Therefore, we hypothesized that loss of *Bap1* in the ENS causes abnormal ENS anatomy. At P15, total myenteric and submucosal neuron density were significantly reduced throughout the bowel, including proximal small intestine, distal small intestine, proximal colon, and distal colon (**Figure 5.3A-D**, and **Supplementary Figures 5.3**, **5.4A-B**). Since imbalance in enteric neuron subtypes can lead to abnormal enteric neural circuits and dysmotility, we also looked at the density of nitrergic neurons. Nitrergic neurons are an abundant and functionally important category of enteric neurons and include interneurons and inhibitory motor neurons (1). We found no difference in overall density of NOS1+ neurons in myenteric and submucosal plexi (**Figure 5.3A-B,E-F, Supplementary Figures 5.3**, **5.4C-D**). However, nitrergic neuron numbers varied greatly between fields of view for both *Tyr-Cre* cKO and control mice. Thus we also assessed the ratio of nitrergic neurons to total neurons in each field of view and preliminary results suggest that nitrergic neurons are reduced proportionally to total neurons in both myenteric and submucosal plexi in all bowel regions assessed (**Figure 5.3G-H** and **Supplementary Figure 5.4E-F**). In *Bap1;Tyr-Cre* mice, only ~80% of migrating ENS precursor cells at day 11.5 of embryonic development (E11.5) are derived from *Tyr-Cre* lineage cells (64) and carry homozygous *Bap1* null alleles. We thus hypothesized that ENS abnormalities would be much more severe in *Bap1;Wnt1-Cre* mice, a mouse model where 100% of the neonatal ENS is derived from ENS precursors carrying *Bap1* knock-out alleles (70).

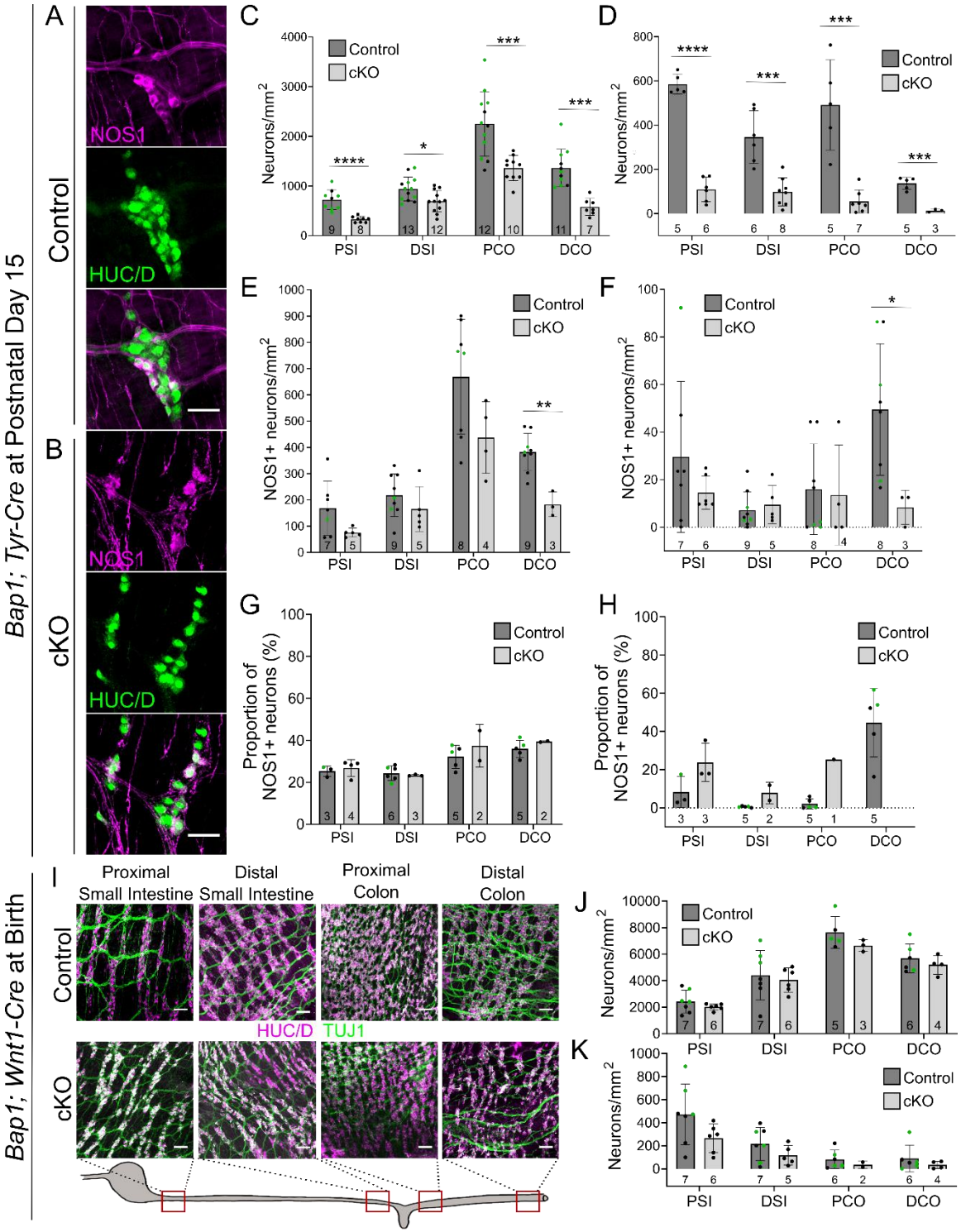
Bap1; Tyr-Cre at Postnatal Day 15
Bap1; Wnt1-Cre at Birth
A
B
Control
cKO
NOS1
HUC/D
C
D
E
F
G
H
I
J
K
Control
cKO
Neurons/mm2
NOS1+ neurons/mm2
Proportion of NOS1+ neurons (%)
PSI
DSI
PCO
DCO
Proximal Small Intestine
Distal Small Intestine
Proximal Colon
Distal Colon
HUC/D TUJ1

Figure 5.3: Preliminary analysis suggested that *Bap1 fl/fl; Tyr-Cre+* mice at postnatal day 15 had decreased total enteric neuron density and proportionally decreased nitrergic neuron density along the bowel. However, neonatal enteric neuron density was unaffected by *Bap1* loss.

(A-B) Representative images of myenteric plexus showing enteric neurons (HUC/D+, green) and nitrergic neurons (NOS1+, magenta) in proximal small intestine for Control (A) and *Bap1 fl/fl; Tyr-Cre* + (cKO; B) mice at postnatal day 15 (P15). (A) Single confocal optical slice. (B) Maximum intensity z-projection. (C-D) Quantification of total neuron density in *Bap1;Tyr-Cre* mice at postnatal day 15 showed decreased neuron density for cKO mice in both myenteric (A) and submucosal plexus (B) as compared to Control mice in all regions of the bowel (Student's t-test; myenteric PSI: $p < 0.0001$, myenteric DSI: $p= 0.0130$, myenteric PCO: $p = 0.0006$, myenteric DCO: $p = 0.0001$, submucosal PSI: $p < 0.0001$, submucosal DSI: $p = 0.0003$, submucosal PCO: $p = 0.0002$, and submucosal DCO: $p = 0.0003$). (E-F) Preliminary analysis of nitrergic neuron (NOS1+) density in *Bap1;Tyr-Cre* mice at P15 suggests no significant decrease in NOS1+ neuron density in myenteric (E) and submucosal plexus (F) except for distal colon (DSI; Student's t-test; myenteric PSI: $p = 0.02829$, myenteric DSI: $p= 0.6083$, myenteric PCO: $p = 0.8402$, myenteric DCO: $p = 0.0.0357$, submucosal PSI: $p = 0.0793$, submucosal DSI: $p = 0.2791$, submucosal PCO: $p = 0.0856$, and submucosal DCO: $p = 0.0011$). (G-H) However, preliminary analysis of the proportion of nitrergic neurons in *Bap1;Tyr-Cre* mice at P15 suggests a proportional decrease of NOS1+ neuron density in myenteric plexus (G) in all bowel regions and submucosal plexus (H) in proximal small intestine (PSI; Student's t-test; $p = 0.1608$). No conclusions can be drawn about submucosal plexus (H) in other bowel regions at this time. (I) Representative images of myenteric plexus showing myenteric enteric neurons (HUC/D+, magenta) and myenteric neurite network (TUJ1+, green) for neonatal (P0) Control and cKO *Bap1;Wnt1-Cre* mice along the bowel. All images are maximum intensity z-projections. (J-K) Preliminary analysis of enteric neuron density in P0 *Bap1;Wnt1-Cre* mice indicates that there is no significant difference between Control and cKO mice in myenteric (G) and submucosal plexus (H; Student's t-test; myenteric PSI: $p = 0.2976$, myenteric DSI: $p= 0.6707$, myenteric PCO: $p = 0.2313$, myenteric DCO: $p = 0.3779$, submucosal PSI: $p = 0.1070$, submucosal DSI: $p = 0.2032$, submucosal PCO: n too small for statistical analysis, and submucosal DCO: $p = 0.3877$). (A) Control genotype is *Bap1 wt/wt; Tyr-Cre* + . (C-K) Control encompasses genotypes *Bap1 wt/wt;Cre*+ or any genotype without *Cre* allele plus *Bap1 fl/wt;Cre* +. cKO genotype is *Bap1 fl/fl;Cre* +. (C-H,J-K) All data derived from mice with the following genotypes are visualized with green data points: *Bap1 wt/wt;Cre* + genotype or any genotype without *Cre* allele. PSI = proximal small intestine, DSI = distal small intestine, PCO = proximal colon, DCO = distal colon. (A-B) Scale bar = 50 μm. (I) Scale bar = 20 μm. All data represented as mean +/- standard deviation. *p<0.05, **p0.01, ***p<0.001, ****p<0.0001

Surprisingly, when we compared the ENS of neonatal *Bap1 fl/fl; Wnt1-Cre*+ (*Wnt1-Cre* cKO) pups to that of control littermates, the ENS of cKO mice appeared unremarkable (**Figure 5.3I**). When we quantified the density of enteric neurons in proximal small intestine, distal small intestine, proximal colon, and distal colon, we found no differences between *Wnt1-Cre* cKO and control ENS (**Figure 5.3J-K**). This suggests that embryonic loss of *Bap1* in the ENS does not affect

the development of a structurally normal way until birth. We hypothesized that enteric neurons without functional BAP1 are possibly lost postnatally. Unfortunately, *Wnt1-Cre* cKO mice did not live beyond the first day of life due to cardiac abnormalities (data not shown), so we turned back to the *Bap1;Tyr-Cre* mouse model to interrogate this hypothesis. We noticed no obvious difference in the percentage of *Tyr-Cre* lineage (TDTOMATO fluorescent reporter- expressing) enteric neurons in P0 *Tyr-Cre* cKO mice as compared to control pups (**Figure 5.4A-B**, quantifications are ongoing). However, by P15, the percentage of *Tyr-Cre* lineage neurons was significantly lower in *Tyr-Cre* cKO myenteric plexus throughout the bowel as compared to wild-type myenteric plexus (**Figure 5.4C-E** and **Supplementary Figure 5.5**). In the submucosal plexus, a significant reduction in TdTomato+ neurons could only be verified in distal colon (**Figure 5.4F** and **Supplementary Figure 5.5**) where the overall number of enteric neuron numbers is also most severely reduced (**Figure 5.3D**). This data supports the hypothesis that conditional loss of *Bap1* allows the development of a normal ENS, but that enteric neurons are either lost postnatally or that there is significantly reduced postnatal proliferation of persistent ENS precursors.

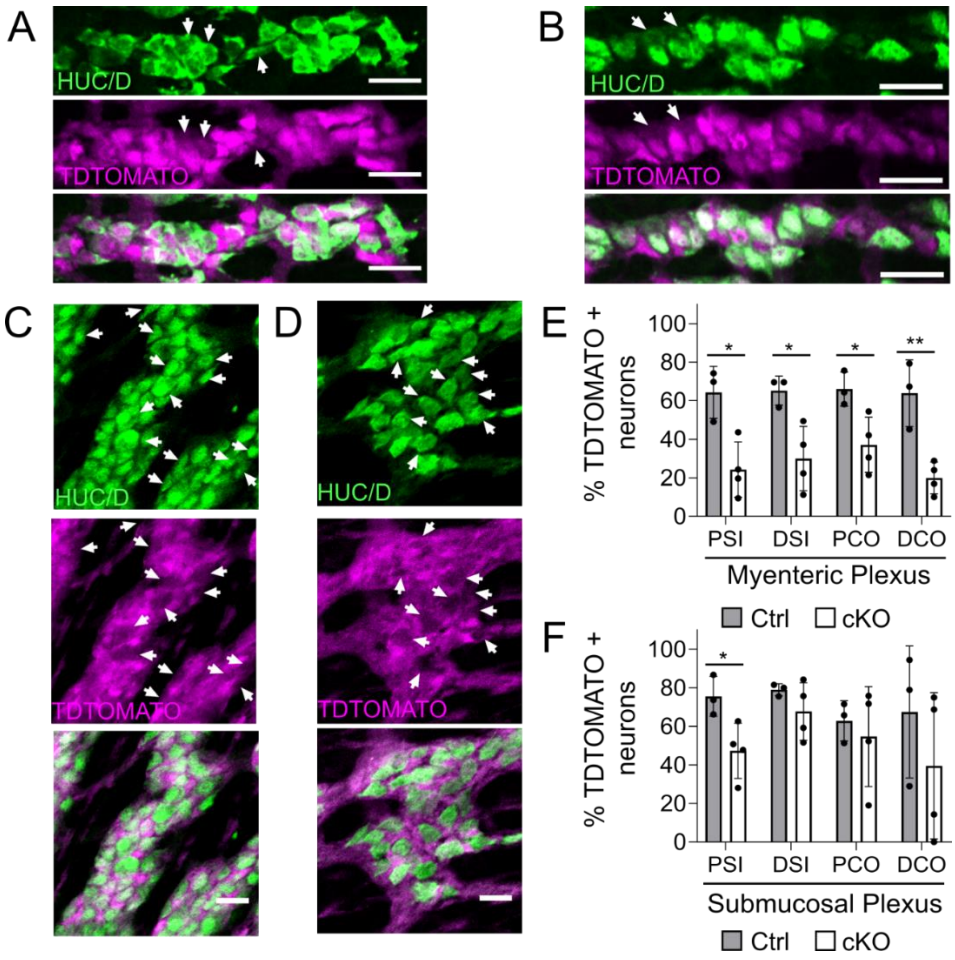

Figure 5.4: Neonatal *Bap1 fl/fl; Tyr-Cre*+ mice appeared to have a normal complement of Tyr-Cre lineage neurons, but lost neurons of the *Tyr-Cre* lineage by postnatal day 15.
(A-B) The vast majority of enteric neurons (HUC/D+, green) of both *Bap1 wt/wt; Tyr-Cre* + (Control, A) and *Bap1 fl/fl; Tyr-Cre* + (cKO, B) mice at birth were derived from enteric neuron precursors of the *Tyr-Cre* lineage (TDTOMATO+, magenta). Images are representative confocal optical slices of distal small intestine myenteric plexus. (C-F) cKO mice preferentially lose *Tyr-Cre* lineage neurons by postnatal day 15 (P15). (C-D) Representative confocal optical slices of proximal colon myenteric plexus for Control (C) and cKO (D) mice. White arrows point to neurons (HUC/D+, green) that do not express TDTOMATO (magenta). (E) Quantification of the proportion of *Tyr-Cre* lineage neurons in the myenteric plexus of P15 Control and cKO mice showed a significant decrease in TDTOMATO+/ *Tyr-Cre* lineage neurons in all bowel regions (PSI: p = 0.013, DSI: p = 0.021, PCO: p = 0.028, DCO: p = 0.006; Student's t-tests; Control = 2 females/ 2 males, cKO = 3 females/ 1male). (F) Quantification of the proportion of *Tyr-Cre* lineage neurons in the submucosal plexus of P15 Control and cKO mice showed a significant decrease in TDTOMATO+/ *Tyr-Cre* lineage neurons in proximal small intestine only (PSI: p = 0.035, DSI: p = 0.263, PCO: 0.635, DCO: 0.362, Student's t-tests). Control = *Bap1 wt/wt; Tyr-Cre*+ and cKO = *Bap1 fl/fl; Tyr-Cre*+. Scale bar = 25 μm.

Neonatal bowel motility is unchanged in Bap1 conditional knock-out mice

We observed a progressive worsening of the bowel phenotype overall (**Figure 5.1E-F** and **Figure 5.2**) and some P15 mice were still gaining weight at a rate similar to their littermates (**Figure 5.1B**) and had normal bowel motility (**Figure 5.2C-D,G** and **Supplementary Figure 3F**). Therefore, we wondered if the normal-appearing neonatal ENS is able to induce neurogenic motility patterns or if the neurons that are present are already functionally abnormal. We chose the *Bap1;Wnt1-Cre* mouse model to assess neonatal bowel motility since 100% of enteric neurons and glia carry the *Bap1* null allele and any functional deficit should be more noticeable in these mice. We compared *in vitro* proximal small intestine motility in P0 *Wnt1-Cre* cKO mice with that of control littermates at birth and were unable to find a difference. As expected (71), we observed CMCs (low frequency/neurogenic contractions) in about half of both *Wnt1-Cre* cKO and control pups (**Figure 5.5A-E** and **Supplementary Figure 5.6A-D**) and there was no difference in the frequency of observed CMCs (**Figure 5.6F**). We also assessed myogenic, high frequency contractions and again found no differences for P0 *Wnt1-Cre* cKO and control mice (**Supplementary Figure 5.6E-F**).

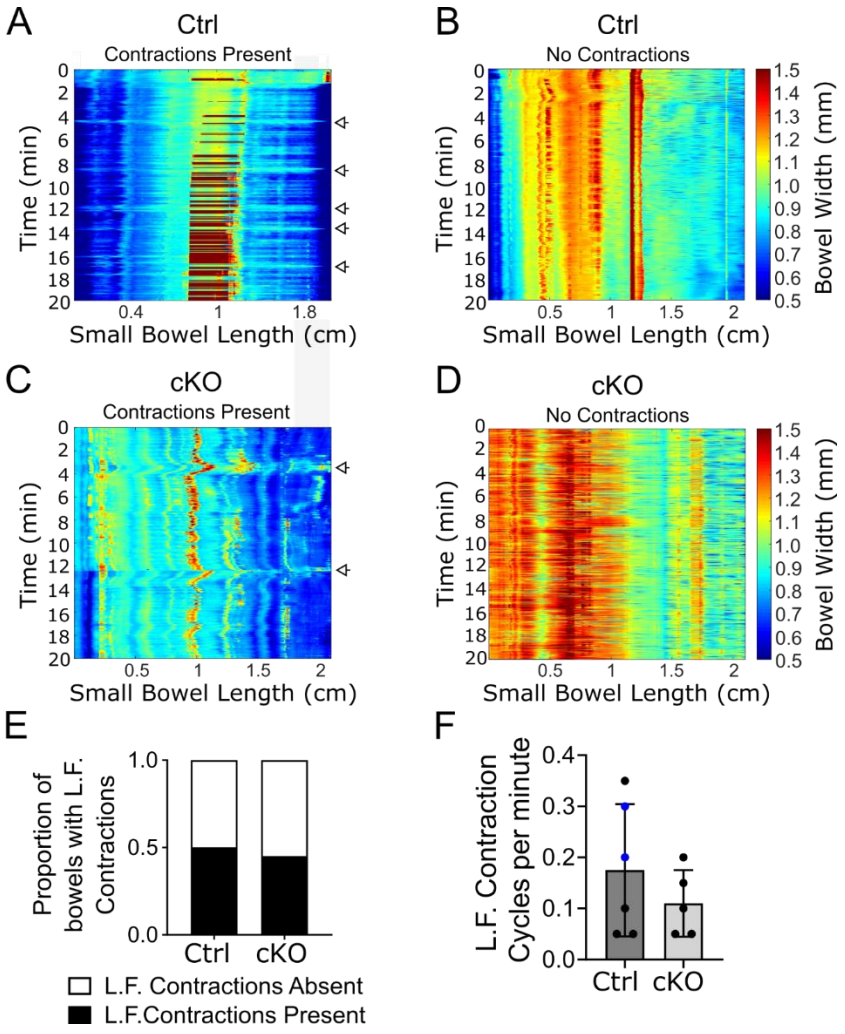

Figure 5.5: Neonatal proximal small bowel motility in *Bap1 fl/fl; Wnt1-Cre*+ mice was normal. (A-D) Representative kymographs depicting bowel width as a function of time and distance along the proximo-distal axis of the cannulated proximal small intestine for Control (Ctrl; A-B) and cKO (C-D) neonatal (P0) mice. Low frequency (L.F.) contractions could be recorded for a subset of P0 Ctrl and cKO pups (A and C; white arrows) while no L.F. contractions were detected for other Ctrl and cKO pups (B and D; Ctrl: n=10 [WT: 5 males/2 females and Het: 1 male/ 2 unknown], cKO: 6 females/ 1 male/ 2 unknown). (E) The proportion of bowels where any L.F. contractions were recorded did not differ for P0 Ctrl (WT: contractions - 3 mice, no contractions - 4 mice, Het: contractions - 2 mice, no contractions - 1 mouse) and P0 cKO mice (contractions - 4 mice, no contractions - 5 mice). (F) The frequency of L.F. contractions did not differ for Ctrl and cKO neonates for which any L.F. contractions could be recorded (p=0.3368, Student's t-test, Ctrl: : 0.18 ± 0.13, cKO: 0.11 ± 0.07 (mean ± stdev)). Data points derived from Het mice are marked by blue color. (A-F) WT refers to *Bap1 wt/wt; Wnt1-Cre* + or any genotype without the *Wnt1-Cre* transgene, Het refers to *Bap1 fl/wt; Wnt1-Cre* + genotype. cKO refers to *Bap1 fl/fl; Wnt1-Cre* + genotype. Data not significant unless otherwise indicated.

Postnatal loss of Bap1 in the ENS does not affect survival, weight gain or colon motility

The ENS in *Bap1* conditional knock-out mice appears to be structurally and functionally normal at birth, but enteric neurons, specifically of the *Tyr-cre* lineage are lost postnatally. These observations led us to ask if *Bap1* has a primary role in the postnatal ENS maintenance with limited effects on prenatal ENS development. We thus deleted *Bap1* in the postnatal ENS either at 8 weeks of age (adult) or between P1 and P7 (early life) in a *Bap1;Ret-CreERT2* mouse model. Deletion of *Bap1* in *Bap1 fl/fl; Ret-CreERT2* + (*Ret-CreERT2* cKO) adult mice or in early life did not affect overall survival of *Ret-CreERT2* cKO mice, despite some toxicity-related lethality across genotypes due to the tamoxifen treatment early in life (**Figure 5.6A-B**). Loss of *Bap1* caused a small increase in percent weight gain in *Ret-CreERT2* cKO treated with tamoxifen in adulthood, but this increase in weight gain did not translate to a clear biologically meaningful increase in raw body weight (the weights of individual adult mice varied greatly at the beginning and end of experimental observation period. cKO: from 23.48g ± 2.96g to 24.49g ± 1.01g, Het: from 23.72g ± 3.41g to 24.77g ± 0.78g, and WT: from 20.73g ± 1.36g to 21.13g ± 0.74g). Weight gain of *Ret-CreERT2* cKO mice was not affected by loss of *Bap1* in early postnatal life (**Figure 5.6C-D**). Preliminary quantification of the proportion of TDTOMATO-expressing neurons in adult mice 1-12 weeks after tamoxifen treatment shows that most enteric neurons (myenteric plexus: 87.02 ± 6.15 across genotypes and submucosal plexus: 96.14 ± 4.62 across genotypes) have undergone Cre-mediated recombination and lost functional *Bap1* alleles (**Figure 6E-G**). However, colon motility appears to be unaffected by postnatal loss of *Bap1* irrespective of the timing of tamoxifen treatment (**Figure 6H**). These observations indicate either that prenatal *Bap1* loss is required for the postnatal dysmotility phenotype and decrease in enteric neuron density, despite a functional, normal-appearing ENS at birth, or that loss of *Bap1* in a small percentage of enteric neurons (1%-20%) is responsible for the observed phenotypes.

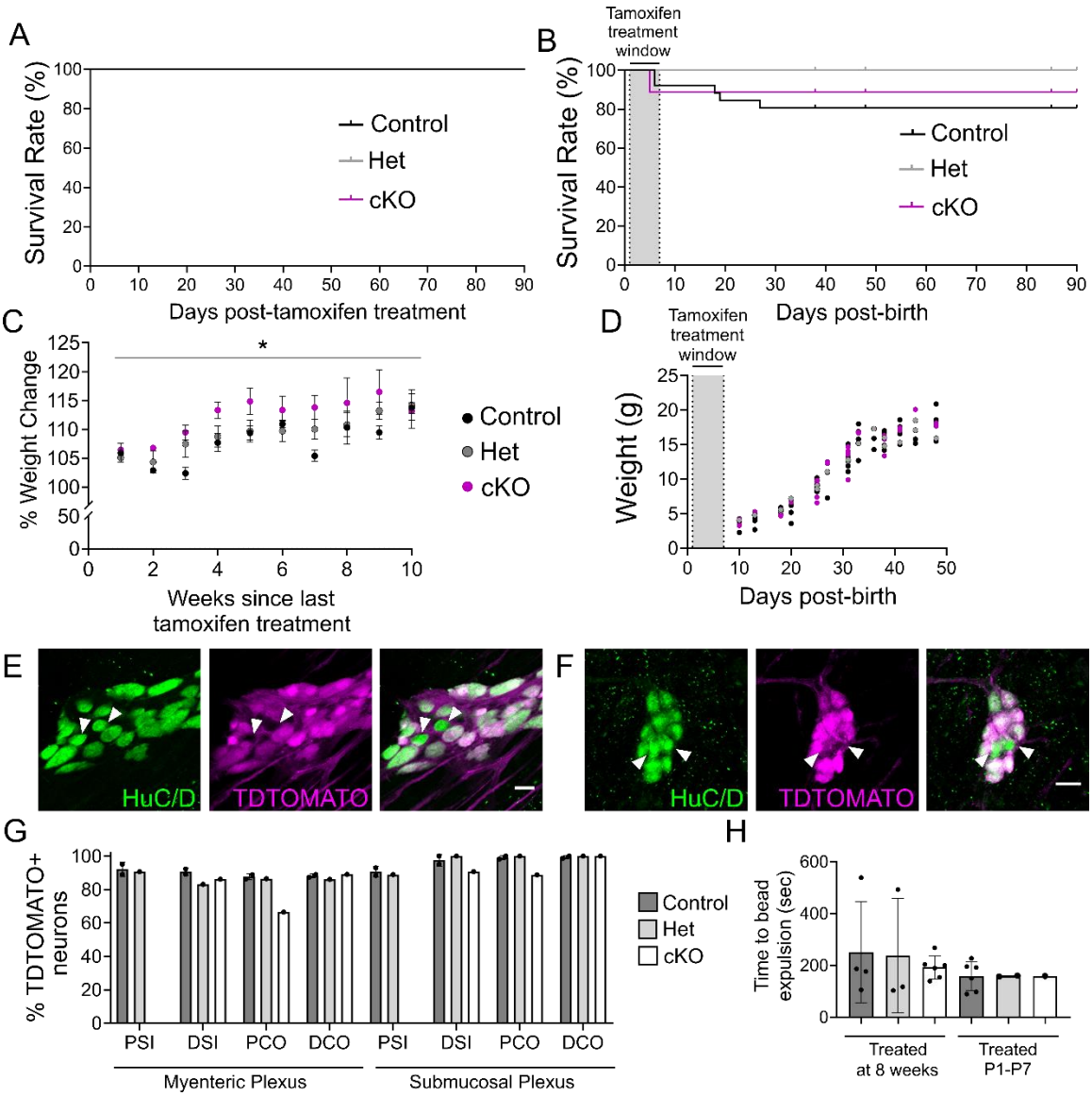

Figure 5.6: Tamoxifen-induced postnatal loss of *Bap1* in the ENS did not affect survival, bowel motility, and possibly post-treatment weight gain.

(A) CRE-mediated excision of *Bap1* allele in *Bap1 fl/fl; Ret-CreERT2* + (cKO) mice at 8 weeks of age did not cause early lethality. Mice were followed for at least 90 days after tamoxifen treatment (cKO: 8 females/ 5 males, Het: 3 females/ 3 males, Control: 4F/1M). (B) Tamoxifen treatment between postnatal day 1 and day 7 (P1-P7) was lethal for a subset of mice, however, no meaningful difference in survival was observed for tamoxifen-treated cKO mice (cKO: 5 females/ 3 males/ 1 not known, Het: 5 females/ 2 males, Control: 11 females/ 11 males/ 4 not known). (C) Tamoxifen-treated adult cKO mice gained and maintained slightly more weight than Control and Het mice between 1 to 10 weeks after tamoxifen treatment with unclear biological significance (p=0.001, Repeated Measures One-way ANOVA mixed effects model with multiple comparisons, p = 0.025;

Control vs. cKO p = 0.016; Het vs. cKO, cKO: 3 females/ 5 males [112.2 ± 3.45], Het: 2 females/ 3 males [109.3 ± 3.14], Control: 3 females [107.8 ± 3.64]). (D) cKO mice treated with tamoxifen between P1-P7 gained weight at the same rate as their Het and Control littermates (p=0.2076, Repeated Measures One-way ANOVA mixed effects model with multiple comparisons, cKO: 5 females/ 2 males, Het: 3 females/ 2 males, Control: 6 females/ 10 males). (E) Proximal colon myenteric plexus in a cKO mouse 1 week after tamoxifen treatment contained some neurons that did not express TDTOMATO (white arrowheads). cKO mouse treated at 8 weeks of age. (F) Proximal colon submucosal plexus in a cKO mouse 1 week after tamoxifen treatment contained some neurons that did not express TDTOMATO (white arrowheads). cKO mouse treated at 8 weeks of age. (G) Preliminary quantification of the proportion of TDTOMATO+ (magenta) enteric neurons (green) shows that tamoxifen treatment at 8 weeks of age led to CRE-mediated recombination in the vast majority of myenteric and submucosal neurons (Control: 2 males (1 week and 12 weeks after treatment), Het: 1 female (12 weeks after treatment), cKO: 1 male (1 week after treatment)) and that the proportion of *Ret-CreERT2* lineage neurons remained constant. (H) Colon bead expulsion latency was normal for cKO mice that were treated with tamoxifen at 8 weeks of age (p = 0.8116, One-way ANOVA, cKO: 4 females/ 1 males, Het: 1 female/ 2 males, Control: 3 females/ 1 males) and colon bead expulsion latency in cKO mice was likely unaffected by tamoxifen treatment between P1-P7 (cKO: 1 female, Het: 2 females, Control: 4 females, 2M). (E-F) Single confocal optical slice. (A-D, G) WT refers to *Bap1 wt/wt; Ret wt/CreERT2* or any genotype without the *CreERT2* knock-in allele. (A-H) Het refers to *Bap1 fl/wt; Ret wt/CreERT2* genotype. cKO refers to *Bap1 fl/fl; Ret wt/CreERT2* genotype. PSI = Proximal Small Intestine, DSI = Distal Small Intestine, PCO = Proximal Colon, and DCO = Distal Colon. (E-F) Scale bar = 20 μm.

Summary

Loss of Bap1 in enteric neural precursors did not affect neonatal enteric nervous system anatomy and function. However, density of *Tyr-Cre* lineage neurons and total neuron density were decreased by P15 in *Tyr-Cre* cKO mice along the entire length of the bowel. By P15, proximal small intestine and colon motility were decreased and *Tyr-cre* cKO mice failed to thrive and died early with greatly distended bowels due to accumulated feces. Postnatal loss of Bap1 in the vast majority of enteric neurons did not cause motility defects, affect weight gain or survival of *RetCreERT2* cKO mice, indicating that prenatal loss of Bap1 in enteric neural precursors is required for postnatal neuron loss and bowel dysmotility or that postnatal loss of Bap1 in very specific neuron subpopulations is responsible for the majority of the observed motility and survival phenotype.

5.5 Discussion and Future Directions

Loss of *Bap1* does not cause Hirschsprung disease

We initially expected that loss of *Bap1* would lead to Hirschsprung disease. This hypothesis was supported by previous studies showing that *Bap1* regulates neural crest lineage differentiation (55) and expression of genes important for enteric neural crest migration (58). We also observed early in this study that the majority of *Tyr-Cre* cKO mice had a patch of white abdominal fur, indicating incomplete embryonic melanocyte migration. Melanocytes are also a neural crest derivative and melanocyte migration defects are associated with Hirschsprung disease (Waardenburg-Shah syndrome (13, 17)). Hirschsprung disease can be caused by disruption of a number of processes, including enteric neural precursor proliferation, survival, and migration (9). *Bap1*'s role as a transcriptional and epigenetic regulator could affect all of these processes. *Bap1* loss could further impair enteric neural precursors differentiation into a full complement of neurons and glia. This could cause ENS structural abnormalities at birth even in the parts of the bowel colonized by enteric neural precursors (36, 72, 73).

To our surprise, the ENS in *Wnt1-Cre* cKO mice appeared anatomically and functionally normal at birth. In neonatal *Wnt1-Cre* cKO mice, overall enteric neuron density was normal along the length of the bowel in both myenteric and submucosal plexi. Additionally, enteric neurons were arranged into enteric ganglia connected by Tuj1+ neurites. Despite the unexpected nature of this observation, the lack of an enteric neural precursor migration defect still needs to be interpreted with caution. Previous studies have shown that Cre-mediated recombination takes place at around E8.5-E9 in the *Bap1;Wnt1-Cre* mouse model (63) and before E10.5 for the *Bap1;Tyr-cre* mouse model (64). However, we do not know how long functional BAP1 protein is retained in migrating enteric neural precursors. It seems unlikely that the functionally and anatomically normal P0 ENS can be solely explained by lingering BAP1 protein that is still able to affect cell signaling until close to birth (more than 9 days after Cre excision in the case of *Bap1;Tyr-Cre* and more than 10 days

later in the case of *Bap1;Wnt1-Cre*). However, ENS migration is completed around E13.5 and the lack of an ENS migration defect could be due to BAP1 protein activity beyond the time point of Cre mediated recombination. We are currently staining embryonic bowel during enteric neuron precursor migration with BAP1 antibodies to visualize whether loss of BAP1 protein was already complete at this stage of development.

Wnt1-Cre cKO *in vitro* proximal small intestine motility also seemed unaffected. Both the proportion of mice for which any neurally mediated contractions could be observed during the observation window and the frequency of recorded contractions was unchanged. These observations support the conclusion that *Bap1* loss does not affect the intrauterine formation of the ENS. It should be noted, however, that assessing bowel motility in neonatal mice is complicated by the relative immaturity of the ENS at that age. Neurologically mediated neurogenic contractions can be observed in proximal small intestine as early as E18.5 (71), but at that same age, neurally mediated contractions are not yet present in the colon (74). The presence of a CMC with a "defined peak of contraction" *in vitro* cannot be directly equated with normal motility patterns that productively propagate a bolus of food towards the anus. To complete the characterization of neonatal bowel motility in cKO pups, we are currently assessing *in vivo* neonatal *Wnt1-Cre* cKO proximal small intestine motility with a FITC Dextran transit assay (analogous to **Figure 5.2A-B**).

The ENS at P15 is abnormal in *Bap1;Tyr-Cre* mice

At P15, *Tyr-Cre* cKO myenteric and submucosal enteric neuron density was reduced along the length of the bowel. This decrease in enteric neuron numbers could be due to a reduction of all ENS neuron subtypes proportional to normal ENS subtype composition or a lack of specific cell populations with complete sparing of other cell types. The change in *Tyr-Cre* cKO enteric neuron density was also accompanied by *in vivo* and *in vitro* bowel dysmotility. Since loss of specific neuron subtypes in particular has been shown to cause dysmotility (30, 34), we decided to evaluate nitrergic (NOS1+) neuron density. Myenteric nitrergic neurons are functionally important since they

include interneurons and inhibitory motor neurons and, in combination with cholinergic enteric neurons, make up >95% of mouse myenteric plexus neurons (1). The data presented here is preliminary and only limited statistical conclusions could be reached, however, it appears that nitrergic neuron density was unchanged despite an overall decrease in neuron density. High variability in NOS1+ neuron numbers in individual fields of view across all genotypes was apparent. This variability made the proportion of NOS1+ neurons to total neurons easier to interpret than nitrergic neuron density since nitrergic neurons could be matched to total neuron numbers for each field of view. We are currently completing the quantification of nitrergic neuron density for the remainder of our P15 sample set.

As a next step, we will assess cholinergic enteric neuron density in P15 *Tyr-Cre* cKO mice. Cholinergic neurons comprise a large subset of submucosal neurons ~41% (75) and a subset of myenteric neurons that is mostly non-overlapping with nitrergic neurons (~70%) (76, 77). So far, we have focused exclusively on enteric neuron density at P0 and P15. However, neonatal enteric glial density as well as postnatal glial survival could also be affected by loss of *Bap1*. Loss or dysfunction of glia could even contribute to the observed functional deficit at P15 (78–80), albeit more subtly than enteric neuron dysfunction.

Loss of *Bap1* may lead to postnatal neuron loss

A postnatal loss of enteric neurons could explain the observed anatomic and functional differences in neonatal versus P15 cKO mice. We observed a worsening of *Tyr-Cre* cKO mouse health over time. At birth, *Tyr-Cre* cKO mice were indistinguishable from their littermates in size and weight and then progressively fell behind their littermates in development and bowel motility defects could be detected in most cKO mice by P15. Interestingly, the rate of phenotype worsening was not uniform. Some *Tyr-Cre* cKO pups stopped gaining weight by P5 and died before P15. In contrast, some P15 *Tyr-Cre* cKO mice exhibited normal colon motility both *in vivo* and *in vitro* and rare *Tyr-Cre* cKO bowels were still free of aggregated feces as late as P20.
282

Loss of only *Tyr-Cre* lineage neurons in cKO mice would be sufficient to explain the overall loss of myenteric neurons in the myenteric plexus. However, the drastic loss of enteric neurons in the submucosal plexus does not correlate with the modest loss of *Tyr-cre* lineage neurons in proximal small intestine and a lack of statistically significant *Tyr-Cre* lineage neuron loss in all other bowel regions. This implies that the presence of *Tyr-Cre* lineage cells also affects the survival of other enteric neurons in the submucosa.

Epithelial changes caused by loss of *Bap1* are of unclear significance

Loss of *Bap1* caused subtle changes in distal small intestine and proximal colon epithelium. We decided to look at the epithelium after we noticed apparent qualitative changes in goblet cell density in *Tyr-Cre* cKO mice (see **Supplementary Figure 5.1A-H**). Assessing epithelial changes also made sense in the context of other observations: *Tyr-Cre* cKO mice sometimes started losing weight and developed diarrhea before any feces had started to accumulate in the distal bowel, which hinted at a possible loss of absorptive capacity for nutrients and water along the bowel. Enteric neurons and glia regulate epithelial turnover and epithelial barrier function (reviewed in **Chapter 1**) and loss of enteric neuron subtype signaling can affect epithelial wound healing capacity (81). The subtle changes we quantified in P15 *Tyr-Cre* cKO pups (e.g. deeper crypts with a proportional increase in goblet cells in proximal colon and a higher density of goblet cells in distal small intestinal crypts but not villi) could be caused directly by altered enteric neuron signaling to epithelial stem cells (82–85), but more likely, the epithelial changes were secondary to prolonged exposure to aggregated feces.

Postnatal loss of *Bap1* in most ENS cells does not cause obvious pathology

Tamoxifen-induced *Bap1* loss in most of the ENS does not seem to affect survival, bowel motility or biologically significant weight change. This could mean that prenatal *Bap1* loss is necessary for the postnatal dysmotility phenotype and decrease in enteric neuron density, despite

a functional, normal-appearing ENS at birth. An alternative possibility is that the observed functional deficits in *Bap1;Tyr-Cre* mice are caused by loss of *Bap1* in a small number of enteric neurons that do not express *Ret* (1-20% of total ENS neurons, see **Figure 5.6G**). We are currently in the process of completing *in vivo* small intestine and colon motility assays for *Bap1;Ret-CreERT2* mice treated with tamoxifen in early life and adulthood to back up our preliminary observations. We are also quantifying enteric neuron density and *Ret-CreERT2* lineage neuron density in *Bap1;Ret-CreERT2* mice treated with tamoxifen at early and later time points to see if enteric neuron survival is affected by postnatal loss of *Bap1*. If we can observe a decrease in enteric neuron density in *Ret-CreERT2* cKO mice compared to wild-type mice after tamoxifen treatment , this would indicate the fascinating possibility that the ENS can buffer a statistically significant loss of enteric neurons without any obvious morbidity and that the functional deficits observed in *Tyr-Cre* cKO mice are caused by dysfunction in a relatively small subset of neurons.

Next steps - towards defining a mechanism

Our next steps will focus on better understanding how *Bap1* is causing postnatal enteric nervous system dysfunction. As a first step, we will look for apoptosis (cleaved caspase 3 staining) and evidence of double-stranded DNA breaks (stain tissue for phosphorylated histone 2AX) (86) in the ENS between P5 and P10. One of *Bap1*'s nuclear roles is facilitating double-stranded DNA break repair (49, 50). Therefore, loss of *Bap1* could cause accumulation of DNA damage resulting in ENS dysfunction and eventually loss of neurons. For example, ENS loss of *Ercc1*, an endonuclease complex subunit required for nucleotide excision repair, causes hypersensitivity to UV irradiation. In this mouse model, the ENS accumulates DNA damage, degenerates after 1 month of age, and animals experience massive colonic distention and death around 4-6 months of age (87). However, the timeline for ENS degeneration and survival in the *Ercc1* cKO mouse model is very different from that in our mice (2-4 weeks for *Bap1* versus 4-6 months for *Ercc1*), and *Ercc1* loss only leads to this drastic phenotype when combined with UV radiation exposure. This

makes accumulation of DNA damage a less likely possibility, yet a possibility we need to exclude. It should also be noted that a lack of apoptotic markers in the postnatal *Bap1;Tyr-Cre* ENS would have to be interpreted with care and cannot exclude cell death since enteric neurons can employ cell death pathways that do not depend on effector caspase activation (88).

We are also evaluating whether histone deacetylase 4 (*Hdac4*) regulation by *Bap1* contributes to the observed postnatal phenotype in the *Bap1;Tyr-Cre* cKO ENS. We were intrigued by the prominent regulatory interaction between *Bap1* and *Hdac4* in early xenopus development. Loss of both *bap1* and *hdac4* was able to rescue the prominent gastrulation and neurulation defects caused by *bap1* loss alone. Deletion of other epigenetic regulators like the polycomb repressor complex 2 subunit *ezh2* did not have any effect (55). We are currently in the process of breeding floxed *Hdac4* alleles into the *Bap1;Tyr-Cre* mouse model to assess the effect of loss of both alleles on survival and bowel phenotype. Preliminary results suggest that *Hdac4* loss by itself is insufficient to correct *Bap1*-induced postnatal ENS dysfunction (data not shown).

Lastly, we are planning to compare single cell ENS transcriptomes from *Bap1;Tyr-Cre* cKO and wild-type mice at P5. We are planning to isolate *Tyr-Cre* lineage/TDTOMATO+ neurons and glia by FACS and assess changes in RNA expression due to *Bap1* loss in comparable ENS cell types (89). This type of analysis can provide indirect evidence of epigenetic dysregulation through large numbers of dysregulated transcripts (56, 57) and may allow us to detect if any specific ENS cell types are most severely affected.

5.6 Acknowledgments

We wish to thank Jenny Yan for her invaluable technical assistance and Beth Maguire for her help with mouse colony management. Funding for the work comes from the Irma and Norman Braman

Endowment, The Children's Hospital of Philadelphia Research Institute, and the Suzi and Scott Lustgarten Center Endowment.

5.7 Authorship Contributions

Conceptualization: SS and ROH; Methodology: SS, JBA, CMW, ROH; Formal Analysis: SS, JBA, RPB, Investigation: SS, JBA, RPB; Resources: ROH and JWH; Writing - original draft: SS, JBA, ROH; Writing - Review and Editing: SS, JBA, RPB, JWH, ROH; Funding Acquisition: ROH and JWH; Supervision: JWH and ROH.

5.8 Supplementary Figures and Tables

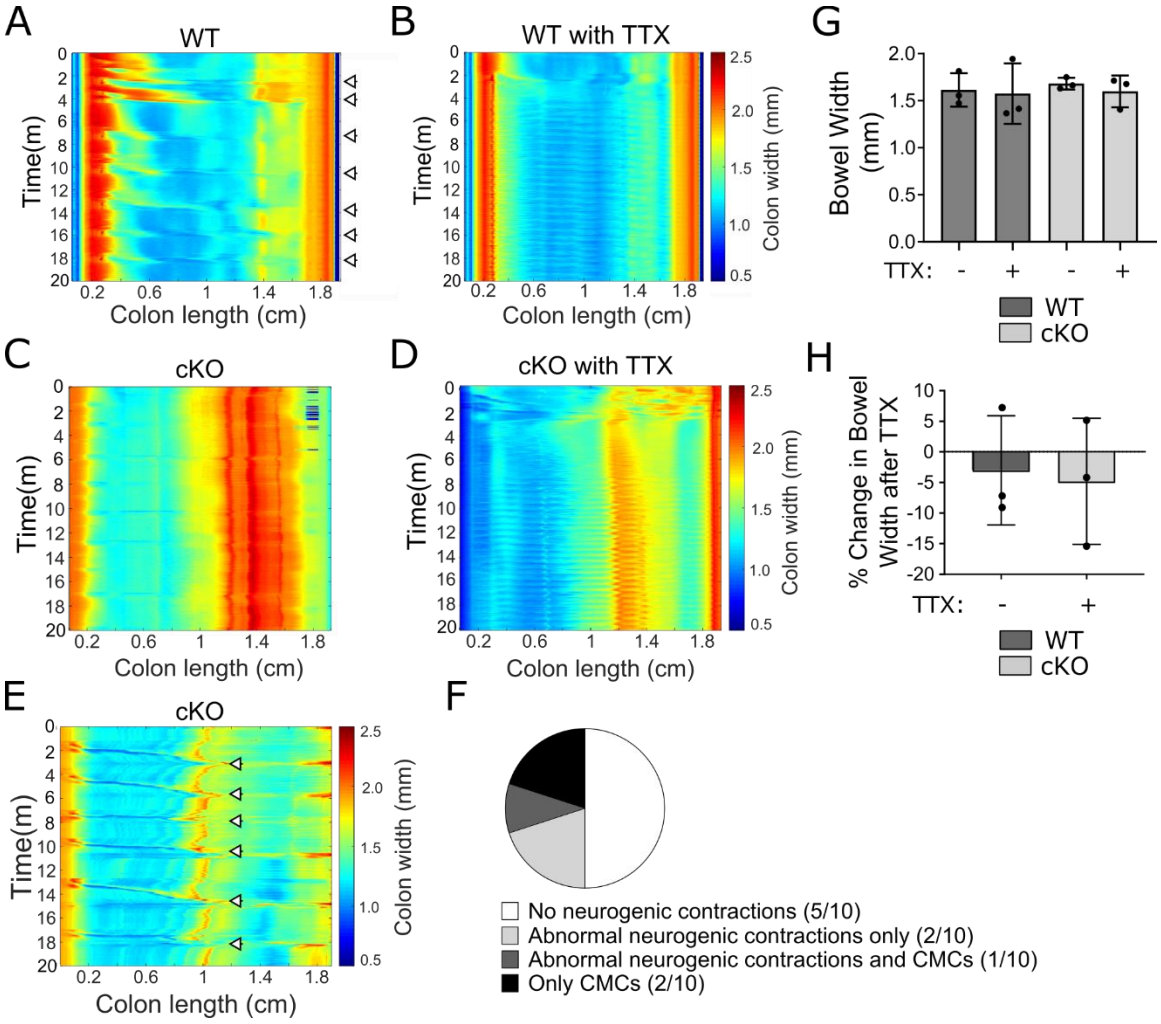

Supplementary Figure 5.1: Motility patterns observed at postnatal day 15 were neurogenic and often abnormal or absent in *Bap1 fl/fl;Tyr-Cre*+ mice.

(A-D) Representative kymographs depicting bowel width as a function of time and distance along the proximo-distal axis of the cannulated colon for WT (*Bap1 wt/wt; Tyr-cre*+; A-B) and cKO (*Bap1 fl/fl; Tyr-Cre*+; C-D) mice at postnatal day 15 (P15). (A-B) Colonic motor complexes (CMC) recorded for P15 WT mice (A; white arrows) disappeared in the presence of tetrodotoxin (TTX, B). (C-D) For some P15 cKO mice, no CMC was recorded (C) and this was also true in the presence of TTX (D). (E) Example kymograph for P15 cKO mouse shows regular but abnormal neurogenic propagating motility patterns. (F) Breakdown of the types of motility patterns observed for P15 cKO mice (n=10). (G) Colon width did not change significantly in the presence of TTX for either P15 WT or cKO mice (cKO: 2 males/1 female, WT: 2 females/1 male). (H) Percent change in colon width as compared to baseline also did not differ significantly for P15 WT and cKO mice (cKO: 2 males/ 1 females, WT: 2 females/ 1 male). (A-E) TTX = tetrodotoxin. (F-G) Graphs show mean +/- standard deviation. Data not significant unless otherwise indicated.

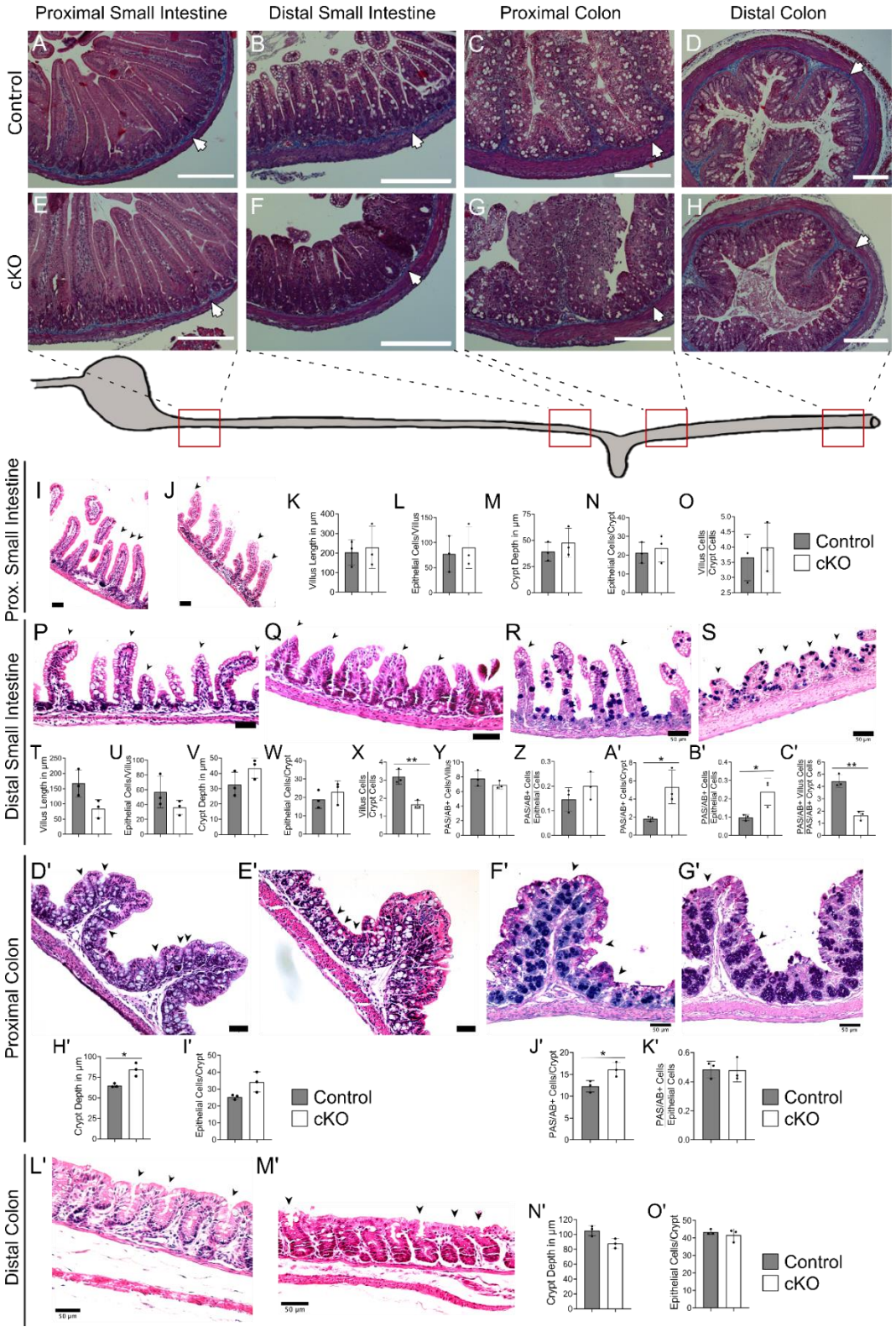
Proximal Small Intestine
Distal Small Intestine
Proximal Colon
Distal Colon
Control
cKO
A
B
C
D
E
F
G
H
Prox. Small Intestine
Distal Small Intestine
Proximal Colon
Distal Colon
I
J
K
L
M
N
O
P
Q
R
S
T
U
V
W
X
Y
Z
A'
B'
C'
D'
E'
F'
G'
H'
I'
J'
K'
L'
M'
N'
O'
Villus Length in µm
Epithelial Cells/Villus
Crypt Depth in µm
Epithelial Cells/Crypt
Villus Cells Crypt Cells
PAS/AB+ Cells/Villus
PAS/AB+ Cells/Crypt
PAS/AB+ Cells Epithelial Cells
PAS/AB+ Villus Cells PAS/AB+ Crypt Cells
Control
cKO
50 µm

Supplementary Figure 5.2: *Bap1 fl/fl; Tyr-Cre*+ mice at postnatal day 15 had altered bowel epithelium.

(A-H) Similar amounts of collagen in the bowel wall were observed in control (A-D) and cKO (E-H) proximal small intestine (A,E), distal small intestine (B,F), proximal colon (C,G), and distal colon (D,H). White arrows indicate trichrome stained collagen in submucosa (blue). Representative images shown. (I-J) Representative images of haematoxylin and eosin-stained proximal small intestine of control (I) and cKO (J) mice. Black arrowheads indicate villi that were included in the quantification. (K-O) No differences could be detected between control and cKO mice in proximal small intestine when comparing villus length (K), number of epithelial cells per villus (L), crypt length (M), and the number of epithelial cells per crypt (N). (O-P) Representative images of haematoxylin and eosin-stained distal small intestine of control (O) and cKO (P) mice. Black arrowheads indicate villi that were included in the quantification. (Q-R) Alcian Blue/Periodic Acid-Schiff staining was used to visualize goblet cells (dark purple spots within epithelium) in distal small intestine of control (Q) and cKO (R) mice. Black arrowheads indicate villi that were included in the quantification. (S-V) No differences in villus length (S), number of epithelial cells per villus (T), crypt depth (U), and number of epithelial cells/crypt (V) could be verified when distal colon epithelium of control and cKO mice was compared. Comparison of average villus length trended towards shorter villi in cKO mice (S, p=0.0533). (W-X) No difference in goblet cell number per villus (W) or per villus epithelial cell number (X) could be found in control versus cKO mice. (Y-Z) cKO distal small intestinal crypts contain a significantly greater number of goblet cells, both when normalizing to crypt depth (Y, p=0.0317) or to crypt epithelial cell numbers (Z, p=0.0315). (A'-B') Representative images of haematoxylin and eosin-stained proximal colon of control (A') and cKO (B') mice. Black arrowheads indicate villi that were included in the quantification. (C'-D') Alcian Blue/Periodic Acid-Schiff staining visualized goblet cells (dark purple spots within epithelium) in proximal colon of control (C') and cKO (D') mice. Black arrowheads point towards villi that were included in the quantification. (E') Proximal colon epithelial crypts were significantly deeper for cKO mice than control mice. (F') However, epithelial cell number per crypt was not significantly different for control and cKO mice (p=0.0675). (G') cKO mice had significantly greater numbers of goblet cells in proximal colon crypts (p=0.035). (H') This increase in goblet cell number disappeared when normalized to the number of epithelial cells per crypt. (I'-J') Representative images of haematoxylin and eosin-stained distal colon of control (I') and cKO (J') mice. Black arrowheads indicate villi that were included in the quantification. (K'-L') Distal colon crypt depth (K') and number of epithelial cells per crypt (L') were not significantly different for control and cKO mice. (A-D) Control refers to *Bap1 wt/wt;Tyr-Cre*+ genotype (n=1, 1 male) or *Bap1 fl/wt; Tyr-Cre*+ (n=4, 3 females/ 1 male). (E-H) cKO refers to *Bap1 fl/fl;Tyr-Cre*+ genotype (n=4, 3 females/ 1 males). (I-O') Control refers to *Bap1 wt/wt;Tyr-Cre*+ genotype (n=3, 2 females/ 1 male). (I-O') cKO refers to *Bap1fl/fl;Tyr-Cre* + genotype (n=3, 2 females/ 1 male). Data is presented as mean ± stdev. Unpaired t test was performed on all data sets to determine significance. Data not significant unless indicated otherwise. *p<0.05. (A-H) Scale bar = 200 μm. (I-M') Scale bar = 50 μm.

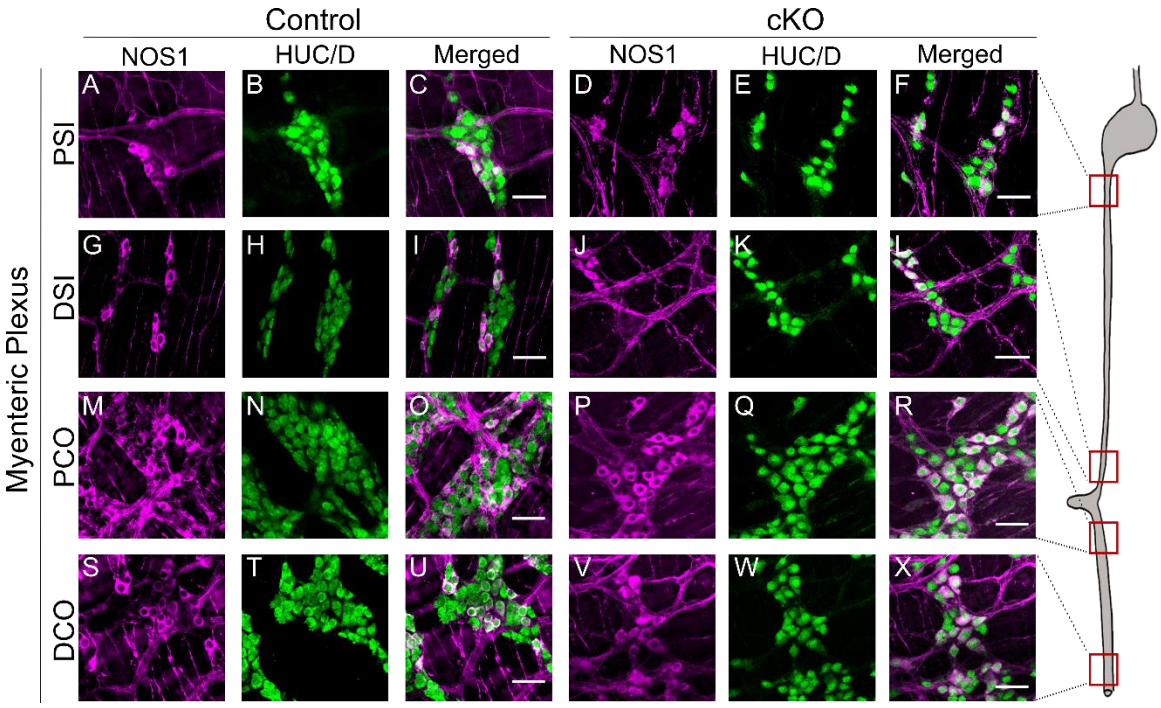

Supplementary Figure 5.3: *Bap1 fl/fl; Tyr-Cre* + mice at postnatal day 15 had decreased total enteric neuron density along the bowel and nitrergic enteric neuron density appears proportionally decreased.

(A-X) Representative images of myenteric plexus along the bowel for *Bap1 wt/wt; Tyr-Cre+* (Control; A-C, G-I, M-O, S-U) and *Bap1 fl/fl; Tyr-Cre* + (cKO; D-F, J-L, P-R, V-X) mice at postnatal day 15. (D-F, J-L, P-R) Maximum intensity z-projections. All other images are single confocal optical slices. PSI = proximal small intestine, DSI = distal small intestine, PCO = proximal colon, DCO = distal colon. Scale bar = 50 μm.

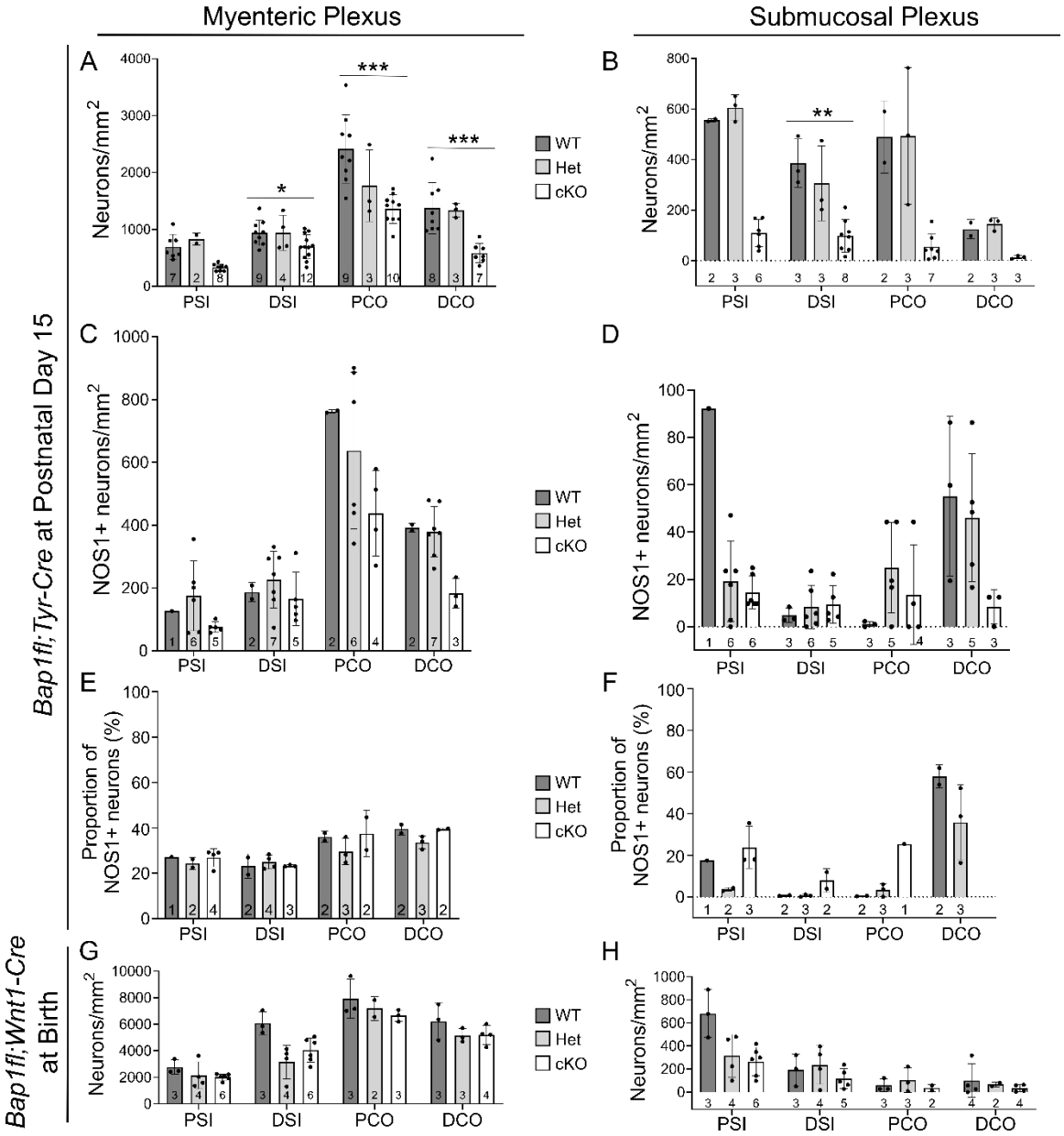

Supplementary Figure 5.4: Preliminary analysis suggests *Bap1 fl/fl; Tyr-Cre* + mice had decreased total enteric neuron density along the bowel by postnatal day 15, but are born with normal neuron density. Nitrergic neurons may decrease proportionally to total neuron numbers.

(A-B) Preliminary analysis of total neuron density in *Bap1;Tyr-Cre* mice at postnatal day 15 (P15) suggests decreased neuron density for cKO mice in both myenteric (A) and submucosal plexus (B) in all regions of the bowel (One-Way ANOVA with Tukey's Multiple Comparisons Test; myenteric PSI: n too small for statistics, myenteric DSI: p= 0.0489, myenteric PCO: p = 0.0005, myenteric DCO: p = 0.0007; submucosal PSI/PCO/DCO: n too small for statistical analysis, submucosal DSI:

p = 0.0011). (C-D) Preliminary analysis of nitrergic neuron density (NOS1+) in P15 *Bap1;Tyr-Cre* mice indicates that there is no difference in NOS1+ neuron density between WT, Het, and cKO bowel in myenteric (C) and submucosal plexus (D) (all n too small for statistical analysis). (E-F) However, preliminary analysis of the proportion of nitrergic neurons in P15 *Bap1;Tyr-Cre* mice suggests a proportional decrease of NOS1+ neuron density in myenteric plexus (E) in all bowel regions (all n too small for statistical analysis). No conclusions can be drawn about submucosal plexus (H) at this time. (G-H) Preliminary analysis of total neuron density in *Bap1;Wnt1-Cre* mice at birth suggests no significant difference between WT, Het, and cKO mice in myenteric (G) and submucosal plexus (H; (all n too small for statistical analysis). (A-G) WT refers to *Bap1 wt/wt; Tyr-Cre* + or any genotype without *Cre* allele, Het refers to *Bap1 fl/wt; Tyr-Cre* +, and cKO refers to *Bap1 fl/fl; Tyr-Cre* +. All data represented as mean +/- standard deviation. *p<0.05, **p0.01, ***p<0.001, ****p<0.0001.

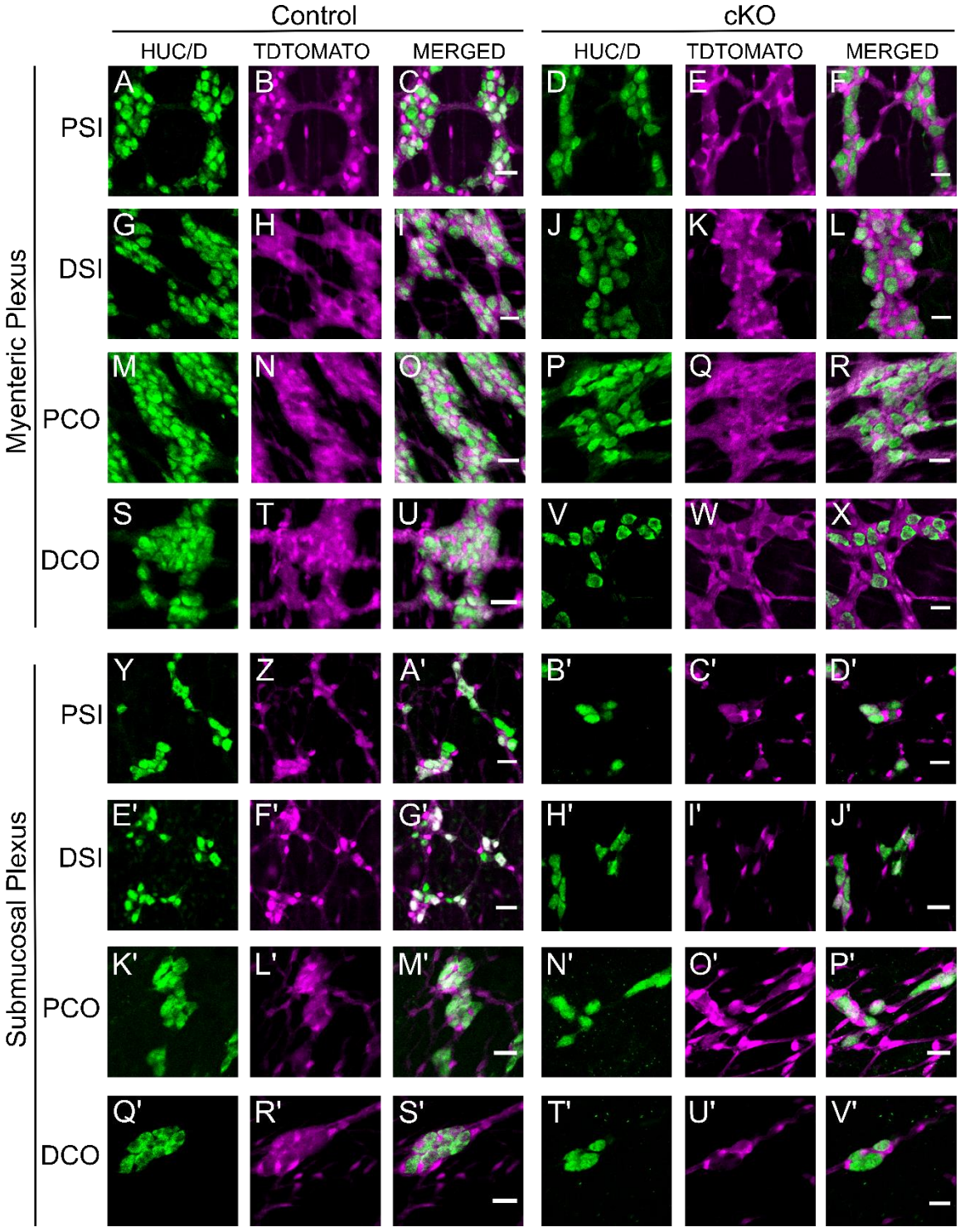

Supplementary Figure 5.5: *Bap1 fl/fl; Tyr-Cre+* mice lose neurons of the *Tyr-Cre* lineage by postnatal day 15.

(A-V') Representative images showing enteric neurons (HUC/D+, green) and neurons of the *Tyr-Cre* lineage (TDTOMATO+, magenta) in different bowel regions for Control (*Bap1 wt/wt; Tyr-Cre*+; D-F, J-L, P-R, V-X, B'-D', H'-J', N'-P', and T'-V') and cKO (*Bap1 fl/fl; Tyr-Cre*+; A-C, G-I, M-O, S-U, Y-A', E'-G', K'-M', and Q'-S') mice at postnatal day 15. (D-F, B'-D', K'-P') Maximum intensity z-projections. All other images are single confocal optical slices. PSI= proximal small intestine, DSI = distal small intestine, PCO = proximal colon, and DCO = distal colon. Scale bar = 25 μm.

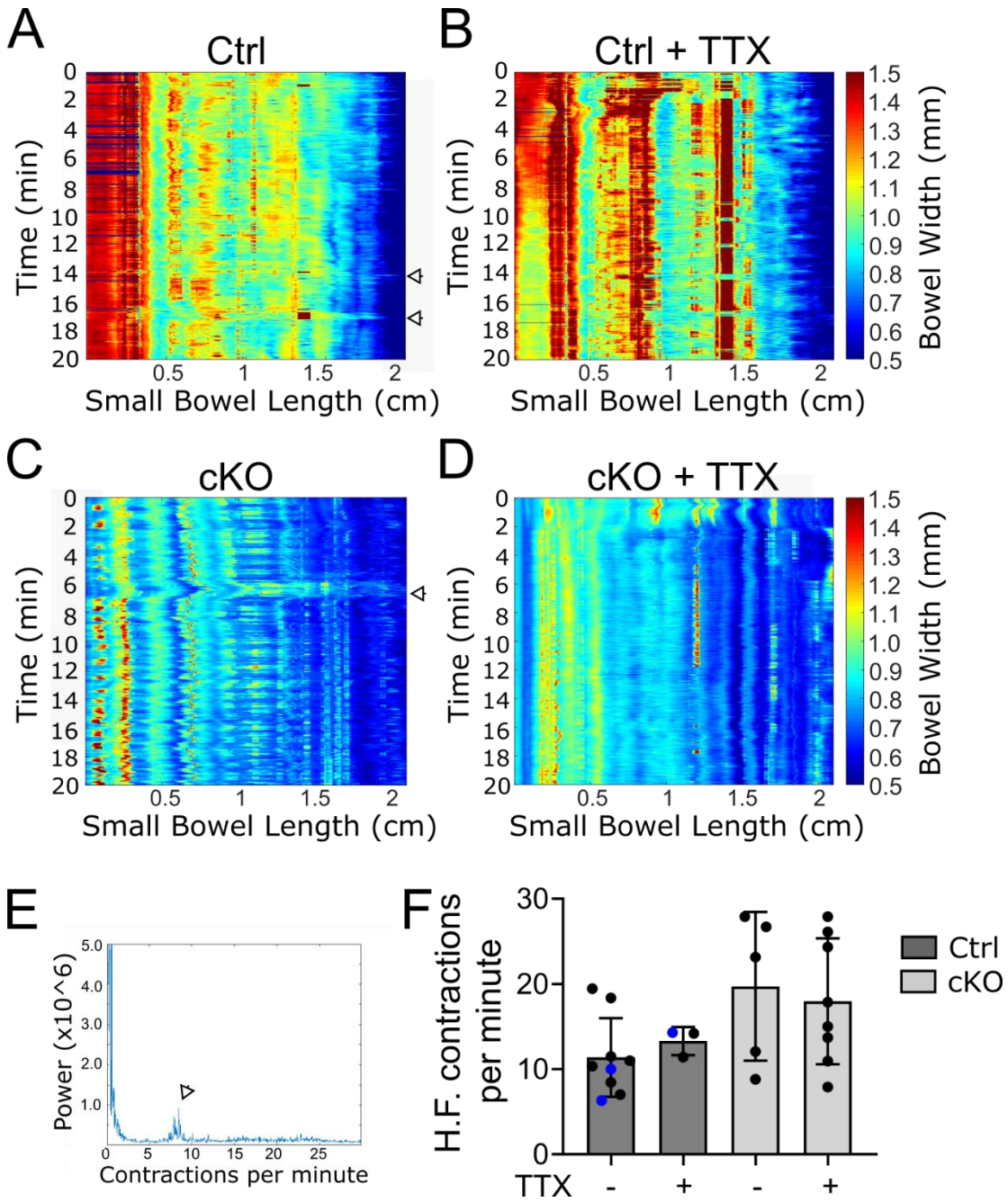

Supplementary Figure 5.6: Neonatal proximal small intestine motility patterns observed *in vitro* are neurogenic and *Bap1 fl/fl; Wnt1-Cre+* mice exhibited normal myogenic contraction frequency at birth.

(A-D) Representative kymographs depicting bowel width as a function of time and distance along the proximo-distal axis of the cannulated proximal small intestine for neonatal control (Ctrl; A-B) and cKO (C-D) mice. (A-B) Low frequency (L.F.) contractions could be recorded for a subset of control mice (A; white arrows) and these L.F. contractions disappeared in the presence of tetrodotoxin (TTX, B). (C-D) Low frequency (L.F.) contractions could also be recorded for a subset

of cKO mice (C; white arrows) and these contractions also disappeared in the presence of tetrodotoxin (TTX, D). (E) Example Fourier transform of the recorded contractions that allows the identification of regularly-occurring myogenic higher frequency contractions (H.F. contractions; white arrow). (F) There was no difference in the frequency of myogenic H.F. contractions recorded for control and cKO neonates and the frequency of contractions was also unaffected by the presence of tetrodotoxin ([No TTX: Ctrl: WT 5 males/ 2 females and Het 1 male/2 unknown (11.38 ± 4.62), cKO: 6 females/ 1 male/ 2 unknown (19.97 ± 7.4)]. [+TTX: Ctrl: 2 male/ 1 unknown (13.30 ± 1.65), KO: 5 females (19.72 ± 8.74)]). Data points derived from Hets are marked by blue color. (A-F) WT refers to *Bap1 wt/wt; Wnt1-Cre*+ or any genotype without the *Wnt1-Cre* transgene. Het refers to *Bap1 fl/wt; Wnt1-Cre*+ genotype. cKO refers to *Bap1 fl/fl; Wnt1-Cre*+ genotype. (F) Data represented as mean ± standard deviation. Data not significant unless otherwise indicated.

Supplementary Table 5.1: ARRIVE Guidelines - General animal husbandry information

Location of Animal facility (types of experiments)	**Childrens' Hospital of Philadelphia**
Facility Type	Conventional: cages are opened at room air, face masks are not required when handling mice
Facility Type	Specific pathogen free, Pathogens detected in room within the past 2 years: MNV (mouse norovirus), Helicobacter not tested but likely present
Bedding	¼ inch corncob (The Andersons, Product 4B)
Cage type	Lab Products (Seaford, DE) 75 sq. in. Ventilated.
Cage cleaning/sterilization	Standard tunnel washer
Mouse diet	Mouse Diet 5015 (Lab Diet), direct from manufacturer: not autoclaved, not irradiated
Light-dark cycle	12/12

Location of Animal facility (types of experiments)	**Childrens' Hospital of Philadelphia**
Temperature	72°F +/- 2°F
Humidity	30-70% depending on the day/season
Water pH and quality	Reverse Osmosis, pH~7, Edstrom automatic watering system
Number of mice per cage	1-5 (20-30g)
Cage Enrichment	house/dome (Bioserve, S3174) and nestlet (Ancare)
Mating strategy	Continuous
Age at weaning	19-20 days
Access to food and water	Continuous
Animal welfare assessment	Daily
Cage changes	1x/week

Supplementary Table 5.2: List of antibodies

Antibody	Concentration	Catalog number	Source
Rabbit anti-NOS1	1:200	AB5380	Sigma; RRID:AB_91824
ANNA-1 (HuC/D)	N/A	N/A	Kind gift from Dr. V. Lennon, Mayo Clinic
Chicken anti-GFP	1:500	GFP-1020	Aves Labs, RRID:AB_10000240
Goat anti-SOX10	1:100	AF2864	R&D Systems, RRID:AB_442208
Rabbit anti-Cleaved Caspase 3	1:150	9661S	Cell Signaling, RRID:AB_2341188
Rabbit anti-H2AX	1:300	A300-081A	Bethyl Laboratories, RRID:AB_203288
Alexa Fluor goat anti-human 647	1:400	A21445	Thermo Fisher Scientific; RRID:AB_2535862
AlexaFluor donkey anti-rabbit 488	1:400	A21206	Thermo Fisher Scientific; RRID:AB_2535792
AlexaFluor donkey anti-rabbit 594	1:400	A21207	Thermo Fisher Scientific; RRID:AB_141637
AlexaFluor donkey anti-rabbit 647	1:400	A31573	Thermo Fisher Scientific; RRID:AB_2536183
AlexaFluor donkey anti-goat 594	1:400	A11058	Thermo Fisher Scientific; RRID:AB_2534105
AlexaFluor goat anti-chicken 488	1:400	A11039	Thermo Fisher Scientific; RRID:AB_142924
AlexaFluor donkey anti-goat 647	1:400	A21447	Thermo Fisher Scientific; RRID:AB_141844
AlexaFluor donkey anti-goat 488	1:400	A11055	Thermo Fisher Scientific; RRID:AB_2534102
AlexaFluor goat anti-rabbit 488	1:400	A31556	Thermo Fisher Scientific; RRID:AB_221605
DyLight donkey anti-human 488	1:200	ab102424	Abcam; RRID:AB_10710634
DyLight donkey anti-human 650	1:200	ab102427	Abcam; RRID:AB_10711474

Supplementary Table 5.3: List of PCR primers for mouse genotyping

Gene (Strain)	Primer Sequence	Band size	Genotyping solution	Reference
Bap1	F: 5'-AGC GTG CTT CTG AAC TGC AGC AAT GTG GAT-3' R: 5'-TTC TGA AAG GGC AGT GGT GGC AAA TGA GAC-3'	Mut: 520bp WT: 423bp	Taq (NEB, Cat#:M0271L)	Personal communication with Dr. J. William Harbour
Gfp (ChAT-EGFP-L10a)	F: 5'-TCA TAG AGG CGC AGA GTT CC-3' R: 5'-CTG AAC TTG TGG CCG TTT AC-3'	Mut: 250bp	KAPA (KAPA Biosystems, Cat#:KK7352)	JAX genotyping protocol (Stock No: 030250)
Cre (Wnt1-Cre and *Tyr-Cre)*	F: 5'-GCA TTA CCG GTC GAT GCA ACG AGT GAT GAG-3' R: 5'-GAG TGA ACG AAC CTG GTC GAA ATC AGT GCG-3'	408bp	KAPA (KAPA Biosystems, Cat #KK7352), Taq (NEB, Cat#:M0271L)	https://mgc.wustl.edu/protocols/pcr_genotyping_primer_pairs
R26R-TdTomato	Common F: 5'-AAA GTC GCT CTG AGT TGT TAT-3' Tg R: 5'-GCG AAG AGT TTG TCC TCA ACC-3' WT R: 5'-GGA GCG GGA GAA ATG GAT ATG-3'	Mut: ~350bp WT: ~600bp	KAPA (KAPA Biosystems, Cat #KK7352), Taq (NEB, Cat#:M0271L)	JAX genotyping protocol (Stock No: 007909)
Hdac4	F: 5'-ATC TGC CCA CCA GAG TAT GTG-3' R: 5'-CTT GTT GAG AAC AAA CTC CTG CAG CT-3'	Mut: 620bp WT: 480bp	Taq (NEB, Cat#:M0271L)	Personal communication with Dr. Kelly A. Hyndman

5.9 References

1. Furness JB, Callaghan BP, Rivera LR, Cho H-J. The enteric nervous system and gastrointestinal innervation: integrated local and central control. *Adv. Exp. Med. Biol.* 2014;817:39–71.

2. Boesmans W, Lasrado R, Vanden Berghe P, Pachnis V. Heterogeneity and phenotypic plasticity of glial cells in the mammalian enteric nervous system. *Glia* 2015;63(2):229–241.

3. Fung C, Vanden Berghe P. Functional circuits and signal processing in the enteric nervous system [Internet]. *Cell. Mol. Life Sci.* [published online ahead of print: May 18, 2020]; doi:10.1007/s00018-020-03543-6

4. Furness JB. *The Enteric Nervous System*. Malden, Mass: Wiley; 2006:

5. Schneider S, Wright CM, Heuckeroth RO. Unexpected Roles for the Second Brain: Enteric Nervous System as Master Regulator of Bowel Function [Internet]. *Annu. Rev. Physiol.* [published online ahead of print: October 31, 2018]; doi:10.1146/annurev-physiol-021317-121515

6. Heuckeroth RO. Hirschsprung disease - integrating basic science and clinical medicine to improve outcomes. *Nat. Rev. Gastroenterol. Hepatol.* 2018;15(3):152–167.

7. Obermayr F, Hotta R, Enomoto H, Young HM. Development and developmental disorders of the enteric nervous system. *Nat. Rev. Gastroenterol. Hepatol.* 2013;10(1):43–57.

8. Knowles CH, Lindberg G, Panza E, De Giorgio R. New perspectives in the diagnosis and management of enteric neuropathies. *Nat. Rev. Gastroenterol. Hepatol.* 2013;10(4):206–218.

9. Lake JI, Heuckeroth RO. Enteric nervous system development: migration, differentiation, and disease. *Am. J. Physiol. Gastrointest. Liver Physiol.* 2013;305(1):G1–24.

10. Kapoor A et al. Population variation in total genetic risk of Hirschsprung disease from common RET, SEMA3 and NRG1 susceptibility polymorphisms. *Hum. Mol. Genet.* 2015;24(10):2997–3003.

11. Luzón-Toro B et al. Mutational spectrum of semaphorin 3A and semaphorin 3D genes in Spanish Hirschsprung patients. *PLoS One* 2013;8(1):e54800.

12. Alves MM et al. Contribution of rare and common variants determine complex diseases-Hirschsprung disease as a model. *Dev. Biol.* 2013;382(1):320–329.

13. Hosoda K et al. Targeted and Natural (Piebald-Lethal) Mutations f Endothelin-B Receptor Gene Produce Megacolon Associated with Spotted Coat Color in Mice. *Ceil, Voi.* 1994;79:1267–1276.

14. Baynash AG et al. Interaction of endothelin-3 with endothelin-B receptor is essential for development of epidermal melanocytes and enteric neurons. *Cell* 1994;79(7):1277–1285.

15. Yamada T et al. Reduced expression of the endothelin receptor type B gene in piebald mice caused by insertion of a retroposon-like element in intron 1. *J. Biol. Chem.* 2006;281(16):10799–10807.

16. Pavan WJ et al. A high-resolution linkage map of the lethal spotting locus: a mouse model for Hirschsprung disease. *Mamm. Genome* 1995;6(1):1–7.

17. Minami SB et al. A clinical and genetic study of 16 Japanese families with Waardenburg syndrome. *Gene* 2019;704:86–90.

18. Lane PW. Association of megacolon with two recessive spotting genes in the mouse. *J. Hered.* 1966;57(1):29–31.

19. Bondurand N et al. Deletions at the SOX10 gene locus cause Waardenburg syndrome types 2 and 4. *Am. J. Hum. Genet.* 2007;81(6):1169–1185.

20. Lane PW, Liu HM. Association of megacolon with a new dominant spotting gene (Dom) in the mouse. *J. Hered.* 1984;75(6):435–439.

21. Paratore C, Eichenberger C, Suter U, Sommer L. Sox10 haploinsufficiency affects maintenance of progenitor cells in a mouse model of Hirschsprung disease. *Hum. Mol. Genet.* 2002;11(24):3075–3085.

22. Southard-Smith EM et al. Comparative analyses of the Dominant megacolon-SOX10 genomic interval in mouse and human. *Mamm. Genome* 1999;10(7):744–749.

23. Musser MA, Correa H, Southard-Smith EM. Enteric neuron imbalance and proximal dysmotility in ganglionated intestine of the Sox10(Dom/+) Hirschsprung mouse model. *Cell Mol Gastroenterol Hepatol* 2015;1(1):87–101.

24. Pingault V et al. Peripheral neuropathy with hypomyelination, chronic intestinal pseudo-obstruction and deafness: a developmental “neural crest syndrome” related to a SOX10 mutation. *Ann. Neurol.* 2000;48(4):671–676.

25. Gargiulo A et al. Filamin A is mutated in X-linked chronic idiopathic intestinal pseudo-obstruction with central nervous system involvement. *Am. J. Hum. Genet.* 2007;80(4):751–758.

26. Chetaille P et al. Mutations in SGOL1 cause a novel cohesinopathy affecting heart and gut rhythm. *Nat. Genet.* 2014;46(11):1245–1249.

27. Bonora E et al. Mutations in RAD21 disrupt regulation of APOB in patients with chronic intestinal pseudo-obstruction. *Gastroenterology* 2015;148(4):771–782.e11.

28. Amiot A et al. Frequency of mitochondrial defects in patients with chronic intestinal pseudo-obstruction. *Gastroenterology* 2009;137(1):101–109.

29. Antonucci A et al. Chronic intestinal pseudo-obstruction. *World J. Gastroenterol.* 2008;14(19):2953–2961.

30. Memic F et al. Transcription and Signaling Regulators in Developing Neuronal Subtypes of Mouse and Human Enteric Nervous System. *Gastroenterology* 2018;154(3):624–636.

31. Morarach K, Mikhailova A, Knoflach V, Memic F. Diversification of molecularly defined myenteric neuron classes revealed by single cell RNA-sequencing [Internet]. *bioRxiv* [published online ahead of print: 2020];https://www.biorxiv.org/content/10.1101/2020.03.02.955757v1.abstract. cited

32. Drokhlyansky E et al. The enteric nervous system of the human and mouse colon at a single-cell resolution [Internet]. *bioRxiv* 2019;746743.

33. Memic F et al. Ascl1 Is Required for the Development of Specific Neuronal Subtypes in the Enteric Nervous System. *J. Neurosci.* 2016;36(15):4339–4350.

34. Wright CM et al. Dlx1/2 mice have abnormal enteric nervous system function [Internet]. *JCI Insight* 2020;5(4). doi:10.1172/jci.insight.131494

35. Blaugrund E et al. Distinct subpopulations of enteric neuronal progenitors defined by time of development, sympathoadrenal lineage markers and Mash-1-dependence. *Development* 1996;122(1):309–320.

36. Hendershot TJ et al. Expression of Hand2 is sufficient for neurogenesis and cell type-specific gene expression in the enteric nervous system. *Dev. Dyn.* 2007;236(1):93–105.

37. Lei J, Howard MJ. Targeted deletion of Hand2 in enteric neural precursor cells affects its functions in neurogenesis, neurotransmitter specification and gangliogenesis, causing functional aganglionosis. *Development* 2011;138(21):4789–4800.

38. Minoux M et al. Gene bivalency at Polycomb domains regulates cranial neural crest positional identity [Internet]. *Science* 2017;355(6332). doi:10.1126/science.aal2913

39. Simões-Costa M, Bronner ME. Establishing neural crest identity: a gene regulatory recipe. *Development* 2015;142(2):242–257.

40. Lasrado R et al. Lineage-dependent spatial and functional organization of the mammalian enteric nervous system. *Science* 2017;356(6339):722–726.

41. Hu N, Strobl-Mazzulla PH, Bronner ME. Epigenetic regulation in neural crest development. *Dev. Biol.* 2014;396(2):159–168.

42. Soldatov R et al. Spatiotemporal structure of cell fate decisions in murine neural crest [Internet]. *Science* 2019;364(6444). doi:10.1126/science.aas9536

43. Kim H, Kang K, Ekram MB, Roh T-Y, Kim J. Aebp2 as an epigenetic regulator for neural crest cells. *PLoS One* 2011;6(9):e25174.

44. Kim H et al. Ablation of Ezh2 in neural crest cells leads to aberrant enteric nervous system development in mice. *PLoS One* 2018;13(8):e0203391.

45. Villalba-Benito L et al. Overexpression of DNMT3b target genes during Enteric Nervous System development contribute to the onset of Hirschsprung disease. *Sci. Rep.* 2017;7(1):6221.

46. Bononi A et al. BAP1 regulates IP3R3-mediated Ca2+flux to mitochondria suppressing cell transformation. *Nature* 2017;546(7659):549–553.

47. Mashtalir N et al. Autodeubiquitination protects the tumor suppressor BAP1 from cytoplasmic sequestration mediated by the atypical ubiquitin ligase UBE2O. *Mol. Cell* 2014;54(3):392–406.

48. Lee H-S, Lee S-A, Hur S-K, Seo J-W, Kwon J. Stabilization and targeting of INO80 to replication forks by BAP1 during normal DNA synthesis. *Nat. Commun.* 2014;5:5128.

49. Ismail IH et al. Germline mutations in BAP1 impair its function in DNA double-strand break repair. *Cancer Res.* 2014;74(16):4282–4294.

50. Yu H et al. Tumor suppressor and deubiquitinase BAP1 promotes DNA double-strand break repair. *Proc. Natl. Acad. Sci. U. S. A.* 2014;111(1):285–290.

51. Yu H et al. The ubiquitin carboxyl hydrolase BAP1 forms a ternary complex with YY1 and HCF-1 and is a critical regulator of gene expression. *Mol. Cell. Biol.* 2010;30(21):5071–5085.

52. Dey A et al. Loss of the tumor suppressor BAP1 causes myeloid transformation. *Science* 2012;337(6101):1541–1546.

53. Ruan H-B et al. O-GlcNAc transferase/host cell factor C1 complex regulates gluconeogenesis by modulating PGC-1α stability. *Cell Metab.* 2012;16(2):226–237.

54. Gambetta MC, Oktaba K, Müller J. Essential role of the glycosyltransferase sxc/Ogt in polycomb repression. *Science* 2009;325(5936):93–96.

55. Kuznetsov JN et al. BAP1 regulates epigenetic switch from pluripotency to differentiation in developmental lineages giving rise to BAP1-mutant cancers. *Sci Adv* 2019;5(9):eaax1738.

56. LaFave LM et al. Loss of BAP1 function leads to EZH2-dependent transformation. *Nat. Med.* 2015;21(11):1344–1349.

57. Campagne A et al. BAP1 complex promotes transcription by opposing PRC1-mediated H2A ubiquitylation. *Nat. Commun.* 2019;10(1):348.

58. Harbour JW et al. Frequent mutation of BAP1 in metastasizing uveal melanomas. *Science* 2010;330(6009):1410–1413.

59. Moon S, Lee Y-K, Lee S-W, Um S-J. Suppressive role of OGT-mediated O-GlcNAcylation of BAP1 in retinoic acid signaling. *Biochem. Biophys. Res. Commun.* 2017;492(1):89–95.

60. Fu M et al. Vitamin A facilitates enteric nervous system precursor migration by reducing Pten accumulation. *Development* 2010;137(4):631–640.

61. Simkin JE, Zhang D, Rollo BN, Newgreen DF. Retinoic acid upregulates ret and induces chain migration and population expansion in vagal neural crest cells to colonise the embryonic gut. *PLoS One* 2013;8(5):e64077.

62. Sato Y, Heuckeroth RO. Retinoic acid regulates murine enteric nervous system precursor proliferation, enhances neuronal precursor differentiation, and reduces neurite growth in vitro. *Dev. Biol.* 2008;320(1):185–198.

63. Danielian PS, Muccino D, Rowitch DH, Michael SK, McMahon AP. Modification of gene activity in mouse embryos in utero by a tamoxifen-inducible form of Cre recombinase. *Curr. Biol.* 1998;8(24):1323–1326.

64. Fu M et al. Retinoblastoma protein prevents enteric nervous system defects and intestinal pseudo-obstruction. *J. Clin. Invest.* 2013;123(12):5152–5164.

65. Kilkenny C, Browne WJ, Cuthill IC, Emerson M, Altman DG. Improving bioscience research reporting: the ARRIVE guidelines for reporting animal research. *Osteoarthritis Cartilage* 2012;20(4):256–260.

66. Guo Y et al. Reduced BAP1 activity prevents ASXL1 truncation-driven myeloid malignancy in vivo [Internet]. *Leukemia* 2018;32(8):1834–1837.

67. Harrington B, Engelen J. Inkscape. *Software available at http://www. inkscape. org* 2004;

68. Corsetti M et al. First translational consensus on terminology and definitions of colonic motility in animals and humans studied by manometric and other techniques. *Nat. Rev. Gastroenterol. Hepatol.* 2019;16(9):559–579.

69. Herath M, Hosie S, Bornstein JC, Franks AE, Hill-Yardin EL. The Role of the Gastrointestinal Mucus System in Intestinal Homeostasis: Implications for Neurological Disorders. *Front. Cell. Infect. Microbiol.* 2020;10:248.

70. Lake JI, Avetisyan M, Zimmermann AG, Heuckeroth RO. Neural crest requires Impdh2 for development of the enteric nervous system, great vessels, and craniofacial skeleton. *Dev. Biol.* 2016;409(1):152–165.

71. Roberts RR et al. The first intestinal motility patterns in fetal mice are not mediated by neurons or interstitial cells of Cajal. *J. Physiol.* 2010;588(Pt 7):1153–1169.

72. Nishino J, Saunders TL, Sagane K, Morrison SJ. Lgi4 promotes the proliferation and differentiation of glial lineage cells throughout the developing peripheral nervous system. *J. Neurosci.* 2010;30(45):15228–15240.

73. Chalazonitis A et al. Neurotrophin-3 Is Required for the Survival–Differentiation of Subsets of Developing Enteric Neurons. *J. Neurosci.* 2001;21(15):5620–5636.

74. Roberts RR, Murphy JF, Young HM, Bornstein JC. Development of colonic motility in the neonatal mouse-studies using spatiotemporal maps. *Am. J. Physiol. Gastrointest. Liver Physiol.* 2007;292(3):G930–8.

75. Mongardi Fantaguzzi C, Thacker M, Chiocchetti R, Furness JB. Identification of neuron types in the submucosal ganglia of the mouse ileum. *Cell Tissue Res.* 2009;336(2):179–189.

76. Qu Z-D et al. Immunohistochemical analysis of neuron types in the mouse small intestine. *Cell Tissue Res.* 2008;334(2):147–161.

77. Sang Q, Young HM. Chemical coding of neurons in the myenteric plexus and external muscle of the small and large intestine of the mouse. *Cell Tissue Res.* 1996;284(1):39–53.

78. Bassotti G, Villanacci V, Antonelli E, Morelli A, Salerni B. Enteric glial cells: new players in gastrointestinal motility?. *Lab. Invest.* 2007;87(7):628–632.

79. McClain J et al. Ca2+ responses in enteric glia are mediated by connexin-43 hemichannels and modulate colonic transit in mice. *Gastroenterology* 2014;146(2):497–507.e1.

80. Rao M et al. Enteric Glia Regulate Gastrointestinal Motility but Are Not Required for Maintenance of the Epithelium in Mice. *Gastroenterology* 2017;153(4):1068–1081.e7.

81. Avetisyan M et al. Hepatocyte Growth Factor and MET Support Mouse Enteric Nervous System Development, the Peristaltic Response, and Intestinal Epithelial Proliferation in Response to Injury. *J. Neurosci.* 2015;35(33):11543–11558.

82. Bjerknes M, Cheng H. Modulation of specific intestinal epithelial progenitors by enteric neurons. *Proc. Natl. Acad. Sci. U. S. A.* 2001;98(22):12497–12502.

83. Puzan M, Hosic S, Ghio C, Koppes A. Enteric Nervous System Regulation of Intestinal Stem Cell Differentiation and Epithelial Monolayer Function. *Sci. Rep.* 2018;8(1):6313.

84. Takahashi T, Shiraishi A, Murata J. The Coordinated Activities of nAChR and Wnt Signaling Regulate Intestinal Stem Cell Function in Mice [Internet]. *Int. J. Mol. Sci.* 2018;19(3). doi:10.3390/ijms19030738

85. Greig CJ, Cowles RA. Muscarinic acetylcholine receptors participate in small intestinal mucosal homeostasis. *J. Pediatr. Surg.* 2017;52(6):1031–1034.

86. Kuo LJ, Yang L-X. Gamma-H2AX - a novel biomarker for DNA double-strand breaks. *In Vivo* 2008;22(3):305–309.

87. Selfridge J, Song L, Brownstein DG, Melton DW. Mice with DNA repair gene Ercc1 deficiency in a neural crest lineage are a model for late-onset Hirschsprung disease. *DNA Repair* 2010;9(6):653–660.

88. Uesaka T et al. Conditional ablation of GFRalpha1 in postmigratory enteric neurons triggers unconventional neuronal death in the colon and causes a Hirschsprung's disease phenotype. *Development* 2007;134(11):2171–2181.

89. Anderson AG, Kulkarni A, Harper M, Konopka G. Single-Cell Analysis of Foxp1-Driven Mechanisms Essential for Striatal Development. *Cell Rep.* 2020;30(9):3051–3066.e7.

CHAPTER 6: APPENDIX A: ROBUST, 3-DIMENSIONAL VISUALIZATION OF HUMAN COLON ENTERIC NERVOUS SYSTEM WITHOUT TISSUE SECTIONING

This chapter has been published in *Gastroenterology* and reprinted here with permission Kahleb D. Graham*, Silvia Huerta López*, Rajarshi Sengupta, Archana Shenoy, Sabine Schneider, Christina M. Wright, Michael Feldman, Emma Furth, Federico Valdivieso, Amanda Lemke, Benjamin J. Wilkins, Ali Naji, Edward J. Doolin, Marthe J. Howard, and Robert O. Heuckeroth. Robust, 3-Dimensional Visualization of Human Colon Enteric Nervous System Without Tissue Sectioning. *Gastroenterology.* 2020 June 1; VOLUME 158, ISSUE 8, P2221-2235.E5. doi: https://doi.org/10.1053/j.gastro.2020.02.035.

* Co-first authors; contributed equally

6.1 Abstract

BACKGROUND & AIMS: Small, 2-dimensional sections routinely used for human pathology analysis provide limited information about bowel innervation. We developed a technique to image human enteric nervous system (ENS) and other intramural cells in 3 dimensions.

METHODS: Using mouse and human colon tissues, we developed a method that combines tissue clearing, immunohistochemistry, confocal microscopy, and quantitative analysis of full-thickness bowel without sectioning to quantify ENS and other intramural cells in 3 dimensions.

RESULTS: We provided 280 adult human colon confocal Z-stacks from persons without known bowel motility disorders. Most of our images were of myenteric ganglia, captured using a 20x objective lens. Full-thickness colon images, viewed with a 10x objective lens, were as large as 4 x 5 mm^2. Colon from 2 pediatric patients with Hirschsprung disease was used to show distal colon without enteric ganglia, as well as a transition zone and proximal pull-through resection margin where ENS was present. After testing a panel of antibodies with our method, we identified 16 antibodies that bind to molecules in neurons, glia, interstitial cells of Cajal, and muscularis

macrophages. Quantitative analyses demonstrated myenteric plexus in 24.5% ± 2.4% of flattened colon Z-stack area. Myenteric ganglia occupied 34% ± 4% of myenteric plexus. Single myenteric ganglion volume averaged 3,527,678 ± 573,832 mm^3 with 38,706 ± 5763 neuron/mm^3 and 129,321 ± 25,356 glia/mm^3. Images of large areas provided insight into why published values of ENS density vary up to 150- fold—ENS density varies greatly, across millimeters, so analyses of small numbers of thin sections from the same bowel region can produce varying results. Neuron subtype analysis revealed that approximately 56% of myenteric neurons stained with neuronal nitric oxide synthase antibody and approximately 33% of neurons produce and store acetylcholine. Transition zone regions from colon tissues of patients with Hirschsprung disease had ganglia in multiple layers and thick nerve fiber bundles without neurons. Submucosal neuron distribution varied among imaged colon regions.

CONCLUSIONS: We developed a 3-dimensional imaging method for colon that provides more information about ENS structure than tissue sectioning. This approach could improve diagnosis for human bowel motility disorders and may be useful for other bowel diseases as well.

6.2 Introduction

The enteric nervous system (ENS) controls most aspects of bowel function and is thought to contain as many neurons as the spinal cord, with approximately 20 neuron and 4–7 glial cell types (1–4). ENS defects can cause debilitating or life-threatening bowel dysfunction, including diverse motility disorders. In many cases, human diseases are well-modeled by mouse mutations that cause striking changes in ENS anatomy (5,6). ENS structural defects are readily visualized in mice via whole-mount staining because murine bowel is thin. In contrast, human ENS is buried in opaque tissue, making visualization challenging, especially because ENS accounts for < 1:10,000 cells in colon wall (our estimate). For this reason, human clinical pathology relies primarily on formalin-fixed paraffin-embedded thin sections to visualize ENS. However, even major ENS defects are difficult to appreciate in sectioned bowel (**Supplementary Figure 6.1**) and human quantitative

analyses provide highly variable results for “normal” colon neuron density (7–9). This variability in “normal” makes structural defects causing bowel motility disorders difficult to define. A few approaches demonstrated elaborate ENS structures in human bowel (10–17), but methods were not reproducible in our hands, technically challenging and time consuming, or failed to demonstrate ENS in large intact regions. We therefore sought to develop robust, highly reproducible methods to visualize cells controlling human colon motility. Our new approach provides 3-dimensional ENS views in large colon regions without sectioning, preserving associations with other bowel cells. This is important because bowel motility requires coordinated muscle contraction and relaxation18 organized by enteric sensory neurons, interneurons, excitatory and inhibitory motor neuron (1,3,19,20), interstitial cells of Cajal (21), enteric glia, muscularis macrophages, platelet-derived growth factor receptor a-immunoreactive cells (or “fibroblast-like cells”), and enteroendocrine cells (1,3). Defining cell type–specific defects that affect bowel motility is most important for life-threatening diseases like Hirschsprung disease (22,23), achalasia (24), gastroparesis (25), and chronic intestinal pseudo-obstruction (26), where improved imaging could provide new ideas about disease pathogenesis or treatment. First, however, we aimed to quantitatively define “normal” ENS anatomy. Here we provide 280 confocal Z-stacks and quantitative data from 14 human adult colons. We also visualized colon ENS from children with Hirschsprung disease, a birth defect where ENS is absent from distal bowel and a hypoganglionic “transition zone” separates aganglionic from proximal ENS-containing colon.

6.3 Methods

Mice

Studies adhere to ARRIVE (Animals in Research: Reporting In Vivo Experiments) guidelines (27) and Institutional Animal Care and Use Committee at Children’s Hospital of Philadelphia (16-001041). P0 Gfrα1 (MGI cat no. 3715269, RRID:MGI:3715269) (28) and wild-type littermate (C57BL/6) were analyzed (9–12 AM). Dam was fed Mouse Diet 5015* (LabDiet, St Louis, MO), not

fasted, housed on corncob (Product 4B; The Andersons, Maumee, OH) in Lab Products (Seaford, DE) caging. Human Tissue Colon was acquired with Children's Hospital of Philadelphia Institutional Review Board (IRB 13-010357) and Perelman School of Medicine at University of Pennsylvania approval (IRB 804376) using Abramson Cancer Center Tumor Tissue Bank or pathology de-identified tissue, providing limited clinical data. Jejunum and pancreas were from the Human Pancreas Analysis Program (IRB exempt).

Human Colon Staining

Detailed protocol is at protocols.io (dx.doi.org/10.17504/ protocols.io.wyeffte).

Tissue Processing

Adult colons remained at ambient temperature until arrival in pathology after routine hospital procedures. Transfer to sterile icecold 1X phosphate-buffered saline (PBS) occurred 61–112 minutes after resection. Staff pathologists provided regions without recognized abnormalities. The laboratory received coded specimens in PBS on ice. While in PBS, fat was removed and tissue was pinned along edges (serosa up) to Sylgard 184 Silicone Elastomer (Dow, Midland, MI) using insect pins. We stretched while pinning, making the colon thin, flat, and uniform thickness. Pins were repositioned several times to stretch colon as muscles relaxed, increasing area 2.6-fold (N = 3, SEM = 0.15) compared to unstretched colon. Pinned tissue was fixed (4% paraformaldehyde, 4C overnight), transferred to PBS, and the edges with pin holes were trimmed. Full-thickness colon was cut with scissors. Most specimens were 1 x 1 cm^2. Larger colonic specimens also stained adequately using this method (eg, 2 x 3 cm^2). Stored tissue (4C, 50% PBS/50% glycerol/0.05% sodium azide) could be stained months later without obvious tissue degradation. Human jejunum, pancreas, and Hirschsprung colon were processed similar to adult colons. Hirschsprung colon was in ice-cold PBS 20–60 minutes after resection. Jejunum and pancreas from transplant donors were in Belzer UW solution (29) (NC0410019; Fisher Scientific, Waltham, MA) immediately after

resection and stored approximately 8 hours before fixation.

Immunohistochemistry

The 1 x 1 cm^2 fixed colons were processed in 24-well VWR Culture Plates (nontreated), 2-cm diameter (cat no. 10861-558). Reagent volumes were 500–1000 µL/well (enough to cover tissue). After washing (PBS, 3 x 5 minutes, room temperature), incubating to permeabilize and remove lipids (100% methanol, 1 hour, on ice), and treating with Dent's bleach (5 mL 30% hydrogen peroxide, 5 mL dimethylsulfoxide, 20 mL 100% methanol) (30) (2 hours, room temperature) to permeabilize and quench auto-fluorescence, colon was washed (PBS, 3 x 5 minutes, room temperature), transferred to 2- mL Eppendorf tubes containing blocking solution (4% normal donkey serum, 0.5% Triton X-100, and 0.05% sodium azide/PBS) and incubated (3 days, 37^0C, New Brunswick Scientific I24 Incubator Shaker, 40–100 rpm). Then we incubated with 1–3 primary antibodies (**Supplementary Table 6.1**) in blocking solution on shaker (14 days, 37^0C, 40–100 rpm) using Parafilm-sealed tubes. Unbound primary antibody was removed (PBS/0.05% sodium azide, 3 washes, 2 hours/wash, plus an overnight wash, on rocker). Secondary antibodies were in PBS/0.05% sodium azide (3 days, 37^0C, on rocker). Excess secondary was removed with PBS/0.05% sodium azide (3 washes, 2 hours/wash, plus additional wash overnight, room temperature, on rocker). Some tested antibodies did not work (**Supplementary Table 6.2**).

Dehydration, Clearing, and Mounting After Immunohistochemistry

Colon was dehydrated in 24-well dishes in graded methanol/PBS (approximately 500 µL/well, extra if needed to cover, 30 minutes/wash: 50% methanol, 70% methanol, 80% methanol, 95% methanol, 100% methanol x3, room temperature, on rocker). Dehydrated colon incubated in Murray's Clear (2:1 benzyl benzoate: benzyl alcohol) (31) until completely translucent (15–30 minutes, room temperature) was mounted on glass slides in Murray's Clear and imaged within 48 hours.

Imaging

Zeiss LSM 710 confocal microscope (10x and 20x PlanApochromat objectives, Zeiss Zen software, version 2.3 14.0.14.201; Zeiss, Oberkochen, Germany) Z-axis increments were 4 mm (10x objective) or 1 mm (20x objective). Each image slice was 900 x 900 (10x) or 1200 x 1200 pixels (20x). The 10x Z-stacks were stitched to cover large regions. Laserscanning operated under multitrack to sequentially acquire multichannel images. Each channel used 100% laser power. Excitation/long-pass emission filters were Alexa Fluor 647 (excitation: 633 nm, emission: 656- to 755-nm filter), Alexa Fluor 594 (excitation: 561 nm, emission: 588- to 656-nm filter), and Alexa Fluor 488 (excitation: 488 nm, emission: 493- to 584-nm filter). Tile scan and Zen stitching were used to assemble multifield images. ImageJ (Java 1.8), Imaris 9.0.2 (Bitplane AG, Zurich Switzerland), Adobe Photoshop CS6, and Inkscape (0.92.3) manipulation was limited to uniform contrast adjustment, cropping, rotating, stitching, assembling Z-stacks, and generating 3-dimensional projections and videos.

Quantitative Analyses Employed Manual and Automated Features

Imaris modules were Crop 3D, Image Processing, Thresholding, Background Subtraction, Surface, Manual Contour, Click Drawing Mode, and Detailed Statistics. ImageJ features were regions of interest, Polygon selection, Straight line tool, Measurements, Scale bar, Z-Project, Split channels, Merge channels, and Duplicate.

Myenteric plexus

Neurons (HuC/D+PHOX2B+) and glia (S100B+) were manually counted in ganglia using 39 randomly selected colon regions (4 right, 5 fields/subject; 3 left, 5 fields/subject; 1 left, 4 fields). Two-dimensional ganglion areas were manually outlined in flattened Z-stacks (4 right, 4 left colon). Using similar manual outlining, we determined percent colon containing myenteric plexus (defined

as ganglia plus thick nerve fiber bundles connecting ganglia), and percent plexus occupied by ganglia (defined as regions with >2 myenteric neurons separated by < 1 cell diameter). For 3-dimensional analyses, individual ganglion volumes were determined by manually outlining at 5- to 7-µm increments within 20x Z-stacks using Click Drawing mode (Surface Contour module; Imaris). Cell density within ganglia was determined by manually counting within defined volumes.

Neuron subtypes

Myenteric neurons (HuC/D+) expressing neuronal nitric oxide synthase (nNOS), choline acetyltransferase (ChAT), or vesicular acetylcholine transporter (VAChT) identified by triple-label immunohistochemistry were manually counted within Z-stacks (5 random fields/subject, 4 right, 4 left, 40 total regions). Maximum neuron diameter was determined manually using ImageJ (6 nNOS+/image, 6 ChAT+/image, five 20x images/subject; 4 right, 4 left; forty 20x images total, 240 nNOS neurons, and 240 ChAT neurons).

Submucosal plexus

Ganglia location was defined in Z-stacks using ImageJ.

Statistics

We used Prism 7 (GraphPad Software, San Diego, CA), D'Agostino & Pearson, and Shapiro-Wilk normality tests with unpaired t tests to compare means. Volumes of manually contoured ganglia used Detailed Statistical Analysis (Imaris). Data are presented as mean ± SEM. Degrees of freedom were 6 for analyses.

6.4 Results

Our goal was to establish highly reproducible, inexpensive, simple techniques to visualize human ENS in 3 dimensions to advance understanding of bowel motility disorders. We tried many published approaches to visualize human ENS (10–13,16,17,32–35), but human colon was incompletely penetrated by antibody, not transparent after clearing, or methods provided only limited views of ENS anatomy after meticulous challenging microdissection. Optimal Clearing, Staining, and Imaging To image ENS in full-thickness colon without perturbing cellular associations, we modified published methods (32,34) to enhance staining and translucency. Our approach worked routinely with 1 x 1 cm^2 colon and can work with larger regions. We reasoned antibodies and light would penetrate better if colon was thin. We therefore pinned and repeatedly stretched colon before fixation to average thickness 800– 1000 µm (**Figure 6.1A**). We kept colon as flat and uniform as possible and avoided drying. We tried staining tissue that had not been stretched before fixation, but reagent penetration was poor, and folded tissue made image interpretation difficult. Methanol, Dent's bleach, prolonged 37^0C incubation and shaking enhanced staining, but took 23 days (**Supplementary Figure 6.2**). Murray's Clear made tissue translucent, but fluorescence in Murray's Clear declined over time so we imaged within 48 hours of immersion. Tissue area underwent shrinkage to 66.9% ± 6.6% of original area measured after fixation (**Supplementary Figure 6.3**), partially reversing stretching

Imaging and Antibody Testing

Colon was easily imaged to a depth of 1000 µm, allowing full-thickness reconstructions of stretched preparations. We identified antibodies binding nerve cell bodies (HuC/D), neuronal and some glial nuclei (PHOX2B), nerve fibers (TuJ1), nerve cell bodies and fibers (PGP9.5), enteric glia (S100β, SOX10), interstitial cells of Cajal (cKIT), muscularis macrophages (Iba1), and enteric neuron subsets (CHAT, VAChT, nNOS, neurofilament 200, neurofilament M, peripherin, calretinin, and somatostatin) (**Figure 6.1B–Q**). We generated 3-dimensional images of many cell types

thought to influence human colon motility and provide 280 adult colon Z-stacks (available at Blackfynn DOI:10.26275/pzek91wx). Our method also worked for human jejunum and pancreas (**Supplementary Figure 6.4**, Supplementary Videos 1 and 2). Quantitative analyses focused on adult human colon.

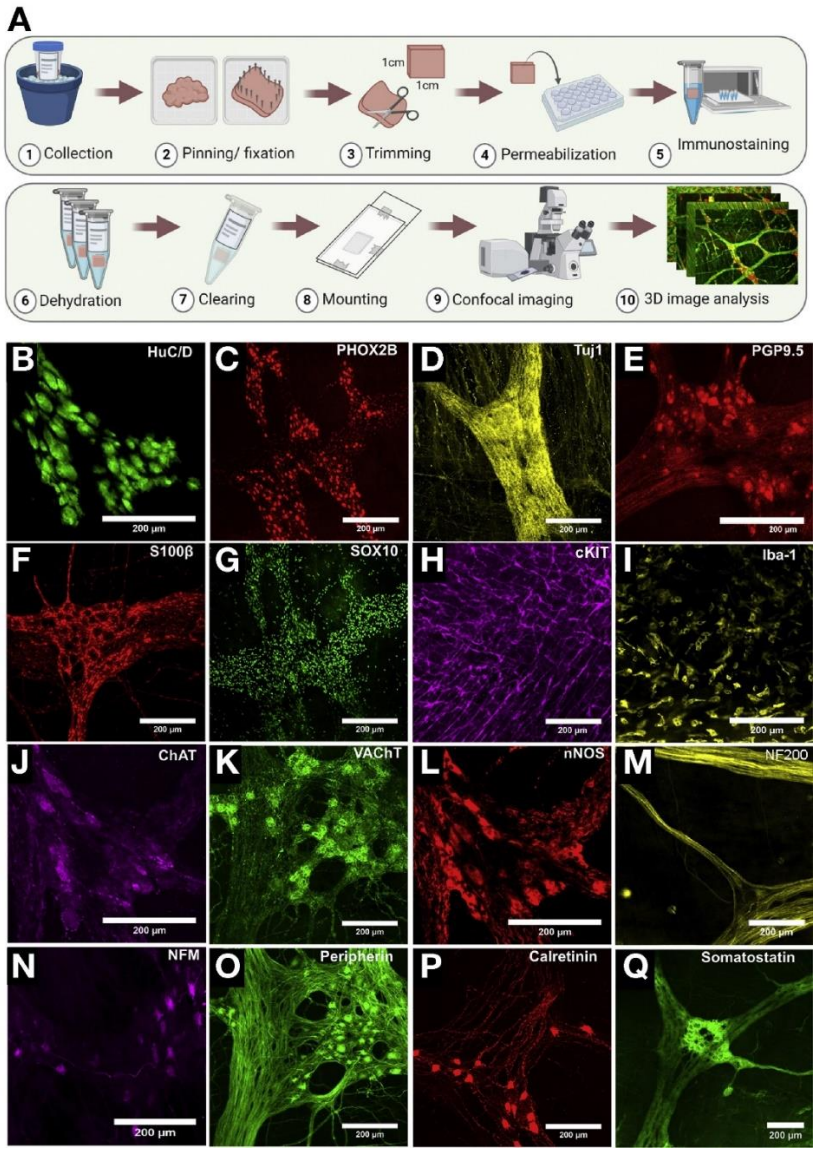

Figure 6.1: Imaging cells controlling human colon motility
(A) Strategy to image without sectioning. (**B–G, J–Q**) Human colon myenteric plexus visualized with 14 antibodies. **(H, I)** Longitudinal muscle interstitial cells of Cajal and muscularis macrophages visualized with cKIT **(H)** and Iba-1 **(I)** antibodies. Scale bars: 200 µm.

Human Colon Enteric Nervous System in 3 Dimensions

To examine normal human colon ENS structure, we analyzed specimens resected for varied clinical indications; all lacked identified motility disorders (**Supplementary Table 4.3**) and adult colon lacked obvious pathology. Three- dimensional imaging of HuC/D, PHOX2B, and S100β stained colon showed enteric neurons clustered into submucosal and myenteric ganglia connected by thick nerve fiber bundles (Supplementary Video 3). Myenteric ganglia appeared larger on average than submucosal ganglia. A few individual neuron cell bodies were within thick circular muscle of all colons (Supplementary Video 3). A rich network of fine nerve fibers and closely associated glia (S100β) was present within circular and longitudinal muscle, with neurites largely parallel to smooth muscle (Supplementary Video 3). Glia were also closely associated with neuronal soma in ganglia (Supplementary Video 4, **Supplementary Figure 6.5**) and nerve fibers were dense near bowel mucosa (Supplementary Video 3).

Human Colon Myenteric Plexus

To establish normal indices, full-thickness colon stained for HuC/D, PHOX2B, and S100β was imaged parallel to bowel surface (**Figure 6.2A**). Confocal Z-stacks were stitched to evaluate large regions (**Figure 6.2A** is 4 x 5 mm^2). For quantitative analyses, we defined “myenteric plexus” as nerve fiber bundles (containing S100β+ glia) and embedded nerve soma (HuC/D+PHOX2B+). We defined “myenteric plexus ganglia” as regions within fiber bundles containing >2 adjacent neuron cell bodies. Using flattened Z-stacks, we determined percent colon containing myenteric plexus or ganglia (**Figure 6.2B**). Although myenteric plexus area was similar in left and right colon (left 26.5% ± 2.5%, right 22.5% ± 4%; P = .4514), more myenteric plexus (left 43% ± 3.2%, right 26% ± 3.7%; P = .0113), and more image area (left 11.6%% ± 1.7%, right 5.3%% ± 0.1%; P = .0116) was

occupied by ganglia in left colon. Two-fold differences in density between left and right colon suggest region-specific normal ranges.

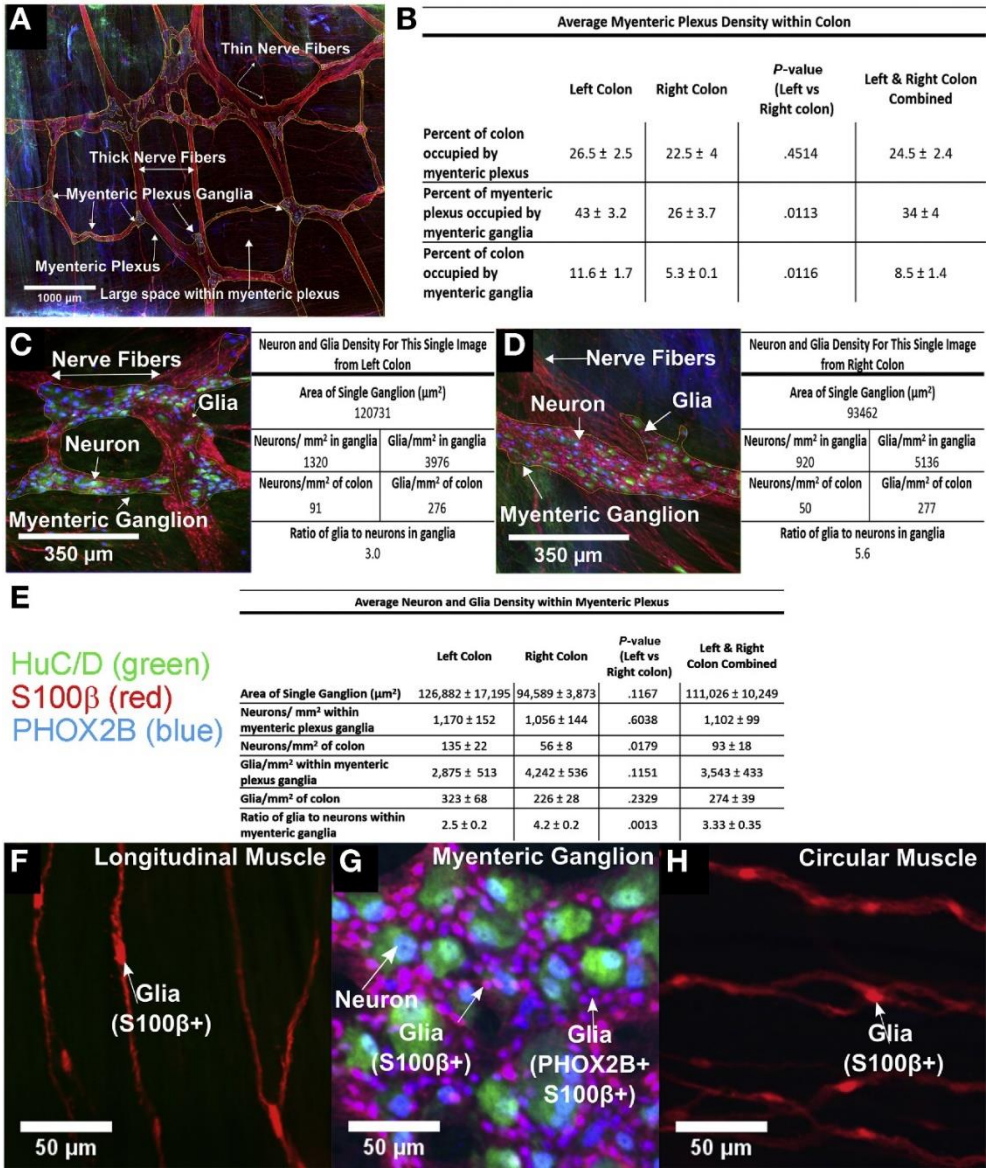

Figure 6.2: Human colon myenteric plexus 2-dimensional analyses

(A) Flattened Z-stack through myenteric plexus (10x objective, stitched fields, 4 x 5 mm^2). Small clustered ganglia have HuC/D+ (*green*) and PHOX2B+ (*blue*) neurons. Nerve fibers are visualized via glial S100β (red). Myenteric plexus and ganglia within plexus were outlined manually (*thin yellow lines*). **(B)** Quantitative data from 4 x 5 mm^2 images like **(A)**. **(C, D)** Flattened Z-stack from colon myenteric ganglia (left **[C]** or right **[D]**) stained for HuC/D (*green*), S100β (*red*), and PHOX2B (*blue*) imaged with 20x objective. Table to right of each image shows quantitative data from that

specific Z-stack. **(E)** Quantitative data from 4 right colon, 5 fields/subject; 3 left colon, 5 fields/ subject; 1 left colon, 4 fields; total neurons counted: 1953 right colon, 2603 left colon; Total glia counted: 8021 right colon, 6423 left colon. Single ganglion areas are from 24 right and 19 left colon ganglia. Cells/mm^2 within these ganglia are based on 5261 neurons and 16,915 glia. **(F, G, H)** Colon stained with HuC/D (*green*), S100β (*red*), and PHOX2B (*blue*) antibodies. PHOX2B+ nuclei include all myenteric neurons and glia within myenteric ganglia **(G)**. Glia in longitudinal **(F)** and circular muscle **(H)** were not PHOX2B immunoreactive. **(A)** Scale bar: 1000 µm. **(C, D)** Scale bar: 350 µm. **(F–H)** Scale bar: 50 µm.

We next determined colon myenteric plexus neuronal and glial density by counting HuC/D+, PHOX2B+, and S100β+ cells (**Figure 6.2C–E**). We discovered all neurons and glia within myenteric ganglia or thick nerve fiber bundles had nuclear PHOX2B immunoreactivity (**Figure 6.2G**). In contrast, glia in thin nerve fibers throughout muscle were not PHOX2B-immunoreactive (**Figure 6.2F and H**). Using 20X Z-stacks, we counted all stained cells in each image. Data are first presented based on 2-dimensional areas, ignoring Z-depth. Quantitative data adjacent to each image were from that specific Z-stack (**Figure 6.2C-D**). Areas containing neurons were considered "ganglia" and outlined (see *thin yellow lines*, **Figure 6.2A**). Mean density data are in **Figure 6.2E**. Although neuron density within myenteric ganglia was similar in left and right colon, neurons/mm2 bowel was greater on left because ganglia occupy a larger percentage of bowel wall (left = 135 ± 22, right 56 ± 8; P = .0179). In contrast, glial density was not statistically different in right vs left colon (glia/mm^2 : left = 323 ± 68, right = 226 ± 28; P = .2329) or within myenteric ganglia (left = 2875 ± 513, right = 4242 ± 536; P = .1151). Interestingly, within ganglia, ratio of glia to neurons was lower in left than right colon (left = 2.5 ± 0.2 glia/neuron, right = 4.2 ± 0.2; P = .0013). To define cell density within myenteric ganglia in 3 dimensions, we manually outlined and counted cells in Zstacks (**Figure 6.3A-B**). Quantitative data for 2 individual images are provided (**Figure 6.3A-B**). Pooled data indicate normal ranges for adult humans without known bowel motility disorders (**Figure 6.3C**).

Estimates for large areas were generated by multiplying cell numbers within ganglia (counted at high magnification in 3-dimensional Z-stacks) by percent colon containing ganglia (measured at low magnification, **Figure 6.2A**). Using 5 regions/individual, cell density estimates

clustered within tight ranges (**Figure 6.3N-O**). Variation was greater between subjects with more variation in left vs right colon.

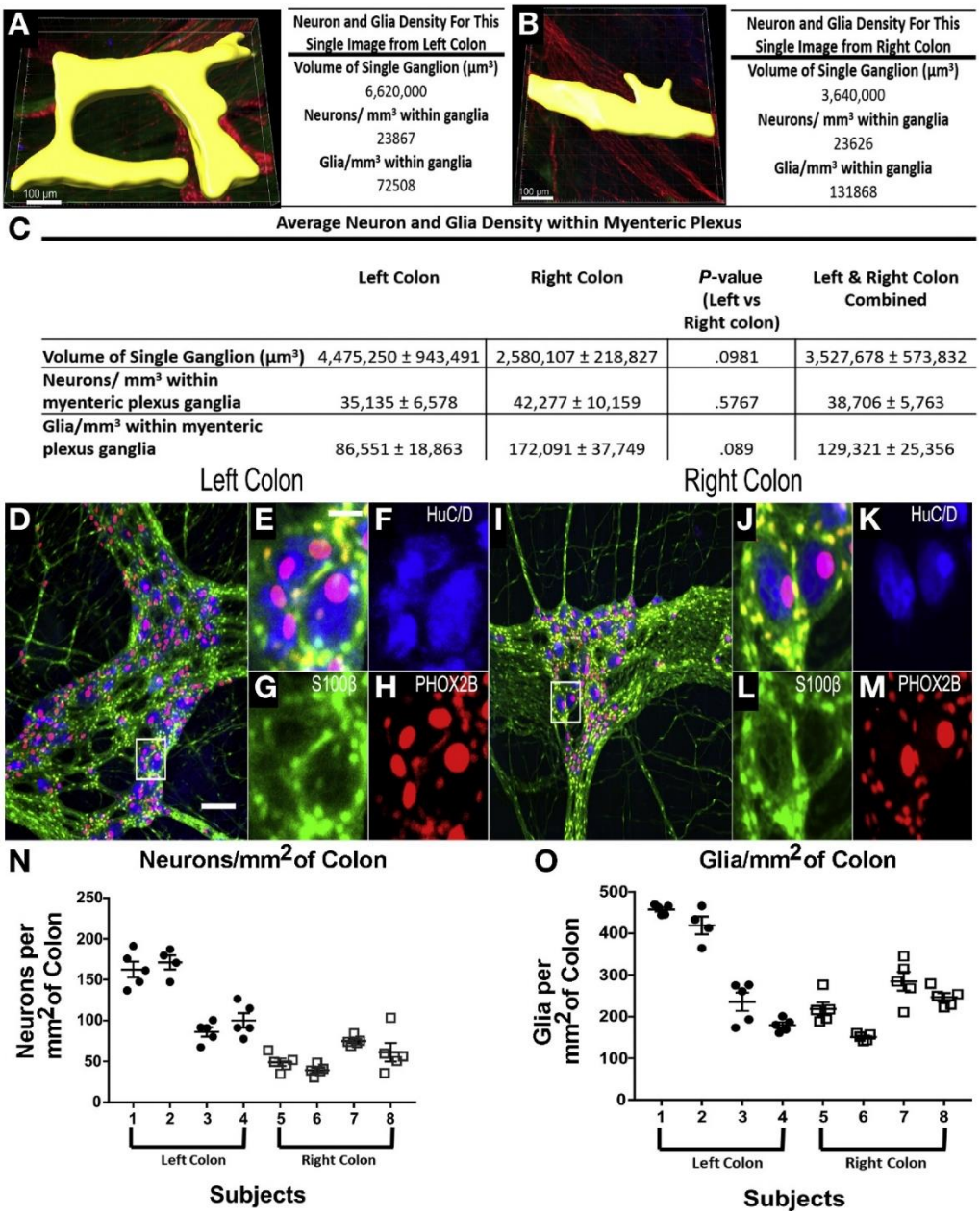

Figure 6.3: Human colon myenteric plexus 2- and 3-dimensional analyses
(A, B) Three-dimensional ganglia volumes (*yellow regions*) (Supplementary Videos 5 and 6 are from these regions). To right of each image are quantitative data from that specific region. **(C)** Cell density based on five 20x fields/subject, 8 subjects (4 left, 4 right colon)), 24 right and 19 left colon ganglia volumes, 5261 neurons and 16,915 glial cells. **(D–M)** Manual neuron and glia counts were

obtained after HuC/D (*blue*), S100β (*green*), and PHOX2B (*red*) staining. **(D, I)** Flattened Z-stacks. **(E–H, J–M)** Single slices and channels from Z-stack. **(N, O)** To estimate cell density over large regions we multiplied density within small regions (like **Figure 6.2C**) by percentage of bowel with myenteric plexus (using images like **Figure 6.2A**). We found little variability in cell density within ganglia, indicated by tight data clusters in individuals. Inter-individual differences primarily reflect percentage of bowel occupied by ganglia in each individual. **(A, B, D, I)** Scale bars: 100 µm. **(E, F, G, H, J, K, L, M)** Use **(E)** scale bar: 25 µm.

We next asked how biopsy size impacts neuron density estimates, recognizing ENS is not uniformly distributed. To do this we divided a single 4 x 5 mm^2 region into 20 x 1 mm^2 zones and analyzed ganglion density in each zone (**Figure 6.4A-B**). If 1 mm^2 is evaluated, widely divergent estimates of ganglion density (0–17%) occur, depending on zone evaluated. Using 4 mm^2 areas, ganglion density estimates were more tightly clustered, but still ranged 3.5%– 11.4%. In contrast, narrow ranges were generated analyzing 9 mm^2 regions. Thus, limited sampling causes diverse enteric neuron density estimates, with greater precision as area evaluated increases.

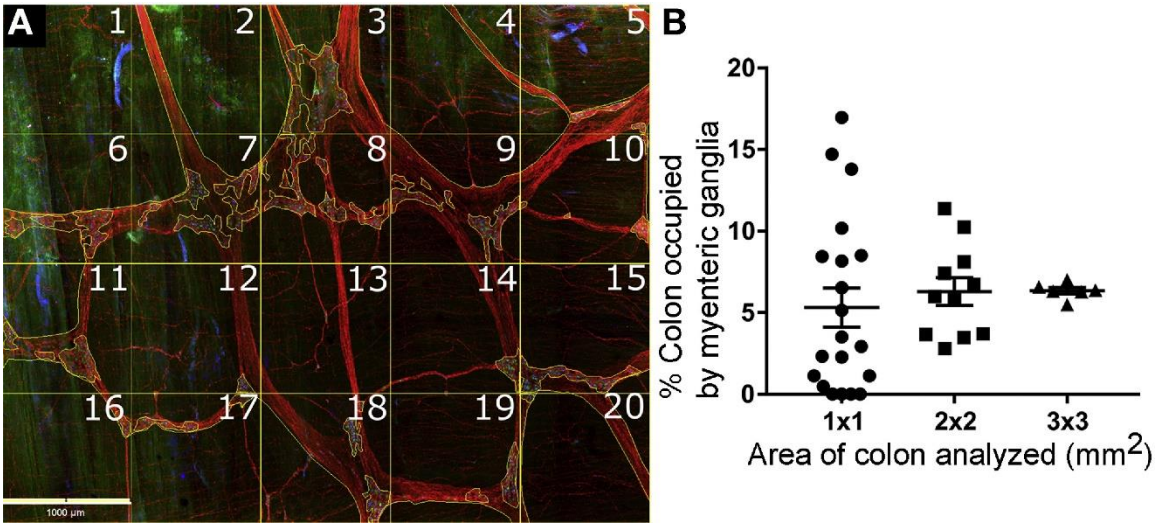

Figure 6.4: Size of region evaluated affects estimated myenteric plexus neuron density
(A) Flattened Z-stack (**Figure 6.2A**) was divided into 20 squares (1 mm^2 each). We determined percentage of each square occupied by ganglia (regions with nerve cell bodies). **(B)** Estimates of percent colon occupied by ganglia using 1 x 1 mm^2 , 2 x 2 mm^2 , or 3 x 3 mm^2 regions. Some 1 x 1 mm^2 regions have no myenteric plexus; others have up to 17% occupied by ganglia. As size of region evaluated increases, estimates of percent area occupied by ganglia become more uniform. Scale bar: 1000 µm.

Neuron Subtype Ratios

Because most myenteric neurons express either nNOS or ChAT and VAChT (1,2,36–39), we defined ratios of these markers in human colon myenteric plexus using ChAT/nNOS/HuC/D (**Figure 6.5A–H**) or ChAT/VAChT/HuC/D staining (**Figure 6.5K–Q**). Using Z-stacks to unambiguously distinguish cytoplasmic staining from overlying neurites, we determined percent neurons (HuC/D+) expressing nNOS, ChAT, both or neither (40 samples, 3359 total neurons evaluated, **Supplementary Table 6.4**). In parallel, we compared ChAT to VAChT staining because murine data suggested ChAT staining is often weak. VAChT was considered "positive" in 1.62-fold more neurons than ChAT, but many VAChT+ cells had faint ChAT staining or high background (**Figure 6.5O–Q**, N = 1902 cells). We hypothesize ChAT alone (at least with this antibody) led to systematic cholinergic neuron undercounting. **Supplementary Table 6.4** explains how we adjusted ChAT+ counts based on VAChT/ChAT data to establish "cholinergic" neuron counts (**Figure 6.5I-J**). We scored approximately 50% of myenteric neurons as nNOS+/noncholinergic (**Figure 6.5I-J**), approximately 28% as cholinergic/nNOS negative, approximately 5% nNOS+/cholinergic, and approximately 16% as nNOS-/noncholinergic. **Figure 6.5I** shows inter-individual variability. **Supplementary Figure 6.6** shows ChAT+ neuron diameters were 32% larger than nNOS+ neurons diameters.

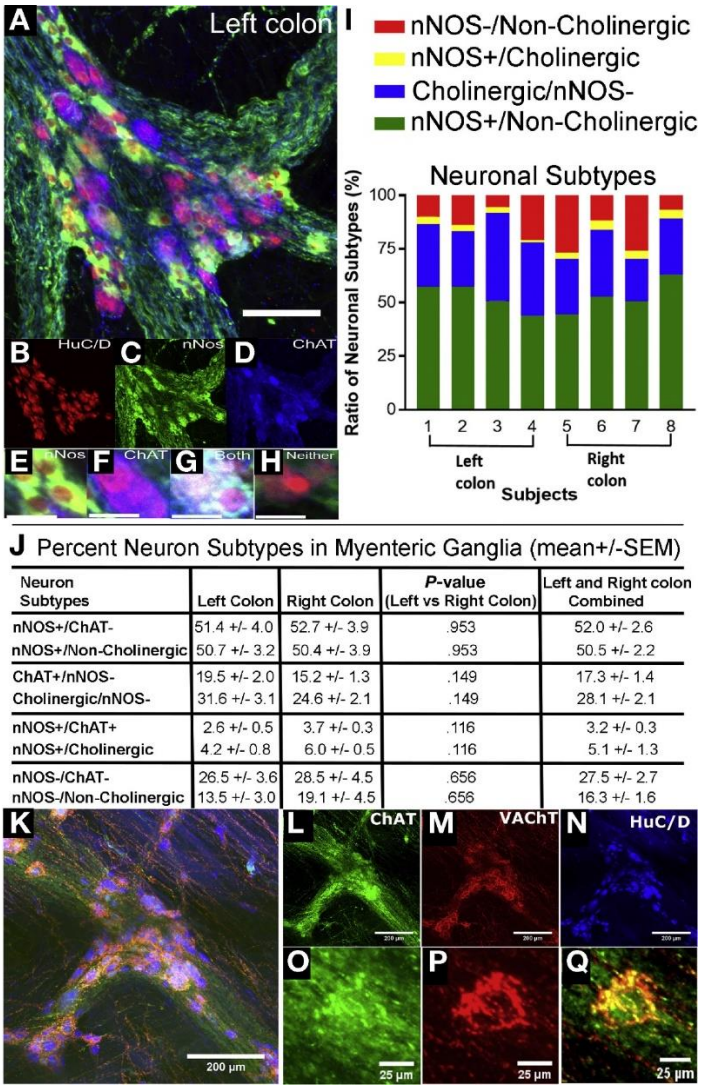

Neuron Subtypes	Left Colon	Right Colon	*P*-value (Left vs Right Colon)	Left and Right colon Combined
nNOS+/ChAT-	51.4 +/- 4.0	52.7 +/- 3.9	.953	52.0 +/- 2.6
nNOS+/Non-Cholinergic	50.7 +/- 3.2	50.4 +/- 3.9	.953	50.5 +/- 2.2
ChAT+/nNOS-	19.5 +/- 2.0	15.2 +/- 1.3	.149	17.3 +/- 1.4
Cholinergic/nNOS-	31.6 +/- 3.1	24.6 +/- 2.1	.149	28.1 +/- 2.1
nNOS+/ChAT+	2.6 +/- 0.5	3.7 +/- 0.3	.116	3.2 +/- 0.3
nNOS+/Cholinergic	4.2 +/- 0.8	6.0 +/- 0.5	.116	5.1 +/- 1.3
nNOS-/ChAT-	26.5 +/- 3.6	28.5 +/- 4.5	.656	27.5 +/- 2.7
nNOS-/Non-Cholinergic	13.5 +/- 3.0	19.1 +/- 4.5	.656	16.3 +/- 1.6

Figure 6.5: Cholinergic/ nitrergic neuron ratios

(A) Flattened Z-stack, human colon myenteric ganglion stained for HuC/D (*red*), nNOS (*green*), and ChAT (*blue*). **(B–D)** Channels for **(A)**. **(E–H)** Sample neurons from **(A)**: **(E)** ChAT+/ nNOS+, **(F)** ChAT+/ nNOS–, **(G)** ChAT+/ nNOS+, **(H)** neither ChAT nor nNOS positive. **(I)** Proportion of neuron classes (8 individuals). **(J)** Average neuron percentages in each class. **(I, J)** We initially evaluated 3360 HuC/D+ cells with ChAT and nNOS antibodies. Subsequent analysis of VAChT/ChAT/ HuC/D staining showed 1.62-fold more neurons would be identified as cholinergic using combined VAChT/ChAT staining compared to ChAT alone (N = 1902 HuC/D+ cells). “Cholinergic numbers” = “ChAT+ numbers” x 1.62. **(K)** Flattened Z-stack, human colon myenteric ganglion stained for ChAT (*green*), VAChT (*red*), and HuC/D (*blue*). **(L–N)** Channels for **(K)**. **(O–Q)** High magnification single confocal slice of neuron from box in **(K)**. We scored this neuron as VAChT+. ChAT immunoreactivity alone was not well localized and ChAT background too high to score this cell as ChAT+ without VAChT staining. (A) Scale bar: 100 µm. **(B–H, O–Q)** Scale bars: 25 µm. **(K–N)** Scale bars: 200 µm. Cell numbers evaluated are in **Supplementary Table 6.4**.

Submucosal Ganglion Location

Additional parameters could be defined via 3-dimensional imaging. For example, human colon submucosal plexus was reported to be in 3 distinct layers (40), but our data suggest ganglia are scattered throughout submucosa, with considerable variability in patterns between evaluated specimens (**Supplementary Figure 6.7**). A subset may have ganglia in definable layers.

Hirschsprung Disease

To highlight clinical utility, we stained colon from children with Hirschsprung disease, a problem where enteric neurons are absent from distal bowel. Resected bowel from pull-through surgery should contain the entire distal aganglionic region, a hypoganglionic transition zone, and ideally normal ENS at proximal margins. This anatomy is difficult to appreciate in paraffin sections (**Figure 6.6A**). In contrast, our 3-dimensional method showed proximal resection margin had a rich ENS network (**Figure 6.6C–H**). Transition zone was relatively hypoganglionic, with unusual features like rows of neurons along nerve fibers (**Figure 6.6B**), myenteric ganglia in more than 1 layer (**Figure 6.7**, slices 23, 29, 42, Supplementary Video 7), thick nerve fiber bundles without neurons (slice 50), and areas without ganglia (slice 144). As expected, distal aganglionic zone was devoid of nerve cell bodies but had extrinsic nerve fibers (**Figure 6.7**, Supplementary Videos 8 and 9).

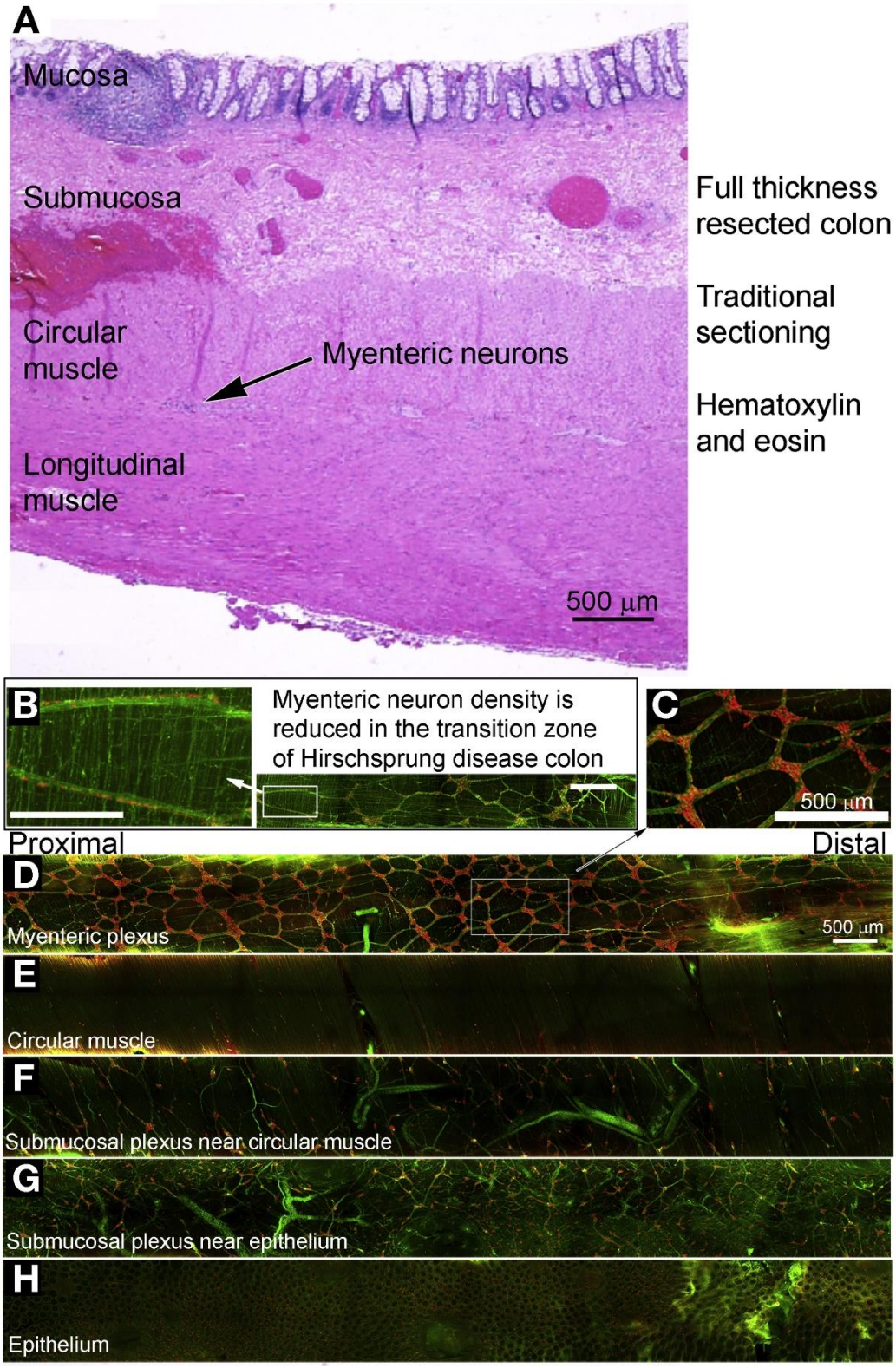
A
Mucosa
Submucosa
Circular muscle
Myenteric neurons
Longitudinal muscle
500 μm
Full thickness resected colon
Traditional sectioning
Hematoxylin and eosin
B
Myenteric neuron density is reduced in the transition zone of Hirschsprung disease colon
C
500 μm
Proximal
Distal
D
Myenteric plexus
500 μm
E
Circular muscle
F
Submucosal plexus near circular muscle
G
Submucosal plexus near epithelium
H
Epithelium

Figure 6.6: Whole mount staining in Hirschsprung disease

(A) Full-thickness colon approximately 4.5 mm from distal resection margin (H&E stained). **(B– H)** Two-month-old Hirschsprung colon stained for nNOS (*green*) and HuC/D (*red*). **(B)** Magnified region from transition zone with enteric neurons along nerve fibers. **(C–H)** Most proximal resection margin for Hirschsprung colon. **(D–H)** Z-stacks slices: **(D)** 49–97, **(E)** 95–96, **(F)** 118– 145, **(G)** 165–176, **(H)** 208– 209. Scale bars: 500 µm. Supplementary Video 7 provides additional images from colon region used to generate **Figure 6.6C–H**).

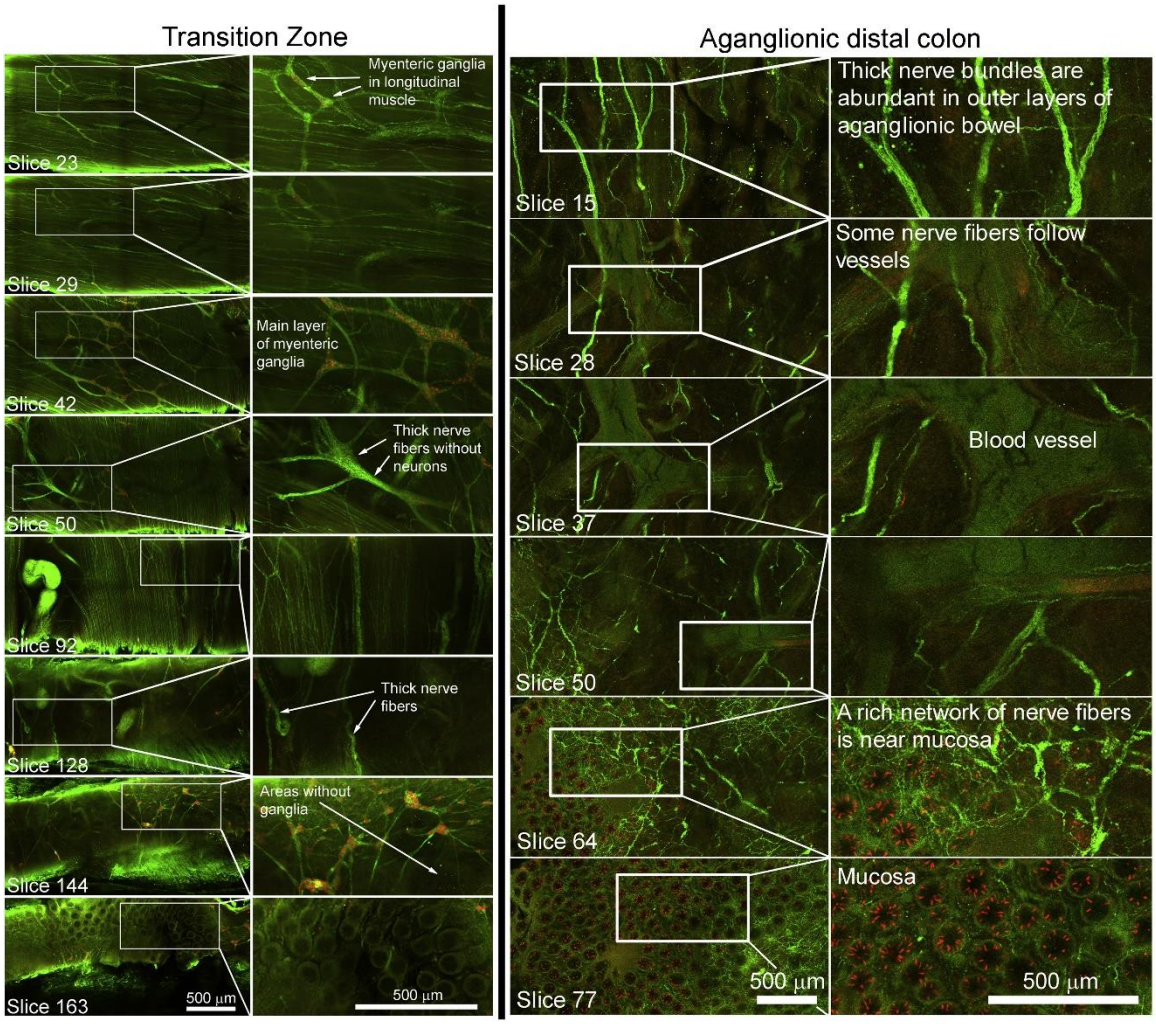

Figure 6.7: Transition zone and distal aganglionic region of Hirschsprung pull through resections

Full-thickness Z-stacks stained with HuC/D (*red*) and nNOS (*green*) antibodies. Identified single slices from Z-stacks in transition zone (*left panel*) and aganglionic region (*right panel*). Higher numbers are closer to mucosa. Scale bars: 500 µm.

6.5 Discussion

Human bowel was estimated to have approximately 500 million enteric neurons controlling most aspects of bowel function (2,3). Our data suggest colon alone has approximately 37 million enteric neurons (approximately 100 neurons/ mm^2 x 1.4 m colon length x 0.15 m circumference (41) x 1,000,000 mm^2 /m^2 x 2.6-fold (stretching) x 0.67-fold (shrinkage with processing)). When ENS is missing or defective, profound bowel dysfunction may occur causing life-threatening problems like Hirschsprung disease (22) and neuropathic chronic intestinal pseudo-obstruction (26). ENS defects may also underlie achalasia (24) and gastroparesis (42), where selective nNOS neuron loss was reported. Furthermore, ENS can be damaged by toxins (eg, chemotherapy) (43–45), systemic disease (diabetes, Parkinson disease) (46–49), inflammation due to infection (50,51), inflammatory bowel disease (52) or necrotizing enterocolitis (53), causing long-term dysmotility and visceral hypersensitivity (54). Unfortunately, until now it has been difficult to visualize human ENS in 3 dimensions. This technical problem limits our understanding of disease mechanisms because full-thickness tissue sections often appear “normal” unless changes are dramatic (eg, complete enteric neuron loss).

Not surprisingly, most of what we know about ENS comes from animal models, in which bowel is thin and muscle is easily dissected from submucosa (5,6,55). In contrast, human bowel is thick (approximately 1000 µm in maximally stretched colon) and muscle layers are difficult to separate from submucosa or each other. For this reason, most human ENS analyses use thin cross-sections (eg, 5 µm), yielding limited data. We hypothesize this problem led to wide variation for “ganglia per 10 mm” (13.5-fold range in rectum) and neurons per ganglia (9-fold range in colon) previously reported (7). Swaminathan and Kapur (9) further identified an approximately 150-fold range for “mean number of ganglion cells per cm” in normal colon (9) and determined reproducible enteric neuron counts require >5 full-circumference sections (estimated at 1.25 mm^2 = 5 sections x approximately 0.005-mm thick section x approximately 50 mm circumference in 8-week-old). Our data suggest 1 mm^2 still yields quite variable neuron density estimates in adult colon and that >9

mm^2 provides more reliable data. Additional problems arise when evaluating human ENS anatomy using thin sections. ENS organization is difficult to appreciate, so dramatic changes can be missed. Nerve fiber bundle orientation is impossible to discern in sections and small nerve fibers are difficult to see, so changes in neurite density or organization are not appreciated. Decades of mouse work suggest 3-dimensional imaging provides much greater insight into disease mechanisms and is essential to see many ENS defects (eg, **Supplementary Figure 6.1**). Thus, robust 3-dimensional methods to visualize human ENS may provide new insight into bowel motility disorders. A few prior studies demonstrated human ENS in 3 dimensions. Myenteric plexus has been visualized by meticulous “fiber by fiber” removal of longitudinal muscle to expose ENS (13,39,56). We tried this, but found it difficult to uncover even small regions, and only cells exposed by dissection could be imaged. Three-dimensional human ENS images were also generated by optical clearing and immunohistochemistry using 300-µm sections (10–12), but we had difficulty replicating this approach, even with significant effort, and few quantitative data were provided from those images.

To overcome these problems, we spent years optimizing clearing and antibody staining for human colon. Our goal was to establish methods that worked well, were easy, and did not require special skill (like microdissection). In addition, we wanted to visualize cells that control bowel motility in 3 dimensions without sectioning that disrupts cellular connections. For this approach to be useful, we need a large library of publicly available images from people without known bowel motility disorders and we need rigorous quantitative data for “normal” ENS anatomy. Our strategy accomplished many of these goals.

Our approach makes colon completely translucent. Large bowel pieces were stained and imaged without sectioning. Confocal imaging permitted visualization of stained cells from serosa to mucosa. Identified antibodies stain neurons, glia, interstitial cells of Cajal, muscularis macrophages, neuron subtypes, and nerve fibers. As expected, some antibodies did not work with our method. We provide 280 three-dimensional Z-stacks of stained adult human colon, highlighting how much we miss with traditional tissue sectioning. We performed substantial quantitative

analyses to define “normal” adult human colon ENS anatomy. Finally, we show images of Hirschsprung disease colon. This is clinically relevant because “transition zone pull through” is thought to commonly cause Hirschsprung disease postoperative morbidity (22), although prolonged processing needed with our approach means it cannot be used for intraoperative decision making. Methods are also applicable to human jejunum and pancreas.

Several observations are worth highlighting. We estimate enteric neurons are < 0.01% of total human colon cells. Myenteric and submucosal plexus resembles ENS in other species, but differences in ENS anatomy between species (57,58) means we need human ENS normal values. Irregular ganglia spacing probably explains dramatic variability in reported enteric neuron densities (7,9) because some thin sections include large ganglia and others lack neurons. Within myenteric ganglia, neuron density was fairly uniform (SEM < 25% of mean neurons/mm^3) and adult human colon had on average 137 ± 20 neurons/myenteric ganglion (**Figure 6.3C**: 38,706 neurons/mm^3 x 0.0035278 mm^3 / ganglion = 137 neurons/ganglion). Uniformity of neuron density within myenteric ganglia contrasts with the 1.65-fold difference in ganglion density within myenteric plexus of right vs left colon (P = .0113). These differences highlight the need to establish region-specific normal ranges for most parameters, although variable ganglion density might simply reflect differences in proximal vs distal colon distensibility.

Enteric glia are much more abundant than neurons, even within myenteric ganglia. Our estimates of glial index (glia to neuron ratio) within ganglia (2.5 left; 4.2 right colon) are lower than prior estimates (5.9–7) (56), but S100β does not label all glia (59,60). Furthermore, 3 left colons were from people with diverticulitis where S100β-labeled enteric glia loss was reported (61). One novel observation was that PHOX2B-immunoreactive nuclei included S100β+ glia and HuC/D+ neurons, but PHOX2B was not detected in enteric glia outside ganglia. Murine data also showed PHOX2B in adult enteric neurons and glia, although mouse images suggest PHOX2B in glia within and outside ganglia (62). These data suggest PHOX2B, a gene mutated in some people with Hirschsprung disease (22), might influence human enteric glial diversity.

We began to define neuron subtype ratios in human colon myenteric plexus because human intestinal motility disorders may result from quantitative or qualitative ENS defects (5,8,22,26,63,64) and nitric oxide–producing enteric neurons are particularly susceptible to injury (65). Because most myenteric neurons produce either nitric oxide or acetylcholine (2), we focused on these subgroups. We found little between-subject variability in noncholinergic nNOS+ neuron prevalence (approximately 50% of myenteric neurons) similar to prior reports indicating 43%–54% of human myenteric neurons were ChAT–/nNOS+ (**Supplementary Table 6.5**) (36–39,66–69). Also consistent with past studies reporting 3%–10% of human colon myenteric neurons produce nNOS and ChAT, we scored 4%–6% of myenteric neurons as nNOS+/cholinergic. We differed substantially from prior studies reporting 36%–56% of human colon myenteric neurons were ChAT+/nNOS– and 2%–7% ChAT–/nNOS– (37–39). Despite using ChAT and VAChT, we scored fewer myenteric neurons as cholinergic/ nNOS– (approximately 28%) and more as noncholinergic/ nNOS– (14%–19%). We suspect the differences are technical (eg, less robust staining with this ChAT antibody using our method). We note, however, that neuron subtype ratios vary between mouse strains and are influenced by diet (70–75) and human subtype ratios are impacted by age (66), diabetes (67), and inflammation (69), so biological variability between subjects is plausible. Clearly, more remains to be done to define human enteric neuron subtype ratios.

Finally, we include many images from distal Hirschsprung disease colon. Although additional studies are needed to define transition zone and “normal” infant ENS, 3-dimensional imaging should facilitate development of intraoperative strategies to avoid transition zone pull through. For example, once transition zone characteristics are well-defined, methods like confocal laser endomicroscopy (76) could be used in the operating room to visualize ENS anatomy. Biopsies could also be evaluated 3-dimensionally in children treated initially by ostomy because they undergo pull-through surgery months later.

Our study has limitations. Subjects were 28–80 years old, with the exception of 2 infants with Hirschsprung disease. Colons were resected for clinical indications. Although we tried to

evaluate only pathology-free regions, diverticulitis-associated inflammation could affect ENS. Exact colon regions are not known (ie, “left” might mean splenic flexure or sigmoid). Specimens were randomly oriented so we cannot distinguish proximal from distal and do not know location along the circumferential colon axis.

Finally, technical obstacles should be noted. Staining takes several weeks, so our method cannot be used intraoperatively. Fluorophores fade after immersion in Murray’s Clear, so efficient confocal imaging is required. Threedimensional imaging takes hours without light sheet microscopy, limiting size of samples that can be imaged. Tissues may dry during prolonged imaging and Murray’s Clear dissolves some plastics. Finally, not all tested antibodies worked well. Nonetheless, our work lays the foundation for future research and suggests new directions for human ENS analyses. We can now visualize human ENS in 3 dimensions in large colon areas with minimal dissection and no sectioning. Our images make it easy to understand why previously reported enteric neuron density estimates vary up to 150-fold. We hope this method will be widely adopted for defining ENS anatomy in adults and children with life-threatening bowel motility disorders where current diagnostic strategies seem most inadequate. We invite others to help us perform quantitative analysis using our images.

6.6 Acknowledgments

The authors thank Pierre Russo for support and encouragement. The authors appreciate the assistance of Deepika Kothakapa, Caitlin Feltcher, Lauren Schmucker, and Andrew Kromer.

6.7 Authorship Contributions

Kahleb D. Graham, MD (Conceptualization: Lead; Data curation: Lead; Formal analysis: Lead; Investigation: Lead; Methodology: Lead; Writing – original draft: Lead; Writing – review & editing: Lead). Silvia Huerta López, BS (Conceptualization: Lead; Data curation: Lead; Formal analysis: Lead; Investigation: Lead; Methodology: Lead; Writing – original draft: Lead; Writing – review &

editing: Lead). Rajarshi Sengupta, PhD (Conceptualization: Supporting; Investigation: Supporting; Methodology: Supporting; Writing – review & editing: Supporting). Archana Shenoy, MD (Investigation: Supporting). Sabine Schneider, BS (Investigation: Supporting; Writing – review & editing: Supporting). Christina M. Wright, BS (Investigation: Supporting; Writing – review & editing: Supporting). Michael Feldman, MD, PhD (Resources: Supporting). Emma Furth, MD (Investigation: Supporting; Resources: Supporting). Federico Valdivieso, BS (Investigation: Supporting; Resources: Supporting). Amanda Lemke, MA (Investigation: Supporting; Project administration: Supporting). Benjamin J. Wilkins, MD, PhD (Investigation: Supporting; Resources: Supporting). Ali Naji, MD, PhD (Funding acquisition: Supporting; Investigation: Supporting). Edward Doolin, MD (Resources: Supporting; Writing – review & editing: Supporting). Marthe J. Howard, PhD (Conceptualization: Supporting; Funding acquisition: Lead; Project administration: Supporting; Writing – review & editing: Supporting). Robert O. Heuckeroth, MD, PhD (Conceptualization: Lead; Data curation: Lead; Formal analysis: Lead; Funding acquisition: Lead; Investigation: Lead; Methodology: Lead; Project administration: Lead; Resources: Lead; Supervision: Lead; Validation: Lead; Visualization: Lead; Writing – original draft: Lead; Writing – review & editing: Lead).

6.8 Funding

This work is supported by the Suzi and Scott Lustgarten Endowment (Robert O. Heuckeroth), the Irma and Norman Braman Endowment (Robert Q5 O. Heuckeroth), The Children's Hospital of Philadelphia Research Institute (Robert O. Heuckeroth), National Institutes of Health (NIH) grants RO1 DK087715 (Robert O. Heuckeroth), March of Dimes 6-FY15-235 (Robert O. Heuckeroth), The Burroughs Wellcome Fund Clinical Scientist Award in Translational Research (grant 1008525) (Robert O. Heuckeroth), Abramson Q16 Cancer Center, NIH 5 F30 DK117546-02 (Christina M. Wright), and NIH SPARC (Stimulating Peripheral Activity to Relieve Conditions) Program Q6 OT2OD023859 (to Marthe J. Howard [principal investigator] and Robert O. Heuckeroth [co-investigator]), and Human Pancreas Analysis Program (https://hpap.pmacs.upenn.edu/), part of

Human Islet Research Network (RRID:SCR_014393; https://hirnetwork.org) grants UC4 DK112217 (Ali Naji). Study sponsors had no role in study design, data collection, analysis or interpretation of data.

6.9 Supplementary Figures and Tables

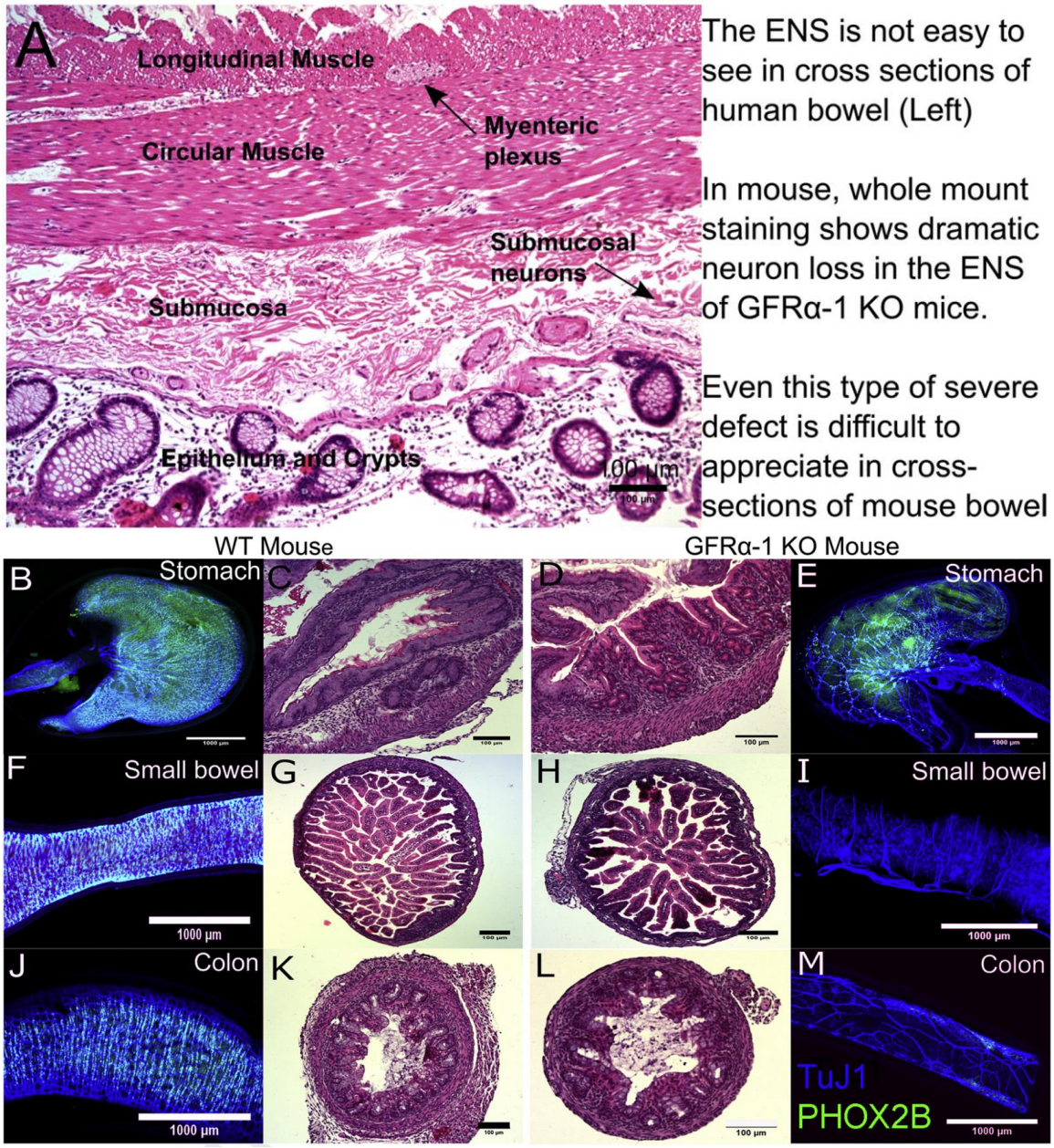

Supplementary Figure 6.1: ENS is difficult to appreciate in bowel sections

(A) Full-thickness human colon. H&E-stained (5-mm paraffin) section, the most common method to evaluate bowel pathology. **(B, F, J)** Rich ENS networks in P0 wild-type mouse stomach **(B)**, small bowel **(F)**, and colon **(J)** are easily seen after TuJ1 (blue)/PHOX2B (green) whole-mount immunohistochemistry. **(E, I, M)** P0 GFRα1–/– mice have few enteric neurons in stomach **(E)** and only extrinsic nerve fibers in small bowel **(I)** and colon **(M)** seen by whole-mount TuJ1 (*blue*)/PHOX2B (*green*) immunohistochemistry. **(C, D, G, H, K, L)** ENS is difficult to appreciate in

H&E-stained 5-mm sections from P0 wild-type stomach (C Q14), small bowel **(G)**, or colon **(K)**. ENS loss is difficult to appreciate in P0 GFRα1–/– stomach **(D)**, small bowel **(H)**, or colon **(L)** 5-mm sections even though magnification is approximately 5–7x higher in sections than whole mounts. **(A, C, D, G, H, K, L)** Scale bar: 100 μm. **(B, E, F, I, J, M)** Scale bar: 1000 μm.

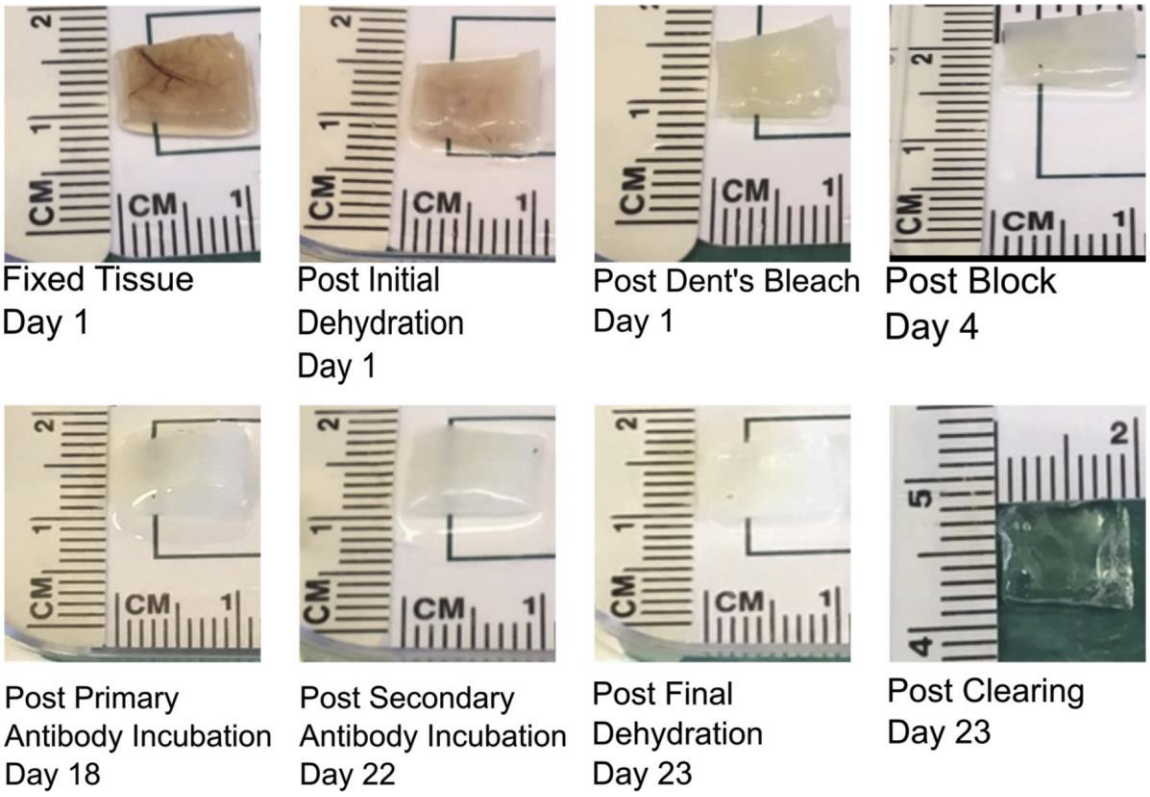

Supplementary Figure 6.2: Tissue processing

A single fixed piece of full-thickness human colon on selected days: tissue is opaque on day 1, but translucent on day 23 when imaging is performed.

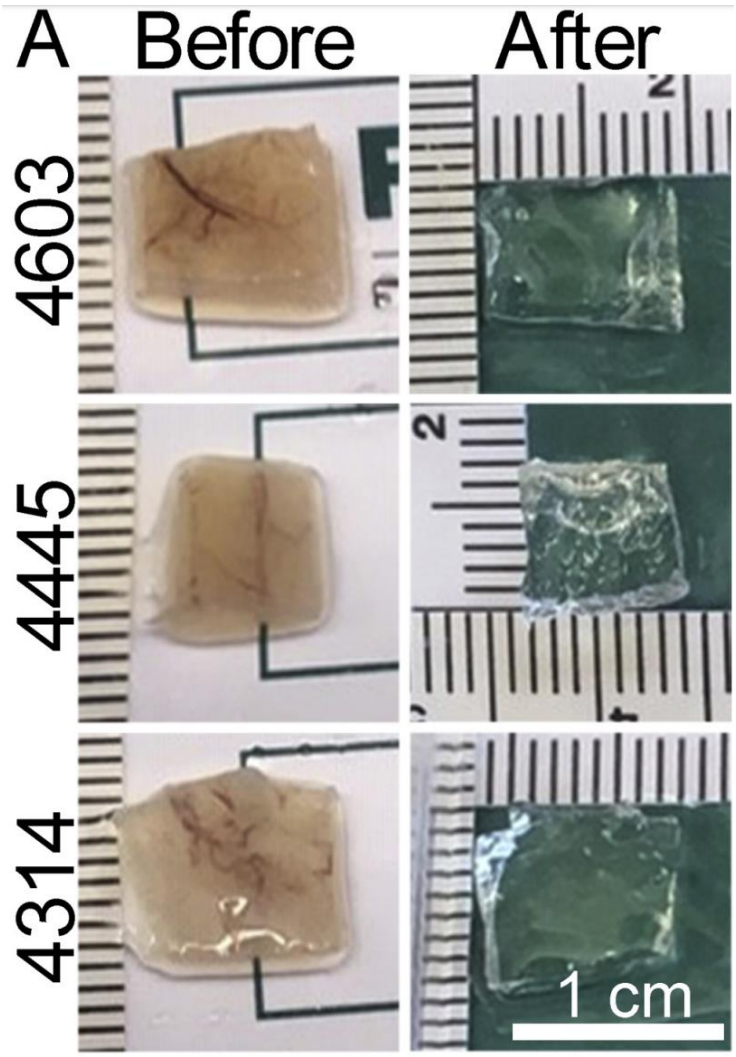

B

Sample Number	Before Processing Area (cm squared)	After Processing Area (cm squared)	% of Original Area
4314	1.076	0.731	67.9
4445	0.703	0.547	77.8
4603	1.028	0.565	55.0
Mean			66.9 +/- 6.6

Supplementary Figure 6.3: Change in tissue area during processing

(A) Before images show fixed stretched colon. After images show tissue ready for imaging. **(B)** Quantitative analysis shows tissue area after processing is 0.67-fold smaller area compared to fixed tissue before processing. The reduction in tissue area during processing partially compensates for the increase in tissue area as we stretch colon before fixation. Because colon stretches and contracts in vivo, images are likely to reflect physiologically relevant dimensions.

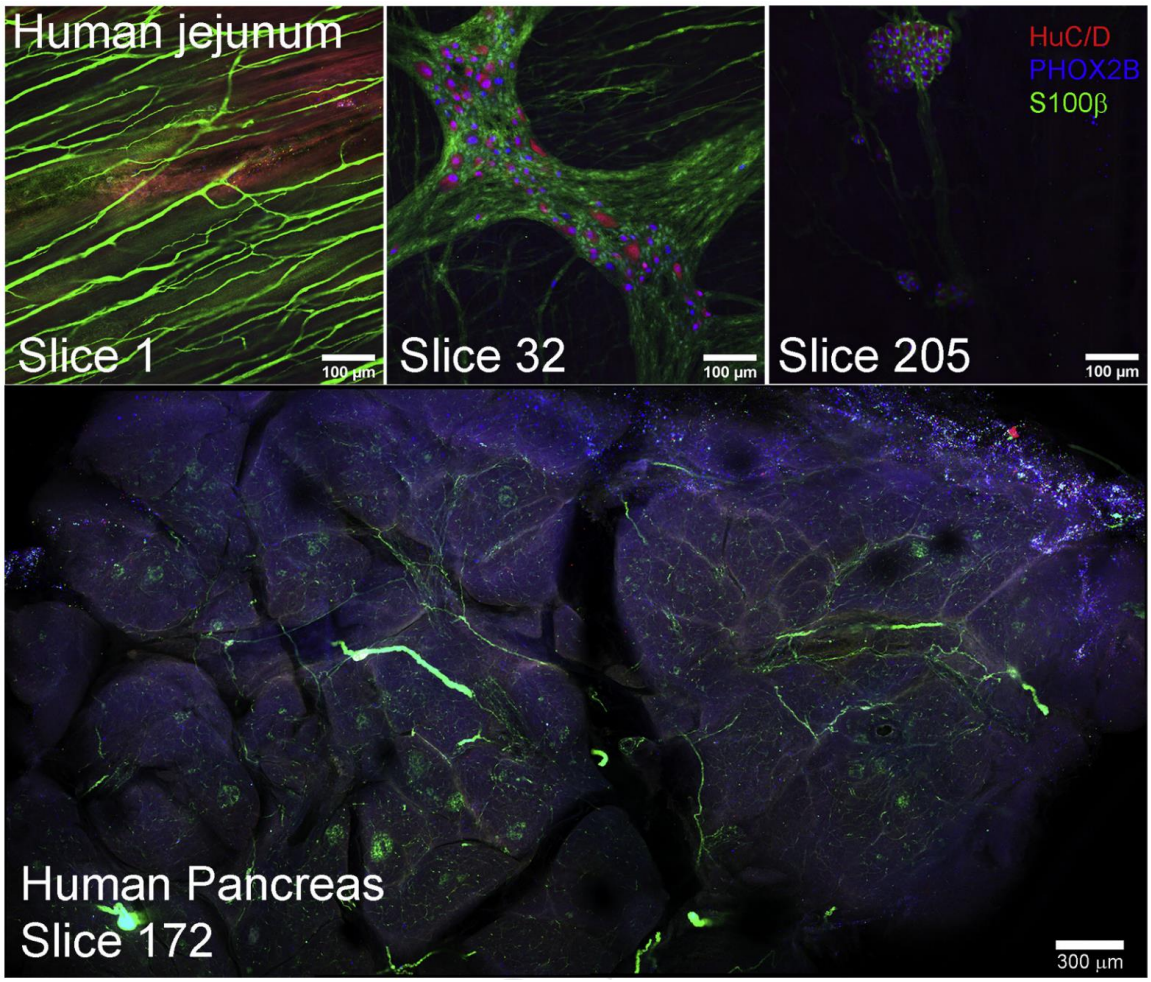

Supplementary Figure 6.4: Human jejunum and human pancreas tissue clearing, immunohistochemistry, and 3-dimensional imaging

Using our method optimized for colon, we stained 1 piece of human jejunum (*top panels*) and 1 piece of human pancreas (*bottom*). Images show single panels from Z-stacks that are available as Supplementary Data.

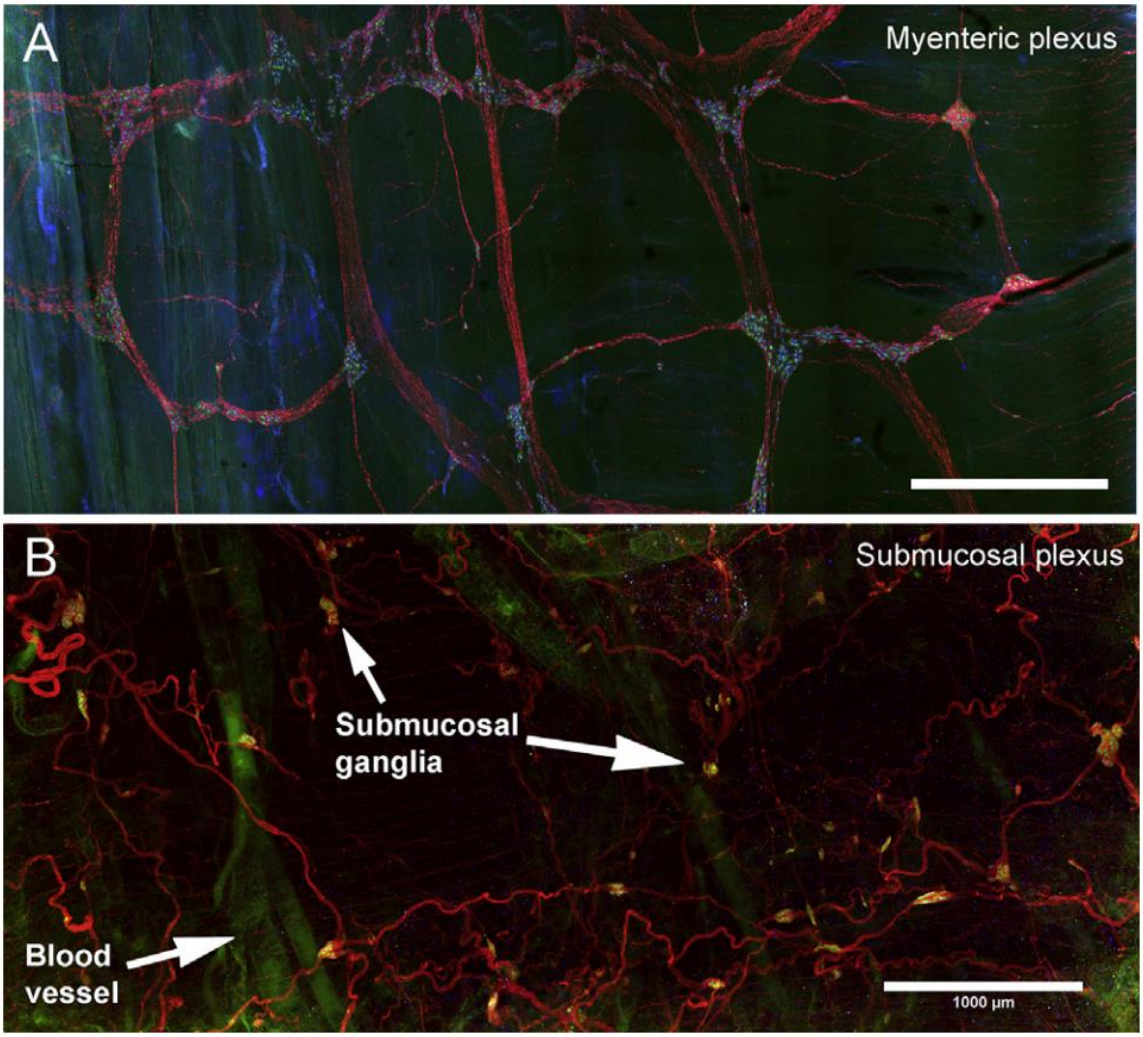

Supplementary Figure 6.5
Large (5.5 x 2.5 mm^2) confocal images. **(A, B)** Flattened Z-stacks of human colon myenteric **(A)** and submucosal plexus **(B)** stained with HuC/D (*green*), PHOX2B (*blue*), and S100β (*red*) antibodies were acquired with 10x objective and stitched. Scale bar: 1000 µm.

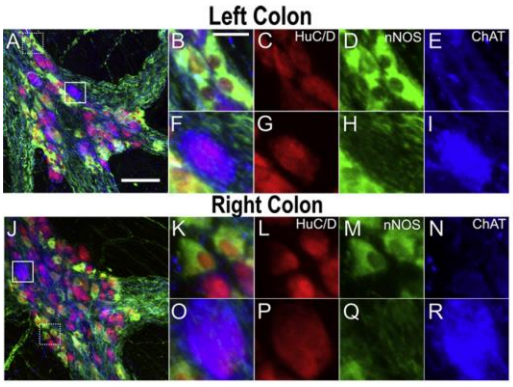

S **Diameter of Neuronal Subtypes**

Diameter of neuron subtypes	Left Colon	Right Colon	P value (Left vs Right Colon)	Left and Right Colon Combined	P value (nNOS+/ChAT- vs ChAT+/nNOS-)
Diameter of nNOS+/CHAT- neurons (µm)	21.7 +/- 1.1	22 +/- 0.76	0.83	21.9 +/- 0.6	0.0003
Diameter of CHAT+/nNOS- neurons (µm)	28.9 +/- 1.8	28.8 +/- 2.3	0.99	28.9 +/- 1.3	

Supplementary Figure 6.6: Largest neuron soma diameter

(A, J) Flattened Z-stack, single human myenteric ganglion from left **(A)** or right colon **(J)** stained for HuC/D (*red*), nNOS (*green*), and ChAT *(blue*). **(B–I, K–R)** Higher magnification images. **(B–E)** nNOS+/ChAT– neurons from dotted line boxed region in **(A)**. **(F–I)** ChAT+/nNOS– neuron from solid line boxed region in **(A). (K–N)** nNOS+/ChAT– neurons from dotted line boxed region in **(J)**. **(O–R)** ChAT+/nNOS– neuron from solid line boxed region in **(J)**. **(S)** Longest neuron diameter (N = 240 nNOS+ and 240 ChAT+ neurons **(A, J)**. **(A)** Scale bar: 100 µm. **(B–I, K–R)** Scale bar: 25 µm.

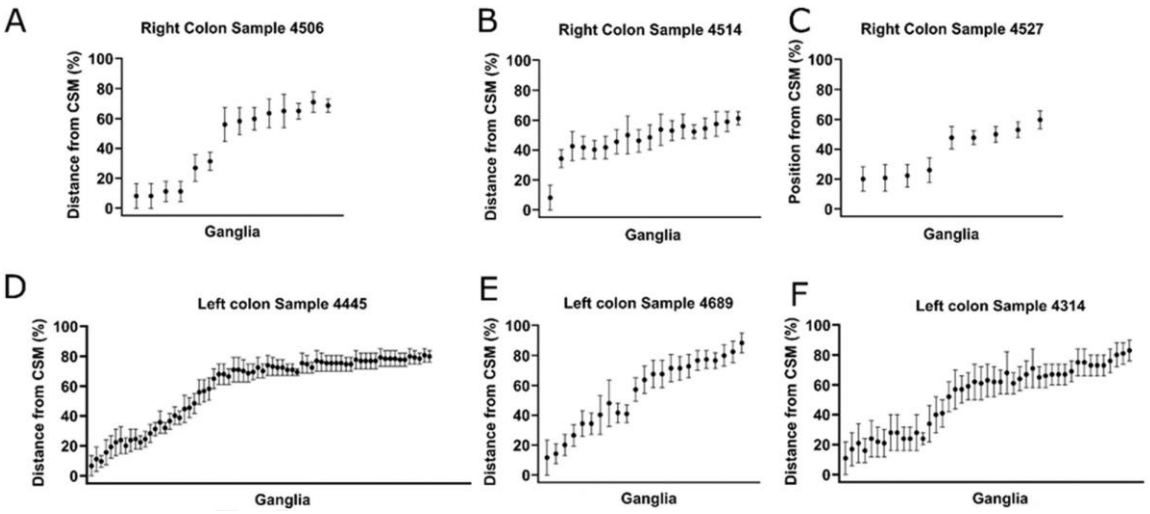

Supplementary Figure 6.7: Quantitative analysis of relative location for ganglia within submucosa

Analysis is based on fullthickness 10X Z-stacks from 6 human colon specimens (**A–C** right colon; **D–F** left colon) stained with antibodies to HuC/D, PHOX2B, and S100b. Because submucosal thickness varied between specimens, we set inner margin of circular smooth muscle (CSM) at 0% and crypt base to 100%. Each dot shows the relative location of a single submucosal ganglion. Bars show positions of all Z-stack slices where submucosal ganglia were present (defined as >2 neuron cell bodies). Area analyzed = 3.6 mm^2 per sample.

Supplementary Table 6.1: Antibodies

Supplemental Table 1

Primary Antibody	Category Number	Species	Source	Concentration	RRID
Hu (C,D)	A21271	Mouse	Invitrogen	1:200	AB_221448
nNOS	AB5380	Rabbit	Millipore	1:100	AB_91824
ChAT	AB144P	Goat	Millipore	1:100	AB_2079751
PGP9.5	AB108986	Rabbit	Abcam	1:50	AB_10891773
Tuj1 (β-Tubulin III)	PRB-435P	Rabbit	Covance	1:2500	AB_291637
C-Kit	AB32363	Rabbit	Abcam	1:100	AB_731513
S100β	AB52642	Rabbit	Abcam	1:100	AB_882426
Peripherin	MAB1527	Mouse	Fisher	1:300	AB_2284441
Iba-1	019-19741	Rabbit	Wako	1:500	AB_839504
Somatostatin	MAB354	Rat	Millipore	1:500	AB_2255365
Calretinin	18-0211	Rabbit	Invitrogen	1:100	AB_86712
Neurofilament 200	N4142	Rabbit	Sigma	1:2000	AB_477272
Neurofilament M	841001	Rabbit	Biolegend	1:1000	AB_2565457
VAChT	139 103	Rabbit	Synaptic Systems	1:1000	AB_887864
PHOX2B	AF4940	Goat	R&D Systems	1:200	AB_10889846
Sox10	AB5727	Rabbit	Millipore	1:50	AB_2195375

Secondary Antibody	Category Number	Species	Source	Concentration	RRID
Goat Alexa Fluor- 647	A21447	Donkey	Invitrogen	1:400	AB_141844
Goat Alexa Fluor- 594	A11058	Donkey	Invitrogen	1:400	AB_142540
Goat Alexa Fluor- 488	A11055	Donkey	Thermo Fisher Scientific	1:400	AB_2534102
Mouse Alexa Fluor- 647	A31571	Donkey	Invitrogen	1:400	AB_162542
Mouse Alexa Fluor- 594	A21203	Donkey	Invitrogen	1:400	AB_141633
Mouse Alexa Fluor- 488	A21202	Donkey	Invitrogen	1:400	AB_141607
Rabbit Alexa Fluor- 647	A31573	Donkey	Invitrogen	1:400	AB_2536183
Rabbit Alexa Fluor- 594	A21207	Donkey	Invitrogen	1:400	AB_141637
Rabbit Alexa Fluor- 488	A21206	Donkey	Thermo Fisher Scientific	1:400	AB_2535792
Rat Alexa Fluor- 594	A21209	Donkey	Thermo Fisher Scientific	1:400	AB_2535795

Supplementary Table 6.2: Antibodies that did not work well with our tissue clearing 3-dimensional imaging method

Supplemental Table 2: Antibodies that **DID NOT** work well with our tissue clearing and 3-dimensional imaging method. These antibodies either gave no signal or too much background staining in our limited testing.

Primary Antibody	Catalog Number	Species	Source	Dilution	RRID
SOX10 (N-20)	sc-17342	Goat	Santa Cruz	1:100	AB_2195374
SOX10	MAB2864	Mouse	R&D Systems	1:100	AB_2195180
TuJ1 (β-Tubulin III)	TUJ89867985	Chicken	Aves Labs	1:500	
S100β	ab52642	Rabbit	Abcam	1:100	AB_882426
cKIT	ab32363	Rabbit	Abcam	1:100	AB_731513
nNOS	AB 5380	Rabbit	Chemicon/ Millipore	1:500	AB_91824
Calretinin	AB1550	Goat	Chemicon	1:500	AB_90764
Alpha-SMA	M0851	Mouse	Dako	1:500	AB_2313736
Tyrosine hydroxylase	AB152	Sheep	Chemicon	1:500	AB_390204
CGRP	ab36001	Goat	Abcam	1:500	AB_725807
Substance P	AB1566	Rabbit	Sigma	1:5000	AB_11213407
Vimentin	V6630	Mouse	Sigma	1:1000	AB_477627
Human GFRα-3	AF670	Goat	Novus Biological	1:200	AB_2110447
Parvalbumin	235	Mouse	SWANT	1:1000	AB_10000343

Supplementary Table 6.3: Demographics

Condition indicates the medical problem that led to colon resection.

Sample Number	Sex	Age	Colon region	Condition
Adult:				
4514	Male	77	Right	Polyp
4656	Male	70	Right	Adenocarcinoma
4504	Male	63	Right	Colon Cancer
4527	Male	63	Right	Crohn's disease
4755	Male	55	Right	Polyp
4506	Male	51	Right	Cancer
4790	Male	51	Right	Colonic mass
4689	Female	80	Left	Colovaginal fistula
4585	Female	63	Left	Sigmoid mass
4443	Female	60	Left	Diverticulitis
4566	Male	59	Left	Sigmoid mass
4557	Male	37	Left	Sessile polyp
4454	Male	36	Left	Diverticulitis
4445	Male	28	Left	Diverticulitis
Pediatric:				
1255	Male	2 months	Recto-sigmoid	Hirschsprung disease
7962	Female	7 months	Recto-sigmoid	Hirschsprung disease
OTHER TISSUES				
HPAP026	Male	24	Jejunum	Organ donor
ICRH117	Male	1	Pancreas	Organ donor

Supplementary Table 6.4: Myenteric neuron subtypes in human colon based on 3359 cells counted in full confocal Z-stacks after ChAT, nNOS and HuC/D antibody staining

Neuron Subtypes	Left Colon	Right Colon	P value (Left vs Right Colon)	Left and Right Colon Combined
nNOS+/ChAT-	51.4 +/- 4.0	52.7 +/- 3.9	0.953	52.0 +/- 2.6
ChAT+/nNOS-	19.5 +/- 2.0	15.2 +/- 1.3	0.149	17.3 +/- 1.4
nNOS+/ChAT+	2.6 +/- 0.5	3.7 +/- 0.3	0.116	3.2 +/- 0.3
nNOS-/ChAT-	26.5 +/- 3.6	28.5 +/- 4.5	0.656	27.5 +/- 2.7

ChAT staining for many neurons was weak and background ChAT staining was higher than desirable. By systematic analysis of human colon stained with antibodies to VAChT, ChAT and HuC/D (N = 1902 cells) we scored 1.62-fold more neurons (HuC/D+) as VAChT+ than ChAT+. Most VAChT+ cells had identifiable but weak ChAT+ staining (See Figure 5O-Q). We consider these cells to be cholinergic neurons. Data in Figure 5I reflect the 1.62-fold adjustment to numbers in the table above. The math is as follows:

Corrected “Cholinergic/nNOS-” = ChAT+/nNOS- x 1.62
Corrected “nNOS+/Cholinergic = ChAT+/nNOS+ x 1.62
Corrected ”nNOS-/Non-Cholinergic” = ChAT-/nNOS- minus reclassified nNOS- neurons
Corrected “nNOS+/Non-Cholinergic” = ChAT-/nNOS+ minus reclassified nNOS+ neurons

Myenteric neuron subtypes in human colon. Numbers are corrected for systematic undercounting when ChAT antibody is used alone. This table is reproduced in Figure 6J.

Neuron Subtypes	Left Colon	Right Colon	P value (Left vs Right Colon)	Left and Right Colon Combined
Non-Cholinergic nNOS+	50.7 +/- 3.2	50.4 +/- 3.9	0.953	50.5 +/- 2.2
Cholinergic nNOS-	31.6 +/- 3.1	24.6 +/- 2.1	0.149	28.1+/- 2.1
Cholinergic nNOS+	4.2 +/- 0.8	6.0 +/- 0.5	0.116	5.1 +/- 1.3
Non-Cholinergic nNOS-	13.5 +/- 3.0	19.1 +/- 4.5	0.656	16.3 +/- 1.6

Supplemental Table 6.5. Previously published data about human colon myenteric neuron subtypes

Neuron subtype percentages		Demographics and colon region	Comment	Ref
ChAT +/nNOS- nNOS +/ChAT- Neither nNOS nor ChAT ChAT+/nNOS+ nNOS/VIP nNOS without VIP	52% 43% 4% 6% 19% 29%	-Ascending colon -5 male/8 female -Cancer surgery -Median age 76 years -Age range 55-86 years --Excluded IBS and slow transit constipation	Myenteric neurons Manuscript also includes data for DiI labeled circular muscle projecting neuron subtypes	36
ChAT+/nNOS- nNOS+ /ChAT- ChAT+/nNOS+ Neither nNOS nor ChAT	48% 43% 4% 5%	-3 transverse colon -5 descending colon -2 sigmoid colon -5 male/5 female -Cancer surgery -Median age 68 years -Age range 52-83 years	Myenteric neurons triple labeled for nNOS/ChAT and HuC/D	37
Control ChAT+/nNOS- (ascending) (transverse) (descending) nNOS+/ChAT- (ascending) (transverse) (descending) ChAT+/nNOS+ ChAT-/nNOS- Slow transit constipation ChAT+/nNOS- (ascending) (transverse) (descending) nNOS+/ChAT- (ascending) (transverse) (descending) ChAT+/nNOS+ ChAT-/nNOS-	 41% 51% 48% 51% 43% 44% 3-4% 2-4% 36% 38 % 42% 54% 52% 49% 3-5% 4-5%	-Control Colon cancer surgery 7 male/5 female Median age 64 years Age range 49-82 years -Colon resection for slow transit constipation (4 females) -Median age 37 years -Ascending, transverse and descending colon	Analysis of ENS in slow transit constipation Triple labeling ChAT/nNOS/HuC/D	38

Neuron subtype percentages	Demographics and colon region	Comment	Ref
ChAT+ 71% nNOS+ 42% -1.3 HuC/D+ neurons/mm/10 years Starting at about 10 neuron/mm for youngest -1.1 ChAT+ neurons/mm/10 years Starting at about 7 neurons/mm for youngest -No change in nNOS+ neurons relate to age	-Descending and sigmoid colon -9 male/7 female -Cancer surgery -33 to 99 years old	ChAT+ myenteric neurons density declined by >50% over interval evaluated, but no change in nNOS+ neuron density Double labeling nNOS/HuC/D or ChAT/HuC/D	66
Neuron counts not reported ChAT immunoreactive area is about 50% lower in diabetic than in control nNOS immunoreactive area is about 80% lower in diabetic than in control	-Colon region not specified -24 male/18 female control -11 male/11 female diabetic -Cancer or polyp surgery -Mean age 62 to 65 years -Age distribution not clear. SEM (?) ~ 2 for ages	9% of control and 18% of diabetics had constipation	67
Distal colon, < 1 year old NADPH diaphorase+ 39% Proximal and distal colon, > 70 year old NADPH diaphorase+ 25%	-3 male/1 female (4-12 months) -1 male/3 female (48-58 years) -4 male/7 female (70-95 years) -Cancer, diverticulitis, anal atresia, polyp anus praeter		
Control: ChAT+ 35% Ulcerative colitis ChAT+ 33%	-2 male/6 female control -Control age 43 to 82 years -3 male/7 female UC	Comparing control to ulcerative colitis (UC) ENS -NSE to label neurons	69

Neuron subtype percentages		Demographics and colon region	Comment	Ref
		-UC age 22 to 68 years		
Descending colon ChAT+ nNOS+ ChAT+/nNOS+ ChAT-/nNOS- Rectum ChAT+ nNOS+ ChAT+/nNOS+ ChAT-/nNOS-	 56% 43% 9% 7% 55% 48% 10% 6%	-8 males/7 females -Cancer surgery -Rectum or descending colon -Median age 63 years -Age range 51-86 years	Whole mount immunohistochemistry	39
Notes: DiI = (1,1¢- didodecyl 3,3,3¢,3¢-indocarbocyanine perchlorate), a lipophilic dye for membrane tracing. IBS = Irritable bowel syndrome NADPH-diaphorase stains nitric oxide producing neurons				

Supplementary Videos 1-9 can be viewed at https://www.gastrojournal.org/article/S0016-5085(20)30262-6/fulltext#supplementaryMaterial .

6.10 References

1. Furness JB, Callaghan BP, Rivera LR, et al. The enteric nervous system and gastrointestinal innervation: integrated local and central control. Adv Exp Med Biol 2014; 817:39–71.
2. Furness JB. The enteric nervous system and neurogastroenterology. Nat Rev Gastroenterol Hepatol 2012; 9:286–294.
3. Schneider S, Wright CM, Heuckeroth RO. Unexpected roles for the second brain: enteric nervous system as master regulator of bowel function. Annu Rev Physiol 2019;81:235–259.
4. Zeisel A, Hochgerner H, Lonnerberg P, et al. Molecular architecture of the mouse nervous system. Cell 2018; 174:999–1014 e22.
5. Lake JI, Heuckeroth RO. Enteric nervous system development: migration, differentiation, and disease. Am J Physiol Gastrointest Liver Physiol 2013;305:G1–G24.
6. Sasselli V, Pachnis V, Burns AJ. The enteric nervous system. Dev Biol 2012;366:64–73.
7. Knowles CH, Veress B, Kapur RP, et al. Quantitation of cellular components of the enteric nervous system in the normal human gastrointestinal tract—report on behalf of the Gastro 2009 International Working Group. Neurogastroenterol Motil 2011;23:115–124.
8. Knowles CH, De Giorgio R, Kapur RP, et al. The London Classification of gastrointestinal neuromuscular pathology: report on behalf of the Gastro 2009 International Working Group. Gut 2010;59:882–887.
9. Swaminathan M, Kapur RP. Counting myenteric ganglion cells in histologic sections: an empirical approach. Hum Pathol 2010;41:1097–1108.
10. Liu YA, Chung YC, Pan ST, et al. 3-D imaging, illustration, and quantitation of enteric glial network in transparent human colon mucosa. Neurogastroenterol Motil 2013;25:e324–e338.
11. Fu YY, Peng SJ, Lin HY, et al. 3-D imaging and illustration of mouse intestinal neurovascular complex. Am J Physiol Gastrointest Liver Physiol 2013;304:G1–G11.

12. Liu YA, Chen Y, Chiang AS, et al. Optical clearing improves the imaging depth and signal-to-noise ratio for digital analysis and three-dimensional projection of the human enteric nervous system. Neurogastroenterol Motil 2011;23:e446–e457.
13. Nemeth L, Yoneda A, Kader M, et al. Three-dimensional morphology of gut innervation in total intestinal aganglionosis using whole-mount preparation. J Pediatr Surg 2001;36:291–295.
14. Krammer HJ, Karahan ST, Sigge W, et al. Immunohistochemistry of markers of the enteric nervous system in whole-mount preparations of the human colon. Eur J Pediatr Surg 1994;4:274–278.
15. Wattchow DA, Porter AJ, Brookes SJ, et al. The polarity of neurochemically defined myenteric neurons in the human colon. Gastroenterology 1997;113:497–506.
16. Krammer HJ, Karahan ST, Rumpel E, et al. Immunohistochemical visualization of the enteric nervous system using antibodies against protein gene product (PGP) 9.5. Anat Anz 1993;175:321–325.
17. Wedel T, Roblick U, Gleiss J, et al. Organization of the enteric nervous system in the human colon demonstrated by wholemount immunohistochemistry with special reference to the submucous plexus. Ann Anat 1999;181:327–337.
18. Keller J, Bassotti G, Clarke J, et al. Expert consensus document: advances in the diagnosis and classification of gastric and intestinal motility disorders. Nat Rev Gastroenterol Hepatol 2018;15:291–308.
19. Furness JB. Integrated neural and endocrine control of gastrointestinal function. Adv Exp Med Biol 2016; 891:159–173.
20. Chambers JD, Bornstein JC, Thomas EA. Insights into mechanisms of intestinal segmentation in guinea pigs: a combined computational modeling and in vitro study. Am J Physiol Gastrointest Liver Physiol 2008;295:G534–G541.
21. Blair PJ, Rhee PL, Sanders KM, et al. The significance of interstitial cells in neurogastroenterology. J Neurogastroenterol Motil 2014;20:294–317.

22. Heuckeroth RO. Hirschsprung disease-integrating basic science and clinical medicine to improve outcomes. Nat Rev Gastroenterol Hepatol 2018;15:152–167.
23. McKeown SJ, Stamp L, Hao MM, et al. Hirschsprung disease: a developmental disorder of the enteric nervous system. Wiley Interdiscip Rev Dev Biol 2013; 2:113129.
24. Bredenoord AJ, Fox M, Kahrilas PJ, et al. Chicago classification criteria of esophageal motility disorders defined in high resolution esophageal pressure topography. Neurogastroenterol Motil 2012;24(Suppl 1):57-65.
25. Nguyen LA, Snape WJ Jr. Clinical presentation and pathophysiology of gastroparesis. Gastroenterol Clin North Am 2015;44:21–30.
26. Di Nardo G, Di Lorenzo C, Lauro A, et al. Chronic intestinal pseudo-obstruction in children and adults: diagnosis and therapeutic options. Neurogastroenterol Motil 2017;29.
27. Kilkenny C, Browne WJ, Cuthill IC, et al. Improving bioscience research reporting: the ARRIVE guidelines for reporting animal research. Osteoarthritis Cartilage 2012; 20:256–260.
28. Uesaka T, Jain S, Yonemura S, et al. Conditional ablation of GFRalpha1 in postmigratory enteric neurons triggers unconventional neuronal death in the colon and causes a Hirschsprung's disease phenotype. Development 2007; 134:2171–2181.
29. Southard JH, Belzer FO. Organ preservation. Annu Rev Med 1995;46:235–247.
30. Dent JA, Polson AG, Klymkowsky MW. A whole-mount immunocytochemical analysis of the expression of the intermediate filament protein vimentin in Xenopus. Development 1989;105:61–74.
31. Dodt HU, Leischner U, Schierloh A, et al. Ultramicroscopy: three-dimensional visualization of neuronal networks in the whole mouse brain. Nat Methods 2007; 4:331–336.
32. Workman MJ, Mahe MM, Trisno S, et al. Engineered human pluripotent-stem-cell-derived intestinal tissues with a functional enteric nervous system. Nat Med 2017; 23:49–59.
33. Hama H, Kurokawa H, Kawano H, et al. Scale: a chemical approach for fluorescence imaging and reconstruction of transparent mouse brain. Nat Neurosci 2011; 14:1481–1488.

34. Belle M, Godefroy D, Couly G, et al. Tridimensional visualization and analysis of early human development. Cell 2017;169:161–173 e12.
35. Erturk A, Mauch CP, Hellal F, et al. Three-dimensional imaging of the unsectioned adult spinal cord to assess axon regeneration and glial responses after injury. Nat Med 2011;18:166–171.
36. Porter AJ, Wattchow DA, Brookes SJ, et al. The neurochemical coding and projections of circular muscle motor neurons in the human colon. Gastroenterology 1997; 113:1916–1923.
37. Murphy EM, Defontgalland D, Costa M, et al. Quantification of subclasses of human colonic myenteric neurons by immunoreactivity to Hu, choline acetyltransferase and nitric oxide synthase. Neurogastroenterol Motil 2007;19:126–134.
38. Wattchow D, Brookes S, Murphy E, et al. Regional variation in the neurochemical coding of the myenteric plexus of the human colon and changes in patients with slow transit constipation. Neurogastroenterol Motil 2008; 20:1298–1305.
39. Ng KS, Montes-Adrian NA, Mahns DA, et al. Quantification and neurochemical coding of the myenteric plexus in humans: no regional variation between the distal colon and rectum. Neurogastroenterol Motil 2018; 30(3).
40. Ibba-Manneschi L, Martini M, Zecchi-Orlandini S, et al. Structural organization of enteric nervous system in human colon. Histol Histopathol 1995;10:17–25.
41. Helander HF, Fandriks L. Surface area of the digestive tract—revisited. Scand J Gastroenterol 2014;49:681–689.
42. Farrugia G. Histologic changes in diabetic gastroparesis. Gastroenterol Clin North Am 2015;44:31–38.
43. Costa DVS, Bon-Frauches AC, Silva A, et al. 5-Fluorouracil induces enteric neuron death and glial activation during intestinal mucositis via a S100BRAGE-NFkappaB-dependent Pathway. Sci Rep 2019;9:665.

44. Macchioni L, Petricciuolo M, Davidescu M, et al. Palmitate lipotoxicity in enteric glial cells: lipid remodeling and mitochondrial ROS are responsible for cyt c release outside mitochondria. Biochim Biophys Acta Mol Cell Biol Lipids 2018;1863:895–908.
45. Stojanovska V, Sakkal S, Nurgali K. Platinum-based chemotherapy: gastrointestinal immunomodulation and enteric nervous system toxicity. Am J Physiol Gastrointest Liver Physiol 2015;308:G223–G232.
46. Chalazonitis A, Rao M. Enteric nervous system manifestations of neurodegenerative disease. Brain Res 2018; 1693:207–213.
47. Del Tredici K, Braak H. Review: sporadic Parkinson's disease: development and distribution of alphasynuclein pathology. Neuropathol Appl Neurobiol 2016; 42:33–50.
48. Yarandi SS, Srinivasan S. Diabetic gastrointestinal motility disorders and the role of enteric nervous system: current status and future directions. Neurogastroenterol Motil 2014;26:611–624.
49. Azpiroz F, Malagelada C. Diabetic neuropathy in the gut: pathogenesis and diagnosis. Diabetologia 2016;59:404–408.
50. Mawe GM. Colitis-induced neuroplasticity disrupts motility in the inflamed and post-inflamed colon. J Clin Invest 2015;125:949–955.
51. White JP, Xiong S, Malvin NP, et al. Intestinal dysmotility syndromes following systemic infection by flaviviruses. Cell 2018;175:1198–1212 e12.
52. Margolis KG, Gershon MD. Enteric Neuronal regulation of intestinal inflammation. Trends Neurosci 2016;39:614–624.
53. Zhou Y, Yang J, Watkins DJ, et al. Enteric nervous system abnormalities are present in human necrotizing enterocolitis: potential neurotransplantation therapy. Stem Cell Res Ther 2013;4:157.

54. Klem F, Wadhwa A, Prokop LJ, et al. Prevalence, risk factors, and outcomes of irritable bowel syndrome after infectious enteritis: a systematic review and meta-analysis. Gastroenterology 2017;152:1042–1054 e1.
55. Young HM, Stamp LA, McKeown SJ. ENS development research since 1983: great strides but many remaining challenges. Adv Exp Med Biol 2016;891:53–62.
56. Hoff S, Zeller F, von Weyhern CW, et al. Quantitative assessment of glial cells in the human and guinea pig enteric nervous system with an anti-Sox8/9/10 antibody. J Comp Neurol 2008;509:356–371.
57. Olsson C, Holmgren S. Autonomic control of gut motility: a comparative view. Auton Neurosci 2011;165:80–101.
58. Christensen J, Stiles MJ, Rick GA, et al. Comparative anatomy of the myenteric plexus of the distal colon in eight mammals. Gastroenterology 1984;86:706–713.
59. Rao M, Nelms BD, Dong L, et al. Enteric glia express proteolipid protein 1 and are a transcriptionally unique population of glia in the mammalian nervous system. Glia 2015;63:2040–2057.
60. Boesmans W, Lasrado R, Vanden Berghe P, et al. Heterogeneity and phenotypic plasticity of glial cells in the mammalian enteric nervous system. Glia 2015;63:229–241.
61. Bassotti G, Battaglia E, Bellone G, et al. Interstitial cells of Cajal, enteric nerves, and glial cells in colonic diverticular disease. J Clin Pathol 2005;58:973–977.
62. Corpening JC, Cantrell VA, Deal KK, et al. A histone2BCerulean BAC transgene identifies differential expression of Phox2b in migrating enteric neural crest derivatives and enteric glia. Dev Dyn 2008;237:1119–1132.
63. Knowles CH, De Giorgio R, Kapur RP, et al. Gastrointestinal neuromuscular pathology: guidelines for histological techniques and reporting on behalf of the Gastro 2009 International Working Group. Acta Neuropathol 2009;118:271–301.

64. Uranga-Ocio JA, Bastus-Diez S, Delkader-Palacios D, et al. Enteric neuropathy associated to diabetes mellitus. Rev Esp Enferm Dig 2015;107:366–373.
65. Rivera LR, Poole DP, Thacker M, et al. The involvement of nitric oxide synthase neurons in enteric neuropathies. Neurogastroenterol Motil 2011;23:980–988.
66. Bernard CE, Gibbons SJ, Gomez-Pinilla PJ, et al. Effect of age on the enteric nervous system of the human colon. Neurogastroenterol Motil 2009;21:746-e46.
67. Chandrasekharan B, Anitha M, Blatt R, et al. Colonic motor dysfunction in human diabetes is associated with enteric neuronal loss and increased oxidative stress. Neurogastroenterol Motil 2011;23:131–138, e26.
68. Hetz S, Acikgoez A, Moll C, et al. Age-related gene expression analysis in enteric ganglia of human colon after laser microdissection. Front Aging Neurosci 2014; 6:276.
69. Neunlist M, Aubert P, Toquet C, et al. Changes in chemical coding of myenteric neurones in ulcerative colitis. Gut 2003;52:84–90.
70. Avetisyan M, Schill EM, Heuckeroth RO. Building a second brain in the bowel. J Clin Invest 2015;125:899–907.
71. Neunlist M, Schemann M. Nutrient-induced changes in the phenotype and function of the enteric nervous system. J Physiol 2014;592:2959–2965.
72. Fu M, Landreville S, Agapova OA, et al. Retinoblastoma protein prevents enteric nervous system defects and intestinal pseudo-obstruction. J Clin Invest 2013; 123:5152–5164.
73. De Quelen F, Chevalier J, Rolli-Derkinderen M, et al. n-3 polyunsaturated fatty acids in the maternal diet modify the postnatal development of nervous regulation of intestinal permeability in piglets. J Physiol 2011;589:4341–4352.